

# THIS WEEK

## EDITORIALS

**TRANSPLANTS** Presumed consent for organs could show the way **p.6**

**WORLD VIEW** Don't lose big-data systems for biology in the cloud **p.7**



**ORIGINS** Fossil shows how modern starfish can spin a tale **p.9**

## More than hot air

*US President Barack Obama gave a fine speech on global warming, but now he must deliver on regulations for coal power and greater fuel economy.*

Before a major speech on the subject last week, it had been two years since US President Barack Obama last waded into the complex arena of energy and climate change. His emphasis then was on an 'all-of-the-above' approach that put oil and natural gas on an even keel with alternative energy sources.

But on 25 June, citing "the overwhelming judgement of science", as well as the country's founding fathers, who charged political leaders "to make decisions with an eye on a longer horizon than the arc of our own political careers", Obama broke a long silence on global warming.

The centrepiece of the president's speech was a pledge to regulate carbon emissions from power plants new and old. The power sector produces some 40% of total US emissions, and administration officials have long said that they would fill the regulatory void if Congress failed to act. Although Obama did not make any specific promises last week, he did lay out a schedule and put the full weight of the White House behind these efforts, which is what they need and deserve.

These commitments are overdue. The US Environmental Protection Agency (EPA) has already proposed a regulation that would essentially ban the construction of new power plants unless they are equipped to capture and sequester carbon. That rule has languished for over a year, and under the new schedule will not be finished for almost another 12 months. Many of Obama's most ardent supporters, as well as his critics, had long assumed that the EPA was already working on regulations for existing power plants. Apparently it wasn't — at least, not in any serious way. Obama has now ordered the agency to issue a regulatory proposal next June and to finalize the rules a year after that, just in time for a major United Nations climate summit in Paris.

Obama's 'climate action plan' contained a variety of other initiatives, including calls for a new round of appliance standards, fuel-economy regulations on heavy-duty vehicles and various efforts intended to prepare the country for a warmer climate. Much of the plan may seem old hat, but that is to the president's credit. Over the years, his administration has cobbled together a broad set of policies that — along with a shift from coal to natural gas and renewables for electricity generation, as well as several years of economic woe — have markedly reduced greenhouse-gas emissions, which registered almost 7% below 2005 levels in 2011.

But the United States still has a long way to go if it is to fulfil its international commitment — a 17% reduction by 2020 — and pursue deep emissions reductions as the century wears on. Having secured historic fuel-economy regulations across the vehicle sector, Obama now has the opportunity to lay down an aggressive set of regulations for the power sector. It will be up to the EPA, working with states, businesses and environmentalists, to determine how to structure the regulations. Rather than focusing purely on technological upgrades such as requiring more efficient boilers, the EPA may be able to improve on broader incentives that would require deeper reductions while, for example,

allowing utilities to work with customers to curb electricity demand.

Obama also hinted that he could deny the proposed Keystone pipeline from Alberta to the United States — if the state department's ongoing analysis determines that it would significantly exacerbate greenhouse-gas emissions. In truth, oil from the tar sands is hardly the dirtiest resource from a climate perspective, but it is not the cleanest either. And even a cursory review of the local environmental impacts suggests plenty of reasons to shift investments towards cleaner alternatives.

**"Obama urged politicians to live up to their obligations as caretakers of the future."**

Regulating greenhouse-gas emissions from the power sector is by far the biggest opportunity, but if the administration feels it can justify a symbolic decision against Keystone and still move a workable and effective regulatory agenda forwards, then so be it.

Whatever form the regulations take, and however ingeniously the administration can work around political opposition, the full scale of the climate challenge is more than any president could accomplish independently of Congress. Obama urged politicians and public servants to rise above the political fray and think beyond the next election, to live up to their obligations not just as "custodians of the present, but as caretakers of the future".

Obama is just six months into his second term, but these are the words of a president who no longer needs to worry about re-election. Obama is now thinking about his place in history. Although his broader climate agenda has been stymied in Congress, Obama has laid out a solid path forward. Now he must follow it through. ■

## Russian roulette

*Reforms without consultation will destroy the Russian Academy of Sciences.*

The Russian Academy of Sciences has seen and survived its share of political turmoil in its nearly 300-year history. Yet recent decades have not been kind: the academy has been in a state of decline since the fall of the Soviet Union in 1991.

When funding, generous in Soviet times, declined drastically in the 1990s, too many of the academy's ageing — and increasingly unproductive — members became preoccupied with securing personal privileges. Last year, an internal assessment of the academy's science managed to conclude that each of the academy's 400 institutes performs world-class research; typically, no external scientists were consulted. In fact, by all measures, only a small fraction of academy institutes can be

considered internationally competitive. Many produce only poor science — and outsiders have criticized the organization again and again for refusing to accept the dire reality of its situation.

The problems have not gone unnoticed by the Russian government. Tensions between the science ministry and the academy have risen in recent years, as the government has become increasingly worried about Russian science's lack of competitiveness. The stand-off approached a dramatic climax last week, when a bill was hastily introduced to the Russian parliament that, if approved, would effectively liquidate the academy in its present form. The academy is ill, of that there is no doubt. But the proposed cure would kill it off. Worse, the bill is marked with the worrisome signs of autocracy that characterize Russian President Vladimir Putin's current regime.

The planned coup would merge the Academy of Sciences with Russia's minor medical and agricultural academies, and would provide all members of the united body with equal status as academicians. The present academy would lose the right to manage its property and, more importantly, would cease to operate research institutes of its own. Existing institutes would be evaluated, and those deemed competitive would in future be run by a new government agency on behalf of the academy. Putin hoped to turn the proposal into law without giving the academy time to respond, although the parliament's final vote has now been postponed to October.

The proposal has caused an outcry from Russian scientists. Researchers have laid down flowers near the academy's headquarters on Leninski Prospect in Moscow in a symbolic funeral for the institution, which was founded in 1724 by Russian Emperor Peter the Great.

However, it is not the bill's aim and content that are most troubling, but the hasty and profoundly undemocratic manner in which it was

conceived. Vladimir Fortov, the academy's newly elected president and a reformer who has announced a number of measures to rejuvenate and restructure the organization (see *Nature* **497**, 420–421, 2013) was not consulted. Neither were the institution's scientific workforce and the trade unions.

Some Western-orientated Russian scientists acknowledge that a number of the proposed changes could be beneficial. In effect, the reform would create a flexible learned body similar to scientific academies in the United States and much of Europe, whose main duties are to provide the government with scientific advice on questions of societal relevance. The task of organizing and funding the research itself would be passed on to a new agency — similar to Germany's Max Planck Society — that, if properly run, could provide basic science in Russia with much-needed vision and impetus.

But such sweeping changes require more time and preparation than Putin seems willing to grant. An organization that employs more than 45,000 scientists cannot be successfully transformed overnight. Russian scientists have a right to be heard and consulted, and they should have been. For the sake of Russian science, members of the parliament should refrain from hastily passing an ill-prepared bill; they should wait until at least the basic technicalities of what is indeed a much-needed reform have been thoroughly worked out and made public. The government and the academy should set up an expert committee of respected scientists and give it at least 12 months to plan the transition. If the result is to be a system that rewards excellence and can give solid advice to those in power, then Russia can wait one more year. ■

***“The academy is ill, of that there is no doubt. But the proposed cure would kill it off.”***

# Presumed consent

*More must be done to boost tissue donation for transplantation and research.*

Despite decades of scientific progress in the field of organ transplantation, there remains a crippling shortage of suitable tissue from willing donors. Actually, make that donors who have made it clear that they would be willing. Surveys in Wales, for example, have shown that although some two-thirds of people asked say that they would be willing to see their heart, liver, lungs and other tissues reused after their death, only half of those people go as far as registering their consent on the organ-donation register. The resulting shortage, according to Mark Drakeford, the Welsh health minister, means that one person dies in his country almost every week while waiting for a donor.

As *Nature* went to press, the Welsh Assembly was voting on a proposed change in the rules. It would see Wales reverse the donation dynamic — on death, an adult's organs will automatically be considered for transplantation, unless that person previously made it clear this was against their wishes. A new register would record the names of those who do not wish to be classed as donors.

If passed, the 'presumed consent' scheme would come into force in 2015. Although the family of someone who died without registering to opt-out would have no legal right to block use of that person's body parts, in practice officials say they would be given the opportunity to show that their loved one would not have wanted to donate. This 'soft' scheme is similar to that in operation in Spain. Austria takes a stronger line and its 'hard' opt-out means that if someone dies without registering their dissent, then their organs are considered fair game.

The vote comes at a time of increasing scrutiny of the way in which tissue taken during hospital procedures is used in medical and scientific research. Last week, *Nature* told the largely unexplored story

of the WI-38 cell line, derived from a fetus aborted from a woman in Sweden (see *Nature* **498**, 422–426; 2013). And Rebecca Skloot's book *The Immortal Life of Henrietta Lacks* (Crown, 2010), the history of the HeLa cell line and the ethical issues it raises, continues to sell. Consent — in medicine and science — has become a key issue.

It also comes at a time when there remains a critical shortage of some tissues for research — the brains of children for example, which are needed for work on autism and schizophrenia. Advocates and patient groups are already working on ways to confront the biggest obstacle — the emotionally fraught conversation with devastated parents who have lost a child (see *Nature* **478**, 427; 2011). By talking to the parents of children with autism about the benefits of donation, for example, they can increase the chances of gaining consent should the worst happen.

Presumed consent, with the burden placed on people and families to opt-out of tissue donation, seems a step too far at present for material needed for scientific research. But are the issues involved that different from those surrounding transplantation? Both promise better health and new life from the waste of death.

One important motivation when it comes to organ donation is that there is little alternative. If someone with a failing organ today does not find a willing donor, they may not see tomorrow. That may not always be the case. As a News Feature on page 20 investigates, researchers are using tissue-engineering techniques to build artificial hearts in the laboratory. A Letter published online this week describes the use of induced pluripotent stem cells to grow human liver tissue in mice (T. Takebe *et al.* *Nature* <http://dx.doi.org/10.1038/nature12271>; 2013). And, last month, Japan announced plans to relax a ban on experiments that mix human and animal cells, which could be used to generate transplantable human organs in pigs.

For now, such research is of little comfort to those waiting for someone else to die. The planned change in Wales goes some way towards making the bodies of the deceased more widely available. And it shows that, given the chance, the kindness of strangers, as well as their consent, can be presumed. ■

➔ **NATURE.COM**  
To comment online,  
click on Editorials at:  
[go.nature.com/xhunqg](http://go.nature.com/xhunqg)





## Biology must develop its own big-data systems

*Too many data-management projects fail because they ignore the changing nature of life-sciences data, argues John Boyle.*

The last week of April was designated Big Data Week. But in modern biology, every week is big-data week: life-sciences research now routinely churns out more information than scientists can analyse without help. That help increasingly comes in the form of expensive data-management systems, but these are hard to design and most are even harder to use. As a result, a long line of data-management projects in the life sciences — many of which I have been involved with — have failed.

The size, complexity and heterogeneity of the data generated in labs across the world can only increase, and the introduction of cloud computing will encourage the same mistakes. Just a stone's throw from where I work, at least three computer companies are already touting cloud-based data-management systems for the life sciences. We need to find ways to manage and integrate data to make discoveries in fields such as genomics, and we need to do this quickly.

At their most basic, data-management systems allow people to organize and share information. In the case of small amounts of uniform data from a single experiment, this can be done with a spreadsheet. But with multiple experiments that produce diverse data — on gene expression, metabolites and protein abundance, for example — we need something more sophisticated.

An ideal data-management system would store data, provide common and secure access methods, and allow for linking, annotation and a way to query and retrieve information. It would be able to cope with data in different locations — on remote servers, on desktops, in a database or spread across different machines — and formats, including spreadsheets, badly named files, blogs or even scanned-in notebooks.

That ideal system does not exist. Most academic organizations have, through trial and error, developed their own in-house systems that work — or just about. The systems have limited functionality and cannot be connected, which makes collaboration difficult. The situation is as unworkable as if every lab in the country had decided to devise its own (poor) document-editing software.

Efforts to introduce overarching data-management systems, to which any and all scientists in a particular field could plug in, have failed for two main reasons. Either they demand that scientists change the format of their data, to allow information to be entered into the system, or they demand that scientists change the way they work, to generate standardized sets of results. The systems are thrust on scientists who are then expected to change, rather than taking the work of scientists as a starting point. It should not be scientists who are required to be flexible; it should be the system that they are being asked to use.

IT SHOULD NOT BE  
THE SCIENTISTS WHO  
ARE REQUIRED TO BE  
**FLEXIBLE;**  
IT SHOULD BE THE  
SYSTEM THAT THEY  
ARE BEING  
**ASKED TO USE.**

These problems are exemplified by the expensive flop that was the US National Cancer Institute's caBIG data-integration project, scrapped last year after almost a decade and tens or even hundreds of millions of dollars. It had admirable goals and seemed workable in theory, but in the end it was too complicated to use. Crucially, caBIG relied on standardized data formats, which called for standardized experiments. Its one-size-fits-all approach fit nearly nobody.

There have been some successes. A widely used system called SRS allows the linking of data held in separate well-structured repositories. And the Biomart project joins up specially designed databases. But these were both fairly bespoke research applications; computer giants Microsoft and IBM are among the commercial firms that have introduced systems that aimed at a wider reach but had little impact.

To be useful to the life-sciences community, a data-management system probably needs to be devised and developed by the life-sciences community. The US National Institutes of Health has a 'Big Data' initiative, and agency head Francis Collins has spoken many times of the need to address the problem. Now is the time for researchers to plan an open data-management system that scientists will want to adopt. Many of the software pieces are already available.

As a starting point, here are three lessons from the successes and failures of the past.

First, the data are going to change. Biological information will always come in varied formats, and these formats cannot be defined in advance. Software engineers hate this. But a useful system must be flexible and updatable.

Second, people are not going to change. Busy scientists will adopt a new system only if it offers substantial benefit and is painless. Many commercial systems are unpopular because they make simple steps such as data retrieval complicated, to stop scientists using several (rival) systems at once.

Third, the problem is not technical. Although the latest kit is always alluring to funders, today's cutting-edge devices will be blunt tomorrow. Data-management systems must be driven by the need to find a workable solution to the problem, not by a desire to make the problem fit the latest fashionable technology.

Development of a biology-friendly system is possible, but it will require a change in mentality. As a useful test, a good data-management system should cost more to maintain, update and change with the times than it does to develop. Otherwise the price is too high. ■

John Boyle will shortly become senior director of bioinformatics at Kymab in Cambridge, UK.  
e-mail: john.boyle@kymab.com

➔ **NATURE.COM**  
Discuss this article  
online at:  
[go.nature.com/zyllsz](http://go.nature.com/zyllsz)

# RESEARCH HIGHLIGHTS

Selections from the  
scientific literature

## NEUROSCIENCE

### A window into nerve repair

Some neurons regenerate better than others.

Researchers led by Vincenzo De Paola at Imperial College London severed nerve cells in mouse brains, using lasers to minimize scarring and inflammation. The authors set glass panes into the skulls of the animals and monitored regrowth in more than 100 neurons for up to a year. More than half of the cut neurons from the deepest layer of the brain's cortex regrew, but only about one-fifth of those in its other layers did. Neurons in the brains of juvenile mice were also more likely to regrow than those in adult brains.

Regrowth depends, at least in part, on the neurons themselves and not just external factors such as neural-support cells, the authors say. They suggest that long-term imaging could be used to test potential neuron-repair strategies in the brains of living animals.

*Nature Commun.* 4, 2038 (2013)

## MATERIALS SCIENCE

### Ratchet action misshapes pearls

Perfectly round pearls (pictured) owe their spherical shape to spiral



growth patterns of nacre, the iridescent material also known as mother of pearl. By contrast, non-spherical pearls such as drop pearls have longitudinal growth fronts positioned such that they work like teeth on a ratchet, spinning the gem as it grows in an oyster.

Julyan Cartwright of the University of Granada, Spain, and his team calculated the forces exerted by nacre particles sticking to and bouncing off the growth fronts of a developing pearl. The forces proved strong enough to rotate the pearl once every 20 days (the speed at which pearls have previously been found to

rotate) and to influence its ultimate shape.

Microscopic control over macroscopic motion could be a useful design principle for building tiny machines, the researchers suggest.

*Langmuir* <http://dx.doi.org/10.1021/la4014202> (2013)

## CANCER

### Drug outdoes standard therapy

A large clinical trial has confirmed the promise of a targeted drug therapy in advanced non-small-cell lung cancer.

The drug crizotinib, which targets an oncogenic protein

encoded by the mutated *ALK* gene, extended progression-free survival in patients with *ALK* mutations by 7.7 months, compared with 3 months for chemotherapy alone. The results from the trial, which included 347 patients, are reported by Alice Shaw at Massachusetts General Hospital in Boston and her colleagues, and come just six years after the discovery of *ALK* fusion mutations in cancer and two years after the drug was approved for non-small-cell lung carcinoma in the United States on the basis of smaller clinical trials.

A related paper from a team also led by Shaw



## ANIMAL BEHAVIOUR

### Familiar nest sites beat better lakes

When common loons (*Gavia immer*, pictured) settle down to breed, they pick sites similar to the ones they hatched in, even if better sites are available.

As part of a 20-year study, researchers led by Walter Piper at Chapman University in Orange, California, tagged and observed birds across glacial lakes in the north-central United States. Loons that were reared on small, acidic lakes tended to settle on similar sites, even though

large, less-acidic lakes can support more and healthier chicks. The researchers suggest that adult loons might survive best on lakes that offer the types of fish and other prey that the birds are most familiar with. A trade-off between reproductive success and survival rate could help to explain the apparently maladaptive habitat choices seen in loons and other species, the authors say.

*Proc. R. Soc. B* 280, 20130979 (2013)

IGNACIO YUFERA/FLPA

AMERICAN CHEMICAL SOCIETY



reports a new mechanism of resistance to crizotinib in one patient, showing that the search for effective targeted treatments must continue.

*N. Engl. J. Med.* 368, 2385–2394; 368, 2395–2401 (2013)

## PALAEOLOGY

## Ancient 'starfish' had a helix

Five rays twisting down from the top of a fossil hint at how creatures such as starfish gained their unusual symmetry.

Starfish, sea urchins and all other known living echinoderms have a symmetry that allows them to be sliced into five identical parts, but some of their counterparts in the Cambrian period, which began about 540 million years ago, were asymmetric or had bilateral symmetry.

Andrew Smith at the Natural History Museum in London and Samuel Zamora at the Smithsonian Institution in Washington DC discovered Cambrian fossils in Morocco that show what stages intermediate to the body plan of living echinoderms might have looked like.

*Helicocystis moroccoensis* (pictured) is the oldest known echinoderm with five-part symmetry; it resembled an egg with its tapered end planted in the sea floor. Its mouth opened upward and its body spiralled down.

*Proc. R. Soc. B* 280, 20131197 (2013)



RICHARD MITHEN

R. SOC.

## ZOOLOGY

## Hot sex for jawless fish

After dancing seductively for their potential mates, male sea lampreys (*Petromyzon marinus*) crank up the heat, literally, using a ridge of tissue on their backs.

Courtship behaviour of lampreys — eel-like, bloodsucking, jawless fishes — includes the male rubbing his ridge against the belly of an interested female. Researchers had assumed that this simply aroused females mechanically, but when Weiming Li and his colleagues at Michigan State University in East Lansing dissected the tissue, they found that ridges from mature males were full of cells packed with oil droplets and cells primed for energy production, a hallmark of heat-producing tissue. The ridge temperature in males jumped by up to 0.3°C in the presence of sexually mature females.

The authors say that the ridge is the first example of a heat-generating sexual trait. *J. Exp. Biol.* 216, 2702–2712 (2013)

## GEOSCIENCE

## Earthquakes sink volcanoes

Giant earthquakes in subduction zones do not just create tsunamis — they can also cause nearby volcanic regions to sink, possibly altering the risk of eruptions.

In subduction zones, one plate of Earth's crust plunges beneath another. Quakes cause the overriding plate to expand and subside. Volcanoes on these plates subside even further, according to satellite radar data from two regions.

Youichiro Takada and Yo Fukushima at Kyoto University, Japan, measured drops in volcanic regions of up to 15 centimetres near the fault that broke in the 2011 magnitude-9.0 Tohoku earthquake. Separately, Matt Pritchard at Cornell

## COMMUNITY CHOICE

The most viewed papers in science

## CROP SCIENCES

## Super-broccoli secret solved

**HIGHLY READ**  
on wiley.com  
in May

A single gene is probably responsible for high levels of sulphur-containing compounds in new commercial varieties of broccoli.

Richard Mithen at the Institute of Food Research in Norwich, UK, and his group analysed hundreds of genetic markers in broccoli hybrids (pictured) bred to produce more glucoraphanin, a compound with reported health benefits. The team had previously created the three hybrid lines by crossing common broccoli (*Brassica oleracea*) and a wild Sicilian cousin (*Brassica villosa*) multiple times. The analysis showed that the hybrids had all inherited a version of a gene from *B. villosa*. The gene, called *Myb28*, also regulates glucoraphanin production in the model plant *Arabidopsis*. Field trials under diverse conditions showed that the hybrids consistently had higher levels of the compound. The plants both drew more sulphur-containing building blocks from the soil and shunted a greater portion of them towards glucoraphanin production. The work paves the way for blinded human studies that assess the health benefits of eating the glucoraphanin-rich broccoli, the authors say.

*New Phytol.* 198, 1085–1095 (2013)



University in Ithaca, New York, and his colleagues measured subsidence of up to 15 centimetres within weeks of the 2010 magnitude-8.8 Maule earthquake off the coast of Chile.

The authors of the Japanese study suggest that the subsidence occurred because reservoirs of magma below the volcanoes sank. By contrast, the authors of the Chilean study say that hydrothermal reservoirs may have drained, causing the ground above to collapse.

*Nature Geosci.* <http://dx.doi.org/10.1038/ngeo1857>; <http://dx.doi.org/10.1038/ngeo1855> (2013)

## AGEING

## Clock blocked by age

A protein linked to ageing and metabolic disease might control the brain's internal clock.

The protein SIRT1 regulates the expression of many genes and has been linked to daily biological cycles called circadian rhythms in tissues such as fat and the liver. Hung-Chun Chang and Leonard Guarente at the Massachusetts Institute of Technology in Cambridge found that in mouse brains, SIRT1 switches on two proteins that are known to regulate circadian rhythms.

Aged mice were slower than young mice to adjust to shifts in light–dark cycles, and expressed lower levels of SIRT1 in the brain region that sets circadian rhythms. Boosting SIRT1 levels shortened animals' adjustment time, whereas depleting SIRT1 lengthened it.

*Cell* 153, 1448–1460 (2013)

**NATURE.COM**

For the latest research published by Nature visit:

[www.nature.com/latestresearch](http://www.nature.com/latestresearch)



# SEVEN DAYS

The news in brief

## EVENTS

### Solar mission

NASA's latest solar mission reached orbit safely on 27 June. The Interface Region Imaging Spectrograph was released by an Orbital Sciences Pegasus XL rocket, which was launched from Vandenberg Air Force Base in Lompoc, California. The US\$181-million spacecraft carries a 20-centimetre ultraviolet telescope and spectrograph, designed to probe the layers of the Sun between its bright surface and its outer atmosphere, or corona (see *Nature* **498**, 279–280; 2013).

## POLICY

### DNA transplants

On 28 June, the UK government announced that it will publish draft regulations later this year with a view to allowing and governing DNA transplants in *in vitro* fertilization that could prevent certain heritable diseases. The United Kingdom may become the first country to legalize the technique, which involves transplanting nuclear DNA from eggs or embryos with faulty mitochondria into healthy donor cells. The regulations will be open to public consultation and debated by parliament in 2014.

### Clinical-trial ethics

US regulators announced plans on 26 June for a public meeting to discuss ethical issues in studies of 'standard of care' treatments — those commonly used in clinical practice. In March, the Office for Human Research Protections (OHRP) criticized a study in infants — the Surfactant, Positive Pressure, and Oxygenation Randomized Trial (SUPPORT) — for failing to adequately disclose risks associated with different blood-oxygen-

saturation levels used to support extremely premature babies. But the criticism stirred controversy among researchers, ethicists and National Institutes of Health officials, prompting the OHRP to schedule a 28 August meeting.

### African power

Over the next five years, the US government will invest US\$7 billion in an initiative to double access to electricity in sub-Saharan Africa, President Barack Obama announced on 30 June. It is estimated that more than two-thirds of people in the region lack electricity. The United States will initially work with six countries — Ethiopia, Ghana, Kenya, Liberia, Nigeria and Tanzania — to increase generation capacity by more

than 10,000 megawatts. The project, called Power Africa, also includes \$9 billion in contributions from industry partners around the world.

### Russian reform

The Russian Academy of Sciences, Russia's main basic-research organization, is facing the most radical overhaul in its 290-year history. A government bill launched on 28 June sets out a plan to merge the academy with two minor academies for medicine and agriculture. Responsibility for its more than 400 research institutes would be transferred to a new government agency. The Russian parliament's final vote on the bill is expected in October. See page 5 and [go.nature.com/be5pyw](http://go.nature.com/be5pyw) for more.

### Obama on climate

Faced with continued political gridlock on climate policy, US President Barack Obama has ordered the Environmental Protection Agency (EPA) to regulate carbon dioxide emissions from existing power plants. The Clean Air Act regulations are the centrepiece of a broader climate strategy unveiled on 25 June and will be developed over the next two years. The president also ordered the EPA to complete work on an existing regulatory proposal covering new power plants. See page 5 for more.

## RESEARCH

### HIV treatment

Two men with HIV may be on the road to being cured, their doctors said on 3 July at



NASA

## Alaskan volcano eruption escalates

An ongoing eruption of Alaska's Pavlof volcano intensified on 25 June, when it spewed an ash plume up to 8.5 kilometres high. Located 1,000 kilometres southwest of Anchorage, Pavlof is one of the state's most active volcanoes. It began erupting in mid-May (pictured on 18 May), and the Alaska Volcano Observatory is watching it closely because of its potential

impact on aeroplane flights across the North Pacific. But four of the nine seismic stations that monitor Pavlof have stopped working in recent years, and budget cuts have prevented the observatory from repairing them. Funding cutbacks have halted real-time monitoring of at least four of Alaska's volcanoes. See [go.nature.com/at8eue](http://go.nature.com/at8eue) for more.

a meeting of the International AIDS Society in Kuala Lumpur, Malaysia. The men received stem-cell transplants to treat blood cancer, then stopped taking their antiretroviral medications, yet have no detectable trace of HIV DNA or RNA in their blood. It is still too early to say whether the men may be the third and fourth people to be essentially cured of HIV (see [go.nature.com/2ka1lq](http://go.nature.com/2ka1lq)). Also at the meeting, the World Health Organization said that HIV patients should begin antiretroviral treatment earlier than previously recommended, while their immune systems are still relatively strong. See [go.nature.com/xchc4b](http://go.nature.com/xchc4b) for more.

## Chimp conclusion

The US National Institutes of Health (NIH) will retire more than 300 research chimpanzees to sanctuaries over the next several years. No more than 50 animals will be available for future studies, which must continue to meet stringent ethical and regulatory standards. The NIH's 26 June announcement acts on a 2011 report by the US Institute of Medicine, which declared most NIH-funded chimpanzee research scientifically unnecessary. The United States is the only major country that conducts invasive chimpanzee research, and the NIH provides

virtually all US federal funding for such work. See [go.nature.com/1nb6rr](http://go.nature.com/1nb6rr) for more.

### PEOPLE



## No trial for Stapel

Dutch social psychologist Diederik Stapel (pictured), who in 2011 was found to have fabricated data in at least 30 published papers, will not face trial for misappropriating government research funds. Instead, in a pre-trial settlement, he has agreed to undertake 120 hours of community service. The Netherlands' public prosecutor's office said on 28 June that the public grants were not misused, as the money was mainly used to pay staff for their work — even though that work was based, in part, on fabricated data. See [go.nature.com/zcquw8](http://go.nature.com/zcquw8) for more.

## Commerce head

Billionaire business executive Penny Pritzker was confirmed by the US Senate on 25 June

as the new US secretary of commerce. Her job will include overseeing the US\$5.3-billion National Oceanic and Atmospheric Administration (NOAA), which accounted for nearly 66% of the commerce department's 2013 budget. Pritzker replaces John Bryson, who resigned in June 2012. The top job at NOAA remains open, however, after marine ecologist Jane Lubchenco left the agency in February.

### FUNDING

## Horizon 2020

European Union (EU) member states and the European Parliament agreed last week on details for Horizon 2020, an EU-wide research initiative set to begin in January 2014. The deal, which must still be formally approved, includes a highly simplified funding model for all participants in the 7-year, €70-billion (US\$91.2-billion) programme. Universities, research institutes and companies will be paid the full direct project costs, plus a 25% flat rate to cover overhead expenses. See page 18 for more.

## Conservation aid

Boosting international aid to the 40 countries where conservation is most underfunded could help to protect one-third of the world's threatened mammals, according to a report released

## COMING UP

### 2–9 JULY

Researchers discuss cosmic-ray physics, neutrino astronomy and dark-matter physics at the 33rd International Cosmic Ray Conference in Rio de Janeiro, Brazil. [go.nature.com/ipljwn](http://go.nature.com/ipljwn)

### 9–11 JULY

Imperial College in London hosts SB6.0, the Sixth International Meeting on Synthetic Biology, where topics include biosecurity risks and applications to human health. [go.nature.com/w8dokr](http://go.nature.com/w8dokr)

on 1 July (A. Waldron *et al.* *Proc. Natl Acad. Sci. USA* <http://dx.doi.org/10.1073/pnas.1221370110>; 2013). The study created a global database of annual conservation spending, and found that funding correlates with a country's land area, gross domestic product and threats to biodiversity. The list of underfunded countries includes Iraq, Senegal and France; such knowledge could inform international spending to prevent species loss, the authors say.

## UK funding

The UK science budget, which has been frozen at an annual £4.6 billion (US\$7 billion) since 2010, will not go up in the 2015–16 financial year, the government said on 26 June. But spending on infrastructure such as research facilities and buildings will increase from £0.6 billion to £1.1 billion, and will rise in line with inflation until 2020–21. The budget also gives an extra £185 million to the Technology Strategy Board, which funds business-led research projects. See [go.nature.com/popd9a](http://go.nature.com/popd9a) for more.

➔ **NATURE.COM**

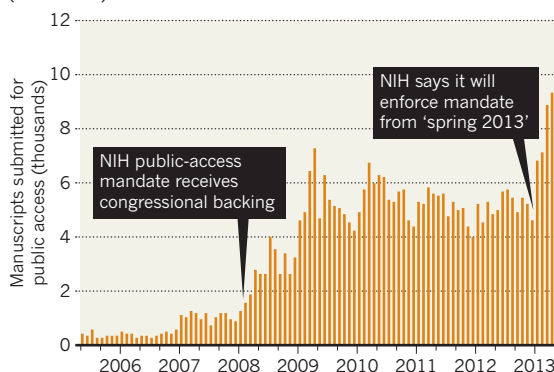
For daily news updates see: [www.nature.com/news](http://www.nature.com/news)

## TREND WATCH

Researchers are submitting skyrocketing numbers of manuscripts for processing by PubMed Central, the freely accessible repository of the US National Institutes of Health (NIH). PubMed has received an average of 8,800 manuscripts per month this year, up from 5,100 per month in 2011 and 2012. Last November, the NIH said that, from spring 2013, it would more rigorously enforce its policy of requiring NIH-funded research to be freely accessible to the public within 12 months of publication.

### PUBLIC-ACCESS SURGE FOR NIH

The US National Institutes of Health has seen a sharp rise in the number of manuscripts submitted to its PubMed Central (free access) database.

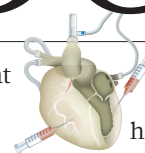


# NEWS IN FOCUS

**SYNTHETIC BIOLOGY** Open-source parts help bioengineers to tinker **p.16**

**IMMIGRATION** US Congress gives foreign scientists more ways to stay **p.17**

**FUNDING** Europe pays a flat rate for steep overhead costs **p.18**



**TISSUE ENGINEERING** What it takes to build a beating heart **p.20**

FABRICE COFFRINI/AFP/GETTY



Bioethanol-fuelled cars are rarer in Europe than those that run on biodiesel, although ethanol is greener.

## ENVIRONMENT

# EU debates U-turn on biofuels policy

*Key vote could signal withdrawal of support from biodiesel.*

BY RICHARD VAN NOORDEN

**T**he European Union (EU) has spent the past 10 years nurturing a €15-billion (US\$20-billion) industry that makes transport fuel from food crops such as soya beans and sugar cane in the hope of cutting greenhouse-gas emissions. Yet for more than half a decade, scientists have warned that many food-based fuels might actually be boosting emissions relative to fossil fuels.

Now the EU could change course by setting a cap on the use of food-based biofuel, but pressure from industry, farming and energy lobbies threatens to limit the reversal. Tensions are rising over how much of the emerging science on biofuel emissions will be included in EU policy ahead of a vote on 10 July by the key

European Parliament committee dealing with the legislation.

Europe began mandating the development and use of biofuels in 2003. The two latest laws on the subject, passed in 2009, require a 6% drop in the carbon footprint of transport fuel by 2020, by which time renewable energy must fuel 10% of the transport sector. Biofuel counts towards that requirement if it produces a 35% emissions saving over fossil fuels, or 50% from 2017 onwards; so far, most of that fuel has come from food crops, helping to generate a thriving biofuels industry based mainly on biodiesel. Europe is even importing rapeseed and vegetable oil to meet demand.

But the original accounting for biofuel emissions was all wrong, as Tim Searchinger, who studies environmental economics at Princeton

University in New Jersey, noted in an influential 2008 article (T. Searchinger *et al. Science* **319**, 1238–1240; 2008). He and his colleagues found that when agricultural land is used to plant bio-fuel crops, fresh land may be ploughed up to accommodate the existing crops that have been edged out. Ultimately, that may drive clearing of forests, peatlands and wetlands rich in sequestered carbon — causing large emissions of carbon dioxide. “It’s kind of obvious if you think about it,” says Searchinger.

Calculating this ‘indirect land-use change’ (ILUC) effect is complicated, because it is based on economic models projecting behaviour 10 or 20 years into the future. The numbers are different for different crops (see ‘Carbon conundrum’). But overall, when land-use effects are taken into account, most varieties of biodiesel turn out to produce more emissions than bioethanol — and often more than fossil fuels.

The effect wipes out more than two-thirds of the carbon emissions that Europe’s renewable-energy policy was supposed to save by 2020, says David Laborde, a researcher at the International Food Policy Research Institute (IFPRI) in Washington DC, which has produced influential reports for the European Commission.

In the United States, the Environmental Protection Agency did take the land-use effect into account in 2010, when it set standards for which fuels count as renewable. Luckily for US farmers, ethanol from maize (corn) — the main biofuel for US vehicles — was given the green light under the agency’s rules.

But the European Commission has ducked the issue in the face of strong resistance from the biofuels industry and Europe’s energy and agricultural sectors.

In October 2012, the commission finally proposed that food-crop fuel quotas be capped at only 5% of transport fuel by 2020 — half of the 10% renewables target — effectively allowing existing facilities to continue recouping investment, but stopping further expansion.

“I think they got it exactly right: the answer is to stop,” says Searchinger. Under the proposal, land-use figures would not be used to select one biofuel over another. But fuel suppliers would have to start including land-use figures produced by the IFPRI when they report the total emissions of their fuels, a hint that the official carbon footprint of Europe’s transport fuel might eventually ►



► incorporate that science.

The European Parliament now gets to battle over the commission's proposals. On 20 June, its energy committee voted to push the cap on food-crop fuels up slightly, to 6.5%. It also removed the stipulation that fuel suppliers report emissions using land-use change figures. Instead, the committee proposed gradually increasing mandates for use of advanced biofuels not made from food crops.

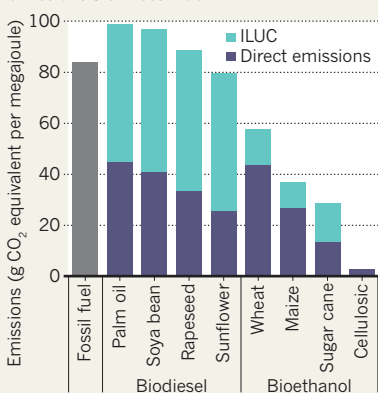
"The science of ILUC is not robust enough for policy," argues Clare Wenner, head of renewable transport policy at the UK Renewable Energy Association in London. But Europe's Joint Research Centre in Brussels says that the models used to calculate the land-use numbers are no less certain than the accepted science on the direct emissions of biofuels — and urges that they be included. The environment committee will vote on its preferred policy on 10 July: its lead negotiator on this issue, Corinne LePage, agrees with the Joint Research Centre and is pushing to incorporate land-use change numbers to distinguish between better and worse food-crop biofuels. But she may not get her way.

The battle does not end there: the main parliament will vote on the issue in September, based largely on what the environment and energy committees recommend. Then Europe's energy ministers will have to reach a compromise on the legislation. Some countries — such as the United Kingdom, the Netherlands and Denmark — want land-use factors to be included, whereas others, including central and eastern European countries with strong biofuel lobbies, do not. Although this month's vote will lay out the main lines of argument, it is conceivable that nothing will be agreed until 2014 — when European Parliament elections in May could set negotiations back to square one. "It's head-bangingly complicated," says Wenner. ■

SOURCE: IFPRI

### CARBON CONUNDRUM

Indirect land-use change (ILUC) effects mean that some biofuels produce more carbon emissions than fossil fuel.



After drinking water was tainted in 2011, people in Mianyang, China, had to take emergency measures.

#### ENVIRONMENTAL POLICY

## China gears up to tackle tainted water

*Government is set to spend 500 million renminbi to clean up groundwater polluted by industry and agriculture.*

BY JIAO LI IN BEIJING

When rumours swirled earlier this year that factories in Weifang, China, were discharging waste water into the region's aquifers — the principal source of drinking water for the city's 9 million residents — citizens flocked to the Web to register their outrage on microblogging site Sina Weibo. The rumours were finally confirmed by officials in late May, further stoking public fears over an already hot issue: the sorry state of the water that so many Chinese people drink.

Now, a massive government investigation has documented the scope of the problem in northern China, and officials have formulated an ambitious plan to tackle it.

About 18% of the water that China uses comes from groundwater, and more than 400 of the country's roughly 655 cities have no other source of drinking water. Much of the groundwater is contaminated, tainted by fertilizers, pesticide residues and dirty waste water used for irrigation in China's vast rural regions, as well as pollutants from mining, the

petrochemical industry, and domestic and industrial waste. Heavy metals are especially problematic, because "once in the groundwater, they don't go away", says Sun Ge, a research hydrologist at the US Department of Agriculture's Forest Service Southern Research Station in Raleigh, North Carolina. "It will be very expensive to clean up, if it is even possible."

In 2006, to assess the scope of the problem, the Chinese Ministry of Land and Resources launched a 6-year investigation focused on the North China Plain, the region most dependent on groundwater, which is home to nearly 130 million people. In late April this year, the government announced a work plan for control of groundwater contamination in the area. "The work plan is actually quite remarkable, and it is certainly a step in the right direction," says Zheng Yan, who studies groundwater pollution and public health at Columbia University in New York.

The extent of the problem is unclear because the full results of the 2006 survey have not been made public. An

**NATURE.COM**  
For a call to tackle China's water crisis, visit:  
[go.nature.com/wxqs3y](http://go.nature.com/wxqs3y)

CHINA DAILY/REUTERS/CORBIS

official at the China Geological Survey, which commissioned the report, declined to offer details for fear of alarming the public. However, the government's action plan acknowledges that the levels of pollution are serious. A 2012 report by the land ministry found that of 4,929 groundwater monitoring sites in 198 prefecture-level administrative regions across the country, 41% had poor water quality. Almost 17% had extremely poor water quality, with levels of iron, manganese, fluoride, nitrites, nitrates, ammonium and heavy metals exceeding safe limits.

Also last year, an article by Zhang Zhaoji, a hydrogeologist at the Chinese Academy of Geological Sciences' Institute of Hydrology and Environmental Geology in Hebei and project leader for the 2006 survey, reported that in the North China Plain, some 35% of shallow groundwater sampling points had been contaminated by human activities (Z. Zhang *et al.* *J. Jilin Univ. Earth Sci. Edn* 42, 1456–1461; 2012). “Water pollution is a more serious problem than the scarcity of water resources,” says Song Xianfang, a hydrologist at the Institute of Geographic Sciences and Natural Resources Research (IGSNRR) in Beijing, part of the Chinese Academy of Sciences.

The contamination rates are “not a surprise, as China is under rapid urbanization and industrialization that bring problems of water pollution for both surface and groundwater”, says Sun. And, although it is hard to prove cause and effect, there will probably be fallout for public health, experts say. Government reports stated that in 2004, China had 38.8 million recorded cases of tooth-enamel damage owing to fluoride exposure; 2.84 million cases of bone disease owing to fluoride exposure; and 9,686 cases of arsenic poisoning.

“These diseases are closely related to environmental and geological factors [and are] especially associated with contaminated groundwater,” says Yang Linsheng, the director of the department of environmental geography and health at the IGSNRR. The Chinese Center for Disease Control and Prevention did not respond to *Nature's* request for an interview.

In its plan, the government says that it will divide the North China Plain into 30 units for pollution prevention and control, which it will separate into three severity

**“Water pollution is a more serious problem than the scarcity of water resources.”**

categories — serious, poor and good — to be addressed differently. The details, which have not been publicly released, include an investment of nearly 500 million renminbi (US\$81 million) between 2013 and 2020 for a raft of measures across the country: to increase pollution assessments and establish a database of results; to control river pollution from agriculture and point sources from industry and landfill; to treat of polluted areas; and to conduct more research into clean-up and prevention strategies. Among other things, researchers will look into the effects of shale-gas development on groundwater.

The plan will also beef up environmental regulation. Experts say that will be a key measure, because the country must become more selective in approving industry projects. It must also enhance regulation of polluters, especially small rural companies such as paper mills. Furthermore, farmers must be educated in the proper use of fertilizers. Openness will be crucial in gaining public trust, experts add. “I would advocate data-sharing and transparency in reporting data,” says Zheng Chunmiao, director of the Center for Water Research at Peking University in Beijing. “Without this, people will be anxious.” ■

## EDUCATION

# Evolution makes the grade

*Kansas, Kentucky and other states will also teach climate-change science.*

BY LAUREN MORELLO

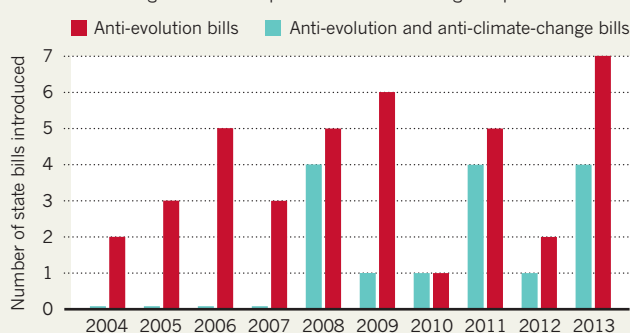
Five US states have adopted science education standards that recommend introducing two highly charged topics — climate-change science and evolution — into classrooms well before high school.

Released in April, the Next Generation Science Standards are the first effort in 15 years to overhaul US science education nationwide. Twenty-six states, working with non-profit science and education groups, developed the guidelines on the basis of recommendations from the US National Research Council. And the measures are being adopted, even in states where climate change and evolution tend to be avoided in the classroom.

In the past two months, education officials in Rhode Island, Kentucky, Kansas, Maryland and Vermont have all approved the standards by overwhelming margins. At least five more states — California, Florida, Maine, Michigan

## BY DESIGN

US state legislatures are increasingly introducing ‘academic freedom’ bills to allow educators to teach creationism. Since 2008, some of these bills would also allow teaching material that promotes climate-change scepticism.



and Washington — may take up the standards in the next few months.

“Whew,” says Minda Berbeco, programmes and policy director at the National Center for Science Education in Oakland, California. “So far, so good.” Swift adoption of the guidelines has been surprising but welcome news for many supporters. Evolution has been a controversial

topic in US education for decades, stretching back to the 1925 ‘monkey trial’ in Tennessee, where the state prosecuted high-school teacher John Scopes for violating a statute that barred the teaching of evolution. In the past decade, those who oppose evolution have sought to enact ‘academic freedom’ laws that would allow creationism to be taught alongside evolution.

Increasingly, that sort of legislation also seeks to promote criticism of mainstream climate science (see ‘By design’). Berbeco says that this allows opponents of evolution and climate-change education to band together. “More people hate evolution and climate change than just evolution alone,” she says.

Laws passed in Louisiana in 2008 and in Tennessee last year allow teachers to present material that undermines global warming and evolution, two subjects that have been specifically singled out in the statutes. Similar bills were introduced this year in Arizona, ►



► Colorado, Kansas and Oklahoma.

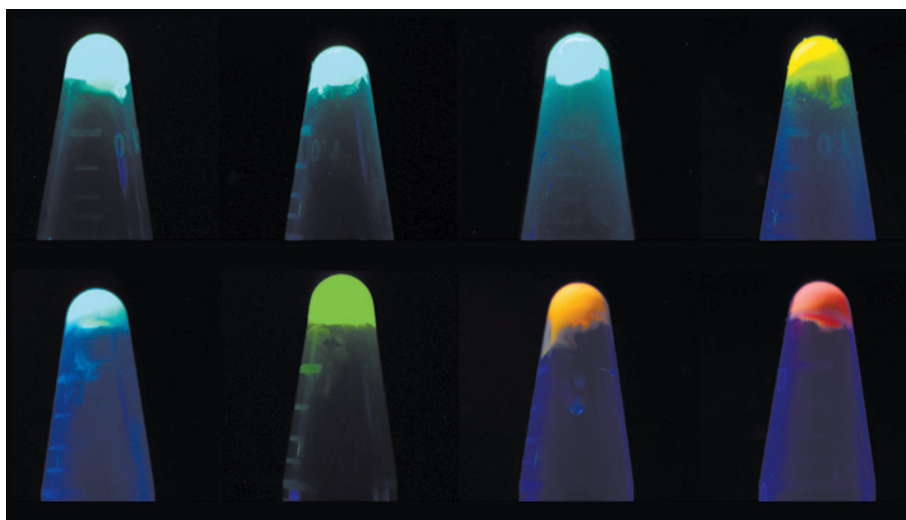
The standards are the first national guidelines to incorporate climate change, which is already taught in some schools. But it has proved daunting for many educators, because the subject requires teaching aspects of biology, physics and chemistry. "It's a little piece of everything," says Rouwenna Lamm, deputy director for national outreach at the Alliance for Climate Education in Oakland. The guidelines recommend introducing the subjects early on, teaching students in middle school that human activities, including the burning of fossil fuels, have warmed the planet. As students get older, that idea should be expanded to encompass discussions of climate models and potential policies to limit greenhouse-gas emissions. Likewise, the guidelines recommend teaching evolution before students reach high-school biology classes, the point at which many states tackle concepts such as natural selection and adaptation.

The standards have faced legal challenges in some states, although the framework has so far escaped unscathed. For example, Kansas lawmakers last month narrowly defeated a measure to block state funding to implement the guidelines — quashing the proposal just hours before lawmakers adjourned for the year. In Kentucky, the state board of education unanimously approved the standards on 5 June, but they must now undergo a public hearing and a subsequent legislative review before teaching can begin.

That places the guidelines squarely in the path of a high-powered critic who will help to steer the legislative review: Mike Wilson, Republican state senator and chairman of the Kentucky Senate's education committee, who is a climate-change sceptic and advocate of intelligent design. "Political correctness bears watching and should never be the arbiter of learning," he wrote in a May article published in *The Courier-Journal*, a Kentucky newspaper.

Robert Bevins, a toxicologist and president of Kentuckians for Science Education, an advocacy group formed in February in part to push for the adoption of the standards, says that he is gearing up for a hard fight. "Kentucky has a love-hate relationship with science," he says, noting that the state has a thriving coal industry that has opposed greenhouse-gas regulations and is also home to the Creation Museum near Petersburg.

Richard Innes, an education analyst with the conservative Bluegrass Institute for Public Policy Solutions in Lexington, Kentucky, predicts that the guidelines will be sent back to the state education board for revision after the public hearing this month. But ultimately, he says, "I think the science standards will go through". ■



Some synthetic fluorescent proteins made by DNA2.0 are now freely available to researchers.

#### BIOTECHNOLOGY

# Bioengineers look beyond patents

*Synthetic-biology company pushes open-source models.*

BY HEIDI LEDFORD

When DNA2.0, a company that synthesizes made-to-order genes, needed to conduct a few routine experiments using a fluorescent protein, its lawyers dug up more than 1,000 US patents covering their use. DNA2.0 decided to avoid the legal thicket by engineering several dozen fluorescent proteins from scratch. But the company, based in Menlo Park, California, was convinced that something had to change.

Last month, DNA2.0 deposited gene sequences encoding three of its fluorescent proteins into an open-access collection of recipes for DNA 'parts', molecular building blocks used to engineer organisms — often bacteria — to carry out specific functions. The company vows not to pursue its patent rights against anyone using the sequences.

Such moves are unusual among larger biotechnology companies, which tend to guard patents fiercely, but for DNA2.0 the choice was strategic, says Claes Gustafsson, the firm's chief commercial officer. Synthetic biologists aim to bring engineering principles to bear on genetic manipulation, and the field's success hinges on the creation of standardized parts that can be combined in predictable ways. The company wants to create incentives for other synthetic-biology firms to design custom organisms for which DNA2.0 can synthesize

the parts. "We have a lot of customers in small biotech companies," Gustafsson says, "and the intellectual-property situation for them is just a nightmare."

Easing that situation will be a key point of discussion next week at the Sixth International Meeting on Synthetic Biology, to be held in London by the BioBricks Foundation, a non-profit organization based in Cambridge, Massachusetts. As patent disputes heat up in some parts of the industry, synthetic biologists are weighing alternatives such as copyrights, which are more straightforward than patents, and open-source parts registries.

Open access to validated molecular components is crucial to the field's success, says Drew Endy, a synthetic biologist at Stanford University in California. Endy says that synthetic biologists are similar to software engineers, with the genetic code as their programming language. The software industry has favoured open-source approaches and copyright protections, because inventions often come faster than patents can be acquired.

The same holds for synthetic biology: if every genetic building block comes with a patent attached, cellular engineers may end up negotiating legal minefields. Few firms will sue a scientist who infringes a patent in the course of academic research, but young synthetic-biology companies are vulnerable.

Two years ago, the BioBricks Foundation



borrowed elements from the open-source software movement to develop a public agreement for designers of synthetic-biology parts. But the 708 parts in the BioBricks open-source collection come from only three donors: DNA2.0, Endy and Ginkgo BioWorks, a synthetic-biology company in Boston, Massachusetts. Commercial use of some of the highest-impact parts is still kept under lock and key by industry or academic labs.

Mark Fischer, a copyright lawyer at Duane Morris in Boston, and a key architect of the BioBricks agreement, says that it is too soon to judge the project. He says that DNA2.0's contribution to the registry is a sign that the movement is taking off. "I think we're now at the dawn of that happening," says Fischer, who also helped to pioneer open-source software agreements.

The open-source push in synthetic biology has also rekindled talk of copyrighting engineered DNA sequences. Copyrights protect certain types of work from being reproduced without permission, but users may substantially modify those creations. The United States started granting such protections to computer programs in the 1960s.

DNA2.0 plans to find out whether DNA sequences can also be shoehorned into the framework. Last year, the company petitioned for US copyright protection of the DNA sequence for a fluorescent green protein, without success, but has launched an appeal. Its plan, says Christopher Holman, a law professor at the University of Missouri–Kansas City who is working with DNA2.0, is to pursue the appeal until the issue is heard in court.

Copyrights are cheaper, easier alternatives to patents, says Endy. They cost \$35 to register, as opposed to the \$100,000 in legal fees and administrative costs that DNA2.0 says it pays for each patent application it files. But Endy worries about the duration of copyright protections, which can last up to 120 years; patents, by contrast, expire after 20.

And patents are still useful for some inventions, says Gustafsson. DNA2.0 will continue to patent some of its engineered genes and proteins. "We play in the same system as everyone else," says Gustafsson. "But we also want to increase our market size." ■

## POLICY

# US Senate backs immigration plan

*Proposal would lift visa caps for US-trained scientists and engineers.*

BY HELEN SHEN

For Gaurav Basu, a graduate scholarship in 2003 helped to fulfil a long-held ambition of pursuing scientific research in the United States. In 2009, Basu, a native of India, earned his PhD in biomedical sciences from Eastern Virginia Medical School in Norfolk.

But Basu is struggling to keep his American dream alive after finishing a postdoctoral fellowship at Old Dominion University in Norfolk in 2011. With his temporary work visa set to expire in 2015, he is now working as a consultant in northern Virginia — and fighting tough odds to stay in the United States permanently by applying for a coveted but scarce 'green card'.

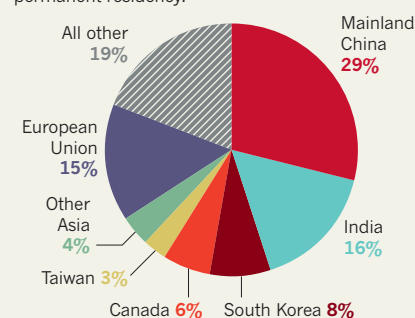
Those green cards could soon flow more freely to scientists such as Basu. After years of debate and many failed attempts, on 27 June the US Senate approved a comprehensive immigration plan that would allow thousands more foreign scientists and engineers to remain in the United States permanently. "It's a phenomenal improvement over the current situation," says Russell Harrison, a senior legislative representative for IEEE-USA in Washington DC, which advocates for US members of the Institute of Electrical and Electronics Engineers.

Under current policy, the number of green cards that can be issued each year is limited to 140,000, a figure that is further reduced by per-country caps. Applicants from countries that send large numbers of immigrants — such as China, India, Mexico and the Philippines — must often wait for years, subsisting on a string of temporary work visas that can be revoked at an employer's discretion.

"Our system is absolutely, utterly broken," says Amy Scott, associate vice-president for federal relations at the Association of

## SHORT STAYS?

Most holders of doctoral degrees who have temporary US work visas come from India and China. Many of them have trouble securing permanent residency.



American Universities in Washington DC.

The Senate bill would end country-based caps and exempt researchers in some disciplines from limits altogether. Applicants with master's or doctoral degrees in science, technology, engineering or mathematics (STEM) obtained from US universities would be eligible to tap an unlimited pool of green cards. And, unlike previous proposals, the bill brings biological and biomedical sciences under the STEM umbrella.

According to the most recent statistics from the National Science Foundation, about 25% of the US science and engineering workforce comes from other countries. People from China and India made up nearly half of PhD holders who received temporary work visas in 2009 (see 'Short stays?'). And many of them lead tenuous lives in their adopted country.

Among them is Somiranjana Ghosh, a senior research associate in molecular genetics at Howard University in ▶

**MORE ONLINE**

## Q &amp; A



New Zealand's science adviser on the country's key research challenges  
[go.nature.com/oigfxf](http://go.nature.com/oigfxf)

## NEWS

- Voyager 1 is going, but not quite gone, from the Solar System [go.nature.com/mugdvh](http://go.nature.com/mugdvh)
- 'Corkscrew' light could turbocharge the Internet [go.nature.com/vyxfgf](http://go.nature.com/vyxfgf)
- Water flow tracks earthquake healing [go.nature.com/b11a4e](http://go.nature.com/b11a4e)

## PODCAST



Catch up with Nature's free audio show  
[go.nature.com/ht2qm2](http://go.nature.com/ht2qm2)

► Washington DC. Ghosh came to the United States from India in 2003 for a postdoctoral fellowship at the National Cancer Institute in Bethesda, Maryland, and finished a second fellowship at Howard University in 2007. He applied for permanent residency in December 2010 and was approved in 2011, but he has yet to receive his green card.

Ghosh also wants to travel abroad, but, without a green card, he could encounter administrative delays when he tries to re-enter the United States. Last year, he turned down an invitation to speak at a conference in France.

Worries about conference travel are a big problem for many postdoctoral fellows on temporary visas, says Benjamin Corb, director of public affairs at the American Society for Biochemistry and Molecular Biology in Rockville,

Maryland. “They just don’t go, so they lose out on that opportunity in their professional career,” he says. That understandable caution can also exact heavy personal costs. Ghosh was too afraid to return to India to see his sister before she died of cancer in January.

**“Our system is absolutely, utterly broken.”**

Ghosh’s visa, unlike a green card, does not allow him to change jobs easily. He would like to move into the field of medical diagnostics and eventually start his own company. “I’m 45 now,” he says. “I want to start my own career.”

Hopes of clearing the green card logjam now rest with the Republican-controlled House of Representatives, and its leaders are preparing separate proposals to address immigration.

Although increased immigration for scientists and engineers enjoys broad bipartisan support, Republicans argue that STEM green cards should be created only at the expense of other categories, such as the annual green card lottery for natives of countries that send few immigrants to the United States. But Democrats, who control the Senate, reject that notion. Any changes to the visa system will require agreement by both sides on a broader suite of hotly contested immigration issues.

For Basu, the stakes may be higher than for most. He and his wife are expecting their first child in three weeks, and he worries that the family may ultimately have to move back to India — away from the life they have created in Virginia. “Our kid will be an American citizen,” says Basu. “We have roots here.” ■

## FUNDING

# European deal cuts red tape

*Horizon 2020 research programme streamlines project reimbursements.*

BY QUIRIN SCHIERMEIER

A deal struck last week during negotiations on the research programme for the next seven years in the European Union (EU) promises a significant change to the way in which institutions are reimbursed for the overhead costs of their research. The agreement for Horizon 2020 sweeps away the onerous red tape involved in the present diverse arrangements and replaces it with an across-the-board 25% reimbursement rate for all.

Although the deal could be a boon for the many European universities with low overheads, which include heating, lighting, rent and facilities maintenance, it has disappointed some operators of large research facilities, mainly those in Western Europe. They warn that the simplified funding rules could harm top-ranking centres with high overheads because they will need reimbursement beyond 25% of the total direct costs.

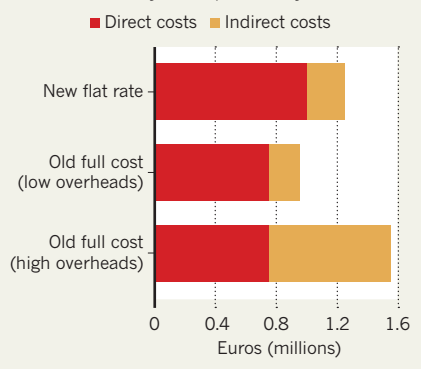
“The new rules threaten to make Horizon 2020 extremely unattractive, particularly for research organizations dedicated to innovation,” says Reimund Neugebauer, president of the Fraunhofer Society, headquartered in Munich, Germany, which carries out contract research for industry.

Details of Horizon 2020, due to start next January, have been under negotiation since February in a series of talks between EU member

► **NATURE.COM**  
Complex accounting rules cost the EU millions:  
[go.nature.com/mc69zw](http://go.nature.com/mc69zw)

## OVERHEAD HEADACHES

A hypothetical €1-million grant would net 25% for indirect costs under new EU rules, contrasting with the variability of the previous system.



states, the European Parliament and the European Commission. The three were united on the programme’s goal to spur economic growth and on its broad themes, which include health and energy research. But the parliament and member states have been squabbling over what accounting rules might best serve Europe’s paperwork-plagued research community. The United States, too, has stumbled over funding of indirect costs (see ‘Transatlantic concerns’), but some had feared that the European deadlock over the issue would delay the start of Horizon 2020.

Keen to simplify the affair, the European Commission and most member states threw their support behind a system that would pay

grant-winners the full direct costs of a project, such as salaries, travel and laboratory supplies, plus a 25% flat rate to cover overheads. Such a move would also please the EU’s auditors — in a report released on 7 June, they slammed the complex funding model used in the organization’s 2007–13 research programme.

But some Members of the European Parliament (MEPs) — backed by the European University Association in Brussels, which represents many of Europe’s universities and research institutes — held that such an approach would make participation in Horizon 2020 unattractive for institutions with high overheads. Universities that run expensive facilities, for example ocean-going research vessels and synchrotron machines, would be left out of pocket, as would organizations such as the Fraunhofer, which have high overheads because the contract research they carry out often involves the use of expensive industry-owned research facilities.

Critics of the flat rate were pushing for the ‘full cost’ reimbursement model used in the last EU research programme. This would have allowed organizations to get 75% of their direct costs plus 100% of their indirect costs — which can sometimes be as high as the direct costs (see ‘Overhead headaches’). In the end, a majority of member states and the commission gained the upper hand in their attempt to simplify the accounting. At the meeting last week, MEPs reluctantly agreed that Horizon 2020 would use only the flat-rate model. The deal must still be formally approved by

► Washington DC. Ghosh came to the United States from India in 2003 for a postdoctoral fellowship at the National Cancer Institute in Bethesda, Maryland, and finished a second fellowship at Howard University in 2007. He applied for permanent residency in December 2010 and was approved in 2011, but he has yet to receive his green card.

Ghosh also wants to travel abroad, but, without a green card, he could encounter administrative delays when he tries to re-enter the United States. Last year, he turned down an invitation to speak at a conference in France.

Worries about conference travel are a big problem for many postdoctoral fellows on temporary visas, says Benjamin Corb, director of public affairs at the American Society for Biochemistry and Molecular Biology in Rockville,

Maryland. “They just don’t go, so they lose out on that opportunity in their professional career,” he says. That understandable caution can also exact heavy personal costs. Ghosh was too afraid to return to India to see his sister before she died of cancer in January.

**“Our system is absolutely, utterly broken.”**

Ghosh’s visa, unlike a green card, does not allow him to change jobs easily. He would like to move into the field of medical diagnostics and eventually start his own company. “I’m 45 now,” he says. “I want to start my own career.”

Hopes of clearing the green card logjam now rest with the Republican-controlled House of Representatives, and its leaders are preparing separate proposals to address immigration.

Although increased immigration for scientists and engineers enjoys broad bipartisan support, Republicans argue that STEM green cards should be created only at the expense of other categories, such as the annual green card lottery for natives of countries that send few immigrants to the United States. But Democrats, who control the Senate, reject that notion. Any changes to the visa system will require agreement by both sides on a broader suite of hotly contested immigration issues.

For Basu, the stakes may be higher than for most. He and his wife are expecting their first child in three weeks, and he worries that the family may ultimately have to move back to India — away from the life they have created in Virginia. “Our kid will be an American citizen,” says Basu. “We have roots here.” ■

## FUNDING

# European deal cuts red tape

*Horizon 2020 research programme streamlines project reimbursements.*

BY QUIRIN SCHIERMEIER

A deal struck last week during negotiations on the research programme for the next seven years in the European Union (EU) promises a significant change to the way in which institutions are reimbursed for the overhead costs of their research. The agreement for Horizon 2020 sweeps away the onerous red tape involved in the present diverse arrangements and replaces it with an across-the-board 25% reimbursement rate for all.

Although the deal could be a boon for the many European universities with low overheads, which include heating, lighting, rent and facilities maintenance, it has disappointed some operators of large research facilities, mainly those in Western Europe. They warn that the simplified funding rules could harm top-ranking centres with high overheads because they will need reimbursement beyond 25% of the total direct costs.

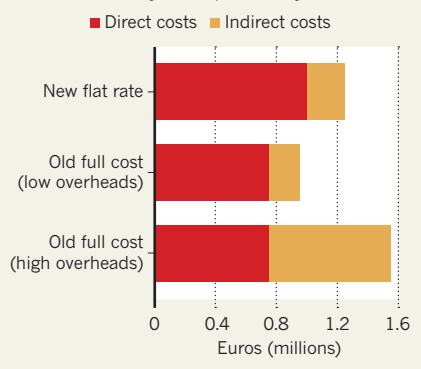
“The new rules threaten to make Horizon 2020 extremely unattractive, particularly for research organizations dedicated to innovation,” says Reimund Neugebauer, president of the Fraunhofer Society, headquartered in Munich, Germany, which carries out contract research for industry.

Details of Horizon 2020, due to start next January, have been under negotiation since February in a series of talks between EU member

► **NATURE.COM**  
Complex accounting rules cost the EU millions:  
[go.nature.com/mc69zw](http://go.nature.com/mc69zw)

## OVERHEAD HEADACHES

A hypothetical €1-million grant would net 25% for indirect costs under new EU rules, contrasting with the variability of the previous system.



states, the European Parliament and the European Commission. The three were united on the programme’s goal to spur economic growth and on its broad themes, which include health and energy research. But the parliament and member states have been squabbling over what accounting rules might best serve Europe’s paperwork-plagued research community. The United States, too, has stumbled over funding of indirect costs (see ‘Transatlantic concerns’), but some had feared that the European deadlock over the issue would delay the start of Horizon 2020.

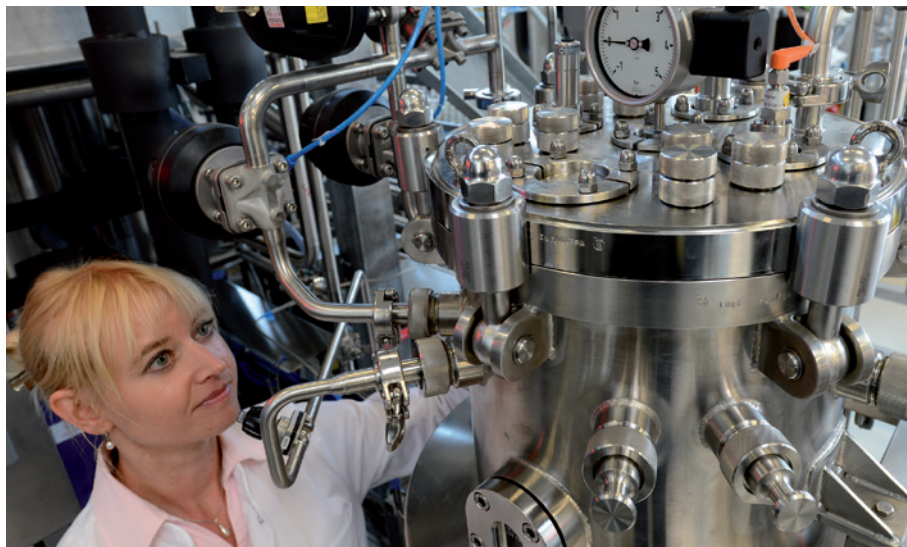
Keen to simplify the affair, the European Commission and most member states threw their support behind a system that would pay

grant-winners the full direct costs of a project, such as salaries, travel and laboratory supplies, plus a 25% flat rate to cover overheads. Such a move would also please the EU’s auditors — in a report released on 7 June, they slammed the complex funding model used in the organization’s 2007–13 research programme.

But some Members of the European Parliament (MEPs) — backed by the European University Association in Brussels, which represents many of Europe’s universities and research institutes — held that such an approach would make participation in Horizon 2020 unattractive for institutions with high overheads. Universities that run expensive facilities, for example ocean-going research vessels and synchrotron machines, would be left out of pocket, as would organizations such as the Fraunhofer, which have high overheads because the contract research they carry out often involves the use of expensive industry-owned research facilities.

Critics of the flat rate were pushing for the ‘full cost’ reimbursement model used in the last EU research programme. This would have allowed organizations to get 75% of their direct costs plus 100% of their indirect costs — which can sometimes be as high as the direct costs (see ‘Overhead headaches’). In the end, a majority of member states and the commission gained the upper hand in their attempt to simplify the accounting. At the meeting last week, MEPs reluctantly agreed that Horizon 2020 would use only the flat-rate model. The deal must still be formally approved by





Research carried out by Germany's Fraunhofer Society might be hampered by European funding rules.

parliament and EU member states, but it is expected to pave the way for Horizon 2020 to start on schedule.

"The parliament managed to safeguard many improvements and substantial simplification for participants," said Christian Ehler, an MEP with the centre-right European People's Party and parliament's lead negotiator for Horizon 2020, in a statement to *Nature*. "But I dread the fact that the parliament had to consent to the council's funding model" because it will dramatically disadvantage some institutions.

Nonetheless, some of Europe's elite research universities are pleased with the promised reduction in red tape. "Having one rule for all is a major improvement," says Kurt Deketelaere, secretary-general of the League of European Research Universities, a partnership of 21 top universities. "Imagine the insane complexity in collaborating with research organizations

and companies which all follow different rules. That system had to go." By and large, says Deketelaere, universities will be better off financially than they were under previous EU research programmes.

But the commission has promised to address the concerns of those unhappy with the new rules. A recent commission working paper seen by *Nature* proposes that more of the costs incurred in operating research facilities could be reimbursed if the money were interpreted as being fully related to a Horizon 2020 project. "We will take the commission at its word," says Neugebauer.

Scientists in the 13 states that have joined the EU since 2004 could benefit from the changes thrashed out last week. Universities and institutes there have less experience in dealing with EU bureaucracy — a prerequisite for claiming and verifying overhead costs. Moreover, their overheads tend to be smaller than those of facilities-rich Western European research centres. As a further sweetener, scientists in these countries who receive a Horizon 2020 grant will get an annual salary bonus of €8,000 (US\$10,400).

The flat-rate system could also help scientists in such countries to win a bigger slice of EU funding, says Krzysztof Frackowiak, director of the Polish Science Contact Agency in Brussels, which helps Polish institutions to negotiate EU red tape. The newer member states "haven't been able to get back from Brussels nearly as much as they paid into European research programmes", he says. ■

## TRANSATLANTIC CONCERNS

### *Flat rate overruled*

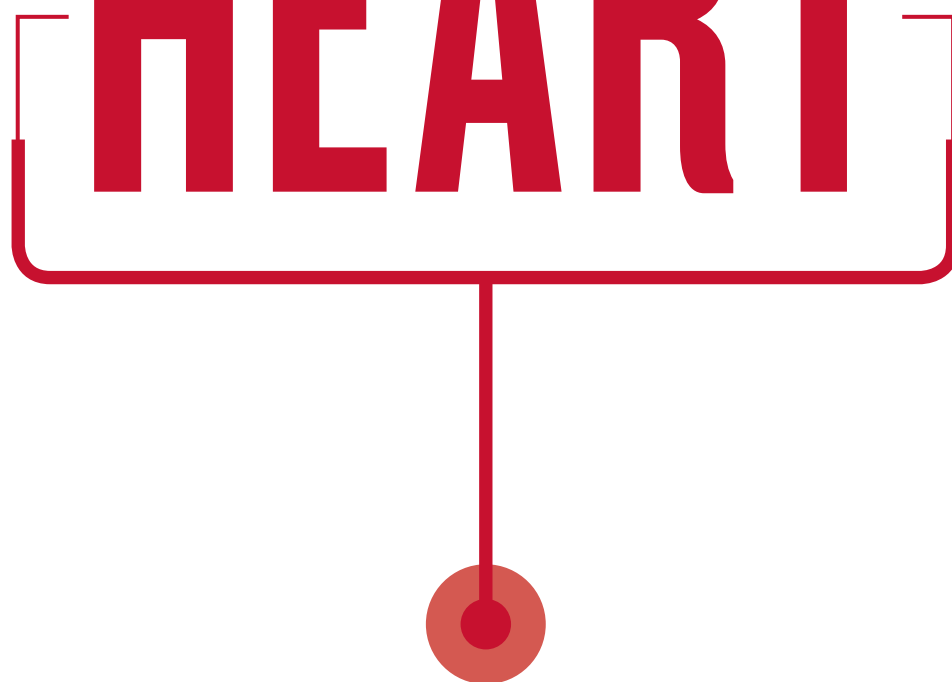
The thorny issue of overhead payments is not restricted to Europe. In the United States, the average reimbursement rate is around 50% of direct project costs, but top institutes such as Harvard University in Cambridge, Massachusetts, receive up to 70% of extra money from federal grants. Critics say that the current practice unfairly favours a few research powerhouses over many other, smaller universities. However, an attempt last year by President Barack Obama's administration to introduce a single flat rate met with fierce opposition from large institutes such as Harvard and the Massachusetts Institute of Technology in Cambridge. The plan was abandoned. **Q.S.**

#### **CORRECTION**

The y-axis in the graphic 'The rise of open access in the News Feature 'The true cost of science publishing' (*Nature* **495**, 426–429; 2013) was mislabelled. The correct version is online at [go.nature.com/e8rsrb](http://go.nature.com/e8rsrb).

*With thousands of people in need of heart transplants, researchers are trying to grow new organs.*

# HOW TO BUILD A HEART



BY BRENDAN MAHER

**D**oris Taylor doesn't take it as an insult when people call her Dr Frankenstein. "It was actually one of the bigger compliments I've gotten," she says — an affirmation that her research is pushing the boundaries of the possible. Given the nature of her work as director of regenerative medicine research at the Texas Heart Institute in Houston, Taylor has to admit that the comparison is apt. She regularly harvests organs such as hearts and lungs from the newly dead, re-engineers them starting from the cells and attempts to bring them back to life in the hope that they might beat or breathe again in the living.

Taylor is in the vanguard of researchers looking to engineer entire new organs, to enable transplants without the risk of rejection by the recipient's immune system. The strategy is simple enough in principle. First remove all the cells from a dead organ — it does not even have to be from a human — then take the protein scaffold left behind and repopulate it with stem cells immunologically matched to the patient in need. *Voilà!* The crippling shortage of transplantable organs around the world is solved.

In practice, however, the process is beset with tremendous challenges. Researchers have had some success with growing and transplanting hollow, relatively simple organs such as tracheas and bladders (see [go.nature.com/zvuxed](http://go.nature.com/zvuxed)). But growing solid organs such as kidneys or

lungs means getting dozens of cell types into exactly the right positions, and simultaneously growing complete networks of blood vessels to keep them alive. The new organs must be sterile, able to grow if the patient is young, and at least nominally able to repair themselves. Most importantly, they have to work — ideally, for a lifetime. The heart is the third most needed organ after the kidney and the liver, with a waiting list of about 3,500 in the United States alone, but it poses extra challenges for transplantation and bioengineering. The heart must beat constantly to pump some 7,000 litres of blood per day without a back-up. It has chambers and valves constructed from several different types of specialized muscle cells called cardiomyocytes. And donor hearts are rare, because they are often damaged by disease or resuscitation efforts, so a steady supply of bioengineered organs would be welcome.

Taylor, who led some of the first successful experiments to build rat hearts<sup>1</sup>, is optimistic about this ultimate challenge in tissue engineering. "I think it's eminently doable," she says, quickly adding, "I don't think it's simple." Some colleagues are less optimistic. Paolo Macchiarini, a thoracic surgeon and scientist at the Karolinska Institute in Stockholm, who has transplanted bioengineered tracheas into several patients, says that although tissue engineering could become routine for replacing tubular structures such as windpipes, arteries and oesophagi, he is "not



confident that this will happen with more complex organs.”

Yet the effort may be worthwhile even if it fails, says Alejandro Soto-Gutiérrez, a researcher and surgeon at the University of Pittsburgh in Pennsylvania. “Besides the dream of making organs for transplantation, there are a lot of things we can learn from these systems,” he says — including a better basic understanding of cell organization in the heart and new ideas about how to fix one.

## THE SCAFFOLD

For more than a decade, biologists have been able to turn embryonic stem cells into beating heart-muscle cells in a dish. With a little electrical pacemaking from the outside, these engineered heart cells even fall into step and maintain synchronous beating for hours.

But getting from twitching blobs in a Petri dish to a working heart calls for a scaffold to organize the cells in three dimensions. Researchers may ultimately be able to create such structures with three-dimensional printing — as was demonstrated earlier this year with an artificial trachea<sup>2</sup> (see *Nature* <http://doi.org/m2q>; 2013). For the foreseeable future, however, the complex structure of the human heart is beyond the reach of even the most sophisticated machines. This is particularly true for the intricate networks of capillaries that must supply the heart with oxygen and nutrients and remove waste products from deep within its tissues. “Vascularity is the major challenge,” says Anthony Atala, a urologist at Wake Forest University in Winston-Salem, North Carolina, who has implanted bio-engineered bladders into patients<sup>3</sup> and is working on building kidneys (see *Nature* <http://doi.org/dw856h>; 2006).

The leading techniques for would-be heart builders generally involve reusing what biology has already created. One good place to see how this is done is Massachusetts General Hospital in Boston, where Harald Ott, a surgeon and regenerative-medicine researcher, demonstrates a method that he developed while training under Taylor in the mid 2000s.

Suspended by plastic tubes in a drum-shaped chamber made of glass and plastic is a fresh human heart. Nearby is a pump that is quietly pushing detergent through a tube running into the heart’s aorta. The flow forces the aortic valve closed and sends the detergent through the network of blood vessels that fed the muscle until its owner died a few days before. Over the course of about a week, explains Ott, this flow of detergent will strip away lipids, DNA, soluble proteins, sugars and almost all the other cellular material from the heart, leaving only a pale mesh of collagen, laminins and other structural proteins: the ‘extracellular matrix’ that once held the organ together.

The scaffold heart does not have to be human. Pigs are promising: they bear all the crucial components of the extracellular matrix, but are unlikely to carry human diseases. And their hearts are rarely

weakened by illness or resuscitation efforts. “Pig tissues are much safer than humans and there’s an unlimited supply,” says Stephen Badyalak, a regenerative-medicine researcher at the University of Pittsburgh.

The tricky part, Ott says, is to make sure that the detergent dissolves just the right amount of material. Strip away too little, and the matrix might retain some of the cell-surface molecules that can lead to rejection by the recipient’s immune system. Strip away too much, and it could lose vital proteins and growth factors that tell newly introduced cells

where to adhere and how to behave. “If you can use a milder agent and a shorter time frame, you get more of a remodelling response,” says Thomas Gilbert, who studies decellularization at ACell, a company in Columbia, Maryland, that produces extracellular-matrix products for regenerative medicine.

Through trial and error, scaling up the concentration, timing and pressure of the detergents, researchers have refined the decellularization process on hundreds of hearts and other organs. It is probably the best-developed stage of the organ-generating enterprise, but it is only the first step. Next, the scaffold needs to be repopulated with human cells.

## THE CELLS

‘Recellularization’ introduces another slew of challenges, says Jason Wertheim, a surgeon at Northwestern University’s Feinberg School of Medicine in Chicago, Illinois. “One, what cells do we use? Two, how many cells do we use? And three, should they be mature cells, embryonic stem cells, iPS [induced pluripotent stem] cells? What is the optimum cell source?”

Using mature cells is tricky to say the least, says Taylor. “You can’t get adult cardiocytes to proliferate,” she says. “If you could, we wouldn’t be having this conversation at all” — because damaged hearts could repair themselves and there would be no need for transplants.

Most researchers in the field use a mixture of two or more cell types, such as endothelial precursor cells to line blood vessels and muscle progenitors to seed the walls of the chambers. Ott has been deriving these from iPS cells — adult cells reprogrammed to an embryonic-stem-cell-like state using growth factors — because these can be taken from a patient in need and used to make immunologically matched tissues.

In principle, the iPS-cell approach could provide the new heart with its full suite of cell types, including vascular cells and several varieties of heart-muscle cell. But in practice, it runs into its own problems. One is the sheer size of a human heart. The numbers are seriously underappreciated, says Ott. “It’s one thing to make a million cells; another to make 100 million or 50 billion cells.” And researchers do not know whether the right cell types will grow when iPS cells are used to recapitulate embryonic development in an adult heart scaffold.

As they colonize the scaffold, some of the immature cells will take root and begin to grow. But urging them to become functional, beating cardiomyocytes requires more than just oxygenated media and growth



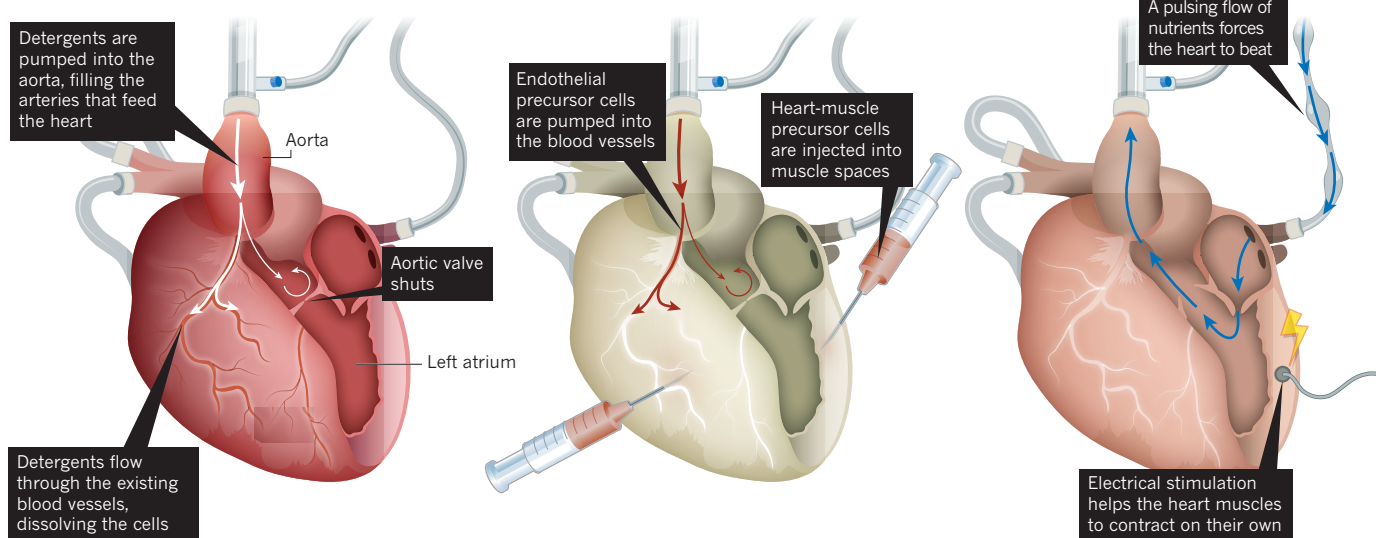
A decellularized human heart awaits rebuilding with an injection of precursor cells.

## ➔ NATURE.COM

To see an experiment with a partially decellularized heart: [go.nature.com/mjnrlg](http://go.nature.com/mjnrlg)

## CUSTOMIZED ORGANS

To construct a new heart, researchers first remove all cells from a donor organ (left), leaving a protein scaffold. That is seeded with cells (centre), which mature under the influence of growth factors and mechanical stimulation (right).



NIK SPENCER/NATURE

factors. “Cells sense their environment,” says Angela Panoskaltsis-Mortari, who has been trying to build lungs for transplant at the University of Minnesota in Minneapolis. “They don’t just sense the factors. They sense the stiffness and the mechanical stress,” which in turn pushes the cells down their proper developmental path.

So researchers must put the heart into a bioreactor that mimics the sensation of beating. Ott’s bioreactors use a combination of electrical signals — akin to a pacemaker — to help to synchronize the beating cardiomyocytes seeded on the scaffold, combined with physical beating motions induced by a pump (see ‘Customized organs’). But researchers face a constant battle in trying to ape the conditions present in the human body, such as changes in heart rate and blood pressure, or the presence of drugs. “The body reacts to things and changes the conditions so quickly it’s probably impossible to mimic that in a bioreactor,” says Badyalak.

When Taylor and Ott were first developing bioreactors, for decellularized and repopulated rat hearts, they had to learn as they went along. “There was a lot of duct tape in the lab,” Ott says. But eventually the hearts were able to beat on their own after eight to ten days in the bioreactor, producing roughly 2% of the pumping capacity of a normal adult rat heart<sup>1</sup>. Taylor says that she has since got hearts from rats and larger mammals to pump with as much as 25% of normal capacity, although she has not yet published the data. She and Ott are confident that they are on the right path.

### THE BEAT

The final challenge is one of the hardest: placing a newly grown, engineered heart into a living animal, and keeping it beating for a long time.

The integrity of the vasculature is the first barrier. Any naked bit of matrix serves as a breeding ground for clots that could be fatal to the organ or the animal. “You’re going to need a pretty intact endothelium lining every vessel or you’re going to have clotting or leakage,” says Gilbert.

Ott has demonstrated that engineered organs can survive for a time. His group has transplanted a single bioengineered lung into a rat, showing that it could support gas exchange for the animal, but the airspace fairly quickly filled with fluids<sup>4</sup>. And an engineered rat-kidney transplant that Ott’s group reported early this year survived without clotting, but had only minimal ability to filter urine, probably because the process had not produced enough of the cell types needed by the kidney<sup>5</sup> (see *Nature* <http://doi.org/m2r>; 2013). Ott’s team and others have implanted reconstructed hearts into rats, generally in the neck, in the abdomen or alongside the animal’s own heart. But although the researchers can feed

the organs with blood and get them to beat for a while, none of the hearts has been able to support the blood-pumping function. The researchers need to show that a heart has much higher ability to function before they can transplant it into an animal bigger than a rat.

With the heart, says Badyalak, “you have to start with something that can function pretty well” from the moment the transplant is in place. “You can’t have something pumping just 1 or 2 or 5% of the ejection fraction of the normal heart and expect to make a difference,” he says, referring to a common measure of pumping efficiency. There is little room for error. “We’re just taking baby steps,” says Panoskaltsis-Mortari. “We’re where people were with heart transplant decades ago.”

The decellularization process being cultivated by Ott and others is already informing the development of improved tissue-based valves and other parts of the heart and other organs. A bioengineered valve, for example, may last longer than mechanical or dead-tissue valves because they have the potential to grow with a patient and repair themselves. And other organs may not need to be replaced entirely. “I’d be surprised if within the next 5–7 years you don’t see the patient implanted with at least part of an artery, lobes of a lung, lobes of a liver,” says Badyalak.

Taylor suspects that partial approaches could aid patients with severe heart defects such as hypoplastic left heart syndrome, in which half the heart is severely underdeveloped. Restoring the other half, “essentially forces you to build the majority of the things you need,” she says.

And these efforts could hold lessons for the development of cell therapies delivered to the heart. Researchers are learning, for example, how heart cells develop and function in three dimensions. In the future, partial scaffolds, either synthetic or from cadavers, could allow new cells to populate damaged areas of hearts and repair them like patches.

The jars of ghostly floating organs might seem like a gruesome echo of the Frankenstein story, but Taylor says her work is a labour of love. “There are some days that I go, ‘Oh my god, what have I gotten into?’ On the other hand, all it takes is a kid calling you, saying ‘Can you help my mother?’ and it makes it all worthwhile.” ■ **SEE EDITORIAL P.6**

**Brendan Maher** is a features editor for *Nature* based in New York.

- Ott, H. C. *et al.* *Nature Med.* **14**, 213–221 (2008).
- Zopf, D. A., Hollister, S. J., Nelson, M. E., Ohye, R. G. & Green, G. E. *N. Engl. J. Med.* **368**, 2043–2045 (2013).
- Atala, A., Bauer, S. B., Soker, S., Yoo, J. J. & Retik, A. B. *Lancet* **367**, 1241–1246 (2006).
- Ott, H. C. *et al.* *Nature Med.* **16**, 927–933 (2010).
- Song, J. J. *et al.* *Nature Med.* **19**, 646–651 (2013).



# COMMENT



**SPACE** An elegy for the disappearing dark, banished by science **p.26**

**ART** Exhibition reveals in the power of unconstrained thought **p.28**

**GENES** US Supreme Court patent rulings set a higher bar for innovation **p.29**

**OBITUARY** Heinrich Rohrer, pioneer of scanning tunnelling microscopy, remembered **p.30**

CARLOS ORTEGA/EPA/CORBIS



The International Center for Tropical Agriculture in Colombia holds 65,000 crop samples from 141 countries.

## Feeding the future

We must mine the biodiversity in seed banks to help to overcome food shortages, urge **Susan McCouch** and colleagues.

Humanity depends on fewer than a dozen of the approximately 300,000 species of flowering plants for 80% of its caloric intake. And we capitalize on only a fraction of the genetic diversity that resides within each of these species. This is not enough to support our food system in the future. Food availability must double in the next 25 years to keep pace with population and income growth around the world. Already, food-production systems are precarious in the face of intensifying demand, climate change, soil degradation and water and land shortages.

Farmers have saved the seeds of hundreds of crop species and hundreds of thousands of 'primitive' varieties (local domesticates called

landraces), as well as the wild relatives of crop species and modern varieties no longer in use. These are stored in more than 1,700 gene banks worldwide. Maintaining the 11 international gene-bank collections alone costs about US\$18 million a year.

The biodiversity stored in gene banks fuels advances in plant breeding, generates billions of dollars in profits, and saves many lives. For example, crossbreeding a single wild species of rice, *Oryza nivara*, which was found after screening more than 6,000 seed-bank accessions, has provided protection against grassy stunt virus disease in almost all tropical rice varieties in Asia for the past 36 years<sup>1</sup>. During the green revolution, high-yielding rice and wheat varieties turned India into a net

food exporter. By 1997, the world economy had accrued annual benefits of approximately \$115 billion from the use of crop wild relatives<sup>2</sup> as sources of environmental resilience and resistance to pests and diseases.

The time is ripe for an effort to harness the full power of biodiversity to feed the world. Plant scientists must efficiently and systematically domesticate new crops and increase the productivity and sustainability of current crop-production systems.

Why does plant breeding need a boost? Because new, high-yielding seeds that are adapted for future conditions are a cornerstone of sustainable, intensified food production<sup>3</sup>. Since the mid-1990s, progress in conventional plant breeding has ►



► slowed, despite the phenomenal yield gains of the past. Part of the reason is that only the tip of the biodiversity iceberg has been explored and used<sup>4</sup>.

Crop wild relatives, landrace varieties and previously undomesticated wild species represent sources of new variation for agriculture. Such plants have survived repeated and extreme environmental challenges, yet their resilience and adaptive capacity remain largely untapped and poorly understood. A wealth of genetic information has been left behind throughout the history of plant domestication and scientific crop improvement. It must now be deployed.

Plant breeders often worry that using wild species or landrace varieties is too risky, scientifically and economically. It took 20 years and 34,000 attempts to cross a domesticated rice variety with a distantly related, highly salt-tolerant wild relative from India before fertile offspring were obtained<sup>5</sup>. It will now take at least 4–5 years of breeding to eliminate unwanted wild characters to generate a new high-yielding, salt-tolerant rice variety (see [go.nature.com/knzt15](http://go.nature.com/knzt15)). That is too long for most plant-breeding programmes, especially in the private sector.

Insufficient genetic and phenotypic information about most of the holdings in gene banks makes plant breeders even more reluctant. Politics has also created obstacles. The Convention on Biological Diversity (see [go.nature.com/njhon](http://go.nature.com/njhon)) is an international treaty that, although vital for consolidating efforts to conserve the diversity of life on Earth, has created significant barriers to the sharing of genetic material, including of domesticated plants and their wild relatives<sup>4</sup>.

Happily, things are changing. The International Treaty on Plant Genetic Resources for Food and Agriculture<sup>6</sup> (ITPGRFA), negotiated in 2004, now governs access to crop diversity. It mandates that a portion of any monetary benefits derived from the commercialization of products from gene-bank materials is put into a fund that supports conservation and sustainable use of crop genetic resources.

On the technical front, we are now able to use a plant's genetic make-up to predict its agronomic potential and traits. Plant breeders commonly use genetic markers to identify individual plants carrying specific genes for disease and pest resistance or stress tolerance, without ever exposing the plants to the relevant agents. Breeders can use genome-wide approaches to eliminate 70–80% of individuals in any generation without having to invest in laborious multi-environment field testing.

### THREE STEPS

How should we begin to mine biodiversity for food security? A logical first step is to obtain a sample of sequence information from the genomes of all non-duplicate plant

samples in the world's gene banks that are available under the terms and conditions of the ITPGRFA — perhaps up to 2 million. This 'fingerprint' for each plant will serve as the basis for assessing genetic relationships, and will make it possible to systematically select subsets of material for in-depth investigations. Sequencing costs are plummeting, making such an effort feasible.

Sequence data provide a genomic 'parts list' that can help to decipher mechanisms that enable plants to adapt to myriad environments, and can guide our remodelling of cropping systems for the future. Linking sequence data with conventional 'passport information' about collection locality and original environment should call attention to the genetic potential of many hidden crop resources.

Second, we must analyse the phenotypes of gene-bank accessions to evaluate their traits and overall performance. This is the most intellectually challenging, complex, costly and time-consuming stage. We cannot hope to evaluate all gene-bank accessions in all relevant environments, even with the advent of high-throughput phenotyping technologies. Using sequence data in combination with phenotypic, geographical and ecological information will enable researchers to target field experiments strategically and to develop models that can predict plant performance. This will make plant breeding faster, more efficient and cheaper.

Assessing the breeding potential of unfamiliar plant materials typically requires them to be crossed with modern, 'elite' varieties. Their offspring are then evaluated in environments of interest to farmers and breeders, over several years. Often, the genetics of high-performing offspring can be traced back to DNA inherited from wild or landrace donors that are agriculturally less productive. For example, the wild tomato species *Solanum pennellii* was used to double commercial tomato yields under a wide range of growing conditions<sup>7</sup>, and the wild rice species *Oryza rufipogon* increased yields of elite varieties of rice by more than 25% (ref. 8). Thus, useful genetic traits are moved across the breeding barrier, expanding the genetic diversity of domesticated plants and opening up new opportunities for environmental resilience and future gains in quality and yield<sup>4</sup>.

A third key step is to create an internationally accessible informatics infrastructure to catalogue the diversity in the world's seed collections. This would link seeds and genetic stocks directly to passport, genomic and phenotypic information<sup>9</sup>, thereby engaging the creativity of geneticists and breeders

and fuelling plant improvement for years to come. This requires an unprecedented effort in data management and sharing. Today, seed data are typically recorded and managed by different people, such as gene-bank curators, agronomists and breeders, often in different institutions and in different database systems.

But it is doable. The Global Biodiversity Information Facility (GBIF) — an online network that facilitates open access to "information about the occurrence of organisms" — provides a good example of such an infrastructure and has changed how biodiversity is studied. But the GBIF does not currently handle the complex genomic data necessary for our efforts.

Most importantly, results from genomics and agronomic research must be connected to the communities that are creating new varieties of crops. An international network of scientists in both the public and the private sectors must work together to provide seeds and plants to farmers and commercial plant breeders for further crossing and testing in different environments. The research community must pay specific attention to the development of locally adapted varieties that meet the needs of the world's poorest farmers.

How much would such a systematic, concerted, collaborative global effort to feed the future cost? We estimate around \$200 million annually. This seems like great value, given that as a society we have spent \$3 billion on sequencing the human genome, \$9 billion on constructing CERN's Large Hadron Collider near Geneva in Switzerland (plus about \$1 billion a year in running costs) and can spend up to \$180 million on a single fighter jet.

After all, as the ecologist Charles Godfray put it: "If we fail on food, we fail on everything". ■

**Susan McCouch** is professor of plant breeding and genetics and of plant biology at Cornell University, Ithaca, New York. e-mail: [mccouch@cornell.edu](mailto:mccouch@cornell.edu)

On behalf of attendees and organizers of the Crop Wild Relative Genomics meeting held in Asilomar, California, in December 2012. See [go.nature.com/nrpoe3](http://go.nature.com/nrpoe3) for full author list.

1. Plucknett, D. L. et al. *Gene Banks and the World's Food* (Princeton Univ. Press, 1987).
2. Pimentel, D. et al. *BioScience* **47**, 747–757 (1997).
3. Godfray, H. C. J. et al. *Science* **327**, 812–818 (2010).
4. Tanksley, S. D. & McCouch, S. R. *Science* **277**, 1063–1066 (1997).
5. Jena, K. K. et al. *Rice Genet. Newsl.* **11**, 78–79 (1994).
6. Food and Agriculture Organization. *International Treaty on Plant Genetic Resources for Food and Agriculture* (FAO, 2009); available at <http://go.nature.com/ikflqh>.
7. Gur, A. & Zamir, D. *PLoS Biol.* **2**, e245 (2004).
8. Imai, I. et al. *Mol. Breed.* **32**, 101–120 (2013).
9. Zamir, D. *PLoS Biol.* **11**, e1001595 (2013).





The Milky Way lights up the night sky above the Navajo trail in Bryce Canyon, Utah.

## ENVIRONMENTAL SCIENCE

# Hymn to fading stars

An exploration of humanity's compulsion to banish darkness is highly enlightening, finds **Tim Radford**.

Here is a paradox: the brilliance of the Enlightenment happened by candlepower. Clarity of vision came courtesy of the dark. The enigmatic night sky must have gleamed everywhere as the giants of the post-Copernican revolution stumbled home from their learned societies. In Birmingham in the English Midlands in the late eighteenth century, Matthew Boulton, James Watt, Erasmus Darwin, Joseph Priestley and Benjamin Franklin met by the full Moon, calling themselves the Lunar Society. The astonishing adventure of science has now almost eliminated true darkness. And for that huge and growing portion of humanity living in cities, it has bleached the night sky of all but a handful of stars.

As Paul Bogard shows in his hymn to vanished darkness, *The End of Night*, this electric overdose comes at a high cost. It may be linked to sleep disorders, changes in migratory behaviour in birds and insects, stress and exhaustion in shift workers, and

even obesity.

Bogard's book is a literary journey — in the space of a few pages, we walk with Virginia Woolf, Charles Dickens and Rétif de la Bretonne. It is also a pilgrimage to our capitals of light. We visit London, with its 1,600 surviving gas lamps; Paris, where 110,000 4.5-watt bulbs illuminate just one courtyard in the Louvre Museum; and Broadway's 'Great White Way' in New York. Bogard hunts true darkness, too: places far from security lights, where nights are so clear and dark that the stars begin to reveal subtle gem-like colours, and the Milky Way emerges as a sight of depth and structure. He goes beyond the broad



**The End of Night: Searching for Natural Darkness in an Age of Artificial Light**  
PAUL BOGARD  
Little, Brown: 2013

splashes of electric brilliance now smeared across continents, seeking places where darkness is conserved and sponsored by bodies such as the International Dark Sky Association in Tucson, Arizona, and the Night Sky Team of the US National Park Service. Bogard dines in Mantua, Italy, with one of the makers of the first world atlas of artificial night sky brightness (see P. Cinzano *et al.* *Mon. Not. R. Astron. Soc.* **328**, 689–707; 2001). He sets off with amateur astronomers in darkest England and the United States. In Las Vegas, Nevada, where the brightest beam on Earth lights up the sky from the apex of the Luxor casino, he still — just — glimpses Rigel and Betelgeuse in the Orion constellation, and Sirius. He talks to researchers and engineers on two continents about the urban compulsion for brightness. Any evidence that ever brighter security lights equal ever greater security is dismissed as dubious: glare creates shadows in which predators can hide. Bogard and his interlocutors also conclude that we may in

WALLY PACHOLKA/ASTROPICS.COM



any case be surrendering to an ancient fear of the dark. The European Union alone, he reports, is estimated to waste €1.7 billion (US\$2.2 billion) a year on needless outdoor lighting.

Bogard visits New York's Museum of Modern Art to contemplate the testimony of Vincent van Gogh's 1889 painting *The Starry Night* and, as a counterweight, Giacomo Balla's 1909 *Street Light* ("Let's kill the moonlight!" was a rallying cry for Italian Futurists). Bogard explores the biology of vision, the capacity of eyes to adjust to ever lower levels of light and the concept of 'seeing' — the odd term stargazers use to record the atmospheric turbulence that makes stars twinkle. He tries to experience the darkness celebrated by Henry David Thoreau at Walden Pond in Concord, Massachusetts, but is stymied by the glow now emanating from the town.

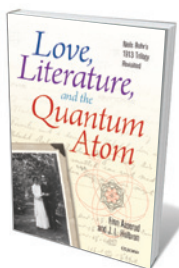
Bogard becomes a midnight sensualist. He goes into Death Valley in California and Nevada, and, training binoculars on the night sky, suddenly feels "as though I'm falling. I have to pull away to find my balance in the dark. The ground on which I'm standing, the cloth of stars above. The great nebula in Orion's belt, the Pleiades, Jupiter so bright and clear it makes me laugh." He visits the Mont-Mégantic Starry Sky Reserve in Quebec Province, Canada, where local communities have turned darkness into astrotourism. (Sadly, the sky is occluded by fog.)

He also considers the victims of 'white nights': prisoners locked in an eternal glare, shift workers trapped in a cycle of sleeplessness, and what you might call electric roadkill. In North America, some 500 species migrate by night and the catalogues of death by electrocution have been enough to trigger a Fatal Light Awareness Programme (FLAP). He cites the murderous night when 50,000 birds followed a beam of light from a Georgia airport straight into the ground and the night when 1,500 migrating grebes in Utah were confused by lights reflected from clouds "and crashed into parking lots they mistook for ponds".

This is a rich book with a rewarding appendix of notes. The straining for descriptive effect occasionally obtrudes; Bogard teaches creative non-fiction to university students, so he will know Samuel Johnson's advice about striking out the fine writing. The book's ambitious scope also necessarily dictates a sacrifice of depth. But these are small things. The big thing is that, as you read it, you too will want to reclaim the night and perhaps rediscover the heavens of the Enlightenment. ■

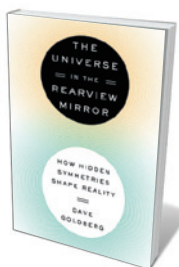
**Tim Radford** is the author of *The Address Book: Our Place in the Scheme of Things*. He was science editor of *The Guardian* until 2005.  
e-mail: [radford.tim@gmail.com](mailto:radford.tim@gmail.com)

## Books in brief



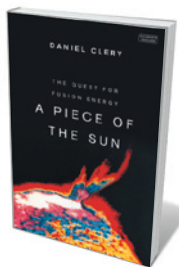
### Love, Literature, and the Quantum Atom: Niels Bohr's 1913 Trilogy Revisited

Finn Aaserud and John L. Heilbron OXFORD UNIVERSITY PRESS (2013)  
Science historian John Heilbron analyses the cultural underpinnings of physicist Niels Bohr's creativity. Bohr's immersion in works by Søren Kierkegaard and other greats of literature and philosophy fed the wellsprings of his quantum atom theory, argues Heilbron (see *Nature* **498**, 27–30; 2013). This is a unique contribution to the fanfare around the centenary of Bohr's theory: it incorporates archivist Finn Aaserud's assemblage of previously unpublished letters between Bohr and his family, and a reprint of Bohr's 'Trilogy' of papers.



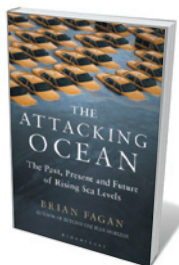
### The Universe in the Rearview Mirror: How Hidden Symmetries Shape Reality

Dave Goldberg DUTTON (2013)  
Who knew symmetry could be so brilliantly entertaining? Physicist Dave Goldberg slings the reader straight in at the deep end of this big physics concept, but with enough masterly wit to keep you afloat. If you've ever longed to know the nitty-gritty on antimatter; puzzled over the exclusion principle; woken up in a cold sweat wondering why you are not a "sentient cloud of helium"; gritted your teeth over the cosmological principle; or been terrified by the beasts of the 'particle zoo', this is for you.



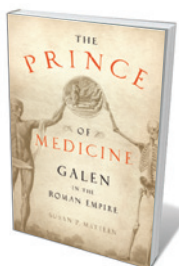
### A Piece of the Sun: The Quest for Fusion Energy

Daniel Clery DUCKWORTH (2013)  
"Fusion seems too good to be true," notes Daniel Clery. But for researchers in this field, making the 'perfect' energy source a reality is central to a power-hungry age. Clery chronicles the march of fusion projects and innovative physicists from the 1940s on. From Peter Thonemann's work on the Zero Energy Thermonuclear Assembly to Lyman Spitzer, Lev Artsimovich and later stars, we enter a prodigious realm of pinch plasmas, stellarators and tokamaks. Despite big hopes and machines to match, harnessing "a piece of the Sun" still faces economic and scientific hurdles, Clery shows.



### The Attacking Ocean: The Past, Present and Future of Rising Sea Levels

Brian Fagan BLOOMSBURY (2013)  
In his wide-ranging study of rising sea levels from the end of the last Ice Age to today, Brian Fagan traces the impact on humanity. The scattered groups that faced early thaws adapted by moving to higher ground. But the growth of populations, industrialization and coastal cities since 1860 has now left hundreds of millions at risk from the sea's climate-driven climb. Hurricane Sandy, Fagan reminds, underlines the need for adaptation strategies and coastal defences from the United States to Bangladesh.



### The Prince of Medicine: Galen in the Roman Empire

Susan P. Mattern OXFORD UNIVERSITY PRESS (2013)  
He was a Greek medic who patched up Roman gladiators — and the emperor Marcus Aurelius. The shadowy figure of Galen, whose treatises dominated Western medicine for centuries, here bursts into life. Susan Mattern shows that he used wine on wounds — although ignorant of its bactericidal properties — and contributed to anatomy (dissecting live Barbary macaques) and pharmacology. He was also arrogant, but Mattern argues that his clinical excellence in a plague-ridden era far outshone his flaws. [Barbara Kiser](#)





Paul Laffoley says viewers can absorb alien inspiration from his *Thanaton III*.

## ARTS

# Think beyond

Joanne Baker plunges into an exhibition on visionaries who break all the rules.

**W**ant to communicate with an extraterrestrial? Place your palms in the hand-shaped outlines and stare into the central disembodied eye of Paul Laffoley's painting *Thanaton III* (1989). The US artist and architect maintains that the graphics, mandalas and symbols gracing the lower part of the canvas were passed on to him by an alien called Quazgaa Klaatu. By touching the painting, Laffoley suggests, you too may absorb that information.

Time travellers and savants are also among the 22 visionaries whose remarkable works are on show at London's Hayward Gallery. The *Alternative Guide to the Universe* exhibition celebrates artists whose ideas lie beyond the mainstream, but are often directed towards solving real-world problems. Following a spate of exhibitions that explore the notions of 'fringe' scientists, inventors and architects — notably at the Wellcome Collection in London and the Institute For

Figuring in Los Angeles, California (see *Nature* 479, 40; 2011) — this wide-ranging show reveals how the power of unconstrained thought might be used for healing, theorizing and utopia-building.

Many of the concepts bear reflection. Laffoley's alien 'speaks' in scientific terms, an assumption also central to the work of the SETI (Search for Extraterrestrial Intelligence) project. And although the alternative quantum theories depicted would never be accepted by a physics journal, they are built around conventional physical concepts such as oscillations and loops. The exhibition's greatest value lies in giving the green light to out-of-the-box thinking.

Architecture steals the show. Most ingenious is Laffoley's proposed design for Das Urpflanze Haus (the primordial plant house),

## ALTERNATIVE GUIDE TO THE UNIVERSE

HAYWARD GALLERY  
London. Until 26 August.

an organic structure that can be grown from genetically altered seeds. Inspired by Johann Wolfgang von Goethe's 1790 description of the archetypal plant, or Urpflanz, as the basis for all botanic growth and form, Laffoley imagines bioengineering a ginkgo tree — one of the oldest known fruiting plants — to sprout pods that people could live in.

He suggests that the high electrical potential of spinach could be harnessed to power such a home and that bioluminescence could light it. This idea is not entirely fanciful: architects and synthetic biologists are already working together on carbonate shells and bioluminescent lighting for buildings (see *Nature* 467, 916–918; 2010).

Laffoley, who *The New York Times* called "one of the most unusual creative minds of our time", believes we are entering a new phase of modernism that will entail an architecture that is physically alive. He calls it the Bauharoque, mixing the Bauhaus school of design's utopian ideals with the theatricality of Baroque art and architecture.

This aesthetic is shared by Canadian architect Richard Greaves's human nests, in which windows dangle and branches and beams canoodle. Greaves doesn't use nails, but binds his cabins with rope so that the structures can move. His precarious shelters, made in a Canadian field from recycled wood and salvaged architectural materials, are on show in photographs and a model.

Equally motile and dramatic are walking, jumping, wall-climbing robot dolls by Wu Yulu, a Chinese farmer and self-taught roboticist. Their shabby, child-like appearance seems more humane than shiny plastic and metal cyborgs, or the robot cosmonauts sketched in the 1950s and 60s by French civil engineer Jean Perdrizet that are also on show.

Physics and maths receive a fresh take here. Philip Blackmarr depicts his 'quantum geometry' in pen-and-ink drawings of vibrating sinusoidal waves so precise that they resemble computer printouts. Connections between the Mayan and Chinese number systems and Goethe's colour theory are explored in rainbow chequerboard paintings by American artist Alfred Jensen. George Widener, a professed 'time traveller' and autistic, can tell immediately what day of the week any future date will fall on, and turns dates into intricate sketches of magic number squares and cities.

Any scientist visiting this alternative universe will find themselves, as I did, poring over blueprints to try to figure out how the machines depicted work, or discerning the mathematical patterns behind the painted squares. Given how much we still don't know, this show importantly asks: are you sure your universe is the right one? ■

Joanne Baker is senior comment editor at *Nature*.

PAUL LAFFOLEY/PHOTO BY LINDA NYLIND

# Correspondence

## US patent rulings will fuel invention

On 13 June, the US Supreme Court denied the validity of patenting genes (*Nature* **498**, 281–282; 2013) — but this is only part of the story. Since 2010, the court has made three separate landmark rulings that give inventors full access to the wellspring of ideas, laws of nature and natural products.

Patent law requires ingenuity and invention for patenting a discovery. The Supreme Court established in 1980 that genetically modifying cells to eat oil, resist pesticides or produce insulin, for example, was a patentable invention.

After the draft human genome was released in 2001, the US Patent and Trademark Office stipulated that only genes of known function could be patented. Into this category fell *BRCA1* and *BRCA2*, the genes mutated in some breast and ovarian cancers, which were patented by the Utah firm Myriad Genetics. But questions arose — hadn't the firm simply extracted a natural product? Did it 'own' the genetic information within?

The court subsequently ruled that a patent that pre-empts all uses of a natural product was disallowed (I was a plaintiff in the case). In separate cases in 2010 and 2012, it also ruled against patents that pre-empt all uses of an abstract idea or of a natural law.

I disagree that these rulings could stifle US innovation: they set a higher bar for genuine invention so that people will gain from better medicines and devices. And they will retain ownership of their genomes.  
**Harry Ostrer** *Albert Einstein College of Medicine, New York, USA.*  
[harry.ostrer@einstein.yu.edu](mailto:harry.ostrer@einstein.yu.edu)

## Will China expand on its carbon trading?

China's current pilot schemes for carbon-emissions trading are the forerunners to a nationwide

carbon market slated for 2016 (*Nature* **498**, 145–146; 2013). This has prompted international speculation that China might adopt an absolute cap on national emissions by 2020. We contend that future Chinese climate policy is unlikely to rely mainly on cap and trade, and so will not depend on the success of pilot schemes.

In our view, the schemes are not likely to deliver a carbon price that reflects its social cost or provides an incentive for long-term investment in low-carbon technologies. The government may bring in other instruments in parallel (such as carbon taxes or mandatory emissions standards), which would distort the carbon price in China as they have in Europe.

The Chinese government should not allow the carbon prices emerging from its pilot trading schemes to distract attention from the real costs of moving to a low-carbon economy.  
**Xi Liang, Francisco Ascuí** *University of Edinburgh, UK.*  
[xi.liang@ed.ac.uk](mailto:xi.liang@ed.ac.uk)  
**David Reiner** *University of Cambridge, UK.*

## Protection for trade of precious rosewood

Madagascar's rosewood trees (*Dalbergia* spp.), prized for their hard, burgundy-coloured wood, are under threat after being exploited to make high-quality furniture and musical instruments.

Earlier this year, rosewoods won greater trade protection at the Convention on International Trade in Endangered Species of Wild Fauna and Flora (CITES) conference in Bangkok. The challenge now, as for CITES designations globally, is to implement and enforce this protection.

Despite previous logging and shipping bans on hardwoods from Madagascar, and even a voluntary CITES Appendix III listing of five *Dalbergia* species in 2011, illegal logging has persisted

in the wake of the country's political turmoil in 2009. The current Appendix II listing will create legal obstacles to illegal trade through a permit system that allows only non-detrimental harvesting practices.

**Meredith A. Barrett** *University of California, San Francisco, USA.*  
[barrettm@chc.ucsf.edu](mailto:barrettm@chc.ucsf.edu)  
**Jason L. Brown, Anne D. Yoder** *Duke University, Durham, North Carolina, USA.*

## Identical twins don't share fingerprints

As chair of the Forensic Identification Standards Committee of the International Association for Identification, I would like to point out an error in your obituary of Joseph Murray regarding the fingerprinting of identical twins (*Nature* **493**, 164; 2013).

Murray did ask for Richard and Ronald Herrick to be fingerprinted to determine whether they were identical before he transplanted a kidney from one to the other (J. E. Murray *Surgery of the Soul*; Watson, 2001). Yet the Boston police archives have no record of the fingerprint request or of its results (I. Truta and M. Sullivan, personal communication).

The twins' fingerprint classification codes were probably tested for similarity, although this would not indicate twinning because unrelated people often share the same classification code. I could find no evidence that "the twins' fingerprints were identical", as the obituary states. Had they been, I am confident that forensic science would have taken notice in 1954.

Different people, including genetically indistinguishable twins, do not deposit identical fingerprints (see, for example, X. Tao *et al.* *PLoS ONE* **7**, e35704; 2012).

**John R. Vanderkolk** *Indiana State Police Laboratory, Fort Wayne, Indiana, USA.*  
[vanderkolkjohn@yahoo.com](mailto:vanderkolkjohn@yahoo.com)

## Latin America should ditch impact factors

Increased reliance on impact factors to evaluate scientific merit is having negative social and environmental effects in Latin America. We should abandon these indicators and concentrate on strengthening regional and national journals and networks for socially and locally relevant research.

Impact-factor rankings have damaged the region for several reasons. Because impact factors are generally low for conservation and ecology articles (compared with those in, say, biotechnology or medicine), these disciplines attract proportionately less funding. Top-tier journals tend to focus on global environmental issues to boost citation rates, at the expense of regionally important ones. And theoretical-ecology journals have higher impact factors than applied-ecology journals.

Together, these metrics are diverting researchers away from regional problems even as socio-ecosystems deteriorate around them. The South American biogeographic region comprises 10% of Earth's surface and hosts 50% of its biodiversity, yet the continent contributed less than 4% of global scientific output in 2010 (see [go.nature.com/hudjwn](http://go.nature.com/hudjwn); in Spanish).

We suggest that Latin America should aim to achieve a genuine knowledge dialogue (see [go.nature.com/ifrnlx](http://go.nature.com/ifrnlx); in Spanish) through confronting regional challenges, rather than focus on increasing its global "brain circulation" (*Nature* **490**, 325; 2012).

**Adrian Monjeau** *Fundación Bariloche; and CONICET, Argentina.*  
[amonjeau@gmail.com](mailto:amonjeau@gmail.com)

**Jaime R. Rau** *University of Los Lagos, Osorno, Chile.*

**Christopher B. Anderson** *CADIC-CONICET; and National University of Tierra del Fuego, Ushuaia, Argentina.*



# Heinrich Rohrer

## (1933–2013)

Co-inventor of the scanning tunnelling microscope.

Heinrich Rohrer, Heini to those who knew him, helped to open the door to nanotechnology. With Gerd Binnig, he produced a device that allowed researchers to image and measure atoms and molecules, and to manipulate them.

Rohrer, who died on 16 May, three weeks before his 80th birthday, was born in 1933, half an hour after his twin sister. He grew up in the village of Buchs in eastern Switzerland. Rohrer studied physics at the Swiss Federal Institute of Technology (ETH) in Zurich, where he remained to pursue a PhD. It was during his PhD years that he first came into contact with the nanometre scale, through studying the properties of superconductors.

After receiving his PhD in 1960, Rohrer pursued a two-year postdoctoral research fellowship at Rutgers University in New Jersey, working on superconductors and metals. At the end of 1963, he joined the IBM Research Laboratory in Rüschlikon, Switzerland, on the recommendation of various peers including physicist Bruno Lüthi, who had worked alongside Rohrer at the ETH.

Towards the end of the 1960s, Rohrer began working on an antiferromagnet called gadolinium aluminate ( $\text{GdAlO}_3$ ) in collaboration with Keith Blazey, another physicist at the IBM lab. Antiferromagnetism is a type of magnetic ordering that vanishes at a certain temperature. The work brought Rohrer into the field of critical phenomena and led to crucial findings about magnetic phase transitions. By this point, the group at the IBM lab had established a world-renowned reputation in critical phenomena, after K. Alex Müller — then head of physical science — had pioneered the field of structural phase transitions.

In the late 1970s, Rohrer's interest shifted towards the complex structure of surface materials. In building ever-faster computers, the semiconductor industry was rapidly approaching the design of chips on the nanoscale. Yet few tools were available to study the structure and properties of materials at this scale. In 1978, Rohrer insisted that the IBM lab hire Gerd Binnig, a young German physicist from Frankfurt University, and the two started to

contemplate a new device. By 1981, the pair had designed the world's first scanning tunnelling microscope (STM).

Unlike conventional microscopes, the STM did not use lenses. Instead, a probe sharpened to a single atom at the tip was

eventually verified by other groups and presented at a workshop on the STM in the Austrian Alps in 1985. Devices such as the atomic force microscope (AFM) — a very high resolution type of scanning microscope that measures the atomic forces between the

tip of a probe and the surface being scanned — have their roots in this meeting. During the last night of the workshop, the mountains were abuzz with crazy ideas about how such microscopes might be used in applications in all sorts of fields, from fundamental physics and chemistry to information technology, quantum computing and molecular electronics, as well as in the life sciences.

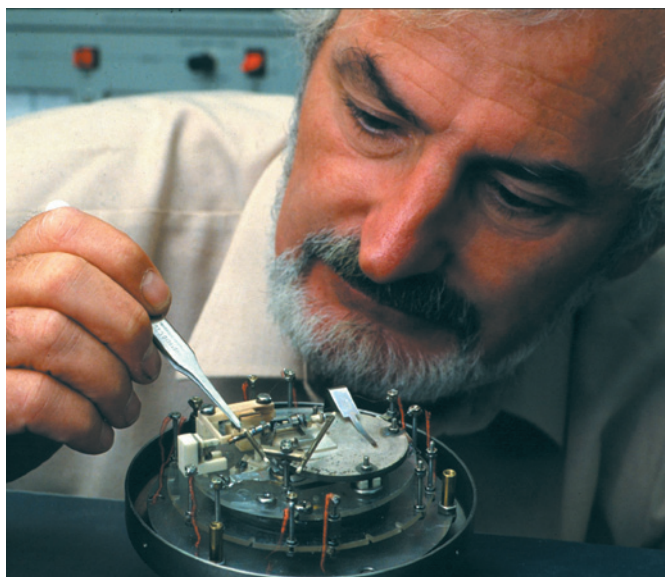
In 1986, Rohrer and Binnig shared half of the Nobel Prize in Physics. The other half of the prize was given to the German physicist Ernst Ruska for inventing the scanning electron microscope, a device that produces images of a sample by scanning it with a focused beam of electrons.

With the emergence of scanning probe microscopes (the STM and the AFM are just two among many types of these), the door to the nanoworld was pushed wide open. Today, such tools are still making a tremendous impact on numerous disciplines.

An extraordinarily charismatic man, Heini went on to promulgate nanoscience and nanotechnology to upcoming generations of researchers. I remember a lecture he gave in South Korea some years ago, which was attended by almost 4,000 high-school and university students. His captivating description of the development of the STM was followed by thunderous applause. In fact, one of the attendees recently told me that it was Heini's talk that inspired him to study physics and nanoscience.

Heini will be deeply missed as a natural leader, a visionary, a stimulating scientist and a wonderful person. He is survived by his wife Rose-Marie Egger, his two daughters Doris Rohrer Hansen and Ellen Rohrer, and two grandchildren. ■

**Christoph Gerber** collaborated with Rohrer at the IBM Research Laboratory for many years. He is at the Swiss Nanoscience Institute, University of Basel, Switzerland. e-mail: christoph.gerber@unibas.ch



moved close enough to the surface of a conductive material, such as silicon or gold, for the electron wavefunctions of the atoms in the tip to overlap with those of the atoms in the conductive surface. (Picture two overlapping electron 'clouds'.) When a voltage was applied to the tip, electrons started to 'tunnel', or 'leak', through the vacuum gap, causing a current to flow from the foremost atom of the tip into the surface.

Moving the tip by the diameter of a single atom changed the current by a factor of a thousand, giving the device its enormous resolution. As the tip was scanned back and forth, it followed the atomic structure of the surface, extending and retracting over dips and bumps. Thus, for the first time, it was possible to get up close and personal with atoms in three dimensions.

Nobody believed that Rohrer and Binnig's experiments demonstrating quantum tunnelling could ever work. A tremendous challenge was bringing the tip only 0.2 nanometres away from the surface (1 nanometre is 1 billionth of a metre). However, a cleverly designed mechanism using the forces of strong magnets did the trick.

Rohrer and Binnig's initial results were



## The cost of children

**An investigation into the causes of the decline in the number of children being born finds that economic motivations are more influential than child mortality or social learning, but also reinforces the relatedness of these factors.**

RUTH MACE

Now that my own children are teenagers and I work in a university in a large city, I can go for weeks without properly interacting with a child. This miserable and unnatural state of being is in part because the society I live in is WEIRD (Western, educated, industrialized, rich and democratic)<sup>1</sup>. But the dramatic and near-universal decline in birth rate and family size that has been one of the most pervasive social changes of the past two centuries, and that continues apace around the world, means that my situation is far from unusual. The question of why fewer babies are being born gets to the heart of what matters to us in life: do we value money, or prestige, or is it reproductive success? Writing in *Proceedings of the National Academy of Sciences*, Shenk *et al.*<sup>2</sup> attempt to disentangle the relative importance of three main classes of influence — risk and mortality, economic and investment, and cultural transmission — on fertility\*.

Demographers have traditionally placed great emphasis on the reduction in mortality as the main cause of the reproductive decline. There is no doubt that this is one driver of the transition to low birth rates, but its failure to predict all aspects of the phenomenon led some researchers to propose the cultural influence of new ideas as a major determinant. Still others have emphasized the effects of the changing costs and benefits of children in the modern world. Shenk and colleagues tried to rank these factors by using a detailed data set from a sample of women in a population that is currently changing from large to small families. This is an elegant and comprehensive study that was much needed.

The setting for the research is the Matlab region of rural Bangladesh, an area that has been the subject of demographic surveillance for many years by the International Centre for Diarrhoeal Disease Research, Bangladesh. The authors interviewed a representative sample of about 1,000 women from this wider study to investigate the relevant socio-economic variables that might be influencing their fertility decisions (Fig. 1). The study is notable for its statistical approach, which attempts to



**Figure 1 | Fertility in decline.** A woman and child from the Matlab region of Bangladesh where Shenk *et al.*<sup>2</sup> conducted research aimed at understanding why women are, on average, having fewer children than in previous decades.

compare the three groups of variables according to their relative effectiveness at predicting the data. To explain to those of us brought up on statistical tests of null hypotheses and *P* values (which my postdocs tell me are now passé), this approach represents a formal method for evaluating the relative success of defined sets of variables (models) at predicting the observed data, using likelihood theory and a measure known as the Akaike information criterion.

The authors found that the economic-and-investment model predicted fertility rates much better than either of the other two models. Their tests show that mortality variables do have a strong influence on the number of births (we have long known that dead babies are quickly 'replaced' with more births), but they seem less relevant to the more interesting question of what determines the final family size of surviving children. Correlates of cultural norms do not seem to have much predictive power. Owning farmland emerges as key, along with several other factors associated with the costs of spreading parental investment

among many offspring. The authors' results also indicate that education is very important, and is one of the things that comprise that parental investment. I have long been an advocate of heritable, transferable resources having a crucial role in fertility decline<sup>3</sup>, so am not surprised by this conclusion, but, as the authors themselves observe, the story may not be as clear cut as the statistics suggest.

It is interesting that this particular population is often held up as an example of one in which fertility declined without the usual correlates of economic development. For example, only a trivial fraction of the Bangladeshi women were in jobs requiring education, and indeed, most married women rarely left their compound. This suggests that the influence of education is more cultural than economic. However, the statistical approach chosen influences the conclusions drawn — the choice of which variables apply to each hypothesis is a key factor, and the data-sampling strategy is another. In this case, Shenk *et al.* listed education in both the economic-and-investment and

\*This News & Views article was published online on 12 June 2013.

the cultural-transmission categories, so the comparison between these two models effectively relies only on the other chosen variables (which may be less important).

It has also been argued that education itself enhances the cultural transmission of low-fertility norms<sup>4,5</sup>, but such interactions were not tested in this study. A multilevel model that incorporates locally clustered rather than randomly dispersed data would be required to identify peer-to-peer, village-level or other contextual effects<sup>6</sup>. Studies at this particular site<sup>7</sup> and elsewhere<sup>8</sup> have shown how religion influences the uptake of contraception, suggesting a significant role for cultural norms. But Shenk and colleagues did not find the influence of religion to be substantial enough — relative to education and other factors — to be included in the cultural-transmission model that was used in the overall model comparison.

One cannot rule out effects that have not been tested for.

Interacting factors make such studies challenging, even with sophisticated statistics. It is clear that cultural transmission is one of the ways by which humans learn that the costs and benefits associated with certain processes — such as raising children — have changed, or might change in the future. Thus, as Shenk *et al.* say, both economics and investment and cultural transmission are important and have complementary effects. The reproductive decisions of those of us with small families do not seem to maximize our genetic fitness, despite the numerous financial, health-related, educational and other individual benefits associated with low fertility<sup>9</sup>. This is one reason why the topic fascinates evolutionary anthropologists, and explains why they have been among the most enthusiastic to pick up the baton handed

on from demographers, and why they continue to run with it. ■

**Ruth Mace** is in the Department of Anthropology, University College London, London WC1E 6BT, UK.  
e-mail: r.mace@ucl.ac.uk

1. Henrich, J., Heine, S. J. & Norenzayan, A. *Behav. Brain Sci.* **33**, 61–83 (2010).
2. Shenk, M. K., Towner, M. C., Kress, H. C. & Alam, N. *Proc. Natl Acad. Sci. USA* **110**, 8045–8050 (2013).
3. Mace, R. *Phil. Trans. R. Soc. B* **353**, 389–397 (1998).
4. Ihara, Y. & Feldman, M. W. *Theor. Popul. Biol.* **65**, 105–111 (2004).
5. Borenstein, E., Kendal, J. & Feldman, M. *Theor. Popul. Biol.* **70**, 92–104 (2006).
6. Colleran, H. *The Evolutionary Anthropology of Fertility Decline in Rural Poland*. PhD thesis, Univ. College London (2013).
7. Munshi, K. & Myaux, J. J. *Dev. Econ.* **80**, 1–38 (2006).
8. Alvergne, A., Gurmu, E., Gibson, M. A. & Mace, R. *PLoS ONE* **6**, e22515 (2011).
9. Goodman, A., Koupil, I. & Lawson, D. W. *Proc. R. Soc. B* **279**, 4342–4351 (2012).

## PLANETARY SCIENCE

# The robustness of planet formation

**The detection of two planets in an open star cluster demonstrates that planetary systems are able to survive disruptive events, such as supernova explosions, during the dense, early stages of the life of such clusters. SEE LETTER P.55**

WILLIAM F. WELSH

On a clear night, a person admiring the heavens may see a few thousand stars. The stars are more or less randomly distributed, although some are gathered in groups known as open clusters, the most famous being the Pleiades (Fig. 1). Stars, and presumably their planets, are born in such clusters. But despite considerable effort<sup>1,2</sup>, evidence for planets in clusters is frustratingly scarce: of more than 850 planets that are currently known<sup>3</sup>, only four reside in clusters<sup>4–6</sup>. And whereas more than 10,000 stars in open clusters have been examined, before the study by Meibom *et al.*<sup>7</sup> reported on page 55 of this issue, no transiting planets had been detected\*. Transits, which are mini-eclipses that occur when a planet passes in front of its star, are especially valuable because they allow a planet's size to be estimated. Meibom and colleagues detected two sub-Neptune-sized transiting planets in the open cluster NGC 6811, out of a sample of only 377 stars. This remarkable success rate was made possible by the ultra-precise data provided by NASA's Kepler Mission<sup>8</sup>.

Dozens of open clusters are easily visible

with a small telescope, enrapturing stargazers with the sparkling of tens to thousands of stars. The stars in a cluster are all kin, born from the same parent molecular cloud — a huge mass of cold gas and microscopic grains teetering on the brink of instability. If a cloud is nudged,

it can be set down a path of cascading gravitational collapse, fragmenting into thousands of dense clumps. These condensations become smaller and smaller, heating up as they compress, until, finally, thermonuclear-fusion ignition occurs and a star is born. Leftover matter that does not form the star will continue to orbit it and may coalesce into planets.

A cluster can be far from a placid environment for planet formation. As stars pass each other, their gravity can tug on planets and planet-forming disks, and stellar winds and intense ultraviolet light from hot young stars can dissipate the star- and planet-forming cloud. The larger and denser the cluster, the more important these effects are. Although NGC 6811 is a small cluster, it is not a young one<sup>9</sup>, and this is significant. As a cluster ages, it 'dissolves' away, its stars mixing with the myriad stars of the Milky Way; sibling stars



ROBERT GENDLER

**Figure 1 | A good age.** The Pleiades star cluster is roughly 100 million years old. By contrast, the open cluster NGC 6811, within which Meibom and colleagues have detected<sup>7</sup> two transiting planets, has survived to an age of 1 billion years.

\*This article and the paper under discussion<sup>7</sup> were published online on 26 June 2013.



become spread across the Galaxy. The time that it takes for the cluster to disperse, between around 10 million and 100 million years, is generally short compared with the lifetime of most stars. But about 10% of clusters persist well beyond that age, their gravity being strong enough to slow the dispersal of the stars.

To have its current number of stars, 1 billion years after its formation, NGC 6811 must have contained a much greater number of stars in the past. Conditions would have been a lot more hostile then than they are today, with numerous stellar encounters and significant evaporation of the natal cloud by hot stars. The planets and planet-forming disks may have even endured several nearby supernova explosions. The discovery of planetary systems that have withstood this challenge tells us that planet formation is robust — nature likes to create planetary systems, and many survive the birthing process.

The planets in NGC 6811 are respectively only 2.8 and 2.9 times Earth's radius. Most of the planets found by Kepler are around this size<sup>10</sup>. The planets' orbital periods are 18 and 16 days, also common for Kepler-discovered bodies. So these two planets seem quite typical. However, Meibom and colleagues could not measure the planets' masses because the host stars were too faint, and so the authors relied on statistical arguments to validate the planets. Using the well-established BLENDER procedure described in the paper's Supplementary Information, Meibom *et al.* estimated that the chance of a planetary transit signal being a false positive was less than 0.24%. It is probably much less than this, as the authors were quite cautious in their estimates, and rightly so, as the validation depends in part on estimating the occurrence rate of planets in clusters, and this is not independently known.

An obvious limitation of the study is that it is based on only two planets in just one cluster. However, the characteristics of the stars in NGC 6811 are similar to those of non-cluster (field) stars, and the occurrence rate of planets in the cluster and in the field were both obtained from Kepler measurements. Thus, the comparison between the two rates is straightforward, without the usual contortions needed to compare surveys that have different sensitivities and biases.

Most stars are thought to have formed in clusters smaller than the primeval NGC 6811, and thus probably in calmer environments. Yet Meibom and colleagues demonstrate that the planetary properties and occurrence rate in NGC 6811 are very similar to those of field stars. This implies that dense open-cluster environments do not significantly destroy planetary systems. Kepler has observed three other clusters, two of which, NGC 6819 and NGC 6791, are considerably older than NGC 6811, and presumably had even more dense and dynamically active nascent environments. NGC 6791 is especially interesting:

a cluster this old, 7 billion to 9 billion years, is rare, particularly given its enrichment of elements heavier than helium. It will be truly fascinating to learn the planet occurrence rate in this cluster. ■

**William F. Welsh** is in the Department of Astronomy, San Diego State University, San Diego, California 92182–1221, USA.  
e-mail: [wwelsh@mail.sdsu.edu](mailto:wwelsh@mail.sdsu.edu)

#### ANCIENT DNA

## Towards a million-year-old genome

**The sequencing of a complete horse genome from a bone dating to around 700,000 years ago sheds light on equine evolution and dramatically extends the known limit of DNA survival. [SEE LETTER P.74](#)**

CRAIG D. MILLAR & DAVID M. LAMBERT

The field of ancient DNA continues to break records. Ancient DNA and genomes provide a window on the recent evolutionary past and often reveal that history is more complex than we previously thought. Following on from the work of the evolutionary biologist Allan Wilson<sup>1</sup> in the early 1980s, ancient DNA studies are now used to address three broad issues: the estimation of molecular rates of change using serially preserved samples; the testing of specific evolutionary hypotheses; and the estimation of changes in genetic diversity and population sizes through time. In this issue, Orlando *et al.*<sup>2</sup> (page 74) address the latter two concepts in their report of the complete genome sequence of a horse that lived around 700,000 years ago. This genome is almost 10 times older than the previous record, which was for a Denisovan<sup>3</sup>, an archaic human dated at approximately 80,000 years before present\*.

The Middle Pleistocene horse genome was obtained using a bone fragment recovered from Arctic permafrost at Thistle Creek, Canada. For comparison, Orlando and colleagues also sequenced the genome of a Late Pleistocene horse (from around 43,000 years before present) and a Przewalski's horse (*Equus ferus przewalskii*). The latter is considered the only remaining truly wild member of the *Equus* genus, and the new data show that it is the closest living relative of the domesticated horse. In addition, the authors sequenced the genomes of five domestic horse breeds (*Equus ferus caballus*) and a donkey (*Equus asinus*). They then used these data to estimate several

1. van Saders, J. L. & Gaudi, B. S. *Astrophys. J.* **729**, 63 (2011).
2. Perryman, M. *The Exoplanet Handbook* 109 (Cambridge Univ. Press, 2011).
3. <http://exoplanetarchive.ipac.caltech.edu>
4. Lovis, C. & Mayor, M. *Astron. Astrophys.* **472**, 657–664 (2007).
5. Sato, B. *et al. Astrophys. J.* **661**, 527–531 (2007).
6. Quinn, S. A. *et al. Astrophys. J.* **756**, L33–L37 (2012).
7. Meibom, S. *et al. Nature* **499**, 55–58 (2013).
8. Koch, D. G. *et al. Astrophys. J.* **713**, L79–L86 (2010).
9. Janes, K., Barnes, S. A., Meibom, S. & Hoq, S. *Astron. J.* **145**, 7–21 (2013).
10. Batalha, N. M. *et al. Astrophys. J. Suppl.* **204**, 24 (2013).

evolutionary and population parameters of the horse, which has been a textbook example in evolutionary biology and palaeontology since early work<sup>4</sup> in the 1950s. For example, they calculate the time to the most recent common

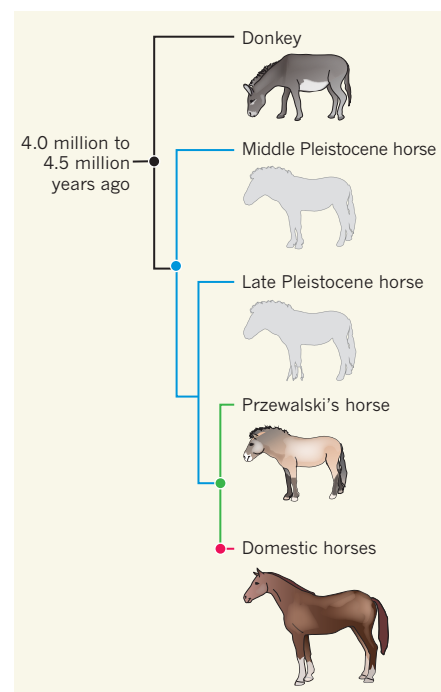


**Figure 1 | Horse origins.** Orlando and colleagues' phylogenetic reconstruction<sup>2</sup> was based on the genomes of the present-day donkey, domestic horses and the Przewalski's horse, and those derived from horse bones dating to approximately 43,000 (Late Pleistocene) and 700,000 (Middle Pleistocene) years ago. This analysis allowed the authors to estimate the time to the most recent common ancestor of all members of the *Equus* genus to be between about 4.0 million and 4.5 million years ago.

\*This article and the paper under discussion<sup>2</sup> were published online on 26 June 2013.



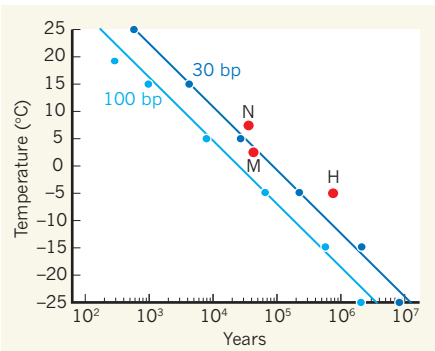


**Figure 2 | Survival of the coldest.** The rate of DNA decay varies with environmental conditions, as indicated by this plot of the estimated half-lives of 30- and 100-base-pair (bp) DNA fragments as a function of temperature<sup>7</sup>. The estimated ages and temperatures of material used to recover the genomes of a Neanderthal (N)<sup>10</sup>, a woolly mammoth (M)<sup>11</sup> and the horse fossil discovered at Thistle Creek, Canada (H)<sup>2</sup>, are shown.

ancestor of members of the *Equus* genus to be between 4.0 million and 4.5 million years ago (Fig. 1), approximately twice the previous estimate.

Orlando *et al.* went on to show that the size of the horse population has fluctuated many times over the past 2 million years, particularly during periods of severe climatic change. Interestingly, they reveal that Przewalski's horse has retained substantial genetic diversity, a feature that could be significant for the species' future conservation. Furthermore, they identify genomic regions in domesticated horses that have been under positive selection; some of these might represent genetic signatures of domestication.

But the implications of this work go well beyond the evolution of horses, by also providing evidence for the limits of DNA survival. Until this study, many experts<sup>5,6</sup> would have thought that it was impossible to recover a genome from a sample of this age because of the rapid degradation of DNA into ever shorter fragments that occurs following the death of an organism. The decay is driven initially by the body's own enzymes, and the actions of enzymes from microorganisms soon follow — death shuts down the normal defences that protect an organism against such fates. This process is, of course, affected by environmental conditions, including the presence of oxygen and water, the microorganisms present, pH and temperature. In general, the colder the environment, the slower the rate of DNA degradation (Fig. 2).

Orlando and colleagues' success is undoubtedly due to the extreme cold in which the bone resided and its resulting preservation, combined with advances in second-generation gene sequencing, including true single-molecule sequencing technology. Technical developments in DNA recovery and the construction of DNA-sequencing libraries also

contributed to the authors' achievements. From this same sample, they were able to sequence 73 proteins, including some found in blood. This illustrates that other methods apart from DNA sequencing can now be applied, on a large scale, to studies of the deep past.

So just how long can animal DNA survive? Recent work has modelled the absolute limits of DNA survival, and suggested that DNA more than 1 million years old may be recoverable from very cold environments<sup>7</sup>. Interestingly, the age of the horse genome recovered by Orlando *et al.* falls comfortably within these predicted limits of DNA survival (Fig. 2), suggesting the tantalizing proposition that complete genomes several millions of years old may be recoverable, given the right environmental conditions. Indeed, Orlando and colleagues' study encourages us to wonder if it might be possible to recover DNA from a wide range of Middle Pleistocene samples. Of particular interest would be material from ancestral human species<sup>8</sup> such as *Homo heidelbergensis* and *Homo erectus*<sup>9</sup>. Such genomic information, in combination with the Denisovan<sup>3</sup> and Neanderthal<sup>10</sup> genomes, would undoubtedly

shed light on the evolution of humans and our hominin ancestors, in much the same way as Orlando and colleagues' study provides insight into the evolution of horses and the survival of DNA itself. ■

**Craig D. Millar** is in the Allan Wilson Centre for Molecular Ecology and Evolution, School of Biological Sciences, University of Auckland, Auckland 1010, New Zealand.

**David M. Lambert** is in the Environmental Futures Centre, Griffith University, Nathan 4111, Australia.

e-mails: [cd.millar@auckland.ac.nz](mailto:cd.millar@auckland.ac.nz); [d.lambert@griffith.edu.au](mailto:d.lambert@griffith.edu.au)

1. Higuchi, R. B., Bowman, B., Freiberger, M., Ryder, O. A. & Wilson, A. C. *Nature* **312**, 282–284 (1984).
2. Orlando, L. *et al.* *Nature* **499**, 74–78 (2013).
3. Meyer, M. *et al.* *Science* **338**, 222–226 (2012).
4. Simpson, G. G. *The Meaning of Evolution* (Yale Univ. Press, 1949).
5. Lindahl, T. *Nature* **362**, 709–715 (1993).
6. Pääbo, S. *et al.* *Annu. Rev. Genet.* **38**, 645–679 (2004).
7. Allentoft, M. E. *et al.* *Proc. R. Soc. B* **279**, 4724–4733 (2012).
8. Wood, B. & Collard, M. *Science* **284**, 65–71 (1999).
9. Rightmire, G. P. *Evol. Anthropol.* **6**, 218–227 (1998).
10. Green, R. E. *et al.* *Science* **328**, 710–722 (2010).
11. Miller, W. *et al.* *Nature* **456**, 387–390 (2008).

#### CANCER

## Mutations close in on gene regulation

**A genome-wide analysis of DNA and RNA sequences, gene expression and DNA modifications in 200 samples of acute myeloid leukaemia sets the stage for data integration and verification that will enhance our understanding of this cancer.**

STEIN AERTS & JAN COOLS

**A**cute myeloid leukaemia exhibits variable genetics, presentation and clinical outcome. Writing in the *New England Journal of Medicine*, Ley and colleagues<sup>1</sup> from the Cancer Genome Atlas Research Network present the first comprehensive genome-wide analysis of DNA sequences, transcribed messenger RNA and microRNA molecules, and DNA modification by methylation, in 200 cases of adult acute myeloid leukaemia (AML). The data, which are publicly available, provide unprecedented insight into the molecular genetics of this cancer and its influence on treatment responses. Although the challenge of integrating and functionally verifying these data remains, the findings are expected to help to explain the biology of AML, and could lead to the development of therapeutic strategies.

Historically, the identification and characterization of individual genetic modifications, such as chromosomal translocations, gene

fusions and gene mutations, have fuelled our understanding of the onset and progression of AML. More recently, whole-genome and whole-exome sequencing studies have further refined this view, identifying mutations in genes in which they were not expected, such as *DNMT3A*, *IDH1*, *PHF6* and *SMC3*. (The exome is the portion of the genome comprising exon sequences — those that form mature mRNA molecules.) Now that our knowledge of DNA-sequence mutations in AML has advanced, it is time for greater integration of this information with data on gene expression.

Deregulation of gene expression is central to cancer development. For example, many cancer-related mutations result in reduced expression of genes that are associated with apoptotic cell death or cell senescence, or alter the expression of genes involved in cell proliferation and differentiation. These changes are often caused by perturbed activity of proteins involved in transcriptional control. Understanding the role of gene expression in

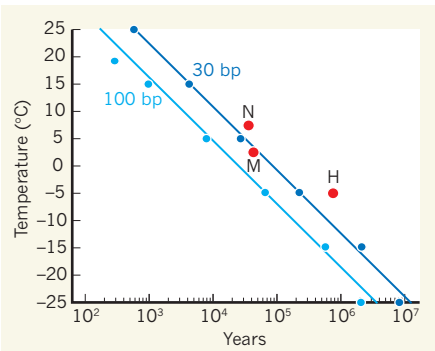


**Figure 2 | Survival of the coldest.** The rate of DNA decay varies with environmental conditions, as indicated by this plot of the estimated half-lives of 30- and 100-base-pair (bp) DNA fragments as a function of temperature<sup>7</sup>. The estimated ages and temperatures of material used to recover the genomes of a Neanderthal (N)<sup>10</sup>, a woolly mammoth (M)<sup>11</sup> and the horse fossil discovered at Thistle Creek, Canada (H)<sup>2</sup>, are shown.

ancestor of members of the *Equus* genus to be between 4.0 million and 4.5 million years ago (Fig. 1), approximately twice the previous estimate.

Orlando *et al.* went on to show that the size of the horse population has fluctuated many times over the past 2 million years, particularly during periods of severe climatic change. Interestingly, they reveal that Przewalski's horse has retained substantial genetic diversity, a feature that could be significant for the species' future conservation. Furthermore, they identify genomic regions in domesticated horses that have been under positive selection; some of these might represent genetic signatures of domestication.

But the implications of this work go well beyond the evolution of horses, by also providing evidence for the limits of DNA survival. Until this study, many experts<sup>5,6</sup> would have thought that it was impossible to recover a genome from a sample of this age because of the rapid degradation of DNA into ever shorter fragments that occurs following the death of an organism. The decay is driven initially by the body's own enzymes, and the actions of enzymes from microorganisms soon follow — death shuts down the normal defences that protect an organism against such fates. This process is, of course, affected by environmental conditions, including the presence of oxygen and water, the microorganisms present, pH and temperature. In general, the colder the environment, the slower the rate of DNA degradation (Fig. 2).

Orlando and colleagues' success is undoubtedly due to the extreme cold in which the bone resided and its resulting preservation, combined with advances in second-generation gene sequencing, including true single-molecule sequencing technology. Technical developments in DNA recovery and the construction of DNA-sequencing libraries also

contributed to the authors' achievements. From this same sample, they were able to sequence 73 proteins, including some found in blood. This illustrates that other methods apart from DNA sequencing can now be applied, on a large scale, to studies of the deep past.

So just how long can animal DNA survive? Recent work has modelled the absolute limits of DNA survival, and suggested that DNA more than 1 million years old may be recoverable from very cold environments<sup>7</sup>. Interestingly, the age of the horse genome recovered by Orlando *et al.* falls comfortably within these predicted limits of DNA survival (Fig. 2), suggesting the tantalizing proposition that complete genomes several millions of years old may be recoverable, given the right environmental conditions. Indeed, Orlando and colleagues' study encourages us to wonder if it might be possible to recover DNA from a wide range of Middle Pleistocene samples. Of particular interest would be material from ancestral human species<sup>8</sup> such as *Homo heidelbergensis* and *Homo erectus*<sup>9</sup>. Such genomic information, in combination with the Denisovan<sup>3</sup> and Neanderthal<sup>10</sup> genomes, would undoubtedly

shed light on the evolution of humans and our hominin ancestors, in much the same way as Orlando and colleagues' study provides insight into the evolution of horses and the survival of DNA itself. ■

**Craig D. Millar** is in the Allan Wilson Centre for Molecular Ecology and Evolution, School of Biological Sciences, University of Auckland, Auckland 1010, New Zealand.

**David M. Lambert** is in the Environmental Futures Centre, Griffith University, Nathan 4111, Australia.

e-mails: [cd.millar@auckland.ac.nz](mailto:cd.millar@auckland.ac.nz); [d.lambert@griffith.edu.au](mailto:d.lambert@griffith.edu.au)

1. Higuchi, R. B., Bowman, B., Freiburger, M., Ryder, O. A. & Wilson, A. C. *Nature* **312**, 282–284 (1984).
2. Orlando, L. *et al.* *Nature* **499**, 74–78 (2013).
3. Meyer, M. *et al.* *Science* **338**, 222–226 (2012).
4. Simpson, G. G. *The Meaning of Evolution* (Yale Univ. Press, 1949).
5. Lindahl, T. *Nature* **362**, 709–715 (1993).
6. Pääbo, S. *et al.* *Annu. Rev. Genet.* **38**, 645–679 (2004).
7. Allentoft, M. E. *et al.* *Proc. R. Soc. B* **279**, 4724–4733 (2012).
8. Wood, B. & Collard, M. *Science* **284**, 65–71 (1999).
9. Rightmire, G. P. *Evol. Anthropol.* **6**, 218–227 (1998).
10. Green, R. E. *et al.* *Science* **328**, 710–722 (2010).
11. Miller, W. *et al.* *Nature* **456**, 387–390 (2008).

#### CANCER

## Mutations close in on gene regulation

**A genome-wide analysis of DNA and RNA sequences, gene expression and DNA modifications in 200 samples of acute myeloid leukaemia sets the stage for data integration and verification that will enhance our understanding of this cancer.**

STEIN AERTS & JAN COOLS

**A**cute myeloid leukaemia exhibits variable genetics, presentation and clinical outcome. Writing in the *New England Journal of Medicine*, Ley and colleagues<sup>1</sup> from the Cancer Genome Atlas Research Network present the first comprehensive genome-wide analysis of DNA sequences, transcribed messenger RNA and microRNA molecules, and DNA modification by methylation, in 200 cases of adult acute myeloid leukaemia (AML). The data, which are publicly available, provide unprecedented insight into the molecular genetics of this cancer and its influence on treatment responses. Although the challenge of integrating and functionally verifying these data remains, the findings are expected to help to explain the biology of AML, and could lead to the development of therapeutic strategies.

Historically, the identification and characterization of individual genetic modifications, such as chromosomal translocations, gene

fusions and gene mutations, have fuelled our understanding of the onset and progression of AML. More recently, whole-genome and whole-exome sequencing studies have further refined this view, identifying mutations in genes in which they were not expected, such as *DNMT3A*, *IDH1*, *PHF6* and *SMC3*. (The exome is the portion of the genome comprising exon sequences — those that form mature mRNA molecules.) Now that our knowledge of DNA-sequence mutations in AML has advanced, it is time for greater integration of this information with data on gene expression.

Deregulation of gene expression is central to cancer development. For example, many cancer-related mutations result in reduced expression of genes that are associated with apoptotic cell death or cell senescence, or alter the expression of genes involved in cell proliferation and differentiation. These changes are often caused by perturbed activity of proteins involved in transcriptional control. Understanding the role of gene expression in



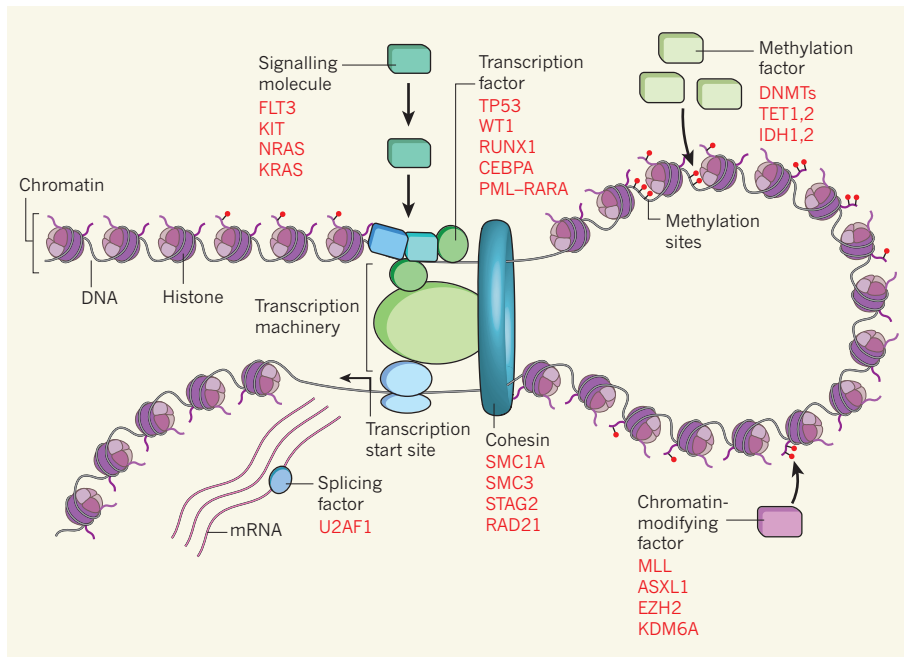


**Figure 1 | Frequent mutations in acute myeloid leukaemia.** The Cancer Genome Atlas Research Network<sup>1</sup> presents an analysis of mutations that are repeatedly seen in patients with acute myeloid leukaemia. All of these mutations can be linked to the regulation of gene expression. They include: mutations in transcription factors and signalling proteins; mutations in factors that regulate the methylation of DNA and associated histone proteins; mutations in the protein complex cohesin, which regulates chromatin structure; and mutations in proteins involved in splicing, a process that regulates the amount and type of mRNA molecules formed. The protein products of mutated genes are shown in red.

cancer will require analysis of epigenetic modifications (structural and chemical genomic changes, such as DNA methylation, that do not change the DNA sequence) and structural changes in chromatin (the complex of DNA and associated histone proteins).

Remarkably, all of the mutations that Ley and colleagues identify in their AML survey, and posit to be cancer-driving, can be associated with the regulation of gene expression (Fig. 1). For example, the authors found several frequent mutations in transcription factors, including TP53, WT1, RUNX1, CEBPA and the PML–RARA fusion protein. The effects of such mutations are directly attributable to the altered regulation of direct and indirect target genes, as shown extensively<sup>2</sup> for regulation by MYC — a transcription factor often mutated in cancer.

Another category of typical cancer drivers is signalling proteins. Altered activity of signalling pathways will affect the activity of downstream transcription factors such as STAT proteins, MYC, ETS, NF- $\kappa$ B and AP-1, and so signalling-protein mutations will also affect gene regulation. According to Ley and colleagues' study, the most frequent of such mutations in AML are in the proteins FLT3, KIT, NRAS and KRAS.

A further category of cancer-driving mutations is those that target chromatin-modifying proteins and DNA methylation factors, which can have broad effects on transcriptional control by promoting or inhibiting the accessibility

of the DNA to transcription factors or other proteins. The most recurrent of these alterations found by the authors were in the genes that encode the proteins MLL, TET2, IDH1, IDH2 and DNMT3A. In addition to these three main categories, the authors identified mutations that affect cohesin, a protein complex that influences structural chromatin interactions, and the spliceosome, a complex that regulates the amount and type of mature RNA transcripts formed.

Several lines of investigation remain to be addressed. How does the interplay of these mutations lead to cancer gene-expression profiles? How do these expression profiles ultimately lead to a proliferation advantage in cancer cells? And how do certain expression profiles represent different cancer characteristics or cancer subtypes that have different clinical properties? Ley *et al.* did not aim to address the enormous challenge of answering these questions, but they have paved the way to do so by providing invaluable data sets for further analysis and integration.

The integration of epigenomic and genomic data with gene-expression data will nevertheless be complicated by the heterogeneity of AML (or that of any other cancer) and the unknown selection process that cancer cells go through before diagnosis and sample collection. It is well established that rare AML stem cells initiate this leukaemia, and it has been suggested that they may also be a source of cells for relapse<sup>3,4</sup>. It is therefore unclear whether the gene-expression

profiles of the bulk of the AML samples in this study will be informative for our understanding of AML development, or if instead we need expression profiles of the stem cells. Patient data alone will probably not be sufficient to optimally unravel significant relationships across all information layers. Animal models, including mice, zebrafish and flies, are increasingly needed to study the effects of cancer mutations and their combinations in a controlled manner.

Another question that arises in relation to gene-regulatory perturbations is to what extent non-coding mutations may contribute to oncogenic processes. The AML study identified a small number of recurrent mutations in microRNAs (small regulatory RNAs that do not encode proteins), but none in *cis*-regulatory control elements (non-coding sequences, such as promoter regions, that typically contain transcription-factor binding sites). However, recent evidence, such as the identification of mutations in the promoter sequence of the *TERT* gene in melanoma cells<sup>5</sup>, suggests that non-coding mutations can be important.

The complexity of gene regulation and our poor understanding of regulatory genomic regions mean that identifying non-coding mutations that affect gene expression is unlikely to be a trivial task. Data from the ENCODE project<sup>6</sup> could help us to prioritize candidate *cis*-regulatory variations, but additional integrative genomics studies will inevitably be necessary. For example, studies using chromatin profiling (using DNase I hypersensitivity or FAIRE-seq assays) or histone modification (using ChIP-seq) during cancer initiation in model organisms could provide additional mechanistic clues about the early stages of cancer development.

We now have an exceptionally clear view of the repertoire of protein-coding driver mutations in AML, how they cluster together and how they can predict patients' responses to therapy<sup>1,7</sup>. But this is not the end — we are only at the beginning of an era in which integration of rich data sets that probe the genome, epigenome and transcriptome will help us to unravel the intricate regulatory connections between genetics and cancer. ■

**Stein Aerts and Jan Cools** are at the Center for Human Genetics, KU Leuven, 3000 Leuven, Belgium. J.C. is also at the VIB Center for the Biology of Disease, KU Leuven.

e-mails: stein.aerts@med.kuleuven.be; jan.cools@cme.vib-kuleuven.be

1. The Cancer Genome Atlas Research Network. *N. Engl. J. Med.* **368**, 2059–2074 (2013).
2. Lin, C. Y. *et al.* *Cell* **151**, 56–67 (2012).
3. Eppert, K. *et al.* *Nature Med.* **17**, 1086–1093 (2011).
4. Ding, L. *et al.* *Nature* **481**, 506–509 (2012).
5. Huang, F. W. *et al.* *Science* **339**, 957–959 (2013).
6. Gerstein, M. B. *et al.* *Nature* **489**, 91–100 (2012).
7. Patel, J. P. *et al.* *N. Engl. J. Med.* **366**, 1079–1089 (2012).

## EARTH SCIENCE

# Hot and deep

The landscape of Afar in Ethiopia (pictured) is tortured, because underlying tectonic plates are pulling apart from each other. Such rifting can lead to continental break-up, and is often accompanied by voluminous magmatism — the production of large amounts of melt. In this issue, Ferguson *et al.* report the cause of this magmatism in Afar (D. J. Ferguson *et al.* *Nature* **490**, 70–73; 2013).

The authors developed a model of magmatism in the region using geochemical data from lavas that erupted along the rift. They conclude that melting is generated at great depths — 80 kilometres or more — and is driven by an unusually hot region of the mantle.

Using another model, Ferguson and colleagues tracked the development of melting at the rift, and found that thinning of the tectonic plate over the past 30 million years has been much less than expected. This suggests that an abrupt phase of plate thinning during the final stages of break-up would be required for an ocean basin to form in Afar. [Andrew Mitchinson](#)



## CANCER

# An acidic link

**Obese people are at higher risk of multiple types of cancer, but why? One explanation could be that obesity enhances the production of pro-inflammatory, and carcinogenic, bile acids by gut microorganisms. [SEE LETTER P.97](#)**

SUZANNE DEVKOTA & PETER J. TURNBAUGH

**T**he rise in the global prevalence of obesity has been accompanied by a wide array of other morbidities, including diabetes, cardiovascular disease and cancer. Despite strong epidemiological data that link obesity to a higher risk of developing numerous cancers, the mechanisms underlying this connection remain unclear. A few important clues have been uncovered: that obesity-associated inflammation contributes to liver cancer<sup>1</sup>; that obesity is associated with marked changes to the trillions of microbes found in the gastrointestinal tract<sup>2</sup>; and that obesity-associated bacteria can produce inflammatory metabolites<sup>3</sup>. On page 97 of this issue, Yoshimoto *et al.*<sup>4</sup> present a plausible link by which deoxycholic acid, an obesity-associated by-product of microbial bile-acid metabolism, might contribute to hepatic inflammation

and the subsequent progression to cancer in obese mice\*.

The authors began by using a strain of mouse in which expression of a gene that induces the senescence-associated secretory phenotype (SASP) can be monitored non-invasively by luminescence. Senescence, or cell-cycle arrest, has conventionally been viewed as a favourable process when trying to correct DNA damage and halt abnormal cell proliferation, but it has more recently been shown that senescent cells are active and can produce pro-inflammatory signalling proteins that promote tumour growth — key hallmarks of SASP<sup>5</sup>. Yoshimoto *et al.* found that tumour initiation with a chemical carcinogen triggered luminescence in the abdomen (indicative of liver cancer) of obese mice fed a high-fat diet, whereas lean mice fed a standard diet were

\*This article and the paper under discussion<sup>4</sup> were published online on 26 June 2013.

protected from liver cancer. The researchers saw a similar response in mice that were deficient in the appetite-regulating hormone leptin, demonstrating that both dietary and genetically induced obesity can promote liver cancer. *In situ* analysis of gene expression in the livers of these obese mice revealed the expression of multiple components of SASP.

But how exactly does obesity stimulate SASP? The authors' experiments using antibiotics implicate obesity-associated gut microbes. Treatment of the mice with a cocktail of four antibiotics resulted in a marked reduction of liver cancer, as did treatment with another antibiotic, vancomycin, to target bacteria in the Firmicutes phylum, which are found at higher abundance in obese animals<sup>6</sup>. Furthermore, the authors detected high serum levels of deoxycholic acid (DCA) in mice fed a high-fat diet, and observed that these levels were reduced by vancomycin treatment. DCA is a secondary bile acid produced by gut microbes such as *Clostridium sordellii*; it is known to be carcinogenic and has long been implicated in colorectal cancer<sup>7</sup>. When the authors inhibited microbial 7 $\alpha$ -dehydroxylation, the biochemical reaction that produces DCA, liver cancer was suppressed in obese mice, whereas when they supplemented antibiotic-treated animals fed a high-fat diet with DCA, carcinogenesis was enhanced.

Together, these results emphasize the key



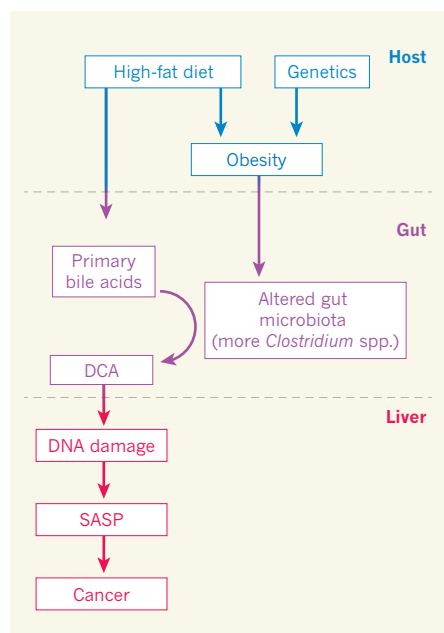


**Figure 1 | How obesity increases cancer risk.**

Yoshimoto *et al.*<sup>4</sup> show that mice that are obese as a result of a high-fat diet or genetic predisposition produce higher levels of deoxycholic acid (DCA), a by-product of the bile-acid metabolism of certain gut microbes. DCA is a carcinogen that can induce DNA damage and the senescence-associated secretory phenotype (SASP), which is associated with tumour growth.

part that bile acids play in mediating host-microbe interactions in the gastrointestinal tract (Fig. 1). Bile acids are typically found at high-millimolar concentrations in the gut lumen, where they are converted to a diverse pool of secondary bile acids, including DCA. Enterohepatic circulation of bile acids provides an efficient route by which these microbial metabolites could reach the liver. A recent study<sup>8</sup> showed that a high-fat diet stimulates bile-acid production that promotes the growth of *Bilophila wadsworthia*, a pathogenic bacterium that causes colitis in genetically susceptible mice. Thus, microbial bile-acid metabolism may provide an under-appreciated mechanism by which our decisions at the dinner table can translate to disastrous consequences for our health.

Now that more links between bile acids and disease are emerging, it will be crucial to revisit how gut microbes metabolize bile acids, and what effects their by-products may have. Could there be 'metabolic powerhouse' organisms that are highly adapted to use bile, similarly to the *Bacteroides* species that metabolize polysaccharides<sup>9</sup>? What are the key genetic and biochemical mechanisms underlying microbial bile-acid metabolism, and what tunes their activity *in vivo*? Multiple factors have already been shown to alter the overall pool of bile acids, including diet<sup>8</sup>, microbial colonization<sup>10</sup> and gastric-bypass surgery<sup>11</sup>, but more work needs to be done to

explore the health implications of these shifts in humans. It will be important to develop comparative approaches that will allow for the comprehensive measurement of the bile-acid composition in various host tissues. These tools could enable us to have a broader understanding of how the consumption of different dietary components alters the bile-acid pool, and whether or not this is a primary host factor that shapes the structure and metabolic activity of gut microbial communities that are associated with diseases such as obesity.

Furthermore, the by-products of microbial bile-acid metabolism are not only passive carcinogens but also active signalling molecules. For example, bile-acid activation of the farnesoid X nuclear receptor and TGR5 in the liver has been shown to regulate lipid and glucose homeostasis, as well the synthesis of the bile acids themselves<sup>12</sup>. These receptors are also found outside the liver in tissues such as the heart, kidney and thymus, suggesting that bile acids have important roles throughout the body.

Yoshimoto and colleagues' work emphasizes the need to consider both host and microbial factors that influence the tumour microenvironment. Continued collaboration between cancer biologists, microbiologists, immunologists and biochemists promises to

provide a mutually beneficial symbiosis aimed at achieving a mechanistic understanding of the many ways in which microbial metabolism can contribute to or be shaped by cancer. This understanding brings with it the promise of better tools for risk assessment, diagnostics and therapeutic intervention. ■

**Suzanne Devkota** is at the Joslin Diabetes Center, Harvard Medical School, Boston, Massachusetts 02215, USA.

**Peter. J. Turnbaugh** is at the FAS Center for Systems Biology, Harvard University, Cambridge, Massachusetts 02138, USA. e-mail: pturnbaugh@fas.harvard.edu

1. Park, E. J. *et al.* *Cell* **140**, 197–208 (2010).
2. Greenblum, S., Turnbaugh, P. J. & Borenstein, E. *Proc. Natl Acad. Sci. USA* **109**, 594–599 (2012).
3. Fei, N. & Zhao, L. *ISME J.* **7**, 880–884 (2013).
4. Yoshimoto, S. *et al.* **499**, 97–101 (2013).
5. Coppe, J. P. *et al.* *PLoS Biol.* **6**, 2853–2868 (2008).
6. Turnbaugh, P. J., Backhed, F., Fulton, L. & Gordon, J. I. *Cell Host Microbe* **3**, 213–223 (2008).
7. Nagengast, N. M. *et al.* *Eur. J. Cancer* **31**, 1067–1070 (1995).
8. Devkota, S. *et al.* *Nature* **487**, 104–108 (2012).
9. Martens, E. C. *et al.* *PLoS Biol.* **9**, e1001221 (2011).
10. Sayin, S. I. *et al.* *Cell Metab.* **17**, 225–235 (2013).
11. Ahmad, N. N., Pfalzer, A. & Kaplan, L. M. *Int. J. Obes.* <http://dx.doi.org/10.1038/ijo.2013.38> (2013).
12. Swann, J. R. *et al.* *Proc. Natl Acad. Sci. USA* **108** (Suppl. 1), 4523–4530 (2011).

## MALARIA

# Sensing when it's time for sex

**Malaria parasites switch between developmental stages to facilitate their transmission to the mosquito vector. This switch seems to be initiated by parasite-to-parasite communication through membrane-bound vesicles.**

LEANN TILLEY & MALCOLM MCCONVILLE

Intercellular communication is crucial for the development of complex multicellular organisms. Single-celled organisms, including bacteria, can also communicate with each other by secreting small molecules that are sensed by their compatriots, as well as other organisms in their vicinity. These signals enable microbes to sense nutrient conditions or environmental stresses and to initiate adaptive growth responses that optimize population survival<sup>1</sup>. Papers by Regev-Rudzki *et al.*<sup>2</sup> in *Cell* and Mantel *et al.*<sup>3</sup> in *Cell Host Microbe* report the identification of an unexpected form of intercellular communication, involving extracellular microvesicles, in the deadly human malaria parasite *Plasmodium falciparum*.

Parasitic microorganisms often switch

between different developmental stages in their animal or human hosts. This trait allows them to invade various host cells and to improve their chances of being transmitted by an intermediate host or vector; in some cases, the switch has been shown to be mediated by secreted parasite factors<sup>4</sup>. In the case of *P. falciparum*, a small proportion of parasites in the rapidly dividing asexual stage — which proliferate in red blood cells (RBCs) of the human host — differentiate into the sexual gametocyte stage that is required for transmission through the *Anopheles* mosquito vector. This switch can be induced by stresses associated with overcrowding, the host immune response or exposure to drugs. Although there is evidence<sup>5</sup> that gametocyte differentiation can be triggered by secreted or released parasite factors, these have not been defined.

The two new reports provide a potential

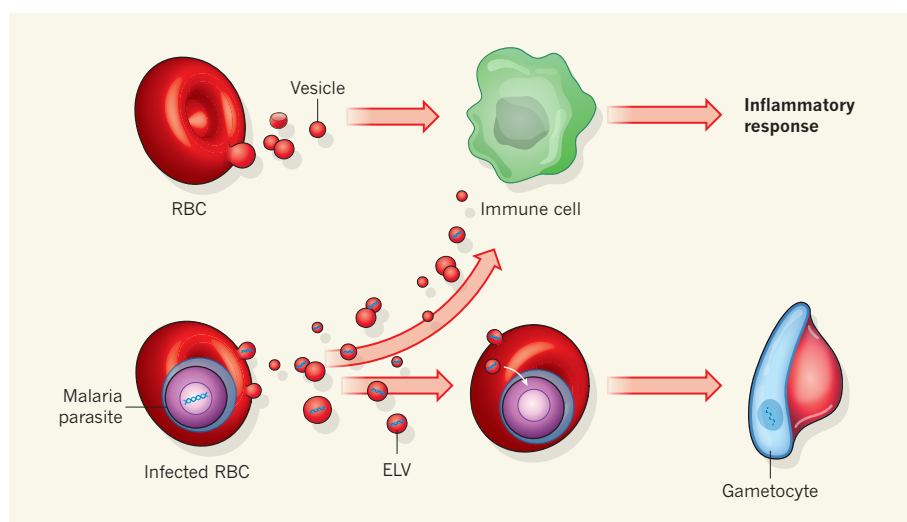


**Figure 1 | Release of vesicles from red blood cells.** Uninfected red blood cells (RBCs) shed cell-membrane-derived vesicles containing damaged cellular components. The vesicles are taken up by immune cells that digest and dispose of this cellular debris. Regev-Rudzki *et al.*<sup>2</sup> and Mantel *et al.*<sup>3</sup> show that RBCs infected with malaria parasites shed more vesicles, and that these exome-like vesicles (ELVs) can mediate transfer of parasite-derived DNA and proteins to other infected RBCs. This provides a form of parasite-to-parasite communication that, among other possible functions, can induce parasites in the recipient cells to differentiate from an asexual to a sexual (gametocyte) form. Vesicle release also contributes to the symptoms of malaria infections by activating inflammatory responses from cells such as macrophages.

mechanism for how asexual-stage parasites generate extracellular signals. Using complementary approaches, the studies demonstrate that small vesicles released from the cell membrane of cultured *P. falciparum*-infected RBCs can mediate the transfer of DNA (specifically, plasmids that encode drug-resistance mediators or fluorescent proteins) from one infected RBC to another. These extracellular vesicles range from 70 to 250 nanometres in diameter<sup>2,3</sup> and contain both RBC and parasite-derived proteins<sup>3</sup>. The authors refer to them as exosome-like vesicles (ELVs)<sup>2</sup> — by analogy to small vesicles that are generated in the endolysosome system of mammalian cells and shed extracellularly — or RBC-derived microvesicles<sup>3</sup>. The term ELVs will be used here.

Circulating microparticles originating from RBCs have previously been reported in patients with malaria<sup>6</sup> and in mice infected with the rodent malaria parasite *Plasmodium berghei*<sup>7</sup>; in the latter, these have been shown to have strong pro-inflammatory activity. Similarly, the ELVs characterized in the current studies seem to be involved in the inflammatory response. They are taken up by other host cells, including macrophages and neutrophils, leading to cell activation and the production of cell-signalling molecules called cytokines (Fig. 1). This may benefit the parasite by increasing the expression of receptors on the endothelial cells to which infected RBCs adhere, thus avoiding parasite clearance in the host's spleen<sup>8</sup>. It may also lead to deregulated inflammation and severe complications, such as cerebral malaria<sup>9</sup>.

Remarkably, both groups found that ELVs are also internalized by other infected RBCs, leading to differentiation of parasites in the recipient cells into gametocytes (Fig. 1). The accumulation of ELVs in the serum of infected individuals may therefore constitute a signal that initiates and regulates the formation of transmissible parasite stages to maximize their passage to the mosquito vector. ELV formation seems to be enhanced by drug treatment<sup>2</sup>, and so this process might also constitute a danger signal that drives the parasite into a resistant state.

The current data provide convincing evidence for parasite-to-parasite communication in *in vitro* cultures, but whether ELVs mediate communication at the low parasite densities that occur *in vivo* remains to be determined. An intriguing possibility is that ELV-mediated sequestration of *P. falciparum*-infected RBCs onto the walls of blood vessels could lead to a local increase in parasite density and aid vesicle-mediated communication.

Although the mechanism by which ELVs are formed is not known, it is well established that uninfected RBCs normally shed membrane vesicles, albeit at a much lower level than *P. falciparum*-infected RBCs. Vesicle shedding in uninfected RBCs is thought to be a mechanism for removing damaged proteins or membrane components<sup>6,10</sup> (Fig. 1). It is tempting to speculate that the malaria parasite has exploited this process to enable cell-to-cell communication. Genetic studies performed by Regev-Rudzki *et al.* suggest that ELV formation depends on the parasite protein PfPTP2, which is associated with vesicles in the RBC



## 50 Years Ago

Investigations were conducted here to determine the effect of a magnetic field on the ripening of green tomatoes (*Lycopersicon esculentum* Mill. Var. V. R. Moscow). Four permanent magnets of considerable strength were utilized. Fruits of uniform maturity were placed between the magnetic poles ... The ripening rates of treated fruits were compared with those of untreated controls in the same room under similar conditions ... In all cases the treated fruits ripened faster than the controls. Furthermore, the fruits nearest the magnetic south ripened faster than those nearest the magnetic north.

From *Nature* 6 July 1963

## 100 Years Ago

In recent issues of *Nature* several correspondents, in referring to the fact that a metal bedstead or a few wires stretched a few feet above the ground will make a wireless antenna, have overlooked a most important point, viz. that with such an antenna the ordinary methods of tuning are quite useless. A piece of wire netting suspended a few feet above the ground makes a most effective aerial, and enables one to receive loud signals from long-distance stations, but signals from Eiffel Tower, Cleethorpes, &c. will all be mixed up, and the ordinary tuner will not separate them effectively ... Wireless signals that are feeble when the surface of the earth is dry, becoming stronger after rain, and the well-known fact that these waves travel much better over sea than over land, all seem to indicate that the aerial waves are at least supplemented by waves that travel along the surface of the earth.

From *Nature* 3 July 1913



cytoplasm. These vesicles bud from membrane sacks called Maurer's clefts (found in infected RBCs) that regulate the transport of parasite proteins to the RBC membrane. PfPTP2 might be directly involved in ELV budding or, alternatively, in regulating the packaging of parasite molecules into the membrane buds. Future studies could assess whether parasites that lack PfPTP2 are deficient in gametocyte formation, or whether other parasite lipids, oligonucleotides or proteins, including those previously implicated in gametocytogenesis<sup>11,12</sup>, are required for this process.

Key questions remain, including: how are large biomolecules, such as DNA plasmids, transferred from the parasite nucleus or cytoplasm to the ELVs, and then targeted to the nucleus of the recipient parasite? This process would require a tortuous journey across several membranes and compartments, including those of the RBC, which lacks its own trafficking machinery. It is conceivable that the nucleic-acid cargo is first packaged into double-membrane vesicles, in a process similar to the formation of exosomes in animal cells. The vesicles could then transport their contents to the cytoplasm of the host RBC. Interestingly, analysis of timing of ELV formation in the two studies raised the possibility that different classes of vesicles are generated during the parasite's early ring stage and late schizont stage, and that these potentially involve different biogenic pathways.

These studies highlight the potential importance of ELVs in immune regulation and of parasite-to-parasite signalling in malaria, and suggest that they are crucial during acute infections and for efficient parasite transmission. However, other functions could also be considered. For example, membrane blebbing might remove oxidized or damaged proteins or lipids and thereby help to maintain the integrity of an infected RBC for long enough to allow the parasite to complete its asexual replication cycle. The findings could also have technical implications, by providing new methods for rapidly generating genetically modified parasites and for the production of gametocytes. Importantly, the formation of ELVs represents a possible new target for antimalarial drugs. Successfully targeting this pathway might both reduce the severity of the infection and interrupt transmission. Field studies and mathematical modelling suggest that inhibiting transmission is crucial to achieving malaria eradication, and these findings may provide a boost to that long-term goal. ■

**Leann Tilley and Malcolm McConville**  
are in the Department of Biochemistry  
and Molecular Biology, Bio21 Molecular  
Science and Biotechnology Institute,  
Parkville, Victoria 3010, Australia.  
**L.T.** is also at the ARC Centre of Excellence  
for Coherent X-ray Science,

University of Melbourne, Parkville.  
e-mails: [ltalley@unimelb.edu.au](mailto:ltalley@unimelb.edu.au);  
[malcolmm@unimelb.edu.au](mailto:malcolmm@unimelb.edu.au)

1. Swift, S. *et al.* *Adv. Microb. Physiol.* **45**, 199–270 (2001).
2. Regev-Rudzki, N. *et al.* *Cell* **153**, 1120–1133 (2013).
3. Mantel, P. Y. *et al.* *Cell Host Microbe* **13**, 521–534 (2013).
4. MacGregor, P., Szöör, B., Savill, N. J. & Matthews, K. R. *Nature Rev. Microbiol.* **10**, 431–438 (2012).
5. Dyer, M. & Day, K. P. *Am. J. Trop. Med. Hyg.* **68**, 403–409 (2003).

6. Nantakomol, D. *et al.* *J. Infect. Dis.* **203**, 700–706 (2011).
7. Couper, K. N. *et al.* *PLoS Pathog.* **6**, e1000744 (2010).
8. Fairhurst, R. M., Bess, C. D. & Krause, M. A. *Microbes Infect.* **14**, 851–862 (2012).
9. Turner, G. D. *et al.* *Am. J. Pathol.* **145**, 1057–1069 (1994).
10. Bosman, G. J., Lasonder, E., Groenen-Dopp, Y. A., Willekens, F. L. & Werre, J. M. *J. Proteomics* **76**, 203–210 (2012).
11. Day, K. P. *et al.* *Proc. Natl Acad. Sci. USA* **90**, 8292–8296 (1993).
12. Gardiner, D. L. *et al.* *Mol. Biochem. Parasitol.* **140**, 153–160 (2005).

## BIOINORGANIC CHEMISTRY

# Enzymes activated by synthetic components

**Synthetic analogues of the catalytic subsite of the hydrogen-producing enzyme HydA1 have been disappointingly inactive. The incorporation of such analogues into the enzyme's active site reveals the requirements for activity. SEE LETTER P.66**

**RYAN D. BETHEL &  
MARCETTA Y. DARENSBOURG**

As our knowledge of biosynthetic pathways evolves, experiments that interfere at specific points in these molecular assembly lines may be judiciously designed. On page 66 of this issue, Berggren *et al.*<sup>1</sup> report just such a strategy in their study of a [FeFe]-hydrogenase enzyme called HydA1, which mediates the remarkably efficient production of hydrogen gas from water-derived hydrogen ions<sup>2–8</sup>. The authors' findings increase our understanding of how the enzyme's active site is constructed\*.

Buried deep within HydA1, the enzyme's active site consists of a [4Fe-4S] cluster (a group of four iron and four sulphur atoms), which serves as a storage and conduit unit for electrons, and a [2Fe] subsite that is the real engine of the catalyst<sup>4</sup>. The [2Fe] subsite is actually a small molecule in which two iron atoms are bound by diatomic ligand molecules (carbon monoxide and cyanide) and connected by a unique dithiolate bridge, SCH<sub>2</sub>XCH<sub>2</sub>S, where the identity of X has been contentious, but could be carbon (CH<sub>2</sub>), oxygen or nitrogen (NH). The subsite is attached to the protein only at the embedded [4Fe-4S] cluster, through a bridge formed by the sulphur atom from a cysteine amino-acid residue.

Organometallic chemists have made synthetic analogues of the subsite that resemble its structure, but these exhibit low catalytic activity for the hydrogen-forming reaction

\*This article and the paper under discussion<sup>1</sup> were published online on 26 June 2013.

in the absence of the protein. A fundamental question is whether these analogues of a small molecule can be recognized at the appropriate point in the biological assembly of the active site of HydA1, and so be inserted into that site. If incorporated into the incomplete protein, would synthetic [2Fe] units be catalytically active? And could the insertion of synthetic analogues into the site be used as a technique to interrogate why their activity is low? More specifically, could this approach be used to identify the elusive bridgehead X of the dithiolate group?

Although a lot is known about the events that control the generation and combination of the components of the [2Fe] subsite, and about the maturase proteins involved<sup>6</sup>, much remains to be clarified. Nevertheless, it is widely accepted that the [2Fe] subsite is built on a scaffold provided by the 'apo' (incomplete) form of an isolable protein known as HydF (ref. 7). Once the [2Fe] unit is formed, the resulting 'holo' (complete) form of HydF serves as a delivery agent, shuttling its cargo to apo-HydA1, where the required [4Fe-4S] cluster resides at the end of a deep cavity<sup>3</sup>. On acceptance of the [2Fe] subunit, HydA1 matures: the channel that provided access for the subunit collapses, generating the complete hydrogenase enzyme in which the [4Fe-4S] cluster and the [2Fe] subunit are fully encapsulated. It has been postulated that cavity collapse causes one carbon monoxide ligand to be lost from the [2Fe] subunit and another to shift into a bridging position between the two irons. This would change the [2Fe] subunit from a symmetrical structure (akin to the structures of its synthetic analogues) to a

cytoplasm. These vesicles bud from membrane sacks called Maurer's clefts (found in infected RBCs) that regulate the transport of parasite proteins to the RBC membrane. PfPTP2 might be directly involved in ELV budding or, alternatively, in regulating the packaging of parasite molecules into the membrane buds. Future studies could assess whether parasites that lack PfPTP2 are deficient in gametocyte formation, or whether other parasite lipids, oligonucleotides or proteins, including those previously implicated in gametocytogenesis<sup>11,12</sup>, are required for this process.

Key questions remain, including: how are large biomolecules, such as DNA plasmids, transferred from the parasite nucleus or cytoplasm to the ELVs, and then targeted to the nucleus of the recipient parasite? This process would require a tortuous journey across several membranes and compartments, including those of the RBC, which lacks its own trafficking machinery. It is conceivable that the nucleic-acid cargo is first packaged into double-membrane vesicles, in a process similar to the formation of exosomes in animal cells. The vesicles could then transport their contents to the cytoplasm of the host RBC. Interestingly, analysis of timing of ELV formation in the two studies raised the possibility that different classes of vesicles are generated during the parasite's early ring stage and late schizont stage, and that these potentially involve different biogenic pathways.

These studies highlight the potential importance of ELVs in immune regulation and of parasite-to-parasite signalling in malaria, and suggest that they are crucial during acute infections and for efficient parasite transmission. However, other functions could also be considered. For example, membrane blebbing might remove oxidized or damaged proteins or lipids and thereby help to maintain the integrity of an infected RBC for long enough to allow the parasite to complete its asexual replication cycle. The findings could also have technical implications, by providing new methods for rapidly generating genetically modified parasites and for the production of gametocytes. Importantly, the formation of ELVs represents a possible new target for antimalarial drugs. Successfully targeting this pathway might both reduce the severity of the infection and interrupt transmission. Field studies and mathematical modelling suggest that inhibiting transmission is crucial to achieving malaria eradication, and these findings may provide a boost to that long-term goal. ■

**Leann Tilley and Malcolm McConville**  
are in the Department of Biochemistry  
and Molecular Biology, Bio21 Molecular  
Science and Biotechnology Institute,  
Parkville, Victoria 3010, Australia.  
**L.T.** is also at the ARC Centre of Excellence  
for Coherent X-ray Science,

University of Melbourne, Parkville.  
e-mails: [ltalley@unimelb.edu.au](mailto:ltalley@unimelb.edu.au);  
[malcolmm@unimelb.edu.au](mailto:malcolmm@unimelb.edu.au)

1. Swift, S. *et al.* *Adv. Microb. Physiol.* **45**, 199–270 (2001).
2. Regev-Rudzki, N. *et al.* *Cell* **153**, 1120–1133 (2013).
3. Mantel, P. Y. *et al.* *Cell Host Microbe* **13**, 521–534 (2013).
4. MacGregor, P., Szöör, B., Savill, N. J. & Matthews, K. R. *Nature Rev. Microbiol.* **10**, 431–438 (2012).
5. Dyer, M. & Day, K. P. *Am. J. Trop. Med. Hyg.* **68**, 403–409 (2003).

6. Nantakomol, D. *et al.* *J. Infect. Dis.* **203**, 700–706 (2011).
7. Couper, K. N. *et al.* *PLoS Pathog.* **6**, e1000744 (2010).
8. Fairhurst, R. M., Bess, C. D. & Krause, M. A. *Microbes Infect.* **14**, 851–862 (2012).
9. Turner, G. D. *et al.* *Am. J. Pathol.* **145**, 1057–1069 (1994).
10. Bosman, G. J., Lasonder, E., Groenen-Dopp, Y. A., Willekens, F. L. & Werre, J. M. *J. Proteomics* **76**, 203–210 (2012).
11. Day, K. P. *et al.* *Proc. Natl Acad. Sci. USA* **90**, 8292–8296 (1993).
12. Gardiner, D. L. *et al.* *Mol. Biochem. Parasitol.* **140**, 153–160 (2005).

## BIOINORGANIC CHEMISTRY

# Enzymes activated by synthetic components

**Synthetic analogues of the catalytic subsite of the hydrogen-producing enzyme HydA1 have been disappointingly inactive. The incorporation of such analogues into the enzyme's active site reveals the requirements for activity. SEE LETTER P.66**

**RYAN D. BETHEL &  
MARCETTA Y. DARENSBOURG**

As our knowledge of biosynthetic pathways evolves, experiments that interfere at specific points in these molecular assembly lines may be judiciously designed. On page 66 of this issue, Berggren *et al.*<sup>1</sup> report just such a strategy in their study of a [FeFe]-hydrogenase enzyme called HydA1, which mediates the remarkably efficient production of hydrogen gas from water-derived hydrogen ions<sup>2–8</sup>. The authors' findings increase our understanding of how the enzyme's active site is constructed\*.

Buried deep within HydA1, the enzyme's active site consists of a [4Fe-4S] cluster (a group of four iron and four sulphur atoms), which serves as a storage and conduit unit for electrons, and a [2Fe] subsite that is the real engine of the catalyst<sup>4</sup>. The [2Fe] subsite is actually a small molecule in which two iron atoms are bound by diatomic ligand molecules (carbon monoxide and cyanide) and connected by a unique dithiolate bridge, SCH<sub>2</sub>XCH<sub>2</sub>S, where the identity of X has been contentious, but could be carbon (CH<sub>2</sub>), oxygen or nitrogen (NH). The subsite is attached to the protein only at the embedded [4Fe-4S] cluster, through a bridge formed by the sulphur atom from a cysteine amino-acid residue.

Organometallic chemists have made synthetic analogues of the subsite that resemble its structure, but these exhibit low catalytic activity for the hydrogen-forming reaction

\*This article and the paper under discussion<sup>1</sup> were published online on 26 June 2013.

in the absence of the protein. A fundamental question is whether these analogues of a small molecule can be recognized at the appropriate point in the biological assembly of the active site of HydA1, and so be inserted into that site. If incorporated into the incomplete protein, would synthetic [2Fe] units be catalytically active? And could the insertion of synthetic analogues into the site be used as a technique to interrogate why their activity is low? More specifically, could this approach be used to identify the elusive bridgehead X of the dithiolate group?

Although a lot is known about the events that control the generation and combination of the components of the [2Fe] subsite, and about the maturase proteins involved<sup>6</sup>, much remains to be clarified. Nevertheless, it is widely accepted that the [2Fe] subsite is built on a scaffold provided by the 'apo' (incomplete) form of an isolable protein known as HydF (ref. 7). Once the [2Fe] unit is formed, the resulting 'holo' (complete) form of HydF serves as a delivery agent, shuttling its cargo to apo-HydA1, where the required [4Fe-4S] cluster resides at the end of a deep cavity<sup>3</sup>. On acceptance of the [2Fe] subunit, HydA1 matures: the channel that provided access for the subunit collapses, generating the complete hydrogenase enzyme in which the [4Fe-4S] cluster and the [2Fe] subunit are fully encapsulated. It has been postulated that cavity collapse causes one carbon monoxide ligand to be lost from the [2Fe] subunit and another to shift into a bridging position between the two irons. This would change the [2Fe] subunit from a symmetrical structure (akin to the structures of its synthetic analogues) to a



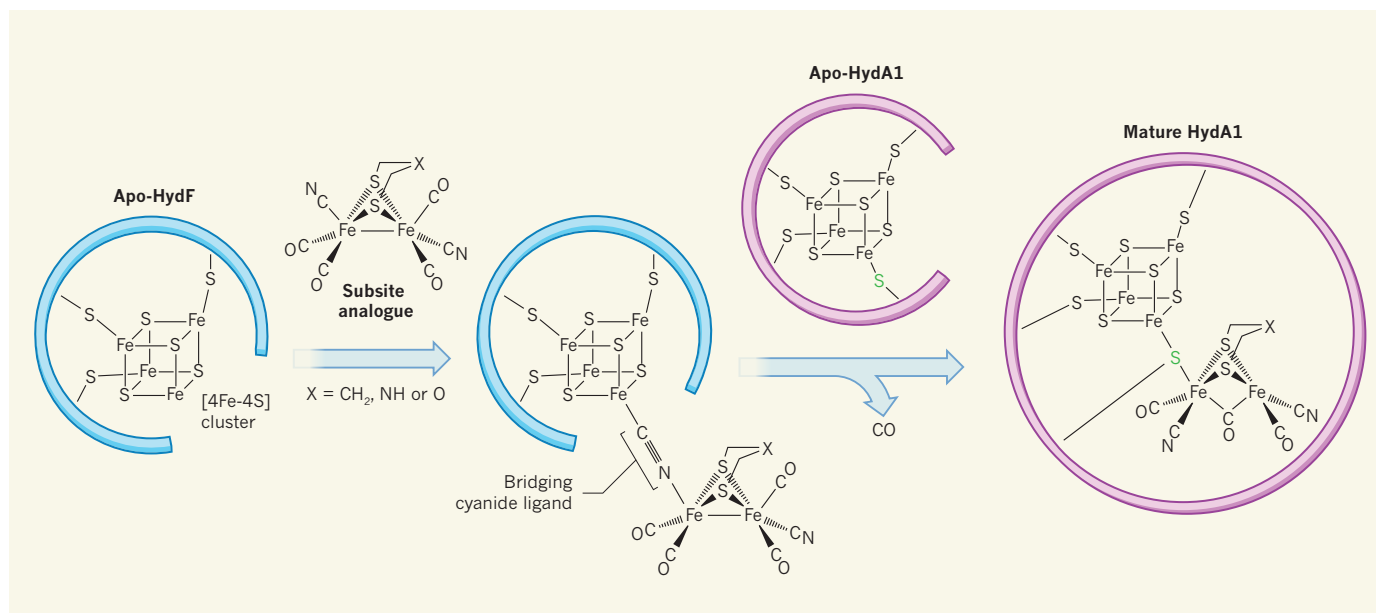


**Figure 1 | Assembly line interrupted.** Berggren *et al.*<sup>1</sup> have bypassed much of the biosynthesis of the HydA1 enzyme, to introduce synthetic analogues of the enzyme's [2Fe] subunit. They observed that the analogues first become incorporated into the apo (incomplete) HydF protein by binding to its [4Fe-4S] cluster, and propose that a cyanide ligand acts as a bridge between iron atoms in the cluster and the subunit analogue. This temporary bridge is used during the transfer of the [2Fe] unit to a similar [4Fe-4S] cluster in apo-HydA1: a sulphur atom (green) from a cysteine amino-acid residue in HydA1 latches onto the [2Fe] cargo, releasing a carbon monoxide (CO) ligand from the subunit and yielding the mature form of HydA1.

'rotated' isomer that is catalytically active<sup>9</sup>.

Berggren *et al.* prepared apo-HydF from the bacterium *Thermotoga maritima* by over-expressing it in *Escherichia coli* bacteria, and then added it to three synthetic analogues of the [2Fe] subunit. The three analogues differed only in the bridgehead atom X, which was carbon, nitrogen or oxygen. Fortunately, the diatomic ligands in the analogues can be easily detected using infrared spectroscopy. This enabled the researchers to track the artificial subunits as they passed from solution into HydF, and eventually into HydA1. Even better, the spectroscopic signatures of synthetic and natural [2Fe] subunits are highly sensitive to changes in their environment. This allowed Berggren and colleagues to confirm that HydF proteins did indeed bind to the synthetic [2Fe] subunits, and that the chemical environment of the diatomic ligands was similar to that found in the isolated, natural form of the protein.

The authors used another spectroscopic technique, electron paramagnetic resonance, to determine how the synthetic [2Fe] subunits are attached to the [4Fe-4S] clusters. This revealed an unexpected role for a cyanide ligand in the subunits. Cyanide ligands have long been known to aggregate metals, as in the widely used pigment Prussian blue. Berggren *et al.* suggest that this ability allows a cyanide ligand to act as a temporary connection between an iron atom in the subunit and one of those in a [4Fe-4S] cluster of apo-HydF (Fig. 1). As HydF transfers its package to apo-HydA1, a cysteine sulphur atom binds the [2Fe] site to form mature HydA1,

the cyanide detaches from the HydF cluster and a carbon monoxide ligand is lost from the subunit.

So, are the semi-synthetic enzymes functional? To answer this question, Berggren and co-workers combined apo-HydA1 with one of the following: an empty scaffold (apo-HydF); HydF bound to the naturally occurring [2Fe] subunit; or HydF bound to each of the artificial [2Fe] subunits. The authors found that no hydrogen gas was produced in reactions using apo-HydF, or for scaffolds bound to artificial [2Fe] subunits in which the bridgehead atom X was carbon or oxygen. However, when they tested the [2Fe] subunit that had a nitrogen bridgehead, they observed vigorous hydrogen-gas production, comparable to that of the naturally occurring enzyme. Notably, under the same assay conditions and in the absence of apo-HydA1, HydF loaded with the nitrogen-bridged subunit was inactive.

The researchers' findings beg the question, can apo-HydA1 be loaded with a synthetic [2Fe] analogue in the absence of HydF? Something similar has already been done: cofactors, such as iron-containing haem, that bind weakly to proteins have been replaced by geometrically similar synthetic catalysts<sup>10,11</sup> simply by mixing the artificial cofactor and the apo-enzyme, without scaffold proteins. Whether the intricacies of apo-HydA1 will recognize and accept a simple synthetic [2Fe] subunit analogue alone is not yet known.

The discovery of an active, semi-synthetic variant of HydA1 is an exciting result. It demonstrates that the complex maturase machinery used to construct the enzyme's active site

can be circumvented, and provides researchers with a simple system for producing active [FeFe]-hydrogenases from various organisms. It also means that inorganic chemists were on the right track with their models of the [2Fe] subunit, even though those models had low catalytic activity — Berggren and colleagues' findings reveal that although a nitrogen in the bridgehead is crucial for hydrogen formation, the subunit cannot function optimally until it is incorporated into the proper protein cavity. ■

**Ryan D. Bethel and Marcetta Y. Darensbourg** are in the Department of Chemistry, Texas A&M University, College Station, Texas 77843, USA.  
e-mails: rbethel@chem.tamu.edu; marcetta@chem.tamu.edu

1. Berggren, G. *et al.* *Nature* **499**, 66–69 (2013).
2. Cendron, L. *et al.* *J. Biol. Chem.* **286**, 43944–43950 (2011).
3. Mulder, D. W. *et al.* *Nature* **465**, 248–252 (2010).
4. Nicolet, Y., Piras, C., Legrand, P., Hatchikian, C. E. & Fontecilla-Camps, J. C. *Structure* **7**, 13–23 (1999).
5. Nicolet, Y., Amara, P., Mouesca, J.-M. & Fontecilla-Camps, J. C. *Proc. Natl Acad. Sci. USA* **106**, 14867–14871 (2009).
6. Posewitz, M. C. *et al.* *J. Biol. Chem.* **279**, 25711–25720 (2004).
7. Shepard, E. M. *et al.* *Proc. Natl Acad. Sci. USA* **107**, 10448–10453 (2010).
8. Kuchenreuther, J. M., Britt, R. D. & Swartz, J. R. *PLoS ONE* **7**, e45850 (2012).
9. Bethel, R. D., Singleton, M. L. & Darensbourg, M. Y. *Angew. Chem. Int. Edn* **49**, 8567–8569 (2010).
10. Ohashi, M. *et al.* *Angew. Chem. Int. Edn* **42**, 1005–1008 (2003).
11. Carey, J. R. *et al.* *J. Am. Chem. Soc.* **126**, 10812–10813 (2004).

# Comprehensive molecular characterization of clear cell renal cell carcinoma

The Cancer Genome Atlas Research Network\*

Genetic changes underlying clear cell renal cell carcinoma (ccRCC) include alterations in genes controlling cellular oxygen sensing (for example, *VHL*) and the maintenance of chromatin states (for example, *PBRM1*). We surveyed more than 400 tumours using different genomic platforms and identified 19 significantly mutated genes. The PI(3)K/AKT pathway was recurrently mutated, suggesting this pathway as a potential therapeutic target. Widespread DNA hypomethylation was associated with mutation of the H3K36 methyltransferase *SETD2*, and integrative analysis suggested that mutations involving the SWI/SNF chromatin remodelling complex (*PBRM1*, *ARID1A*, *SMARCA4*) could have far-reaching effects on other pathways. Aggressive cancers demonstrated evidence of a metabolic shift, involving downregulation of genes involved in the TCA cycle, decreased AMPK and PTEN protein levels, upregulation of the pentose phosphate pathway and the glutamine transporter genes, increased acetyl-CoA carboxylase protein, and altered promoter methylation of miR-21 (also known as *MIR21*) and *GRB10*. Remodelling cellular metabolism thus constitutes a recurrent pattern in ccRCC that correlates with tumour stage and severity and offers new views on the opportunities for disease treatment.

Kidney cancers, or renal cell carcinomas (RCC), are a common group of chemotherapy-resistant diseases that can be distinguished by histopathological features and underlying gene mutations<sup>1</sup>. Inherited predisposition to RCC has been shown to arise from genes involved in regulating cellular metabolism, making RCC a model for the role of an oncologic-metabolic shift, commonly referred to as the 'Warburg effect', leading to malignancy<sup>2</sup>. The most common type of RCC, clear cell renal cell carcinoma (ccRCC), is closely associated with *VHL* gene mutations that lead to stabilization of hypoxia inducible factors (*HIF-1 $\alpha$*  and *HIF-2 $\alpha$* , also known as *HIF1A* and *EPAS1*) in both sporadic and familial forms. *PBRM1*, a subunit of the PBAF SWI/SNF chromatin remodelling complex, as well as histone deubiquitinase *BAP1* and histone methyltransferase *SETD2*, were recently found to be altered in ccRCC<sup>3–5</sup>, implicating major roles for epigenetic regulation of additional functional pathways participating in the development and progression of the disease. Oncogenic metabolism and epigenetic reprogramming have thus emerged as central features of ccRCC.

In the present study, clinical and pathological features, genomic alterations, DNA methylation profiles, and RNA and proteomic signatures were evaluated in ccRCC. We accrued more than 500 primary nephrectomy specimens from patients with histologically confirmed ccRCC that conformed to the requirements for genomic study defined by the Cancer Genome Atlas (TCGA), together with matching 'normal' genomic material. Samples were restricted to those that contained at least 60% tumour nuclei (median 85%) by pathological review (clinical data summary provided in Supplementary Table 1). A data freeze representing 446 samples was generated from at least one analytical platform ('Extended' data set) and data from all platforms were available for 372 samples for coordinated, integrative analyses ('Core' data set) (Supplementary Data 1, Supplementary Table 2). No substantial batch effects in the data that might confound analyses were detected (Supplementary Figs 1–20).

## Somatic alterations

The global pattern of somatic alterations, determined from analysis of 417 samples, is shown in Fig. 1a. DNA hybridizations showed that recurrent arm-level and focal somatic copy number alterations

(SCNAs) occurred at a fewer sites than is generally observed in other cancers ( $P < 0.0004$ ; Supplementary Figs 21–22 and Supplementary Table 3). However, SCNAs that were observed more commonly involved entire chromosomes or chromosome arms, rather than focal events (17% vs 0.4%, Fig. 1b). Notably, the most frequent arm-level events involved loss of chromosome 3p (ref. 6; 91% of samples), encompassing all of the four most commonly mutated genes (*VHL*, *PBRM1*, *BAP1* and *SETD2*).

The data also suggested lower and more variable tumour cellularity<sup>7</sup> in the accrued samples, compared to conventional pathological review (median 54%  $\pm$  14%). This may reflect stromal or endothelial cell contributions, or tumour cell heterogeneity. A recent study of multiple samples from single tumours has demonstrated significant regional genomic heterogeneity, but with shared mutations in frequently mutated genes and convergent evolution of other common gene level events<sup>8</sup>. The mutation frequencies of key genes (*VHL*, *PBRM1* and so on), as well as copy number gains and losses found here, were, however, consistent with previous reports. Tumour purity was therefore not determined to be a limitation in the current study.

Arm level losses on chromosome 14q, associated with loss of *HIF1A*, which has been predicted to drive more aggressive disease<sup>9</sup>, were also frequent (45% of samples). Gains of 5q were observed (67% of samples) and additional focal amplifications refined the region of interest to 60 genes in 5q35, which was particularly informative as little has been known about the importance of this region in ccRCC since the 5q gain was initially described. Focal amplification also implicated the protein kinase C member *PRKCI* (ref. 10), and the MDS1 and EVI1 complex locus *MECOM* at 3p26, the p53 regulator *MDM4* at 1q32, *MYC* at 8q24 and *JAK2* on 9p24. Focally deleted regions included the tumour suppressor genes *CDKN2A* at 9p21 and *PTEN* at 10q23, putative tumour suppressor genes *NEGR1* at 1p31, *QKI* at 6q26, and *CADM2* at 3p12 and the genes that are frequently deleted in cancer, *PTPRD* at 9p23 and *NRXN3* at 14q24 (ref. 11).

Whole-exome sequencing (WES) of tumours from 417 patients identified 36,353 putative somatic mutations, including 16,821 missense mutations, 6,383 silent mutations and 2,999 indels, with an average of

\*Lists of participants and their affiliations appear at the end of the paper.



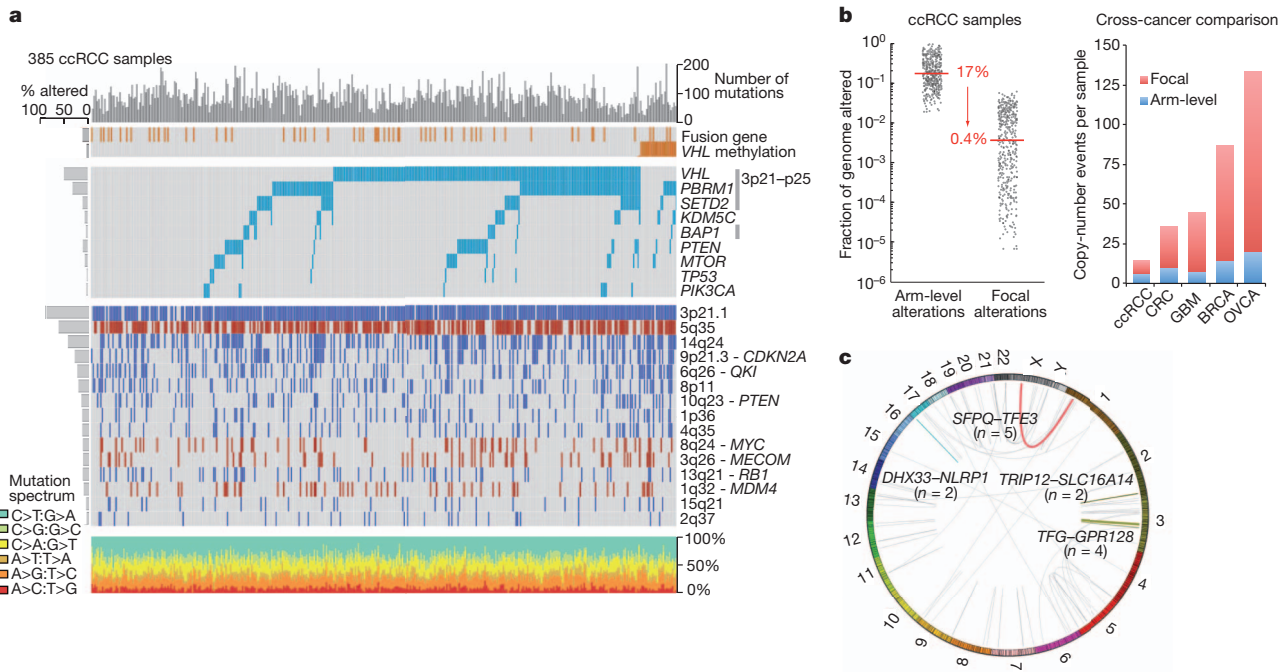


**Figure 1 | Somatic alterations in ccRCC.** **a**, Top histogram, mutation events per sample; left histogram, samples affected per alteration. Upper heat map, distribution of fusion transcripts and *VHL* methylation across samples ( $n = 385$  samples, with overlapping exome/SCNA/RNA-seq/methylation data); middle heat map, mutation events; bottom heat map, copy number gains (red) and losses (blue). Lower chart, mutation spectrum by indicated categories.

$1.1 \pm 0.5$  non-silent mutations per megabase (Supplementary Figs 23–25). Mutations from 50 genes with high apparent somatic mutation frequencies (Supplementary Table 4) were independently validated using alternative sequencing instrumentation (Supplementary Fig. 26). In tumours from 22 patients, whole-genome sequencing was also used to validate and calibrate the WES data and confirmed 83% of the WES mutation-calls (Supplementary Tables 5 and 6). In line with results of previous studies (Supplementary Tables 7 and 8), the validated mutation data identified nineteen significantly mutated genes (SMGs) (false discovery rate (FDR)  $< 0.1$ ), with *VHL*, *PBRM1*, *SETD2*, *KDM5C*, *PTEN*, *BAP1*, *MTOR* and *TP53* representing the eight most extreme members ( $q < 0.00001$ ) (Fig. 1a). Eleven additional SMGs were of considerably lower significance ( $q < 0.1$ – $0.5$ ) but included known cancer genes. Among all SMGs, only mutation of *BAP1* correlated with poor survival outcome (Supplementary Fig. 27)<sup>12</sup>. Approximately 20% of cases had none of the 19 recorded SMGs, although many contained rare mutations in other known oncogenes or tumour suppressors, involving survival associations, illustrating the genetic complexity of ccRCC<sup>8</sup> (Supplementary Figs 28–30 and Supplementary Table 9).

Eighty-four putative RNA fusions were identified in 416 ccRCC samples<sup>13</sup>. Eleven of thirteen predicted events (Fig. 1c) were validated using targeted methods, consistent with an 85% true-positive rate (Supplementary Table 10 and Supplementary Figs 31–35). A recurrent *SFPQ-TFE3* fusion (previously linked to non-clear cell translocation-associated RCC<sup>14</sup>) was found in five samples, all of which were *VHL* wild type, indicating either that these tumours are a clear cell variant or that translocation-associated renal tumours may be histologically indistinguishable from conventional ccRCC. Furthermore, the TFE3 protein as well as an X(p11) rearrangement was found in three of those samples, where there were available slides.

## DNA methylation profiles

We observed epigenetic silencing of *VHL* in about 7% of ccRCC tumours, which was mutually exclusive with mutation of *VHL* (Fig. 1a), reflecting the central role of this locus in ccRCC<sup>15</sup>. An additional 289 genes showed

evidence of epigenetic silencing in at least 5% of tumours. The top-ranked gene by inverse correlation between gene expression and DNA methylation was *UQCRH*, hypermethylated in 36% of the tumours. *UQCRH* has been previously suggested to be a tumour suppressor<sup>16</sup>, but not linked to ccRCC. Interestingly, increasing promoter hypermethylation frequency correlated with higher stage and grade (Fig. 2a, b).

We also evaluated the global consequences of mutation in specific epigenetic modifiers. Mutations in *SETD2*, a non-redundant H3K36 methyltransferase, were associated with increased loss of DNA methylation at non-promoter regions (Fig. 2c, d). This discovery is consistent with the emerging view that H3K36 trimethylation may be involved in the maintenance of a heterochromatic state<sup>17</sup>, whereby DNA methyltransferase 3A (DNMT3A) binds H3K36me3 and methylates nearby DNA<sup>18</sup>. Thus, reductions of H3K36me3 through *SETD2* inactivation could lead indirectly to regional loss of DNA methylation.

## RNA expression

Unsupervised clustering methods identified four stable subsets in both mRNA (m1–m4) and miRNA (mi1–mi4) expression data sets (Fig. 3a and Supplementary Figs 36–39). Supervised clustering revealed the similarity of these new mRNA classes to the previously reported ccA and ccB expression subtypes<sup>19</sup>, with cluster m1 corresponding to ccA and ccB divided between m2 and m3 (Supplementary Table 11). Cluster m4 probably accounts for the roughly 15% of tumours previously unclassified in the ccA/ccB classification scheme. Similarly, the survival advantage previously observed for ccA cases was again identified for m1 tumours (Fig. 3b).

The m1 subtype was characterized by gene sets associated with chromatin remodelling processes and a higher frequency of *PBRM1* mutations (39% in m1 vs 27% in others,  $P = 0.027$ ). Deletion of *CDKN2A* (53% vs 26%;  $P < 0.0001$ ) and mutations in *PTEN* (11% vs 1%;  $P < 0.0001$ ) were more frequent in m3 tumours (Supplementary Fig. 5). The m4 group showed higher frequencies of *BAP1* mutations (17% vs 7%;  $P = 0.002$ ) and base-excision repair; however, this group

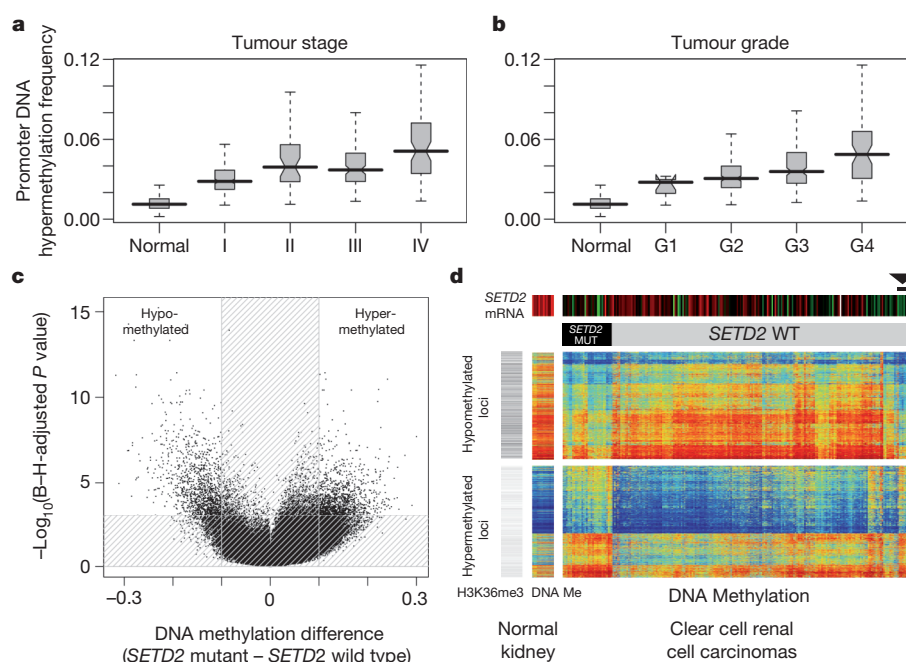


**Figure 2 | DNA methylation and ccRCC.**  
**a, b,** Overall promoter DNA hypermethylation frequency in the tumour increases with rising stage (**a**) and grade (**b**). The promoter DNA hypermethylation frequency is calculated as the percentage of CpG loci hypermethylated among 15,101 loci which are unmethylated in the normal kidney tissue and normal white blood cells (boxplots, median with 95% confidence interval). **c,** Volcano plots showing a comparison of DNA methylation for *SETD2* mutant versus non-mutant tumours ( $n = 224$ , HumanMethylation450 platform). Unshaded area: CpG loci with Benjamini–Hochberg (B–H) FDR = 0.001 and difference in mean beta value  $> 0.1$  ( $n = 2,557$ ). **d,** Heat map showing CpG loci with *SETD2* mutation-associated DNA methylation (from part **c**); blue to red indicates low to high DNA methylation. The loci are split into those hypomethylated (top panel;  $n = 1,251$ ) or hypermethylated (bottom panel;  $n = 1,306$ ) in *SETD2* mutants. Top colour bars indicate *SETD2* mRNA expression (red: high, green: low) and *SETD2* mutation status. Grey-scale row-side colour bar on left-hand side represents the relative number of overlapping reads, based on H3K36me3 ChIP-seq experiment in normal adult kidney (<http://nihroadmap.nih.gov/epigenomics/>); black, high read count. DNA methylation patterns include 14 normal kidney samples. Among the tumours without *SETD2* mutations, six (arrowhead) have both the signature pattern of *SETD2* mutation and low *SETD2* mRNA expression.

also harboured more *mTOR* mutations (12% vs 4%;  $P = 0.01$ ) and ribosomal gene sets.

Survival differences evident in miRNA-based subtypes (Supplementary Figs 40–44) correlated with the mRNA data (Fig. 3b–d). For example, miR-21, previously shown to demonstrate strong regulatory interactions in ccRCC<sup>20</sup> and with established roles in metabolism<sup>17,21,22</sup> correlated strongly with worse outcome, and DNA promoter methylation levels inversely correlated with expression of miR-21, miR-10b and miR-30a (Supplementary Tables 12–14). miRNA interactions thus represent a significant component of the epigenetic regulation observed in ccRCC.

## Integrative data analyses

We used a combination of approaches for integrative pathway analysis. The HotNet<sup>23</sup> algorithm uses a heat diffusion model, to find sub-networks distinguished by both the frequency of mutation in genes (nodes in the network) and the topology of interactions between genes (edges in the network). In ccRCC, HotNet identified twenty-five sub-networks of genes within a genome-scale protein–protein interaction network (Supplementary Table 15 and Supplementary Fig. 45). The largest and most frequently mutated network contained *VHL* and interacting partners. The second most frequently mutated sub-network included *PBRM1*, *ARID1A* and *SMARCA4*, key genes in the PBAF *SWI/SNF* chromatin remodelling complex.

We also inferred activities for known pathways, by using the PARADIGM algorithm to incorporate mutation, copy and mRNA expression data, with pathway information catalogued in public databases. This method identified a highly significant sub-network of 2,398 known regulatory interactions, connecting 1,218 molecular features (645 distinct proteins) (Supplementary Figs 46–49 and Supplementary Tables 16 and 17). Several ‘active’ transcriptional ‘hubs’ were identified, by searching for transcription factors with targets that were inferred to be active in the PARADIGM network. The active hubs found included HIF1A/ARNT, the transcription factor program activated by *VHL* mutation, as well as MYC/MAX, SP1, FOXM1, JUN and FOS. These hubs, together with

several other less well-studied transcription factors, interlink much of the transcriptional program promoting glycolytic shift, de-differentiation and growth promotion in ccRCC.

We next searched for causal regulatory interactions connecting ccRCC somatic mutations to these transcriptional hubs, using a bi-directional extension to HotNet (‘TieDIE’) and identified a chromatin-specific sub-network (Fig. 4a and Supplementary Figs 50–52). TieDIE defines a set of transcriptional targets, whose state in the tumour cells is proposed to be influenced by one or more of the significantly mutated genes. The chromatin modification pathway intersects a wide variety of processes, including the regulation of hormone receptors (for example, *ESR1*), RAS signalling via the *SRC* homologue (*SHC1*), immune-related signalling (for example, *NFKB1* and *IL6*)<sup>24</sup>, transcriptional output (for example, *HIF1A*, *JUN*, *FOS* and *SP1*), DNA repair (via *BAP1*) and beta-catenin (*CTNNB1*) and transforming growth factor (TGF)- $\beta$  (*TGFBR2*) signalling via interactions with a *SMARCB1*–*PBRM1*–*ARID1A* complex. The complexity of these interactions reflects the potential for highly pleiotropic effects following primary events in chromatin modification genes.

The mutations in the chromatin regulators *PBRM1*, *BAP1* and *SETD2* were differentially associated with altered expression patterns of large numbers of genes when compared to samples bearing a background of *VHL* mutation (Supplementary Tables 18–21 and Supplementary Fig. 53). Each chromatin regulator had a distinct set of downstream effects, reflecting diverse roles for chromatin remodelling in the transcriptome.

Additionally, an unsupervised pathway analysis using the MEMO algorithm<sup>25</sup> identified mutually exclusive patterns of alterations targeting multiple components of the PI(3)K/AKT/MTOR pathway in 28% of the tumours (Fig. 4b and Supplementary Table 22). Interestingly, the altered gene module included two genes from the broad amplicon on 5q35.3: *GNB2L1* and *SQSTM1*. Both these genes have previously been associated with activation of PI(3)K signalling<sup>26,27</sup>. Furthermore, mRNA expression levels of these two genes were correlated with both DNA copy number increases and alteration status of the PI(3)K pathway (Supplementary Figs 54–55). The mutual exclusivity module also includes



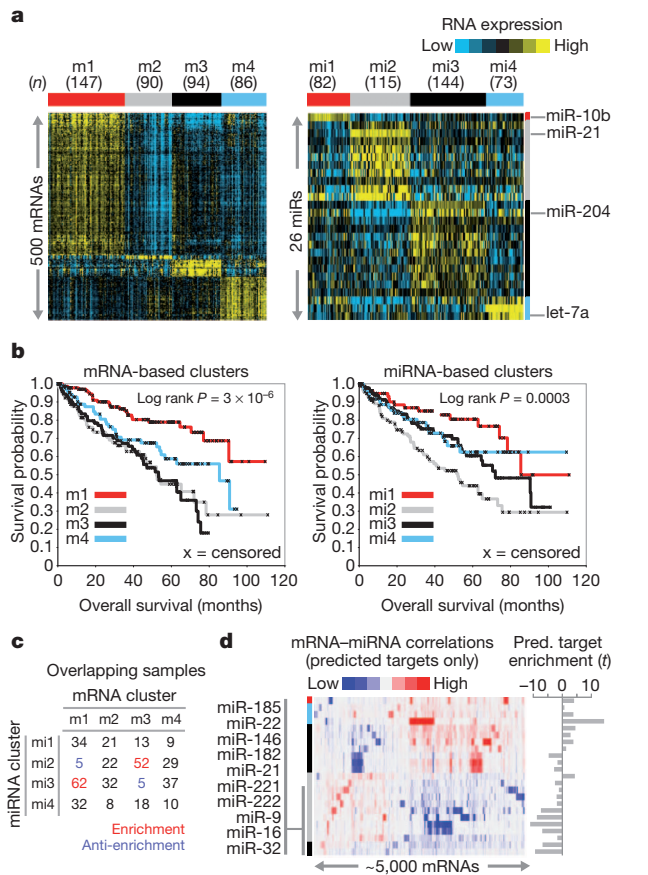


**Figure 3 | mRNA and miRNA patterns reflect molecular subtypes of ccRCC.** **a**, Tumours were separated into four sample groups (that is, 'clusters') by unsupervised analyses, on the basis of either differentially expressed mRNA patterns (left panel, showing 500 representative genes: m1–m4) or differentially expressed miRNA patterns (right panel, showing 26 representative miRNAs: mi1–mi4). **b**, Significant differences in patient survival were identified for both the mRNA-based clusters (left panel) and the miRNA-based clusters (right panel). **c**, Numbers of samples overlapping between the two sets of clusters, with significant concordance observed between m1 and mi3 and between m3 and mi2; red, significant overlap ( $P < 10^{-5}$ , chi-squared test). **d**, mRNA–miRNA correlations, for predicted targeting interactions. Rows indicate miRNAs from **a** (indicated by cluster-specific colour bar); columns, mRNAs (5,000 differentially regulated genes selected for average RPKM  $> 10$  and at least one predicted miRNA interaction); mRNA–miRNA entries with no predicted targeting are white. To the right of the correlation matrix,  $t$  statistics (Spearman's rank) indicate group target enrichment.

frequent overexpression of EGFR, which correlates with increased phosphorylation of the receptor (Supplementary Fig. 56), and which has been previously associated with lapatinib response in ccRCC<sup>28</sup>.

### Correlations with survival

Where unsupervised analyses had indicated that common molecular patterns were associated with patient survival, we sought to further define molecular prognostic signatures at the levels of mRNA, miRNA, DNA methylation and protein. Data were divided into 'discovery' ( $n = 193$ ) and 'validation' ( $n = 253$ ) sets and platform-specific signatures were defined using Cox analyses<sup>24</sup>. Kaplan–Meier analysis for each signature showed statistically significant associations with survival in the validation subset (Fig. 5a and Supplementary Fig. 57). Multivariate Cox analyses, incorporating established clinical variables, showed that the mRNA, miRNA and protein signatures provided additional prognostic power (Supplementary Table 23). In addition, these signatures could provide molecular clues as to the drivers of aggressive cancers.

Top protein correlates of worse survival included reduced AMP-activated kinase (AMPK) and increased acetyl-CoA carboxylase (ACC)

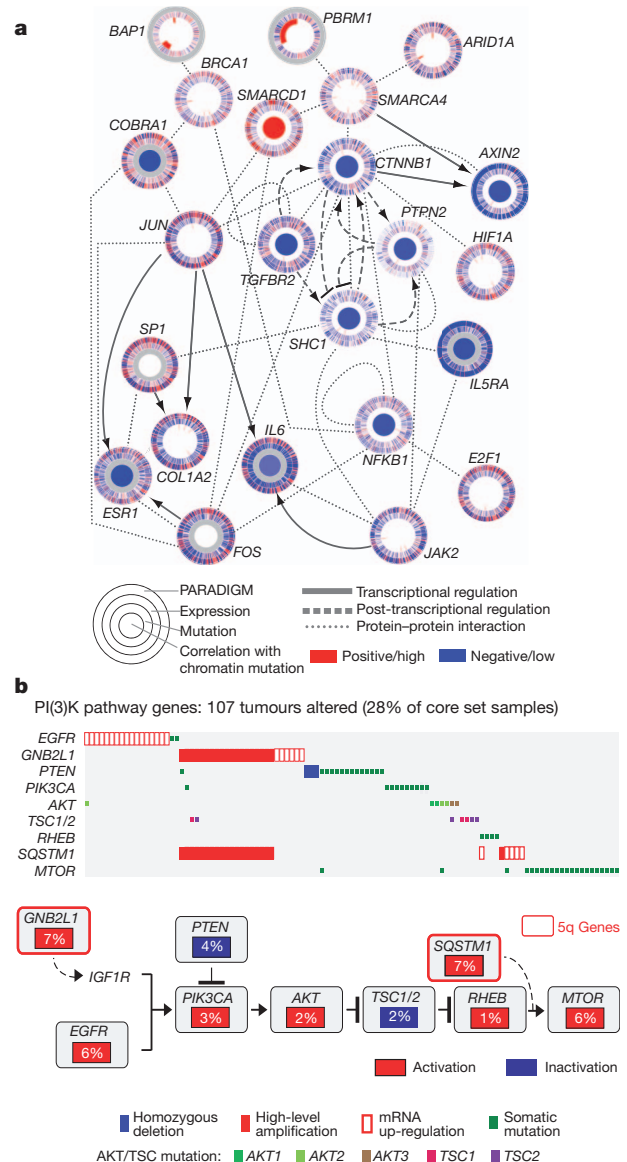


**Figure 4 | Genomically-altered pathways in ccRCC.** **a**, Alterations in chromatin remodelling genes were predicted to affect a large network of genes and pathways (larger implicated network in Supplementary Information). Each gene is depicted as a multi-ring circle with various levels of data, plotted such that each 'spoke' in the ring represents a single patient sample (same sample ordering for all genes). 'PARADIGM' ring, bioinformatically inferred levels of gene activity (red, higher activity); 'Expression', mRNA levels relative to normal (red, high); 'Mutation', somatic event; centre, correlation of gene expression or activity to mutation events in chromatin-related genes (red, positive). Protein-protein relationships inferred using public resources. **b**, For the PI(3)K/AKT/MTOR pathway (altered in ~28% of tumours), the MEMO algorithm identified a pattern of mutually exclusive gene alterations (somatic mutations, copy alterations and aberrant mRNA expression) targeting multiple components, including two genes from the recurrent amplicon on 5q35.3. The alteration frequency and inferred alteration type (blue for inactivation and red for activation) is shown for each gene in the pathway diagram.

(Supplementary Fig. 58). Together, downregulation of AMPK and upregulation of ACC activity contribute to a metabolic shift towards increased fatty acid synthesis<sup>29</sup>. A metabolic shift to an altered use of key metabolites and pathways was also apparent when considering the full set of genes involved in the core metabolic processes, including a shift towards a 'Warburg effect'-like state (Fig. 5b). Poor prognosis correlated with downregulation of AMPK complex and the Krebs cycle genes, and with upregulation of genes involved in the pentose phosphate pathway

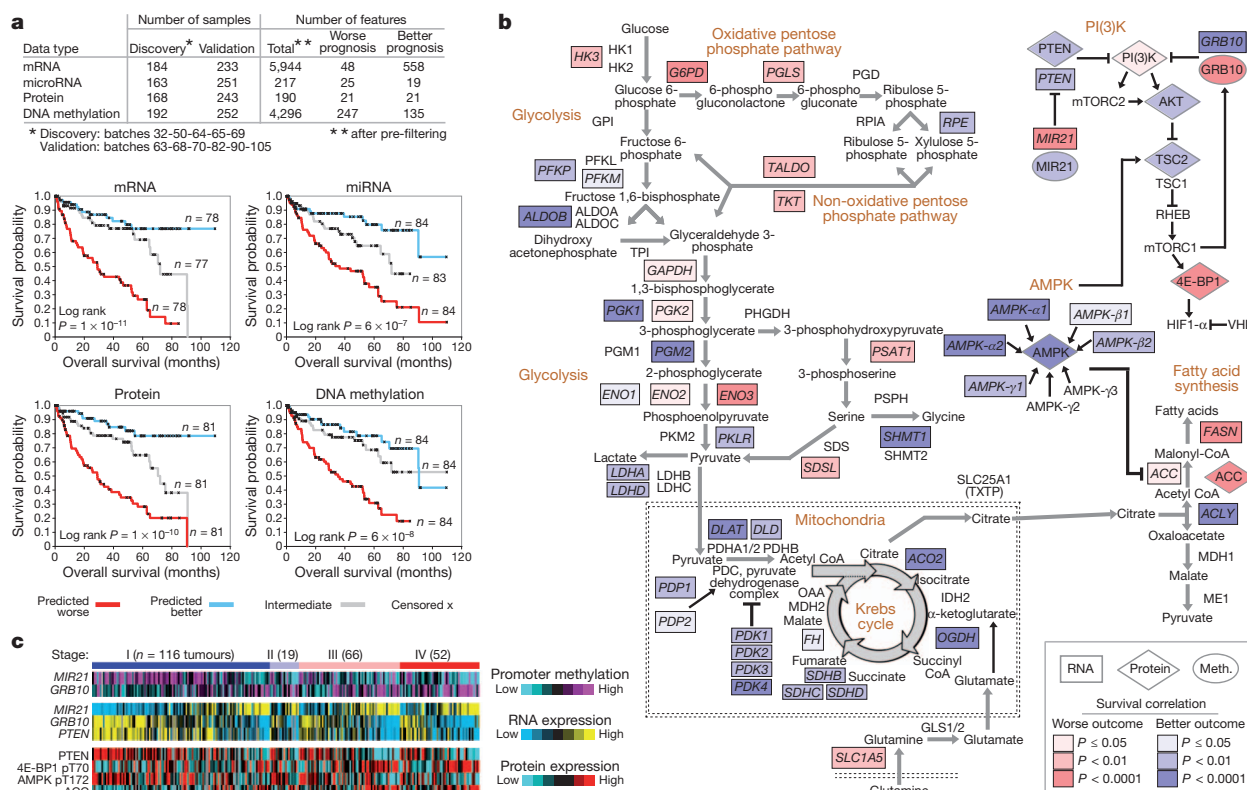


**Figure 5 | Molecular correlates of patient survival involve metabolic pathways.** **a**, Sample profiles were separated into discovery and validation subsets, with the top survival correlates within the discovery subset being defined for each of the four platforms examined (mRNA, microRNA, protein, DNA methylation). Kaplan–Meier plots show results of applying the four prognostic signatures to the validation subset, comparing survival for patients with predicted higher risk (red, top third of signature scores), lower risk (blue, bottom third) or intermediate risk (grey, middle third); successful predictions were observed in each case. **b**, When viewed in the context of metabolism, the molecular survival correlates highlight a widespread metabolic shift, with tumours altering their usage of key pathways and metabolites (red and blue

(*G6PD*, *PGLS*, *TALDO* (also known as *TALDO1P1*), *TKT*) and fatty acid synthesis (*FASN*, *ACC* (also known as *ACACA*)).

Examination of potential genetic or epigenetic drivers of a glycolytic shift led us to identify methylation events involving *MIR21* and *GRB10*, with decreased promoter methylation of each gene (thereby higher expression) being associated with worse or better outcome, respectively (Fig. 5b, Supplementary Fig. 59 and Supplementary Table 24). Both genes regulate the PI(3)K pathway: miR-21 is inducible by high glucose levels and downregulates *PTEN*<sup>22</sup>; whereas the tumour suppressor *GRB10* negatively regulates PI(3)K and insulin signalling<sup>30</sup>. Promoter methylation of *MIR21* and *GRB10* were coordinated with their mRNA expression patterns, as well as with the mRNA expression of other key genes and protein expression in the metabolic pathways (Fig. 5c and Supplementary Fig. 60). In addition to the PI(3)K pathway (Fig. 5b and Supplementary Fig. 61), molecular survival correlations involved several pro-metastatic matrix metalloproteinases (Supplementary Fig. 62).

## Discussion

Our study sampled a single site of the primary tumour, in a disease with a potentially high level of tumour heterogeneity<sup>8</sup>. The extent to which convergent evolutionary events are a common theme in ccRCC remains to be determined, but may indicate that critical genes will be represented across the tumour landscape for an individual mass. In general, the large sample size seemed to overcome the intrinsic challenges of studying a genetically complex disease, revealing rare variants

shading representing the correlation of increased gene expression with worse or better survival respectively, univariate Cox based on extended cohort). Worse survival correlates with upregulation of pentose phosphate pathway genes (*G6PD*, *PGLS*, *TALDO* and *TKT*), fatty acid synthesis genes (*ACC* and *FASN*), and PI(3)K pathway enhancing genes (*MIR21*). Better survival correlates with upregulation of AMPK complex genes, multiple Krebs cycle genes and PI(3)K pathway inhibitors (*PTEN*, *TSC2*). Additionally, specific promoter methylation events, including hypermethylation of PI(3)K pathway repressor *GRB10*, associate with outcome. **c**, Heat map of selected key features from the metabolic shift schematic (**b**) demonstrating coordinate expression by stage at DNA methylation, RNA, and protein levels (data from validation subset).

at rates similar to what has been described previously<sup>3</sup>. The samples, taken from primary tumour specimens, were reflective of patients fit for either definitive or cytoreductive nephrectomy, whereas future work could explore the genomic landscape of metastatic lesions.

Pathway and integrated analyses highlighted the importance of the well-known VHL/HIF pathway, the newly emerging chromatin remodelling/histone methylation pathway, and the PI(3)K/AKT pathway. The observation of chromatin modifier genes being frequently mutated in ccRCC strongly supports the model of nucleosome dynamics, providing a key function in renal tumorigenesis. Although the mechanistic details remain to be defined as to how such modulation promotes tumour formation, the data presented here revealed alterations in DNA methylation associated with *SETD2* mutations. As an epigenetic process that can potentially modify many transcriptional outputs, these mutational events have the potential to change the landscape of the tumour genome through altered expression of global sets of genes and genetic elements. Molecular correlates of patient survival further implicated PI(3)K/AKT as having a role in tumour progression, involving specific DNA methylation events. The PI(3)K/AKT pathway presents a strong therapeutic target in ccRCC, supporting the potential value of MTOR and/or related pathway inhibitor drugs for this cancer<sup>31,32</sup>.

Cross-platform molecular analyses indicated a correlation between worsened prognosis in patients with ccRCC and a metabolic shift involving increased dependence on the pentose phosphate shunt, decreased AMPK, decreased Krebs cycle activity, increased glutamine transport and fatty acid production. These findings are consistent



with the isotopomer spectral analysis of a pair of *VHL*<sup>-/-</sup> clear cell kidney cancer cell lines, both of which were notably derived from patients with aggressive, metastatic disease, which revealed a dependence on reductive glutamine metabolism for lipid biosynthesis<sup>33</sup>. The metabolic shift identified in poor prognosis ccRCC remarkably mirrors the Warburg metabolic phenotype (increased glycolysis, decreased AMPK, glutamine-dependent lipogenesis) identified in type 2 papillary kidney cancer characterized by mutation of the Krebs cycle enzyme, fumarate hydratase<sup>33</sup>. Further studies to dissect out the role of the commonly mutated chromosome 3 chromatin remodelling genes, *PBRM1*, *SETD2* and *BAP1*, in ccRCC tumorigenesis and their potential role in the metabolic remodelling associated with progression of this disease will hopefully provide the foundation for the development of effective forms of therapy for this disease.

## METHODS SUMMARY

Specimens were obtained from patients, with appropriate consent from institutional review boards. Using a co-isolation protocol, DNA and RNA were purified. In total, 446 patients were assayed on at least one molecular profiling platform, which platforms included: (1) RNA sequencing, (2) DNA methylation arrays, (3) miRNA sequencing, (4) Affymetrix single nucleotide polymorphism (SNP) arrays, (5) exome sequencing, and (6) reverse phase protein arrays. As described above and in the Supplementary Methods, both single platform analyses and integrated cross-platform analyses were performed.

Received 25 October 2012; accepted 24 April 2013.

Published online 23 June 2013.


- Linehan, W. M., Walther, M. M. & Zbar, B. The genetic basis of cancer of the kidney. *J. Urol.* **170**, 2163–2172 (2003).
- Linehan, W. M., Srinivasan, R. & Schmidt, L. S. The genetic basis of kidney cancer: a metabolic disease. *Nature Rev. Urol.* **7**, 277–285 (2010).
- Dalglish, G. L. *et al.* Systematic sequencing of renal carcinoma reveals inactivation of histone modifying genes. *Nature* **463**, 360–363 (2010).
- Guo, G. *et al.* Frequent mutations of genes encoding ubiquitin-mediated proteolysis pathway components in clear cell renal cell carcinoma. *Nature Genet.* **44**, 17–19 (2012).
- Varela, I. *et al.* Exome sequencing identifies frequent mutation of the SWI/SNF complex gene *PBRM1* in renal carcinoma. *Nature* **469**, 529–542 (2011).
- Zbar, B., Brauch, H., Talmadge, C. & Linehan, M. Loss of alleles of loci on the short arm of chromosome 3 in renal cell carcinoma. *Nature* **327**, 721–724 (1987).
- Carter, S. L. *et al.* Absolute quantification of somatic DNA alterations in human cancer. *Nature Biotechnol.* **30**, 413–421 (2012).
- Gerlinger, M. *et al.* Intratumor heterogeneity and branched evolution revealed by multiregion sequencing. *N. Engl. J. Med.* **366**, 883–892 (2012).
- Shen, C. *et al.* Genetic and functional studies implicate HIF1 $\alpha$  as a 14q kidney cancer suppressor gene. *Cancer Discov.* **1**, 222–235 (2011).
- Eder, A. M. *et al.* Atypical PKC $\alpha$  contributes to poor prognosis through loss of apical basal polarity and cyclin E overexpression in ovarian cancer. *Proc. Natl Acad. Sci. USA* **102**, 12519–12524 (2005).
- Herbers, J. *et al.* Significance of chromosome arm 14q loss in nonpapillary renal cell carcinomas. *Genes Chromosomes Cancer* **19**, 29–35 (1997).
- Hakimi, A. *et al.* Adverse outcomes in clear cell renal cell carcinoma with mutations of 3p21 epigenetic regulators BAP1 and SETD2: a report by MSKCC and the KIRC TCGA research network. *Clin. Cancer Res.* <http://dx.doi.org/10.1158/1078-0432.CCR-12-3886> (2013).
- Lewis, B. P., Shih, I., Jones-Rhoades, M., Bartel, D. & Burge, C. Prediction of mammalian microRNA targets. *Cell* **115**, 787–798 (2003).
- Clark, J. *et al.* Fusion of splicing factor genes *PSF* and *NonO* (*p54<sup>nrb</sup>*) to the *TFE3* gene in papillary renal cell carcinoma. *Oncogene* **15**, 2233–2239 (1997).
- Herman, J. G. *et al.* Silencing of the VHL tumor-suppressor gene by DNA methylation in renal carcinoma. *Proc. Natl Acad. Sci. USA* **91**, 9700–9704 (1994).
- Modena, P. *et al.* *UQCRRH* gene encoding mitochondrial hinge protein is interrupted by a translocation in a soft-tissue sarcoma and epigenetically inactivated in some cancer cell lines. *Oncogene* **22**, 4586–4593 (2003).
- Wagner, E. J. & Carpenter, P. B. Understanding the language of Lys36 methylation at histone H3. *Nature Rev. Mol. Cell Biol.* **13**, 115–126 (2012).
- Dhayan, A. *et al.* The Dnmt3a PWWP domain reads histone 3 lysine 36 trimethylation and guides DNA methylation. *J. Biol. Chem.* **285**, 26114–26120 (2010).
- Brannon, A. R. *et al.* Molecular stratification of clear cell renal cell carcinoma by consensus clustering reveals distinct subtypes and survival patterns. *Genes Cancer* **1**, 152–163 (2010).
- Liu, H. *et al.* Identifying mRNA targets of microRNA dysregulated in cancer: with application to clear cell renal cell carcinoma. *BMC Syst. Biol.* **4**, 51 (2010).
- Creighton, C. J. *et al.* Integrated analyses of microRNAs demonstrate their widespread influence on gene expression in high-grade serous ovarian carcinoma. *PLoS ONE* **7**, e34546 (2012).
- Dey, N. *et al.* MicroRNA-21 orchestrates high glucose-induced signals to TOR complex 1, resulting in renal cell pathology in diabetes. *J. Biol. Chem.* **286**, 25586–25603 (2011).
- Vandin, F., Upfal, E. & Raphael, B. J. Algorithms for detecting significantly mutated pathways in cancer. *J. Comput. Biol.* **18**, 507–522 (2011).
- The Cancer Genome Atlas Research Network. Integrated genomic analyses of ovarian carcinoma. *Nature* **474**, 609–615 (2011).
- Ciriello, G., Cerami, E., Sander, C. & Schultz, N. Mutual exclusivity analysis identifies oncogenic network modules. *Genome Res.* **22**, 398–406 (2012).
- He, X., Wang, J., Messing, E. M. & Wu, G. Regulation of receptor for activated C kinase 1 protein by the von Hippel-Lindau tumor suppressor in IGF-I-induced renal carcinoma cell invasiveness. *Oncogene* **30**, 535–547 (2011).
- Duran, A. *et al.* p62 is a key regulator of nutrient sensing in the mTORC1 pathway. *Mol. Cell* **44**, 134–146 (2011).
- Ravaud, A. *et al.* Lapatinib versus hormone therapy in patients with advanced renal cell carcinoma: a randomized phase III clinical trial. *J. Clin. Oncol.* **26**, 2285–2291 (2008).
- Tong, W. H. *et al.* The glycolytic shift in fumarate-hydratase-deficient kidney cancer lowers AMPK levels, increases anabolic propensities and lowers cellular iron levels. *Cancer Cell* **20**, 315–327 (2011).
- Yu, Y. *et al.* Phosphoproteomic analysis identifies Grb10 as an mTORC1 substrate that negatively regulates insulin signaling. *Science* **332**, 1322–1326 (2011).
- Motzer, R. J. *et al.* Efficacy of everolimus in advanced renal cell carcinoma: a double-blind, randomised, placebo-controlled phase III trial. *Lancet* **372**, 449–456 (2008).
- Hudes, G. *et al.* Temsirolimus, interferon alfa, or both for advanced renal-cell carcinoma. *N. Engl. J. Med.* **356**, 2271–2281 (2007).
- Metallo, C. M. *et al.* Reductive glutamine metabolism by IDH1 mediates lipogenesis under hypoxia. *Nature* **481**, 380–384 (2012).

Supplementary Information is available in the online version of the paper.

**Acknowledgements** We wish to thank all patients and families who contributed to this study. A full list of grant support and acknowledgments is included in the supplement.

**Author Contributions** The Cancer Genome Atlas research network contributed collectively to this study. Biospecimens were provided by the tissue source sites and processed by the Biospecimen Core Resource. Data generation and analyses were performed by the genome-sequencing centers, cancer genome-characterization centers and genome data analysis centers. All data were released through the Data Coordinating Center. Project activities were coordinated by the NCI and NHGRI project teams. The following TCGA investigators of the Kidney Analysis Working Group contributed substantially to the analysis and writing of this manuscript: Project leaders: Richard A. Gibbs, W. Marston Linehan. Data Coordinator: Margaret Morgan. Analysis Coordinators: Chad J. Creighton, Roel G. W. Verhaak. Manuscript Coordinators: Richard A. Gibbs, Chad J. Creighton. Writing Team: W. Marston Linehan, Chad J. Creighton, W. Kimryn Rathmell, Roel G. W. Verhaak, Richard A. Gibbs. DNA Sequence analysis: David A. Wheeler, Kristian Cibulskis. mRNA analysis: Roel G. W. Verhaak, A. Rose Brannon, W. Kimryn Rathmell, Wandaliz Torres-Garcia. microRNA analysis: A. Gordon Robertson, Andy Chu, Preethi H. Gunaratne. DNA methylation analysis: Hui Shen, Peter W. Laird. Copy number analysis: Rameen Beroukhi, Sabina Signoretti. Protein analysis: Dimitra Tsavachidou, Yiling Lu, Gordon B. Mills. Pathway/Integrated Analysis: Rehan Akbani, Giovanni Ciriello, Chad J. Creighton, Suzanne S. Fei, Anders Jacobsen, Evan O. Pailu, Ben Raphael, Sheila M. Reynolds, Christopher J. Ricketts, Nikolaus Schultz, Joshua M. Stuart, Fabio Vandin. Clinical Data: W. Kimryn Rathmell, A. Ari Hakimi, Johanna Gardener, Candace Shelton. Pathology and Clinical Expertise: James Hsieh, Marston W. Linehan, Pheroze Tamboli, W. Kimryn Rathmell, Victor Reuter.

**Author Information** All of the primary sequence files are deposited in CGHub (file IDs in Supplementary Information) and all other data are deposited at the Data Coordinating Center (DCC) for public access (<http://cancergenome.nih.gov/>). Reprints and permissions information is available at [www.nature.com/reprints](http://www.nature.com/reprints). The authors declare no competing financial interests. Readers are welcome to comment on the online version of the paper. Correspondence and requests for materials should be addressed to R.A.G. (agibbs@bcm.edu) or W.M.L. (linehanm@mail.nih.gov).

 This work is licensed under a Creative Commons Attribution-NonCommercial-Share Alike 3.0 Unported licence. To view a copy of this licence, visit <http://creativecommons.org/licenses/by-nc-sa/3.0>

## The Cancer Genome Atlas Research Network

**Analysis working group:** Baylor College of Medicine Chad J. Creighton<sup>1,2</sup>, Margaret Morgan<sup>1</sup>, Preethi H. Gunaratne<sup>1,3</sup>, David A. Wheeler<sup>1</sup>, Richard A. Gibbs<sup>1</sup>; **BC Cancer Agency** A. Gordon Robertson<sup>4</sup>, Andy Chu<sup>4</sup>; **Broad Institute** Rameen Beroukhi<sup>5,6</sup>, Kristian Cibulskis<sup>6</sup>; **Brigham & Women's Hospital** Sabina Signoretti<sup>7,54,59</sup>; **Brown University** Fabio Vandin<sup>8</sup>; Hsin-Ta Wu<sup>8</sup>, Benjamin J. Raphael<sup>8</sup>; **The University of Texas MD Anderson Cancer Center** Roel G. W. Verhaak<sup>9</sup>, Pheroze Tamboli<sup>10</sup>, Wandaliz Torres-Garcia<sup>9</sup>, Rehan Akbani<sup>9</sup>, John N. Weinstein<sup>9</sup>; **Memorial Sloan-Kettering Cancer Center** Victor Reuter<sup>11</sup>, James J. Hsieh<sup>12</sup>, A. Rose Brannon<sup>11</sup>, A. Ari Hakimi<sup>12</sup>, Anders Jacobsen<sup>13</sup>, Giovanni Ciriello<sup>13</sup>, Boris Reva<sup>13</sup>; **National Cancer Institute** Christopher J. Ricketts<sup>14</sup>, W. Marston Linehan<sup>14</sup>; **University of California Santa Cruz** Joshua M. Stuart<sup>15</sup>; **University of North Carolina, Chapel Hill** W. Kimryn Rathmell<sup>16</sup>; **University of Southern California** Hui Shen<sup>17</sup>, Peter W. Laird<sup>17</sup>; **Genome sequencing centres:** Baylor College of Medicine Donna Muzny<sup>1</sup>, Caleb Davis<sup>1</sup>, Margaret Morgan<sup>1</sup>, Liu Xi<sup>1</sup>,

Kyle Chang<sup>1</sup>, Nipun Kakkar<sup>1</sup>, Lisa R. Treviño<sup>1</sup>, Susan Benton<sup>1</sup>, Jeffrey G. Reid<sup>1</sup>, Donna Morton<sup>1</sup>, Harsha Doddapaneni<sup>1</sup>, Yi Han<sup>1</sup>, Lora Lewis<sup>1</sup>, Huyen Dinh<sup>1</sup>, Christie Kovar<sup>1</sup>, Yiming Zhu<sup>1</sup>, Jireh Santibanez<sup>1</sup>, Min Wang<sup>1</sup>, Walker Hale<sup>1</sup>, Divya Kalra<sup>1</sup>, Chad J. Creighton<sup>1,2</sup>, David A. Wheeler<sup>1</sup>, Richard A. Gibbs<sup>1</sup>; **Broad Institute** Gad Getz<sup>6,57</sup>, Kristian Cibulskis<sup>6</sup>, Michael S. Lawrence<sup>6</sup>, Carrie Sougnez<sup>2</sup>, Scott L. Carter<sup>6</sup>, Andrey Sivachenko<sup>6</sup>, Lee Lichtenstein<sup>6</sup>, Chip Stewart<sup>6</sup>, Doug Voet<sup>6</sup>, Sheila Fisher<sup>6</sup>, Stacey B. Gabriel<sup>6</sup>, Eric Lander<sup>6</sup>; **Genome characterization centres: Broad Institute** Rameen Beroukhi<sup>5,6,54,56</sup>, Steve E. Schumacher<sup>6,56</sup>, Barbara Tabak<sup>6,56</sup>, Gordon Saksena<sup>6</sup>, Robert C. Onofrio<sup>6</sup>, Scott L. Carter<sup>6</sup>, Andrew D. Cherniack<sup>6</sup>, Jeff Gentry<sup>6</sup>, Kristin Ardlie<sup>6</sup>, Carrie Sougnez<sup>2</sup>, Gad Getz<sup>6,57</sup>, Stacey B. Gabriel<sup>6</sup>, Matthew Meyerson<sup>6,7,54</sup>; **BC Cancer Agency** A. Gordon Robertson<sup>4</sup>, Andy Chu<sup>4</sup>, Hye-Jung E. Chun<sup>4</sup>, Andrew J. Mungall<sup>4</sup>, Payal Sipahimalani<sup>4</sup>, Dominik Stolfi<sup>4</sup>, Adrian Ally<sup>4</sup>, Miruna Balasundaram<sup>4</sup>, Yaron S. N. Butterfield<sup>4</sup>, Rebecca Carsen<sup>4</sup>, Candace Carter<sup>4</sup>, Eric Chuah<sup>4</sup>, Robin J. N. Coope<sup>4</sup>, Noreen Dhalla<sup>4</sup>, Sharon Garski<sup>4</sup>, Ranabir Guin<sup>4</sup>, Carrie Hirst<sup>4</sup>, Martin Hirst<sup>4</sup>, Robert A. Holt<sup>4</sup>, Chandra Lebovitz<sup>4</sup>, Darlene Lee<sup>4</sup>, Haiyan I. Li<sup>4</sup>, Michael Mayo<sup>4</sup>, Richard A. Moore<sup>4</sup>, Erin Pleasance<sup>4</sup>, Patrick Plettner<sup>4</sup>, Jacqueline E. Schein<sup>4</sup>, Arash Shafiei<sup>4</sup>, Jared R. Slobodan<sup>4</sup>, Angela Tam<sup>4</sup>, Nina Thiessen<sup>4</sup>, Richard J. Varhol<sup>4</sup>, Natasia Wye<sup>4</sup>, Yongjun Zhao<sup>4</sup>, Inanc Birol<sup>4</sup>, Steven J. M. Jones<sup>4</sup>, Marco A. Marra<sup>4</sup>; **University of North Carolina, Chapel Hill** J. Todd Auman<sup>18</sup>, Donghui Tan<sup>19</sup>, Corbin D. Jones<sup>20</sup>, Katherine A. Hoadley<sup>16,21,22</sup>, Piotr A. Mieczkowski<sup>22</sup>, Lisle E. Mose<sup>21</sup>, Stuart R. Jefferys<sup>22</sup>, Michael D. Topal<sup>21,22</sup>, Christina Liquori<sup>16</sup>, Yidi J. Turman<sup>16</sup>, Yan Shi<sup>16</sup>, Scot Waring<sup>16</sup>, Elizabeth Buda<sup>16</sup>, Jesse Walsh<sup>16</sup>, Junyuan Wu<sup>16</sup>, Tom Bodenheimer<sup>16</sup>, Alan P. Hoyle<sup>16</sup>, Janae V. Simons<sup>16</sup>, Mathew G. Soloway<sup>16</sup>, Saianand Balu<sup>16</sup>, Joel S. Parker<sup>16</sup>, D. Neil Hayes<sup>16,23</sup>, Charles M. Perou<sup>16,21,22</sup>; **Harvard Medical School** Raju Kucherlapati<sup>24,25</sup>, Peter Park<sup>25,26,27</sup>; **University of Southern California & Johns Hopkins University** Hui Shen<sup>17</sup>, Timothy Triche Jr<sup>17</sup>, Daniel J. Weisenberger<sup>17</sup>, Phillip H. Lai<sup>17</sup>, Moiz S. Bootwalla<sup>17</sup>, Dennis T. Maglinte<sup>17</sup>, Swapna Mahurkar<sup>17</sup>, Benjamin P. Berman<sup>17</sup>, David J. Van Den Berg<sup>17</sup>, Leslie Cope<sup>28</sup>, Stephen B. Baylin<sup>28</sup>, Peter W. Laird<sup>17</sup>; **Genome data analysis: Baylor College of Medicine** Chad J. Creighton<sup>12</sup>, David A. Wheeler<sup>17</sup>; **Broad Institute** Gad Getz<sup>6,57</sup>, Michael S. Noble<sup>6</sup>, Daniel DiCara<sup>6</sup>, Hailei Zhang<sup>6</sup>, Juok Cho<sup>6</sup>, David I. Heiman<sup>6</sup>, Nils Gehlenborg<sup>6,26</sup>, Doug Voet<sup>6</sup>, William Mallard<sup>6</sup>, Pei Lin<sup>6</sup>, Scott Frazier<sup>6</sup>, Petar Stojanov<sup>6,54</sup>, Yingchun Lu<sup>6</sup>, Lihua Zhou<sup>6</sup>, Jaegil Kim<sup>6</sup>, Michael S. Lawrence<sup>6</sup>, Lynda Chin<sup>6,31</sup>; **Brown University** Fabio Vandin<sup>8</sup>, Hsin-Ta Wu<sup>8</sup>, Benjamin J. Raphael<sup>8</sup>; **Buck Institute for Research on Aging** Christopher Benz<sup>55</sup>, Christina Yau<sup>55</sup>; **Institute for Systems Biology** Sheila M. Reynolds<sup>29</sup>, Ilya Shmulevich<sup>29</sup>; **The University of Texas MD Anderson Cancer Center** Roel G.W. Verhaak<sup>9</sup>, Wandaliz Torres-Garcia<sup>9</sup>, Rahul Vegesna<sup>9</sup>, Hoon Kim<sup>9</sup>, Wei Zhang<sup>10</sup>, David Cogdell<sup>10</sup>, Eric Jonasz<sup>9</sup>, Zhiyong Ding<sup>9</sup>, Yiling Lu<sup>30</sup>, Rehan Akbani<sup>9</sup>, Nianxiang Zhang<sup>9</sup>, Anna K. Unruh<sup>9</sup>, Tod D. Casasent<sup>9</sup>, Chris Wakefield<sup>9</sup>, Dimitra Tsavachidou<sup>30</sup>, Lynda Chin<sup>6,31</sup>, Gordon B. Mills<sup>30</sup>, John N. Weinstein<sup>9</sup>; **Memorial Sloan-Kettering Cancer Center** Anders Jacobsen<sup>13</sup>, A. Rose Brannon<sup>11</sup>, Giovanni Ciriello<sup>13</sup>, Nikolaus Schultz<sup>13</sup>, A. Ari Hakimi<sup>12</sup>, Boris Reva<sup>13</sup>, Yevgeniy Antipin<sup>13</sup>, Jianjiong Gao<sup>13</sup>, Ethan Cerami<sup>13</sup>, Benjamin Gross<sup>13</sup>, B. Arman Aksoy<sup>13</sup>, Rileen Sinha<sup>13</sup>, Nils Weinhold<sup>13</sup>, S. Onur Sumer<sup>13</sup>, Barry S. Taylor<sup>13</sup>, Ronglai Shen<sup>13</sup>, Irina Ostrovnya<sup>32</sup>, James J. Hsieh<sup>12</sup>, Michael F. Berger<sup>11</sup>, Marc Ladanyi<sup>12</sup>, Chris Sander<sup>13</sup>; **Oregon Health & Science University** Suzanne S. Fei<sup>33</sup>, Andrew Stout<sup>33</sup>, Paul T. Spellman<sup>33</sup>; **Stanford University** Daniel L. Rubin<sup>34</sup>, Tiffany T. Liu<sup>34</sup>; **University of California Santa Cruz** Joshua M. Stuart<sup>15</sup>, Sam Ng<sup>15</sup>, Evan O. Paull<sup>15</sup>, Daniel Carlin<sup>15</sup>, Theodore Goldstein<sup>15</sup>, Peter Waltman<sup>15</sup>, Kyle Elliott<sup>15</sup>, Jing Zhu<sup>15</sup>, David Haussler<sup>15,35</sup>; **University of Houston** Preethi H. Gunaratne<sup>13</sup>, Weimin Xiao<sup>3</sup>; **Biospecimen core resource: International Genomics Consortium** Candace Shelton<sup>36</sup>, Johanna Gardner<sup>36</sup>, Robert Penny<sup>36</sup>, Mark Sherman<sup>36</sup>, David Mallery<sup>36</sup>, Scott Morris<sup>36</sup>, Joseph Paulauskis<sup>36</sup>, Ken Burnett<sup>36</sup>, Troy Shelton<sup>36</sup>; **Tissue source sites: Brigham & Women's Hospital** Sabina Signoretti<sup>7,54,59</sup>, **Dana-Farber Cancer Institute** William G. Kaelin<sup>54,60</sup>, Toni Choueiri<sup>54</sup>; **Georgetown University** Michael B. Atkins<sup>37</sup>; **International Genomics Consortium** Robert Penny<sup>36</sup>, Ken Burnett<sup>36</sup>, David Mallery<sup>36</sup>, Erin Curley<sup>36</sup>; **Memorial Sloan-Kettering Cancer Center** Satish Tickoo<sup>11</sup>, Victor Reuter<sup>11</sup>; **University of North Carolina at Chapel Hill** W. Kimryn Rathmell<sup>16</sup>, Leigh Thorne<sup>16</sup>, Lori Boice<sup>16</sup>, Mei Huang<sup>16</sup>, Jennifer C. Fisher<sup>16</sup>; **National Cancer Institute** W. Marston Linehan<sup>14</sup>, Cathy D. Vocke<sup>14</sup>, James Peterson<sup>14</sup>, Robert Worrell<sup>14</sup>, Maria J. Merino<sup>14</sup>, Laura S. Schmidt<sup>14,38</sup>; **The University of Texas MD Anderson Cancer Center** Pheroze Tamboli<sup>10</sup>, Bogdan A. Czerniak<sup>10</sup>, Kenneth D. Aldape<sup>10</sup>, Christopher G. Wood<sup>39</sup>; **Fox Chase Cancer Center** Jeff Boyd<sup>40</sup>, JoEllen Weaver<sup>40</sup>; **Helen F. Graham Cancer Center at Christiana Care** Mary V. Iacocca<sup>41</sup>, Nicholas Petrelli<sup>41</sup>, Gary Witkin<sup>41</sup>, Jennifer Brown<sup>41</sup>, Christine Czerwinski<sup>41</sup>, Lori Huelsenbeck-Dill<sup>41</sup>, Brenda Rabeno<sup>41</sup>; **Penrose-St. Francis Health Services** Jerome Myers<sup>42</sup>, Carl Morrison<sup>42</sup>, Julie Bergsten<sup>42</sup>, John Eckman<sup>42</sup>, Jodi Harr<sup>42</sup>, Christine Smith<sup>42</sup>, Kelinda Tucker<sup>42</sup>, Leigh Anne Zach<sup>42</sup>; **Roswell Park Cancer Institute** Wiam Bshara<sup>43</sup>, Carmelo Gaudio<sup>43</sup>, Carl Morrison<sup>43</sup>; **University of Pittsburgh** Rajiv Dhir<sup>44</sup>, Jodi Maranchie<sup>44</sup>, Joel Nelson<sup>44</sup>, Anil Parwani<sup>44</sup>; **Cureline** Olga Potapova<sup>45</sup>; **St. Petersburg City Clinical Oncology Dispensary** Konstantin Fedosenko<sup>46</sup>; **Mayo Clinic** John C. Cheville<sup>58</sup>, R. Houston Thompson<sup>58</sup>; **Disease working group: Brigham & Women's Hospital** Sabina Signoretti<sup>7,54,59</sup>; **Dana-Farber Cancer Institute** William G. Kaelin<sup>54,60</sup>; **Georgetown University** Michael B. Atkins<sup>37</sup>; **Memorial Sloan-Kettering Cancer Center** Satish Tickoo<sup>11</sup>, Victor Reuter<sup>11</sup>; **National Cancer Institute** W. Marston Linehan<sup>14</sup>, Cathy D. Vocke<sup>14</sup>, James Peterson<sup>14</sup>, Maria J. Merino<sup>14</sup>, Laura S. Schmidt<sup>14,38</sup>; **The University of Texas MD Anderson Cancer Center** Pheroze Tamboli<sup>10</sup>; **Weill Cornell Medical College** Juan M. Mosquera<sup>47</sup>, Mark A. Rubin<sup>47</sup>; **Massachusetts General Hospital** Michael L. Blute<sup>48</sup>; **University of North Carolina, Chapel Hill** W. Kimryn Rathmell<sup>16</sup>; **Data coordination centre: Todd Pihl**<sup>49</sup>, Mark Jensen<sup>49</sup>, Robert Sfeir<sup>49</sup>, Ari Kahn<sup>49</sup>, Anna Chu<sup>49</sup>, Prachi Kothiyal<sup>49</sup>, Eric Snyder<sup>49</sup>, Joan Pontius<sup>49</sup>, Brenda Ayala<sup>49</sup>, Mark Backus<sup>49</sup>, Jessica Walton<sup>49</sup>, Julien Baboud<sup>49</sup>, Dominique Berton<sup>49</sup>, Matthew Nicholls<sup>49</sup>, Deepak

Srinivasan<sup>49</sup>, Rohini Raman<sup>49</sup>, Stanley Girshik<sup>49</sup>, Peter Kigonya<sup>49</sup>, Shelley Alonso<sup>49</sup>, Rashmi Sanbhatti<sup>49</sup>, Sean Barletta<sup>49</sup>, David Pot<sup>49</sup>; **Project team: National Cancer Institute** Margi Sheth<sup>50</sup>, John A. Demchok<sup>50</sup>, Tanja Davidisen<sup>50</sup>, Zhining Wang<sup>50</sup>, Liming Yang<sup>50</sup>, Roy W. Tarnuzzer<sup>50</sup>, Jiashan Zhang<sup>50</sup>, Greg Eley<sup>51</sup>, Martin L. Ferguson<sup>52</sup>, Kenna R. Mills Shaw<sup>50</sup>; **National Human Genome Research Institute** Mark S. Guyer<sup>53</sup>, Bradley A. Ozenberger<sup>53</sup> & Heidi J. Sofia<sup>53</sup>.

<sup>1</sup>Human Genome Sequencing Center, Baylor College of Medicine, Houston, Texas 77030, USA. <sup>2</sup>Dan L. Duncan Cancer Center, Baylor College of Medicine, Houston, Texas 77030, USA. <sup>3</sup>Department of Biology & Biochemistry, University of Houston, Houston, Texas 77204, USA. <sup>4</sup>Canada's Michael Smith Genome Sciences Centre, BC Cancer Agency, Vancouver, British Columbia V5Z, Canada. <sup>5</sup>Department of Medicine, Harvard Medical School, Boston, Massachusetts 02215, USA. <sup>6</sup>The Eli and Edythe L. Broad Institute of Massachusetts Institute of Technology and Harvard University, Cambridge, Massachusetts 02142, USA. <sup>7</sup>Department of Pathology, Harvard Medical School, Boston, Massachusetts 02215, USA. <sup>8</sup>Department of Computer Science, Brown University, Providence, Rhode Island 02912, USA. <sup>9</sup>Department of Bioinformatics and Computational Biology, The University of Texas MD Anderson Cancer Center, Houston, Texas 77030, USA. <sup>10</sup>Department of Pathology, The University of Texas MD Anderson Cancer Center, Houston, Texas 77030, USA. <sup>11</sup>Department of Pathology, Memorial Sloan-Kettering Cancer Center, New York, New York 10065, USA. <sup>12</sup>Human Oncology and Pathogenesis Program, Memorial Sloan-Kettering Cancer Center, New York, New York 10065, USA. <sup>13</sup>Computational Biology Center, Memorial Sloan-Kettering Cancer Center, New York, New York 10065, USA. <sup>14</sup>Urologic Oncology Branch, Center for Cancer Research, National Cancer Institute, Bethesda, Maryland 20892, USA. <sup>15</sup>Department of Biomolecular Engineering and Center for Biomolecular Science and Engineering, University of California Santa Cruz, Santa Cruz, California 95064, USA. <sup>16</sup>Lineberger Comprehensive Cancer Center, University of North Carolina at Chapel Hill, Chapel Hill, North Carolina 27599, USA. <sup>17</sup>USC Epigenome Center, University of Southern California, Los Angeles, California 90033, USA. <sup>18</sup>Eshelman School of Pharmacy, University of North Carolina at Chapel Hill, Chapel Hill, North Carolina 27599, USA. <sup>19</sup>Carolina Center for Genome Sciences, University of North Carolina at Chapel Hill, Chapel Hill, North Carolina 27599, USA. <sup>20</sup>Department of Biology, University of North Carolina at Chapel Hill, Chapel Hill, North Carolina 27599, USA. <sup>21</sup>Department of Pathology and Laboratory Medicine, University of North Carolina at Chapel Hill, Chapel Hill, North Carolina 27599, USA. <sup>22</sup>Department of Genetics, University of North Carolina at Chapel Hill, Chapel Hill, North Carolina 27599, USA. <sup>23</sup>Department of Internal Medicine, Division of Medical Oncology, University of North Carolina at Chapel Hill, Chapel Hill, North Carolina 27599, USA. <sup>24</sup>Department of Genetics, Harvard Medical School, Boston, Massachusetts 02215, USA. <sup>25</sup>Division of Genetics, Brigham and Women's Hospital, Boston, Massachusetts 02115, USA. <sup>26</sup>The Center for Biomedical Informatics, Harvard Medical School, Boston, Massachusetts 02115, USA. <sup>27</sup>Informatics Program, Children's Hospital, Boston, Massachusetts 02115, USA. <sup>28</sup>Cancer Biology Division, The Sidney Kimmel Comprehensive Cancer Center at Johns Hopkins University, Baltimore, Maryland 21231, USA. <sup>29</sup>Institute for Systems Biology, Seattle, Washington 98109, USA. <sup>30</sup>Department of Systems Biology, The University of Texas MD Anderson Cancer Center, Houston, Texas 77030, USA. <sup>31</sup>Department of Genomic Medicine, University of Texas MD Anderson Cancer Center, Houston, Texas 77054, USA. <sup>32</sup>Department of Epidemiology and Biostatistics, Memorial Sloan-Kettering Cancer Center, New York, New York 10065, USA. <sup>33</sup>Department of Molecular & Medical Genetics, Oregon Health & Science University, Portland, Oregon 97239, USA. <sup>34</sup>Department of Radiology, Stanford University Medical Center, Stanford, California 94305, USA. <sup>35</sup>Howard Hughes Medical Institute, University of California Santa Cruz, Santa Cruz, California 95064, USA. <sup>36</sup>International Genomics Consortium, Phoenix, Arizona 85004, USA. <sup>37</sup>Georgetown-Lombardi Comprehensive Cancer Center, Georgetown University, Washington DC 20057, USA. <sup>38</sup>Basic Science Program, SAIC-Frederick, Inc., Frederick National Lab, Frederick, Maryland 21702, USA. <sup>39</sup>Department of Urology, The University of Texas MD Anderson Cancer Center, Houston, Texas 77030, USA. <sup>40</sup>Cancer Biology Program, Fox Chase Cancer Center, Philadelphia, Pennsylvania 19111, USA. <sup>41</sup>Helen F. Graham Cancer Center, Christiana Care, Newark, Delaware 19713, USA. <sup>42</sup>Penrose-St. Francis Health Services, Colorado Springs, Colorado 80907, USA. <sup>43</sup>Department of Pathology, Roswell Park Cancer Institute, Buffalo, New York 14263, USA. <sup>44</sup>Department of Pathology, University of Pittsburgh, Pittsburgh, Pennsylvania 15213, USA. <sup>45</sup>Cureline, Inc. South San Francisco, California 94080, USA. <sup>46</sup>St Petersburg City Clinical Oncology Dispensary, St Petersburg 198255, Russia. <sup>47</sup>Department of Pathology and Laboratory Medicine, Weill Cornell College of Medicine, New York, New York 10065, USA. <sup>48</sup>Department of Urology, Massachusetts General Hospital, Boston, Massachusetts 02114, USA. <sup>49</sup>SRA International, 4300 Fair Lakes Court, Fairfax, Virginia 22033, USA. <sup>50</sup>The Cancer Genome Atlas Program Office, Center for Cancer Genomics, National Cancer Institute, Bethesda, Maryland 20892, USA. <sup>51</sup>TCGA Consultant, Scicentis, LLC, Atlanta, Georgia 30666, USA. <sup>52</sup>MLF Consulting, Arlington, Massachusetts 02474, USA. <sup>53</sup>National Human Genome Research Institute, National Institutes of Health, Bethesda, Maryland 20892, USA. <sup>54</sup>Department of Medical Oncology, Dana-Farber Cancer Institute, Boston, Massachusetts 02215, USA. <sup>55</sup>Buck Institute for Research on Aging, Novato, California 94945, USA. <sup>56</sup>Department of Cancer Biology, Dana-Farber Cancer Institute, Boston, Massachusetts 02215, USA. <sup>57</sup>Cancer Center and Department of Pathology, Massachusetts General Hospital, 55 Fruit St, Boston, Massachusetts 02114. <sup>58</sup>Mayo Clinic, Rochester, Minnesota 55905, USA. <sup>59</sup>Department of Pathology, Brigham and Women's Hospital, Boston, Massachusetts 02215, USA. <sup>60</sup>Howard Hughes Medical Institute, Chevy Chase, Maryland 20815, USA.



# 53BP1 is a reader of the DNA-damage-induced H2A Lys 15 ubiquitin mark

Amélie Fradet-Turcotte<sup>1</sup>, Marella D. Canny<sup>1</sup>, Cristina Escribano-Díaz<sup>1</sup>, Alexandre Orthwein<sup>1</sup>, Charles C. Y. Leung<sup>1</sup>, Hao Huang<sup>1</sup>, Marie-Claude Landry<sup>1</sup>, Julianne Kitevski-LeBlanc<sup>2,3,4</sup>, Sylvie M. Noordermeer<sup>1</sup>, Frank Sicheri<sup>1,2,3</sup> & Daniel Durocher<sup>1,2</sup>

**53BP1 (also called TP53BP1) is a chromatin-associated factor that promotes immunoglobulin class switching and DNA double-strand-break (DSB) repair by non-homologous end joining. To accomplish its function in DNA repair, 53BP1 accumulates at DSB sites downstream of the RNF168 ubiquitin ligase. How ubiquitin recruits 53BP1 to break sites remains unknown as its relocalization involves recognition of histone H4 Lys 20 (H4K20) methylation by its Tudor domain. Here we elucidate how vertebrate 53BP1 is recruited to the chromatin that flanks DSB sites. We show that 53BP1 recognizes mononucleosomes containing dimethylated H4K20 (H4K20me2) and H2A ubiquitinated on Lys 15 (H2AK15ub), the latter being a product of RNF168 action on chromatin. 53BP1 binds to nucleosomes minimally as a dimer using its previously characterized methyl-lysine-binding Tudor domain and a carboxy-terminal extension, termed the ubiquitination-dependent recruitment (UDR) motif, which interacts with the epitope formed by H2AK15ub and its surrounding residues on the H2A tail. 53BP1 is therefore a bivalent histone modification reader that recognizes a histone ‘code’ produced by DSB signalling.**

DNA double-strand breaks (DSBs) elicit a cascade of protein recruitment on the chromatin surrounding DNA lesions that regulates DNA damage repair and signalling<sup>1,2</sup>. 53BP1 is an important effector of this DSB response, as it promotes repair by non-homologous end joining (NHEJ)<sup>3</sup> by opposing DNA end resection<sup>4</sup>, the initiating step in homologous recombination. In mice, 53BP1 is necessary for immunoglobulin class switching<sup>5,6</sup> and dysfunctional telomere fusions<sup>7</sup>, two processes that rely on NHEJ. Furthermore, 53BP1 deficiency in mice leads to a near-complete reversal of the phenotypes associated with loss of BRCA1, including tumorigenesis<sup>4,8</sup>. 53BP1 must accumulate on the chromatin surrounding DSBs to accomplish its functions<sup>9</sup>. At the molecular level, 53BP1 acts as a recruitment platform for RIF1, its effector protein during DSB repair by NHEJ<sup>10–13</sup>. 53BP1 accumulation at DSB sites, as monitored by formation of ionizing radiation (IR)-induced subnuclear foci, requires the recognition of histone methylation, in particular H4K20me2 (ref. 14), by its tandem Tudor domain<sup>15</sup> (Fig. 1a). However, the formation of 53BP1 foci also requires the RNF168 E3 ligase<sup>1,2</sup>, raising the question of how a ubiquitin ligase promotes the accumulation of a methylated histone binding protein at sites of DNA damage. The current models of 53BP1 recruitment to DSB sites propose that H4K20 methylation is either induced or becomes available for 53BP1 binding after DNA damage<sup>16–19</sup>. For example, it has been proposed that JMJD2A and L3MBTL1, which bind to H4K20me2, are removed in a ubiquitination-dependent manner from the chromatin surrounding DSB sites, to allow 53BP1 binding<sup>18,19</sup>. In aggregate, these models indicate that increased accessibility of H4K20me2 at DSB sites might be sufficient to trigger 53BP1 recruitment.

## Identification of the 53BP1 UDR

We reasoned that if the above model was strictly correct, the 53BP1 orthologue from fission yeast, Crb2, should also form IR-induced foci in human cells. Indeed, Crb2 contains a tandem Tudor domain that binds to H4K20me2 (Fig. 1a)<sup>14</sup>. Crb2 accumulates at DSB sites in an H4K20me2-binding-dependent manner<sup>16,20</sup>, but fission yeast does

not have a recognizable RNF168 homologue, as it arose later during evolution. When expressed in human cells as a GFP fusion, Crb2 failed to form IR-induced foci whereas 53BP1 formed foci that co-localized with  $\gamma$ -H2AX (Fig. 1b). As expected, the accumulation of 53BP1 at DSB sites was dependent on H4K20me2 recognition because the 53BP1 D1521R mutation, which disrupts this activity of the Tudor domain, impaired the ability of 53BP1 to form IR-induced foci (Fig. 1b). The inability of Crb2 to accumulate at DSB sites in human cells was not due to a failure of Crb2 to interact with human H4K20me2, as it associated with human chromatin in a Tudor-dependent manner, as determined by fluorescence recovery after photobleaching (FRAP) (Supplementary Fig. 2a–d) and cellular subfractionation (Supplementary Fig. 2e). These experiments suggested that 53BP1 recruitment to break sites might be largely independent of an increased accessibility of H4K20me2 in damaged chromatin.

These observations provided an opportunity to map the region that endows 53BP1 with the ability to accumulate at DSB sites in an RNF168-dependent manner. We refer to this putative region as the ubiquitination-dependent recruitment (UDR) motif. We thus prepared various chimaeras between Crb2 and the minimal focus-forming region (FFR) of 53BP1, which consists of the Tudor domain flanked by an amino-terminal oligomerization region and a C-terminal extension<sup>21,22</sup> (that is, 53BP1 residues 1220–1711; Fig. 1a). We separated the 53BP1(FFR) and Crb2 into three regions that were swapped between the two proteins, in various combinations. The chimaeras prepared are illustrated in Fig. 1c and, to facilitate the identification of the chimaeras, segments were labelled ‘S’ if derived from 53BP1 and ‘C’ if derived from Crb2. Because 53BP1 can oligomerize<sup>21</sup>, all experiments were carried out in cells depleted of endogenous 53BP1.

The domain-swapping experiments first confirmed that the Crb2 Tudor domain can recognize H4K20me2 in human chromatin, as the Crb2 Tudor domain inserted into the 53BP1(FFR) supported localization to break sites (Fig. 1c, d). Second, introduction of the sequence immediately C-terminal of the 53BP1 Tudor domain into Crb2 (CC5

<sup>1</sup>Samuel Lunenfeld Research Institute, Mount Sinai Hospital, 600 University Avenue, Toronto, Ontario M5G 1X5, Canada. <sup>2</sup>Department of Molecular Genetics, University of Toronto, Ontario M5S 3E1, Canada. <sup>3</sup>Department of Biochemistry, University of Toronto, Ontario M5S 3E1, Canada. <sup>4</sup>Department of Chemistry, University of Toronto, Ontario M5S 3E1, Canada.

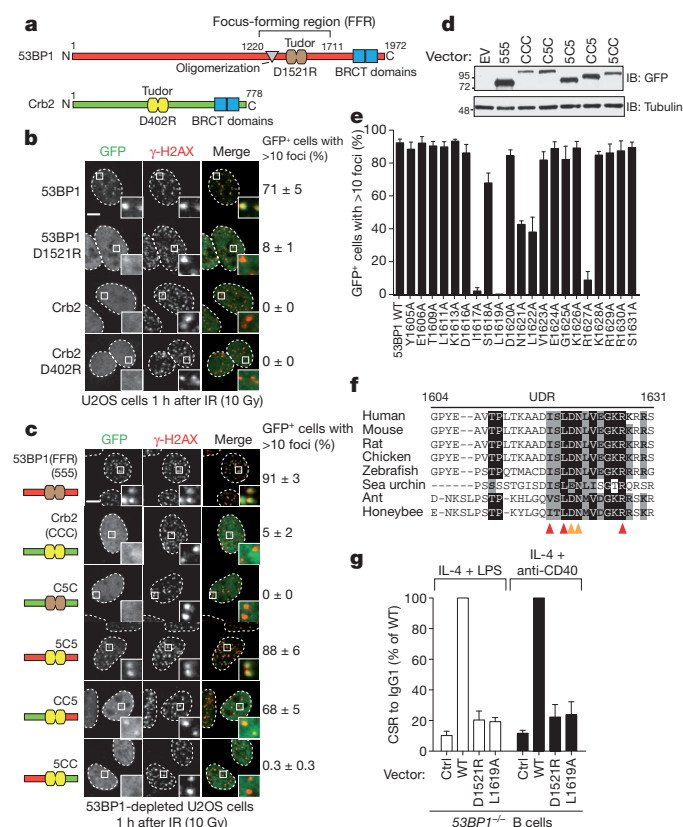


**Figure 1 | Identification of the 53BP1 UDR.** **a**, Schematic representation of 53BP1 and Crb2. **b**, U2OS cells transfected with GFP-53BP1 and GFP-Crb2 expression vectors were irradiated (10 Gy) and processed for GFP imaging and  $\gamma$ -H2AX immunofluorescence (mean  $\pm$  s.e.m.,  $n = 4$  except for 53BP1 WT, where  $n = 5$ ). **c**, 53BP1-depleted U2OS cells transfected with the indicated GFP-53BP1/Crb2-derived expression vectors were irradiated (10 Gy) and processed as described in **a** (mean  $\pm$  s.e.m.,  $n = 5$  except for 5CC and C5C, where  $n = 3$ ). **d**, Analysis of GFP fusion protein expression by immunoblotting. The migration of molecular mass markers (kDa) is indicated on the left. EV, empty vector; IB, immunoblot. **e**, 53BP1-depleted U2OS cells transfected with vectors expressing the indicated GFP-53BP1 mutants (residues 1220–1631) were irradiated (10 Gy) and processed as in **a** (mean  $\pm$  s.e.m.,  $n = 3$  except for WT, where  $n = 7$ , L1613A and L1619A, where  $n = 4$ , and S1631A, where  $n = 6$ ). **f**, Alignment of the UDR region in 53BP1 orthologues. Arrows indicate conserved residues. **g**, Relative levels of class switching to IgG1 in 53BP1<sup>-/-</sup> murine B cells transduced with the indicated retroviruses (mean  $\pm$  s.d.,  $n = 3$  except for L1619A, where  $n = 2$ ).

chimaera) produced a protein that accumulated into IR-induced foci that co-localized with  $\gamma$ -H2AX (Fig. 1c, d). Notably, the accumulation of the CC5 chimaera at DSB sites was dependent on RNF168 (Supplementary Fig. 3a, b), strongly suggesting that sequences C-terminal of the 53BP1 Tudor compose the UDR. We further narrowed down the UDR to the region between residues 1604 and 1631 (Supplementary Fig. 3c–e).

Next, we performed alanine-scanning mutagenesis of the UDR, in the context of 53BP1(1220–1631), to identify residues that participate in the recruitment of 53BP1 to DNA damage sites. These studies identified five residues (I1617, L1619, N1621, L1622 and R1627) the mutation of which to alanine disrupts 53BP1 recruitment to DSB sites, with the I1617A and L1619A mutations having the strongest impact (Fig. 1e and Supplementary Fig. 4). The importance of L1619 and L1622 in 53BP1 recruitment to break sites was observed previously<sup>21</sup>. Introduction of these five mutations in the context of full-length 53BP1 also impaired IR-induced focus formation, confirming their importance for accumulation at DSB sites (Supplementary Fig. 5). The five residues important for the activity of the UDR are clustered in a 12-amino-acid residue

segment that is highly conserved among 53BP1 orthologues in organisms that have a recognizable RNF8 pathway (Fig. 1f).

## The UDR is required for 53BP1 function

RIF1 is the 53BP1 effector during DSB repair<sup>10–13</sup>. We therefore examined the contribution of the UDR in promoting RIF1 IR-induced focus formation. We tested eight UDR mutations introduced in a short interfering RNA (siRNA)-resistant 53BP1 vector: the five mutations that affect 53BP1 recruitment and three others (K1613A, D1616A and E1624A) that do not. We also included in these assays 53BP1 and 53BP1(D1521R), our positive and negative controls, respectively. We observed that the mutations that impaired 53BP1 accumulation at DSB sites also abrogated RIF1 foci after IR (Supplementary Fig. 5). These results indicated that the UDR is critical for the function of 53BP1 in the DSB response. In further support of this observation, reconstitution of 53BP1<sup>-/-</sup> murine B cells with either the D1521R or L1619A mutants failed to restore class switch recombination (CSR) from IgM to IgG1, whereas reintroduction of wild-type 53BP1 restored CSR (Fig. 1g and Supplementary Fig. 6). Furthermore, the UDR-defective L1619A mutant was unable to restore resistance to IR-induced DSBs in DT40 53BP1<sup>-/-</sup> cells, or to restrict homologous recombination in BRCA1 and 53BP1 co-depleted cells (Supplementary Fig. 7). Together, these results indicate that the UDR is necessary for the biological functions of 53BP1.

## 53BP1 binds to ubiquitinated nucleosomes

Next, we sought to determine the mechanism by which the UDR promotes 53BP1 recruitment to DSB sites. We first considered that the UDR might increase the affinity of 53BP1 for H4K20me2 due to its location; that is, apposed to the Tudor domain. We expressed GST–53BP1 fusion proteins consisting of the tandem Tudor domain with (Tudor–UDR) or without (Tudor) the UDR region and examined binding to a H4K20me2-derived peptide in pull-down assays. We observed that both proteins interacted equally well with H4K20me2 in a manner that required the D1521 residue (Fig. 2a). The L1619A

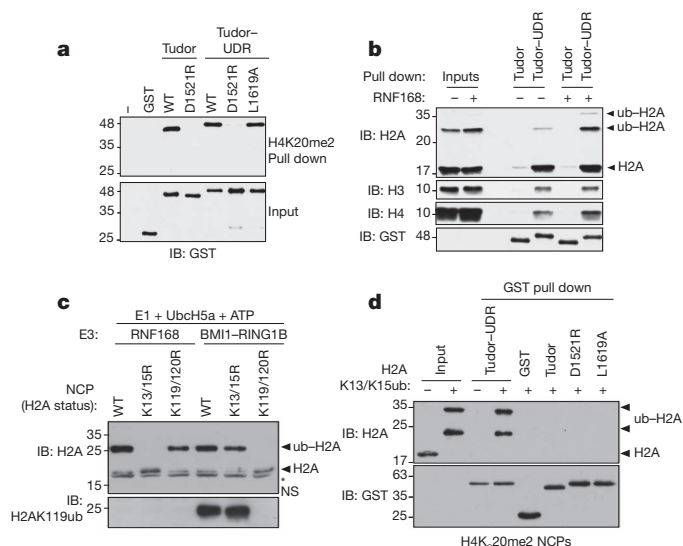


**Figure 2 | 53BP1 binds to ubiquitinated nucleosomes.** **a**, Streptavidin pull-downs of the indicated GST fusion proteins with a biotinylated H4K20me2 peptide. IB, immunoblot. **b**, Chromatin from HEK293 cells expressing Flag-RNF168 (+) or not (-) were subjected to pull-down assays with the indicated GST fusion proteins. **c**, Ubiquitination of the indicated NCPs by RNF168 and BMI1-RING1B. NS, nonspecific band. **d**, Pull-down assays of NCPs containing H4K<sub>20</sub>me2 with the indicated GST fusion proteins. NCPs were ubiquitinated with RNF168 as the E3 (+); a reaction without E1 (-) was used as a negative control. The migration of molecular mass markers (kDa) is indicated on the left.



mutation, which abolishes UDR activity, had no effect on H4K20me2 binding (Fig. 2a), indicating that the UDR does not have an impact on recognition of H4K20me2, at least in the context of a peptide.

An alternative function of the UDR might be that it promotes the interaction of 53BP1 with chromatin. To test this possibility, we prepared polynucleosome-enriched extracts obtained from micrococcal nuclease digestion of human chromatin. Because RNF168 overexpression can trigger 53BP1 accumulation on chromatin<sup>23</sup>, even in the absence of RNF8 (ref. 24), we prepared a set of extracts from cells that either overexpressed RNF168 (ref. 25), or that were transfected with an empty vector. RNF168 was recently shown to catalyse a new histone mark, H2AK13/K15 monoubiquitination (H2AK13/K15ub)<sup>26,27</sup>, and thus we sought to test whether 53BP1 could potentially bind to nucleosomes containing RNF168-ubiquitinated H2A. Immunoblotting of H2A showed that the global levels of H2A ubiquitination (ub-H2A) did not greatly change after RNF168 overexpression (Fig. 2b) because H2AK119ub, which is catalysed by E3s such as BMI1-RING1B<sup>28</sup>, is much more abundant than H2AK13ub or K15ub. These extracts were then subjected to GST pull-down assays using either the 53BP1 Tudor domain or the extended Tudor-UDR module. In the absence of exogenous RNF168 expression, we observed a UDR-dependent interaction between 53BP1 and histones H2A, H3 and H4 (Fig. 2b). However, in the presence of RNF168, we observed a marked increase in the retrieval of mono- and diubiquitinated H2A by the Tudor-UDR protein (Fig. 2b). Together, these results indicated that the UDR may stimulate two modes of interaction between 53BP1 and nucleosomes: one mode that is independent of histone ubiquitination, and which may reflect the constitutive interaction of 53BP1 with chromatin; and a second mode of interaction that is dependent on H2A ubiquitination by RNF168, and which may represent the interaction that leads to 53BP1 accumulation at DSB sites.

### 53BP1 recognizes H2AK15ub

Because the above experiments were carried out with polynucleosomes, the interactions observed could be the product of avidity between the dimeric 53BP1 fusion protein and the multimeric nucleosomal arrays. Therefore, we tested whether we could detect binding between 53BP1 and fully recombinant monomeric nucleosome core particles (NCPs) (Supplementary Fig. 8a). We used an N-terminal fragment of RNF168 in ubiquitination reactions with UbcH5, which recapitulated H2AK13/K15 ubiquitination<sup>26</sup> (Fig. 2c and Supplementary Fig. 8b–d). To generate H2AK119ub, we used a recombinant BMI1-RING1B complex as the E3 (Fig. 2c and Supplementary Fig. 8b, c). For histone methylation, we produced methyl-lysine analogue versions of H4K20me2 (H4K<sub>C</sub>20me2) and H3K9me2 (H3K<sub>C</sub>9me2)<sup>29</sup> before octamer and nucleosome assembly.

We first assembled H4K<sub>C</sub>20me2-containing NCPs and subjected them to ubiquitination reactions in the presence of RNF168 to produce H2AK13/K15ub (Fig. 2d). As a control, we also carried out reactions without E1 and, as expected, no H2A ubiquitination was detected (Fig. 2d). The products of these two reactions were used in GST-pull-down

assays with various fusion proteins derived from 53BP1. We observed a marked, ubiquitination-dependent interaction between the 53BP1 Tudor-UDR fusion and NCPs (Fig. 2d) that was not seen with the GST protein alone, the 53BP1 Tudor domain alone, the D1521R mutant or, finally, the L1619A mutant that disrupts UDR function. Together, these data indicate that the 53BP1 Tudor-UDR module promotes binding to methylated and ubiquitinated mononucleosomes in a manner that involves the same residues that are necessary for 53BP1 accumulation at DSB sites.

Next, we examined whether the binding of 53BP1 to NCPs was specific to H4K20me2 and H2AK13/K15ub. We assembled a series of NCPs that contained H4K<sub>C</sub>20me2, H3K<sub>C</sub>9me2 or their unmodified lysine counterparts. These NCPs were then used in ubiquitination reactions with RNF168 to produce H2AK13/K15ub-containing NCPs. When these NCPs were interrogated for binding to the 53BP1 Tudor-UDR module, we observed a specific interaction between 53BP1 and the NCPs containing H4K<sub>C</sub>20me2 (and H2AK13/K15ub) but not those containing H3K<sub>C</sub>9me2 or the unmodified H4K20 (Fig. 3a and Supplementary Fig. 9a). Next, we used H4K<sub>C</sub>20me2-containing NCPs as substrates in ubiquitination reactions with RNF168 or BMI1-RING1B. Both reactions produced similar levels of monoubiquitinated H2A (Fig. 3b) but when they were used in GST pull-down assays with the 53BP1 Tudor-UDR module, we only observed an interaction with the RNF168-ubiquitinated NCPs. Importantly, we excluded the possibility that the binding was due to the presence of diubiquitinated H2A in the RNF168 sample (Supplementary Fig. 9b). From these results, we conclude that the interaction between 53BP1 and nucleosomes requires the presence of both H4K20me2 and H2AK13/K15ub.

Whereas RNF168 can ubiquitinate H2A K13 or K15 *in vitro* and *in vivo*<sup>26,27</sup>, we tested whether 53BP1 displayed selectivity towards K13ub or K15ub. To do so, we assembled H4K<sub>C</sub>20me2-containing NCPs with either H2AK13R or H2AK15R substitutions to leave K15 or K13, respectively, as the only residue ubiquitinated by RNF168 (Fig. 3c). To our surprise, when these ubiquitinated NCPs were used in pull-down assays, we found that the 53BP1 Tudor-UDR protein interacted specifically with NCPs containing H2AK15ub (Fig. 3c). This result indicates that 53BP1 has the ability to discriminate between two closely positioned ubiquitinated lysine residues on H2A.

### Molecular basis of H2AK15ub selectivity

One possible cause for the 53BP1 selectivity towards H2AK15ub could be the presence of sequence elements in the H2A N-terminal tail that are recognized by 53BP1. We noted that three mutations (K9R, A14S and R17S) were sufficient to convert the sequence surrounding K13 in the H2AK15R mutant into the sequence that normally surrounds H2AK15 (Fig. 4a). We found that the resulting mutant (H2AK15Rm3), when ubiquitinated, bound robustly to the 53BP1 Tudor-UDR module (Fig. 4a). We conclude that additional residues in the H2A N terminus contribute to the binding of 53BP1 to H2AK15ub-containing nucleosomes.

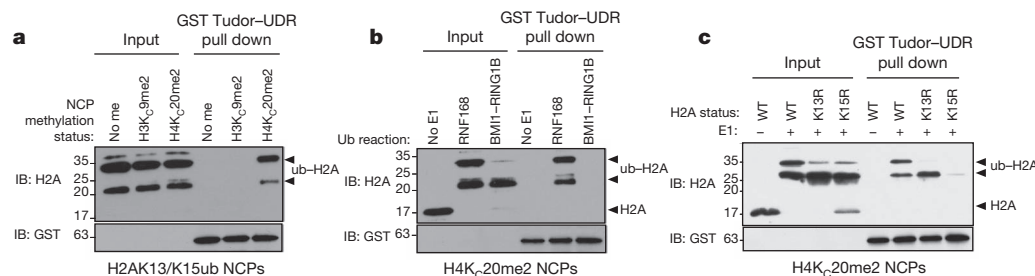


**Figure 3 | 53BP1 is a bivalent reader of the H4K20me2 and H2AK15ub histone marks.** **a**, Pull-down assays of RNF168-ubiquitinated NCPs containing unmethylated histone H4 and H3 (no me), H4K<sub>C</sub>20me2 or H3K<sub>C</sub>9me2 with GST-Tudor-UDR. IB, immunoblot. **b**, Pull-down assays of NCPs ubiquitinated with the indicated E3s by GST-Tudor-UDR. A reaction

without E1 (No E1) acts as a negative control. **c**, GST-Tudor-UDR pull-down assays of the indicated NCPs ubiquitinated with RNF168 (+); a reaction lacking E1 (–) was used as negative control. The migration of molecular mass markers (kDa) is indicated on the left.

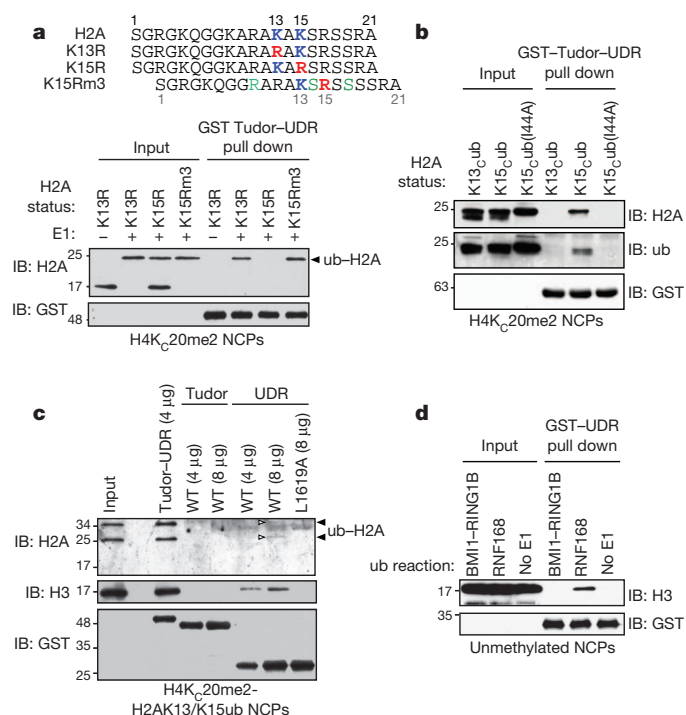


**Figure 4 | Determinants of H2AK15ub recognition.** **a**, Top panel: sequence of the H2A N termini of various mutants. Mutations are highlighted in colour. Bottom panel: GST-Tudor-UDR pull-down assays of RNF168-ubiquitinated NCPs (+) assembled with H4K<sub>20</sub>me2 and the indicated H2A mutants. A reaction without E1 (–) was used as control. IB, immunoblot. **b**, GST-Tudor-UDR pull-down assays of NCPs with the indicated H2A ubiquitinations. **c**, Pull-down assays of RNF168-ubiquitinated H4K<sub>20</sub>me2 NCPs with the indicated fusion proteins. A white arrowhead highlights faint ub-H2A bands. **d**, GST-UDR pull-down assays of unmethylated NCPs that were either ubiquitinated with the indicated E3 or not (no E1). The migration of molecular mass markers (kDa) is indicated on the left.

We next investigated whether ubiquitin recognition contributed to the 53BP1–NCP interaction. Ubiquitin contains a hydrophobic patch centred on its I44 residue that contributes to most ubiquitin-dependent interactions<sup>30</sup>, and therefore we sought to test whether the ubiquitin I44 residue was important for 53BP1 recognition of H2AK15ub–NCP complexes. We used chemical ubiquitination by disulphide exchange<sup>31</sup> to prepare NCPs that contained H2A chemically ubiquitinated on H2AK13 (H2AK<sub>13</sub>ub), H2AK15 (H2AK<sub>15</sub>ub) and H2AK15 ubiquitinated with Ub(I44A) (H2AK<sub>15</sub>ub(I44A); Fig. 4b). Those NCPs were then used in pull-down assays with the Tudor–UDR module. As expected, we found that the interaction was selective for H2AK<sub>15</sub>ub (Fig. 4b). However, H2AK<sub>15</sub>ub(I44A)-containing NCPs were unable to be retrieved by 53BP1 (Fig. 4b), suggesting that ubiquitin recognition participates in the interaction of 53BP1 with H2AK15ub.

In aggregate, our results support a model where the Tudor–UDR module comprises two histone-modification-binding domains: the Tudor domain that binds H4K20me2, and the UDR, which may interact directly with H2AK15ub. In support of this model, the transfer of the 53BP1 UDR onto the Crb2 Tudor domain endowed it with the ability to robustly bind to RNF168-ubiquitinated and H4K20me2-containing NCPs (Supplementary Fig. 10a–d). This observation prompted us to produce the isolated UDR, as a GST fusion protein, and to assess its binding properties. As expected, the isolated UDR did not bind to H4K20me2 (Supplementary Fig. 10e). However, when H2AK13/K15ub-containing NCPs were incubated with increasing amounts of the isolated UDR, we observed a dose-dependent retrieval of NCPs in a manner that required the critical L1619 residue (Fig. 4c). This weak binding of the UDR to NCPs was specific to RNF168-dependent ubiquitination (Fig. 4d) and, as expected, was independent of H4K20me2

given the absence of the Tudor domain (Fig. 4d and Supplementary Fig. 11a). Interestingly, we failed to detect either an interaction between the UDR and free ubiquitin by nuclear magnetic resonance or an interaction between the UDR and a ubiquitinated H2A peptide in a pull-down experiment (Supplementary Fig. 11b, c). These results indicate that the UDR recognizes H2AK15ub specifically in the context of the nucleosome.

## Discussion

In response to DSBs, ATM signalling triggers a first wave of chromatin ubiquitination that is dependent on RNF8 (ref. 2). The role of RNF8, and its E2 UBC13, is to trigger the recruitment of RNF168 to DSB sites where it catalyses H2AK13/K15 monoubiquitination. Together, our work identifies 53BP1 as a bivalent histone modification reader that recognizes nucleosomes modified with H4K20me2 and the DNA-damage-inducible H2AK15ub mark (Supplementary Fig. 1). We propose that the engagement of H4K20me2 by the Tudor domain positions the UDR in the correct orientation to contact the epitope formed by H2AK15ub, a scenario supported by modelling (Supplementary Fig. 12). In the Supplementary Data section, we also present evidence that 53BP1 recognizes nucleosomes minimally as a dimer (Supplementary Figs 13 and 14). Together, these observations indicate that 53BP1 may alter nucleosomal array structure either by acting similarly to a wheel-clamp if a dimer engages a mononucleosome (Supplementary Fig. 1), or by acting as a ubiquitination-dependent nucleosome crosslinker if it can bridge adjacent nucleosomes (Supplementary Fig. 1). These plausible binding modes may be central to the function of 53BP1 as an inhibitor of end resection.

Our experiments also identify the first, to our knowledge, site-specific reader of histone ubiquitination. 53BP1 is likely to be one of many readers that interpret the various histone ubiquitination marks identified so far. Proteins such as ASH2L (for H2BK120ub)<sup>32</sup>, RNF168 and RNF169 (for H2AK13/K15ub)<sup>25</sup> are prime candidates for ubiquitin mark readers. RNF169 presents an attractive case because it acts as a competitive inhibitor of 53BP1 (refs 25, 33). These observations and the identification of 53BP1 as an H2AK15ub reader further emphasize the need to decipher the chromatin modification landscape, its regulation and its interpretation, at sites of DNA damage.

## METHODS SUMMARY

Human cell lines were maintained at 37 °C and 5% CO<sub>2</sub> atmosphere whereas the avian DT40 cells were grown at 39.5 °C and 5% CO<sub>2</sub> atmosphere. Immunofluorescence microscopy and fluorescent protein imaging were carried out as described previously<sup>11,25</sup>. Recombinant protein production and pull-down assays were carried out as described previously<sup>25,34</sup>.

**Full Methods** and any associated references are available in the online version of the paper.

Received 8 February; accepted 24 May 2013.

Published online 12 June 2013.

- Lukas, J., Lukas, C. & Bartek, J. More than just a focus: The chromatin response to DNA damage and its role in genome integrity maintenance. *Nature Cell Biol.* **13**, 1161–1169 (2011).
- Jackson, S. P. & Durocher, D. Regulation of DNA damage responses by ubiquitin and SUMO. *Mol. Cell* **49**, 795–807 (2013).
- Nakamura, K. *et al.* Genetic dissection of vertebrate 53BP1: a major role in non-homologous end joining of DNA double strand breaks. *DNA Repair* **5**, 741–749 (2006).
- Bunting, S. F. *et al.* 53BP1 inhibits homologous recombination in Brca1-deficient cells by blocking resection of DNA breaks. *Cell* **141**, 243–254 (2010).
- Ward, I. M. *et al.* 53BP1 is required for class switch recombination. *J. Cell Biol.* **165**, 459–464 (2004).
- Manis, J. P. *et al.* 53BP1 links DNA damage-response pathways to immunoglobulin heavy chain class-switch recombination. *Nature Immunol.* **5**, 481–487 (2004).
- Dimitrova, N., Chen, Y. C., Spector, D. L. & de Lange, T. 53BP1 promotes non-homologous end joining of telomeres by increasing chromatin mobility. *Nature* **456**, 524–528 (2008).



8. Bouwman, P. *et al.* 53BP1 loss rescues BRCA1 deficiency and is associated with triple-negative and BRCA-mutated breast cancers. *Nature Struct. Mol. Biol.* **17**, 688–695 (2010).
9. Bothmer, A. *et al.* Regulation of DNA end joining, resection, and immunoglobulin class switch recombination by 53BP1. *Mol. Cell* **42**, 319–329 (2011).
10. Zimmermann, M., Lottersberger, F., Buonomo, S. B., Sfeir, A. & de Lange, T. 53BP1 regulates DSB repair using Rif1 to control 5' end resection. *Science* **339**, 700–704 (2013).
11. Escibano-Díaz, C. *et al.* A cell cycle-dependent regulatory circuit composed of 53BP1–RIF1 and BRCA1–CtIP controls DNA repair pathway choice. *Mol. Cell* **49**, 872–883 (2013).
12. Di Virgilio, M. *et al.* Rif1 prevents resection of DNA breaks and promotes immunoglobulin class switching. *Science* **339**, 711–715 (2013).
13. Chapman, J. R. *et al.* RIF1 is essential for 53BP1-dependent nonhomologous end joining and suppression of DNA double-strand break resection. *Mol. Cell* **49**, 858–871 (2013).
14. Botuyan, M. V. *et al.* Structural basis for the methylation state-specific recognition of histone H4–K20 by 53BP1 and Crb2 in DNA repair. *Cell* **127**, 1361–1373 (2006).
15. Huyen, Y. *et al.* Methylated lysine 79 of histone H3 targets 53BP1 to DNA double-strand breaks. *Nature* **432**, 406–411 (2004).
16. Sanders, S. L. *et al.* Methylation of histone H4 lysine 20 controls recruitment of Crb2 to sites of DNA damage. *Cell* **119**, 603–614 (2004).
17. Pei, H. *et al.* MMSET regulates histone H4K20 methylation and 53BP1 accumulation at DNA damage sites. *Nature* **470**, 124–128 (2011).
18. Acs, K. *et al.* The AAA-ATPase VCP/p97 promotes 53BP1 recruitment by removing L3MBTL1 from DNA double-strand breaks. *Nature Struct. Mol. Biol.* **18**, 1345–1350 (2011).
19. Mallette, F. A. *et al.* RNF8- and RNF168-dependent degradation of KDM4A/JMJD2A triggers 53BP1 recruitment to DNA damage sites. *EMBO J.* **31**, 1865–1878 (2012).
20. Nakamura, T. M., Moser, B. A., Du, L. L. & Russell, P. Cooperative control of Crb2 by ATM family and Cdc2 kinases is essential for the DNA damage checkpoint in fission yeast. *Mol. Cell. Biol.* **25**, 10721–10730 (2005).
21. Zgheib, O., Pataky, K., Brugger, J. & Halazonetis, T. D. An oligomerized 53BP1 tudor domain suffices for recognition of DNA double-strand breaks. *Mol. Cell. Biol.* **29**, 1050–1058 (2009).
22. Pryde, F. *et al.* 53BP1 exchanges slowly at the sites of DNA damage and appears to require RNA for its association with chromatin. *J. Cell Sci.* **118**, 2043–2055 (2005).
23. Gudjonsson, T. *et al.* TRIP12 and UBR5 suppress spreading of chromatin ubiquitylation at damaged chromosomes. *Cell* **150**, 697–709 (2012).
24. Stewart, G. S. *et al.* The RIDDLE syndrome protein mediates a ubiquitin-dependent signaling cascade at sites of DNA damage. *Cell* **136**, 420–434 (2009).
25. Panier, S. *et al.* Tandem protein interaction modules organize the ubiquitin-dependent response to DNA double-strand breaks. *Mol. Cell* **47**, 383–395 (2012).
26. Mattioli, F. *et al.* RNF168 ubiquitinates K13–15 on H2A/H2AX to drive DNA damage signaling. *Cell* **150**, 1182–1195 (2012).
27. Gatti, M. *et al.* A novel ubiquitin mark at the N-terminal tail of histone H2As targeted by RNF168 ubiquitin ligase. *Cell Cycle* **11**, 2538–2544 (2012).
28. Wang, H. *et al.* Role of histone H2A ubiquitination in Polycomb silencing. *Nature* **431**, 873–878 (2004).
29. Simon, M. D. *et al.* The site-specific installation of methyl-lysine analogs into recombinant histones. *Cell* **128**, 1003–1012 (2007).
30. Dikic, I., Wakatsuki, S. & Walters, K. J. Ubiquitin-binding domains—from structures to functions. *Nature Rev. Mol. Cell Biol.* **10**, 659–671 (2009).
31. Chen, J., Ai, Y., Wang, J., Haracska, L. & Zhuang, Z. Chemically ubiquitylated PCNA as a probe for eukaryotic translesion DNA synthesis. *Nature Chem. Biol.* **6**, 270–272 (2010).
32. Wu, L. *et al.* ASH2L regulates ubiquitylation signaling to MLL: trans-regulation of H3 K4 methylation in higher eukaryotes. *Mol. Cell* **49**, 1108–1120 (2013).
33. Poulsen, M., Lukas, C., Lukas, J., Bekker-Jensen, S. & Mailand, N. Human RNF169 is a negative regulator of the ubiquitin-dependent response to DNA double-strand breaks. *J. Cell Biol.* **197**, 189–199 (2012).
34. Juang, Y. C. *et al.* OTUB1 co-opts Lys48-linked ubiquitin recognition to suppress E2 enzyme function. *Mol. Cell* **45**, 384–397 (2012).

**Supplementary Information** is available in the online version of the paper.

**Acknowledgements** We are grateful to R. Szilard, J. Côté and S. Panier for critically reading the manuscript; to L.-L. Du, A. Nussenzweig, Y. Tong and C. Arrowsmith for plasmids; to M. Cook and A. Rosebrock for centrifugal elutriation; and to B. Sauriol for help with FRAP data analysis. A.F.-T. and A.O. both receive post-doctoral fellowships from the CIHR; C.E.-D. is an Ontario Post-doctoral Fellow; J.K.-L. receives a post-doctoral fellowship from the Leukemia and Lymphoma Society; and C.C.Y.L. and M.-C.L. are post-doctoral fellows of the Canadian Breast Cancer Foundation (Ontario Division). D.D. is the Thomas Kierans Chair in Mechanisms of Cancer Development and a Canada Research Chair (Tier 1) in the Molecular Mechanisms of Genome Integrity. Work in the D.D. laboratory was supported by CIHR grant MOP84297 and grant GL2-01-010 from the Ontario Research Fund.

**Author Contributions** A.F.-T. initiated the project, carried out most of the cell biological experiments, found the interaction between ubiquitinated H2A and 53BP1, and contributed to the experimental design and data interpretation. M.D.C. produced the recombinant nucleosomes. A.F.-T. and M.D.C. and carried out the recombinant nucleosome pull-down studies. C.E.-D. examined RIF1 focus formation, the role of the UDR in homologous recombination and helped with some immunofluorescence experiments. A.O. carried out the class switching experiments and the DT40 work. C.C.Y.L. helped with protein binding studies and generated the nucleosome model shown in Supplementary Fig. 12. M.-C.L. helped with the FRAP experiments. J.K.-L. carried out chemical ubiquitination and mass spectrometry to verify histone methylation. H.H. carried out the NMR experiments. S.M.N. carried out mass spectrometry to verify H4K20 methylation. F.S. supervised H.H. D.D. supervised the project and wrote the manuscript with input from the other authors.

**Author Information** Reprints and permissions information is available at [www.nature.com/reprints](http://www.nature.com/reprints). The authors declare no competing financial interests. Readers are welcome to comment on the online version of the paper. Correspondence and requests for materials should be addressed to D.D. ([durocher@lunenfeld.ca](mailto:durocher@lunenfeld.ca)).

## METHODS

**Cell culture and plasmid transfection.** Human cell culture media were supplemented with 10% fetal bovine serum (FBS) and maintained at 37 °C and 5% CO<sub>2</sub> atmosphere. U-2-OS (U2OS) cells were cultured in McCoy's medium (Gibco). HEK293T and HeLa DR-GFP cells were cultured in DMEM (Gibco). HCT116 Flp-In T-REX Flag and Flag-RNF168 stably transfected cell lines were cultured in DMEM supplemented with 250 µg ml<sup>-1</sup> hygromycin B and 5 µg ml<sup>-1</sup> blasticidin. CT116 Flp-In T-REX Flag and Flag-RNF168 stably transfected cell lines were described previously<sup>25</sup>. U2OS and HEK293T cells were purchased from ATCC and HeLa DR-GFP cells were a gift from the laboratory of R. Greenberg. All cell lines were tested negative for mycoplasma contamination. To induce protein expression in these cell lines, 5 µg ml<sup>-1</sup> doxycycline was added to the culture medium for 24 h. DT40 cells were obtained from the laboratory of D. Xu and grown at 39.5 °C, 5% CO<sub>2</sub> in RPMI 1640 medium (Gibco) supplemented with 10% fetal calf serum, 1% chicken serum and 0.1 mM β-mercaptoethanol. Plasmid transfections were generally carried out using Lipofectamine 2000 Transfection Reagent (Invitrogen) or Effectene (Qiagen).

Unless stated otherwise, for microscopy experiments, cells were fixed 1 h after irradiation (10 Gy). The DNA was also counter-stained with DAPI (not shown) and used to trace the outline of the nuclei.

**Retroviral restitution of 53BP1 in B cells.** Class switching to IgG1 was assayed in 53BP1<sup>-/-</sup> murine primary B cells complemented with 53BP1 (1-1711) and mutants thereof by retroviral delivery. Mature B lymphocytes were isolated from the spleens of two males and one female 8–15-week-old 53BP1<sup>-/-</sup> C57BL/6 strain 129-Trp53bp1tm1Jc/J mice<sup>3</sup> by depletion of CD43<sup>+</sup> cells using CD43 microbeads (Miltenyi Biotec) according to the manufacturer's instructions. Mice were obtained from Jackson laboratories. Purified B cells were re-suspended at a concentration of 10<sup>6</sup> cells ml<sup>-1</sup> in the presence of 50 ng ml<sup>-1</sup> IL-4 (Preprotech) and 25 µg ml<sup>-1</sup> LPS (Sigma-Aldrich) or 1 µg ml<sup>-1</sup> agonist anti-CD40 (BD) to allow B-cell proliferation/activation. Retroviral particles were collected from the supernatant of Plat-E packaging cells<sup>35</sup> transfected with 10 µg of the different retroviral pMX constructs. Retroviral supernatants were passed through a 0.45 µm filter and then ultracentrifuged at 20,000g at 25 °C for 90 min through a 20% sucrose layer to obtain purified virus. B cells were subsequently infected with the retroviral concentrate in the presence of 8 µg ml<sup>-1</sup> polybrene (Sigma-Aldrich) and 20 mM HEPES, pH 7.5 by plate centrifugation. The B-cell medium was subsequently changed and replaced with fresh RPMI medium supplemented with 50 ng ml<sup>-1</sup> IL-4 and 25 µg ml<sup>-1</sup> LPS or 1 µg ml<sup>-1</sup> agonist anti-CD40 to induce class switching to IgG1. CSR was analysed 3 days after infection by flow cytometry as described previously<sup>11</sup>. Experiments with 53BP1<sup>-/-</sup> mice (Trp53bp1<sup>tm1Jc/tm1Jc</sup>) were carried out according to regulatory standards and were approved by the Mount Sinai Hospital animal care committee (Protocol AUP 0200a).

**Chromatin pull down.** HEK293 chromatin-enriched extracts were prepared essentially as described<sup>25</sup>. Chromatin pull downs were performed with 2.5 µg of recombinant GST-tagged proteins immobilized on glutathione sepharose 4B (GE Healthcare) in chromatin pull-down buffer (CPB: 50 mM Tris-HCl, pH 7.5, 100 mM NaCl, 1 mM dithiothreitol (DTT)) for 1 h at 4 °C. Pull downs were then carried out by mixing 125 µg of chromatin-enriched extract isolated from cells stably expressing Flag-RNF168 in a final volume of 1.5 ml for 3 h at 4 °C. Pull downs were then washed four times with 1 ml of CPB and eluted in 2× Laemmli SDS-PAGE sample buffer for analysis by immunoblotting.

**NCP reconstitution.** Recombinant histones were purified essentially as described<sup>36,37</sup>. Briefly, after preparation of inclusion bodies, the histones were purified under denaturing conditions on either a HiPrep 16/60 Sephacryl S-300 HR (GE Healthcare) size exclusion column or a 5 ml HiTrap SP HP (GE Healthcare) cation exchange column. Fractions containing the purified histones were pooled and extensively dialysed into water and 2 mM β-mercaptoethanol before lyophilization. His6-G76C ubiquitin and His6-I44A/G76C ubiquitin to be installed on H2A K13C or K15C were purified over a Ni-NTA column (Qiagen) and the His tag was removed with TEV protease. DTT was added to the ubiquitin to reduce any oxidized bonds and then quickly buffer exchanged into degassed water (with no DTT) using a PD-10 column (GE Healthcare). The reduced ubiquitin was immediately snap frozen and lyophilized to dryness. Octamers were refolded by mixing the four histones in equimolar ratios, followed by dialysis into 2 M NaCl, and then purified on a Superdex 200 10/300 GL size exclusion column (GE Healthcare). Nucleosome core particles (NCPs) were reconstituted as described<sup>36</sup>. The 151-base pair DNA used to wrap the mononucleosomes was obtained from an EcoRV digest of 32x601 DNA plasmid (a gift from C. Arrowsmith).

**Histone labelling.** The installation of a dimethyl-lysine analogue (di-MLA) at the mutated cysteine of the H4K20C protein or H3K9C (C110A) protein was done exactly as described previously<sup>29</sup>. The di-MLA installation was confirmed by mass spectrometry for the H3K9me2 protein, and by mass spectrometry and immunoblotting against H4K20me2 for the H4K20me2 full-length protein. Once

labelled, the H4K20me2 and H3K9me2 proteins were refolded into octamers as described in the 'NCP reconstitution' section above.

Installation of a modified wild-type or I44A mutant ubiquitin was achieved by disulphide-directed conjugation. H2A K15C or K13C were conjugated with G76C ubiquitin or I44A/G76C ubiquitin via disulphide exchange before octamer refolding. Specifically, the cysteine on the histone was activated by dissolving 5 mg of lyophilized H2A in 1 ml of water containing 5 mM TCEP. Then 5 mg of DTNP (2,2'-dithiobis(5-nitropyridine); Sigma Aldrich) dissolved in 2 ml of acetic acid was added to the histone and this mixture was agitated at room temperature overnight. The activated histone reaction was then dialysed extensively against water before purification by S75 10/300 gel filtration (GE Healthcare) in conjugation reaction buffer. The conjugation reaction was set up in 6 M guanidinium-HCl, 50 mM Tris-HCl pH 6.9 at room temperature with a 2:1 ratio of lyophilized ubiquitin to degassed activated histone. After 1 h, the completion of the reaction was confirmed by mass spectrometry. Unconjugated ubiquitin and any oxidized ubiquitin-ubiquitin conjugates were removed in subsequent gel filtration runs.

**In vitro ubiquitination of the NCP.** Nucleosomes were ubiquitinated by incubating 2.5 µg recombinant mononucleosomes with 30 nM E1, 1.5 µM UbcH5a, 4 µM RNF168 (1-113) or BMI1-RING1B complex, 22 µM ubiquitin or methylated ubiquitin (Boston Biochem), and 3.33 mM ATP in a buffer containing 50 mM Tris-HCl, pH 7.5, 100 mM NaCl, 10 mM MgCl<sub>2</sub>, 1 µM ZnOAc and 1 mM DTT at 30 °C for 2 h.

**NCP pull-down assays.** NCP pull downs were done in a total volume of 100 µl by using 15–20 µl ubiquitination reaction and 4 or 8 µg GST- or MBP-protein coupled to glutathione sepharose 4B (GE Healthcare) or amylose resin (New England Biolabs), respectively, in the same buffer as the peptide pull downs, except containing 0.1% BSA. Pull-down reactions were incubated for 2 h at 4 °C. Pull downs were then washed three times with 0.5 ml of the pull-down buffer plus 0.1% BSA and eluted in 2× Laemmli SDS-PAGE sample buffer for analysis by immunoblotting.

**Plasmids.** The GFP-53BP1 expression vector (DDp1910) resistant to siRNA 53BP1 no. 1 (ThermoFisher D-003548-01) was described previously<sup>11</sup>. The GFP was swapped for mCherry using the KpnI-AscI sites to generate pcDNA5-mCherry-FRT/TO-53BP1 (DDp2005). The 53BP1 deletion vectors (consisting of residues 1220–1711, 1220–1631, 1484–1603, 1484–1631 or 1604–1631) were created by inserting PCR-amplified fragments (derived from DDp1910) into the NotI and ApaI sites of pcDNA5-GFP-FRT/TO; EcoRI and NotI sites of pcDNA5-Flag-FRT/TO-DmrA (DDp1911) and pcDNA5-HA-FRT/TO-DmrC (DDp1912); and in the BamHI and EcoRI sites of a modified pETM-30-02 vector in which the ORF of GST was inserted between the hexahistidine tag and the TEV cleavage site or between the BamHI and PstI sites of pMAL-c2X (New England Biolabs). Mammalian expression vectors for the components of the heterodimerization system were generated by PCR amplification of DmrA (FKBP12) and DmrC (FRB) from pLVX-Het-2 and pLVX-Het-1 (iDimerize Inducible Heterodimer System, Clontech), respectively, and by ligation into the BamHI and EcoRI sites of pcDNA5-Flag-FRT/TO and pcDNA5-HA-FRT/TO (DDp1915). The GFP-Crb2 and GFP-CC (that is, residues 1–507 of Crb2) vectors (DDp1913 and DDp1914, respectively) were constructed by inserting PCR-amplified fragments of Crb2 into the NotI and ApaI sites of pcDNA5-GFP-FRT/TO or pcDNA5-GFP-NLS-FRT/TO (DDp1916). The source of the Crb2 coding sequence was the pJK148-Crb2 plasmid (gift from L.-L. Du)<sup>38</sup>. Chimaeras of 53BP1 and Crb2 were obtained by annealing overlapping PCR fragments (where 555 = amino acids 1220–1483, 1484–1603, 1604–1711; and CCC = amino acids 1–357, 358–507, 507–708). The annealed fragments were then ligated into the NotI and ApaI sites of pcDNA5-GFP-NLS-FRT/TO (DDp1916). The GST-Crb2 Tudor domain (that is, residues 358–507 of Crb2) alone or fused to 53BP1 UDR (residues 1604–1631), yielding GST-Tudor(C) and GST-Tudor(C)-UDR(5) vectors, respectively, were constructed by inserting PCR-amplified sequences into the BamHI and EcoRI sites of a modified pETM-30-02 described above. Bacterial expression vectors for histones (His<sub>6</sub>-human H2A in pET15b, His<sub>6</sub>-human H2B in pET15b, *Xenopus laevis* H3 in pET3d and *X. laevis* H4 in pET3a) were obtained from C. Arrowsmith. The RNF168 bacterial expression vector (residues 1–113; DDp1878) was obtained by PCR amplification of the DDp1109 (ref. 25) and cloned into pPROEX HTa (Invitrogen) using the BamHI and SpeI sites. The BMI1-His<sub>6</sub> (residues 1–108) bacterial expression vector (DDp1886) was obtained by PCR amplification of pGEX-4T1-BMI1(1–108) and cloned into pET24b(+) using NdeI and XhoI sites. The RING1B (residue 1–116) bacterial expression vector (DDp1887) was obtained by PCR amplification of pET28-MHL-RINGb(1–120) and cloned into pGEX-6P-1 using the BamHI and NotI sites. pGEX-4T1-BMI1(1–108) and pET28-MHL-RINGb(1–120) were gifts of Y. Tong. The retroviral vector pMX-53BP1 (1–1711) and its D1521R derivative were gifts of A. Nussenzweig<sup>9</sup>. All mutations were introduced by site-directed mutagenesis using QuikChange (Stratagene) and all plasmids were sequence-verified.



**Subcellular fractionation.** A cytoplasmic fraction (CYTO) was obtained by collecting HEK293 cells in EBC1 buffer (50 mM Tris-HCl pH 7.5, 100 mM NaCl, 0.5% IGEPAL CA-630, 1 mM EDTA, 1 mM DTT, 1× protease inhibitors—Complete, EDTA-free; Roche). After centrifugation at 1,000g for 15 min at 4 °C, the nuclear pellet was re-suspended and periodically vortexed in EBC2 buffer (50 mM Tris-HCl pH 7.5, 300 mM NaCl, 5 mM CaCl<sub>2</sub>, 1× protease inhibitors—Complete, EDTA-free; Roche) over 30 min. Following centrifugation at 1,000g for 15 min, the supernatant was harvested as the nuclear soluble fraction (NS). The remaining insoluble chromatin fraction was then solubilized by micrococcal nuclease digestion for 30 min at 30 °C and centrifugation at 1,000g for 15 min; the supernatant was collected as the nuclear soluble fraction (CHR).

**RNA interference.** All siRNAs used in this study were single duplex siRNAs purchased from ThermoFisher. RNA interference (RNAi) transfections (40 nM) were performed using DharmaFECT 1 (ThermoFisher) or RNAiMax (Invitrogen) in a forward transfection mode, following the manufacturer's protocol. The individual siRNA duplexes used were: 53BP1 (ThermoFisher, D-003548-01, target sequence: 5'-GAGAGCAGAUCCUUUA-3'), RNF168 (ThermoFisher, D-007152-04, target sequence: 5'-GAAGAGUCGUGCCUACUGAUU-3'), BRCA1 (ThermoFisher D-003461-05, target sequence: 5'-CAGCUACCCUCCAUCUAUUAU-3') and non-targeting control siRNA (ThermoFisher, D-001210-02, target sequence: 5'-UAAGGCUAUGAAGAGAUAC-3'). Except when stated otherwise, siRNAs were transfected 48 h before cell processing.

**Antibodies.** We used the following antibodies: mouse anti-53BP1 (clone 19, BD Biosciences), rabbit anti-53BP1 (A300-273A, Bethyl), mouse anti-γ-H2AX (clone JBW301, Millipore), rabbit anti-γ-H2AX (no. 2577, Cell Signaling Technologies), rabbit anti-BRCA1 (no. 07-434, Millipore), rabbit anti-KAP1 (A300-274A, Bethyl), goat anti-RIF1 (N20) (sc55979, Santa Cruz), mouse anti-Flag (clone M2, Sigma), mouse anti-tubulin (clone DM1A, Calbiochem), mouse anti-GFP (Roche), rabbit anti-cyclin A (gift from M. Pagano), mouse anti-HA (F-7, sc-7392, Santa Cruz), rabbit anti-H2A (ab18255, Abcam), rabbit anti-H4 (NBP1-19404, Novus Biologicals), rabbit anti-H3 (ab1791, Abcam), rabbit anti-H2B (ab1790, Abcam), rabbit anti-H4K20me2 (9759, Cell Signaling Technologies), rabbit anti-GST (sc-459, Santa Cruz), mouse anti-MBP (E8032, NEB), rabbit anti-ubiquitin (Z0458, Dako) and mouse anti-actin (CP01, Calbiochem). Peroxidase-afiniPure goat anti-rabbit IgG (111 035 144, Jackson ImmunoResearch) and HRP-linked sheep anti-mouse IgG (NA931, GE Healthcare) were used as secondary antibodies in immunoblotting. The following antibodies were used as secondary antibodies in immunofluorescence microscopy: Alexa Fluor 488 goat anti-mouse, Alexa Fluor 488 donkey anti-mouse, Alexa Fluor 555 goat anti-mouse, Alexa Fluor 555 goat anti-rabbit, Alexa Fluor 555 donkey anti-goat, Alexa Fluor 647 donkey anti-mouse (Molecular Probes).

**Fluorescence recovery after photobleaching (FRAP).** For FRAP experiments, cells were seeded onto 25-mm round coverslips, transferred to a Chamlide Chamber and imaged using a Quorum WaveFX Spinning Disc Confocal System (Quorum Technologies) equipped with a ×63 oil objective and a temperature-controlled chamber (37 °C, 5% CO<sub>2</sub>). All images were acquired using Velocity Software (Improvision). FRAP experiments were performed 24 h after cell transfection. Five images were acquired before photobleaching a region of interest using a Photonic Instruments Mosaic (450–515 nm Ar laser, 0.6 s) to achieve at least 60–70% of measured fluorescence loss. Images were then acquired every 0.08 s for 20 s. Image processing was performed using Velocity and included photobleaching and background correction. Recovery time was obtained by fitting a single exponential equation. As the image set of each sample was acquired with nonuniform time intervals, a cubic spline interpolation technique was used to resample data on a common time base.

**Recombinant protein production.** GST and MBP fusions proteins were produced as previously described<sup>25,34</sup>. Briefly, MBP and GST proteins expressed in

*Escherichia coli* were purified on amylose (New England Biolabs) or glutathione sepharose 4B (GE Healthcare) resins according to the batch method described by the manufacturer and stored in 50 mM HEPES pH 7.5, 150 mM NaCl, 5% glycerol. His<sub>6</sub>-UbcH5a and His<sub>6</sub>-RNF168 (1–113) were purified on Ni-NTA agarose (Qiagen) and stored in 50 mM Tris-HCl pH 7.5, 1 mM EDTA, 10% glycerol. For NMR, the proteins were further purified by gel filtration in NMR buffer (S75 10/300 HiPrep Superdex, GE Healthcare). The pET24b(+)-Bmi1 and pGEX-6p-1-RING1B expression plasmids were co-transformed and the proteins were purified as a complex as described<sup>39</sup>.

**Peptides.** The H4K20me2 peptide (H4K20me2: biotin-YGKGGAKRHR-K(me2)-VLRD) was purchased from BioBasic and the H2AK15ub peptide (biotin-spacer-ARAKAK(ub)SRSSR; Spacer = 8-amino-3,6-dioxaoctanoic acid) was purchased from Lifesensors Inc.

Peptide pull downs were performed by incubating 2.5 μM MBP or GST-tagged 53BP1 proteins with 25 μM of the indicated biotinylated histone H4-derived peptide in peptide pull-down buffer (PPB) (50 mM Tris-HCl pH 8.0, 150 mM NaCl, 0.05% NP-40, 1% BSA). After 2 h at 4 °C, 10 μl of the pull-down reaction mixture was removed as input control and 10 μl of streptavidin-Dynabeads (Dyna) were added to the pull-down mixture and incubated for an additional 30 min at 4 °C. The Dynabeads were then washed twice with 750 μl PPB, twice with 750 μl of 50 mM Tris-HCl pH 8.0, 150 mM NaCl and were then eluted in 25 μl × 2 Laemmli SDS-PAGE sample buffer for analysis by immunoblotting.

**Gel filtration.** Estimation of the GST-53BP1 Tudor-UDR and MBP-53BP1 Tudor-UDR molecular masses in solution was done by gel filtration analysis using a 24-ml S200 Superdex column (S200 10-300 GL, (GE Healthcare)) in 50 mM HEPES pH 7.5, 150 mM NaCl. Approximately 400 μg of purified GST or MBP-tagged protein was injected onto the column. The molecular mass of each sample was estimated according to the elution profile of gel filtration standard molecular weight markers (151–1901, Bio-Rad).

**NMR spectroscopy.** NMR data were acquired at 25 °C on a 600 MHz Bruker AVANCE III spectrometer equipped with a 1.7 mm TCI CryoProbe. Two-dimensional <sup>1</sup>H, <sup>15</sup>N HSQC (heteronuclear single quantum coherence) spectra were collected for 0.2 mM <sup>15</sup>N-ubiquitin in the absence or presence of GST, GST-53BP1-UDR (1604–1631) or CDC34. All NMR samples were prepared in 50 mM HEPES, pH 7.5, 100 mM NaCl, 1 mM DTT and 10% D<sub>2</sub>O. Backbone resonance assignments for human ubiquitin have been reported previously<sup>40</sup>. Residue A46 was not seen in the spectra, and therefore was excluded from analysis.

**Mass spectrometry.** Electrospray ionization mass spectrometry analysis was performed on an Agilent LC/MSD TOF mass spectrometer. Samples were diluted in 0.1% trifluoroacetic acid before analysis. Deconvolution was performed using Agilent MassHunter workstation software for the analysis of modified histones.

35. Morita, S., Kojima, T. & Kitamura, T. Plat-E: an efficient and stable system for transient packaging of retroviruses. *Gene Ther.* **7**, 1063–1066 (2000).
36. Dyer, P. N. *et al.* Reconstitution of nucleosome core particles from recombinant histones and DNA. *Methods Enzymol.* **375**, 23–44 (2004).
37. Luger, K., Mader, A. W., Richmond, R. K., Sargent, D. F. & Richmond, T. J. Crystal structure of the nucleosome core particle at 2.8 Å resolution. *Nature* **389**, 251–260 (1997).
38. Nakamura, T. M., Du, L. L., Redon, C. & Russell, P. Histone H2A phosphorylation controls Crb2 recruitment at DNA breaks, maintains checkpoint arrest, and influences DNA repair in fission yeast. *Mol. Cell. Biol.* **24**, 6215–6230 (2004).
39. Bentley, M. L. *et al.* Recognition of UbcH5c and the nucleosome by the Bmi1/Ring1b ubiquitin ligase complex. *EMBO J.* **30**, 3285–3297 (2011).
40. Wang, A. C., Grzesiek, S., Tschudin, R., Lodi, P. J. & Bax, A. Sequential backbone assignment of isotopically enriched proteins in D<sub>2</sub>O by deuterium-decoupled HA(CA)N and HA(CAC)N. *J. Biomol. NMR* **5**, 376–382 (1995).

# The same frequency of planets inside and outside open clusters of stars

Søren Meibom<sup>1</sup>, Guillermo Torres<sup>1</sup>, Francois Fressin<sup>1</sup>, David W. Latham<sup>1</sup>, Jason F. Rowe<sup>2</sup>, David R. Ciardi<sup>3</sup>, Steven T. Bryson<sup>2</sup>, Leslie A. Rogers<sup>4</sup>, Christopher E. Henze<sup>2</sup>, Kenneth Janes<sup>5</sup>, Sydney A. Barnes<sup>6,7</sup>, Geoffrey W. Marcy<sup>8</sup>, Howard Isaacson<sup>8</sup>, Debra A. Fischer<sup>9</sup>, Steve B. Howell<sup>2</sup>, Elliott P. Horch<sup>10</sup>, Jon M. Jenkins<sup>11</sup>, Simon C. Schuler<sup>12</sup> & Justin Crepp<sup>13</sup>

**Most stars and their planets form in open clusters. Over 95 per cent of such clusters have stellar densities too low (less than a hundred stars per cubic parsec) to withstand internal and external dynamical stresses and fall apart within a few hundred million years<sup>1</sup>. Older open clusters have survived by virtue of being richer and denser in stars (1,000 to 10,000 per cubic parsec) when they formed. Such clusters represent a stellar environment very different from the birthplace of the Sun and other planet-hosting field stars. So far more than 800 planets have been found around Sun-like stars in the field<sup>2</sup>. The field planets are usually the size of Neptune or smaller<sup>3–5</sup>. In contrast, only four planets have been found orbiting stars in open clusters<sup>6–8</sup>, all with masses similar to or greater than that of Jupiter. Here we report observations of the transits of two Sun-like stars by planets smaller than Neptune in the billion-year-old open cluster NGC6811. This demonstrates that small planets can form and survive in a dense cluster environment, and implies that the frequency and properties of planets in open clusters are consistent with those of planets around field stars in the Galaxy.**

Previous planet surveys in clusters have suffered from insufficient sensitivity to detect small planets, and from sample sizes barely large enough to find the less common larger planets<sup>9</sup>. The recent discovery by the Doppler method of two giant planets around Sun-like stars in the Praesepe open cluster<sup>8</sup> set a preliminary lower limit to the rate of occurrence of hot Jupiters in that cluster. This frequency is not inconsistent with that in the field, after accounting for the enriched metallicity of Praesepe<sup>10</sup> and the positive correlation between stellar metallicity and the frequency of giant planets<sup>11</sup>. However, it does not address the frequency of smaller planets such as those more commonly found around field stars. NASA's Kepler telescope is sensitive enough to detect planets of the size of Neptune or smaller, using the transit technique.

Our detection of two mini-Neptunes (two to four Earth radii,  $R_{\oplus}$ ) in NGC6811 is the result of a survey of 377 stars in the cluster as part of The Kepler Cluster Study<sup>12</sup>. The two planets, Kepler-66b and Kepler-67b, have radii of  $2.8R_{\oplus}$  and  $2.9R_{\oplus}$  and are each transiting (passing in front of) a Sun-like star in NGC6811 once every 17.8 and 15.7 days, respectively. Kepler-66b and Kepler-67b are the smallest planets to be found in a star cluster, and the first cluster planets seen to transit their host stars, which enables the measurement of their sizes.

The properties derived for the two planets depend directly on the properties determined for their parent stars (Kepler-66 and Kepler-67). Because the members of NGC6811 form a coeval, co-spatial and chemically homogeneous collection of stars, they trace a distinct sequence in the colour–magnitude diagram (Fig. 1a). This allows both their commonly held properties (such as age and distance) and their individual physical characteristics (such as masses, radii and temperatures) to be determined reliably from stellar evolution models<sup>13,14</sup>. Kepler-66b and Kepler-67b therefore join a small group of planets with precisely determined ages,

distances and sizes. Table 1 lists the model-derived properties of the two planets and their host stars. Figure 1a shows the locations of Kepler-66 and Kepler-67 in the colour–magnitude diagram for NGC6811, and Fig. 2 displays their phase-folded transit light curves reduced and calibrated by the Kepler pipeline<sup>15</sup>.

The membership of Kepler-66 and Kepler-67 to NGC6811 was established from a five-year radial-velocity survey (see Supplementary Information). They are both secure radial-velocity members of NGC6811 and are located squarely on the cluster sequence in the colour–magnitude diagram (Fig. 1a). Their rotation periods listed in Table 1 were determined from the periodic, out-of-transit, brightness variations in the Kepler light curves, caused by star spots being carried around as the star spins (see Supplementary Information). The rotation periods provide additional confirmation of cluster membership, as they obey the distinct relationship between stellar rotation and colour observed for other members of NGC6811. Figure 1b shows the colour versus rotation period diagram plotted for radial-velocity members of the cluster<sup>16</sup>.

Because of the large distance to NGC6811, the two host stars are too faint (see Table 1) for their radial velocities to be measured with sufficient precision to confirm the status of Kepler-66b and Kepler-67b as true planets in the usual way, that is, by establishing that their masses are in the planetary range. To validate them as planets we instead applied a statistical procedure known as BLENDER (see Supplementary Information), by which we have demonstrated that they are much more likely to be planets than false positives. We determined probabilities of only 0.0019 and 0.0024 that Kepler-66b and Kepler-67b are false positives.

To establish whether finding two mini-Neptunes in NGC6811 is consistent with the rate of occurrence of planets in the field, we conducted a Monte Carlo experiment using the known spectral type and magnitude distributions of the 377 member stars. We simulated true planets adopting distributions of planet sizes and orbital periods corresponding to those found in the Kepler field, along with planet occurrence rates based on a statistical study of the Kepler candidates that accounts for the incidence of false positives as well as incompleteness<sup>5</sup>. We retained only the simulated planets that would be detectable by Kepler on the basis of real noise estimates for each star. We repeated the simulation 1,000 times to predict the average number of transiting planets of all sizes we would expect to detect among the known cluster members observed by Kepler, as well as their period and size distributions (Fig. 3). The result,  $4.0 \pm 2.0$  planets, is consistent with our two planet detections. The expected number of  $2.2 \pm 1.5$  mini-Neptunes is also consistent with our detection of two such planets, and the lack of smaller and larger transiting planets in NGC6811 similarly agrees with their predicted detection rates of  $1.2 \pm 1.1$  for Earths and super-Earths ( $0.8–2R_{\oplus}$ ) and  $0.6 \pm 0.6$  for giant planets ( $>4R_{\oplus}$ ). Together, the results

<sup>1</sup>Harvard-Smithsonian Center for Astrophysics, Cambridge, Massachusetts 02138, USA. <sup>2</sup>NASA Ames Research Center, Moffett Field, California 94035, USA. <sup>3</sup>NASA Exoplanet Science Institute, California Institute of Technology, Pasadena, California 91125, USA. <sup>4</sup>California Institute of Technology, Pasadena, California 91125, USA. <sup>5</sup>Boston University, Boston, Massachusetts 02215, USA. <sup>6</sup>Leibniz-Institute for Astrophysics, Potsdam 14467, Germany. <sup>7</sup>Space Science Institute, Boulder, Colorado 80301, USA. <sup>8</sup>University of California, Berkeley, Berkeley, California 94720, USA. <sup>9</sup>Yale University, New Haven, Connecticut 06520, USA. <sup>10</sup>Southern Connecticut State University, New Haven, Connecticut 06515, USA. <sup>11</sup>SETI Institute/NASA Ames Research Center, Moffett Field, California 94035, USA. <sup>12</sup>National Optical Astronomy Observatory, Tucson, Arizona 85719, USA. <sup>13</sup>University of Notre Dame, Notre Dame, Indiana 46556, USA.



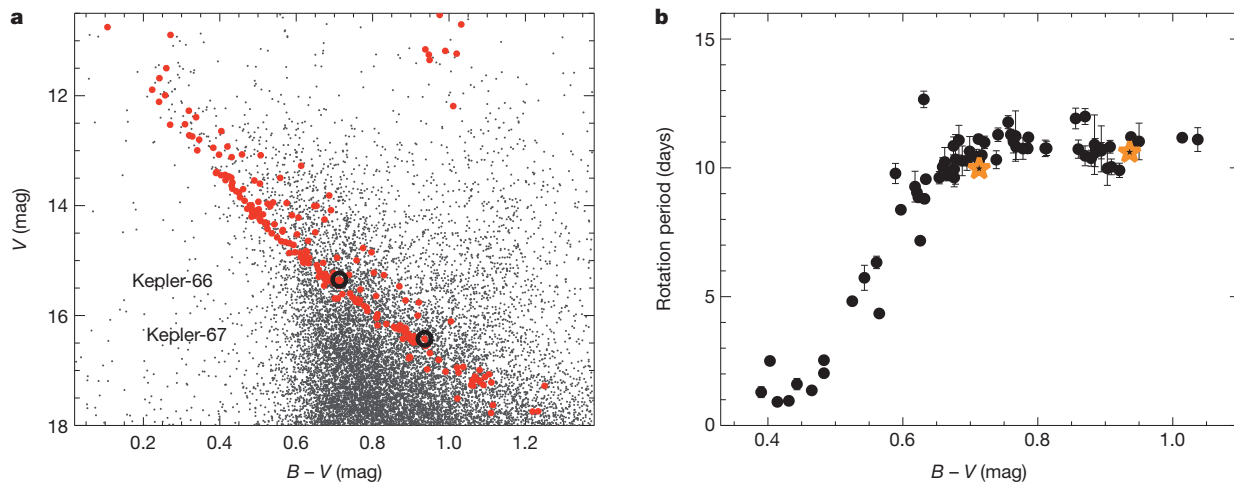


**Figure 1 | The colour-magnitude and colour-period diagrams for NGC6811.** **a**, The colour-magnitude diagram for stars within a 1-degree-diameter field centred on NGC6811 with the locations of Kepler-66 and Kepler-67 marked by black circles. Cluster members, marked with larger red dots, trace a well-defined relationship between stellar mass (colour,  $B - V$ ) and luminosity (brightness,  $V$ ) that can be fitted by stellar evolution models to determine the age and distance of NGC6811 as well as the masses and radii of its members. By this method NGC6811 is found to be  $1.00 \pm 0.17$  billion years old and

imply that the planet frequency in NGC6811 is consistent with that of the field.

The members of NGC6811 fall entirely within the range of stellar spectral types selected for the Kepler planet survey, and the slightly sub-solar metallicity of NGC6811 (ref. 17) is close to the average metallicity of the Galactic disk population from which the Kepler targets are drawn. Therefore, correlations between planet frequency and stellar mass and/

$1,107 \pm 90$  parsecs distant<sup>17</sup>. **b**, The colour-period diagram for 72 NGC6811 members<sup>16</sup>. The rotation periods are determined from periodic brightness variations in the Kepler light curves, and the error bars represent the dispersion of multiple period measurements. As in the colour-magnitude diagram, cluster members trace a well-defined relation between stellar colour and rotation period. The locations of Kepler-66 and Kepler-67 on the cluster sequence are marked by orange star symbols.

**Table 1 | Stellar and planetary parameters for Kepler-66 and Kepler-67**

Stellar properties	Kepler-66	Kepler-67
Right ascension	19 h 35 min 55.573 s	19 h 36 min 36.799 s
Declination	46° 41' 15.906"	46° 09' 59.181"
Spectral type	G0V	G9V
Effective temperature, $T_{\text{eff}}$ (K)	$5,962 \pm 79$	$5,331 \pm 63$
$\log[\text{Surface gravity (cm s}^{-2}\text{)}]$	$4.484 \pm 0.023$	$4.594 \pm 0.022$
Rotation period (days)	$9.97 \pm 0.16$	$10.61 \pm 0.04$
Mass (solar masses)	$1.038 \pm 0.044$	$0.865 \pm 0.034$
Radius (solar radii)	$0.966 \pm 0.042$	$0.778 \pm 0.031$
Density (solar)	$1.15 \pm 0.15$	$1.89 \pm 0.17$
Visual magnitude, $V$	15.3	16.4
Age (billion years)		$1.00 \pm 0.17$
Distance (parsec)		$1,107 \pm 90$
Metallicity, $Z$		$0.012 \pm 0.003$
Planetary parameters	Kepler-66b	Kepler-67b
Orbital period (days)	$17.815815 \pm 0.000075$	$15.72590 \pm 0.00011$
Impact parameter	$0.56 \pm 0.26$	$0.37 \pm 0.21$
Time of mid-transit (BJD)	$2454967.4854 \pm 0.0025$	$2454966.9855 \pm 0.0048$
Planet-to-star radius ratio	$0.02646 \pm 0.00097$	$0.03451 \pm 0.0013$
Scaled semi-major axis ( $a/R_{\text{star}}$ )	$30.3 \pm 1.0$	$32.4 \pm 1.1$
Semi-major axis (AU)	$0.1352 \pm 0.0017$	$0.1171 \pm 0.0015$
Radius ( $R_{\oplus}$ )	$2.80 \pm 0.16$	$2.94 \pm 0.16$

The age, distance and chemical composition of NGC6811 were determined from a maximum-likelihood fit of stellar evolution models<sup>13,14</sup> to the cluster sequence in the colour-magnitude diagram using Bayesian statistics and a Markov-chain Monte Carlo algorithm<sup>17</sup>. The best-fitting stellar isochrone<sup>14</sup> and photometric measurements in all available bandpasses (UBV, griz, JHK and D51 magnitude) were used to derive the effective temperatures, surface gravities, masses, radii and densities for Kepler-66 and Kepler-67. The transit and orbital parameters (period, impact parameter, time of mid-transit, radius ratio, and scaled semi-major axis) for Kepler-66b and Kepler-67b were derived from the Kepler photometry using a Markov-chain Monte Carlo procedure with the mean stellar density as a prior<sup>28</sup>. The parameters for Kepler-67b account for minor dilution from a close companion to the star described in section 3.2 of the Supplementary Information. Errors given for stellar and planetary parameters are  $1\sigma$  uncertainties. BJD is barycentric Julian date, and AU is astronomical units.

or metallicity are not a concern when comparing the frequency and size distribution of planets in NGC6811 to that of the field. The detection of Kepler-66b and Kepler-67b thus places the first robust constraint on the frequency of small planets in open clusters relative to the field.

The comparison in Fig. 3 of the orbital periods and radii of Kepler-66b and Kepler-67b with those in our simulated distributions shows that the sizes and orbital properties of the two planets are similar to those of the most common types of field planets ( $2-3R_{\oplus}$ , and orbital periods between 10 and 20 days). This suggests that the sizes and orbital properties of planets in open clusters are also not unlike those in the field.

The masses, structures and compositions of Kepler-66b and Kepler-67b can be constrained using theoretical models. With radii in excess of  $2R_{\oplus}$ , the two planets probably contain significant quantities of volatiles in the form of astrophysical ices and up to a few per cent of H or He by mass. Volatile-poor rocky planets this large would have Saturn-like masses of 82–117 Earth masses (assuming an Earth-like composition with 32% iron core and 68% silicates by mass), and would be larger and more massive than any rocky exoplanet discovered to date. Instead, Kepler-66b and Kepler-67b are likely to have structures and compositions that resemble that of Neptune and, following mass-radius relations for exoplanets in the field<sup>18</sup>, probably have masses less than 20 Earth masses (see Supplementary Information).

For NGC6811 to have survived a billion years, the initial number density of stars in the cluster must have been at least that of the Orion Trapezium cluster (about 13,000 per cubic parsec) and thus more than two orders of magnitude greater than that of the typical cluster formed in a molecular cloud (about a hundred stars per cubic parsec; ref. 1). Highly energetic phenomena including explosions, outflows and winds often associated with massive stars would have been common in the young cluster. The degree to which the formation and evolution of planets is influenced by a such a dense and dynamically and radiatively hostile environment is not well understood, either observationally or theoretically<sup>19–25</sup>. The formation of planets takes place in the circumstellar disks during the first few million years of a star's life, which is the typical lifetime of disks<sup>26</sup>. We estimated the number and mass-distribution of stars in NGC6811 at the time Kepler-66b and Kepler-67b formed by fitting a canonical initial mass function<sup>27</sup> to the current distribution of masses for members in the cluster (see Supplementary Information). The calculation suggests that the cluster contained

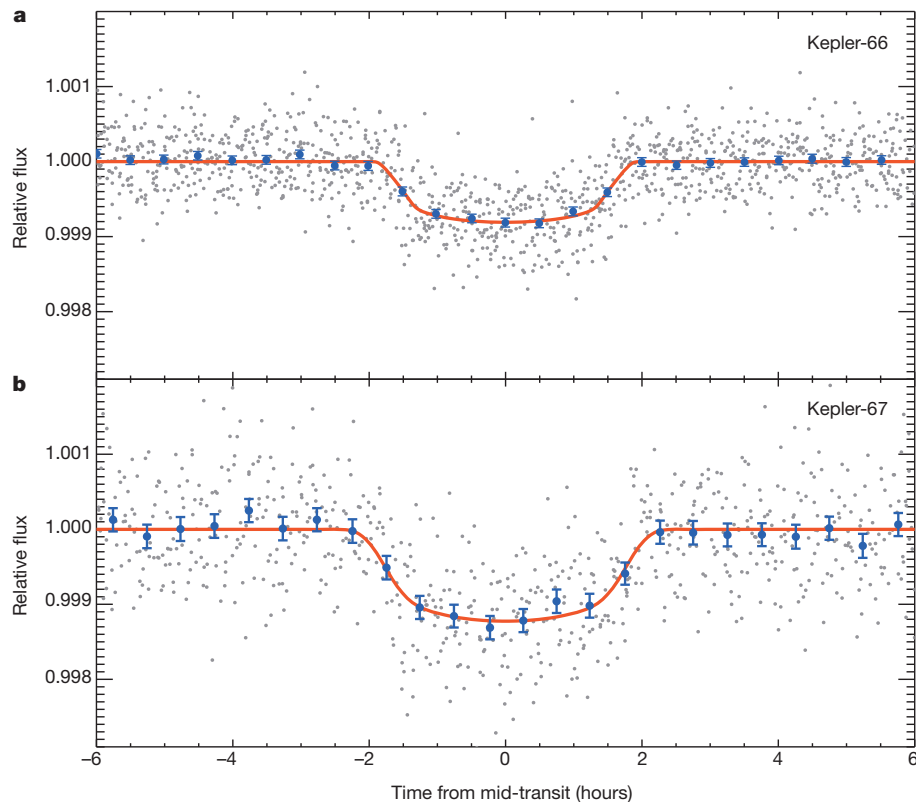


**Figure 2 | Transit light curves.** **a, b,** The Kepler light curves for Kepler-66 (**a**) and Kepler-67 (**b**). The photometric measurements (grey points) were acquired in long cadence mode (30-min total exposures) and have been detrended<sup>28</sup>, normalized to the out-of-transit flux level, and phase-folded on the

periods of the transiting planets. The blue data points and error bars represent the same data phase-binned in 30-min intervals and the standard error of the mean, respectively. Transit models smoothed to the same cadence are overplotted in red.

at least 6,000 stars during the era of planet formation, including several O stars (masses greater than 20 solar masses) and more than one hundred B stars (masses between 3 and 20 solar masses). The discovery of two mini-Neptunes in NGC6811 thus provides evidence that the formation and long-term stability of small planets is robust against

stellar densities that are extremely high for open clusters, and the violent deaths and high-energy radiation of nearby massive stars.

Received 6 November 2012; accepted 2 May 2013.

Published online 26 June 2013.

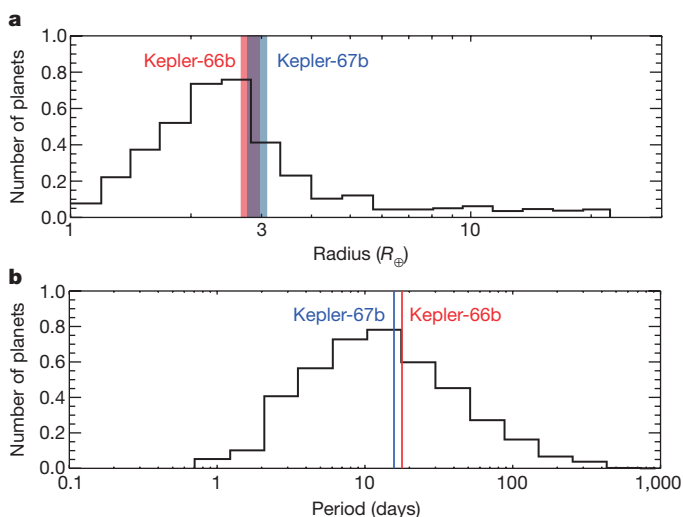


**Figure 3 | Distribution of planetary properties.** **a, b,** Histograms of planetary radii (**a**) and orbital periods (**b**) of simulated transiting planets expected in NGC6811, accounting for incompleteness and assuming the same period and size distribution and occurrence rate as in the field<sup>5</sup>. The properties of Kepler-66b and Kepler-67b are similar to those of the most commonly expected planets. The widths of the red and blue vertical lines reflect  $\pm 1\sigma$  errors in the radii and periods of the two planets.

1. Lada, C. J. & Lada, E. A. Embedded clusters in molecular clouds. *Annu. Rev. Astron. Astrophys.* **41**, 57–115 (2003).
2. The Extrasolar Planets Encyclopaedia. <http://exoplanet.eu> (2012).
3. Mayor, M. *et al.* The HARPS search for southern extra-solar planets XXXIV. Occurrence, mass distribution and orbital properties of super-Earths and Neptune-mass planets. *Astron. Astrophys.* (submitted); preprint at <http://arxiv.org/abs/1109.2497>.
4. Howard, A. *et al.* Planet occurrence within 0.25 AU of solar-type stars from Kepler. *Astrophys. J. Suppl.* **201**, 15–35 (2012).
5. Fressin, F. *et al.* The false positive rate of Kepler and the occurrence of planets. *Astrophys. J.* **766**, 81–99 (2013).
6. Sato, B. *et al.* A planetary companion to the Hyades giant Epsilon Tauri. *Astrophys. J.* **661**, 527–531 (2007).
7. Lovis, C. & Mayor, M. Planets around evolved intermediate-mass stars. I. Two substellar companions in the open clusters NGC2423 and NGC4349. *Astron. Astrophys.* **472**, 657–664 (2007).
8. Quinn, S. *et al.* Two “b”s in the beehive: the discovery of the first hot Jupiters in an open cluster. *Astrophys. J.* **756**, L33–L36 (2012).
9. van Saders, J. L. & Gaudi, B. S. Ensemble analysis of open cluster transit surveys: upper limits on the frequency of short-period planets consistent with the field. *Astrophys. J.* **729**, 63–76 (2011).
10. Pace, G., Pasquini, L. & Francois, P. Abundances of four open clusters from solar stars. *Astron. Astrophys.* **489**, 403–412 (2008).
11. Fischer, D. A. & Valenti, J. The planet-metallicity correlation. *Astrophys. J.* **622**, 1102–1117 (2005).
12. Meibom, S. The Kepler Cluster Study. *Bull. Am. Astron. Soc.* **43**, (AAS Meeting 218) abstr. 311.03 (2011).
13. Yi, S. *et al.* Toward better age estimates for stellar populations: the  $Y^2$  isochrones for solar mixture. *Astrophys. J. Suppl.* **136**, 417–437 (2001).
14. Girardi, L., Bressan, A., Bertelli, G. & Chiosi, C. Evolutionary tracks and isochrones for low- and intermediate-mass stars: from 0.15 to 7  $M_{\odot}$ , and from  $Z=0.0004$  to 0.03. *Astron. Astrophys.* **141** (Suppl.), 371–383 (2000).
15. Jenkins, J. M. *et al.* Overview of the Kepler Science Processing Pipeline. *Astrophys. J.* **713**, L87–L91 (2010).



16. Meibom, S. *et al.* The Kepler Cluster Study: stellar rotation in NGC6811. *Astrophys. J.* **733**, L9–L12 (2011).
17. Janes, K., Barnes, S. A., Meibom, S. & Hoq, S. NGC6811: an intermediate-age cluster in the Kepler field. *Astron. J.* **145**, 7–21 (2013).
18. Weiss, L. M. *et al.* The mass of KOI-94d and a relation for planet radius, mass, and incident flux. *Astrophys. J.* **768**, 14–32 (2013).
19. Scally, A. & Clarke, C. Destruction of protoplanetary discs in the Orion nebula cluster. *Mon. Not. R. Astron. Soc.* **325**, 449–456 (2001).
20. Bonnell, I. A. *et al.* Planetary dynamics in stellar clusters. *Mon. Not. R. Astron. Soc.* **322**, 859–865 (2001).
21. Smith, K. W. & Bonnell, I. A. Free-floating planets in stellar clusters? *Mon. Not. R. Astron. Soc.* **322**, L1–L4 (2001).
22. Fregeau, J. M., Chatterjee, S. & Rasio, F. A. Dynamical interactions of planetary systems in dense stellar environments. *Astrophys. J.* **640**, 1086–1098 (2006).
23. Adams, F. C., Proszkow, E. M., Fatuzzo, M. & Myers, P. C. Early evolution of stellar groups and clusters: environmental effects on forming planetary systems. *Astrophys. J.* **641**, 504–525 (2006).
24. Malmberg, D. *et al.* Close encounters in young stellar clusters: implications for planetary systems in the solar neighbourhood. *Mon. Not. R. Astron. Soc.* **378**, 1207–1216 (2007).
25. Spurzem, R., Giersz, M., Heggie, D. C. & Lin, D. N. C. Dynamics of planetary systems in star clusters. *Astrophys. J.* **697**, 458–482 (2009).
26. Haisch, K. E., Lada, E. A. & Lada, C. J. Disk frequencies and lifetimes in young clusters. *Astrophys. J.* **553**, L153–L156 (2001).
27. Kroupa, P. The IMF of simple and composite populations. *Astron. Soc. Pacif. Conf. Ser.* **390**, 303–315 (2008).
28. Gautier, T. N. *et al.* Kepler-20: a Sun-like star with three sub-Neptune exoplanets and two Earth-size candidates. *Astrophys. J.* **749**, 15–33 (2012).

**Supplementary Information** is available in the online version of the paper.

**Acknowledgements** Kepler was competitively selected as the tenth Discovery mission. Funding for this mission is provided by NASA's Science Mission Directorate. S.M. acknowledges support through NASA grant NNX09AH18A (The Kepler Cluster Study)

and from the Kepler mission via NASA Cooperative Agreement NCC2-1390. G.T. acknowledges support through NASA's Kepler Participating Scientist Program grant NNX12AC75G. L.A.R. acknowledges NASA support through Hubble Fellowship grant HF-51313.01-A awarded by the Space Telescope Science Institute, which is operated by the Association of Universities for Research in Astronomy, Inc., for NASA, under contract NAS 5-26555.

**Author Contributions** S.M. is the Principal Investigator of The Kepler Cluster Study and led the writing of the paper and the effort to identify members of NGC6811. He worked with G.T. and F.F. on characterization and validation of Kepler-66b and Kepler-67b, and with K.J. and S.A.B. on determination of the properties of NGC6811. G.T. developed the BLENDER software used to validate the planets, and determined the stellar properties of the host stars. F.F. worked on the BLENDER validation of the two planets and the Monte-Carlo simulation of the cluster yield. D.W.L. contributed follow-up spectroscopy of host stars. J.F.R. performed the light-curve analysis to extract the planet characteristics. D.R.C. provided constraints on angular separation of potential background blends from adaptive optics imaging. S.T.B. performed pixel-level centroid analysis. C.E.H. assisted in running BLENDER on the NASA Pleiades supercomputer. L.A.R. modelled the planets' interior structure to constrain the range of possible masses and compositions. K.J. led the supporting photometric study from which the bulk properties of NGC6811 are derived. S.A.B. participated in the acquisition of ground-based spectroscopic and photometric data on NGC6811. G.W.M. and H.I. obtained and analysed high-resolution Keck HIRES spectra of the host stars used for the BLENDER analysis. D.A.F. analysed HIRES spectra using the Spectroscopy Made Easy software. S.B.H. and E.P.H. obtained and analysed speckle observations of the host stars. J.M.J. led the efforts of data collection, data processing and data review that yielded the Kepler time series photometry. S.C.S. did spectroscopic analysis of stellar members of NGC6811 to aid in the determination of cluster parameters including metallicity. J.C. obtained adaptive optics imaging observations.

**Author Information** Reprints and permissions information is available at [www.nature.com/reprints](http://www.nature.com/reprints). The authors declare no competing financial interests. Readers are welcome to comment on the online version of the paper. Correspondence and requests for materials should be addressed to S.M. ([smeibom@cfa.harvard.edu](mailto:smeibom@cfa.harvard.edu)).

# Global resurfacing of Mercury 4.0–4.1 billion years ago by heavy bombardment and volcanism

Simone Marchi<sup>1</sup>, Clark R. Chapman<sup>2</sup>, Caleb I. Fassett<sup>3</sup>, James W. Head<sup>4</sup>, W. F. Bottke<sup>2</sup> & Robert G. Strom<sup>5</sup>

**The most heavily cratered terrains on Mercury have been estimated to be about 4 billion years (Gyr) old<sup>1–4</sup>, but this was based on images of only about 45 per cent of the surface; even older regions could have existed in the unobserved portion. These terrains have a lower density of craters less than 100 km in diameter than does the Moon<sup>1,3,5</sup>, an observation attributed to preferential resurfacing on Mercury. Here we report global crater statistics of Mercury's most heavily cratered terrains on the entire surface. Applying a recent model for early lunar crater chronology<sup>6</sup> and an updated dynamical extrapolation to Mercury<sup>7</sup>, we find that the oldest surfaces were emplaced just after the start of the Late Heavy Bombardment (LHB) about 4.0–4.1 Gyr ago. Mercury's global record of large impact basins<sup>8</sup>, which has hitherto not been dated, yields a similar surface age. This agreement implies that resurfacing was global and was due to volcanism, as previously suggested<sup>1,5</sup>. This activity ended during the tail of the LHB, within about 300–400 million years after the emplacement of the oldest terrains on Mercury. These findings suggest that persistent volcanism could have been aided by the surge of basin-scale impacts during this bombardment.**

The earliest geological features that have been detected on Mercury, the heavily cratered terrains, show signs of ancient resurfacing as shown by the intercrater smooth plains. Early work, based on partial coverage by Mariner 10 images, suggested that both volcanism<sup>1</sup> and basin ejecta<sup>9</sup> could have been responsible for the formation of the intercrater plains. Recent work<sup>10</sup> based on high-resolution imaging from MESSENGER (MErcury Surface, Space ENvironment, GEochemistry, and Ranging) presented evidence that the extensive intercrater plains seen in the heavily cratered terrains resulted from an early period of volcanism, although clear volcanic sources for these ancient units have not yet been identified. The timing and areal extent of this proposed resurfacing on Mercury, and the specific role of volcanism, have been unknown.

As is true for other terrestrial bodies, except the Earth and the Moon, Mercury's relative geological chronology has been inferred from observations of the impact crater record (see, for example, ref. 11), with absolute ages then extrapolated from the better-constrained lunar crater chronology<sup>12–14</sup>. Here we measure crater size–frequency distributions for the most heavily cratered terrains on Mercury to determine their absolute ages. The age of the most heavily cratered terrains is an important benchmark for Mercury, because it provides an upper limit for the formation of subsequent major geological units such as the widespread volcanic smooth plains in the annulus surrounding the Caloris basin<sup>15</sup> and in high northern latitudes of Mercury<sup>16</sup>. The currently visible impactor population in the terrestrial planet region, namely near-Earth objects, is now well characterized for kilometre-sized asteroids<sup>17</sup>, although impact rates and size distributions are less certain for earlier epochs. By using current models of the impact rate in the inner solar system, a model production function for lunar cratering has been developed and extrapolated to Mercury<sup>7</sup>. More recently, an independent model<sup>18</sup> found comparable results.

We initially identified the most heavily cratered terrains on Mercury using a preliminary global crater catalogue<sup>5</sup>, then defined their boundaries on a new MESSENGER global mosaic. We concentrated on two regions of high crater density (Supplementary Fig. 1): the northern heavily cratered terrains (NHCT; Fig. 1) and a heavily cratered area at southern latitudes east of Rembrandt basin unseen by Mariner 10 (Supplementary Fig. 1). The NHCT is a surviving remnant of a once larger heavily cratered terrain. Adjacent regions experienced more substantial resurfacing by the northern volcanic plains, the circum-Caloris volcanic plains, and by young basins east of the NHCT. The region east of Rembrandt was studied in a similar manner and produced comparable results (Supplementary Fig. 2), so we restrict discussion in this paper to the NHCT region.

The next step was to use a model production function of craters to model the observed cumulative number of craters at least 25 km in diameter on NHCT (see Supplementary Fig. 2). The model production function was obtained<sup>7</sup> by using an impactor size–frequency distribution resembling that of the main asteroid belt<sup>7,19,20</sup>, which has provided a suitable fit to old units on Mercury, the Moon and Mars. As can be seen, the model production function fits the NHCT data quite well, ensuring that our model is well suited to studying the early cratering on Mercury.

Cratering data for the northern heavily cratered terrains are plotted in both cumulative and R-plot formats<sup>21</sup> in Fig. 2. The associated lunar data come from crater counts on specific ancient lunar terrains<sup>20</sup>. The pre-Nectarian terrains were defined as a particular portion of the northern farside highlands. They represent one of the oldest lunar terrains, with a crater spatial density that slightly exceeds that of the NHCT on Mercury. The post-Nectarian crater size–frequency distribution is representative of terrains coeval with or younger than the Nectaris basin, a stratigraphic benchmark in lunar history<sup>22</sup>.

In general, we find that the spatial density of craters from the lunar and Mercurian terrains in Fig. 2b approaches empirical saturation equilibrium, which is thought to occur at  $R = 0.2$ – $0.3$ , for diameters near 100 km (ref. 23), but they fall well below this level for craters that are considerably larger or smaller. The shapes of the NHCT and lunar pre-Nectarian terrains crater size–frequency distributions also resemble that of the lunar nearside highlands crater size–frequency distribution<sup>1,20</sup>. The question is whether these ancient units have reached crater saturation or whether they still represent the size–frequency distribution of the impactor population. The characteristics of the crater size–frequency distributions on the NHCT and pre-Nectarian terrains lead us to adopt the view that those terrains are in production (see Supplementary Information for discussion).

To interpret the ancient crater size–frequency distribution on Mercury within the context of lunar chronology, we need to account for the differences between Mercury and the Moon concerning impact velocities, gravitational focusing and other factors that affect crater scaling relationships. Using the current Moon-crossing and Mercury-crossing asteroid populations derived from ref. 24, we find that on average

<sup>1</sup>NASA Lunar Science Institute, Southwest Research Institute, Boulder, Colorado 80302, USA. <sup>2</sup>Southwest Research Institute, Boulder, Colorado 80302, USA. <sup>3</sup>Department of Astronomy, Mount Holyoke College, South Hadley, Massachusetts 01075, USA. <sup>4</sup>Department of Geological Sciences, Brown University, Providence, Rhode Island 02912, USA. <sup>5</sup>Department of Planetary Sciences, University of Arizona, Tucson, Arizona 85721, USA.



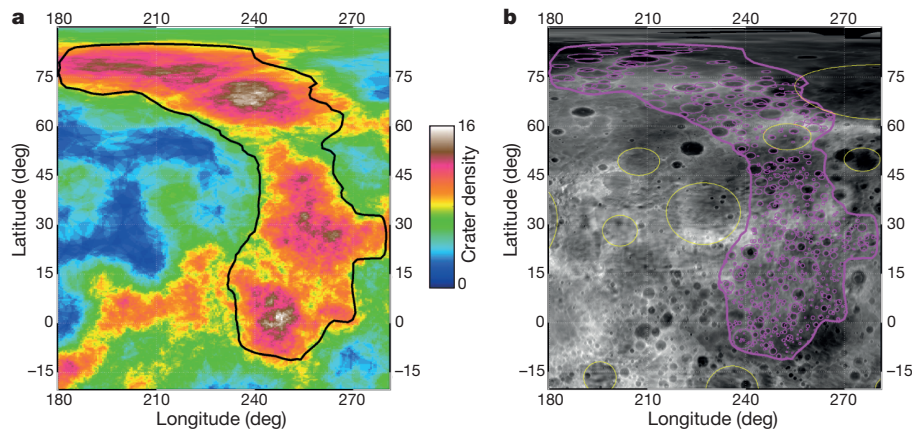


**Figure 1 | The northern heavily cratered terrains of Mercury.** Crater measurements were made from a global mosaic with a resolution of 500 m per pixel based on MESSENGER images obtained during its first year orbiting Mercury. Our reliance on the global mosaic for actual crater measurements was augmented, for a few regions of poorer imaging and for some highly degraded craters, by a global digital terrain model having a resolution of about 1,300 m per pixel produced from wide-angle camera images by R. Gaskell (personal communication, 2012). **a**, Crater areal density (in number of craters at least 25 km in diameter per  $10^5 \text{ km}^2$ ) obtained by averaging over a radius of 300 km.

about 3–3.5-fold as many craters in the size range relevant for this work (20–300 km) should form on Mercury as on the Moon (Supplementary Fig. 3). In this work we adopt a conservative factor of 3 (valid at 20 km), a value consistent with an independent estimate<sup>18</sup>. Furthermore, we adopted a recently revised early lunar chronology<sup>6</sup> for ages older than 3 Gyr (Fig. 3). The earliest declining lunar bombardment was due to planetesimals left over from terrestrial planet formation. Beginning about 4.1 Gyr ago there was a spike in the bombardment rate (the LHB) due to asteroids ejected from the primordial asteroid belt by sweeping resonances in the wake of late giant planet migration<sup>25</sup>, which declined over at least the subsequent 0.6 Gyr. This is manifested in the cumulative plot by the break in slope at 4.1 Gyr ago. We also plot in Fig. 3

the expected cumulative cratering flux for Mercury, appropriately scaled by the factor discussed above. The results show that the NHCT has an age of about 4.0–4.1 Gyr and therefore is likely to be several hundreds of million years younger than the most ancient lunar terrains (interpreted in ref. 6 to be about 4.4 Gyr old). Even if both the lunar and Mercurian heavily cratered terrains were in an empirical saturation equilibrium state, the age difference between the Moon and Mercury would be reduced but Mercury's NHCT crater retention age would still be post-Nectarian.

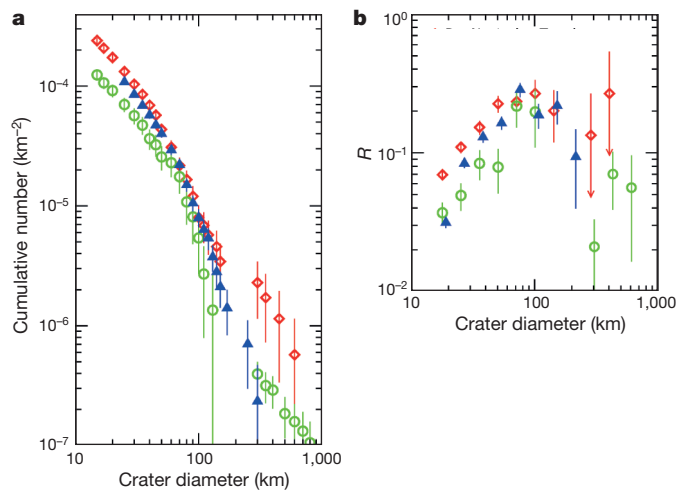


**Figure 2 | Comparison of Mercury cratering data with key lunar units.** The measured craters on the NHCT (blue triangles) are plotted in a cumulative form (**a**) and on an  $R$ -plot (**b**), obtained by normalizing the cumulative size–frequency distributions to a power law  $D^{-2}$ , where  $D$  is the crater diameter. Pre-Nectarian terrains (red diamonds) encompass a portion of the lunar northern farside<sup>20,22</sup>. The post-Nectarian crater size–frequency distribution (green circles) was obtained by taking the crater size–frequency distribution (for  $D < 300 \text{ km}$ ) found near or on terrains resurfaced by the formation of Nectaris basin<sup>20</sup> and then adding 12 post-Nectaris basins<sup>22</sup>, all of which had  $D > 300 \text{ km}$ . Error bars correspond to Poisson statistics.

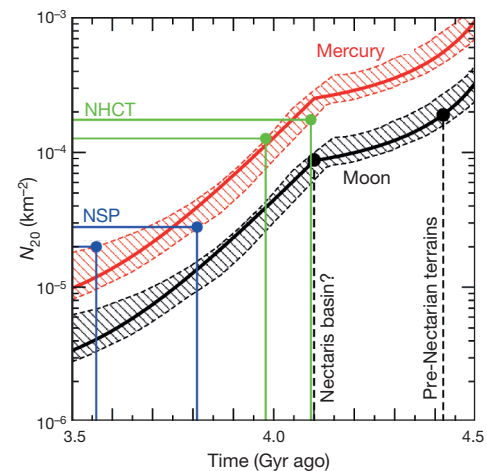


**Figure 3 | Mercury and lunar crater chronologies.** The solid black curve shows the number of lunar craters larger than 20 km per unit surface ( $N_{20}$ ), corresponding to the best model<sup>6</sup>. The slope transition at 4.1 Gyr ago marks the onset of the LHB<sup>6</sup>. The inferred age of the pre-Nectarian terrains is also shown, as well as a putative age for the Nectaris basin of 4.1 Gyr (refs 6, 20, 25). The black hatched region represents the envelope of uncertainties in the lunar chronology, as discussed in ref. 6. The Mercury crater chronology (red curve) is obtained by scaling the lunar chronology by a factor of 3. The model uncertainty in the factor of 3 is not considered because it lies within the chronology envelope. The horizontal green lines indicate the range of  $N_{20}$  estimated for the NHCT (see Supplementary Fig. 2), which translates into a range of ages spanning from about 4.0 to about 4.1 Gyr ago. The horizontal blue lines indicate the range of  $N_{20}$  for the northern smooth plains (NSP; see Supplementary Fig. 2)<sup>16</sup>, which translates into a range of ages spanning from about 3.55 to about 3.8 Gyr ago.

We can arrive at a similar conclusion by looking at the record of large basins on the Moon and Mercury (that is, more than 300 km in diameter)<sup>8</sup>. On the Moon there are about 12–15 such basins younger than Nectaris<sup>22,26</sup>. If the scaling factor derived above is applicable to large LHB-era impactors, which is plausible (see, for example, ref. 25), we would expect about 36–45 basins on Mercury to have accumulated over the same timescale. This number is close to the  $46 \pm 7$  basins (certain and probable) observed on Mercury<sup>8</sup>, and is consistent with our predicted younger age for Mercury's surface. Moreover, the merged large basin size–frequency distribution and NHCT crater size–frequency distribution match remarkably well the model production function over nearly two orders of magnitude in crater sizes (see Supplementary Fig. 4). This strongly suggests that the entire surface of Mercury was resurfaced 4.0–4.1 Gyr ago and that the most ancient crater record (including all visible basins) was produced by impactors having a main belt-like size–frequency distribution.

The end of widespread smooth plains volcanism (see, for example, ref. 16) represents another benchmark in Mercury's history. Using our model production function chronology, we find that the northern smooth volcanic plains<sup>16</sup>, which along with the contemporary plains surrounding Caloris basin account for about 17% of the entire surface, were emplaced about 3.55–3.8 Gyr ago (Fig. 3 and Supplementary Fig. 2).

These findings provide compelling evidence for a widespread process, probably volcanism, that erased up to hundreds of millions of years of Mercury's earlier crater history. Moreover, the fact that the globally distributed large basins and the NHCT yield similar ages suggests that the resurfacing was global in nature (see, for example, ref. 10). Our data further indicate that widespread volcanism declined rapidly during the LHB relative to the Moon<sup>27</sup>, and ended about 3.55–3.8 Gyr ago. After that time, volcanism was much more restricted, occurring only in small patches or within large impact basins<sup>28</sup>.

Widespread volcanism on Mercury was occurring at the same time as the increase in the impact flux at the start of the LHB period. From an impact statistics point of view, the onset of the LHB was probably followed by a slight delay before the first large basin-forming collisions took place. The fact that our age estimate for Mercury's NHCT is slightly younger than the start of the LHB is consistent with heavy bombardment and basin formation occurring at the same time as global volcanism. Also significant is the cessation of major volcanism near the end of LHB basin formation, thus showing a temporal link between impact flux and volcanism. These findings, coupled with the prediction of a relatively thin lithosphere of Mercury<sup>29</sup>, support the idea that large impacts may have triggered voluminous volcanism<sup>30,31</sup>. Vital remaining issues are to what extent and in what ways the impact process had a role in internal melt generation, ascent and eruption.

Received 30 November 2012; accepted 2 May 2013.

1. Strom, R. G. Origin and relative age of lunar and Mercurian intercrater plains. *Phys. Earth Planet. Inter.* **15**, 156–172 (1977).
2. Leake, M. A. *The Intercrater Plains of Mercury and the Moon: their Nature, Origin, and Role in Terrestrial Planet Evolution*. PhD thesis, Univ. of Arizona (1982).
3. Strom, R. G. & Neukum, G. in *Mercury* (eds Vilas, F., Chapman, C. R. & Matthews, M. S.) 336–373 (Univ. Arizona Press, 1988).
4. Neukum, G., Oberst, J., Hoffmann, H., Wagner, R. & Ivanov, B. A. Geologic evolution and cratering history of Mercury. *Planet. Space Sci.* **49**, 1507–1521 (2001).
5. Fassett, C. I. *et al.* The global population of large craters on Mercury and comparison with the Moon. *Geophys. Res. Lett.* **38**, L10202 (2011).
6. Morbidelli, A. *et al.* A sawtooth-like timeline for the first billion years of lunar bombardment. *Earth Planet. Sci. Lett.* **355–356**, 144–151 (2012).
7. Marchi, S. *et al.* A new chronology for the Moon and Mercury. *Astron. J.* **137**, 4936–4948 (2009).

8. Fassett, C. I. *et al.* Large impact basins on Mercury: global distribution, characteristics, and modification history from MESSENGER orbital data. *J. Geophys. Res.* **117**, E00L08, <http://dx.doi.org/10.1029/2012JE004154> (2012).
9. Wilhelms, D. E. Mercurian volcanism questioned. *Icarus* **28**, 551–558 (1976).
10. Strom, R. G. *et al.* Mercury crater statistics from MESSENGER flybys: implications for stratigraphy and resurfacing history. *Planet. Space Sci.* **59**, 1960–1967 (2011).
11. Shoemaker, E. M. *et al.* Interplanetary correlation of geologic time. *Adv. Astronaut. Sci.* **8**, 70–89 (1963).
12. Hartmann, W. K. *et al.* in *Basaltic Volcanism on the Terrestrial Planets* (eds McGetchin, T. R., Pepin, R. O. & Phillips, R. J.) 1049–1127 (Pergamon, 1981).
13. Neukum, G. & Ivanov, B. A. in *Hazards Due to Comets and Asteroids* (eds Gehrels, T., Matthews, M. S. & Schumann, A.) 359–416 (Univ. of Arizona Press, 1994).
14. Stöffler, D. & Ryder, G. Stratigraphy and isotope ages of lunar geologic units: chronological standard for the inner Solar System. *Space Sci. Rev.* **96**, 9–54 (2001).
15. Strom, R. G. *et al.* Mercury cratering record viewed from MESSENGER's first flyby. *Science* **321**, 79–81 (2008).
16. Head, J. W. *et al.* Flood volcanism in the northern high latitudes of Mercury revealed by MESSENGER. *Science* **333**, 1853–1856 (2011).
17. Mainzer, A. *et al.* NEOWISE observations of near-Earth objects: preliminary results. *Astrophys. J.* **743**, 156–173 (2011).
18. Le Feuvre, M. & Wieczorek, M. A. Nonuniform cratering of the Moon and a revised crater chronology of the inner Solar System. *Icarus* **214**, 1–20 (2011).
19. Strom, R. G. *et al.* The origin of planetary impactors in the inner Solar System. *Science* **309**, 1847–1850 (2005).
20. Marchi, S. *et al.* The onset of the lunar cataclysm as recorded in its ancient crater populations. *Earth Planet. Sci. Lett.* **325**, 27–38 (2012).
21. Crater Analysis Techniques Working Group. Standard techniques for presentation and analysis of crater size-frequency data. *Icarus* **37**, 467–474 (1979).
22. Wilhelms, D. E. *The Geologic History of the Moon* (US Geological Survey Professional Paper 1348, 1987).
23. Hartmann, W. K. Does crater 'saturation equilibrium' occur in the solar system? *Icarus* **60**, 56–74 (1984).
24. Bottke, W. F. *et al.* Debaised orbital and absolute magnitude distribution of the near-Earth objects. *Icarus* **156**, 399–433 (2002).
25. Bottke, W. F. *et al.* An Archaean heavy bombardment from a destabilized extension of the asteroid belt. *Nature* **485**, 78–81 (2012).
26. Fassett, C. I. *et al.* Lunar impact basins: stratigraphy, sequence and ages from superposed impact crater populations measured from Lunar Orbiter Laser Altimeter (LOLA) data. *J. Geophys. Res.* **117**, E00H06, <http://dx.doi.org/10.1029/2011JE003951> (2012).
27. Hiesinger, H., Head, J. W., Wolf, U., Jaumann, R. & Neukum, G. in *Recent Advances and Current Research Issues in Lunar Stratigraphy* (eds Ambrose, W. A. & Williams, D. A.) 1–51 (Geological Society of America Special Paper 477, 2011).
28. Marchi, S. *et al.* The effects of the target material properties and layering on the crater chronology: the case of Raditladi and Rachmaninoff basins on Mercury. *Planet. Space Sci.* **59**, 1968–1980 (2011).
29. Smith, D. E. The equatorial shape and gravity field of Mercury from MESSENGER flybys 1 and 2. *Icarus* **209**, 88–100 (2010).
30. Elkins-Tanton, L. T. & Hager, B. H. Giant meteoroid impacts can cause volcanism. *Earth Planet. Sci. Lett.* **239**, 219–232 (2005).
31. Ivanov, B. A. & Melosh, H. J. Impacts do not initiate volcanic eruptions: eruptions close to the crater. *Geology* **31**, 869–872 (2003).

Supplementary Information is available in the online version of the paper.

**Acknowledgements** The contributions of S.M. and W.F.B. were supported by the NASA Lunar Science Institute (Center for Lunar Origin and Evolution at the Southwest Research Institute in Boulder, Colorado—NASA Grant NNA09DB32A; Center for Lunar Science and Exploration at the Lunar and Planetary Institute in Houston, Texas). S.M. is grateful for being welcomed as a collaborator with the Geology Discipline Group of MESSENGER. C.R.C.'s contribution was supported by the MESSENGER Project. The MESSENGER Project is supported by the NASA Discovery Program under contracts NASW-00002 to the Carnegie Institution of Washington and NAS5-97271 to the Johns Hopkins University Applied Physics Laboratory.

**Author Contributions** S.M. and C.R.C. performed the new crater measurements. S.M. and W.F.B. computed the impact rates. C.I.F., J.W.H. and R.G.S. provided earlier crater catalogues. All authors contributed to a discussion of the results and their implications, and to writing and revising the manuscript.

**Author Information** Reprints and permissions information is available at [www.nature.com/reprints](http://www.nature.com/reprints). The authors declare no competing financial interests. Readers are welcome to comment on the online version of the paper. Correspondence and requests for materials should be addressed to S.M. ([marchi@boulder.swri.edu](mailto:marchi@boulder.swri.edu)).



# Reduction of the radiative decay of atomic coherence in squeezed vacuum

K. W. Murch<sup>1</sup>, S. J. Weber<sup>1</sup>, K. M. Beck<sup>2</sup>, E. Ginossar<sup>3</sup> & I. Siddiqi<sup>1</sup>

Quantum fluctuations of the electromagnetic vacuum are responsible for physical effects such as the Casimir force and the radiative decay of atoms, and set fundamental limits on the sensitivity of measurements. Entanglement between photons can produce correlations that result in a reduction of these fluctuations below the ordinary vacuum level, allowing measurements that surpass the standard quantum limit in sensitivity<sup>1–5</sup>. The effects of such ‘squeezed states’ of light on matter were first considered in a prediction<sup>6</sup> of the radiative decay rates of atoms in squeezed vacuum. Despite efforts to demonstrate such effects in experiments with natural atoms<sup>7–9</sup>, a direct quantitative observation of this prediction has remained elusive. Here we report a twofold reduction of the transverse radiative decay rate of a superconducting artificial atom coupled to continuum squeezed vacuum. The artificial atom is effectively a two-level system formed by the strong interaction between a superconducting circuit and a microwave-frequency cavity. A Josephson parametric amplifier is used to generate quadrature-squeezed electromagnetic vacuum. The observed twofold reduction in the decay rate of the atom allows the transverse coherence time,  $T_2$ , to exceed the ordinary vacuum decay limit,  $2T_1$ . We demonstrate that the measured radiative decay dynamics can be used to reconstruct the Wigner distribution of the itinerant squeezed state. Our results confirm a canonical prediction<sup>6</sup> of quantum optics and should enable new studies of the quantum light–matter interaction.

The quantization of the electromagnetic field implies a minimum uncertainty relation for non-commuting observables such as photon number and phase, or the two quadrature amplitudes,  $X_1$  and  $X_2$ , of a mode of the electromagnetic field. The electromagnetic vacuum is a minimum-uncertainty state with quantum fluctuations distributed equally between the two quadratures. Parametric amplifiers operating in the optical<sup>10–12</sup> and microwave<sup>13–19</sup> domain have been used to produce squeezed states of the electromagnetic field, wherein the fluctuations in one quadrature are increased and fluctuations in the other quadrature are reduced below the ordinary vacuum level, allowing for an improvement in measurement sensitivity<sup>1–5</sup>. The focus of our research, however, is to reveal the effects of squeezed vacuum on the radiative properties of an atom. In the optical domain, only a few experiments have explored the squeezed light–atom interaction, in studies in free space<sup>7,8</sup> and in a cavity quantum electrodynamics architecture<sup>9</sup>. Our experiment is in the microwave domain and uses a hybrid quantum bit (qubit)—an effective two-level atom formed by the strong light–matter dipole interaction between a superconducting circuit and a microwave-frequency cavity. We use a Josephson parametric amplifier to produce a spectrally broadband squeezed vacuum in the modes of a transmission line that are resonant with the atomic transition. The architecture of a one-dimensional radiative environment<sup>6,9,20,21</sup> and the strong coupling available in circuit quantum electrodynamics<sup>22</sup> enable us to engineer the radiative decay to be solely into the modes of the transmission line that are occupied by squeezed vacuum. Thus, we are able to explore the radiative decay dynamics of an atom in squeezed vacuum systematically.

The itinerant electromagnetic field generated by a degenerate parametric amplifier may be approximately described in terms of the squeezing moments,  $M$  and  $N$ , which are related to the frequency correlations of the output field. In the limit of large amplifier bandwidth  $\langle a^\dagger(\omega)a(\omega') \rangle = N\delta(\omega - \omega')$  and  $\langle a(\omega)a(\omega') \rangle = M\delta(\omega + \omega' - 2\omega_0)$ , where  $a(\omega')$  and  $a^\dagger(\omega)$  are respectively the creation and annihilation operators of the output field of the amplifier at frequencies  $\omega'$  and  $\omega$ ,  $\omega_0$  is the centre frequency of the amplifier,  $\delta(x)$  is the Dirac delta function and angle brackets denote expectation values. Squeezed states occur when  $N < M < \sqrt{N(N+1)}$ . The radiative decay dynamics of an atom that couples to broadband squeezed vacuum centred at the atomic transition frequency is governed by the optical Gardiner–Bloch equations<sup>6</sup>:

$$\begin{aligned}\dot{\langle \sigma_x \rangle} &= -\gamma(N - M + 1/2)\langle \sigma_x \rangle \\ \dot{\langle \sigma_y \rangle} &= -\gamma(N + M + 1/2)\langle \sigma_y \rangle \\ \dot{\langle \sigma_z \rangle} &= -\gamma(2N + 1)\langle \sigma_z \rangle + \gamma\end{aligned}\quad (1)$$

Here  $\sigma_x$ ,  $\sigma_y$  and  $\sigma_z$  are the pseudospin operators for a two-level atom,  $\gamma$  is the radiative linewidth of the atom and a dot denotes a time derivative. As shown in Fig. 1, the  $X_2$  quadrature of the electromagnetic vacuum is squeezed, and a coherent field along this axis induces rotations of the atom about the  $\hat{y}$  axis of the Bloch sphere. By setting  $M = N = 0$  in equation (1), we recover the case of radiative decay into ordinary electromagnetic vacuum, where the transverse coherence decays half as fast as the longitudinal coherence ( $T_2 = 2T_1 = 2/\gamma$ ). In contrast, the radiative decay into squeezed vacuum is characterized by the timescales  $\tilde{T}_x = T_1/(N - M + 1/2)$ ,  $\tilde{T}_y = T_1/(N + M + 1/2)$  and  $\tilde{T}_z = T_1/(2N + 1)$ , which respectively describe the radiative decay of coherence when the qubit is prepared along the  $\pm\hat{x}$ ,  $\pm\hat{y}$  or  $\pm\hat{z}$  axes of the Bloch sphere. In the limit of large squeezing, it is predicted<sup>6</sup> that  $\tilde{T}_y$  and  $\tilde{T}_z$  are reduced and that the transverse decay time,  $\tilde{T}_x$ , is increased beyond the value of  $2T_1$  owing to the reduced fluctuations in the  $X_2$  quadrature of the vacuum.

A simplified schematic diagram of our experiment is shown in Fig. 1b. We realized an effective two-level system using the hybrid qubit formed by a superconducting transmon<sup>23</sup> circuit resonantly coupled to the transverse electric TE<sub>101</sub> mode of a three-dimensional (3D) superconducting cavity<sup>24</sup>. The transition frequency of the effective qubit was  $\omega_q/2\pi = 5.8989$  GHz with a measured longitudinal decay time constant of  $T_1 = 0.65 \pm 0.02$   $\mu$ s (mean  $\pm$  s.e.m.), set by deliberate coupling to the 50- $\Omega$  environment. In Supplementary Information, we show in detail that the radiative interaction of the hybrid qubit with squeezed vacuum is that of an idealized atom interacting directly with squeezed vacuum. We generated squeezed vacuum by pumping a lumped-element Josephson parametric amplifier (LJPA) with two tones at frequencies  $\omega_1$  and  $\omega_2$ , which were evenly spaced about the qubit transition frequency<sup>25</sup> and satisfied  $\omega_0 = (\omega_1 + \omega_2)/2 = \omega_q$ . The bandwidth of the squeezing was 13 MHz, which is sufficient to fulfil the large bandwidth assumption based on the radiative

<sup>1</sup>Quantum Nanoelectronics Laboratory, Department of Physics, University of California, Berkeley, California 94720, USA. <sup>2</sup>Department of Physics, MIT–Harvard Center for Ultracold Atoms, and Research Laboratory of Electronics, Massachusetts Institute of Technology, Cambridge, Massachusetts 02139, USA. <sup>3</sup>Advanced Technology Institute and Department of Physics, University of Surrey, Guildford GU2 7XH, UK.

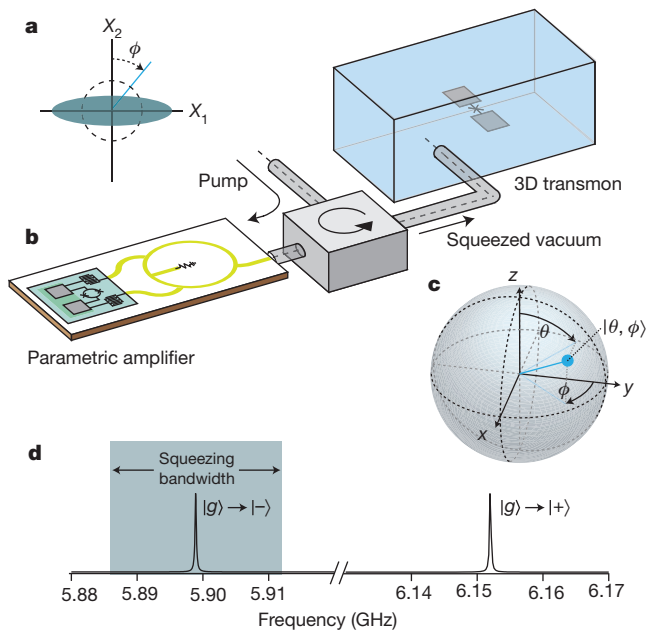


**Figure 1 | Simplified experiment set-up.** **a**, The phase space of a mode of the electromagnetic field is described in terms of its quadrature amplitudes,  $X_1$  and  $X_2$ . The Gaussian variance of the vacuum state is shown as a dashed line, and a squeezed state as the blue-grey region. **b**, A lumped-element Josephson parametric amplifier is used to generate squeezed vacuum that is coupled to the input port of a hybrid qubit (3D transmon) through a circulator with coaxial cables. A second port (not shown) is used for readout. This port is weakly coupled and has negligible influence on the relaxation. **c**, The state of a two-level atom may be represented on the Bloch sphere with angles  $\theta$  and  $\phi$  describing the latitude and longitude, respectively. **d**, The resonant strong light-matter dipole interaction of the transmon circuit with the 3D cavity results in two states,  $|+\rangle$  and  $|-\rangle$ . The bandwidth of the squeezing is centred about  $\omega_q$ , the transition frequency between the ground state and  $|-\rangle$ , and is large compared with the natural linewidth of the transition.

linewidth of the qubit,  $\gamma/2\pi = 240$  kHz. The output of the amplifier was connected with coaxial cables to the strongly coupled port of the superconducting cavity.

To demonstrate the effect of squeezed vacuum on the transverse decay of the qubit, we conducted Ramsey measurements at different angles along the equator of the Bloch sphere. The Ramsey measurements consisted of an initial  $\pi/2$  rotation about the  $-\hat{x}\cos(\phi) + \hat{y}\sin(\phi)$  axis, followed by a second  $\pi/2$  rotation about the  $\hat{x}\sin(\omega_{\text{mod}}t) - \hat{y}\cos(\omega_{\text{mod}}t)$  axis, applied at variable time  $t$ . Modulation of the rotation angle of the second  $\pi/2$  pulse at frequency  $\omega_{\text{mod}}$  resulted in oscillatory Ramsey fringes without detuning. Figure 2a shows  $\langle\sigma_z\rangle$  as a function of time and angle with the squeezing turned off;  $\langle\sigma_z\rangle$  exhibits exponentially damped, sinusoidal oscillations with angular frequency  $\omega_{\text{mod}}$  and phase  $\phi$ , with a uniform decay time  $T_2^* = 1.08(4)$   $\mu\text{s}$ . The fact that  $T_2^*$  is less than  $2T_1$  indicates the presence of a small amount of pure dephasing characterized by a time scale  $T_\phi = 6.6 \pm 0.5$   $\mu\text{s}$ . Figure 2b shows the results of the Ramsey measurement when the LJPA pump was turned on to generate squeezed vacuum for the variable duration between the first and second  $\pi/2$  pulses. The power gain of the amplifier was 4 dB. The transverse decay in the presence of squeezed vacuum reveals two timescales,  $T_x = 1.67$   $\mu\text{s}$  and  $T_y = 0.28$   $\mu\text{s}$ , which describe the exponential decay of coherence when the qubit is prepared along the  $\pm\hat{x}$  and  $\pm\hat{y}$  axes, respectively. Subtracting the pure dephasing from the measured timescales gives the radiative transverse decay times,  $\tilde{T}_x = 2.2$   $\mu\text{s}$  and  $\tilde{T}_y = 0.29$   $\mu\text{s}$ . The interaction with squeezed vacuum both enhances decay along the  $\hat{y}$  axis, owing to the increased fluctuations in the  $X_1$  quadrature of the field, and suppresses decay along the  $\hat{x}$  axis, owing to the reduced fluctuations in  $X_2$ .

The radiative decay dynamics in the presence of squeezed vacuum can be presented as a trajectory of the Bloch vector. To illustrate this,

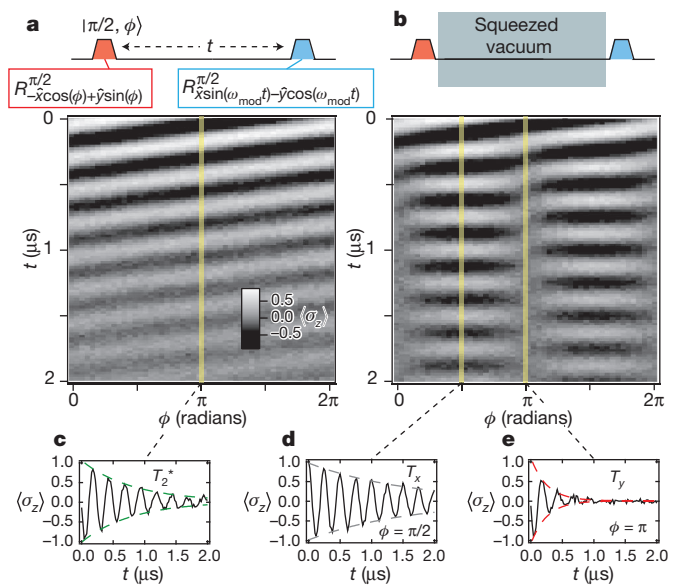


**Figure 2 | Transverse decay into squeezed vacuum.** **a**, The Ramsey measurement as a function of angle consisted of a first  $\pi/2$  rotation about the  $-\hat{x}\cos(\phi) + \hat{y}\sin(\phi)$  axis, to prepare the in the state  $|\pi/2, \phi\rangle$  (in the notation of Fig. 1), followed by a second  $\pi/2$  rotation about the  $\hat{x}\sin(\omega_{\text{mod}}t) - \hat{y}\cos(\omega_{\text{mod}}t)$  axis applied at variable time  $t$ . The two-dimensional plot shows  $\langle\sigma_z\rangle$  as a function of  $t$  and  $\phi$ ;  $\langle\sigma_z\rangle$  is characterized by sinusoidal decay with a uniform decay constant  $T_2^*$  and phase  $\phi$ . **b**, The transverse decay into squeezed vacuum was measured by turning the pump for the LJPA on between the qubit pulses. The two-dimensional plot indicates that after rapid decay of coherence along the  $\pm\hat{y}$  axes, the resulting coherence along the  $\pm\hat{x}$  axes decays with time constant  $T_x > T_2^*$ . **c**, The Ramsey measurement for the qubit prepared along the  $-\hat{y}(\phi = \pi)$  axis with the squeezing off. **d**, **e**, The Ramsey measurement in the presence of squeezed vacuum for the qubit prepared along the  $+\hat{x}(\phi = \pi/2)$  (**d**) and  $-\hat{y}(\phi = \pi)$  (**e**) axes.

we prepared the qubit in an initial state  $|i\rangle$  with a  $0.67\pi$  rotation about the  $-\hat{x}\cos(\phi) + \hat{y}\sin(\phi)$  axis with  $\phi = 0.83\pi$ . After this preparation, the pump of the LJPA was turned on for a variable duration to generate squeezed vacuum. After this variable period of time, we tomographically reconstructed the qubit state either using  $\pi/2$  rotations around the  $\hat{x}$  and  $\hat{y}$  axes followed by state readout in the  $\sigma_z$  basis, to determine the Bloch vector components  $\langle\sigma_x\rangle$  and, respectively,  $\langle\sigma_y\rangle$ ; or using no rotation and state readout in the  $\sigma_z$  basis, to determine  $\langle\sigma_z\rangle$ . The trajectory of the Bloch vector, displayed in Fig. 3, follows the expected decay dynamics based on equation (1) with fast decay along the  $\hat{y}$  and  $\hat{z}$  axes and slow relaxation along  $\hat{x}$ . The final state of the qubit is described by  $\langle\sigma_x\rangle \rightarrow 0$ ,  $\langle\sigma_y\rangle \rightarrow 0.07$  and  $\langle\sigma_z\rangle \rightarrow 0.36$ . The steady-state value of  $\langle\sigma_z\rangle$  is consistent with a bath of  $N = 0.88$  photons, which characterizes the average photon occupation of the squeezed state. The remnant coherence along the  $\hat{y}$  axis is the result of a small coherent component of the squeezed state. In combination with the radiative decay of the qubit, this coherent drive, which is characterized by a Rabi frequency  $\Omega_R \ll 1/T_1$ , results in a steady-state coherence<sup>26</sup>,  $\langle\sigma_y\rangle_{\text{ss}} \propto \Omega_R T_1$ . From our measurements, we find that  $\Omega_R \approx 2\pi \times 10$  kHz, consistent with the 65-dB on/off ratio of our qubit manipulation pulses.

Because the qubit's decay dynamics are sensitive to altered vacuum fluctuations, they can be used to probe squeezed states of light. Previously, noise and correlation measurements have been used to characterize the squeezed states generated by microwave parametric amplifiers<sup>17–19,27</sup>. Similarly, qubits have been used to reconstruct localized non-classical states of light tomographically<sup>28,29</sup>. Here we use the qubit's decay dynamics to reconstruct, to second order, the Wigner distribution for the itinerant squeezed state generated by the LJPA. From  $T_2$ , the measured decay constant of  $\langle\sigma_z\rangle$ , and  $\tilde{T}_x$ , we determine that  $N = 0.88$  and  $M = 1.08$ , from which the Gaussian variances  $\sigma_I^2 = 2(N + M + 1/2)$  and  $\sigma_Q^2 = 2(N - M + 1/2)$  are calculated.



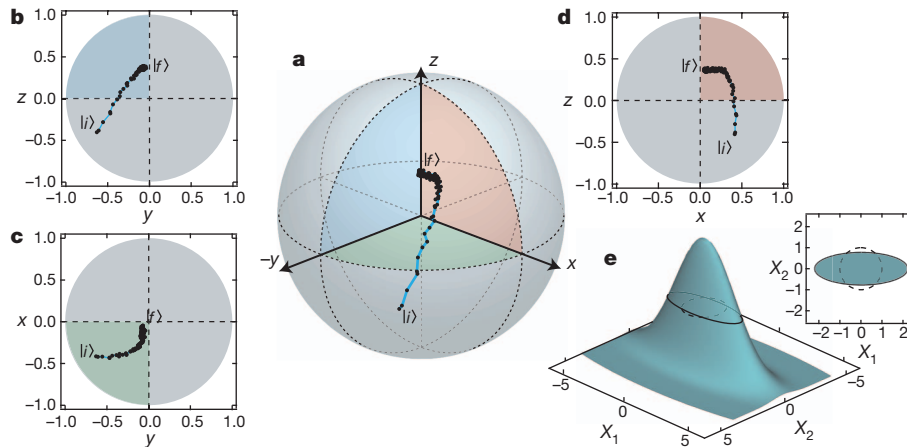


**Figure 3 | Radiative decay dynamics in squeezed vacuum.** **a–d**, Quantum state tomography with measurements equally spaced between 0 and 3  $\mu\text{s}$  shows the evolution of the Bloch vector between initial state  $|i\rangle = |0.67\pi, 0.83\pi\rangle$  and final state  $|f\rangle$ . The dynamics are characterized by fast decay along  $\hat{y}$  and  $\hat{z}$  and

slow decay along  $\hat{x}$ . **e**, From the radiative decay rates, we tomographically reconstruct the Wigner quasiprobability distribution of the itinerant squeezed vacuum mode at  $\omega_0$ . Inset, Gaussian half-widths of the squeezed (solid) and vacuum (dashed) states.

Figure 3e shows the reconstructed Wigner distribution for the squeezed mode at frequency  $\omega_0$ . In Fig. 4a, we display the effective decay constants for different values of the detuning  $\delta = \omega_0 - \omega_q$  between the centre frequency of the pump and the qubit. The decay constants  $T_x$  and  $T_y$  depend strongly on the detuning near resonance, highlighting the tell-tale evidence of interaction with squeezed vacuum where  $T_x > 2T_1$ . When the detuning is large, the squeezing axis rotates rapidly with respect to the qubit axis and the decay times approach a constant value of  $2T_1/(2N + 1)$ . The solid black and red lines in Fig. 4a indicate the expected dependence of  $T_x$  and  $T_y$  on  $\delta$  as discussed in Supplementary Information.

In Fig. 4b, we display the decay constants measured for different bias conditions of the LJPA, obtained by changing the power of the pump tones. The transverse decay rates were measured as shown in Fig. 2, and we use the measured value of  $T_z$  to determine  $N$ . As expected, larger LJPA gain results in larger amounts of squeezing with an associated increase in  $T_x$  and decrease in  $T_y$  and  $T_z$ . Figure 4c displays  $M - N$  versus  $N$ . The reduction of  $M$  from its maximum allowed value, shown as a dashed line, may be attributed to two possible sources: losses in the microwave components between the LJPA and the qubit,

and non-ideal performance of the LJPA characterized by added thermal noise. If we assume that the LJPA produces an ideal squeezed state, with  $M = \sqrt{N(N+1)}$ , then the degradation can be accounted for by an attenuation of the squeezed vacuum from the LJPA by a factor of  $\eta = 0.5$ . Attenuation degrades the squeezed vacuum by absorbing correlated photons, thereby making the quadrature fluctuations tend towards the ordinary vacuum fluctuations. This level of attenuation is consistent with the anticipated insertion loss between the LJPA and the qubit due to the microwave components we used. For  $N > 1$ , however, it seems that the performance of the LJPA may become non-ideal as indicated by the slight reduction in  $M - N$  for  $N > 1$ .

Our results demonstrate the ability to alter the vacuum environment of a two-level atom to a degree that has so far not been achieved in atomic and molecular systems, allowing the direct study of a long-sought aspect of the light–matter interaction. Our system also demonstrates the strength of using superconducting artificial atoms as sensitive detectors of the quantum states of the electromagnetic field. Future studies with squeezed light and superconducting qubits may enhance the fidelity of quantum gates, enable the generation of multi-qubit entanglement<sup>30</sup> and allow the study of non-Markovian quantum baths.

Our results demonstrate the ability to alter the vacuum environment of a two-level atom to a degree that has so far not been achieved in atomic and molecular systems, allowing the direct study of a long-sought aspect of the light–matter interaction. Our system also demonstrates the strength of using superconducting artificial atoms as sensitive detectors of the quantum states of the electromagnetic field. Future studies with squeezed light and superconducting qubits may enhance the fidelity of quantum gates, enable the generation of multi-qubit entanglement<sup>30</sup> and allow the study of non-Markovian quantum baths.

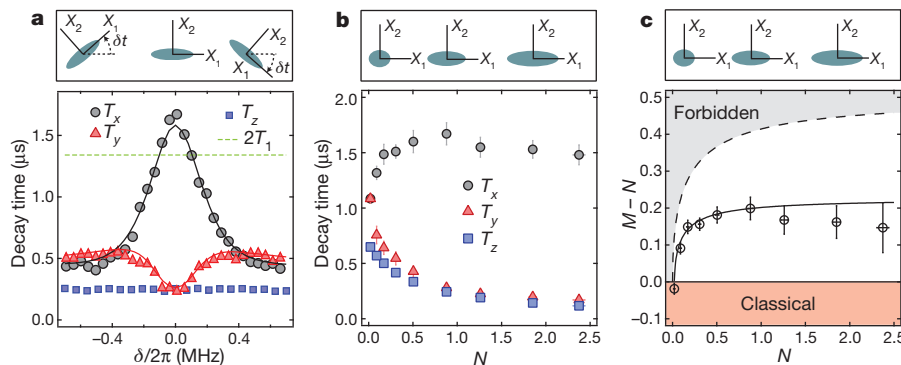


**Figure 4 | Dependence of the transverse and longitudinal decay times on LJPA detuning and bias.** **a**, Effective decay constants versus the detuning of the centre frequency of the LJPA from the qubit,  $\delta = \omega_0 - \omega_q$ . The decay constants  $T_x$  and  $T_y$  show a dependence on the detuning of the squeezing from the qubit transition frequency: on resonance  $T_x$  reaches its maximum value and  $T_y$  reaches its minimum value. The ordinary vacuum decay limit,  $2T_1$  is shown for comparison. The solid lines show the theoretical dependence of  $T_x$  (black) and  $T_y$  (red) on the detuning. The upper sketch indicates how detuning causes the squeezing ellipse to rotate relative to the qubit coordinates. **b**, Measured

values of  $T_x$ ,  $T_y$  and  $T_z$  for increasing LJPA gain versus  $N$ . Error bars indicate the s.e.m. based on 10 successive measurements. The upper panel indicates how the aspect ratio of the squeezed state changes for increasing  $N$ . **c**,  $M - N$  versus  $N$ . The dashed line indicates a minimum-uncertainty squeezed state, which is expected for ideal squeezing. The solid line indicates the expected dependence for a quantum efficiency of  $\eta = 0.5$ . The grey region indicates values of  $M$  and  $N$  that are forbidden and the red region indicates values of  $M$  and  $N$  that correspond to classical states of light.

## METHODS SUMMARY

Owing to the finite temperature of the 50- $\Omega$  environment and other sources of noise, a small average number of photons,  $N_{\text{th}}$ , are expected to contaminate the vacuum environment of the qubit. This bath of thermal photons both reduces the measured energy decay time  $T_1$  from its intrinsic value by a factor of  $1/(2N_{\text{th}} + 1)$  and increases the equilibrium excited state population. We determined the equilibrium excited-state population to be 1.8% using a Rabi population measurement<sup>31</sup>, allowing us to place an upper limit on the number of thermal photons that characterize our vacuum environment, of  $N_{\text{th}} \leq 0.019$ , and, thus, on the intrinsic radiative decay time,  $T_1 = 0.67 \mu\text{s}$ . We observe a transverse decay rate of  $T_x > 2T_1$ , indicating that, even in the presence of thermal photons, we have demonstrated interaction with fluctuations below the ordinary vacuum level. Although their effects are small, these thermal photons were included in our determination of  $N$  and  $M$ .

The qubit was composed of a transmon circuit with charging energy  $E_C/h = 208 \text{ MHz}$  and Josephson energy  $E_J/h = 23.27 \text{ GHz}$ , coupled to a 3D aluminium cavity with resonance frequency  $\omega_c/2\pi = 6.0456 \text{ GHz}$  at rate  $g/2\pi = 126 \text{ MHz}$ . The cavity was equipped with two ports: a strongly coupled port that limited the quality factor to  $Q = 1.1 \times 10^4$  and a weakly coupled port. Outgoing signals from the qubit passed through several circulators and filters before amplification with a HEMT (high-electron-mobility transistor) amplifier at 2.7 K. The qubit was enclosed in successive layers of superconducting and magnetic shields and anchored to the mixing chamber stage of a dilution refrigerator with a base temperature of 20 mK. State readout was performed using the Jaynes–Cummings nonlinearity technique<sup>32</sup> by driving the weakly coupled port of the cavity at 6.0467 GHz and integrating the first 200 ns of transmitted signal. Further details of the experimental set-up are given in Supplementary Information.

The LJPA was composed of a two-junction SQUID (superconducting quantum interference device) formed of 1- $\mu\text{A}$  Josephson junctions shunted with 1 pF of capacitance and isolated from the input ports of a  $180^\circ$  hybrid coupler with interdigitated capacitors that resulted in a quality factor of  $Q_{\text{LJPA}} = 100$ . The LJPA was flux-biased to have a low power resonance at 5.897 GHz. The differential port of the hybrid coupler was connected to the strongly coupled port of the qubit with coaxial lines through two circulators and a  $-20\text{-dB}$  coupler that allowed the injection of the qubit manipulation pulses. Using numerical modelling of the LJPA, we found that the values of  $N$  obtained from the  $T_2$  timescale were consistent with the measured power gain of the amplifier at each bias condition. Additional characterization of the LJPA is described in Supplementary Information.

A single microwave source was used to generate the qubit preparation, tomography and LJPA pump pulses. The LJPA pump was obtained by driving an  $I$ – $Q$  mixer with a tone at 540 MHz and adjusting the d.c. offsets to suppress the carrier.

Received 22 January; accepted 1 May 2013.

1. Treps, N. *et al.* Surpassing the standard quantum limit for optical imaging using nonclassical multimode light. *Phys. Rev. Lett.* **88**, 203601 (2002).
2. Grangier, P., Slusher, R. E., Yurke, B. & LaPorta, A. Squeezed-light enhanced polarization interferometer. *Phys. Rev. Lett.* **59**, 2153–2156 (1987).
3. Xiao, M., Wu, L.-A. & Kimble, H. J. Precision measurement beyond the shot-noise limit. *Phys. Rev. Lett.* **59**, 278–281 (1987).
4. Goda, K. *et al.* A quantum-enhanced prototype gravitational-wave detector. *Nature Physics* **4**, 472–476 (2008).
5. Polzik, E. S., Carri, J. & Kimble, H. J. Spectroscopy with squeezed light. *Phys. Rev. Lett.* **68**, 3020–3023 (1992).
6. Gardiner, C. W. Inhibition of atomic phase decays by squeezed light: a direct effect of squeezing. *Phys. Rev. Lett.* **56**, 1917–1920 (1986).
7. Georgiades, N. P., Polzik, E. S., Edamatsu, K., Kimble, H. J. & Parkins, A. S. Nonclassical excitation for atoms in a squeezed vacuum. *Phys. Rev. Lett.* **75**, 3426–3429 (1995).
8. Dayan, B., Pe'er, A., Friesem, A. A. & Silberberg, Y. Two photon absorption and coherent control with broadband down-converted light. *Phys. Rev. Lett.* **93**, 023005 (2004).
9. Turchette, Q. A., Georgiades, N. P., Hood, C. J., Kimble, H. J. & Parkins, A. S. Squeezed excitation in cavity QED: experiment and theory. *Phys. Rev. A* **58**, 4056–4077 (1998).
10. Slusher, R. E., Hollberg, L. W., Yurke, B., Mertz, J. C. & Valley, J. F. Observation of squeezed states generated by four-wave mixing in an optical cavity. *Phys. Rev. Lett.* **55**, 2409–2412 (1985).

11. Ourjoumtsev, A. *et al.* Observation of squeezed light from one atom excited with two photons. *Nature* **474**, 623–626 (2011).
12. Brooks, D. *et al.* Non-classical light generated by quantum-noise-driven cavity optomechanics. *Nature* **488**, 476–480 (2012).
13. Castellanos-Beltran, M. A., Irwin, K. D., Hilton, G. C., Vale, L. R. & Lehnert, K. W. Amplification and squeezing of quantum noise with a tunable Josephson metamaterial. *Nature Phys.* **4**, 929–931 (2008).
14. Bergeal, N. *et al.* Phase preserving amplification near the quantum limit with a Josephson ring modulator. *Nature* **465**, 64–68 (2010).
15. Roch, N. *et al.* Widely tunable, nondegenerate three-wave mixing microwave device operating near the quantum limit. *Phys. Rev. Lett.* **108**, 147701 (2012).
16. Hatridge, M., Vijay, R., Slichter, D. H., Clarke, J. & Siddiqi, I. Dispersive magnetometry with a quantum limited squid parametric amplifier. *Phys. Rev. B* **83**, 134501 (2011).
17. Eichler, C. *et al.* Observation of two-mode squeezing in the microwave frequency domain. *Phys. Rev. Lett.* **107**, 113601 (2011).
18. Bergeal, N., Schackert, F., Frunzio, L. & Devoret, M. H. Two-mode correlation of microwave quantum noise generated by parametric down-conversion. *Phys. Rev. Lett.* **108**, 123902 (2012).
19. Flurin, E., Roch, N., Mallet, F., Devoret, M. H. & Huard, B. Generating entangled microwave radiation over two transmission lines. *Phys. Rev. Lett.* **109**, 183901 (2012).
20. Ginossar, E. & Levit, S. Semiconductor microstructure in a squeezed vacuum: electron-hole plasma luminescence. *Phys. Rev. B* **72**, 075333 (2005).
21. Parkins, A. S., Zoller, P. & Carmichael, H. J. Spectral linewidth narrowing in a strongly coupled atom-cavity system via squeezed-light excitation of a “vacuum” Rabi resonance. *Phys. Rev. A* **48**, 758–763 (1993).
22. Schoelkopf, R. J. & Girvin, S. M. Wiring up quantum systems. *Nature* **451**, 664–669 (2008).
23. Koch, J. *et al.* Charge-insensitive qubit design derived from the Cooper pair box. *Phys. Rev. A* **76**, 042319 (2007).
24. Paik, H. *et al.* Observation of high coherence in Josephson junction qubits measured in a three-dimensional circuit QED architecture. *Phys. Rev. Lett.* **107**, 240501 (2011).
25. Kamal, A., Marblestone, A. & Devoret, M. Signal-to-pump back action and self-oscillation in double-pump Josephson parametric amplifier. *Phys. Rev. B* **79**, 184301 (2009).
26. Carmichael, H. J., Lane, A. S. & Walls, D. F. Resonance fluorescence from an atom in a squeezed vacuum. *Phys. Rev. Lett.* **58**, 2539–2542 (1987).
27. Mallet, F. *et al.* Quantum state tomography of an itinerant squeezed microwave field. *Phys. Rev. Lett.* **106**, 220502 (2011).
28. Hofheinz, M. *et al.* Synthesizing arbitrary quantum states in a superconducting resonator. *Nature* **459**, 546–549 (2009).
29. Kirchmair, G. *et al.* Observation of quantum state collapse and revival due to the single-photon Kerr effect. *Nature* **495**, 205–209 (2013).
30. Hald, J., Sørensen, J. L., Schori, C. & Polzik, E. S. Spin squeezed atoms: a macroscopic entangled ensemble created by light. *Phys. Rev. Lett.* **83**, 1319–1322 (1999).
31. Geerlings, K. *et al.* Demonstrating a driven reset protocol for a superconducting qubit. *Phys. Rev. Lett.* **110**, 120501 (2013).
32. Reed, M. D. *et al.* High-fidelity readout in circuit quantum electrodynamics using the Jaynes–Cummings nonlinearity. *Phys. Rev. Lett.* **105**, 173601 (2010).

Supplementary Information is available in the online version of the paper.

**Acknowledgements** We thank C. Macklin, N. Roch and Lev S. Bishop for discussions. This research was supported in part (K.W.M., S.J.W. and I.S.) by the Office of Naval Research (N00014-13-1-0150) and the Office of the Director of National Intelligence (ODNI), Intelligence Advanced Research Projects Activity (IARPA), through the Army Research Office (W911NF-11-1-0029). All statements of fact, opinion or conclusions contained herein are those of the authors and should not be construed as representing the official views or policies of IARPA, the ODNI or the US government. E.G. acknowledges support from EPSRC (EP/I026231/1). K.M.B. acknowledges support from US NSF GRFP (0645960) and IGERT (0801525).

**Author Contributions** K.W.M. and S.J.W. performed the experiment and analysed the data. S.J.W. fabricated the qubit and parametric amplifier. K.W.M. wrote the manuscript. K.M.B. helped with the experimental set-up, provided theoretical support and wrote Supplementary Information. E.G. designed the experiment and provided theoretical support. All work was carried out under the supervision of I.S.

**Author Information** Reprints and permissions information is available at [www.nature.com/reprints](http://www.nature.com/reprints). The authors declare no competing financial interests. Readers are welcome to comment on the online version of the paper. Correspondence and requests for materials should be addressed to K.W.M. ([katernm@berkeley.edu](mailto:katernm@berkeley.edu)).



# Biomimetic assembly and activation of [FeFe]-hydrogenases

G. Berggren<sup>1,2†</sup>, A. Adamska<sup>3\*</sup>, C. Lambertz<sup>4\*</sup>, T. R. Simmons<sup>1\*</sup>, J. Esselborn<sup>4</sup>, M. Atta<sup>1</sup>, S. Gambarelli<sup>5</sup>, J.-M. Mouesca<sup>5</sup>, E. Reijerse<sup>3</sup>, W. Lubitz<sup>3</sup>, T. Happe<sup>4</sup>, V. Artero<sup>1</sup> & M. Fontecave<sup>1,2</sup>

Hydrogenases are the most active molecular catalysts for hydrogen production and uptake<sup>1,2</sup>, and could therefore facilitate the development of new types of fuel cell<sup>3–5</sup>. In [FeFe]-hydrogenases, catalysis takes place at a unique di-iron centre (the [2Fe] subsite), which contains a bridging dithiolate ligand, three CO ligands and two CN<sup>−</sup> ligands<sup>6,7</sup>. Through a complex multienzymatic biosynthetic process, this [2Fe] subsite is first assembled on a maturation enzyme, HydF, and then delivered to the apo-hydrogenase for activation<sup>8</sup>. Synthetic chemistry has been used to prepare remarkably similar mimics of that subsite<sup>1</sup>, but it has failed to reproduce the natural enzymatic activities thus far. Here we show that three synthetic mimics (containing different bridging dithiolate ligands) can be loaded onto bacterial *Thermotoga maritima* HydF and then transferred to apo-HydA1, one of the hydrogenases of *Chlamydomonas reinhardtii* algae. Full activation of HydA1 was achieved only when using the HydF hybrid protein containing the mimic with an azadithiolate bridge, confirming the presence of this ligand in the active site of native [FeFe]-hydrogenases<sup>9,10</sup>. This is an example of controlled metalloenzyme activation using the combination of a specific protein scaffold and active-site synthetic analogues. This simple methodology provides both new mechanistic and structural insight into hydrogenase maturation and a unique tool for producing recombinant wild-type and variant [FeFe]-hydrogenases, with no requirement for the complete maturation machinery.

Complexes **1**<sup>11–13</sup>, **2**<sup>14</sup> and **3**<sup>15</sup> (Fig. 1a) represent the closest synthetic mimics of the [2Fe] subsite in HydA1. They all share the same primary coordination sphere with four CO, two CN<sup>−</sup> and a bridging dithiolate ligand. They do however differ in the nature of the central bridgehead atom of the dithiolate: carbon in **1**, nitrogen in **2** and oxygen in **3**. The nature of this atom in the enzyme [2Fe] subsite has been a matter of controversy<sup>7,9,10,16</sup>. Anaerobic reaction of HydF from *T. maritima*

(expressed in *Escherichia coli*), containing a [4Fe-4S] cluster<sup>17</sup> and named ‘HydF’ in the following, with a tenfold molar excess of complex **1**, **2** or **3**, led to new hybrid species, x-HydF (x = **1**, **2** or **3** respectively), that could be isolated in pure form and characterized. Indeed, in all cases, iron quantification showed an increase from  $3.9 \pm 0.4$  to  $5.6 \pm 0.4$  iron atoms per protein, and the ultraviolet–visible spectrum of these hybrids displayed features consistent with a ~1:1 ratio of the synthetic complexes and the HydF protein (Supplementary Fig. 1a–c).

Fourier transform infrared (FTIR) spectroscopy is a convenient method for characterizing metalloproteins such as hydrogenases containing CO and CN<sup>−</sup> ligands<sup>18</sup>. Thus, further evidence for the incorporation of synthetic complexes in HydF was obtained from their FTIR spectra, which contained CN<sup>−</sup>-stretching bands between 2,000 and 2,100 cm<sup>−1</sup> and four partly overlapping CO-stretching bands in the 1,800–2,000 cm<sup>−1</sup> range (Fig. 2b and Supplementary Table 1). The high-energy bands underwent a 40 cm<sup>−1</sup> shift on <sup>13</sup>C-labelling of the CN<sup>−</sup> ligands (Supplementary Fig. 2). Interestingly, the width of the FTIR bands is still identical to those of the unbound complexes (Fig. 2a) but their positions show strong similarities to those of *Clostridium acetobutylicum* HydF (Fig. 2b and Supplementary Table 1), a HydF preparation isolated from a strain of *C. acetobutylicum* expressing the complete maturase machinery (including HydE and HydG)<sup>19</sup>. *Clostridium acetobutylicum* HydF contains, in addition to a [4Fe-4S] cluster, a still-undefined [2Fe] centre and is capable of activating the apo form of HydA1<sup>19</sup>. Although the width of the FTIR bands of the hybrids would suggest a ligand conformational freedom similar to that of the unbound complexes, the position of the FTIR bands is a clear indication that the synthetic complexes closely mimic the natural [2Fe] subsite in HydF.

The arrangements in which the synthetic complexes are bound to HydF and its [4Fe-4S] cluster are not evident from the FTIR spectra. In particular, FTIR spectroscopy does not allow terminal and bridging cyanide ligands to be definitively distinguished (see below and

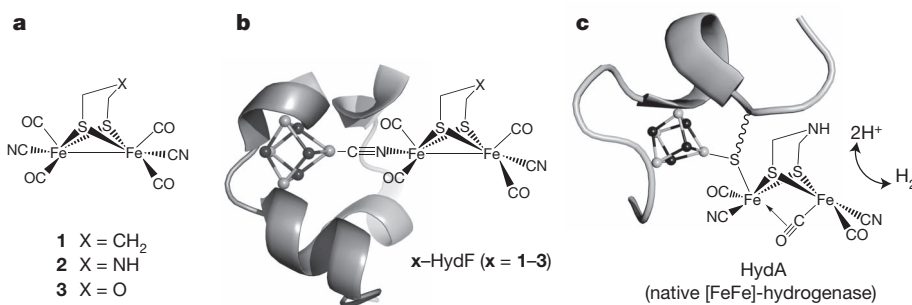


**Figure 1 | Structures of the di-iron clusters discussed in the study.** **a**, The synthetic mimics **1**<sup>11–13</sup>, **2**<sup>14</sup> and **3**<sup>15</sup>. **b**, Proposed structure for the x-HydF (x = **1**–**3**) hybrid proteins. **c**, The H-cluster (active site) of

[FeFe]-hydrogenase. The protein ribbon and the [4Fe-4S] clusters (shown as balls and sticks with Fe shown as white spheres) are shown only schematically.

<sup>1</sup>Laboratoire de Chimie et Biologie des Métaux (CEA/Université Grenoble 1/CNRS), 17 rue des Martyrs, F-38054 Grenoble Cedex 9, France. <sup>2</sup>Collège de France, 11 place Marcelin-Berthelot, F-75231 Paris Cedex 5, France. <sup>3</sup>Max-Planck-Institut für Chemische Energiekonversion, Stiftstrasse 34–36, 45470 Mülheim an der Ruhr, Germany. <sup>4</sup>Lehrstuhl Biochemie der Pflanzen, AG Photobiotechnologie, Ruhr Universität Bochum, Universitätsstrasse 150, 44801 Bochum, Germany. <sup>5</sup>Laboratoire de Chimie Inorganique et Biologique (CEA-INAC, Université Grenoble 1, UMR-E 3), 17 rue des Martyrs, F-38054 Grenoble Cedex 9, France. <sup>†</sup>Present address: Department of Biochemistry and Biophysics, Stockholm University, Svante Arrhenius väg 16, 106 91 Stockholm, Sweden.

\*These authors contributed equally to this work.

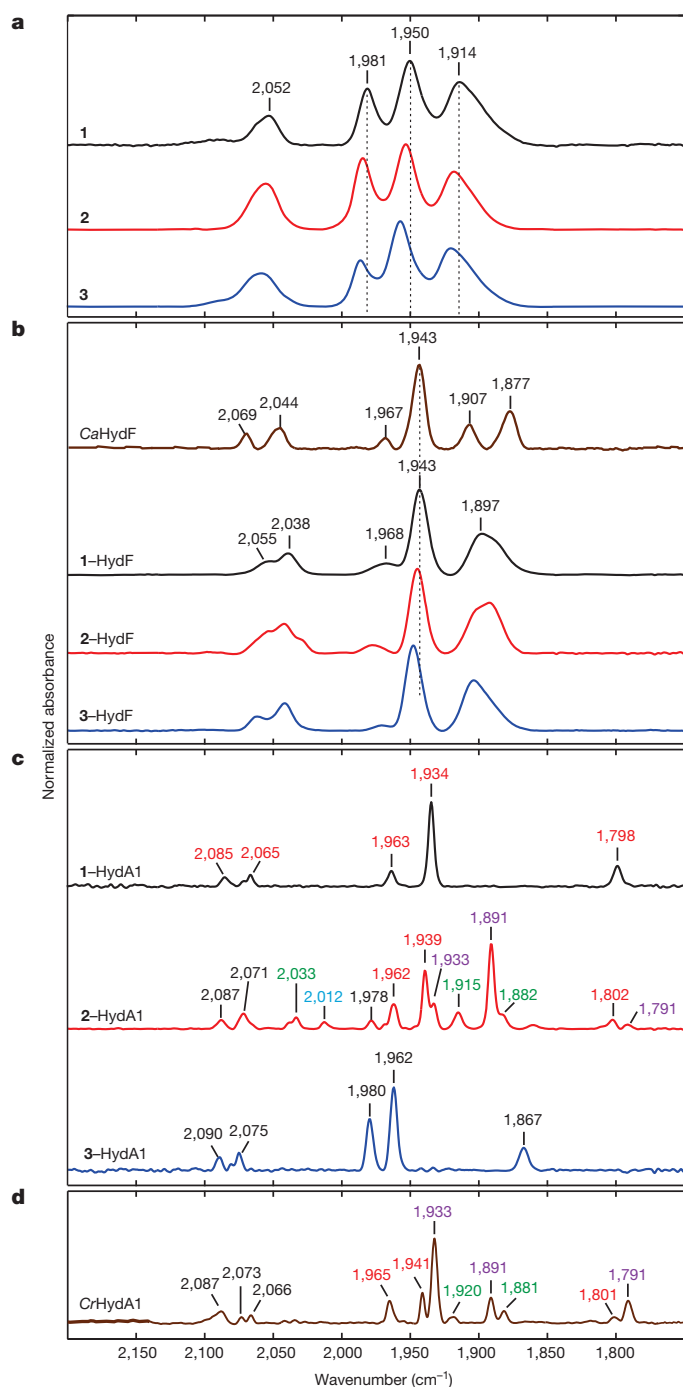


**Figure 2 | Normalized FTIR spectra recorded in liquid solution at 15 °C.** **a**, Complexes 1–3. **b**, *Clostridium acetobutylicum* (Ca)HydF (from ref. 19) and x-HydF (x = 1–3) hybrid species. **c**, HydA1 after treatment of apo-HydA1 with 1-HydF (1-HydA1), 2-HydF (2-HydA1) and 3-HydF (3-HydA1). Peak positions in the spectrum of 2-HydA1 are colour coded to indicate the contributions from H<sub>ox</sub> (red), H<sub>red</sub> (violet), H<sub>sred</sub> (green) and H<sub>ox-CO</sub> (blue) (see Supplementary Fig. 6 for a complete data set). **d**, HydA1 from *C. reinhardtii* expressed in *C. acetobutylicum* (CrHydA1) (ref. 18). Colour code as in **c**. Samples of complexes 1–3 and x-HydF (x = 1–3) were prepared in HEPES buffer (20 mM, 100 mM KCl) pH 7.5. Samples of x-HydA1 were prepared in 10 mM Tris-HCl buffer pH 8 containing sodium dithionite (2 mM).

Supplementary Discussion)<sup>20</sup>. Electron paramagnetic resonance (EPR) and two-dimensional hyperfine sub-level correlation (HYSCORE) spectroscopies are more powerful in this respect. They demonstrate a close interaction between the cluster and the synthetic complex, as

revealed for the case of 1-HydF. First, the EPR spectrum of the spin-half ( $S = 1/2$ )  $[4\text{Fe-4S}]^{1+}$  cluster in dithionite-reduced 1-HydF was markedly different from that of the reduced cluster in unloaded HydF, with the high-field feature at  $g = 1.90$  ( $g$  is the Landé factor) in HydF shifted to  $g = 1.93$  in 1-HydF (Fig. 3a). A comparable shift was observed in the case of hybrids 2-HydF and 3-HydF (Supplementary Fig. 3). The absence of additional signals indicated that, in all cases, the synthetic complex remained in the EPR-silent Fe(I)Fe(I) state (both iron centres are in a low-spin  $S = 1/2$  configuration but are anti-ferromagnetically coupled, leading to a diamagnetic  $S = 0$  ground state).

Second, pulsed EPR spectroscopy unambiguously demonstrated that the  $[4\text{Fe-4S}]$  cluster and the  $[2\text{Fe}]$  subsite analogue shared a  $\text{CN}^-$  ligand in 1-HydF. For this purpose we used a nuclear coherence-transfer experiment, CF-NF<sup>21</sup>, correlating the combination frequencies (CF) with the nuclear frequencies (NF), which is more sensitive than HYSCORE spectroscopy for disordered systems and best adapted for the observation of  $^{13}\text{C}$  signals in the presence of weakly coupled  $^{14}\text{N}$  atoms. This is the first time to our knowledge that a metalloprotein has been characterized in such an experiment. The CF-NF spectrum of 1-HydF (Fig. 3b, right) displayed peaks from distant  $^{13}\text{C}$  carbon atoms present in natural abundance. When 1 was prepared with  $^{13}\text{C}$ -labelled  $\text{CN}^-$ , the spectrum of 1-HydF displayed a new feature reflecting coupling of the unpaired electron in the  $[4\text{Fe-4S}]$  cluster with the  $^{13}\text{C}$  nucleus, characterized by a hyperfine coupling constant of  $4.0 \pm 0.2$  MHz (Fig. 3b, left). As shown in Supplementary Fig. 4, the HYSCORE spectrum of reduced 1-HydF displayed an additional feature consistent with the presence of a nitrogen atom weakly coupled to the  $[4\text{Fe-4S}]$  cluster in 1-HydF. The hyperfine coupling constant ( $a_N \leq 1$  MHz) is significantly smaller than those generally obtained when a N atom is directly coordinated to an Fe-S cluster<sup>17,22,23</sup> ( $a_N$  in the range of 4–7 MHz).

These coupling constants are consistent with a  $\text{CN}^-$  ligand bridging one iron of the  $[4\text{Fe-4S}]$  cluster and one iron of 1, as established by density functional theory (DFT) calculations (a detailed description of the DFT calculations is provided as Supplementary Discussion and in Supplementary Tables 2–5). More precisely, computed hyperfine coupling constants indicate that the cyanide C atom is bound to one iron atom belonging to a mixed-valence ( $\text{Fe}^{2.5+}$ ) iron of the  $[4\text{Fe-4S}]$  cluster and that the N atom is bound to the di-iron complex, implying cyanide linkage isomerism on formation of 1-HydF, as found in the synthesis of Prussian blue analogues<sup>24</sup> and other molecular metal clusters<sup>20,25</sup>. Furthermore, DFT calculated values of CO and CN stretching frequencies (2,010 and 2,060  $\text{cm}^{-1}$ ) of a 1-HydF model, containing a CN ligand bridging the  $[4\text{Fe-4S}]$  cluster and complex 1, are well in the range of the experimental values (2,038 and 2,055  $\text{cm}^{-1}$ ; see Supplementary Discussion and Supplementary Table 6).

The hybrid x-HydF proteins were studied for their potential to activate apo-HydA1 from *C. reinhardtii* containing a single  $[4\text{Fe-4S}]$  cluster and no  $[2\text{Fe}]$  subsite<sup>26</sup>. A pure preparation of apo-HydA1 was incubated anaerobically with 10 equiv. of the hybrid protein, the optimal excess ratio (Supplementary Fig. 5), in phosphate buffer pH 6.8 at 37 °C for 30 min, and hydrogen evolution was monitored under standard conditions (Methods)<sup>26</sup>. No  $\text{H}_2$  evolution could be detected using HydF, 1-HydF or 3-HydF (Fig. 4). In contrast, vigorous  $\text{H}_2$  evolution was observed using 2-HydF, corresponding to a specific activity of 700–800  $\mu\text{mol H}_2$  per min per mg HydA1, comparable to the activity values reported for wild-type HydA1<sup>27</sup>, thus indicating complete maturation/activation of HydA1 by 2-HydF<sup>28</sup> (Fig. 4 and Supplementary Fig. 5). Furthermore, activation by 2-HydF was more efficient than by *C. acetobutylicum* HydF (specific activity, 350–400), assayed under the same conditions (Fig. 4). Indeed, *C. acetobutylicum* HydF provided full activation only when present in larger excess<sup>19</sup>. 2-HydF by itself did not show any hydrogenase activity. Finally, apo-HydA1 was treated with a fourfold excess of x-HydF (x = 1, 2 or 3), under reducing conditions, then separated from HydF by affinity chromatography and analysed by FTIR spectroscopy. In all cases, the

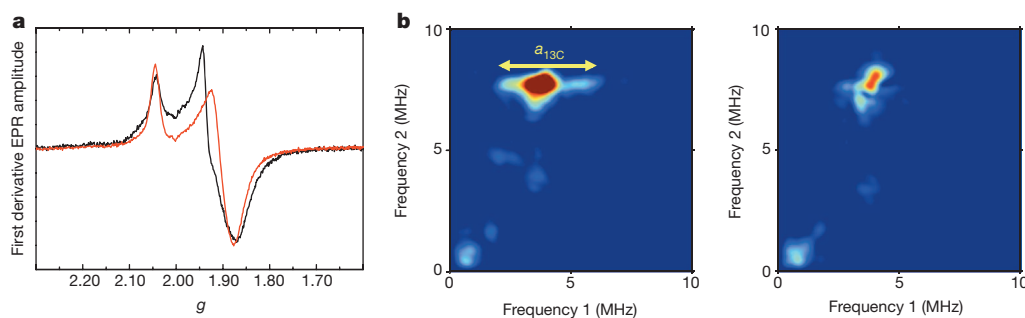


**Figure 3 | Continuous wave and pulsed EPR spectra of 1-HydF.** **a**, X-band EPR spectra recorded at 10 K for dithionite-reduced 1-HydF (red line) and HydF (black line) in 50 mM Tris-HCl buffer, 150 mM NaCl, 5 mM sodium dithionite, pH 8. Microwave power, 100  $\mu\text{W}$ ; modulation amplitude, 1 mT; microwave frequency, 9.39 GHz. The shoulder observed at  $g = 1.90$  in the 1-HydF spectrum, corresponding to a few per cent of the total signal intensity, is assigned to a small fraction of HydF lacking **1**. **b**, X-band two-dimensional pulsed electron spin echo envelope modulation (ESEEM) spectroscopy

(CF-NF) of 1-HydF labelled with  $^{13}\text{CN}^-$  (left) and unlabelled 1-HydF (right). The horizontal ridge seen at a frequency  $\nu_2$  of 7.7 MHz along the frequency 2 axis ( $\nu_2$  being equal to  $2\nu_{13\text{C}}$  with  $\nu_{13\text{C}}$  the Zeeman frequency of a  $^{13}\text{C}$  nuclear spin) is attributed to a hyperfine interaction ( $a_{13\text{C}}$ ) between a  $^{13}\text{C}$  nucleus and the paramagnetic [4Fe-4S] cluster. Its extension ( $\Delta\nu_1$ ) along the frequency 1 axis yields the magnitude of the coupling ( $\Delta\nu_1 = 4.0 \text{ MHz} = a_{13\text{C}}$ ). This feature is absent from the unlabelled 1-HydF spectrum.

presence of characteristic narrow Fe–CO and Fe–CN bands demonstrated that the synthetic complex had been transferred from HydF to HydA1 (Fig. 2c and Supplementary Fig. 6). The FTIR spectrum of HydA1 after treatment with 2-HydF shows a strong correspondence to that of fully active wild-type HydA1 (Fig. 2d)<sup>18</sup>. Specifically, both species exist as a mixture of oxidized ( $\text{H}_{\text{ox}}$ ), reduced ( $\text{H}_{\text{red}}$ ) and super-reduced ( $\text{H}_{\text{red}}$ ) redox states of the H-cluster (the H-cluster is the complete active site of HydA shown in Fig. 1c) that all participate in the catalytic cycle<sup>18</sup>. Furthermore, after flushing with CO, a complete conversion to  $\text{H}_{\text{ox}}$ -CO occurred (Supplementary Fig. 7).

These data demonstrate that **2** is efficiently transferred from HydF to apo-HydA1, where it acquires the structure of the natural active [2Fe] subsite. This implies isomerization of one  $\text{CN}^-$  ligand, replacement of one CO by a cysteinyl ligand of the proximal [4Fe-4S] cluster in HydA1 and conformational rearrangement to adopt the inverted square pyramid structure required for opening a substrate binding site on the distal iron atom of the [2Fe] subsite (Fig. 1)<sup>29</sup>. We note that 1-HydA1 and 3-HydA1 both show 'H-cluster-like' FTIR signatures. In fact, the FTIR spectrum of 1-HydA1 has strong similarities with the  $\text{H}_{\text{ox}}$ -state (Fig. 2c and Supplementary Fig. 6) whereas the FTIR spectrum of 3-HydA1 does not resemble that of any known H-cluster redox state, but seems to indicate a pure redox state and even shows a band assigned to a bridging CO.

Besides unequivocally demonstrating that nitrogen is the bridge-head atom in the dithiolate ligand of the H-cluster, these results shed

light on a number of important questions regarding hydrogenase maturation. They strongly support the hypothesis that HydF transiently binds a di-iron precursor of the active [2Fe] subsite of HydA1 and suggest stabilization through interactions with the [4Fe-4S] cluster. The structure of this natural precursor is likely to be very close to that of **2**. Further investigation of HydA1 maturation by the hybrid system, combining site-directed mutagenesis experiments and synthetic manipulation of the [2Fe] subsite (for example, isotopic labelling as shown here with  $^{13}\text{CN}$ ), will probably provide additional insight into the transfer mechanism and the structure of both HydF and HydA1 binding sites. These data also demonstrate the unique properties of the HydA1 protein binding pocket in converting the otherwise inactive complex **2** into an active catalyst. More importantly, this novel artificial hybrid maturase system provides a unique, simple and straightforward biotechnological tool for producing active recombinant hydrogenases, with no requirement for coexpression with the still incompletely characterized complex biosynthetic machinery.

Because this procedure has been shown to work with proteins (HydF from *T. maritima* and HydA1 from *C. reinhardtii*) from two completely different organisms, it is very likely that [FeFe]-hydrogenases from other microorganisms, overexpressed in their apo form in *E. coli* (which lacks the maturation machinery), could also be activated through simple reaction with 2-HydF. This reaction could thus be used for exploring a large variety of [FeFe]-hydrogenases—for example, from different species or derived from directed mutagenesis—with the aim of finding the most active and stable enzymes for exploitation in biotechnological processes of  $\text{H}_2$  production<sup>30</sup> as well as in bioelectrodes in (photo)electrolysers or fuel cells<sup>3–5</sup>.

## METHODS SUMMARY

Recombinant *T. maritima* HydF protein was isolated, and its [4Fe-4S] cluster introduced using enzymatic reconstitution, as previously described<sup>17</sup>. The synthetic complexes **1**<sup>11–13</sup>, **2**<sup>14</sup> and **3**<sup>15</sup> were prepared as previously described with slight modifications of the purification procedures described in the Supplementary Information. Hybrid proteins (1-HydF, 2-HydF and 3-HydF) were prepared under strictly anaerobic conditions in a glove-box. In a standard experiment, 150  $\mu\text{M}$  HydF in 50 mM Tris-HCl, 150 mM NaCl, buffer pH 8 was incubated with a tenfold molar excess of the complex (**1**, **2** or **3**) for 30 min. The protein was then desalted on a NAP-25 cartridge (GE Healthcare) and concentrated with Amicon Ultra centrifugal filters 10K (Millipore). The protein was stored in liquid nitrogen.

*In vitro* maturation of apo-HydA1 from *C. reinhardtii* overexpressed in *E. coli* by the HydF hybrids was assayed as previously described<sup>19</sup>. Apo-HydA1 was incubated in 0.1 M potassium phosphate buffer pH 6.8, 2 mM sodium dithionite with an excess of the respective x-HydF hybrid protein for 30 min at 37 °C in a total volume of 400  $\mu\text{l}$ . The specific hydrogenase activity was determined as described<sup>19</sup> by transferring the maturation solution to a 1.6 ml reaction mixture containing 100 mM sodium dithionite and 10 mM methyl viologen in the same buffer. For

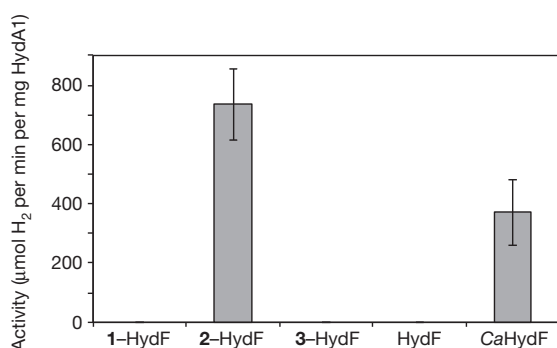


**Figure 4 | Specific hydrogenase activity of reconstituted HydA1.** Activity of HydA1 ( $\mu\text{mol H}_2$  per min per mg HydA1) was measured in the presence of methyl viologen (10 mM) and sodium dithionite (100 mM) after *in vitro* maturation of apo-HydA1 for 30 min at 37 °C with 10 equiv. of x-HydF (x = 1–3), HydF or *C. acetobutylicum* (Ca)HydF. The value for the last was obtained after a 60-min reaction and was taken from ref. 23. Data show mean  $\pm$  s.d.



FTIR measurements, apo-HydA1 and 4 equiv. x-HydF were incubated in 10 mM Tris-HCl pH 8.0, 2 mM sodium dithionite for 1 h at 37 °C and HydA1 was purified through a strep tag affinity column.

**Full Methods** and any associated references are available in the online version of the paper.

**Received 20 January; accepted 29 April 2013.**

**Published online 26 June 2013.**

1. Tard, C. & Pickett, C. J. Structural and functional analogues of the active sites of the [Fe]-, [NiFe]-, and [FeFe]-hydrogenases. *Chem. Rev.* **109**, 2245–2274 (2009).
2. Cracknell, J. A., Vincent, K. A. & Armstrong, F. A. Enzymes as working or inspirational electrocatalysts for fuel cells and electrolysis. *Chem. Rev.* **108**, 2439–2461 (2008).
3. Hambourger, M. *et al.* [FeFe]-hydrogenase-catalyzed H<sub>2</sub> production in a photoelectrochemical biofuel cell. *J. Am. Chem. Soc.* **130**, 2015–2022 (2008).
4. Krishnan, S. & Armstrong, F. A. Order-of-magnitude enhancement of an enzymatic hydrogen-air fuel cell based on pyrenyl carbon nanostructures. *Chem. Sci.* **3**, 1015–1023 (2012).
5. Ciaccafava, A. *et al.* An innovative powerful and mediatorless H<sub>2</sub>/O<sub>2</sub> biofuel cell based on an outstanding bioanode. *Electrochem. Commun.* **23**, 25–28 (2012).
6. Peters, J. W., Lanzilotta, W. N., Lemon, B. J. & Seefeldt, L. C. X-ray crystal structure of the Fe-only hydrogenase (Cpl) from *Clostridium pasteurianum* to 1.8 angstrom resolution. *Science* **282**, 1853–1858 (1998).
7. Nicolet, Y., Piras, C., Legrand, P., Hatchikian, C. E. & Fontecilla-Camps, J. C. *Desulfovibrio desulfuricans* iron hydrogenase: the structure shows unusual coordination to an active site Fe binuclear center. *Structure* **7**, 13–23 (1999).
8. Mulder, D. W. *et al.* Stepwise [FeFe]-hydrogenase H-cluster assembly revealed in the structure of HydA<sup>AFRC</sup>. *Nature* **465**, 248–251 (2010).
9. Nicolet, Y. *et al.* Crystallographic and FTIR spectroscopic evidence of changes in Fe coordination upon reduction of the active site of the Fe-only hydrogenase from *Desulfovibrio desulfuricans*. *J. Am. Chem. Soc.* **123**, 1596–1601 (2001).
10. Silakov, A., Wenk, B., Reijerse, E. & Lubitz, W. <sup>14</sup>N HYSCORE investigation of the H-cluster of [FeFe] hydrogenase: evidence for a nitrogen in the dithiol bridge. *Phys. Chem. Chem. Phys.* **11**, 6592–6599 (2009).
11. Le Cloirec, A. *et al.* A di-iron dithiolate possessing structural elements of the carbonyl/cyanide sub-site of the H-centre of Fe-only hydrogenase. *Chem. Commun.* 2285–2286 (1999).
12. Lyon, E. J., Georgakaki, I. P., Reibenspies, J. H. & Darensbourg, M. Y. Carbon monoxide and cyanide ligands in a classical organometallic complex model for Fe-only hydrogenase. *Angew. Chem. Int. Edn Engl.* **38**, 3178–3180 (1999).
13. Schmidt, M., Contakes, S. M. & Rauchfuss, T. B. First generation analogues of the binuclear site in the Fe-only hydrogenases: [Fe<sub>2</sub>(μ-SR)<sub>2</sub>(CO)<sub>4</sub>(CN)<sub>2</sub>]<sup>2-</sup>. *J. Am. Chem. Soc.* **121**, 9736–9737 (1999).
14. Li, H. X. & Rauchfuss, T. B. Iron carbonyl sulfides, formaldehyde, and amines condense to give the proposed azadithiolate cofactor of the Fe-only hydrogenases. *J. Am. Chem. Soc.* **124**, 726–727 (2002).
15. Song, L. C., Yang, Z. Y., Bian, H. Z. & Hu, Q. M. Novel single and double diiron oxadithiolates as models for the active site of [Fe]-only hydrogenases. *Organometallics* **23**, 3082–3084 (2004).
16. Pandey, A. S., Harris, T. V., Giles, L. J., Peters, J. W. & Szilagy, R. K. Dithiomethylether as a ligand in the hydrogenase H-cluster. *J. Am. Chem. Soc.* **130**, 4533–4540 (2008).
17. Brazzolotto, X. *et al.* The [Fe-Fe]-hydrogenase maturation protein HydF from *Thermotoga maritima* is a GTPase with an iron-sulfur cluster. *J. Biol. Chem.* **281**, 769–774 (2006).
18. Adamska, A. *et al.* Identification and characterization of the “super-reduced” state of the H-cluster in [FeFe] hydrogenase: a new building block for the catalytic cycle? *Angew. Chem. Int. Ed.* **51**, 11458–11462 (2012).
19. Czech, I., Silakov, A., Lubitz, W. & Happe, T. The [FeFe]-hydrogenase maturase HydF from *Clostridium acetobutylicum* contains a CO and CN<sup>-</sup> ligated iron cofactor. *FEBS Lett.* **584**, 638–642 (2010).
20. Geiss, A. & Vahrenkamp, H. M. (μ-CN)Fe(μ-CN)M<sup>+</sup> chains with phthalocyanine iron centers: preparation, structures, and isomerization. *Inorg. Chem.* **39**, 4029–4036 (2000).
21. Hubrich, M., Jeschke, G. & Schweiger, A. The generalized hyperfine sublevel coherence transfer experiment in one and two dimensions. *J. Chem. Phys.* **104**, 2172–2184 (1996).
22. Gambarelli, S., Luttringer, F., Padovani, D., Mulliez, E. & Fontecave, M. Activation of the anaerobic ribonucleotide reductase by S-adenosylmethionine. *ChemBioChem* **6**, 1960–1962 (2005).
23. Chen, D. W., Walsby, C., Hoffman, B. M. & Frey, P. A. Coordination and mechanism of reversible cleavage of S-adenosylmethionine by the [4Fe-4S] center in lysine 2,3-aminomutase. *J. Am. Chem. Soc.* **125**, 11788–11789 (2003).
24. Coronado, E. *et al.* Pressure-tuning of magnetism and linkage isomerism in iron(II) hexacyanochromate. *J. Am. Chem. Soc.* **127**, 4580–4581 (2005).
25. Shatruk, M. *et al.* Properties of Prussian blue materials manifested in molecular complexes: observation of cyanide linkage isomerism and spin-crossover behavior in pentanuclear cyanide clusters. *J. Am. Chem. Soc.* **129**, 6104–6116 (2007).
26. Happe, T. & Naber, J. D. Isolation, characterization and N-terminal amino-acid-sequence of hydrogenase from the green-alga *Chlamydomonas reinhardtii*. *Eur. J. Biochem.* **214**, 475–481 (1993).
27. Kamp, C. *et al.* Isolation and first EPR characterization of the [FeFe]-hydrogenases from green algae. *Biochim. Biophys. Acta Bioenerg.* **1777**, 410–416 (2008).
28. Sybirna, K. *et al.* *Shewanella oneidensis*: a new and efficient system for expression and maturation of heterologous [FeFe] hydrogenase from *Chlamydomonas reinhardtii*. *BMC Biotechnol.* **8**, 73–81 (2008).
29. Darensbourg, M. Y., Lyon, E. J., Zhao, X. & Georgakaki, I. P. The organometallic active site of [Fe] hydrogenase: models and entatic states. *Proc. Natl Acad. Sci. USA* **100**, 3683–3688 (2003).
30. Mertens, R. & Liese, A. Biotechnological applications of hydrogenases. *Curr. Opin. Biotechnol.* **15**, 343–348 (2004).

**Supplementary Information** is available in the online version of the paper.

**Acknowledgements** G.B. acknowledges support from the Bengt Lundqvist Minnesfond, FORMAS (contract number 213-2010-563) and the Swedish Royal Academy of Sciences. This work was supported by the French National Research Agency (ANR) through grant 07-BLAN-0298-01 and the Labex programme (ARCANE, 11-LABX-003). V.A. acknowledges support from the European Research Council under the European Union's Seventh Framework Programme (FP/2007-2013/ERC Grant Agreement no. 306398). T.H. was supported by the Deutsche Forschungsgemeinschaft (HA 255/2-1), the BMBF (Bio-H2) and the Volkswagen foundation (LigH2t). A.A., E.R. and W.L. thank the Max Planck Society for financial support, and A. Silakov for providing the FTIR processing software.

**Author Contributions** G.B., V.A., M.A., W.L., T.H. and M.F. designed the research; G.B. and T.R.S. prepared and characterized synthetic complexes and hybrid species; C.L., J.E. and G.B. contributed to maturation experiments and H<sub>2</sub> evolution measurements; A.A. and C.L. performed FTIR measurements; G.B. and S.G. performed EPR measurements; J.-M.M. did DFT calculations; and M.F., G.B., E.R. and V.A. wrote the paper.

**Author Information** Reprints and permissions information is available at [www.nature.com/reprints](http://www.nature.com/reprints). The authors declare no competing financial interests. Readers are welcome to comment on the online version of the paper. Correspondence and requests for materials should be addressed to M.F. ([marc.fontecave@cea.fr](mailto:marc.fontecave@cea.fr)).

## METHODS

All chemicals were purchased from Sigma-Aldrich and used as received unless otherwise stated. NMR was recorded on a Bruker AC300 using the residual solvent peak as internal standard. Complex  $(\text{Et}_4\text{N})_2[\text{Fe}_2(\text{adt})(\text{CO})_4(\text{CN})_2]$  (**2**,  $\text{adt}^{2-} = 2$ -azapropanedithiolate)<sup>14</sup> was synthesized following literature procedure, and  $(\text{Et}_4\text{N})_2[\text{Fe}_2(\text{pdt})(\text{CO})_4(\text{CN})_2]$  (**1**,  $\text{pdt}^{2-} = \text{propanedithiolate}$ )<sup>11</sup>,  $(\text{Et}_4\text{N})_2[\text{Fe}_2(\text{pdt})(\text{CO})_4(^{13}\text{CN})_2]$ <sup>31</sup> and  $(\text{Et}_4\text{N})_2[\text{Fe}_2(\text{odt})(\text{CO})_4(\text{CN})_2]$  (**3**,  $\text{odt}^{2-} = 2$ -oxopropanedithiolate)<sup>15</sup> were prepared by modified literature procedures (see Supplementary Information) and their thin-film solution FTIR spectra were recorded on a Perkin Elmer Spectrum-100 spectrometer. *TmHydF* (referred to as *HydF* throughout the text) was overexpressed, purified and its [4Fe-4S] cluster reconstituted as previously described<sup>17</sup>. Apo-CrHydA1 (referred to as apo-HydA1 throughout the text) was overexpressed in *E. coli* BL21 DE3 ΔiscR using growth conditions and a pET plasmid as previously published for the production of active HydA1 in *E. coli*<sup>32</sup>.

Protein purity was assessed by gel electrophoresis by loading samples on Any kD Mini-Protean TGX precast gels (Biorad) alongside Precision Plus Protein standards (Biorad). Migration was achieved on a Mini-Protean apparatus (Biorad) at 200 V for 30 min. Protein concentrations were determined with the Biorad Protein Assay, using bovine serum albumin as a standard as well as by optical absorption measurements. Aerobic ultraviolet–visible absorption spectra were recorded on a Cary 1Bio spectrophotometer (Varian) and anaerobic measurements were made with a fibre-optic-fitted UvikonXL spectrophotometer (BioTek Instruments). Iron and sulphur quantification were performed following the methods of refs 33 and 34, respectively. The specific hydrogenase activity was determined as described previously<sup>35</sup>.

**Spectroscopic characterization.** FTIR spectra of protein samples were recorded on a Bruker IFS 66 v/s FTIR spectrometer equipped with a Bruker MCT (mercury cadmium telluride) detector. The spectrometer was controlled by Bruker Opus software. All measurements were performed at 15 °C with a resolution of 2 cm<sup>-1</sup>. The spectra were accumulated in the double-sided, forward-backward mode with 1,000 scans. Data were processed using custom-written routines in the MATLAB programming environment. FTIR samples of complexes **1–3** and x-HydF (x = **1–3**) were prepared in HEPES buffer (20 mM, 100 mM KCl) pH 7.5. FTIR samples of x-HydA1 were prepared in 10 mM Tris-HCl buffer pH 8.0 containing sodium dithionite (10 mM). For the FTIR measurement of matured HydA1, apo-HydA1 was washed twice with 10 mM Tris-HCl pH 8.0, 2 mM sodium dithionite (a buffer referred to below as TPW2) by concentration and dilution to remove any trace of desthiobiotin originating from the prior purification of apo-HydA1 by strep-tag affinity chromatography. 100 μl of TPW2 buffer containing 100 μM apo-HydA1 and a fourfold molar excess of the hybrid protein (1-HydF, 2-HydF or 3-HydF, respectively) was incubated for 60 min at 37 °C. Afterwards, 500 μl of TPW2 buffer was added, and the solution was loaded on a 750 μl Strep-Tactin Superflow (IBA) column. The HydA1 protein was separated from 1-HydF (1-HydA1), 2-HydF (2-HydA1) or 3-HydF (3-HydA1) by affinity chromatography

using 10 mM Tris-HCl pH 8.0, 2 mM sodium dithionite, 200 mM NaCl as washing buffer and TPW2 buffer, 2.5 mM desthiobiotin for elution. The isolated protein was concentrated using Amicon Ultra centrifugal filters 10K (Millipore) and stored as described previously<sup>36</sup>. For the FTIR spectra shown in Supplementary Fig. 7, the preparation was done as described above with 2-HydF but without the final purification step.

X-band EPR spectra were recorded on a Bruker ESP 300D spectrometer equipped with an Oxford Instruments ESR 900 flow cryostat. Protein samples were anaerobically reduced with 10 molar equivalents of sodium dithionite before freezing. Hyperfine sublevel correlation (HYSCORE) spectra and their Combination Frequency (CF) – Nuclear Frequency (NF) variants were recorded on a Bruker Elexsys E-580 X band (frequency, 9.71 GHz) pulsed spectrometer with a Bruker ER4118X dielectric resonator and continuous-flow He cryostat (Oxford Instruments CF935) controlled by an Oxford Instruments temperature controller ITC 503. Experiments (128 × 128 data set) were performed at 8 K using the standard four-pulse sequence ( $\pi/2 - \tau - \pi/2 - t_1 - \pi - t_2 - \pi/2 - \text{echo}$ ) with a nominal pulse width of 16 ns for  $\pi/2$  pulses, a  $\tau$  value of 132 ns and a pulse repetition rate of 1 kHz. In the HYSCORE experiment, the delays before ( $t_1$ ) and after ( $t_2$ ) the mixing  $\pi$  pulse were incremented in 20-ns steps from an initial value ( $t_{\text{ini}} = 200$  ns) according to the following formula:  $t_1 = t_{\text{ini}} + d_1$  and  $t_2 = t_{\text{ini}} + d_2$ . In the CF-NF experiment,  $t_1$  and  $t_2$  were incremented in 20-ns steps according to the following formula:  $t_1 = t_{\text{ini}} + d_1$  and  $t_2 = t_{\text{ini}} + d_1 + d_2$ . The value of  $t_{\text{ini}}$  was chosen to be as long as 1,000 ns to remove as much as possible the broad features arising from <sup>14</sup>N quadrupole coupling. Unwanted echoes were removed by four-step phase cycling. The background decay in both dimensions was subtracted using a linear fit followed by apodization with a Hamming window and zero-filling to 2,048 points in each dimension. The 2D Fourier transform magnitude spectrum was then calculated. The static magnetic field was set at 3,600 G ( $g_{\perp}$ ).

**DFT calculations.** These were performed using the ADF2012 quantum chemistry code (see Supplementary Discussion). Hyperfine coupling constants were computed using the parameter-free PBE0 exchange-correlation potential with triple- $\zeta$  basis sets (+ two polarization functions) and unfrozen cores.

- Fiedler, A. T. & Brunold, T. C. Combined spectroscopic/computational study of binuclear Fe(I)–Fe(I) complexes: implications for the fully-reduced active-site cluster of Fe-only hydrogenases. *Inorg. Chem.* **44**, 1794–1809 (2005).
- Kuchenreuther, J. M. *et al.* High-yield expression of heterologous [FeFe] hydrogenases in *Escherichia coli*. *PLoS ONE* **5**, e15491 (2010).
- Fish, W. W. Rapid colorimetric micromethod for the quantitation of complexed iron in biological samples. *Methods Enzymol.* **158**, 357–364 (1988).
- Beinert, H. Semi-micro methods for analysis of labile sulfide and of labile sulfide plus sulfane sulfur in unusually stable iron sulfur proteins. *Anal. Biochem.* **131**, 373–378 (1983).
- Hemschmeier, A., Melis, A. & Happe, T. Analytical approaches to photobiological hydrogen production in unicellular green algae. *Photosynth. Res.* **102**, 523–540 (2009).
- Stripp, S. T. *et al.* How oxygen attacks [FeFe] hydrogenases from photosynthetic organisms. *Proc. Natl Acad. Sci. USA* **106**, 17331–17336 (2009).

# Melting during late-stage rifting in Afar is hot and deep

D. J. Ferguson<sup>1</sup>, J. MacLennan<sup>2</sup>, I. D. Bastow<sup>3</sup>, D. M. Pyle<sup>4</sup>, S. M. Jones<sup>5</sup>, D. Keir<sup>6</sup>, J. D. Blundy<sup>7</sup>, T. Plank<sup>1</sup> & G. Yirgu<sup>8</sup>

Investigations of a variety of continental rifts and margins worldwide have revealed that a considerable volume of melt can intrude into the crust during continental breakup<sup>1–8</sup>, modifying its composition and thermal structure. However, it is unclear whether the cause of voluminous melt production at volcanic rifts is primarily increased mantle temperature or plate thinning<sup>1,2,8–12</sup>. Also disputed is the extent to which plate stretching or thinning is uniform or varies with depth with the entire continental lithospheric mantle potentially being removed before plate rupture<sup>13–16</sup>. Here we show that the extensive magmatism during rifting along the southern Red Sea rift in Afar, a unique region of sub-aerial transition from continental to oceanic rifting, is driven by deep melting of hotter-than-normal asthenosphere. Petrogenetic modelling shows that melts are predominantly generated at depths greater than 80 kilometres, implying the existence of a thick upper thermo-mechanical boundary layer in a rift system approaching the point of plate rupture. Numerical modelling of rift development shows that when breakup occurs at the slow extension rates observed in Afar, the survival of a thick plate is an inevitable consequence of conductive cooling of the lithosphere, even when the underlying asthenosphere is hot. Sustained magmatic activity during rifting in Afar thus requires persistently high mantle temperatures, which would allow melting at high pressure beneath the thick plate. If extensive plate thinning does occur during breakup it must do so abruptly at a late stage, immediately before the formation of the new ocean basin<sup>16</sup>.

The geological record at rifted margins often preserves evidence for voluminous magmatism during continental breakup<sup>1,2</sup>. However, the principal control on the creation of this thick transitional igneous crust remains a matter of considerable debate. Some authors suggest that small-scale convection within the mantle beneath thinned plates can account for the syn-rift melting<sup>10</sup>; others have argued that increased mantle temperatures are also required, either via a short-lived thermal pulse<sup>9</sup> or from a sustained increase that persists to the early stages of seafloor spreading<sup>7</sup>. Also debated is the mechanism by which the thickness of the continental lithosphere is reduced from 100–150 km (ref. 14) to almost zero at the point of plate rupture. Some models propose that the lower-mantle lithosphere is preferentially removed at an early stage of breakup<sup>13</sup>, possibly by stretching<sup>14</sup> or detachment<sup>16</sup>; others suggest that a significant portion of the lithospheric mantle remains until the final stage of plate thinning<sup>16</sup>.

Ethiopia offers an excellent opportunity to understand how mantle temperature and plate thinning covary during rifting because it exposes several stages of rift development, including the final stages of transition to oceanic spreading in northern Afar<sup>17</sup>. This setting offers a distinct advantage over studies on passive continental margins, where inferences from the geological record cannot be compared directly to a priori constraints on features such as mantle temperature (for example, seismic wave speeds).

Conventional rifting models<sup>18</sup> predict a present-day thinning factor (initial thickness divided by final thickness) for the Afar lithosphere of approximately 3, in contrast to seismic data, which show that current crustal thinning in most of Afar has a factor of only <2. This discrepancy between observed and predicted crustal thickness is likely to be partly the result of ‘magma-compensated’ thinning<sup>7</sup>, whereby extensive melt addition to the crust<sup>3,4,6</sup> has reduced net thinning, with a possible further contribution from magmatically accommodated extension<sup>5</sup>. However, the response of the lower part of the Ethiopian lithosphere to extension remains unclear and it is debated whether the lower plate has been preferentially thinned<sup>14</sup>, effectively compensating for the modest net crustal attenuation, or whether a significant thickness of the lithospheric mantle remains intact<sup>17</sup>. A related controversy concerns the temperature of the Afar mantle<sup>13,19</sup>, which exerts a fundamental control on the depth and extent of melting and is therefore a key parameter in understanding the ongoing magmatism and thermal structure of the upper mantle.

Here we address these issues by developing a petrogenetic model for current rift-related magmatism in Afar. We test our petrogenetic results using a numerical model of rift development to investigate how the lithosphere has evolved over 30 million years of rifting and magmatism. Our results provide new constraints on plate thickness and mantle potential temperature  $T_p$ , thereby aiding discrimination between competing models for magmatism and extension during the final stages of continental breakup.

We used mafic lavas erupted from on- and off-axis vents and fissures from the seismically and volcanically active Dabbahu segment<sup>5,20</sup>, which is part of the Red Sea rift in west-central Afar (Fig. 1; Supplementary Tables 1 and 2). All lavas are enriched in incompatible trace elements compared to typical mid-ocean ridge basalt and have trace-element characteristics similar to the Ethiopian flood basalts<sup>21</sup>, which were erupted at about 30 million years ago, during the early stages of rifting and hotspot tectonism<sup>22</sup> (Fig. 2). The off-axis lavas have consistently more enriched characteristics than their axial counterparts, including higher ratios of light rare earth elements (REE) to heavy REE (that is, La/Sm; Fig. 2) and of middle REE to heavy REE (that is, Tb/Yb; Fig. 2) and they also have different major-element compositions (Supplementary Table 2). These geochemical trends occur over short length scales (around 20 km), with the implication that the plumbing systems feeding the main rift zone and off-axis volcanoes are separate throughout the crust. Calculated equilibrium pressure  $P$  and temperature  $T$  conditions between the major-element composition of the lavas and mantle peridotite (Fig. 3e; see Methods) indicate that the axial lavas preserve compositions consistent with conditions in the mantle at 2.3–2.6 GPa and 1,472–1,489 °C. Off-axis lavas give consistently lower and more variable values of 1,301–1,396 °C and 1.1–1.9 GPa.

We interpret these different thermal regimes as resulting from variations in the magma plumbing systems between these two regions. The

<sup>1</sup>Lamont-Doherty Earth Observatory, Columbia University, Palisades, New York 10964, USA. <sup>2</sup>Department of Earth Sciences, University of Cambridge, Cambridge CB2 3EQ, UK. <sup>3</sup>Department of Earth Science and Engineering, Imperial College London, London SW7 2AZ, UK. <sup>4</sup>Department of Earth Sciences, University of Oxford, Oxford OX1 3AN, UK. <sup>5</sup>School of Geography, Earth and Environmental Science, University of Birmingham, Birmingham B15 2TT, UK. <sup>6</sup>National Oceanography Centre Southampton, University of Southampton, Southampton SO14 3ZH, UK. <sup>7</sup>Department of Earth Sciences, University of Bristol, Bristol BS8 1RJ, UK. <sup>8</sup>Department of Earth Sciences, Addis Ababa University, Addis Ababa, Ethiopia.



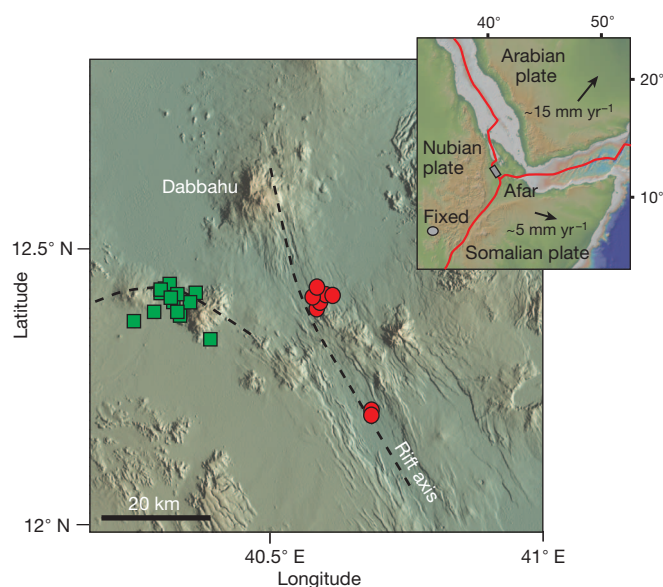


**Figure 1 | Map of the Dabbahu–Manda Hararo magmatic segment.** The Dabbahu–Manda Hararo rift zone has formed along the on-land section of the Red Sea rift system, near the rift–rift–rift triple junction (red lines shown in inset; rectangle shows location of main figure). Symbols show locations of on-axis (circles) and off-axis (squares) lava samples. The magma chamber feeding recent axial dyke intrusions<sup>5</sup> and eruptions<sup>20</sup> is located beneath the central part of the segment. Arrows in the inset show motions of Somalian and Arabian plates relative to a fixed point (oval) in Nubia.

on-axis melts appear to be extracted in a rapid and/or chemically isolated fashion, thus preserving  $P$ – $T$  conditions that reflect a mean of primary melting processes, consistent with our trace-element modelling presented here. In contrast, the off-axis lavas are likely to have been modified during ascent by reactive re-equilibration at lower  $P$ – $T$  conditions within the lithospheric mantle.

We constrained the conditions of mantle melting using the observed REE concentrations of the lavas, which during mantle melting vary as a function of source composition, lithology and melt productivity with depth<sup>23</sup>. A key feature of these REE melting models is the effect on the medium REE/heavy REE values in the melt phase caused by the presence of residual garnet in the melting lithology. Garnet preferentially retains the heavy REE within its crystal lattice, so melts generated at

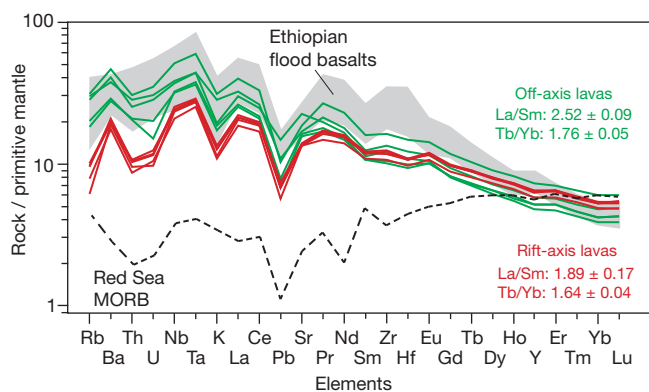


**Figure 2 | Trace-element compositions of mafic lavas from Afar.** Lavas erupted from off-axis vents show consistent enrichments in the most incompatible elements compared to those from the axial part of the rift zone. The grey area shows compositions of Ethiopian flood basalts identified as mostly closely resembling the Afar hotspot/plume<sup>21</sup>. Both the current Afar lavas and the older flood basalts show similar enrichments in incompatible elements compared to average mid-ocean ridge basalt (MORB) compositions. Listed ratios of La/Sm and Tb/Yb are means with  $1\sigma$  variations. Compositions are normalized to that of primitive mantle.

higher pressure where garnet is stable will have higher medium REE/heavy REE compared to those generated by melting at lower pressures in its absence. Our REE modelling (see Methods) therefore acts partly as a melting barometer, which we used to constrain how the composition of the accumulated melt reflects the distribution of polybaric melt production throughout the region of mantle melting.

We started with simple forward models of melting during passive upwelling of mantle peridotite<sup>8</sup>. In this model, steady-state adiabatic fractional melting occurs at a given mantle  $T_p$  and up to a specified depth. We initially tested melting of normal-temperature mantle ( $T_p = 1,350 \pm 50^\circ\text{C}$ ; ref. 24), where melting occurs according to the geodynamic model for Afar of ref. 13 with the onset of melting between depths of 70 km and 80 km and melt production continues until a depth of 40 km. The compositions of melts generated from these regimes (Fig. 3a) do not match the observed REE concentrations and we found a particularly poor fit to the relative concentration ratios.

Next we used a series of forward models at various  $T_p$  values and melting intervals, from which we found that the erupted melts can be matched best by mantle melting at elevated  $T_p$  ( $1,450^\circ\text{C}$ ; similar to that proposed for Afar by ref. 19), with a relatively deep onset (about 95 km) and termination (about 80 km) of melting (Fig. 3b). This short melting interval led to a greater overall contribution from melts generated in the garnet stability field (over 86 km depth), which is required to retain the relatively high medium REE/heavy REE observed in the erupted melts. These results therefore imply that melt production beneath Afar initiates at relatively high pressures and temperatures, and does not continue to shallow depths.

We developed our model further by using the inversion scheme of ref. 23 to obtain physical melting conditions from the observed REE concentrations. As before, we examined shallow melting regimes associated with lower  $T_p$  values, but because such melting is initiated above the garnet stability field, varying the melting rate with depth cannot lead to a closer match with the observed melts (Supplementary Fig. 1a). Increasing mantle  $T_p$  to allow initial melting to occur in the garnet stability field led to an improved fit to the observed melts, but in cases where melting is allowed to continue to shallow depths, the requirement to preserve the high medium REE/heavy REE leads to very low or negligible melt production being predicted in the upper parts of the melting region. Using the thermal conditions given by the major-element  $P$ – $T$  results, which suggest a melting path close to the mantle adiabat for a  $T_p$  of  $1,450^\circ\text{C}$  (Fig. 3), we obtained a very close fit to the REE composition of the axial lavas where melting occurs between depths of approximately 95–80 km (Fig. 3c), in excellent agreement with the forward model with similar parameters (Fig. 3b).

The clear results from both these REE models are that (1) temperatures hotter than normal ambient mantle (that is,  $T_p > 1,300$ – $1,400^\circ\text{C}$ , ref. 24) are required to generate deep melting, and (2) melting initiated at depths below the garnet–spinel phase transition and insignificant melt generation occurred at depths shallower than about 80 km. The equilibration pressures calculated for these lavas of about 2.5 GPa (Fig. 3e) are consistent with pooling of melts from this melting region. An inversion model for the off-axis melt compositions with the same parameters yields similar results (Supplementary Fig. 1b), but with a slightly lower overall extent of melting (that is, a shorter melting column), suggesting that upwelling and melting have become focused beneath the rift axis and that off-axis volcanism is fed by melts from the margins of the melting region.

Our geochemical modelling shows that significant asthenospheric upwelling and melting beneath central Afar is presently confined to depths greater than around 80 km. Thus, although our results do not provide precise constraints on lithospheric thickness, they clearly demonstrate that melting at shallower depths is suppressed, implying that the thermo-mechanical boundary layer beneath Afar remains relatively thick. Plate reconstructions<sup>25</sup> show that since rift initiation at about 30 million years ago, Afar has extended by a factor of around 3, from a starting rift width of approximately 100 km, at rates not exceeding

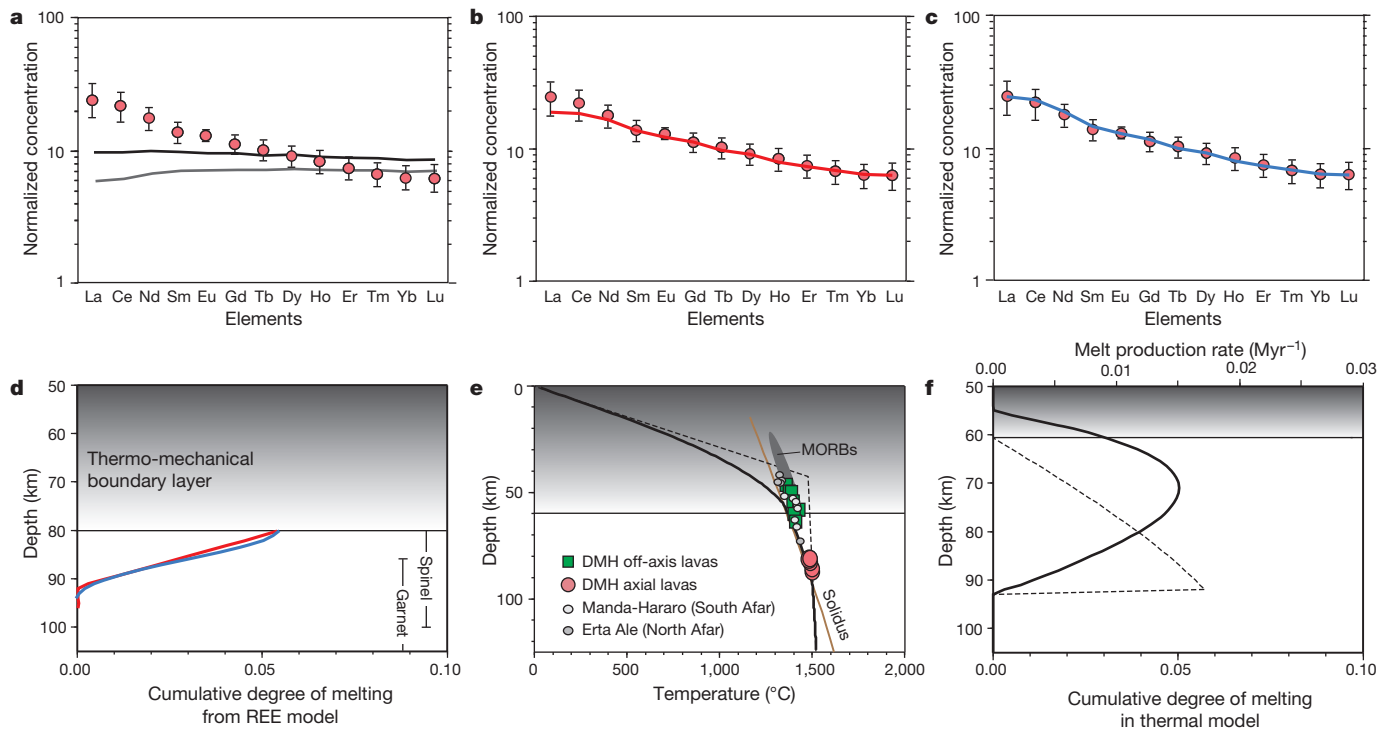


**Figure 3 | Results of REE and rifting models.** a–c, Observed (circles) and predicted (lines) REE concentrations. a, Results from a forward model (melting stops at 40 km) at  $T_p$  values of 1,350 °C ( $F_{\text{max}} = 0.12$ ; black line) and 1,400 °C ( $F_{\text{max}} = 0.18$ ; grey line). b, Results of the best-fit REE forward model (melting stops at 80 km), for a  $T_p$  value of 1,450 °C ( $F_{\text{max}} = 0.055$ ). c, Results of the best-fit inversion model for a  $T_p$  value of 1,450 °C ( $F_{\text{max}} = 0.055$ ). d, Cumulative degree of melting with depth for the best-fitting inversion model (blue line) and from the forward model (red line), both with a  $T_p$  of 1,450 °C. Error bars are 1 s.d. e and f, Pressure–temperature conditions of mantle–melt equilibria for Afar lavas and predicted geothermal gradient and melting conditions after 30 million years of rifting. Melting occurs when the temperature of the

20 mm  $\text{yr}^{-1}$  (ref. 26): equivalent to those of ultra-slow-spreading oceanic ridges<sup>27</sup>. Conventional instantaneous plate stretching models<sup>18</sup> predict a present-day lithospheric thickness of less than 40 km (assuming an initial thickness of about 125 km), with the implication that melting and upwelling should be markedly shallower than is observed. However, finite-duration rifting models show that when extension occurs at low strain rates, such as those observed in Afar, the base of the lithosphere may be strongly affected by conductive cooling<sup>28</sup>.

We quantify this effect for Afar using a numerical finite-duration rifting and melting model<sup>28,29</sup> (see Methods) to examine how the history of rifting may have affected melt production and plate thinning. This approach adds to the petrological and REE modelling by explicitly examining the relationships between rifting, mantle upwelling, the geotherm (and hence lithospheric thickness) and melting. Unlike in the REE model, which assumes steady-state adiabatic melting, the generation of melts during upwelling in the thermal model considers both the advection and conduction of heat. We track the development of the geotherm and associated melting during 30 million years of rifting at strain rates appropriate for Afar.

The results (Fig. 3e, f) show that lithospheric thinning and mantle melting are significantly reduced in comparison with an instantaneous stretching model (also shown in Fig. 3e). The average depth of melting at 30 million years is predicted to be about 80 km, with the onset of melting at 95 km and no melt production occurring at depths shallower than 60 km. The greater lithospheric thickness and melting depth in the finite-duration rifting model than in the instantaneous case arise both because low upwelling rates permit significant conductive cooling, and also because the geotherm and melting region have not yet evolved to a steady state. These results show that the presence of

upwelling mantle oversteps the solidus (orange line in e). The thick line in e shows the temperature profile affected by conductive cooling (30 million years of rifting) compared to the model with instantaneous extension (dashed line). No melting is predicted above a depth of 60 km (shaded area) because the instantaneous melting rate (thin line in f) falls to zero. The time-dependent cumulative degree of melting from the thermal model after 30 million years of rifting (thick line in f) shows good agreement with the REE results and is significantly less than that predicted by the instantaneous rifting model (dashed line in e). The portion of the cumulative melt degree curve (thick line) that decreases upward in f represents mantle that melted previously but has now moved upwards.  $T_p$  is 1,450 °C. DMH, Dabbahu–Manda Hararo rift zone.

the thick thermal boundary layer in Afar implied by the petrogenetic results is an inevitable consequence of the protracted breakup process occurring here. Owing to the different and complementary assumptions inherent in the REE and thermal modelling techniques (steady-state adiabatic melting versus evolving thermal regime) we do not expect a direct correlation between cumulative melting curves predicted by these (see Methods). However, the two classes of model give generally consistent results and both predict similar extents of melting beneath a 60–80-km-thick lithosphere (Supplementary Fig. 2).

Geophysical studies from Ethiopia and elsewhere have demonstrated the significant role of magma intrusion in modifying crustal compositions and maintaining crustal thickness during continental rifting<sup>1–7,16</sup>. Both our modelling approaches show that the ongoing magmatism here requires the underlying mantle to have an elevated potential temperature of around 1,450 °C, allowing partial melting to occur at high pressures beneath a 60–80-km-thick lithospheric lid. This mantle  $T_p$  is consistent with previous estimates by ref. 19 as well as the markedly slow seismic wave speeds observed in the Ethiopian mantle<sup>6,16</sup>. Although shallow magmatic processes in the Afar crust currently have some affinity with those observed at the mid-ocean ridges<sup>5,17</sup>, our results show that net lithospheric thinning of this slowly extending continental lithosphere remains modest. If a new ocean basin were to open here an abrupt phase of late-stage plate thinning would therefore probably be required<sup>16</sup>.

## METHODS SUMMARY

**P–T conditions of mantle–melt equilibration.** A peridotitic, rather than pyroxenitic, source was determined using diagnostic elemental ratios such as Zn/Fe and Mn/Fe (Supplementary Fig. 1). P–T conditions of mantle–melt equilibria were

calculated using the Si and Mg thermobarometer of ref. 30 for lavas with  $\text{MgO} > 7 \text{ wt\%}$  and assuming an  $\text{H}_2\text{O}$  content of 0.5 wt%. These were corrected for olivine removal to be in equilibrium with Mg-rich olivine compositions of  $\text{Fo}_{90}$  (90% forsterite) using an Fe–Mg olivine–melt partition coefficient of 0.3 and  $\text{Fe}^{3+}/\Sigma\text{Fe}$  of 0.16, determined from oxygen fugacity conditions constrained by analysis of V in olivine and the host lavas.

**REE melting calculations.** The source composition for melting models was calculated by matching the Nd isotopic composition of lavas by mixing primitive and depleted mantle. Forward<sup>8</sup> and inversion<sup>23</sup> REE models were then used to estimate the cumulative degree of melting against depth relationship present in the mantle. For the inversion we used REE data from high MgO lavas, corrected for fractionation. Melting was assumed to be fractional and the garnet–spinel transition depth was set at 86–100 km based on experimental studies.

**Two-dimensional rifting model.** We modelled a square-sided rift undergoing pure shear stretching with a total strain of 3 over 30 million years, in line with ref. 26. The equilibrium thickness of the lithosphere was 125 km. Thermal structure was tracked using a two-dimensional explicit finite difference scheme that includes vertical and lateral advection and conduction of heat and adiabatic cooling. The local instantaneous melt production rate was calculated using expressions in ref. 29, which account for depressurization and change in thermal structure. Parameterizations in ref. 8 were used for solidus, liquidus and melting progress. Cumulative degree of melting was calculated by integrating the melting rate over time, accounting for mantle upwelling. The geotherm and melting results in Fig. 3 are from the centre of the model.

**Full Methods** and any associated references are available in the online version of the paper.

**Received 8 December 2012; accepted 1 May 2013.**

- White, R. & McKenzie, D. Magmatism at rift zones: the generation of volcanic continental margins and flood basalts. *J. Geophys. Res.* **94**, 7685–7729 (1989).
- White, R. *et al.* Lower-crustal intrusion on the North Atlantic continental margin. *Nature* **452**, 460–464 (2008).
- Hammond, J. O. S. *et al.* The nature of the crust beneath the Afar triple junction: evidence from receiver functions. *Geochem. Geophys. Geosyst.* **12**, Q12004 (2011).
- Keranen, K., Klemperer, S. L., Gloaguen, R., EAGLE Working Group. Three-dimensional seismic imaging of a protoridge axis in the Main Ethiopian rift. *Geology* **32**, 949–952 (2004).
- Wright, T. J. *et al.* Magma-maintained rift segmentation at continental rupture in the 2005 Afar dyking episode. *Nature* **442**, 291–294 (2006).
- Bastow, I. D., Pilidou, S., Kendall, J.-M. & Stuart, G. W. Melt-induced seismic anisotropy and magma assisted rifting in Ethiopia: evidence from surface waves. *Geochem. Geophys. Geosyst.* **11**, Q0AB05 (2010).
- Thybo, H. & Nielsen, C. A. Magma-compensated crustal thinning in continental rift zones. *Nature* **457**, 873–876 (2009).
- McKenzie, D. & Bickle, M. J. The volume and composition of melt generated by extension of the lithosphere. *J. Petrol.* **29**, 625–679 (1988).
- Nielsen, T. K. & Hopper, J. R. From rift to drift: mantle melting during continental breakup. *Geochem. Geophys. Geosyst.* **5**, Q07003 (2004).
- Boutillier, R. R. & Keen, C. E. Small-scale convection and divergent plate boundaries. *J. Geophys. Res.* **104**, 7389–7403 (1999).
- Armitage, J. J., Collier, J. S. & Minshall, T. A. The importance of rift history for volcanic margin formation. *Nature* **465**, 913–917 (2010).
- Shillington, D. J. *et al.* Abrupt transition from magma-starved to magma-rich rifting in the eastern Black Sea. *Geology* **37**, 7–10 (2009).
- Rychert, C. A. *et al.* Volcanism in the Afar Rift sustained by decompression melting with minimal plume influence. *Nature Geosci.* **5**, 406–409 (2012).
- Huisman, R. & Beaumont, C. Depth-dependent extension, two-stage breakup and cratonic underplating at rifted margins. *Nature* **473**, 74–78 (2011).
- Esedo, R., van Wijk, J., Coblenz, D. & Meyer, R. Uplift prior to continental breakup: indication for removal of mantle lithosphere? *Geosphere* **8**, 1078–1085 (2012).
- Bastow, I. D. & Keir, D. The protracted development of the continent–ocean transition in Afar. *Nature Geosci.* **4**, 248–250 (2011).
- Hayward, N. J. & Ebinger, C. J. Variations in the along-axis segmentation of the Afar Rift system. *Tectonics* **15**, 244–257 (1996).
- McKenzie, D. Some remarks on the development of sedimentary basins. *Earth Planet. Sci. Lett.* **40**, 25–32 (1978).
- Rooney, T. O., Herzberg, C. & Bastow, I. D. Elevated mantle temperature beneath East Africa. *Geology* **40**, 27–30 (2012).
- Ferguson, D. J. *et al.* Recent rift related volcanism in Afar, Ethiopia. *Earth Planet. Sci. Lett.* **292**, 409–418 (2010).
- Pik, R., Deniel, C., Coulon, C., Yirgu, G. & Marty, B. Isotopic and trace element signatures of Ethiopian flood basalts: evidence for plume–lithosphere interactions. *Geochim. Cosmochim. Acta* **63**, 2263–2279 (1999).
- Hoffman, C. *et al.* Timing of the Ethiopian flood basalt event and implications for plume birth and global change. *Nature* **389**, 838–841 (1997).
- McKenzie, D. & O’Nions, K. G. Partial melt distributions from inversion of rare earth element concentrations. *J. Petrol.* **32**, 1021–1091 (1991).
- Herzberg, C. *et al.* Temperatures in ambient mantle and plumes: constraints from basalts, picrites, and komatiites. *Geochem. Geophys. Geosyst.* **8**, Q02006 (2007).
- Eagles, G., Gloaguen, R. & Ebinger, C. J. Kinematics of the Danakil microplate. *Earth Planet. Sci. Lett.* **203**, 607–620 (2002).
- Wolfenden, E., Ebinger, C., Yirgu, G., Renne, P. R. & Kelley, S. P. Evolution of a volcanic rifted margin: southern Red Sea, Ethiopia. *Geol. Soc. Am. Bull.* **117**, 846–864 (2005).
- Dick, H. J. B., Lin, J. & Schouten, H. An ultraslow-spreading class of ocean ridge. *Nature* **426**, 405–412 (2003).
- Jarvis, G. T. & McKenzie, D. Sedimentary formation with finite extension rates. *Earth Planet. Sci. Lett.* **48**, 42–52 (1980).
- Bown, J. W. & White, R. S. Effect of finite extension rate on melt generation at rifted continental margins. *J. Geophys. Res.* **100**, 18011–18029 (1995).
- Lee, C.-T. A., Luffi, P., Plank, T., Dalton, H. & Leeman, W. P. Constraints on the depths and temperatures of basaltic magma generation on Earth and other terrestrial planets using new thermobarometers for mafic magmas. *Earth Planet. Sci. Lett.* **279**, 20–33 (2009).

**Supplementary Information** is available in the online version of the paper.

**Acknowledgements** We acknowledge help and support by members of the NERC Afar Rift Consortium. This project was supported by a NERC consortium grant. D.J.F. acknowledges support from a LDEO postdoctoral fellowship.

**Author Contributions** D.J.F., D.M.P., J.D.B. and G.Y. planned the project and conducted fieldwork in Afar. Geochemical analysis and modelling was by D.J.F., J.M., D.M.P., J.D.B. and T.P. and S.M.J. did the numerical rifting model. D.J.F. took the lead in writing the manuscript with contributions from I.D.B., J.M., D.K., S.M.J. and others.

**Author Information** Reprints and permissions information is available at [www.nature.com/reprints](http://www.nature.com/reprints). The authors declare no competing financial interests. Readers are welcome to comment on the online version of the paper. Correspondence and requests for materials should be addressed to D.J.F. ([davef@ldeo.columbia.edu](mailto:davef@ldeo.columbia.edu)).



## METHODS

**Source lithology and thermobarometry.** Diagnostic elemental ratios such as Zn/Fe (Supplementary Fig. 3; ref. 31) indicate an origin for the observed basalts predominantly by peridotite melting. Equilibrium  $P$  and  $T$  conditions for the lavas and mantle peridotite, shown in Fig. 3e, were calculated using a Si and Mg thermobarometer<sup>30</sup>. Before applying the thermobarometer, lavas with MgO > 7 wt% (Supplementary Table 1) were corrected for olivine fractionation by incremental olivine addition using an Fe–Mg olivine–melt partition coefficient of 0.3 until equilibrium with 90% forsterite (Fo<sub>90</sub>) olivine. An important factor in this correction is the Fe<sup>3+</sup>/ΣFe ratio in the melt and we use a value of 0.16 determined directly for the Afar lavas using oxygen fugacity conditions constrained by analysis of V in olivine and melts using the methods of refs 32 and 33. The limited volatile data<sup>34</sup> available for basaltic melts from Afar suggests that pre-eruptive H<sub>2</sub>O contents are relatively low and we use an assumed value of 0.5 wt%. Using 0.1 wt% or 1 wt% leads to temperature estimates that are about 10 °C higher or lower respectively. Several factors can affect the final major element composition of the melts and the calculated  $P$ – $T$  relations therefore reflect some mean of these<sup>35</sup>. In the case of the axial lavas we interpret these to be mean melting conditions. The off-axis lavas give a lower range of  $P$ – $T$  estimates, implying at least partial re-equilibration as shallower depths within the lithosphere/thermal boundary layer, demonstrating variations in melt transport between the rift axis and off-axis volcanoes.

**REE melting models.** The starting mantle source composition was calculated by matching the Nd isotopic composition of the lavas ( $\epsilon_{\text{Nd}}$  of about 5; Supplementary Table 2) by mixing primitive and depleted mantle end-member compositions from refs 36 and 37. ( $\epsilon_{\text{Nd}} = [(^{143}\text{Nd}/^{144}\text{Nd}_{\text{sample}})/(^{143}\text{Nd}/^{144}\text{Nd}_{\text{CHUR}}) - 1] \times 10^4$ , where CHUR is 'chondritic uniform reservoir' with a  $^{143}\text{Nd}/^{144}\text{Nd}$  of 0.512638.) REE inversion modelling<sup>23</sup> was used to estimate the relationship between the cumulative degree of melting and depth present in the mantle. Partition coefficients were taken from the compilation of ref. 39 and the garnet–spinel transition depth was set from 86–100 km in the model runs, based on the experimental results of ref. 40. The initial source lithology was 59.8% olivine, 21.1% orthopyroxene, 7.6% clinopyroxene and 11.5% garnet for garnet peridotite; and 57.8% olivine, 27% orthopyroxene, 11.9% clinopyroxene and 3.3% spinel for spinel peridotite. Melting was assumed to be fractional, and the melts were integrated over a triangular melting region with a constant upwelling rate. This melting geometry recovers lower melt fractions in the garnet field than inversion models with a one-dimensional column, so we believe that our conclusion of deep melting at high  $T_p$  is not strongly dependent on the melting geometry. Only high-MgO basalts were used in the inversion runs, which were corrected for 30% fractionation using the methods of ref. 24. Cumulative melting curves from the inversion modelling were compared with theoretical curves for adiabatic upwelling at different mantle potential temperatures (the forward model). These curves were calculated using the parameterization of ref. 8, but with an entropy of fusion of  $350 \text{ J kg}^{-1} \text{ °C}^{-1}$  (ref. 41).

**Numerical thermal rifting model.** We modelled a square-sided rift undergoing pure shear stretching (that is, linear variation in upwelling rate with depth) with a total strain factor ( $\beta$ ) of 3 over a period of 30 million years. Strain rate in the most recent ten million years of rifting was set to 1.5 times the strain rate in the first 20 million years because there is evidence that strain rate has accelerated during the rifting period<sup>26</sup>. The initial rift width of 65 km was chosen to give a final width of 400 km. The equilibrium thickness of the lithosphere was set to 125 km. Evolution of the thermal structure of the lithosphere was tracked using a two-dimensional explicit finite difference scheme that includes vertical and lateral advection and conduction of heat<sup>42</sup> with the addition of adiabatic cooling. The geotherm and melting results plotted in Fig. 3e are from the centre of the model. Local instantaneous melt production rate was calculated using equation (7) in ref. 29, which accounts for both depressurization through upwelling and also temperature change by advection and conduction of heat. The parameterizations

of ref. 8 were used for solidus, liquidus and melting progress. Cumulative degree of melting was calculated by integrating the instantaneous melt production rate over time, accounting for ongoing mantle upwelling through the melting region.

**Comparison of REE and thermal rift models.** The two approaches offer complementary insights into melting beneath Afar, but several important differences should be borne in mind when comparing the results. First, the thermal rifting model evolves over time, whereas the REE melting model assumes steady state. Second, conductive cooling in the thermal model allows a sub-adiabatic melting path and suppresses melting as the material moves upward, whereas the forward REE melting model assumes an adiabatic melting path up to the specified top of the melting region. These differences mean that cumulative degree of melting can both increase and decrease upwards in any snapshot of the thermal rift model, but it can only increase upwards in the REE melting model. The portion of the cumulative melt degree curve that decreases upward (Fig. 3f) represents mantle that melted previously but has now welled up and out of the melting region. Therefore the thermal and REE models are expected to be most closely comparable in the deepest part of the melting region, where the cumulative degree of melting increases upwards, and Supplementary Fig. 2b shows an excellent match in this region. The base of the lithosphere is specified as a single value in the REE model, while in the thermal model it is calculated as the zone over which progress of melting decays from a maximum to zero. Given these different definitions, it is encouraging that there is a difference of only 9 km between the top of the melting region in the best-fitting REE models (80 km) and the depth of maximum melting progress automatically determined by the thermal model (71 km) (Fig. 3d, f). Results can also be compared in terms of degrees of melting and proportions of total melting within the garnet and spinel stability zones, which determine the REE concentrations in the melt (Supplementary Fig. 2a). The models all involve the onset of melting at 93–96 km. At 86 km (top of garnet stability) the thermal rifting model has melted by 2.37%, and 37% of the total melt is generated in the garnet field. For the best REE forward (or inversion) model, 2.6% (or 2.9%) melting has occurred at the top of the garnet stability field and 48% (or 54%) of the total melt is generated in the garnet field. Therefore, the thermal rifting model and the forward and inverse REE models are comparable in terms of predicted REE concentrations.

1. Le Roux, V., Lee, C.-T. A. & Turner, S. J. Zn/Fe systematics in mafic and ultramafic systems: implications for detecting major element heterogeneities in the Earth's mantle. *Geochim. Cosmochim. Acta* **74**, 2779–2796 (2010).
2. Canil, D. Vanadium in peridotites, mantle redox and tectonic environments: Archean to present. *Earth Planet. Sci. Lett.* **195**, 75–90 (2002).
3. Kress, V. C. & Carmichael, S. E. The compressibility of silicate liquids containing Fe<sub>2</sub>O<sub>3</sub> and the effect of composition, temperature oxygen fugacity and pressure on their redox states. *Contrib. Mineral. Petrol.* **108**, 82–92 (1991).
4. Field, L. *et al.* Integrated field, satellite and petrological observations of the November 2010 eruption of Erta Ale. *Bull. Volcanol.* **74**, 2251–2271 (2012).
5. Asimow, P. & Longhi, J. The significance of multiple saturation points in the context of polybaric near-fractional melting. *J. Petrol.* **45**, 2349–2367 (2004).
6. Workman, R. K. & Hart, S. R. Major and trace element composition of the depleted MORB mantle (DMM). *Earth Planet. Sci. Lett.* **231**, 53–72 (2005).
7. McDonough, W. F. & Sun, S.-S. The composition of the Earth. *Chem. Geol.* **120**, 223–253 (1995).
8. White, R. S., McKenzie, D. & O'Nions, R. K. Oceanic crustal thickness from seismic measurements and rare earth element inversions. *J. Geophys. Res.* **97**, 19683–19715 (1992).
9. Gibson, S. A. & Geist, D. Geochemical and geophysical estimates of lithospheric thickness variation beneath Galápagos. *Earth Planet. Sci. Lett.* **300**, 275–286 (2010).
10. Robinson, J. A. C. & Wood, B. J. The depth of the spinel to garnet transition at the peridotite solidus. *Earth Planet. Sci. Lett.* **164**, 277–284 (1998).
11. Kojitani, H. & Akaogi, M. Melting enthalpies of mantle peridotite: calorimetric determinations in the system CaO–MgO–Al<sub>2</sub>O<sub>3</sub>–SiO<sub>2</sub> and application to magma generation. *Earth Planet. Sci. Lett.* **153**, 209–222 (1997).
12. White, N. & Bellingham, P. A two-dimensional inverse model for extensional sedimentary basins. 1. Theory. *J. Geophys. Res.* **107**, 2259 (2002).

# Recalibrating *Equus* evolution using the genome sequence of an early Middle Pleistocene horse

Ludovic Orlando<sup>1\*</sup>, Aurélien Ginolhac<sup>1\*</sup>, Guojie Zhang<sup>2\*</sup>, Duane Froese<sup>3</sup>, Anders Albrechtsen<sup>4</sup>, Mathias Stiller<sup>5</sup>, Mikkel Schubert<sup>1</sup>, Enrico Cappellini<sup>1</sup>, Bent Petersen<sup>6</sup>, Ida Moltke<sup>4,7</sup>, Philip L. F. Johnson<sup>8</sup>, Matteo Fumagalli<sup>9</sup>, Julia T. Vilstrup<sup>1</sup>, Maanasa Raghavan<sup>1</sup>, Thorfinn Korneliussen<sup>1</sup>, Anna-Sapfo Malaspinas<sup>1</sup>, Josef Vogt<sup>6</sup>, Damian Szklarczyk<sup>10†</sup>, Christian D. Kelstrup<sup>10</sup>, Jakob Vinther<sup>11†</sup>, Andrei Dolocan<sup>12</sup>, Jesper Stenderup<sup>1</sup>, Amhed M. V. Velazquez<sup>1</sup>, James Cahill<sup>5</sup>, Morten Rasmussen<sup>1</sup>, Xiaoli Wang<sup>2</sup>, Jiumeng Min<sup>2</sup>, Grant D. Zazula<sup>13</sup>, Andaine Seguin-Orlando<sup>1,14</sup>, Cecilie Mortensen<sup>1,14</sup>, Kim Magnussen<sup>1,14</sup>, John F. Thompson<sup>15</sup>, Jacobo Weinstock<sup>16</sup>, Kristian Gregersen<sup>1,17</sup>, Knut H. Røed<sup>18</sup>, Vera Eisenmann<sup>19</sup>, Carl J. Rubin<sup>20</sup>, Donald C. Miller<sup>21</sup>, Douglas F. Antczak<sup>21</sup>, Mads F. Bertelsen<sup>22</sup>, Søren Brunak<sup>6,23</sup>, Khaled A. S. Al-Rasheid<sup>24</sup>, Oliver Ryder<sup>25</sup>, Leif Andersson<sup>20</sup>, John Mundy<sup>26</sup>, Anders Krogh<sup>1,4</sup>, M. Thomas P. Gilbert<sup>1</sup>, Kurt Kjær<sup>1</sup>, Thomas Sicheritz-Ponten<sup>6,23</sup>, Lars Juhl Jensen<sup>10</sup>, Jesper V. Olsen<sup>10</sup>, Michael Hofreiter<sup>27</sup>, Rasmus Nielsen<sup>28</sup>, Beth Shapiro<sup>5</sup>, Jun Wang<sup>2,26,29,30</sup> & Eske Willerslev<sup>1</sup>

The rich fossil record of equids has made them a model for evolutionary processes<sup>1</sup>. Here we present a 1.12-times coverage draft genome from a horse bone recovered from permafrost dated to approximately 560–780 thousand years before present (kyr BP)<sup>2,3</sup>. Our data represent the oldest full genome sequence determined so far by almost an order of magnitude. For comparison, we sequenced the genome of a Late Pleistocene horse (43 kyr BP), and modern genomes of five domestic horse breeds (*Equus ferus caballus*), a Przewalski's horse (*E. f. przewalskii*) and a donkey (*E. asinus*). Our analyses suggest that the *Equus* lineage giving rise to all contemporary horses, zebras and donkeys originated 4.0–4.5 million years before present (Myr BP), twice the conventionally accepted time to the most recent common ancestor of the genus *Equus*<sup>4,5</sup>. We also find that horse population size fluctuated multiple times over the past 2 Myr, particularly during periods of severe climatic changes. We estimate that the Przewalski's and domestic horse populations diverged 38–72 kyr BP, and find no evidence of recent admixture between the domestic horse breeds and the Przewalski's horse investigated. This supports the contention that Przewalski's horses represent the last surviving wild horse population<sup>6</sup>. We find similar levels of genetic variation among Przewalski's and domestic populations, indicating that the former are genetically viable and worthy of conservation efforts. We also find evidence for continuous selection on the immune system and olfaction throughout horse evolution. Finally, we identify 29 genomic regions among horse breeds that deviate from neutrality and show low levels of genetic variation compared to the Przewalski's horse. Such regions could correspond to loci selected early during domestication.

In 2003, we recovered a metapodial horse fossil at the Thistle Creek site in west-central Yukon Territory, Canada (Fig. 1a). The fossil was

from an interglacial organic unit associated with the Gold Run volcanic ash, dated to  $735 \pm 88$  kyr BP<sup>2,3</sup> (Fig. 1b). Relict ice wedges below the unit indicate persistent permafrost since deposition (Supplementary Information, section 1.1), whereas the organic unit, hosting the fossil, indicates a period of permafrost degradation, or a thaw unconformity<sup>7</sup>, during a past interglacial as warm or warmer than present<sup>3</sup>, and rapid deposition during either marine isotope stage 19, 17 or 15. This indicates that the fossil dates to approximately 560–780 kyr BP. The metapodial shows typical caballine morphology, consistent with Middle rather than the smaller Late Pleistocene horse fossils from the area (Fig. 1c and Supplementary Information, section 1.2). This age is consistent with small mammal fossils from this unit indicating a Late Irvingtonian, or Middle Pleistocene, age<sup>3</sup>, and infinite radiocarbon dates<sup>8</sup>.

Theoretical<sup>9</sup> and empirical evidence<sup>10</sup> indicates that this age approaches the upper limit of DNA survival. So far, no genome-wide information has been obtained from fossil remains older than 110–130 kyr BP<sup>11</sup>. Time-of-flight secondary ion mass spectrometry (TOF-SIMS) on the ancient horse bone revealed secondary ion signatures typical of collagen within the bone matrix (Fig. 2a and Supplementary Table 7.1), and high-resolution tandem mass spectrometry sequencing<sup>12</sup> revealed 73 proteins, including blood-derived peptides (Supplementary Information, section 7.4). This is consistent with good biomolecular preservation, suggesting possible DNA survival. Therefore, we conducted larger-scale destructive sampling for genome sequencing.

We used Illumina and Helicos sequencing to generate 12.2 billion DNA reads from the Thistle Creek metapodial. Mapping against the horse reference genome yielded  $\sim 1.12\times$  genome coverage. We based the size distribution of ancient DNA templates on collapsed Illumina

<sup>1</sup>Centre for GeoGenetics, Natural History Museum of Denmark, University of Copenhagen, Øster Voldgade 5–7, 1350 Copenhagen K, Denmark. <sup>2</sup>Shenzhen Key Laboratory of Transomics Biotechnologies, BGI-Shenzhen, Shenzhen 518083, China. <sup>3</sup>Department of Earth and Atmospheric Sciences, University of Alberta, Edmonton, Alberta T6G 2E3, Canada. <sup>4</sup>The Bioinformatics Centre, Department of Biology, University of Copenhagen, Ole Maaloes Vej 5, 2200 Copenhagen, Denmark. <sup>5</sup>Department of Ecology and Evolutionary Biology, University of California, Santa Cruz, California 95064, USA. <sup>6</sup>Center for Biological Sequence Analysis, Department of Systems Biology, Technical University of Denmark, DK-2800 Lyngby, Denmark. <sup>7</sup>Department of Human Genetics, The University of Chicago, Chicago, Illinois 60637, USA. <sup>8</sup>Department of Biology, Emory University, Atlanta, Georgia 30322, USA. <sup>9</sup>Department of Integrative Biology, University of California, Berkeley, California 94720, USA. <sup>10</sup>Novo Nordisk Foundation Center for Protein Research, Faculty of Health and Medical Sciences, University of Copenhagen, Blegdamsvej 3b, 2200 Copenhagen, Denmark. <sup>11</sup>Jackson School of Geosciences, The University of Texas at Austin, 1 University Road, Austin, Texas 78712, USA. <sup>12</sup>Texas Materials Institute, The University of Texas at Austin, Austin, Texas 78712, USA. <sup>13</sup>Government of Yukon, Department of Tourism and Culture, Yukon Palaeontology Program, PO Box 2703 L2A, Whitehorse, Yukon Territory Y1A 2C6, Canada. <sup>14</sup>Danish National High-throughput DNA Sequencing Centre, University of Copenhagen, Øster Farimagsgade 2D, 1353 Copenhagen K, Denmark. <sup>15</sup>NABsys Inc, 60 Clifford Street, Providence, Rhode Island 02903, USA. <sup>16</sup>Archeology, University of Southampton, Avenue Campus, Highfield, Southampton SO17 1BF, UK. <sup>17</sup>Zoological Museum, Natural History Museum of Denmark, University of Copenhagen, Universitetsparken 15, 2100 Copenhagen, Denmark. <sup>18</sup>Department of Basic Sciences and Aquatic Medicine, Norwegian School of Veterinary Science, Box 8146 Dep, N-0033 Oslo, Norway. <sup>19</sup>Département histoire de la Terre, UMR 5143 du CNRS, paléobiodiversité et paléoenvironnements, MNHN, CP 38, 8, rue Buffon, 75005 Paris, France. <sup>20</sup>Science for Life Laboratory, Department of Medical Biochemistry and Microbiology, Uppsala University, SE-751 23 Uppsala, Sweden. <sup>21</sup>Baker Institute for Animal Health, Cornell University, Ithaca, New York 14853, USA. <sup>22</sup>Center for Zoo and Wild Animal Health, Copenhagen Zoo, 2000 Frederiksberg, Denmark. <sup>23</sup>Novo Nordisk Foundation Center for Biosustainability, Technical University of Denmark, DK-2970 Hørsholm, Denmark. <sup>24</sup>Zoology Department, College of Science, King Saud University, Riyadh 11451, Saudi Arabia. <sup>25</sup>San Diego Zoo's Institute for Conservation Research, Escondido, California 92027, USA. <sup>26</sup>Department of Biology, University of Copenhagen, Ole Maaloes Vej 5, 2200 Copenhagen, Denmark. <sup>27</sup>Department of Biology, The University of York, Wentworth Way, Heslington, York YO10 5DD, UK. <sup>28</sup>Departments of Integrative Biology and Statistics, University of California, Berkeley, Berkeley, California 94720, USA. <sup>29</sup>King Abdulaziz University, Jeddah 21589, Saudi Arabia. <sup>30</sup>Macau University of Science and Technology, Avenida Wai long, Taipa, Macau 999078, China. †Present addresses: Bioinformatics Group, Institute of Molecular Life Sciences, University of Zurich, Winterthurerstrasse 190, CH-8057 Zurich, Switzerland (D.S.); Departments of Earth Sciences and Biological Sciences, University of Bristol BS8 1UG, UK (Ja.V.).

\*These authors contributed equally to this work.

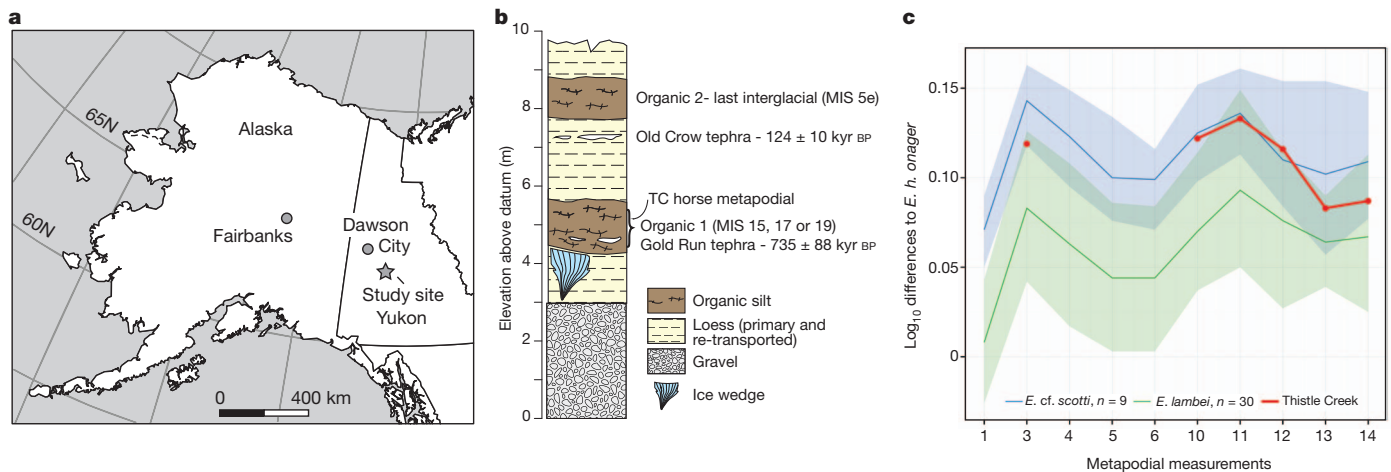


**Figure 1 | The early Middle Pleistocene horse metapodial from Thistle Creek (TC).** **a**, Geographical localization. **b**, Stratigraphic setting. **c**, Morphological comparison to Middle and Late Pleistocene horses from Beringia. Simpson's ratio diagrams contrasting  $\log_{10}$  differences in 10 metapodial measurements between horse fossils and a reference (*E. hemionus onager*) are shown for a series of 9 and 30 horses from the Middle and the Late Pleistocene era, respectively (Supplementary Information, section 1.2). The full

read pairs (Supplementary Fig. 4.4), yielding an average length of 77.5 base pairs (bp). The specimen is male based on X to autosomal chromosome coverage (Supplementary Information, section 4.2b) and the presence of Y-chromosome markers (Supplementary Information, section 4.1d). Endogenous read content was lower for Illumina (0.47%) than Helicos (4.21%) using standard<sup>8</sup> or improved<sup>13</sup> single-strand template preparation procedures. This is probably due to 3' ends available at nicks, resistance of undamaged modern DNA contaminants to denaturation, and Helicos ability to sequence short templates. Despite this, endogenous DNA content was >16.6–20.0-fold lower than for Saqqaq Palaeo-Eskimo<sup>14</sup> and Denisovan specimens<sup>15</sup>, both sequenced to high depth.

Several observations support genome sequence authenticity. First, a 348-bp mitochondrial control region segment was replicated independently (Supplementary Fig. 2.2 and Supplementary Information, section 2.4). Second, phylogenetic analyses on data obtained with two sequencing platforms in different laboratories are consistent (Supplementary Fig. 8.4), ruling out post-purification contamination. Third, autosomal, Y-chromosomal and mitochondrial DNA analyses place the Thistle Creek specimen basal to Late Pleistocene and modern horses (Fig. 3a and Supplementary Figs 8.1–8.4). Fourth, we found signs of severe biomolecular degradation, including levels of cytosine deamination at overhangs considerably higher than observed in 28 younger permafrost-preserved fossils from the Late Pleistocene (Fig. 2c, Supplementary Fig. 6.40 and Supplementary Table 6.1) and protein deamidation levels<sup>12,16</sup> (Fig. 2b and Supplementary Information, section 7.5) greater than those reported for younger permafrost-preserved bones.

We additionally sequenced genomes of a 43-kyr-old (pre-domestication) horse (1.8× coverage), a modern donkey (16×; Supplementary Fig. 4.1), 5 modern domestic horses (Arabian, Icelandic, Norwegian fjord, Standardbred and Thoroughbred; 7.9×–21.1×) and one modern Przewalski's horse (9.6×; Supplementary Table 2.1), considered to possibly represent the last surviving wild horse population. We used this data set to address fundamental questions in horse evolution: (1) the timing of the origins of the genus *Equus*; (2) the demographic history of modern horses; (3) the divergence time of horse populations forming the Przewalski's and domestic lineages; (4) the extent to which the Przewalski's horse has remained isolated from domestic relatives; (5) the timing of gene expansions within the horse genome; (6) the identification of genes potentially under selection during horse evolution.

As no accepted *Equus* fossils exist before 2.0 Myr BP<sup>4,5</sup> (Supplementary Information, section 9.1d), the date of the last common ancestor that

distribution range between minimal and maximal values is presented within shaded areas. Numbers reported on the x axis refer to the following measurements: 1, maximal length; 3, breadth at the middle of the diaphysis; 4, depth at the middle of the diaphysis; 5, proximal breadth; 6, proximal depth; 10, distal supra-articular breadth; 11, distal articular breadth; 12, depth of the keel; 13, least depth of medial condyle; 14, greatest depth of medial condyle.

gave rise to extant horses versus donkeys, asses and zebras<sup>17</sup> remains heavily debated. Proposed dates extend as early as 4.2–4.5 Myr BP on the basis of palaeontological estimates<sup>18</sup> to over 6.0 Myr BP according to molecular analyses<sup>19</sup>. We addressed this issue by taking advantage of the established age for the Thistle Creek horse. As a sample cannot be older than the population it belonged to, we explored a full range of possible calibrations for the *Equus* most recent common ancestor (MRCA) and calculated the divergence time between the populations of the ancient Thistle Creek horse and modern horses<sup>20</sup> (Supplementary Information, section 10.1). Calibrations resulting in divergence times younger than the Thistle Creek bone age were rejected, providing a credible confidence range for the MRCA of *Equus*. We found rates consistent with the *Equus* MRCA living 3.6–5.8 Myr BP to be compatible with our data (Fig. 3b and Supplementary Figs 10.1–10.3). We also found support for slower mutation rates in horse than human (Supplementary Information, section 8.4 and Supplementary Table 8.5), implying a minimal date of 4.07 Myr BP for the MRCA of *Equus* (Supplementary Figs 10.1–10.3). We therefore propose 4.0–4.5 Myr BP for the MRCA of all living *Equus*, in agreement with recent molecular findings<sup>17</sup> and the oldest palaeontological records for the monodactyle *Plesippus simplicidens*, which some<sup>18</sup> consider the earliest fossil of *Equus*. Our result indicates that the evolutionary timescale for the origin of contemporary equid diversity is at least twice that commonly accepted.

Second, we reconstructed horse population demography over the last 2 Myr. The pairwise sequential Markovian coalescent (PSMC) approach<sup>21</sup> shows that horses experienced a population minimum approximately 125 kyr BP, corresponding to the last interglacial when environmental conditions were similar to now throughout their range. The population expanded during the cold stages of marine isotope stage (MIS) 4 and 3 as grasslands expanded. A peak was reached 25–50 kyr BP and was followed by an approximately 100-fold collapse, probably resulting from major climatic changes and related grassland contraction after the Last Glacial Maximum<sup>22</sup> (Fig. 4 and Supplementary Figs 9.4–9.5). A similar demographic history was inferred from Bayesian skyline reconstructions using 23 newly characterized ancient mitochondrial genomes (Supplementary Fig. 9.6). These results support suggestions<sup>22</sup> that climatic changes are major demographic drivers for horse populations. PSMC analyses also revealed two earlier demographic phases (Fig. 4b and Supplementary Figs 9.4–9.5), with population sizes peaking 190–260 kyr BP and 1.2–1.6 Myr BP, respectively, followed by 1.7-fold and 8.1-fold collapses. Extremely low population sizes were inferred approximately 500–800 kyr BP, a time period



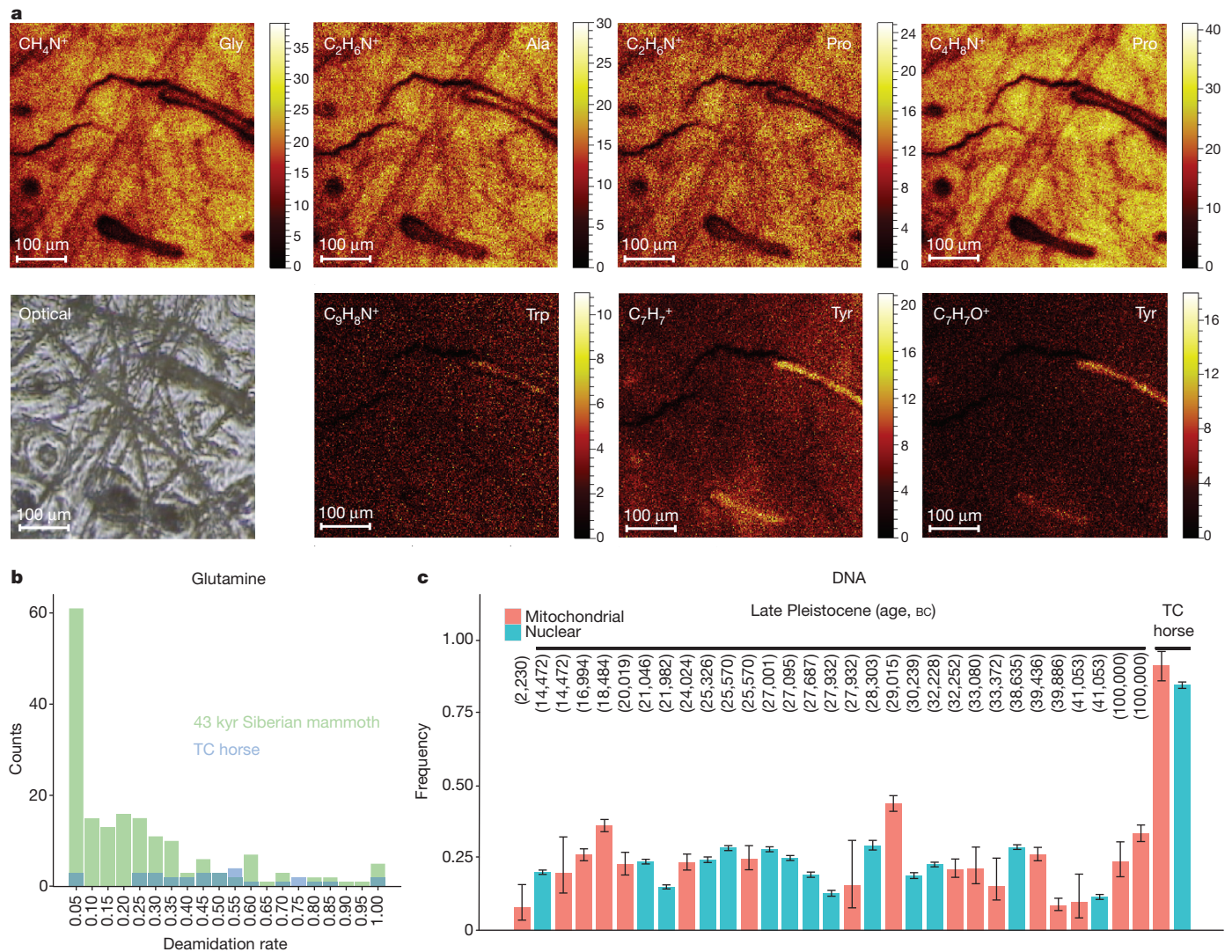


**Figure 2 | Amino acid, protein and DNA preservation of the Thistle Creek horse bone.** **a**, Amino acid signatures. Secondary ions, characteristic of five amino acids over- or under-represented in collagen, were detected by TOF-SIMS (Supplementary Information, section 7.1). The size of secondary ion maps is  $500 \times 500 \mu\text{m}^2$  with a resolution of  $256 \times 256$  pixels. **b**, Glutamine deamidation. The observed distribution of glutamine deamidation levels (Supplementary Information, section 7.5) is blue for the Thistle Creek (TC) horse bone and green for a 43-kyr-old Siberian mammoth bone.

that covers the divergence time of the Thistle Creek and contemporary horse populations. This result may relate to population fragmentation when horses colonized Eurasia from America, in agreement with the earliest presence of horses in Eurasia 750 kyr BP<sup>4</sup>.

We next investigated whether Przewalski's horse indeed represents the last survivor of wild horses. Native to the Mongolian steppes, this horse was listed as extinct in the wild (IUCN red list<sup>23</sup>) but has been reassigned to endangered after successful conservation and reintroduction. Using maximum likelihood phylogenetic analyses and topological tests (Supplementary Information, sections 8.2–8.3), we found that the Przewalski's horse genome falls outside a monophyletic group of domestic horses. The MRCA of Przewalski's and domestic horse sequences dates to 341–431 kyr BP (Supplementary Table 8.3), a period consistent with previous estimates<sup>6</sup>. We estimated the divergence time between populations of Przewalski's and domestic horses to approximately 38–72 kyr BP (Supplementary Tables 10.4–10.6). Our 43 kyr BP horse genome branched off before the Przewalski's and domestic horse lineages diverged (Fig. 3a). This specimen belonged to a population that diverged from that leading to modern horses approximately 89–167 kyr BP

(Supplementary Figs 10.1–10.3 and Supplementary Table 10.5), providing a maximal boundary for the younger divergence between Przewalski's and domestic horses.

Using quartet alignments and *D* statistics<sup>24</sup> (Supplementary Information, sections 12.1–12.3) we found no evidence for admixture between the Przewalski's horse and the individual horse breeds investigated in this study using either the donkey or the ancient Thistle Creek genome as out-group (Supplementary Tables 12.1–S12.3). Scanning the Przewalski's horse genome, we also found no long tracts of shared polymorphisms with domestic horses (Supplementary Fig. 12.3), as would be expected if recent admixture occurred after the last wild individual was captured in the 1940s<sup>25</sup>. Rather, we identified long tracts of variation unique to the Przewalski's horse genome, including genes involved in immunity, cytoskeleton, metabolism and the central nervous system that could have been specifically selected in this lineage (Supplementary Information, section 12.6). The average levels of polymorphism present in the Przewalski's horse genome are greater than those observed in the Icelandic, Standardbred and Arabian horse genomes (Supplementary Fig. 5.5 and Supplementary Table 11.10). Thus, unadmixed lineages

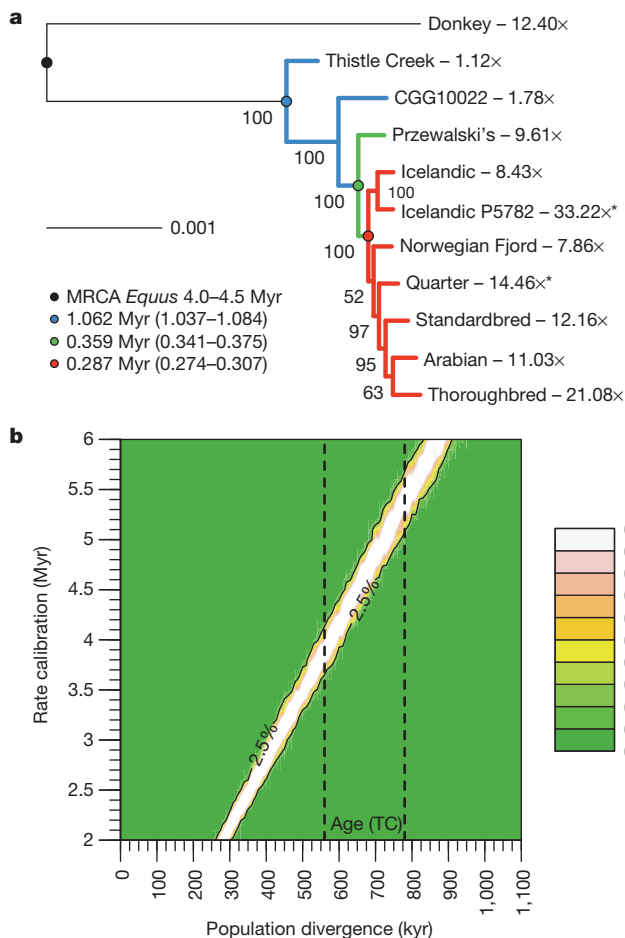


**Figure 3 | Horse phylogenetic relationships and population divergence times.** **a**, Maximum likelihood phylogenetic inference. We performed a supermatrix analysis of 5,359 coding genes (Supplementary Information, section 8.3a, 100 bootstrap pseudo-replicates) and estimated the average age for the main nodes (r8s semi-parametric penalized likelihood (PL) method, Supplementary Information, section 8.3c; see Supplementary Table 8.3 for other analyses). Asterisk indicates previously published horse genomes.

**b**, Population divergence times. We used ABC to recover a posterior distribution for the time when two horse populations split over a full range of possible mutation rate calibrations (Supplementary Information, section 10.1). The first population included the Thistle Creek horse; the second consisted of modern domestic horses. A conservative age range for the Thistle Creek horse is reported between the dashed lines (560–780 kyr).

for certain functionally important gene families<sup>26</sup> (Supplementary Information, section 5.1c). Our data set revealed that a limited fraction of horse paralogues (1.7%, representing 258 paralogues) showed no hits among donkey reads, suggesting that most horse paralogues expanded before the origin of the genus *Equus* some 4.0–4.5 Myr BP. Among these 258 regions, 11 L1 retrotransposons and one copy of a keratin gene are absent from the ancient Thistle Creek horse genome but present in the 43 kyr horse and modern horses (Supplementary Table 5.3), suggesting an expansion before their MRCA some 500–626 kyr BP (Supplementary Table 8.3). Similarly, 44 L1-retrotransposon paralogues were found only in modern horse genomes (Supplementary Table 5.4), indicating that expansion of L1 retrotransposons has remained active since then.

Finally, we identified loci potentially selected in modern horses (Supplementary Figs 11.1–11.2), focusing on regions showing unusual densities of derived mutations (Supplementary Information, section 11.1). We caution that local variations in mutation and recombination rates, as well as misalignments, may result in similar signatures at neutrally evolving regions. Functional clustering analyses revealed significant enrichment for immunity-related and olfactory receptor genes (Supplementary Table 11.4), two categories also enriched for non-synonymous single nucleotide polymorphisms (SNPs) (Supplementary Information, section 5.2d). Additionally, we identified 29 regions showing deviation from neutrality and significant reduction in genetic diversity among modern domestic horses compared to Przewalski's horse (Supplementary Tables 11.8–11.9). Such regions could correspond to loci that have been selected and transmitted to all horse breeds investigated here after divergence from the Przewalski's horse population,

are still present in the endangered Przewalski's horse population, with levels of allelic diversity that can support long-term survival of captive breeding stocks despite descending from only 13–14 wild individuals<sup>25</sup>.

The sequencing of the horse reference genome showed increased paralogous expansion rates in horses compared to humans and bovines

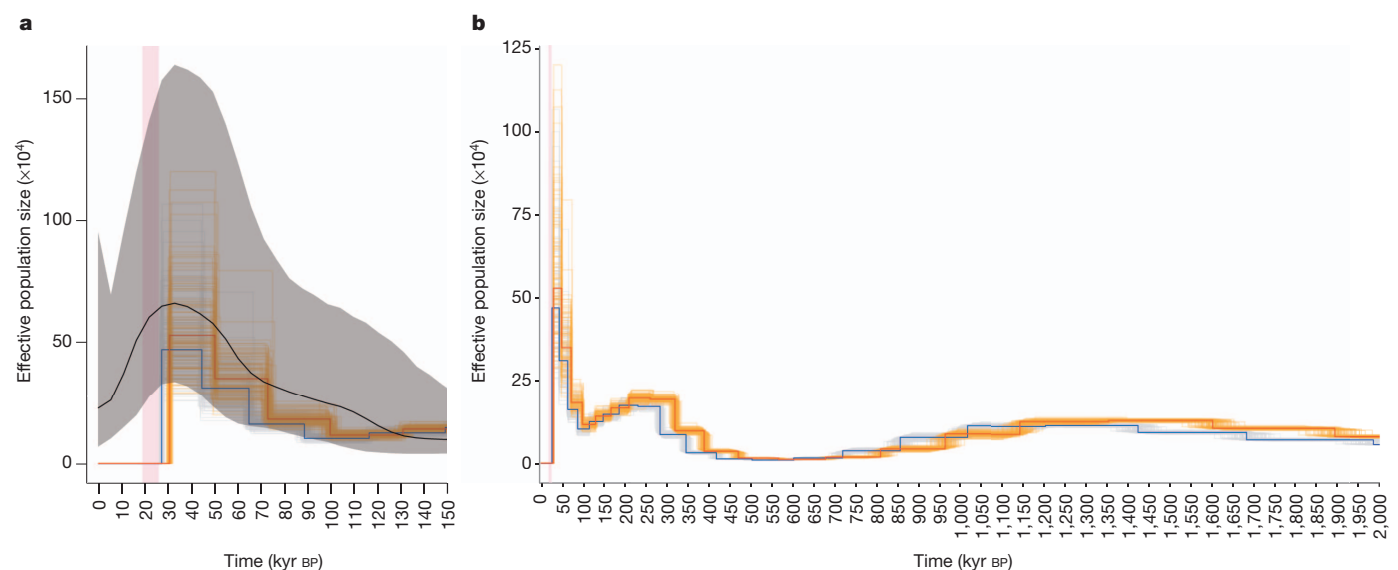


**Figure 4 | Horse demographic history.** **a**, Last 150 kyr BP. PSMC based on nuclear data (100 bootstrap pseudo-replicates) and Bayesian skyline inference based on mitochondrial genomes (median, black; 2.5% and 97.5% quantiles, grey) are presented following the methodology described in Supplementary Information, section 9. The Last Glacial Maximum (19–26 kyr BP) is shown in

pink. **b**, Last 2 Myr BP. PSMC profiles are scaled using the new calibration values proposed for the MRCA of all living members of the genus *Equus* (4.0 Myr, blue; 4.5 Myr, red), and assuming a generation time of 8 years (for other generation times, see Supplementary Figs 9.4 and 9.5).



possibly related to domestication. These regions include genes for the KIT ligand critical for haematopoiesis, spermatogenesis and melanogenesis, and myopalladin involved in sarcomere organization.

Our study has pushed the timeframe of palaeogenomics back by almost an order of magnitude. This enabled us to readdress a range of questions related to the evolution of *Equus*—a group representing textbook examples of evolutionary processes. The Thistle Creek genome also provided us with direct estimates of the long-term rate of DNA decay<sup>27</sup>, revealing that a significant fraction (6.0–13.3%) of short (25-bp) DNA fragments may survive over a million years in the geosphere (Supplementary Fig. 6.42). Thus, procedures maximizing the retrieval of short, but still informative, DNA may provide access to resources previously considered to be much too old. Methods have recently been developed for increasing the sequencing depth of ancient genomes<sup>15</sup> but do not increase the percentage of endogenous sequences retrieved. Overcoming this technical challenge with whole-genome enrichment approaches, and lower sequencing costs, will make retrieval of higher coverage genomes from specimens with low endogenous DNA content practical and economical.

## METHODS SUMMARY

Ancient horse extracts and DNA libraries were prepared in facilities designed to analyse ancient DNA following standard procedures<sup>8,12</sup>. Protein sequencing was performed using nanoflow liquid chromatography tandem mass spectrometry<sup>28</sup>. DNA sequencing was performed using Illumina and Helicos sequencing platforms<sup>8,13</sup>. Reads were aligned to the horse reference genome<sup>26</sup> and *de novo* assembled donkey scaffolds using BWA<sup>29</sup>. Maximum-likelihood DNA damage rates were estimated from nucleotide misincorporation patterns. Population divergence times were estimated disregarding transitions to limit the impact of replication of damaged DNA and following ref. 20 with quartet genome alignments instead of trios and implementing approximate Bayesian computation (ABC).

**Online Content** Any additional Methods, Extended Data display items and Source Data are available in the online version of the paper; references unique to these sections appear only in the online paper.

Received 30 October 2012; accepted 30 May 2013.

Published online 26 June 2013.

1. Franzen, J. L. *The Rise of Horses: 55 Million Years of Evolution* (Johns Hopkins Univ. Press, 2010).
2. Froese, D. G., Westgate, J. A., Reyes, A. V., Enkin, R. J. & Preece, S. J. Ancient permafrost and a future, warmer Arctic. *Science* **321**, 1648 (2008).
3. Westgate, J. A. *et al.* Gold Run tephra: A Middle Pleistocene stratigraphic and paleoenvironmental marker across west-central Yukon Territory, Canada. *Can. J. Earth Sci.* **46**, 465–478 (2009).
4. Eisenmann, V. Origins, dispersals, and migrations of *Equus* (Mammalia, Perissodactyla). *Courier Forschungsinstitut Senckenberg* **153**, 161–170 (1992).
5. Forsten, A. Mitochondrial-DNA timetable and the evolution of *Equus*: Comparison of molecular and paleontological evidence. *Ann. Zool. Fenn.* **28**, 301–309 (1992).
6. Goto, H. *et al.* A massively parallel sequencing approach uncovers ancient origins and high genetic variability of endangered Przewalski's horses. *Genome Biol. Evol.* **3**, 1096–1106 (2011).
7. Reyes, A. V., Froese, D. G. & Jensen, B. J. Response of permafrost to last interglacial warming: field evidence from non-glaciated Yukon and Alaska. *Quat. Sci. Rev.* **29**, 3256–3274 (2010).
8. Orlando, L. *et al.* True single-molecule DNA sequencing of a Pleistocene horse bone. *Genet. Res.* **21**, 1705–1719 (2011).
9. Lindahl, T. Instability and decay of the primary structure of DNA. *Nature* **362**, 709–715 (1993).
10. Willerslev, E. *et al.* Ancient biomolecules from deep ice cores reveal a forested southern Greenland. *Science* **317**, 111–114 (2007).
11. Miller, W. *et al.* Polar and brown bear genomes reveal ancient admixture and demographic footprints of past climate change. *Proc. Natl Acad. Sci. USA* **109**, E2382–E2390 (2012).
12. Cappellini, E. *et al.* Proteomic analysis of a pleistocene mammoth femur reveals more than one hundred ancient bone proteins. *J. Proteome Res.* **11**, 917–926 (2012).
13. Ginolhac, A. *et al.* Improving the performance of True Single Molecule Sequencing for ancient DNA. *BMC Genomics* **13**, 177 (2012).
14. Rasmussen, M. *et al.* Ancient human genome sequence of an extinct Palaeo-Eskimo. *Nature* **463**, 757–762 (2010).
15. Meyer, M. *et al.* A high-coverage genome sequence from an archaic Denisovan individual. *Science* **338**, 222–226 (2012).
16. van Doorn, N. L., Wilson, J., Holland, H., Soressi, M. & Collins, M. J. Site-specific deamidation of glutamine: a new marker of bone collagen deterioration. *Rapid Commun. Mass Spectrom.* **26**, 2319–2327 (2012).
17. Vilstrup, J. T. *et al.* Mitochondrial phylogenomics of modern and ancient equids. *PLoS ONE* **8**, e55950 (2013).
18. McFadden, B. J. & Carranza-Castaneda, O. Cranium of *Dinohippus mexicanus* (Mammalia Equidae) from the early Pliocene (latest Hemphillian) of central Mexico and the origin of *Equus*. *Bull. Florida Museum Nat. History* **43**, 163–185 (2002).
19. Weinstock, J. *et al.* Evolution, systematics, and phylogeography of Pleistocene horses in the new world: a molecular perspective. *PLoS Biol.* **3**, e241 (2005).
20. Green, R. E. *et al.* A draft sequence of the Neandertal genome. *Science* **328**, 710–722 (2010).
21. Li, H. & Durbin, R. Inference of human population history from individual whole-genome sequences. *Nature* **475**, 493–496 (2011).
22. Lorenzen, E. D. *et al.* Species-specific responses of Late Quaternary megafauna to climate and humans. *Nature* **479**, 359–364 (2011).
23. International Union for Conservation of Nature. IUCN Red List of Threatened Species, Version 2010.1, <http://www.iucnredlist.org> (downloaded 11 March 2010).
24. Reich, D. *et al.* Genetic history of an archaic hominin group from Denisova Cave in Siberia. *Nature* **468**, 1053–1060 (2010).
25. Bowling, A. T. *et al.* Genetic variation in Przewalski's horses, with special focus on the last wild caught mare, 231 Orlitza III. *Cytogenet. Genome Res.* **102**, 226–234 (2003).
26. Wade, C. M. *et al.* Genome sequence, comparative analysis, and population genetics of the domestic horse. *Science* **326**, 865–867 (2009).
27. Allentoft, M. E. *et al.* The half-life of DNA in bone: measuring decay kinetics in 158 dated fossils. *Proc. R. Soc. Lond. B* **279**, 4724–4733 (2012).
28. Kelstrup, C. D., Young, C., Lavalley, R., Nielsen, M. L. & Olsen, J. V. Optimized fast and sensitive acquisition methods for shotgun proteomics on a quadrupole orbitrap mass spectrometer. *J. Proteome Res.* **11**, 3487–3497 (2012).
29. Li, H. & Durbin, R. Fast and accurate short read alignment with Burrows-Wheeler transform. *Bioinformatics* **25**, 1754–1760 (2009).

**Supplementary Information** is available in the online version of the paper.

**Acknowledgements** We thank T. Brand, the laboratory technicians at the Danish National High-throughput DNA Sequencing Centre and the Illumina sequencing platform at SciLifeLab-Uppsala for technical assistance; J. Clausen for help with the donkey samples; S. Rasmussen for computational assistance; J. N. MacLeod and T. Kalbfleisch for discussions involving the re-sequencing of the horse reference genome; and S. Sawyer for providing published ancient horse data. This work was supported by the Danish Council for Independent Research, Natural Sciences (FNU); the Danish National Research Foundation; the Novo Nordisk Foundation; the Lundbeck Foundation (R52-A5062); a Marie-Curie Career Integration grant (FP7 CIG-293845); the National Science Foundation ARC-0909456; National Science Foundation DBI-0906041; the Searle Scholars Program; King Saud University Distinguished Scientist Fellowship Program (DSFP); Natural Science and Engineering Research Council of Canada; the US National Science Foundation DMR-0923096; and a grant RC2 HG005598 from the National Human Genetics Research Institute (NHGRI). A.G. was supported by a Marie-Curie Intra-European Fellowship (FP7 IEF-299176). M.F. was supported by EMBO Long-Term Post-doctoral Fellowship (ALTF 229-2011). A.-S.M. was supported by a fellowship from the Swiss National Science Foundation (SNSF). Mi.S. was supported by the Lundbeck foundation (R82-5062).

**Author Contributions** L.O. and E.W. initially conceived and headed the project; G.Z. and Ju.W. headed research at BGI; L.O. and E.W. designed the experimental research project set-up, with input from B.S. and R.N.; D.F. and G.D.Z. provided the Thistle Creek specimen, stratigraphic context and morphological information, with input from K.K.; K.H.R., B.S., K.G., D.C.M., D.F.A., K.A.S.A.-R. and M.F.B. provided samples; L.O., J.T.V., Ma.R., M.H., C.M. and J.S. did ancient and modern DNA extractions and constructed Illumina DNA libraries for shotgun sequencing; Ja.W. did the independent replication in Oxford; Ma.S. did ancient DNA extractions and generated target enrichment sequence data; Ji.M. and X.W. did Illumina libraries on donkey extracts; K.M., C.M. and A.S.-O. performed Illumina sequencing for the Middle Pleistocene and the 43-kyr-old horse genomes, the five domestic horse genomes and the Przewalski's horse genome at Copenhagen, with input from Mo.R.; Ji.M. and X.W. performed Illumina sequencing for the Middle Pleistocene and the donkey genomes at BGI; J.F.T. headed true Single DNA Molecule Sequencing of the Middle Pleistocene genome; A.G., B.P. and Mi.S. did the mapping analyses and generated genome alignments, with input from L.O. and A.K.; Jo.V. and T.S.-P. did the metagenomic analyses, with input from A.G., B.P., S.B. and L.O.; Jo.V. and T.S.-P. did the *ab initio* prediction of the donkey genes and the identification of the Y chromosome scaffolds, with input from A.G. and Mi.S.; L.O., A.G. and P.L.F.J. did the damage analyses, with input from I.M.; A.G. did the functional SNP assignment; A.M.V.V. and L.O. did the PCA analyses, with input from O.R.; B.S. did the phylogenetic and Bayesian skyline reconstructions on mitochondrial data; Mi.S. did the phylogenetic and divergence dating based on nuclear data, with input from L.O.; A.G. did the PSMC analyses using data generated by C.J.R. and L.A.; L.O. and A.G. did the population divergence analyses, with input from J.C., R.N. and M.F.; L.O., A.G. and T.K. did the selection scans, with input from A.-S.M. and R.N.; A.A., I.M. and M.F. did the admixture analyses, with input from R.N.; L.O. and A.G. did the analysis of paralogues and structural variation; Ja.W. and A.D. did the amino-acid composition analyses; E.C., C.D.K., D.S., L.J.J. and J.V.O. did the proteomic analyses, with input from M.T.P.G. and A.M.V.V.; L.O. and V.E. performed the morphological analyses, with input from D.F. and G.D.Z.; L.O. and E.W. wrote the manuscript, with critical input from M.H., B.S., Jo.M. and all remaining authors.

**Author Information** All sequence data have been submitted to Sequence Read Archive under accession number SRA082086 and are available for download, together with final BAM and VCF files, *de novo* donkey scaffolds, and proteomic data at <http://geogenetics.ku.dk/publications/middle-pleistocene-omics>. Reprints and permissions information is available at [www.nature.com/reprints](http://www.nature.com/reprints). The authors declare no competing financial interests. Readers are welcome to comment on the online version of the paper. Correspondence and requests for materials should be addressed to L.O. (Lorlando@snm.ku.dk), Ju.W. (wangjun30@gmail.com) or E.W. (ewillerslev@snm.ku.dk).



## METHODS

**Genome sequencing.** All fossil specimens were extracted in facilities designed to analyse ancient DNA using silica-based extraction procedures<sup>30,31</sup> (Supplementary Information, section 2). A total number of 16 ancient horse extracts were built into Illumina libraries (Supplementary Information, section 2) and shotgun-sequenced at the Centre for GeoGenetics (Supplementary Tables 2.3 and 4.9). The full mitochondrial genome of a total number of 16 ancient horse specimens was captured using MYselect in-solution target enrichment kit (Supplementary Information, section 3.3b) following library construction<sup>32</sup>, and sequenced at Penn State/UCSC (Supplementary Tables 2.4 and 4.10). The combination of shotgun sequencing and capture-based sequencing performed in those two laboratories resulted in the characterization of 23 novel pseudo-complete ancient horse mitochondrial genomes (Supplementary Table 8.1). Additional sequencing was compatible with the characterization of draft nuclear genomes of two ancient horse specimens (Supplementary Tables 4.9 and 4.11): that of a Middle Pleistocene horse from Thistle Creek (560–780 kyr BP), and that of a Late Pleistocene horse from the Taymyr Peninsula (CGG10022, cal. 42,012–40,094 BC; Supplementary Table 2.3). The Thistle Creek horse draft genome was characterized using Illumina (11,593,288,435 reads, Supplementary Table 3.2; coverage = 0.74×, Supplementary Table 4.11) and Helicos sequence data (654,292,583 reads, Supplementary Table 3.5; coverage = 0.38×, Supplementary Table 4.11). Ancient specimens were radiocarbon dated at Belfast 14Chrono facilities (Supplementary Tables 2.3 and 2.4). The Middle Pleistocene Thistle Creek horse bone is associated with infinite radiocarbon dates.

Modern equine genomes from five modern horse breeds (Arabian, Icelandic, Norwegian fjord, Standardbred, Thoroughbred), one Przewalski's horse individual and one domestic donkey were characterized using Illumina paired-end sequencing (Supplementary Information, sections 3.1.b.3–3.1.b.4). DNA was extracted and prepared into libraries (Supplementary Information, section 2.2) in laboratories located in buildings physically separated from ancient DNA laboratory facilities. Modern horse genomes were sequenced at the Danish National High-Throughput DNA Sequencing Centre whereas the donkey genome was characterized at BGI, Shenzhen (Supplementary Information, 3.1). Trimmed reads were aligned to the horse reference genome EquCab2.0 (ref. 26), excluding the mitochondrial genome and chrUn, using BWA<sup>29</sup> (Supplementary Information, section 4.2). We generated a draft *de novo* assembly of the donkey genome using de Bruijn graphs as implemented within SOAPdenovo<sup>33</sup> (Supplementary Information, section 4.1.a), built gene models using Augustus<sup>34</sup> and SpyPhy<sup>35</sup> (Supplementary Information, section 4.1.b), and identified candidate scaffolds originating from the X and Y chromosomes (Supplementary Information, sections 4.1.c and 4.1.d). Sequence reads were also aligned against *de novo* assembled donkey scaffolds (Supplementary Information, section 4.2). For all genomes characterized in this study, we estimated that overall error rates were low (Supplementary Information, section 4.4.a), with type-specific error rates inferior to  $5.3 \times 10^{-4}$ , except for ancient genomes where post-mortem DNA damage inflated the GC→AT mis-incorporation rates (Supplementary Table 4.12). Metagenomic assignment of all reads generated from the Thistle Creek horse bone was performed using BWA-sw<sup>36</sup> and mapping against a customized database, which included all bacterial, fungal and viral genomes available (Supplementary Information, section 4.3).

**Genomic variation.** SNPs were called for modern genomes using the mpileup command from SAMtools (0.1.18)<sup>37</sup> and bcftools, and were subsequently filtered using vcutils varFilter and stringent quality filter criteria (Supplementary Information, section 5.2). We compared overall SNP variation levels (Supplementary Information, sections 5.2b and 11.2; Supplementary Table 11.10) present in modern horse genomes. We also compared genotypic information extracted from the genomes characterized in this study to that of 362 horse individuals belonging to 14 modern domestic breeds and 9 Przewalski's horses<sup>38</sup>. Genotype and the breed/population of origin were converted into PLINK map and ped formats<sup>39</sup> and further analysed using the software Smartpca of EIGENSOFT 4.0 (ref. 40). PCA plots were generated using R 2.12.2 (ref. 41) (Supplementary Figs 5.6–5.14). Filtered SNPs that passed our quality criteria (Supplementary Information, section 5.2.a) were categorized into a series of functional and structural genomic classes using the Perl script variant\_effect\_predictor.pl version 2.5 (ref. 42) available at Ensembl and the EquCab2.0 annotation database version 65 (Supplementary Information, section 5.2b). We also screened our genome data for a list of 36 loci that have been associated with known phenotypic defects and/or variants (Supplementary Information, section 5.2e and Supplementary Tables 5.19 and 5.20). We systematically looked in the donkey genome for the presence of genes that have been identified in the horse reference genome as paralogues. This was performed by downloading from Ensembl a list of 15,310 paralogues and extracting genomic coordinates of the 15,171 paralogues that were located on the 31 autosomes and the X chromosome. We next calculated the average depth-of-coverage of these regions using the alignment of donkey reads against the horse reference genome. A total number of 258 paralogues exhibited no hit and were

putatively missing from the donkey genome. We further tested for the presence of those paralogues in the different ancient horse genomes characterized here, using a model where observed depth-of-coverage in ancient individual (Illumina data) is a function of the depth-of-coverage observed in a modern horse male individual, local %GC and read length (Supplementary Information, section 5.1.c). A similar model was used for identifying segmental duplications in modern equid genomes (Supplementary Information, section 5.1b).

**DNA damage.** We estimated DNA damage levels in the Thistle Creek horse sample and compared these to the DNA damage levels observed among other Pleistocene horse fossil bones, all associated with more recent ages (Supplementary Tables 2.3 and 2.4). All fossil specimens analysed were permafrost-preserved, limiting environmental-dependent variation in DNA damage rates<sup>43</sup>. DNA fragmentation and nucleotide mis-incorporation patterns were plotted using the mapDamage package<sup>44</sup> (Supplementary Information, section 6.2). We then developed a DNA damage likelihood model after the model presented in ref. 45, with slight modifications, where ancient DNA fragments consist of four non-overlapping regions from 5' to 3' ends: (1) a single-stranded overhang; (2) a double-stranded region that extends until a single-strand break is encountered; (3) a double-stranded region that extends 3' of the single strand break previously mentioned, and; (4) a single stranded overhang (Supplementary Information, section 6.3 and Supplementary Fig. 6.39). All model parameters were estimated using maximum likelihood. Confidence intervals were found by taking each parameter in turn and slowly adjusting that parameter while maximizing the likelihood with respect to all other parameters until finding the points above and below with likelihood 1.92 units below the maximum. Finally, we used the model framework presented in ref. 27 to recover direct estimates of DNA survival rates from next-generation sequence data (Supplementary Information, section 6.4). We restricted our analyses (1) to the distribution of templates showing sizes superior to the modal size category; and (2) to collapsed paired-end reads, as the size of the latter corresponds to the exact size of ancient DNA fragments inserted in the DNA library.

**Amino acid and proteomic analyses.** A sample of the Middle Pleistocene Thistle Creek horse bone was embedded in Epothin resin under sterile conditions, cut and polished until chemical analysis of the sample surface could be performed with a time-of-flight secondary ion mass spectrometer (TOF-SIMS) instrument (Supplementary Information, section 7). We also performed high-resolution mass spectrometry (MS)-based shotgun proteomics analysis using two fragments from the Middle Pleistocene Thistle Creek horse bone (weighing 86 and 78 mg, respectively) in order to retrieve large-scale molecular information. The overall methodological approach follows the procedure that was previously applied to survey the remains of the bone proteome from three mammoth specimens living approximately 11–43 kyr ago<sup>12</sup>, although with significant improvements (Supplementary Information, sections 7.2–7.3). Strict measures to avoid contamination and exclude false-positive results were implemented at every step, allowing to confidently profile 73 ancient bone proteins (from the attribution of 659 unique peptides based on 13,030 spectra). Raw spectrum files were searched on a local workstation using the MaxQuant algorithm version 1.2.2.5 (ref. 46) and the Andromeda peptide search engine<sup>47</sup> against the target/reverse list of horse proteins available from Ensembl (EqCab2.64.pep.all), the IPI v.3.37 human protein database and the common contaminants such as wool keratins and porcine trypsin, downloaded from Uniprot. The spectra were also searched against the Uniprot protein database, taxonomically restricted to chordates, and non-horse peptides were identified and eventually removed. Proteomic data were further compared to similar information already generated from fossil specimens collected in Siberian permafrost and temperate environments. Proteome-wide incidence of deamidation was estimated in relation with protein recovery to further assess the molecular state of preservation of ancient proteins.

**Phylogenetic analyses.** The CDS of protein-coding genes were selected from the Ensembl website, keeping the transcripts with the most exons in cases where multiple records were found for a single gene. We then extracted corresponding genomic coordinates, filtered for DNA damage/sequencing errors, and aligned each gene using MAFFT G-INS-i ('ginsi')<sup>48,49</sup> (Supplementary Information, section 8.3a). Phylogenetic analysis was carried out using a super-matrix approach. First RAXML v7.3.2<sup>50</sup> was run to generate the parsimony starting trees. The final tree inference was performed using RAXML-Light v1.1.1<sup>51</sup> and one GTRGAMMA model of nucleotide substitutions for each gene partition (codon positions 1 and 2, versus 3). Node support was estimated using 100 bootstrap pseudo-replicates. Bootstrap trees were dated using 'r8s', using the PL method and the Truncated Newton (TN) algorithm, with a smoothing value of 1,000 (ref. 52), or using the Langley-Fitch (LF) method (Supplementary Information, section 8.3.c). The date of the root node was constrained to 4.0–4.5 Myr, the date of CGG10022 was fixed to 43 kyr, and the date of the Thistle Creek specimen was constrained to 560–780 kyr BP. We also performed phylogenetic analyses of whole mitochondrial

genomes (Supplementary Information, section 8.1), Y chromosome (Supplementary Information, section 8.2) and a series of topological tests using approximately unbiased tests as implemented in the CONSEL makermt program<sup>33</sup> (Supplementary Information, section 8.3b).

**Demographic reconstructions.** Past population demographic changes were reconstructed from whole diploid genome information using the pairwise sequentially Markovian coalescent model (PSMC)<sup>21</sup> and excluding sequence data originating from sex chromosomes and scaffolds (Supplementary Information, section 9). For low coverage genomes ( $<20\times$ ), we applied a correction based on an empirical uniform false-negative rate. Three different generation times of 5, 8 and 12 years were considered in agreement with the range of generation times reported in the literature<sup>23,54–56</sup>. Mutation rates were estimated using quartet genome alignments where the donkey was used as out-group (Supplementary Information, section 10.1c). We also reconstructed past horse population demographic changes by means of Bayesian skyline plots using the software BEAST v1.7.2 (refs 57, 58) (Supplementary Information, section 9.2). Complete mitochondrial genomes were aligned and partitioned as described in Supplementary Information, section 8.1b, and a strict clock model was selected. We ran two independent MCMC chains of 50 million iterations each, sampling from the posterior every 5,000 iterations. We discarded the first 10% of each chain as burn-in, and after visual inspection in Tracer v1.5<sup>59</sup> to ensure that the replicate chains had converged on similar values, combined the remainder of the two runs.

**Population split.** We followed the method presented in ref. 20 to estimate the population divergence date of ancient and modern horses (Supplementary Information, section 10.1). This method was also applied to date the population divergence of Przewalski's horses and domestic horses (Supplementary Information, section 10.2), as both our phylogenetic analyses and admixture tests supported those as two independent populations (Supplementary Information, sections 8.3 and 12). In this method, we focus on heterozygous sites in one of the two populations and randomly sample one of the two possible alleles (ancestral or derived) in the individual belonging to the first population. The number of times a derived allele is sampled ( $F$  statistics) can be used to recover a full posterior distribution of the population divergence time using (serial) coalescent simulations and approximate Bayesian computation (ABC) (Supplementary Information, section 10.1). For dating the divergence time between the Przewalski's horse population and domestic breeds, we also performed coalescent simulations using ms<sup>60</sup> assuming different divergence times in order to compute the expected relative occurrences of 4 genotype configurations (Supplementary Information, section 10.2b). We assumed that no gene flow occurred after the population split, in agreement with the absence of detectable levels of admixture. The divergence time was then estimated by minimizing the root mean square deviation (r.m.s.d.) between observed and expected genotype configurations. We minimized the r.m.s.d. using a golden search algorithm. We repeated the minimization from different starting values to ensure convergence.

**Selection scans.** We used quartet alignments including the donkey as out-group, one ancient horse and two modern horses to scan for genomic regions where the two modern horses shared unusual accumulation of derived alleles (Supplementary Information, section 11.1). We used a sliding window approach on the entire genome, with a window size of 200 kb and calculated an unbiased proxy for selection using the 'delta technique' (see for example ref. 61). We then used an outlier approach to identify candidate loci with a conservative false-positive rate of 0.01. We further retrieved transcript IDs from the different genomic regions identified and performed functional clustering analyses in DAVID<sup>62</sup>. We estimated genetic diversity (theta Watterson) within the Przewalski's horse population and among modern horse breeds using sliding windows of 50 kb. For this, we estimated the population scaled mutation rate and used an empirical Bayes method where we took the uncertainty of the data into account by using genotype likelihoods instead of calling genotypes. We computed the genotype likelihoods assuming a model similar to that of SAMtools version 0.1.18 (ref. 37) (Supplementary Information, section 11.2). Genomic windows showing excessive proportions of segregating sites with regards to species divergence ( $>5\%$ ) or coverage  $<90\%$  were discarded. We estimated Tajima's  $D$  following the same procedure and identified genomic regions showing minimal Tajima's  $D$  values and low genetic diversity among breeds but not in the Przewalski's horse population as a conservative set of gene candidates for positive selection among modern horse breeds. Finally, we scanned modern horse genomes for long homozygosity tracts, which could be indicative of selective sweeps<sup>63</sup>. We used 2-Mb sliding windows and ignored sites showing coverage inferior to 8. This resulted in the identification of 456 outlier regions within 8 modern horse genomes.

**Admixture analyses.** In order to investigate if there was evidence for gene flow between the Przewalski's horse population and four modern horse domestic breeds (Arabian, Icelandic, Norwegian fjord and Standardbred), we performed ABBA-BABA tests<sup>20,24</sup>. To avoid introducing bias due to differences in sequencing

depth we based the tests on data achieved by sampling one allele randomly from each horse at each site. First we used the domestic donkey as out-group, then the Middle Pleistocene Thistle Creek horse. When using the Thistle Creek horse as out-group we removed all sites showing transitions to avoid spurious patterns resulting from nucleotide misincorporations related to post-mortem DNA damage. We estimated the standard error of the test statistic using 'delete-m Jackknife for unequal m' with 10-Mb blocks<sup>64</sup> (Supplementary Information, section 12.1). We also scanned genome alignments to record the proportion of shared SNPs between Przewalski's horse and each horse breed (Supplementary Information, section 12.6), a proxy for recent admixture events that are expected to result in the introgression of alleles from the admixer to the admixed genome and long tracts of shared polymorphisms. Finally, we compared our Przewalski's horse individual to other individuals with different levels of admixture in their pedigree. We extracted genotype information from the Przewalski's horse genome for SNP coordinates already genotyped across 9 Przewalski horse individuals<sup>38</sup>. Genotypic information from two Mongolian horses was added as out-group. We next selected the best model of nucleotide substitution using modelgenerator v0.85 (ref. 65) and performed maximum likelihood phylogenetic analyses using PhyML 3.0 (ref. 66) (Supplementary Information, section 12.5). We further confirmed the phylogenetic position of our Przewalski's horse individual together with Rosa (KB3838), Basil (KB7413) and Roland (KB3063), three individuals for which no admixture with domestic horses could be detected in previous studies<sup>25</sup> by means of Approximate-Unbiased (AU) and Shimodeira-Hasegawa (SH-) tests, as implemented in CONSEL<sup>53</sup>. **Morphological analyses.** We measured the metapodial of Thistle Creek early Middle Pleistocene bone for 6 dimensions, despite incomplete preservation of its distal end (Supplementary Information, section 1.2). These measurements were compared to 30 metatarsals of *E. lambei*, 9 metatarsals of *E. cf. scotti* of Klondike, Central Yukon, Canada (Supplementary Information, section 1.2) and to extant horses (Supplementary Information, section 1.3). Comparisons were made using Simpson's ratio diagrams that provide a standard and accurate comparison of both size and shape, for a single bone or a group of bones (Supplementary Figs 1.2 and 1.3). We also measured taxonomically informative morphometric features on the skull and post-cranial complete skeleton of the modern Przewalski's horse specimen that was genome sequenced. We compared those to a collection of horse measurements available for horses, filtering for specimens of similar age and using principal component analyses (Supplementary Information, section 1.4).

30. Orlando, L. *et al.* Revisiting the recent evolutionary history of equids using ancient DNA. *Proc. Natl Acad. Sci. USA* **106**, 21754–21759 (2009).
31. Rohland, N. & Hofreiter, M. Ancient DNA extraction from bones and teeth. *Nature Protocols* **2**, 1756–1762 (2007).
32. Meyer, M. & Kircher, M. Illumina sequencing library preparation for highly multiplexed target capture and sequencing. *Cold Spring Harb. Protoc.* **6**, <http://dx.doi.org/10.1101/pdb.prot5448> (2010).
33. Luo, R. *et al.* SOAPdenovo2: an empirically improved memory-efficient short-read de novo assembler. *GigaScience* **1**, 18 (2012).
34. Stanke, M., Steinkamp, R., Waack, S. & Morgenstern, B. AUGUSTUS: a web server for gene finding in eukaryotes. *Nucleic Acids Res.* **32**, W309–W312 (2004).
35. Carlton, J. M. *et al.* Draft genome sequence of the sexually transmitted pathogen *Trichomonas vaginalis*. *Science* **315**, 207–212 (2007).
36. Li, H. & Durbin, R. Fast and accurate long-read alignment with Burrows-Wheeler transform. *Bioinformatics* **26**, 589–595 (2010).
37. Li, H. *et al.* The Sequence alignment/map (SAM) format and SAMtools. *Bioinformatics* **25**, 2078–2079 (2009).
38. McCue, M. E. *et al.* A high density SNP array for the domestic horse and extant *Perissodactyla*: utility for association mapping, genetic diversity, and phylogeny studies. *PLoS Genet.* **8**, e1002451 (2012).
39. Purcell, S. *et al.* PLINK: a tool set for whole-genome association and population-based linkage analyses. *Am. J. Hum. Genet.* **81**, 559–575 (2007).
40. Patterson, N., Price, A. L. & Reich, D. Population structure and eigenanalysis. *PLoS Genet.* **2**, e190 (2006).
41. R Development Core Team. A language and environment for statistical computing. <http://www.R-project.org> (R Foundation for Statistical Computing, 2011).
42. McLaren, W. *et al.* Deriving the consequences of genomic variants with the Ensembl API and SNP Effect Predictor. *Bioinformatics* **26**, 2069–2070 (2010).
43. Smith, C. I., Chamberlain, A. T., Riley, M. S., Stringer, C. & Collins, M. J. The thermal history of human fossils and the likelihood of successful DNA amplification. *J. Hum. Evol.* **45**, 203–217 (2003).
44. Ginolhac, A., Rasmussen, M., Gilbert, T. M., Willerslev, E. & Orlando, L. mapDamage: testing for damage patterns in ancient DNA sequences. *Bioinformatics* **27**, 2153–2155 (2011).
45. Briggs, A. W. *et al.* Patterns of damage in genomic DNA sequences from a Neandertal. *Proc. Natl Acad. Sci. USA* **104**, 14616–14621 (2007).
46. Cox, J. & Mann, M. MaxQuant enables high peptide identification rates, individualized p.p.b.-range mass accuracies and proteome-wide protein quantification. *Nature Biotechnol.* **26**, 1367–1372 (2008).
47. Cox, J. *et al.* Andromeda: a peptide search engine integrated into the MaxQuant environment. *J. Proteome Res.* **10**, 1794–1805 (2011).

48. Katoh, K., Misawa, K., Kuma, K. & Miyata, T. MAFFT: a novel method for rapid multiple sequence alignment based on fast Fourier transform. *Nucleic Acids Res.* **30**, 3059–3066 (2002).
49. Katoh, K. & Toh, H. Recent developments in the MAFFT multiple sequence alignment program. *Brief. Bioinform.* **9**, 286–298 (2008).
50. Stamatakis, A. RAXML-VI-HPC: maximum likelihood-based phylogenetic analyses with thousands of taxa and mixed models. *Bioinformatics* **22**, 2688–2690 (2006).
51. Stamatakis, A. *et al.* RAXML-Light: a tool for computing Terabyte phylogenies. *Bioinformatics* **28**, 2064–2066 (2012).
52. Sanderson, M. J. r8s: inferring absolute rates of molecular evolution and divergence times in the absence of a molecular clock. *Bioinformatics* **19**, 301–302 (2003).
53. Shimodaira, H. & Hasegawa, M. CONSEL: for assessing the confidence of phylogenetic tree selection. *Bioinformatics* **17**, 1246–1247 (2001).
54. Lippold, S., Matzke, N. J., Reissmann, M. & Hofreiter, M. Whole mitochondrial genome sequencing of domestic horses reveals incorporation of extensive wild horse diversity during domestication. *BMC Evol. Biol.* **11**, 328 (2011).
55. Achilli, A. *et al.* Mitochondrial genomes from modern horses reveal the major haplogroups that underwent domestication. *Proc. Natl Acad. Sci. USA* **109**, 2449–2454 (2012).
56. Warmuth, V. *et al.* Reconstructing the origin and spread of horse domestication in the Eurasian steppe. *Proc. Natl Acad. Sci. USA* **109**, 8202–8206 (2012).
57. Drummond, A. J. & Rambaut, A. BEAST: Bayesian evolutionary analysis by sampling trees. *BMC Evol. Biol.* **7**, 214 (2007).
58. Drummond, A. J., Suchard, M. A., Xie, D. & Rambaut, A. Bayesian phylogenetics with BEAUti and the BEAST 1.7. *Mol. Biol. Evol.* **29**, 1969–1973 (2012).
59. Rambaut, A. & Drummond, A. J. Tracer v1. 5, <http://beast.bio.ed.ac.uk/Tracer> (2009).
60. Hudson, R. R. Generating samples under a Wright-Fisher neutral model of genetic variation. *Bioinformatics* **18**, 337–338 (2002).
61. Zhang, Z. *Computational Molecular Evolution* (Oxford Univ. Press, 2006).
62. Huang, D. W., Sherman, B. T. & Lempicki, R. A. Systematic and integrative analysis of large gene lists using DAVID Bioinformatics Resources. *Nature Protocols* **4**, 44–57 (2009).
63. Nielsen, R. Molecular signatures of natural selection. *Annu. Rev. Genet.* **39**, 197–218 (2005).
64. Busing, F. M. T. A., Meijer, E. & Van Der Leeden, R. Delete-*m* Jackknife for Unequal *m*. *Stat. Comput.* **9**, 3–8 (1999).
65. Keane, T. M., Creevey, C. J., Pentony, M. M., Naughton, T. J. & McInerney, J. O. Assessment of methods for amino acid matrix selection and their use on empirical data shows that ad hoc assumptions for choice of matrix are not justified. *BMC Evol. Biol.* **6**, 29 (2006).
66. Guindon, S. *et al.* New algorithms and methods to estimate Maximum-Likelihood phylogenies: assessing the performance of PhyML 3.0. *Syst. Biol.* **59**, 307–321 (2010).



# Variation and genetic control of protein abundance in humans

Linfeng Wu<sup>1\*</sup>, Sophie I. Candille<sup>1\*</sup>, Yoonha Choi<sup>1</sup>, Dan Xie<sup>1</sup>, Lihua Jiang<sup>1</sup>, Jennifer Li-Pook-Than<sup>1</sup>, Hua Tang<sup>1</sup> & Michael Snyder<sup>1</sup>

Gene expression differs among individuals and populations and is thought to be a major determinant of phenotypic variation. Although variation and genetic loci responsible for RNA expression levels have been analysed extensively in human populations<sup>1–5</sup>, our knowledge is limited regarding the differences in human protein abundance and the genetic basis for this difference. Variation in messenger RNA expression is not a perfect surrogate for protein expression because the latter is influenced by an array of post-transcriptional regulatory mechanisms, and, empirically, the correlation between protein and mRNA levels is generally modest<sup>6,7</sup>. Here we used isobaric tag-based quantitative mass spectrometry to determine relative protein levels of 5,953 genes in lymphoblastoid cell lines from 95 diverse individuals genotyped in the HapMap Project<sup>8,9</sup>. We found that protein levels are heritable molecular phenotypes that exhibit considerable variation between individuals, populations and sexes. Levels of specific sets of proteins involved in the same biological process covary among individuals, indicating that these processes are tightly regulated at the protein level. We identified *cis*-pQTLs (protein quantitative trait loci), including variants not detected by previous transcriptome studies. This study demonstrates the feasibility of high-throughput human proteome quantification that, when integrated with DNA variation and transcriptome information, adds a new dimension to the characterization of gene expression regulation.

We used isobaric tandem mass tag (TMT)-based quantitative mass spectrometry to determine protein expression variation of lymphoblastoid cell lines (LCLs) derived from 95 ethnically diverse individuals genotyped in the HapMap Consortium. The samples consisted of 53 Caucasians of northern and western European ancestry (CEU); 33 Yorubans of African ancestry from Ibadan, Nigeria (YRI); eight Han Chinese from Beijing (CHB); and one Japanese from Tokyo (JPT). CHB and JPT were grouped together as East Asians (ASN). The ASN individuals were unrelated whereas the CEU and YRI groups included trios (mother, father and offspring), and had 42 and 23 unrelated individuals, respectively. In each experiment, we used unique TMT tags to label trypsin-digested peptides from six cell lines, including a reference cell line (GM12878) and five other cell lines followed by two-dimensional liquid chromatography tandem mass spectrometry (2D LC-MS/MS) analysis (Fig. 1a).

Fifty-one experiments were performed that included biological replicates; each resulted in an average of 54,000 high-confidence peptide identifications and quantifications. Protein expression in a cell line was quantified relative to the reference cell line, using peptides that uniquely mapped to a gene and lacked any known polymorphic protein coding variant among the 95 individuals (Supplementary Methods). A total of 5,953 proteins were quantified based on the analysis of 2,159,989 peptide spectra (Supplementary Table 1). To

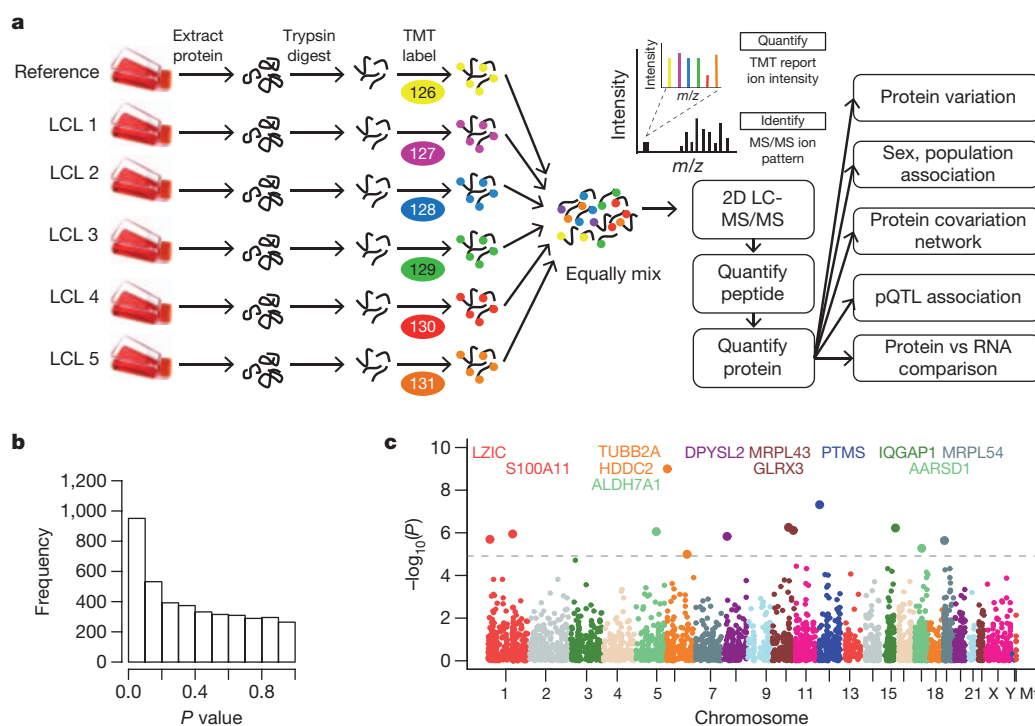


**Figure 1 | Overview of workflow and protein association with ethnicity.** **a**, Flow chart of experimental scheme. In each experiment, peptide digests from a reference cell line (GM12878) and five other cell lines were each labelled with one of the TMT-sixplex tags. Labelled peptides were equally mixed and subjected to identification and quantification by mass spectrometry, and then used for protein quantification. A total of 51 experiments were performed. **b**, The *P* value distribution for the difference in protein levels between CEU and YRI shows enrichment at small *P* values. **c**, *P* value of protein level differences between CEU and YRI plotted as a function of the genomic coordinate for each protein. The dashed line is at significance threshold Bonferroni  $P = 0.05$ . All of the proteins that passed the threshold are highlighted with larger dots and labelled with gene names. Proteins that differed between CEU and YRI are distributed throughout the genome.

<sup>1</sup>Department of Genetics, Stanford University School of Medicine, Stanford, California 94305, USA.

\*These authors contributed equally to this work.

ensure adequate sample size and statistical power, most of the analyses described below focused on the 4,053 proteins that were detected in more than 50% of the 74 unrelated individuals.

To assess reproducibility, we analysed the correlation of protein level measurements between replicate and non-replicate cell lines. We observed that the Spearman's rank correlation coefficient among non-replicates was much less than that of biological replicates, with median values 0.19 versus 0.56 (Supplementary Fig. 1a), suggesting that the TMT-based quantitative mass spectrometry technique can reproducibly detect variation in protein expression across individuals.

We observed considerable inter-individual protein variation: a median of 5.7% of the proteome changed more than 1.5-fold between pairs of individuals (Supplementary Fig. 1b). This figure is probably an underestimate because of precursor ion interference<sup>10,11</sup>. Although the CEU, YRI and ASN HapMap cell lines were established in separate batches and differ in age, the coefficients of variation (CV) estimated in the different populations are highly correlated (Spearman's rank correlation coefficients 0.68–0.82, Supplementary Fig. 1c and Supplementary Table 2), indicating that the level of inter-individual protein variation is similar across populations; therefore the observed pattern of protein variation is unlikely to be dominated by these exogenous factors. Furthermore, by estimation of potential peptide phosphorylation, we found little evidence that the measurements of protein variation were influenced by post-translational modification (Supplementary Fig. 2).

To characterize the most and least variable proteins, we performed Gene Ontology (GO) category analysis and found that the most variable proteins were enriched in immune response, whereas the least variable proteins were enriched in housekeeping processes (Supplementary Fig. 3). These findings are similar to those observed in previous mRNA studies<sup>12</sup>. However, caution should be taken when comparing variability between proteins, because peptide ratios measured by isobaric tag-based mass spectrometry can be distorted during precursor ion isolation<sup>10,11</sup>. Because precursor ion interference mostly compresses the peptide ratio towards one, the underlying variation in some protein expressions may be substantially underestimated. Nonetheless, our results demonstrate a considerable variation in protein levels, particularly in immune response proteins.

As a proof of principle demonstrating that the protein measurements reflect biological variation, we sought to detect protein variation associated with biological attributes such as sex and ethnicity. To avoid the correlation between parents and offspring, we only used unrelated individuals for the analyses below, with the exception of the heritability calculations, which were based on the trios.

To identify proteins differentially expressed between males ( $n = 36$ ) and females ( $n = 38$ ), we regressed protein levels on sex, adjusting for average population differences (Supplementary Table 3). The distribution of  $P$  values for proteins exhibiting sex differences shows a modest enrichment at small  $P$  values (Supplementary Fig. 4a). At a false discovery rate (FDR) of 10%, 12 proteins are differentially expressed between sexes, among which seven have a Bonferroni corrected  $P$  value  $< 0.05$  and all seven map to the X or the Y chromosome (Supplementary Fig. 4b). These results indicate that our study captures bona fide variation in protein expression.

Similarly, we examined population differences in protein expression. We focused on the CEU and YRI unrelated individuals (42 CEU versus 23 YRI), as the ASN sample size was smaller. At an FDR of 10%, 247 proteins are differentially expressed between CEU and YRI (Supplementary Table 4). The distribution of  $P$  values for population differences shows a much greater enrichment of small  $P$  values than for sex differences, and they are distributed throughout the genome (Fig. 1b, c). This finding further corroborates that our study can detect meaningful biological differences in protein expression.

Proteins that are part of the same complex or in the same biological process might be expected to vary synchronously, indicative of a coordinated regulation of biological components and pathways. To determine if this is the case and to identify proteins that exhibit covariation, we

constructed protein covariation networks using sparse partial correlation estimation<sup>13</sup>. In a sparse network, which connects proteins showing the strongest evidence of direct correlation (Supplementary Methods), 223 edges connect 278 proteins; these include five major clusters, each with at least 9 proteins (that is, nodes) (Fig. 2 and Supplementary Table 5). We performed GO category analysis for the five clusters; three were enriched in protein metabolic process ( $P = 4 \times 10^{-4}$ ), translation ( $P = 2 \times 10^{-9}$ ) and glycolysis ( $P = 2 \times 10^{-11}$ ), respectively. We also found many smaller clusters that consisted of subunits of protein complexes, for example, minichromosome maintenance complex components. Many of these edges connect known interacting proteins. Enrichment analysis showed that the known interacting proteins are significantly enriched in the protein covariation network ( $P = 5 \times 10^{-6}$ ). Relaxing the stringency of direct correlation while maintaining high statistical confidence, assessed by permutation and sub-sampling analyses (Supplementary Methods), yielded a denser network with 1,012 edges connecting 944 proteins, featuring a 'megacuster' of proteins that is enriched in translation ( $P = 2 \times 10^{-6}$ ) (Supplementary Table 6). These results demonstrated that protein expression in a cell is highly coordinated and that, for several important biological processes (for example, translation and glycolysis), tight control of protein levels is maintained.

We also investigated the correspondence between protein–protein covariation and RNA–RNA covariation obtained by RNA sequencing (RNA-seq) in CEU and YRI LCLs<sup>2,3</sup>. We observed that covarying proteins tend to correspond to covarying RNAs with median correlation 0.42 for CEU and 0.21 for YRI (Supplementary Fig. 5). However, protein and RNA do not correlate perfectly, indicating that variation in protein levels is not entirely regulated through RNA expression.

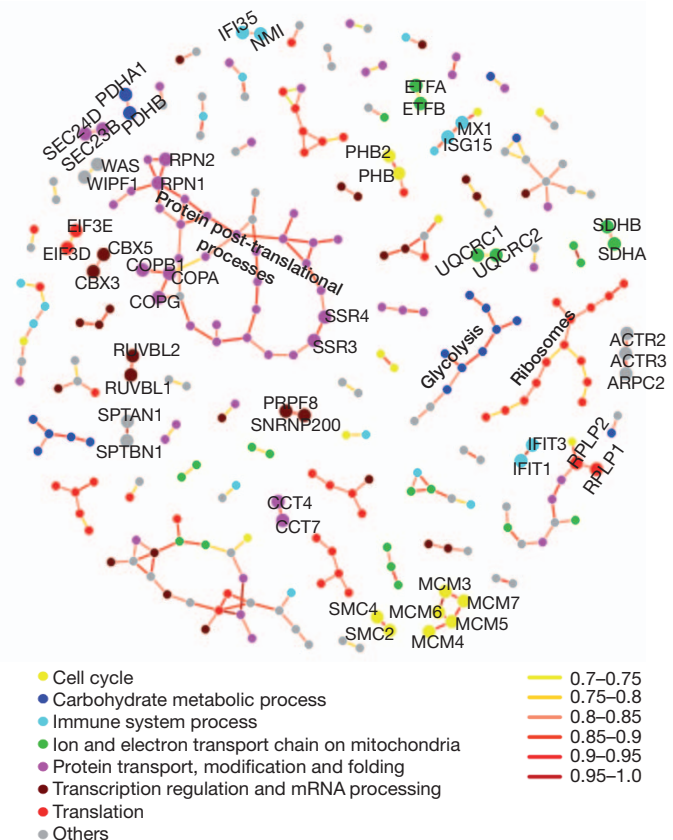


**Figure 2 | Protein covariation network generated by sparse partial correlation estimation.** Nodes represent proteins. Edges represent connection by covariation. This sparse network displays the 223 strongest connections among 278 proteins. Protein function is annotated by node colour. Edge colour is categorized according to correlation value. Known protein–protein interacting pairs are highlighted in larger nodes and labelled with gene names.

To assess the extent and nature of the genetic factors that affect protein levels, we estimated the 'narrow-sense' heritability of protein levels, which represents the additive genetic component of protein levels and is estimated as the slope of regressing the offspring trait values on the average trait values of their parents. Median heritability of protein levels was 0.06 and 0.17 in CEU and YRI, respectively; 38% of the CEU proteins and 47% of the YRI proteins had a heritability higher than 0.2, respectively (Supplementary Fig. 6 and Supplementary Table 7). Overall, proteins in YRI cell lines show greater heritability than in CEU cell lines. Previous analyses on RNA level heritability have shown a similar trend<sup>1</sup>, which may be attributable to the newer age of the YRI cell lines relative to the CEU cell lines.

We also tested the association of *cis* genetic variation with protein levels using HapMap phase III genotypes<sup>9</sup>. We limited the search for protein quantitative trait loci (pQTLs) to those single nucleotide polymorphisms (SNPs) located between  $\pm 20$  kilobases (kb) of the gene region with minor allele frequency (MAF)  $>10\%$  in our samples. We performed a *cis*-pQTL analysis separately in CEU and YRI, and in CEU, YRI and ASN combined, in an effort to reveal pQTLs common to all populations. Multiple loci throughout the genome displayed an excess of small *P* values (Fig. 3a and Supplementary Fig. 7a). At a 10% FDR threshold, we detected 33, 13 and 77 genes with at least one significant pQTL in CEU, YRI and in all three populations combined, respectively (Table 1 and Supplementary Table 8). Of the 77 genes with a pQTL in the analysis combining all three populations, 34 were also identified in the CEU and/or YRI population. Indeed, the CEU pQTLs are highly enriched for significant *P* values and tend to have consistent regression coefficients or effect sizes in YRI (Supplementary Fig. 7b, c). These results suggest that there is a considerable overlap in the genetic architecture of protein expression across populations. The lower number of significant pQTLs detected in YRI is probably a consequence of the smaller sample size.

To what extent do the genetic determinants that affect RNA levels coincide with those that regulate protein levels? To address this question the genetic regions that affect protein expression (pQTLs) were

compared with those that affect RNA expression (eQTLs) previously identified in HapMap individuals using RNA-seq methods<sup>2,3</sup>. For each pQTL SNP, we obtained the *P* value for its association with RNA expression in CEU and YRI. Overall, we observed enrichment for small *P* values (Supplementary Fig. 8 and Supplementary Table 8), and we estimate that approximately one-half of pQTLs are probably also eQTLs. However, many pQTLs do not correspond to eQTLs, even at a relaxed statistical stringency. We note that the numbers of pQTLs detected in this study are relatively small due to the limited sample size. Therefore, the proportions of genetic variants contributing to both protein and mRNA variation and specific to protein variation should be considered as approximations. Nonetheless, our results indicate that despite an overlap between eQTLs and pQTLs, many pQTLs are distinct from eQTLs.

Manual inspection of the individual pQTLs revealed interesting variants in several cases. *OAS1* (2'-5'-oligoadenylate synthase 1) is an essential protein involved in the innate immune response to viral infection. Mutations in *OAS1* have been associated with susceptibility to viral infection<sup>14</sup>. We identified a pQTL for *OAS1*. The variant showing the strongest correlation with *OAS1* protein level is located at a splice site (rs10774671), where the G allele is associated with higher protein level than the A allele. *OAS1* protein levels were calculated based on the quantification of 14 unique peptides, all of which are located before the splice site variant. Nine of them are shared by all known *OAS1* isoforms in the literature. All of the used peptides have the same expression orientation at rs10774671, indicating that this SNP is associated with total protein level variation (Supplementary Fig. 9). The G allele at rs10774671 has previously been associated with higher enzyme activity but the underlying mechanism is unknown<sup>15</sup>. Our data indicate that this variant may influence the overall *OAS1* protein expression, in addition to giving rise to different isoforms.

A second example, *IMPA1* (inositol monophosphatase 1), is a putative target for lithium in the treatment of bipolar disorder<sup>16</sup>, but no *IMPA1* genetic variant has been associated with bipolar disease<sup>17</sup>, nor has an eQTL been identified for this gene in recent RNA-seq

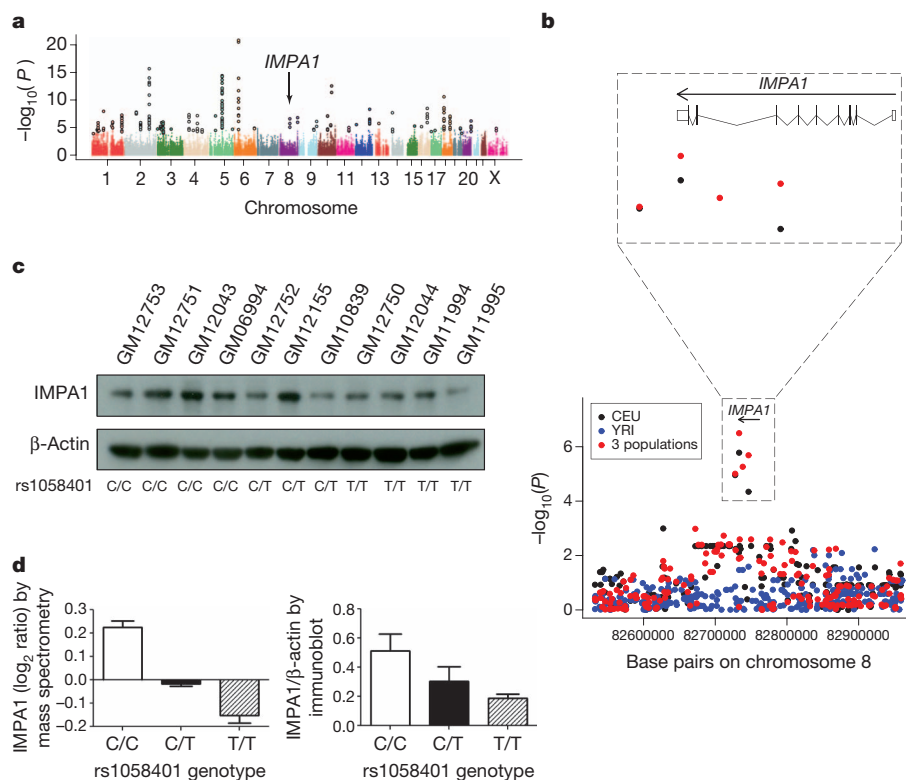


**Figure 3 | Loci associated with protein expression levels.** **a**, Identification of *cis*-pQTLs in all three populations combined ( $n = 72$ ). The *P* value and genomic coordinates for each protein/*cis*-SNP association test are plotted in the Manhattan plot. pQTLs with protein level multiple testing corrected *P* value  $<0.001$  are highlighted with a bigger dot size and a black outline. Multiple loci throughout the genome displayed an excess of small *P* values. The arrow indicates the location of the *IMPA1* gene which contains a significant *cis*-pQTL. **b**, Overview of *IMPA1* protein level and SNP genotype association in CEU, YRI and all populations combined. The bottom plot is the fine mapping of *cis*-pQTL for *IMPA1* based on HapMap phases I, II and III genotypes release 28. Each dot represents a tested SNP. Dot colours represent testing groups. The arrow is indicative of the chromosome location and transcription direction of the *IMPA1* gene. There are several highly significant associations near the *IMPA1* region in CEU and all three populations combined (CEU, YRI and ASN). The exact locations of these associations in the *IMPA1* gene region are illustrated in the top plot. The most significant SNP is rs1058401, located in *IMPA1* 3' UTR. **c**, Validation of *IMPA1* protein expression level. *IMPA1* protein expression level was validated by immunoblotting in 11 CEU individuals, with their genotype at rs1058401 labelled at the bottom. **d**, The bar plots show the mean of *IMPA1* protein level of these 11 individuals in each rs1058401 genotype, based on data measured by quantitative mass spectrometry and by densitometry of immunoblot. Error bars indicate standard error of the mean.



**Table 1 | Number of *cis*-pQTLs at different FDR**

Group	Number of LCLs	Number of proteins	Number of tests	Number of genes with a pQTL		
				10% FDR	20% FDR	30% FDR
CEU	41	3,984	116,556	33	54	122
YRI	22	4,017	121,405	13	34	50
Three populations*	72	4,021	130,505	77	134	239

\*CEU, YRI and ASN populations combined.

studies<sup>2,3</sup>. We found that SNP rs1058401, located at the 3' untranslated region (UTR) of the *IMPA1* gene, is associated with protein levels. We first explored a fine *cis*-pQTL mapping of the *IMPA1* gene using denser SNP coverage. We selected all the SNPs within  $\pm 200$  kb of the *IMPA1* gene from HapMap phases I, II and III with a MAF  $> 5\%$ . Several SNPs on or near the 3' UTR show significant pQTL effect in CEU and in the three populations combined (Fig. 3b). We validated this pQTL by immunoblot analyses in both CEU and YRI (Fig. 3c, d and Supplementary Fig. 10). The results are consistent with the data obtained using mass spectrometry, confirming that rs1058401 is indeed associated with *IMPA1* protein levels.

We also evaluated the correlation between *IMPA1* protein and mRNA levels, and observed a poor correlation between protein and mRNA in the combined sample ( $r = 0.04$ ,  $P = 0.76$ , Supplementary Fig. 11) or in CEU alone ( $r = -0.19$ ,  $P = 0.27$ ). However, protein and mRNA levels do show moderate correlation in YRI ( $r = 0.50$ ,  $P = 0.02$ ). The rs1058401 SNP showed no evidence of association with RNA levels measured in CEU ( $P = 0.56$ ), moderate evidence of association with RNA levels in YRI ( $P = 0.008$ ), and much stronger evidence of association with protein levels ( $P = 3 \times 10^{-7}$ , in the combined populations analysis). We checked whether this SNP is associated with mRNA decay rate using results from a recent report<sup>18</sup>, and found no support for such a hypothesis. Therefore, this pQTL may have a significant role in regulating gene expression at the translational level.

We describe the first systematic interrogation of the genetic effects on the human proteome using isobaric tag-based quantitative mass spectrometry. Our results demonstrate the power of quantitative mass spectrometry data for analysis of protein co-regulation and uncovering genetic effects influencing protein abundance. With a larger number of cell lines and improvement of mass spectrometry technology, the number of pQTLs is likely to increase substantially. Some, but not all, pQTLs overlap with those identified in eQTL studies. These results indicate that distinct and diverse genetic mechanisms control gene expression at many different levels, suggesting that important and complementary knowledge can be acquired by systematically characterizing the human proteome.

## METHODS SUMMARY

Lymphoblastoid cell lines (LCLs) from 95 HapMap individuals were obtained from the Coriell Institute for Medical Research. All trypsin-digest mixtures were analysed on an LTQ Orbitrap Velos (Thermo Scientific) equipped with an online 2D nanoACQUITY UPLC System (Waters) as previously described, with modifications<sup>19</sup>. The acquired mass spectrometry raw data were searched against a human International Protein Index (IPI) database, version 3.75<sup>20</sup>, concatenated with a decoy database with all the protein sequences in reverse order, using SEQUEST algorithm<sup>21</sup> (Proteome Discoverer software, version 1.2, Thermo Scientific). The correspondence between proteins, genes (Ensembl gene IDs) and genomic loci was established based on the protein and gene cross-reference tables of IPI database version 3.87 and transcript sequences of Ensembl database release 62. Screening of peptides overlapping with protein coding changes was based on genotypes and annotation releases by the HapMap and 1000 Genomes Project<sup>9,22,23</sup>. To estimate the false discovery rate for sex, population and pQTL analyses, the QVALUE Bioconductor package was used<sup>24</sup>. For full methods, see Supplementary Information.

Received 16 August 2012; accepted 26 April 2013.

Published online 15 May 2013.

1. Stranger, B. E. *et al.* Population genomics of human gene expression. *Nature Genet.* **39**, 1217–1224 (2007).

2. Montgomery, S. B. *et al.* Transcriptome genetics using second generation sequencing in a Caucasian population. *Nature* **464**, 773–777 (2010).
3. Pickrell, J. K. *et al.* Understanding mechanisms underlying human gene expression variation with RNA sequencing. *Nature* **464**, 768–772 (2010).
4. Stranger, B. E. *et al.* Patterns of *cis* regulatory variation in diverse human populations. *PLoS Genet.* **8**, e1002639 (2012).
5. Kasowski, M. *et al.* Variation in transcription factor binding among humans. *Science* **328**, 232–235 (2010).
6. Schwanhäusser, B. *et al.* Global quantification of mammalian gene expression control. *Nature* **473**, 337–342 (2011).
7. de Sousa Abreu, R., Penalva, L. O., Marcotte, E. M. & Vogel, C. Global signatures of protein and mRNA expression levels. *Mol. Biosyst.* **5**, 1512–1526 (2009).
8. Ong, S. E. & Mann, M. Mass spectrometry-based proteomics turns quantitative. *Nature Chem. Biol.* **1**, 252–262 (2005).
9. Altshuler, D. M. *et al.* Integrating common and rare genetic variation in diverse human populations. *Nature* **467**, 52–58 (2010).
10. Ow, S. Y. *et al.* iTRAQ underestimation in simple and complex mixtures: “the good, the bad and the ugly”. *J. Proteome Res.* **8**, 5347–5355 (2009).
11. Karp, N. A. *et al.* Addressing accuracy and precision issues in iTRAQ quantitation. *Mol. Cell. Proteomics* **9**, 1885–1897 (2010).
12. Li, J., Liu, Y., Kim, T., Min, R. & Zhang, Z. Gene expression variability within and between human populations and implications toward disease susceptibility. *PLoS Comput. Biol.* **6**, e1000910 (2010).
13. Peng, J., Wang, P., Zhou, N. & Zhu, J. Partial correlation estimation by joint sparse regression models. *J. Am. Stat. Assoc.* **104**, 735–746 (2009).
14. Lim, J. K. *et al.* Genetic variation in *OAS1* is a risk factor for initial infection with West Nile virus in man. *PLoS Pathog.* **5**, e1000321 (2009).
15. Bonnevie-Nielsen, V. *et al.* Variation in antiviral 2',5'-oligoadenylate synthetase (2'5'AS) enzyme activity is controlled by a single-nucleotide polymorphism at a splice-acceptor site in the *OAS1* gene. *Am. J. Hum. Genet.* **76**, 623–633 (2005).
16. Agam, G. *et al.* Knockout mice in understanding the mechanism of action of lithium. *Biochem. Soc. Trans.* **37**, 1121–1125 (2009).
17. Sjöholt, G. *et al.* Examination of *IMPA1* and *IMPA2* genes in manic-depressive patients: association between *IMPA2* promoter polymorphisms and bipolar disorder. *Mol. Psychiatry* **9**, 621–629 (2004).
18. Pai, A. A. *et al.* The contribution of RNA decay quantitative trait loci to inter-individual variation in steady-state gene expression levels. *PLoS Genet.* **8**, e1003000 (2012).
19. Chen, R. *et al.* Personal omics profiling reveals dynamic molecular and medical phenotypes. *Cell* **148**, 1293–1307 (2012).
20. Kersey, P. J. *et al.* The International Protein Index: an integrated database for proteomics experiments. *Proteomics* **4**, 1985–1988 (2004).
21. Eng, J. K., McCormack, A. L. & Yates, J. R. An approach to correlate tandem mass spectral data of peptides with amino acid sequences in a protein database. *J. Am. Soc. Mass Spectrom.* **5**, 976–989 (1994).
22. Frazer, K. A. *et al.* A second generation human haplotype map of over 3.1 million SNPs. *Nature* **449**, 851–861 (2007).
23. Abecasis, G. R. *et al.* An integrated map of genetic variation from 1,092 human genomes. *Nature* **491**, 56–65 (2012).
24. Storey, J. D. & Tibshirani, R. Statistical significance for genomewide studies. *Proc. Natl Acad. Sci. USA* **100**, 9440–9445 (2003).

**Supplementary Information** is available in the online version of the paper.

**Acknowledgements** We thank S. Montgomery for providing gene-level RNA sequencing measurements of CEU LCLs. This work was supported by NIH grants to M.S. and H.T.

**Author Contributions** L.W. performed all the experimental work, mass spectrometry-related data analysis and part of the statistical data analysis. S.I.C. performed most of the statistical data analysis. Y.C. performed the protein covariation analysis. D.X. performed the screening of allele-specific peptides. L.J. helped on instrument maintenance. J.L.-P.-T. contributed text and comments to the manuscript. L.W. and S.I.C. wrote the manuscript and participated in detailed discussion of study design and data analysis at all stages of the study. M.S. and H.T. designed and supervised the project.

**Author Information** Mass spectrometry raw data and searching results have been deposited in Peptide Atlas and are available at <http://www.peptideatlas.org/PASS/PASS00230>. Reprints and permissions information is available at [www.nature.com/reprints](http://www.nature.com/reprints). The authors declare no competing financial interests. Readers are welcome to comment on the online version of the paper. Correspondence and requests for materials should be addressed to M.S. (mmpsnyder@stanford.edu) or H.T. (huatang@stanford.edu).

# A single pair of interneurons commands the *Drosophila* feeding motor program

Thomas F. Flood<sup>1\*</sup>, Shinya Iguchi<sup>1\*</sup>, Michael Gorczyca<sup>1\*</sup>, Benjamin White<sup>2</sup>, Kei Ito<sup>3</sup> & Motojiro Yoshihara<sup>1</sup>

Many feeding behaviours are the result of stereotyped, organized sequences of motor patterns. These patterns have been the subject of neuroethological studies<sup>1,2</sup>, such as electrophysiological characterization of neurons governing prey capture in toads<sup>1,3</sup>. However, technical limitations have prevented detailed study of the functional role of these neurons, a common problem for vertebrate organisms. Complexities involved in studies of whole-animal behaviour can be resolved in *Drosophila*, in which remote activation of brain cells by genetic means<sup>4</sup> enables us to examine the nervous system in freely moving animals to identify neurons that govern a specific behaviour, and then to repeatedly target and manipulate these neurons to characterize their function. Here we show neurons that generate the feeding motor program in *Drosophila*. We carried out an unbiased screen using remote neuronal activation and identified a critical pair of brain cells that induces the entire feeding sequence when activated. These ‘feeding neurons’ (here abbreviated to Fdg neurons for brevity) are also essential for normal feeding as their suppression or ablation eliminates sugar-induced feeding behaviour. Activation of a single Fdg neuron induces asymmetric feeding behaviour and ablation of a single Fdg neuron distorts the sugar-induced feeding behaviour to become asymmetric, indicating the direct role of these neurons in shaping motor-program execution. Furthermore, recording neuronal activity and calcium imaging simultaneously during feeding behaviour<sup>5</sup> reveals that the Fdg neurons respond to food presentation, but only in starved flies. Our results demonstrate that Fdg neurons operate firmly within the sensorimotor watershed, downstream of sensory and metabolic cues and at the top of the feeding motor hierarchy, to execute the decision to feed.

To identify neurons controlling feeding behaviour we have behaviourally screened flies in which randomly targeted neurons are activated to induce the feeding motor program in a small, temperature-controlled chamber (Supplementary Fig. 2). To genetically target random sets of neurons, we took advantage of the collection of NP (Nippon) lines<sup>6</sup>. Each of these lines expresses the yeast transcription factor Gal4 in a different stereotyped pattern of neurons that depends on the *GAL4* insertion site<sup>7</sup>. Gal4-expressing cells were activated by mating flies of each line to flies with a transgene encoding a rat cold-activated cation channel, TRPM8 (ref. 8), or a *Drosophila* heat-activated-channel, TRPA1 (ref. 9), under the control of upstream activating sequences (UAS) recognized by Gal4. A screen of 835 NP lines identified the *GAL4* line NP883, which showed continuous feeding behaviour with *TrpA1* at increased temperature. The induced behaviour was compared with natural feeding behaviour<sup>2</sup> (Fig. 1a–d, Supplementary Figs 3, 4 and Supplementary Videos 1, 2). The natural feeding pattern, evoked by contact with food, is characterized by an initial cessation of locomotion followed by the sequential execution of eight basic motor patterns (Fig. 1a) for taking up food by repeated proboscis extension/retraction and opening/closing labellar lobes at the tip of the proboscis. This behavioural sequence was reproduced in a food-free environment by TRPA1-mediated activation of neurons in the Gal4-expressing pattern

(Fig. 1b and Supplementary Video 2). The TRPA1-induced sequence was well-coordinated and indistinguishable from natural feeding behaviour in the duration of proboscis extension, labellar contact with the substrate and proboscis retraction (Fig. 1d). We observed repeated labellar opening even with the rostrum and haustellum immobilized (Supplementary

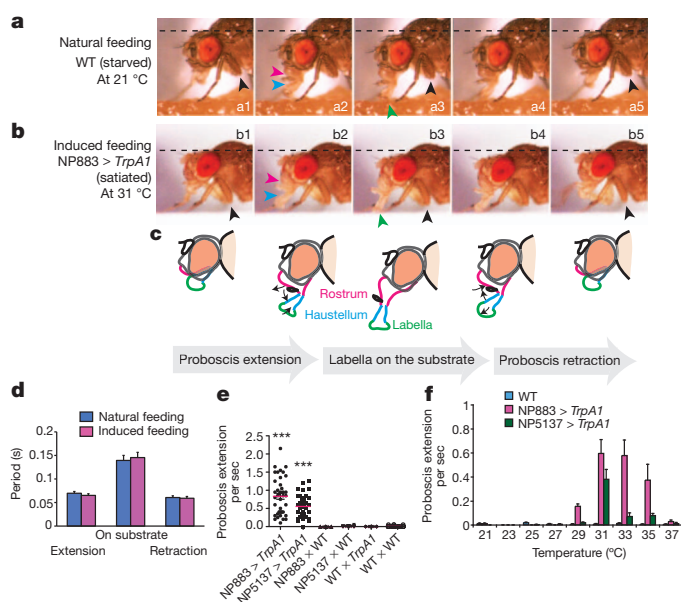


**Figure 1 | Thermogenetic activation reproduced coordinated natural feeding behaviour.** **a**, Natural feeding behaviour of a starved wild-type (WT) fly on normal food at 21 °C, consisting of eight basic motor patterns: (1) all main joints of the fly's forelegs (black arrowheads) bend to bring the head closer to the food (dashed horizontal lines for comparison of head heights); (2) the rostrum (magenta arrowheads) projects forward (a1 to a3) while (3) the haustellum (blue arrowheads) extends downward (a1 to a3), resulting in protrusion of the proboscis; (4) the paired lobes at the tip of the proboscis, called labella (green arrowheads), open upon touching the food to take up food (a2 to a3); (5) taking food, the labella close (a3 to a4) and (6) the rostrum and (7) the haustellum retract, returning the entire proboscis to its original position while (8) the forelegs (black arrowheads) raise the body to its original position (a3 to a5). **b**, TRPA1-induced proboscis extension in a satiated NP883 > *TrpA1* fly at 31 °C with the eight basic motor patterns indistinguishable from **a**. No food was present. **c**, Schematic drawings depict unfolding sequence of major segments of proboscis. **d**, Comparison of time taken for each step in proboscis extension in **c**.  $n = 22$  for each genotype. **e**, Proboscis-extension rate of free-running, satiated flies observed singly in an arena without food at 31 °C for each genotype (see Methods for description of the other line, NP5137, with a similar expression pattern to NP883 (Supplementary Fig. 8c)). Magenta bars denote mean values. \*\*\* $P < 0.001$  (see Methods for statistics).  $n = 40$  for each genotype. **f**, Temperature dependence of proboscis-extension rate without food for free-running, satiated flies for each genotype.  $n = 40$  for each genotype at each temperature. Error bars in all figures are s.e.m.

<sup>1</sup>Department of Neurobiology, University of Massachusetts Medical School, Worcester, Massachusetts 01605, USA. <sup>2</sup>Laboratory of Molecular Biology, National Institute of Mental Health, Bethesda, Maryland 20892, USA. <sup>3</sup>Institute of Molecular and Cellular Biosciences, University of Tokyo, Tokyo 113-0032, Japan.

\*These authors contributed equally to this work.

Fig. 5 and Supplementary Video 2), demonstrating independence of the induced behavioural sequence from sensory cues, which have been thought to be required for labellar lobe opening after contact with food<sup>2,10</sup>. Although flies in which the feeding program was induced by TRPA1 stimulation generally opened their labella upon touching the plastic/glass substrate of the chamber (Fig. 1b b2–b3, Supplementary Figs 3b, 4b), some did so without touching the substrate (Supplementary Fig. 4c, d and Supplementary Video 2). The induced feeding thus represents a ‘fixed action pattern’<sup>11</sup>, which is completely executed without food or substrate, although the natural feeding must be coordinated with sensory stimuli as well. To quantify the feeding behaviour induced by stimulation of neurons in the NP883 pattern we adopted the extension and retraction of the rostrum and haustellum (numbers 2, 3, 6 and 7 in the sequence outlined in the legend of Fig. 1a), referred to as ‘proboscis extension’. Measured by this index, the induced feeding behaviour observed in NP883 > *TrpA1* flies at increased temperature required both the NP883-*GAL4* insertion and the *TrpA1* transgene (Fig. 1e) and exhibited a temperature dependence consistent with the activation properties of the *Drosophila* TRPA1 channel (Fig. 1f). Feeding was acutely induced in both sexes (Supplementary Fig. 6).

An essential component of feeding behaviour not measured by proboscis extension is the rhythmic activity of the pharyngeal pump, which is used for swallowing food<sup>2,12,13</sup>. To assess whether the behaviour induced in NP883 > *TrpA1* flies included activation of the pharyngeal pump, we fluorescently labelled the pharyngeal muscles using green fluorescent protein expressed under control of the enhancer in the myosin heavy chain (*Mhc*) locus (*Mhc*-GFP)<sup>14</sup> (Fig. 2a, b) so that they could be observed through the cuticle. These muscles, m11, m12-1 and m12-2, (Fig. 2b–d) are attached to the upper sclerotized plate out of two sclerotized plates, which lie on top of one another (Fig. 2e and Supplementary Fig. 7a). Observing the action of the pump using a dye-coloured sugar solution to visualize fluid flow upon presentation to a starved fly revealed the dynamics of pump movement shown in Fig. 2a–e, Supplementary Fig. 7a–c and Supplementary Video 3. In brief, m12-1, m12-2 and m11 sequentially contract and relax in an alternating manner to lift first the anterior and then the posterior parts of the upper plate to generate rhythmic peristaltic waves of the upper plate, which move ingested material from the mouth to the oesophagus between the two plates. Counting of individual pump cycles under m12-1 and m12-2 (Fig. 2f) revealed that sucrose-induced feeding in a starved fly was mediated by vigorous pumping at 6–8 Hz when the temperature was set at 29 °C, with the rate declining gradually as the fly became satiated, then leading to a fully swollen crop in 2 min (Fig. 2g). When we tested NP883 > *TrpA1* flies in the *Mhc*-GFP background we found that temperature increase induced intermittent pumping that was indistinguishable from natural pumping (Supplementary Video 3). Satiated NP883 > *TrpA1* flies showed only occasional pumping at 21 °C, but pumped the sugarless dye solution at 6–8 Hz at 29 °C in a pattern indistinguishable from that of wild-type starved flies with sucrose solution (magnified plots in Fig. 2g). Satiated wild-type flies used as controls showed much less pumping of the dye solution, even at 29 °C, compared to NP883 > *TrpA1* flies at the same temperature (Fig. 2g), as total pumping pulses were quantified to show a sevenfold difference (Supplementary Fig. 7d). Although the induced total pumping during 2 min was 40% lower than the sucrose-induced pumping of starved wild-type flies (Supplementary Fig. 7d), comparison of rates (Fig. 2h) showed that the NP883 > *TrpA1* flies maintained pumping at the same steady-state rate as starved wild-type flies, although the latter initially pumped more vigorously in response to sucrose. By measuring the net amount of ingested fluid, we observed that, in the first 2 min, induced pharyngeal pumping led to ingestion of 4.7-fold more fluid than wild-type controls (Supplementary Fig. 7e), and after approximately 5 min led to a fully swollen crop, although the crop was not filled at 2 min (Fig. 2g and Supplementary Video 3). Taken together, our results demonstrate that the activation of Gal4-expressing cells in

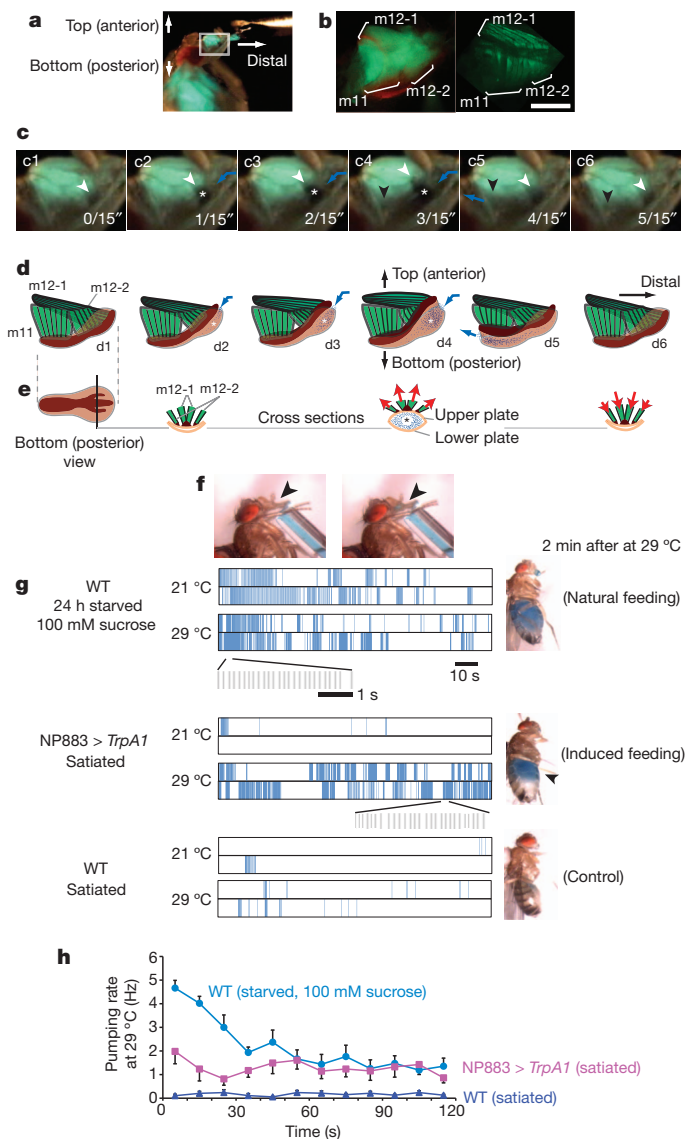


**Figure 2 | Thermogenetically induced food ingestion through the pharyngeal pump.** **a–e**, Mechanism of pharyngeal pump for normal ingestion in a wild-type fly. A fly starved for 24 h was fed an aqueous 100 mM sucrose solution with blue dye. **a**, A side view. Muscles are highlighted with *Mhc*-GFP. Area in white box is magnified in **c**. **b**, Micrographs (left, dissection microscope; right, confocal microscope) to illustrate muscle structure. Each of three muscle fibre groups, m11, m12-1 and m12-2, consists of several muscle fibres, forming the pharyngeal pump. m12-1 was described previously as 12 (ref. 12), whereas m12-2 was identified in this study with the help of *Mhc*-GFP. Scale bar, 100  $\mu$ m. **c**, Still images at 21 °C (Supplementary Video 3). White arrowheads denote edge of m12-1; black arrowheads denote edge of m11. Blue arrows denote flow of ingested material. Asterisks denote the main lumen enlarged (also in **d** and **e**). **d**, **e**, Schematic diagram for muscle movement. The two sclerotized plates are depicted as light brown, whereas the apodeme, which protrudes from the upper plate and is attached to the muscles, is depicted as dark brown. **f**, Visualization of ingestion with blue dye in the space under m12-1 and m12-2 (arrowheads) for counting a single pulse in **g**. Left, closed state without dye; right, open state with dye. The proboscis of the fly was allowed to move freely as in its natural state. **g**, Representative raster plots (two for each condition) to show pumping events during a 2-min period at 21 °C and 29 °C. Right, representative flies for each 29 °C groups after 2 min. Arrowhead, belly with sugarless dye without starvation. **h**, Pumping rates plotted at every 10 s in 29 °C groups in **g**.  $n = 11$  (wild type, sucrose), 11 (NP883 > *TrpA1*), 18 (wild type, control). Error bars denote s.e.m.



NP883 produces the complete feeding motor program consisting of all essential motor patterns, including pharyngeal pumping.

To identify the specific neurons within the NP883 expression pattern (Fig. 3a and Supplementary Figs 8a, b, 9) that activate feeding behaviour, we used the ‘flip-out *GAL80*’ technique<sup>15</sup>, in which the initially ubiquitous expression of *Gal80*, an inhibitor of *Gal4*-mediated transcription, is eliminated in small numbers of neurons by the flippase-mediated random removal of the *GAL80* gene (see Methods). By this means, we simultaneously expressed *TRPA1* and GFP in small subsets of the NP883 pattern and identified the GFP-labelled neurons, whose presence we could correlate with *TRPA1*-induced feeding. From screening 1,243 flies (Supplementary Fig. 10) we dissected the flies that showed a proboscis-extension rate of six times per min or above, a value not observed in non-flipped-out specimens (Supplementary Table 1). Examination of the 40 proboscis-extension-positive flies led to the identification of one type of interneuron, the GFP expression of which correlated with flies having a higher proboscis-extension frequency as seen in the histogram of Fig. 3b. We termed this pair of interneurons Fdg neurons. They possess a distinct and stereotypical morphology with extensive arborization (Fig. 3d, Supplementary Figs 10c and 11, and Supplementary Video 5), which can be unambiguously identified in the full expression pattern of NP883 (arrowheads in Fig. 3a). They are located in the subesophageal ganglion (SEG (also called SOG)), where axons of gustatory sensory neurons terminate<sup>16–18</sup> (the primary gustatory centre in the fly brain) and where motoneurons for mouth-part muscles extend their dendritic arborizations<sup>10</sup>. To understand information flow to and from the Fdg neuron, we defined its cellular architecture in relation to these sensory inputs and motor outputs by the flip-out *GAL80* with synaptic markers (Fig. 3e and Supplementary Fig. 12). Figure 3b shows the distribution of proboscis-extension rate in the ‘Fdg neuron with GFP group’ to be significantly skewed to high

values in contrast to the ‘no Fdg neuron with GFP’ group by Mann–Whitney’s *U*-test. By contrast, another identified neuron type within the NP883 pattern, which we called ALLH (antennal lobe and lateral hone) neurons (Supplementary Fig. 13a, b), did not exhibit such a skew (Fig. 3c). In addition, none of the other six prominent SEG cell types within the NP883 expression pattern showed a statistically significant correlation between GFP expression and proboscis-extension frequency (Supplementary Fig. 13). This was also the case for all cells outside of the SEG (Supplementary Table 2), suggesting that the Fdg neuron is responsible for the feeding behaviour with higher proboscis-extension rates (see also Supplementary Note 1).

Supplementary Fig. 10d shows the induced behaviour (Supplementary Video 4) of a fly that had strong GFP expression only in a single Fdg neuron, as shown in Fig. 3d and Supplementary Fig. 10c. The behaviour induced by *TRPA1* in this fly clearly included all eight motor patterns of the natural feeding program following the initial cessation of locomotion, indicating that activation of a single Fdg neuron can induce the entire sequence of feeding behaviour. It should be noted that the feeding behaviour observed in Fdg-neuron-positive flies contrasted with that of NP883 > *TrpA1* flies in that it included more walking (Supplementary Video 4) and lacked the leg tremors observed in NP883 > *TrpA1* flies (Supplementary Video 2), probably owing to suppression of *TRPA1* expression in other cells by *Gal80*. In these respects, the behaviour resulting from the activation of individual Fdg neurons more closely mimicked natural feeding behaviour. Interestingly, we observed an unusual directionality to the proboscis extensions produced by flies in which single Fdg neurons were activated. As shown in Supplementary Fig. 10e, Supplementary Video 4 and Supplementary Table 2, proboscis extension was consistently directed towards the side the GFP-expressing Fdg neuron was on. This asymmetric regulation of proboscis extension by the Fdg neuron suggests that each Fdg neuron may selectively regulate the strength of proboscis muscle contraction on the same side of the body, consistent with the observation that presentation of food to gustatory receptors on one side of the body leads to proboscis extension on that side (Supplementary Video 1).

To determine whether Fdg neuron activity is required for natural feeding, we first suppressed activity of all neurons in the NP883-*GAL4* pattern by the expression of an inward rectifier potassium channel, *Kir*<sup>19</sup>, leading to abolishment of natural feeding behaviour in response to sucrose (Supplementary Fig. 14 and Supplementary Video 6). The main sugar-sensing neurons of the labellum, which express the gustatory receptor *GR5A*<sup>16,17</sup>, terminate in the vicinity of the dendrite of the Fdg neuron, but careful confocal analysis revealed no direct contact between the processes of the two types of neuron (Supplementary Fig. 15). To determine whether the Fdg neurons receive indirect input from the sugar-sensing neurons, we assayed their response to gustatory stimuli by calcium imaging using a genetically encoded  $\text{Ca}^{2+}$  indicator, *GCaMP3.0* (ref. 20), driven by NP883-*GAL4*. To achieve this, we used a specially designed setup (that is, the feeding circuit/fly brain live imaging and electrophysiology stage, or FLIES) to visualize SEG neurons through an opening in the head<sup>5</sup> (Fig. 4a, b). As shown in Fig. 4c, stimulation of the labellar lobes of a starved fly with 400 mM sucrose resulted in brief lobe opening, and a simultaneous, large increase in *GCaMP3.0* fluorescence in the cell body of the Fdg neuron (Supplementary Video 7). This response was specific insofar as an adjacent neuron, which we called LPE (lateral peri-esophageal) (Supplementary Figs 13 and 16a), showed no increase in *GCaMP3.0* fluorescence, even in starved flies (Supplementary Fig. 17a). Furthermore, red fluorescent protein (RFP) fluorescence did not change with the sucrose stimulus (Fig. 4c and Supplementary Fig. 17a). Interestingly, neither labellar opening nor  $\text{Ca}^{2+}$  increase in the Fdg neuron was observed in satiated flies (Supplementary Fig. 17). Our results thus indicate that sucrose acutely activates the Fdg neurons, and that this response is contingent on the metabolic state of the animal.

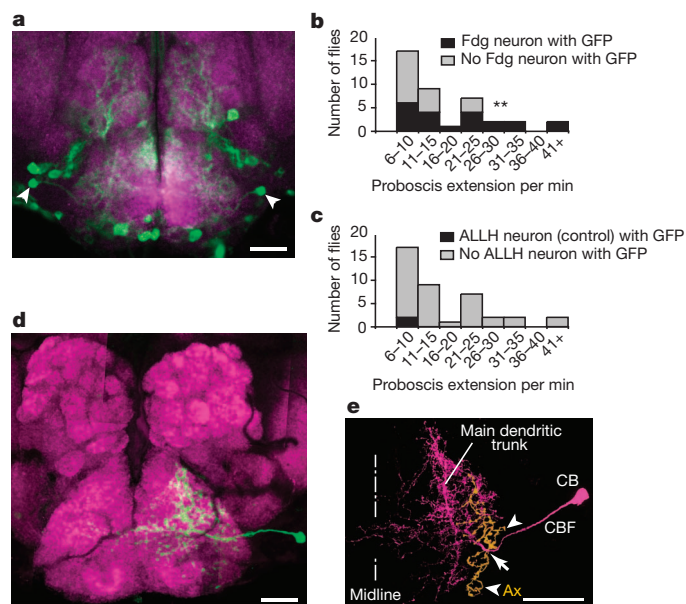


**Figure 3 | Identification of the Fdg neuron.** **a**, Full expression pattern of NP883 in the SEG as a confocal section, which covers both Fdg neurons (arrowheads). **b**, **c**, A histogram of proboscis-extension rate in 40 proboscis-extension-positive (proboscis extension > five times per min) flies, with GFP detected in Fdg neuron (**b**) or ALLH neuron (**c**) filled in black.  $**P < 0.01$ , Mann–Whitney’s *U*-test between ‘with GFP’ and ‘no GFP’. **d**, The Fdg neuron, labelled with anti-GFP antibody (green). A confocal montage of the SEG (lower half) and antennal lobes (upper half), with the neuropil marker antibody, nc82 (magenta). **e**, Fdg neuron with the presumptive axon digitally traced in deep yellow, on the basis of synaptic marker analyses in Supplementary Fig. 12. Arrow indicates position where the axon posteriorly branches off from cell body fibre (CBF), then, the sub-branches travel dorsally and ventrally as axon terminals (Ax, arrowheads). CB, cell body. All scale bars, 30  $\mu\text{m}$ .

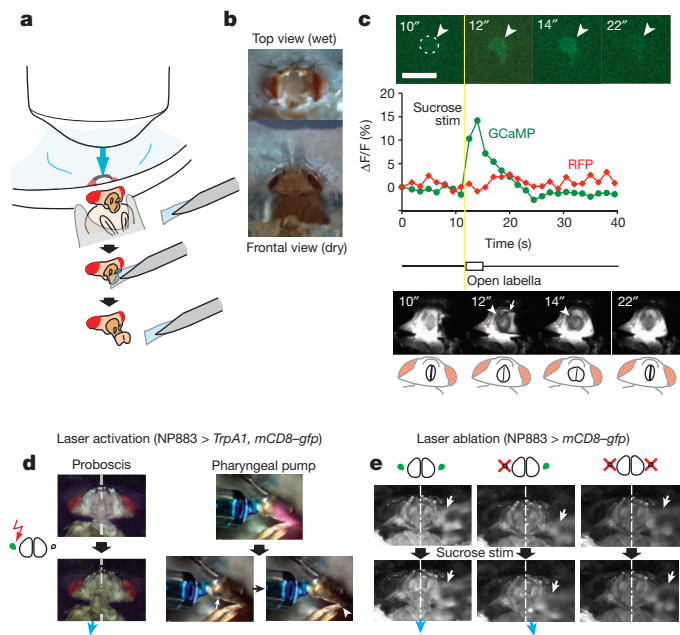


**Figure 4 | Functional analyses of Fdg neuron.** **a, b**, Experimental design with FLIES chamber<sup>5</sup> for experiments in this figure. **c**,  $\text{Ca}^{2+}$  imaging of Fdg neuron when NP883 > *GCaMP3.0*; *mCD8-rfp* flies were stimulated with 400 mM sucrose. Top, a representative *GCaMP3.0* fluorescence at the cell body of Fdg neuron (arrowheads) in a starved fly. Dashed circle denotes quantified area outlining an Fdg neuron cell body. Scale bar, 10  $\mu\text{m}$ . Middle, a time course of *GCaMP3.0*/RFP fluorescence as ratios to the initial fluorescence in a representative example. Bottom, labellar lobe opening (arrowheads) with other parts of proboscis immobilized. Arrow, sucrose wick for stimulation. Quantification and statistics are given in Supplementary Fig. 17. **d**, Laser activation of a single Fdg neuron in a satiated fly. Left panels, proboscis extension to the fly's right side in response to laser stimulation of the fly's right Fdg neuron cell body to activate TRPA1 under a two-photon microscope. Right panels, pump movement induced by laser activation of a single Fdg neuron on either side. Dye solution was applied through a capillary tube as shown in Fig. 2f, to see ingestion through the pharyngeal pump (white arrow) and the oesophagus (arrowhead) immediately after laser illumination. **e**, Laser ablation of a single Fdg neuron. A cell body of a single Fdg neuron was intensely illuminated under a two-photon microscope. Blue arrows denote sucrose-induced proboscis-extension directions before (left panels) and after (middle panels) ablation. Right panels, abolishment of sucrose-induced proboscis extension after ablation of both Fdg neurons. Chain lines denote fly's midline. White arrows denote sucrose wick.

The FLIES setup allowed us to image and focally heat the cell body of a single Fdg neuron expressing TRPA1 and GFP using limited illumination of the infrared laser of a two-photon microscope for activation of the Fdg neuron (see Methods and Supplementary Fig. 16b). As expected from the results of our flip-out *GAL80* studies, this stimulus caused immediate asymmetric proboscis extension to the side of the stimulated neuron (Fig. 4d and Supplementary Video 8). It also induced pump movement (Fig. 4d and Supplementary Video 8). By contrast, selective illumination of an LPE neuron, located only 10–20  $\mu\text{m}$  from the Fdg neuron (Supplementary Figs 13 and 16a, c), failed to induce proboscis extension or pump movement at the same stimulus level (see Methods and Supplementary Video 8). These results directly confirmed that activation of a single Fdg neuron can trigger feeding behaviour in a specific manner.

To test the requirement for the Fdg neuron in natural feeding behaviour, we selectively ablated Fdg neurons in starved NP883 > *gfp* flies using stronger laser illumination (see Methods and Supplementary Fig. 16d). Ablation of the Fdg neuron on one side, followed by stimulation with 400 mM sucrose, triggered proboscis extension in the direction opposite to the ablated side, whereas ablation of the Fdg neurons on both sides completely eliminated the response to sucrose

(Fig. 4e and Supplementary Video 9). In control experiments, ablation of the nearby LPE neuron did not affect the proboscis-extension response, again demonstrating the specificity of the manipulation. Consistent with the results of Kir suppression (Supplementary Fig. 14), these results demonstrate that Fdg neurons are essential for natural feeding in the fly and demonstrate the absence of neurons with redundant function.

The induction of the entire feeding program by Fdg neuron activation contrasts with the effects of activating motor neurons that innervate muscles of the proboscis<sup>21</sup> or the pharyngeal pump<sup>22</sup>. The induction of feeding by Fdg neurons is likewise distinct from that produced by stimulation of neurons that co-express neuropeptide Y and agouti-related protein in the mammalian hypothalamus, which has long latencies (that is, minutes versus seconds) and involves indirect regulation of motor output<sup>23</sup>. Their activity encodes metabolically derived motivational cues and contrasts with that of the Fdg neurons, which clearly encode integrated information of both gustatory and metabolic origin, and drive motor output in a manner that is perhaps most reminiscent of the 'command neurons' (interneurons whose natural activity triggers a specific motor program) first described in the crayfish<sup>24</sup>. The motor—as opposed to motivational—function of the Fdg neurons is evident in their asymmetric control of proboscis extension, which indicates a specific role of each Fdg neuron in contraction of a subset of the proboscis musculature. How the Fdg neurons coordinate the various motor patterns involved in feeding remains to be determined. Pump rhythms (Fig. 2), like the well-characterized movements of the crustacean stomatogastric nervous system, may result from the action of a central pattern generator governed by intrinsic membrane properties and inhibitory interactions of the component neurons<sup>25</sup>. Recently, co-activation of motoneurons controlling m11 and m12-1 has been shown to generate rhythmic contractions of the pharyngeal pump<sup>22</sup>, and activation of these neurons by the Fdg neurons might be the source of the pump central pattern generator<sup>2</sup>. As seen in Supplementary Video 5, the large dendritic arborization of the Fdg neuron, which is reminiscent of the putative feeding neurons of toads<sup>1,3</sup> and courtship neurons of *Drosophila*<sup>26</sup>, suggest a role in integrating information beyond sugar and starvation cues, including perhaps other gustatory cues, such as bitter or salty, and signals of other modalities. In any case, our laser ablation experiments suggest that inputs that govern feeding responses probably pass through the single pair of Fdg neurons. The identification of these neurons here and the demonstration of their pivotal position in the feeding circuit open the door to systematic future experiments on their roles in sensory integration and its plasticity in fly feeding behaviour.

## METHODS SUMMARY

In behavioural observation, the temperature was maintained within  $\pm 1^\circ\text{C}$  of a set temperature. Immunohistochemistry was performed according to a protocol described previously<sup>27</sup> with a modification for adult brains.  $\text{Ca}^{2+}$  imaging as well as laser activation and inactivation were performed using FLIES apparatus, which was designed to expose the brain of a fly for general purposes such as live imaging, electrophysiology and to keep the fly's proboscis dry and free for movement<sup>5</sup>. A sugar-free saline (1.5 mM  $\text{Ca}^{2+}$ ) used previously for *Drosophila* electrophysiology<sup>28</sup> was continuously perfused at  $21^\circ\text{C}$ . The head capsule was opened by a tungsten 'sword', which was originally designed for dissection of a *Drosophila* embryo used in study of synaptic plasticity<sup>29</sup>, and by 'scissors', which are forceps modified to act as scissors<sup>5</sup>. An ultrathin, smooth, traditional Japanese Washi paper, Gampi-shi (Haibara), was used as a wick for sugar stimulus<sup>5</sup>.

**Full Methods** and any associated references are available in the online version of the paper.

Received 31 December 2012; accepted 22 April 2013.

Published online 9 June 2013.

1. Ewert, J. P. Neural correlates of key stimulus and releasing mechanism: a case study and two concepts. *Trends Neurosci.* **20**, 332–339 (1997).
2. Dethier, V. G. *Hungry Fly* (Harvard University Press, 1976).
3. Matsushima, T., Satou, M. & Ueda, K. Medullary reticular neurons in the Japanese toad: morphologies and excitatory inputs from the optic tectum. *J. Comp. Physiol. A* **166**, 7–22 (1989).

4. Lima, S. Q. & Miesenbock, G. Remote control of behavior through genetically targeted photostimulation of neurons. *Cell* **121**, 141–152 (2005).
5. Yoshihara, M. Simultaneous recording of calcium signals from identified neurons and feeding behavior of *Drosophila melanogaster*. *J. Vis. Exp.* **62**, e3625 (2012).
6. Yoshihara, M. & Ito, K. Improved Gal4 screening kit for large-scale generation of enhancer-trap strains. *Drosoph. Inf. Serv.* **83**, 199–202 (2000).
7. O'Kane, C. J. & Gehring, W. J. Detection in situ of genomic regulatory elements in *Drosophila*. *Proc. Natl Acad. Sci. USA* **84**, 9123–9127 (1987).
8. Peabody, N. C. *et al.* Characterization of the decision network for wing expansion in *Drosophila* using targeted expression of the TRPM8 channel. *J. Neurosci.* **29**, 3343–3353 (2009).
9. Hamada, F. N. *et al.* An internal thermal sensor controlling temperature preference in *Drosophila*. *Nature* **454**, 217–220 (2008).
10. Singh, R. N. Neurobiology of the gustatory systems of *Drosophila* and some terrestrial insects. *Microsc. Res. Tech.* **39**, 547–563 (1997).
11. Tinbergen, N. *The Study of Instinct* (Clarendon Press, 1989).
12. Miller, A. in *Biology of Drosophila* (ed. Demerec, M.) 420–534 (John Wiley & Sons, 1950).
13. Ferris, G. F. in *Biology of Drosophila* (ed. Demerec, M.) 368–419 (John Wiley & Sons, 1950).
14. Gajewski, K. M. & Schulz, R. A. CF2 represses *Actin 88F* gene expression and maintains filament balance during indirect flight muscle development in *Drosophila*. *PLoS ONE* **5**, e10713 (2010).
15. Struhl, G. & Basler, K. Organizing activity of wingless protein in *Drosophila*. *Cell* **72**, 527–540 (1993).
16. Wang, Z., Singhvi, A., Kong, P. & Scott, K. Taste representations in the *Drosophila* brain. *Cell* **117**, 981–991 (2004).
17. Thorne, N., Chromey, C., Bray, S. & Amrein, H. Taste perception and coding in *Drosophila*. *Curr. Biol.* **14**, 1065–1079 (2004).
18. Miyazaki, T. & Ito, K. Neural architecture of the primary gustatory center of *Drosophila melanogaster* visualized with GAL4 and LexA enhancer-trap systems. *J. Comp. Neurol.* **518**, 4147–4181 (2010).
19. Hagiwara, S., Miyazaki, S., Moody, W. & Patlak, J. Blocking effects of barium and hydrogen ions on the potassium current during anomalous rectification in the starfish egg. *J. Physiol.* **279**, 167–185 (1978).
20. Tian, L. *et al.* Imaging neural activity in worms, flies and mice with improved GCaMP calcium indicators. *Nature Methods* **6**, 875–881 (2009).
21. Gordon, M. D. & Scott, K. Motor control in a *Drosophila* taste circuit. *Neuron* **61**, 373–384 (2009).
22. Manzo, A., Silies, M., Gohl, D. M. & Scott, K. Motor neurons controlling fluid ingestion in *Drosophila*. *Proc. Natl Acad. Sci. USA* **109**, 6307–6312 (2012).
23. Aponte, Y., Atasoy, D. & Sternson, S. M. AGRP neurons are sufficient to orchestrate feeding behavior rapidly and without training. *Nature Neurosci.* **14**, 351–355 (2011).
24. Wiersma, C. A. & Ikeda, K. Interneurons commanding swimmeret movements in the Crayfish, *Procambarus clarki* (Girard). *Comp. Biochem. Physiol.* **12**, 509–525 (1964).
25. Marder, E. & Bucher, D. Understanding circuit dynamics using the stomatogastric nervous system of lobsters and crabs. *Annu. Rev. Physiol.* **69**, 291–316 (2007).
26. Kimura, K., Hachiya, T., Koganezawa, M., Tazawa, T. & Yamamoto, D. Fruitless and doublesex coordinate to generate male-specific neurons that can initiate courtship. *Neuron* **59**, 759–769 (2008).
27. Yoshihara, M., Rheuben, M. B. & Kidokoro, Y. Transition from growth cone to functional motor nerve terminal in *Drosophila* embryos. *J. Neurosci.* **17**, 8408–8426 (1997).
28. Yoshihara, M. *et al.* Selective effects of neuronal-synaptobrevin mutations on transmitter release evoked by sustained versus transient  $Ca^{2+}$  increases and by cAMP. *J. Neurosci.* **19**, 2432–2441 (1999).
29. Yoshihara, M., Adolfsen, B., Galle, K. T. & Littleton, J. T. Retrograde signaling by Syt 4 induces presynaptic release and synapse-specific growth. *Science* **310**, 858–863 (2005).

**Supplementary Information** is available in the online version of the paper.

**Acknowledgements** We thank S. Waddell for discussions, fly stocks and reading of the manuscript; T. Lee for discussions and fly stocks; A. Sakurai for reading of the manuscript; S. Reppert for support; M. Alkema and T. Ip for discussions; members of the NP consortium for NP lines; T. Awasaki, C. Kao, V. Budnik, P. Garrity, M. Freeman, M. Rosbash, Y.-N. Jan, L. Luo, S. Sigrist, K. Scott, T. Tanimura, L. Looger, M. Ramaswami and K. Gajewski for fly stocks; K. Ikeda, T. Tanimura and H. Ishimoto for technical advices; A. Taylor and R. Seeham for technical help; and N. Yoshihara for material information. This work was supported by National Institute of Mental Health Grant MH85958, and the Worcester Foundation (to M.Y.), the National Institute of Mental Health Intramural Research Program (B.W.), the summer program of the Japan Society for the Promotion of Science/National Science Foundation (to T.F.F.), and a Japan Science and Technology Agency CREST grant (to K.I.).

**Author Contributions** M.Y., S.I., T.F.F. and M.G. designed the research. T.F.F. screened GAL4 lines under the supervision of K.I. and M.Y. T.F.F., S.I. and M.Y. performed behavioural analyses. S.I. performed analyses of ingestion and pump movement while M.Y. visualized the pump movement. M.G., S.I., K.I. and M.Y. performed neuroanatomy. S.I. and M.Y. did the fly genetics. M.Y. performed calcium imaging. S.I. and M.Y. performed experiments of laser activation and laser ablation with the technical assistance of M.G. B.W. contributed TRPM8 and essential advice. M.Y., M.G. and T.F.F. wrote the paper with assistance from S.I., B.W. and K.I.

**Author Information** Reprints and permissions information is available at [www.nature.com/reprints](http://www.nature.com/reprints). The authors declare no competing financial interests. Readers are welcome to comment on the online version of the paper. Correspondence and requests for materials should be addressed to M.Y. (Motojiro.Yoshihara@umassmed.edu).



## METHODS

**Immunohistochemistry.** We performed immunolabelling according to a protocol described previously<sup>27</sup> with a modification for adult brains (see Supplementary Methods for details).

**Saline and dissection tools.** A sugar-free saline used previously for *Drosophila* embryonic electrophysiology was also used in this study<sup>28</sup>. The saline contained (in mM): NaCl, 140; KCl, 2; MgCl<sub>2</sub>, 4.5; CaCl<sub>2</sub>, 1.5; and HEPES-NaOH, 5 (pH 7.1). The head capsule was opened by a tungsten 'sword', which was originally designed for dissection of a *Drosophila* embryo used in study of synaptic plasticity<sup>29</sup>, and by 'scissors', which are forceps modified to act as scissors<sup>5</sup>.

**Fly strains.** *Drosophila* crosses were performed at 21 °C or 25 °C according to standard protocols. Canton S was used as the wild-type control. Transgenic strains were balanced with *FM7c*, *CyO*, *TM3* or *TM6B* chromosomes. *UAS-TRPM8* has been previously described<sup>8</sup>. *UAS-TrpA1* (ref. 9) was obtained from P. Garrity. *UAS-mCD8-mCherry* was made by A. Sheehan, and generously provided by M. Freeman before publication. *Mhc-gfp* was from K. Gajewski<sup>14</sup>, *UAS-mCD8-gfp*<sup>30</sup> and a heat-shock-flippase (*HS-FLP*) strain<sup>15</sup> were from T. Lee. *>Tubulin-GAL80>* (in which '>' denotes a flip recombination target, FRT, sequence to be recognized by flippase; the '*Tubulin-GAL80*' sequence between the two FRT sequences is excised when flippase is provided; and *Tubulin* is used for ubiquitous expression of Gal80), made by G. Struhl, was from M. Roshbash<sup>31</sup>, *elav-GAL80* (ref. 32) was from Y.-N. Jan, *Mhc-GAL80* (ref. 33) was from L. Luo, *Cha-GAL80* (ref. 34) was from S. Waddell, *UAS-brp-gfp*<sup>35</sup> and *UAS-nAChR-gfp* (*UAS-Dα7-gfp*)<sup>36</sup> were from S. Sigrist, *UAS-n-syb-gfp*<sup>37</sup> was from M. Ramaswami, *Gr5a-gfp-IRES-gfp-IRES-gfp*<sup>38</sup> was from K. Scott, *UAS-Kir2.1* (ref. 39) was from V. Budnik, *tubP-GAL80*<sup>45</sup> (temperature sensitive)<sup>40</sup> was from S. Waddell, *UAS-GCaMP3.0* (ref. 20) was from L. Looger and *UAS-mCD8-rfp* was from T. Awasaki<sup>41</sup>.

We used two *GAL4* strains that were established by the NP consortium<sup>6</sup>. The NP883 line has a *GAL4* insertion approximately 500 base pairs 5' upstream of the untranslated region of *Cyp6a14* (ref. 42), a locus encoding a member of the cytochrome P450 family, which functions for electron transfer. Although none of the *GAL4* lines screened showed temperature-induced behaviour similar to NP883, another NP line not included in the screen, NP5137, was later identified as having an insertion at a more proximal site to the coding region of *Cyp6a14* (ref. 42). This line exhibited a similar pattern of feeding behaviour (Fig. 1e, f) when driving TRPA1, and included Fdg neuron in its expression pattern common to NP883 (Supplementary Fig. 8c).

**Observation of fly behaviour.** For observing TRPA1-induced behaviour, we used a custom-built plastic chamber (Supplementary Fig. 2), which enabled the temperature gradient to be maintained within  $\pm 1$  °C from its floor to ceiling (height 4 mm) at experimental temperatures. The chamber was designed to fit snugly into a Nunc 35-mm plastic dish, and temperature was regulated by a TS-4 SPD Controller (Physitemp) and monitored with an IT-23 probe connected to a microprobe thermometer, BAT-10 (Physitemp) (Supplementary Fig. 2). The inside of the fly chamber was cleaned after each use. We observed fly behaviour by the usual techniques (see Supplementary Methods).

For observing labellar movement with immobilized proboscis (Supplementary Fig. 5), we anaesthetized a fly in a 15-ml plastic tube immersed in ice, and placed the fly in a Pipetman tip with its tip cut to expose its head<sup>43</sup>. The rostrum and haustellum of the fly's proboscis were fixed using light-curing glue (Tetric EvoFlow, Ivoclar Vivadent). The fly held in the Pipetman tip was videotaped for 1 min at 21 °C. Then, the Pipetman tip holding the fly was placed in the temperature-controlled chamber pre-warmed to 31–32 °C. One minute later, when the temperature monitored by the temperature probe reached 31–32 °C, we videotaped the labellar lobes for 1 min. After that, we took the Pipetman tip holding the fly out from the chamber and placed it in the room at 21 °C, and we videotaped labellar lobes for 1 min.

**Visualization and quantification of pump movement and quantification of dye ingestion amount.** For visualization of pump movement, a fly with *Mhc-gfp*<sup>14</sup> was constrained in a Pipetman tip as stated above. For natural feeding, an aqueous 100 mM sucrose solution with 0.03 mg ml<sup>-1</sup> Brilliant Blue FCF (Acros Organics) was provided to a 24-h-starved fly through a hypodermic needle. For visualizing m11, the hypodermic needle was placed anterior to make the rostrum fully protracted. For induced feeding, the rostrum of a fly with NP883 > *TrpA1* with *Mhc-gfp* constrained in a Pipetman tip was glued to be immobilized at fully protracted position with light curing glue. Then, the Pipetman tip was placed in the temperature-controlled chamber with small holes, through which a hypodermic needle passed to provide the blue dye solution. The hypodermic needle was loaded on a joystick manipulator (Narishige, MN-151) and connected with a flexible plastic tube to an injector (Narishige, IM-5B) to constantly supply dye solution. Fluorescence from *Mhc-GFP* was observed using Leica MZ10F with a charge-coupled device (CCD) camera for videotaping. This fluorescence was supplemented with additional light from fibre optics to visualize the fly's mouthpart structures. We

noticed that, in partially satiated wild-type flies and sometimes in NP883 > *TrpA1* flies, contractions of m12-1 and m12-2 were not necessarily associated with those of m11 (Supplementary Video 3), causing backward flow from the spherical lumen<sup>22</sup> (Supplementary Video 3). To quantify ingestion directly, we therefore measured the net amount of ingested fluid as follows.

For quantification of pump movement and ingestion amount, a tethered fly on its back was provided with the dye solution through a glass capillary tube, which was loaded on a manipulator and connected to an injector as stated above. The glass capillary allowed us to measure the amount of solution ingested by measuring the length of dye solution filling the capillary. In the same experiments, the fly was videotaped with a CCD camera through a Nikon SMZ-800, and dye movement under m12-1 and m12-2 (Fig. 2f) was characterized.

**Flipping screening for feeding flies.** We used flies with the following genotype for flipping experiments for TRPA1 and GFP: *HS-FLP* (X chromosome); > *Tubulin-GAL80* > *UAS-TrpA1/NP883* (second chromosomes); *UAS-mCD8-gfp/+* (third chromosomes). We used flies with the following genotype for flipping experiments for TRPA1, mCherry and BRP-GFP: *HS-FLP* (X-chromosome); > *Tubulin-GAL80* > *UAS-TrpA1/NP883* (second chromosomes); *UAS-mCD8-mCherry UAS-brp-gfp/+* (third chromosomes). A series of similar experiments was also performed using *UAS-n-syb-gfp*<sup>37</sup> instead of *UAS-brp-gfp*. We used flies with the following genotype for flipping experiments for TRPA1, mCherry and nAChR-GFP: *HS-FLP* (X chromosome); > *Tubulin-GAL80* > *UAS-TrpA1/NP883* (second chromosomes); *UAS-mCD8-mCherry UAS-nAChR-gfp/+* (third chromosomes). We used flies with the following genotype for flipping experiments for TRPA1, mCherry and GR5A-GFP: *Gr5a-gfp-IRES-gfp-IRES-gfp/HS-FLP* (X chromosome); > *Tubulin-GAL80* > *UAS-TrpA1/NP883* (second chromosomes); *UAS-mCD8-mCherry/+* (third chromosomes).

These flies were aged 2–5 days after eclosion and tested at 37 °C to observe feeding behaviour. Behaviour was quantified by counting proboscis extensions for 1 min after an incubation period of 30 s upon introduction into the behavioural chamber. Heat shock was not necessary as flipping was active at normal temperature (21 °C). For assessing asymmetry, we analysed movie frames with bottom views, and judged asymmetry if the centre of labella extended beyond 5% of the distance between the midline and lateral edge of the fly's head at least three times.

For describing Fdg neuron branching pattern, more than ten samples with an isolated and complete Fdg neuron were analysed in detail from the behavioural screening described in the text. For each analysis of cellular architecture, at least four good samples for each genotype were analysed in detail by isolating, immunolabelling and microscoping more than ten feeding-positive flies from each series of behavioural screening.

**Suppression by Kir2.1 channel.** The inward rectifier potassium channel<sup>19,44</sup> Kir2.1 (ref. 39) was expressed exclusively in the adult stage using the TARGET system<sup>40</sup> to avoid any developmental effects. Flies with NP883, *UAS-Kir2.1*, *tubP-GAL80*<sup>45</sup> were reared at 19 °C, and collected within 1 day after eclosion. NP883, *UAS-Kir2.1* flies were lethal, thus, the suppression by Gal80<sup>45</sup> through development was mandatory. The flies were starved and temperature-shifted in the protocols depicted in Supplementary Fig. 14. They were starved in a vial with a wet paper towel at the bottom. Starved flies were anaesthetized by chilling in a test tube standing on ice, and gently held by Pipetman tip as previously described<sup>43</sup>. For observation of proboscis extension response (PER), the proboscis was stimulated by a 100-mM aqueous sucrose solution on a wick inserted into a 1-ml syringe<sup>5</sup>. A special ultrathin, smooth, traditional Japanese Washi paper, Gampi-shi (Haibara), was used as a wick. This was sturdy and held solution well and was transparent when wet, all improvements for reducing experimental variation when compared to KimWipes<sup>43</sup>. After making a very small droplet of sugar solution at the wick, the piston of the syringe was pulled, and at the moment when the droplet was sucked, the wet surface of the Washi wick was applied to the tip of proboscis. These manipulations were done quickly to prevent the animal from drinking sucrose solution and mitigating its starved state (Supplementary Video 6). Before sucrose application water was applied to make sure the fly was not thirsty. If the fly responded just to water, it was given water to the point of satiation. Each fly was given five presentations of sucrose solution and PER was counted. Between each sucrose presentation water was applied to clean labellar lobes. As no difference between males and female was recognized, half of the results were from male flies and half were from females.

For observation of free-running behaviour with Kir2.1, flies of certain genotype were placed individually in a chamber (3.5 mm × 10 mm, 2 mm height) with a sheet (1-mm thickness) of standard fly food on one side (10 mm × 2 mm). Behaviour was observed for 2 min and videotaped in the 2.5 mm × 10 mm (2 mm height) space through the top glass (3.5 mm × 10 mm) at each time point for each genotype. Proboscis extension that reached the food was counted for 30 s, 1–1.5 min after placing the fly into the chamber, and proboscis extension per minute was calculated.

**Calcium imaging with observation of proboscis extension response.**  $\text{Ca}^{2+}$  imaging as well as laser activation and ablation were performed using FLIES, which was designed to expose the brain of a fly for general purposes such as live imaging, electrophysiology and to keep the fly's proboscis dry and free for movement<sup>5</sup>.  $\text{Ca}^{2+}$  imaging was performed by a method modified from that previously reported<sup>5</sup>. An adult fly was anesthetized in a 15-ml plastic tube standing on ice and set in a tube attached to a FLIES apparatus. Light-curing glue was used to seal the proximally adjacent part of the rostrum to the inner edge of the chamber's hole. To minimize movement artefact, we immobilized the proboscis, which we kept half extended to prevent the pump unit from bumping into and from occluding the SEG, with light-curing glue leaving only labellar lobes free to move. In the saline described above, the head capsule was opened by the tungsten 'sword', and by the 'scissors' to better clip the cuticle and trachea and expose the SEG. The oesophagus, muscle 16 (ref. 12) and the antennal nerves were removed, and air sacks were stretched to the side to expose an Fdg neuron's cell body and to avoid movements that could add noise to the  $\text{Ca}^{2+}$  signal.  $\text{Ca}^{2+}$  imaging was performed following a previous report<sup>45</sup>. We scanned the cell body of an Fdg neuron through a 40 $\times$  water immersion lens (0.80 numerical aperture), using the spinning disk confocal laser system, CSU X1 (Improvision/Yokogawa) using Velocity software, v4.3, on a BX51WI microscope (Olympus). mCD8-RFP was co-expressed to check movement artefact, and GCaMP3.0 and mCD8-RFP were labelled at the same time. GCaMP3.0 signal was imaged with an exposure time of 300 ms of 491-nm laser for detection, and mCD8-RFP fluorescence was imaged with a 535-nm laser with an exposure time of 100 ms every 1.4 s. GCaMP3.0 fluorescence and mCD8-RFP fluorescence at the cell body of a Fdg neuron were quantified at a region of interest using the Velocity software (Improvision). Identification of a Fdg neuron by its location was confirmed by immunolabelling with anti-GFP antibody recognizing GCaMP 3.0 after  $\text{Ca}^{2+}$  imaging experiments. Throughout the experiments, saline was slowly (one drop per second) perfused. Perfusion dramatically reduced the spontaneous movement of a proboscis, which is one key source of movement artefact. The proboscis was stimulated by an aqueous sucrose solution in the same manner as PER experiments with Kir suppression. Labellar bristles (Supplementary Fig. 3a) sensed the sucrose and the proboscis extended reproducibly if flies were starved for 24 h immediately before PER experiments (Supplementary Video 7). PER behaviour was monitored and recorded through a CCD camera attached to a dissection microscope (SMZ-800, Nikon) supported by a swing arm at the same time as GCaMP3.0 was being imaged by the spinning disk confocal microscope<sup>5</sup>. In the case of NP883 > *GCaMP3.0* flies, starvation effect is accelerated probably due to interaction between GCaMP3.0 and cellular  $\text{Ca}^{2+}$  ions, and these flies show a full PER in response to 100 mM sucrose by only 13 h of starvation. Starvation for too long, such as for 24 h, decreases the probability of PER. Therefore, we started dissection in this series of  $\text{Ca}^{2+}$  imaging experiments at around 13 h of starvation. To gain an unambiguous response, we stimulated with 400 mM sucrose because weak responses by 100 mM sucrose tended to be confused with background activity or movement artefact even after several attempts to reduce movement artefact as stated above. We checked PER by 100 mM sucrose before dissection, and only flies exhibiting PER behaviour were dissected. For satiated experiments, flies were placed in a grape juice/yeast pasted food vial for more than 1 h, and only flies that did not show a PER to sucrose stimulation were dissected. We took data within 1.5 h after starting dissection. Details of these methods were published<sup>5</sup>, but many details were improved from the published methods to minimize movement artefact to unambiguously detect small responses in Fdg neurons.

**Laser activation and laser ablation of an Fdg neuron.** The FLIES apparatus was used, and experiments were performed under the Zeiss two-photon microscope, LSM 7 MP. The fly was set into the FLIES apparatus stated above, but the proboscis was left free for observation of its movement, especially for testing asymmetry of proboscis extension. Dissection was done in the same manner as in the  $\text{Ca}^{2+}$  imaging experiments. We used the same saline as that used for  $\text{Ca}^{2+}$  imaging in this series of laser activation and ablation experiments.

For laser activation, we first briefly imaged a satiated NP883 > *TrpA1*; *mCD8-gfp* fly and identified an Fdg neuron and an LPE neuron (control), limiting infrared illumination as much as possible to avoid triggering activity (Supplementary Fig. 16). Then we set a 15.4- $\mu\text{m}$  (55 pixel at 3 $\times$  zoomed condition; pixel size, 0.28  $\mu\text{m}$ ) diameter region of interest surrounding the cell body (Fdg neuron or LPE neuron). We set the circle so that its diameter was twice the diameter of the cell, so as not to miss the cell body even after small movements, which were inevitable because the proboscis was moving freely. Using the 'test bleaching' program of the LSM 7 MP system's Zen software, we scanned the area of the circle for 120 ms total (four iterations) with 20% power at a laser setting of 870 nm. We set the scan speed at 5, which corresponded to a pixel dwell time of 12.61  $\mu\text{s}$ , and selected the 'zoom bleach' function on the software. This scanning protocol was repeated three times approximately 10 s apart. We could see an obvious proboscis extension, usually by the third scanning but sometimes earlier, presumably by a facilitative effect. Only one

neuron was illuminated for each preparation either for Fdg neuron or LPE neuron to exclude the possibility of activating the cell as a result of repeated laser scanning. At the end of the experiment, a live scan of the cell body was taken, and no obvious damage was observed (Supplementary Fig. 16b, c). We positioned a Nikon SMZ-800 stereomicroscope supported with a swing arm in front of the fly to observe and videotape movement of the proboscis, using fibre illumination. To suppress background TRPA1 opening and to improve the spatiotemporal resolution of laser activation, we perfused saline chilled to 21  $^{\circ}\text{C}$  during the entire experiment.

For laser activation observing pump movement, a similar experimental setup was used as described above, except the oesophagus was left intact to allow proper ingestion of dye aqueous solution. The rostrum of the proboscis was extended out with gentle vacuum and glued to the eaves of the FLIES apparatus with light curing glue to visualize the pharyngeal pump. Before activation, flies were allowed access to ingest dye solution to avoid dehydration. Numbers of samples were: 4 (Fdg neuron for proboscis extension), 5 (Fdg neuron for pumping), 5 (LPE neuron for proboscis extension), 5 (LPE neuron for pumping). All preparation for the Fdg neuron showed positive effects; that is, proboscis extension in the direction to the same side as illuminated Fdg neuron, or a pump pulse just after laser illumination on either side of Fdg neuron. Control illumination on LPE neuron had no obvious effect on proboscis extension or pump pulses. In the absence of TRPA1 expression, we saw no induction of feeding behaviour upon infrared illumination of the Fdg neuron, also confirming the specificity of the manipulation (data not shown,  $n = 5$ ).

For laser ablation, we used basically the same type of experimental setup as that for laser activation. We first briefly imaged a starved NP883 > *mCD8-gfp* fly and identified an Fdg neuron and an LPE neuron. Then we set 2.8- $\mu\text{m}$  (10 pixel at 3 $\times$  zoomed condition; pixel size, 0.28  $\mu\text{m}$ ) diameter circle inside the targeted cell body (Fdg neuron or LPE neuron). We set the scan speed at 4, which corresponded to a pixel dwell time of 25.21  $\mu\text{s}$ , and selected the 'zoom bleach' function within the software. Using the 'test bleaching' program, we scanned the area of the circle for 10 ms as total (five iterations) with 30% power at 870 nm. The strong laser made a damaged-looking cell body (arrowhead in Supplementary Fig. 16d) to confirm that the cell was ablated. In some cases, we could observe a small, transient bubble, which shrank and disappeared in a few seconds, then ended up with the aforementioned damaged look. Before and after ablation, we tested PER with 400 mM sucrose stimulation. We perfused saline chilled to 21  $^{\circ}\text{C}$  during all experiments. After ablation of a neuron, we waited for 15 min until ablation effect appeared on PER. Numbers of samples were: 5 (Fdg neuron), 5 (LPE neuron). All Fdg neuron ablation gave consistent results with those in Fig. 4e and Supplementary Video 9, whereas ablation of LPE neuron showed no recognizable effect on proboscis extension.

For assessing asymmetry both in laser activation and in laser ablation, we analysed movie frames, and judged asymmetry if the midline of the labella extended beyond 5% of the distance between the midline and the lateral edge of the fly's head.

**Statistics.** All statistical analyses were performed according to standard methods<sup>46</sup> using Prism, v5.0a (GraphPad Software) and Excel (Microsoft).

For statistics in Fig. 1e, the six groups were analysed with the Kruskal–Wallis test using a one-way analysis of variance by ranks, and the significant difference between groups was found ( $P < 0.0001$ ). \*\*\* denotes  $P < 0.001$  by Dunn's post-hoc multiple comparison test between progeny from this cross: NP883  $\times$  *UAS-TrpA1* (NP883 > *TrpA1*), compared to these crosses NP883  $\times$  wild type, wild type  $\times$  *UAS-TrpA1*, or wild type  $\times$  wild type. The same post-hoc analysis was performed for the NP5137 line.

30. Lee, T. & Luo, L. Mosaic analysis with a repressible cell marker for studies of gene function in neuronal morphogenesis. *Neuron* **22**, 451–461 (1999).
31. Shang, Y., Griffith, L. C. & Rosbash, M. Light-arousal and circadian photoreception circuits intersect at the large PDF cells of the *Drosophila* brain. *Proc. Natl Acad. Sci. USA* **105**, 19587–19594 (2008).
32. Yang, C. H. et al. Control of the postmating behavioral switch in *Drosophila* females by internal sensory neurons. *Neuron* **61**, 519–526 (2009).
33. Pauli, A. et al. Cell-type-specific TEV protease cleavage reveals cohesin functions in *Drosophila* neurons. *Dev. Cell* **14**, 239–251 (2008).
34. Kitamoto, T. Conditional disruption of synaptic transmission induces male-male courtship behavior in *Drosophila*. *Proc. Natl Acad. Sci. USA* **99**, 13232–13237 (2002).
35. Fouquet, W. et al. Maturation of active zone assembly by *Drosophila* Bruchpilot. *J. Cell Biol.* **186**, 129–145 (2009).
36. Leiss, F. et al. Characterization of dendritic spines in the *Drosophila* central nervous system. *Dev. Neurobiol.* **69**, 221–234 (2009).
37. Estes, P. S., Ho, G. L., Narayanan, R. & Ramaswami, M. Synaptic localization and restricted diffusion of a *Drosophila* neuronal synaptobrevin-green fluorescent protein chimera *in vivo*. *J. Neurogenet.* **13**, 233–255 (2000).
38. Fischler, W., Kong, P., Marella, S. & Scott, K. The detection of carbonation by the *Drosophila* gustatory system. *Nature* **448**, 1054–1057 (2007).
39. Baines, R. A., Uhler, J. P., Thompson, A., Sweeney, S. T. & Bate, M. Altered electrical properties in *Drosophila* neurons developing without synaptic transmission. *J. Neurosci.* **21**, 1523–1531 (2001).

40. McGuire, S. E., Le, P. T., Osborn, A. J., Matsumoto, K. & Davis, R. L. Spatiotemporal rescue of memory dysfunction in *Drosophila*. *Science* **302**, 1765–1768 (2003).
41. Awasaki, T., Lai, S. L., Ito, K. & Lee, T. Organization and postembryonic development of glial cells in the adult central brain of *Drosophila*. *J. Neurosci.* **28**, 13742–13753 (2008).
42. Hayashi, S. *et al.* GETDB, a database compiling expression patterns and molecular locations of a collection of Gal4 enhancer traps. *Genesis* **34**, 58–61 (2002).
43. Shiraiwa, T. & Carlson, J. R. Proboscis extension response (PER) assay in *Drosophila*. *J. Vis. Exp.* **3**, 193 (2007).
44. Kubo, Y., Baldwin, T. J., Jan, Y. N. & Jan, L. Y. Primary structure and functional expression of a mouse inward rectifier potassium channel. *Nature* **362**, 127–133 (1993).
45. Marella, S. *et al.* Imaging taste responses in the fly brain reveals a functional map of taste category and behavior. *Neuron* **49**, 285–295 (2006).
46. Zar, J. *Biostatistical Analysis* 4th edn (Prentice Hall, 1999).



# High-resolution analysis with novel cell-surface markers identifies routes to iPS cells

James O'Malley<sup>1</sup>, Stavroula Skylaki<sup>2</sup>, Kumiko A. Iwabuchi<sup>1</sup>, Eleni Chantzoura<sup>1</sup>, Tyson Ruetz<sup>1</sup>, Anna Johnsson<sup>3</sup>, Simon R. Tomlinson<sup>1</sup>, Sten Linnarsson<sup>3</sup> & Keisuke Kaji<sup>1</sup>

The generation of induced pluripotent stem (iPS) cells presents a challenge to normal developmental processes. The low efficiency and heterogeneity of most methods have hindered understanding of the precise molecular mechanisms promoting, and roadblocks preventing, efficient reprogramming. Although several intermediate populations have been described<sup>1–7</sup>, it has proved difficult to characterize the rare, asynchronous transition from these intermediate stages to iPS cells. The rapid expansion of minor reprogrammed cells in the heterogeneous population can also obscure investigation of relevant transition processes. Understanding the biological mechanisms essential for successful iPS cell generation requires both accurate capture of cells undergoing the reprogramming process and identification of the associated global gene expression changes. Here we demonstrate that in mouse embryonic fibroblasts, reprogramming follows an orderly sequence of stage transitions, marked by changes in the cell-surface markers CD44 and ICAM1, and a Nanog-enhanced green fluorescent protein (Nanog-eGFP) reporter. RNA-sequencing analysis of these populations demonstrates two waves of pluripotency gene upregulation, and unexpectedly, transient upregulation of several epidermis-related genes, demonstrating that reprogramming is not simply the reversal of the normal developmental processes. This novel high-resolution analysis enables the construction of a detailed reprogramming route map, and the improved understanding of the reprogramming process will lead to new reprogramming strategies.

Several reports have suggested that reprogramming progresses in an ordered manner<sup>3,5,6,8–10</sup>. To identify markers whose expression changed concurrent with pluripotency gene expression, we performed time course microarray analysis using a piggyBac transposon-based secondary reprogramming system<sup>3,11</sup> (Supplementary Fig. 2a). Of a number of candidate cell-surface markers, *Cd44* and *Icam1* (also known as *CD54*) demonstrated the most dynamic expression changes throughout secondary mouse embryonic fibroblast (MEF) reprogramming (Supplementary Fig. 2b). For further investigation, we generated an efficient secondary reprogramming system in which doxycycline-mediated induction of the reprogramming factors could be monitored by an mOrange reporter placed after the 2A-peptide-linked reprogramming cassette *c-Myc-Klf4-Oct4-Sox2* (MKOS)<sup>12</sup>, and endogenous *Nanog* promoter activation could be followed by expression of enhanced green fluorescent protein (eGFP)<sup>13</sup> (Supplementary Fig. 3). Reprogramming cultures were supplemented with vitamin C and an Alk inhibitor, both of which enhance reprogramming efficiency<sup>10,14,15</sup>. In this secondary reprogramming system, Nanog-eGFP<sup>+</sup> cells appeared as early as day 6, and >60% of mOrange<sup>+</sup> transgene-expressing cells were found to be Nanog-eGFP<sup>+</sup> by day 12 (Supplementary Figs 4 and 5a). Most mOrange<sup>+</sup> transgene-expressing cells lost expression of *Thy1* (also known as *CD90*) and gained E-cadherin (also known as *Cdh1*) expression by day 4 (Supplementary Fig. 5b, c). Expression of stage-specific embryonic antigen 1 (SSEA-1, also known as *Fut4*) barely

changed after day 8, with a gradual gain of Nanog-eGFP<sup>+</sup> cells in both SSEA-1<sup>+</sup> and SSEA-1<sup>−</sup> cell populations (Supplementary Fig. 5d). Consistent with heterogeneous expression of SSEA1 in iPS and embryonic stem (ES) cells, it was not possible to delineate the reprogramming process accurately using SSEA-1 (Supplementary Fig. 6). By contrast, the appearance of CD44<sup>−</sup> and ICAM1<sup>+</sup> cells at later time points closely correlated with Nanog-eGFP expression (Supplementary Fig. 5e, f). Double staining for CD44 and ICAM1 revealed that a distinct series of population changes occur during reprogramming (Fig. 1). Initially, MEFs displayed high CD44 and broad ICAM1 expression, with most becoming ICAM1<sup>−</sup> by day 6, along with the appearance of a minor CD44<sup>−</sup> ICAM1<sup>−</sup> cell population. By day 8, CD44<sup>−</sup> populations appeared enriched, and at day 12 almost all cells displayed an iPS/ES-cell-like CD44<sup>−</sup> ICAM1<sup>+</sup> profile, of which more than 60% expressed Nanog-eGFP. Consistent with the observation that Nanog expression is not necessarily a sign of completed reprogramming<sup>16</sup>, Nanog-eGFP<sup>+</sup> cells were observed even before cells obtained this iPS/ES-cell-like phenotype (CD44<sup>−</sup> ICAM1<sup>+</sup>). Both ICAM1<sup>+</sup> and ICAM1<sup>−</sup>-sorted MEFs demonstrated similar fluorescence-activated cell sorting (FACS) profile changes during reprogramming (Supplementary Fig. 7). Immunofluorescence for CD44 and ICAM1 revealed that reprogramming is not synchronized even within individual colonies (Supplementary Fig. 8). Secondary reprogramming of the non-polycistronic iPS cell line 6c (refs 3, 11) and primary reprogramming using MKOS and *Oct4-P2A-Sox2-T2A-Klf4-E2A-cMyc* (OSKM)<sup>17</sup> piggyBac transposons resulted in similar ICAM1 and CD44 profile changes, indicating their suitability for use in other systems and contexts (Supplementary Fig. 9). These findings demonstrated the asynchronous but stepwise manner of reprogramming, and highlighted the potential usefulness of CD44 and ICAM1 to isolate intermediate reprogramming subpopulations.

Next, we aimed to confirm that the observed CD44/ICAM1 profile changes reflected the transition of individual cells from one stage to the next, and not merely the loss of one major population and expansion of another minor population. CD44<sup>+</sup> ICAM1<sup>−</sup> (gate 1), CD44<sup>−</sup> ICAM1<sup>−</sup> (gate 2) and CD44<sup>−</sup> ICAM1<sup>+</sup> (gate 3) cell populations, either Nanog-eGFP<sup>+</sup> (that is, 1NG<sup>+</sup>, 2NG<sup>+</sup> and 3NG<sup>+</sup>) or Nanog-eGFP<sup>−</sup> (1NG<sup>−</sup>, 2NG<sup>−</sup> and 3NG<sup>−</sup>), were isolated by cell-sorting at day 10 of reprogramming and re-plated in reprogramming conditions (Fig. 2a). After 3 days, both NG<sup>+</sup> and NG<sup>−</sup> cells progressed in the order of gates 1 to 2 to 3 (Fig. 2b). This progression correlated well with increased Nanog-eGFP<sup>+</sup> colony-forming potential (c.f.p.), with 3NG<sup>+</sup> cells displaying similar clonogenicity to fully reprogrammed iPS cells (Fig. 2c). Of cells with the same CD44/ICAM1 profile, Nanog-eGFP expression correlated with a higher c.f.p. (for example, 1NG<sup>−</sup> versus 1NG<sup>+</sup>).

To examine the progression of the reprogramming process more accurately, cells from each gate were sorted, and their expression of CD44/ICAM1/Nanog-eGFP was re-analysed after 24 h (Fig. 2d). On the basis of total cell numbers in each gate after 24 h (Supplementary Fig. 10), we generated a reprogramming route map representing differences in the

<sup>1</sup>MRC Centre for Regenerative Medicine, University of Edinburgh, Edinburgh BioQuarter, 5 Little France Drive, Edinburgh EH16 4UU, UK. <sup>2</sup>Stem Cell Dynamics Research Unit, Helmholtz Center Munich, Ingolstädter Landstraße 1, 85764 Neuherberg, Germany. <sup>3</sup>Laboratory for Molecular Neurobiology, Department of Medical Biochemistry and Biophysics, Karolinska Institute, Scheeles väg 1, SE-171 77 Stockholm, Sweden.

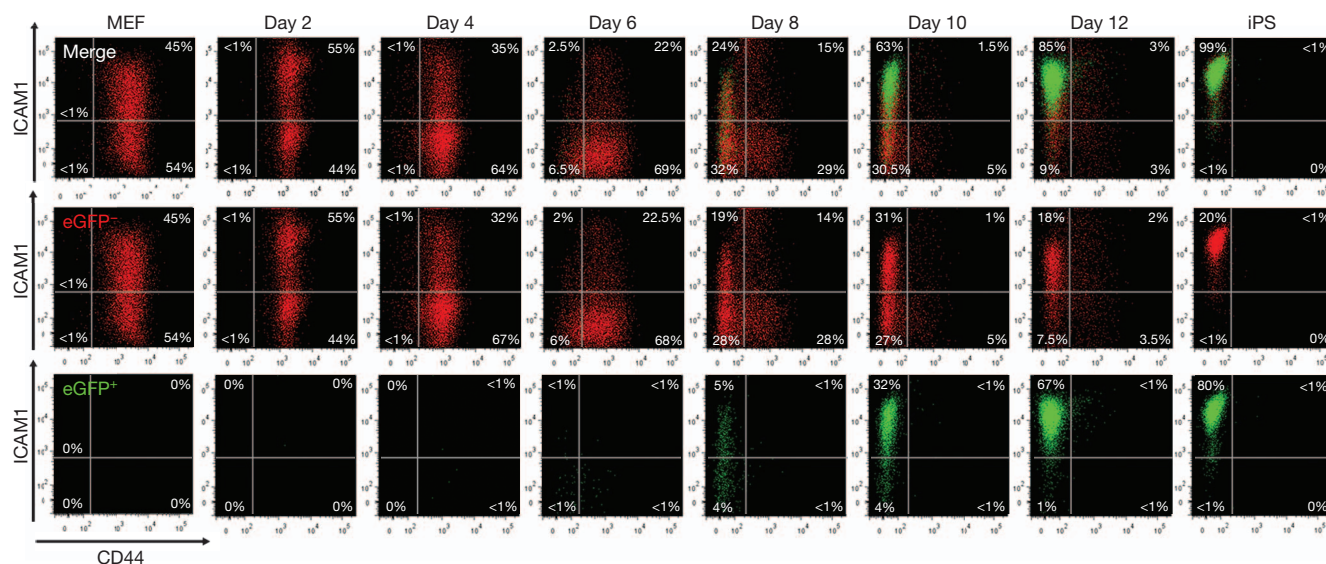


**Figure 1 | FACS analysis during secondary reprogramming of MEFs with CD44/ICAM1 double staining.** Loss of CD44 expression was rapidly followed by ICAM1 upregulation and Nanog-eGFP expression. By day 12, most cells

displayed an ICAM<sup>+</sup>/CD44<sup>-</sup> ES-cell-like profile. Red denotes Nanog-eGFP<sup>-</sup> cells; green denotes Nanog-eGFP<sup>+</sup> cells.

efficiency of these stage transitions and in Nanog-eGFP<sup>+</sup> c.f.p. (Fig. 2e). Similar results were obtained when each subpopulation was sorted at day 8 (Supplementary Fig. 11). This analysis revealed that reaching a Nanog-eGFP<sup>+</sup> state is a rate-limiting step—as few cells overcame this barrier in the 24 h assay—and those that do so reprogram more efficiently than their Nanog-eGFP<sup>-</sup> counterparts, consistent with the role of *Nanog* as an accelerator of reprogramming and the gateway to pluripotency<sup>18,19</sup>.

To determine global gene expression changes during these stage transitions, we carried out RNA-sequencing analysis using a highly

multiplexed sample bar-coding system<sup>20–26</sup> (see Methods and Supplementary Table 1). Hierarchical clustering using the complete list of differentially expressed genes (DEGs) revealed four major branches: (1) MEFs; (2) 1NG<sup>-/+</sup> and 2NG<sup>-</sup>; (3) 2NG<sup>-/+</sup> and 3NG<sup>-/+</sup>; and (4) 3NG<sup>+</sup> sorted at day 15 (3NG<sup>+</sup>D15), iPS and ES cells (Fig. 3a). There was a prominent gene expression difference between 3NG<sup>+</sup> and 3NG<sup>+</sup>D15 cells, with the latter being more similar to iPS and ES cells (Fig. 3a and Supplementary Fig. 12), possibly reflecting the observed difference in the c.f.p. in the absence of doxycycline (Supplementary

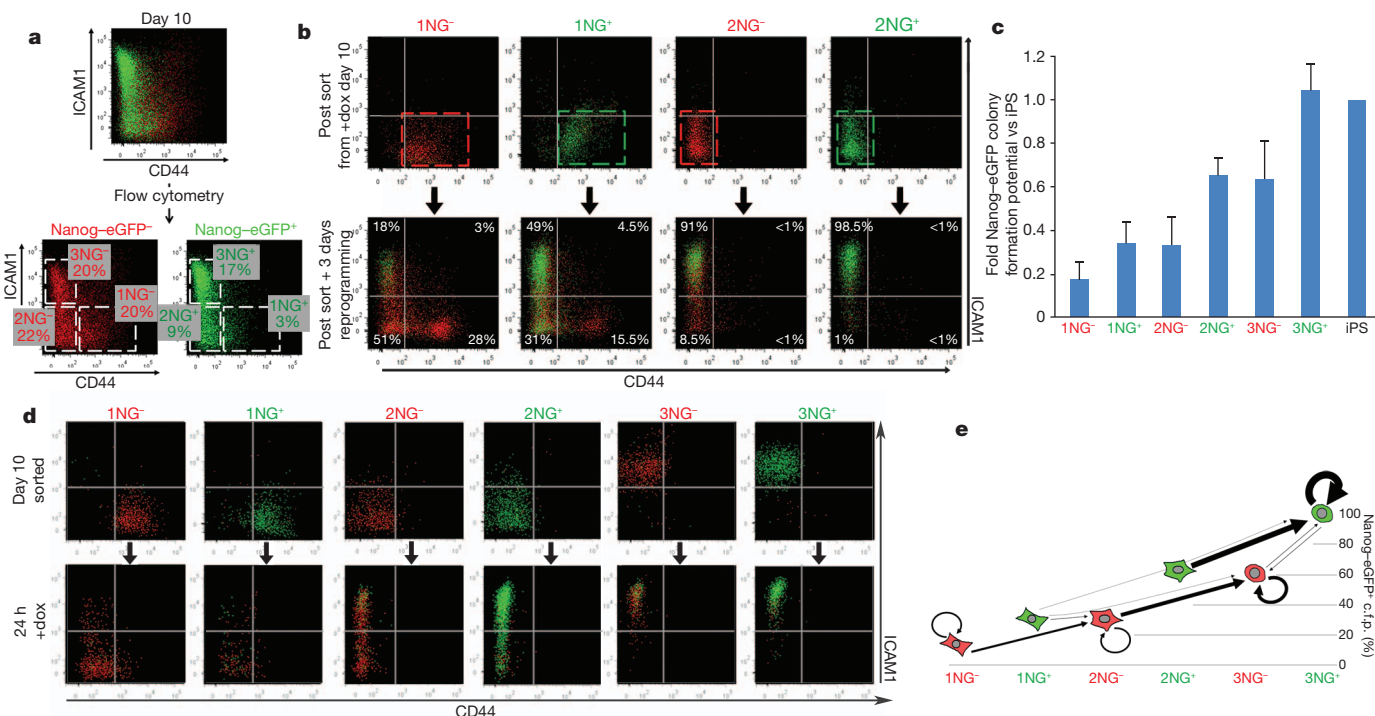


**Figure 2 | CD44/ICAM1 subpopulations represent distinct stages of reprogramming.** **a**, Nanog-eGFP<sup>+</sup> (NG<sup>+</sup>) and Nanog-eGFP<sup>-</sup> (NG<sup>-</sup>) cells were subdivided into CD44<sup>+</sup> ICAM1<sup>-</sup> (gate 1), CD44<sup>-</sup> ICAM1<sup>-</sup> (gate 2) and CD44<sup>-</sup> ICAM1<sup>+</sup> (gate 3) populations at day 10 of reprogramming. **b**, FACS analysis of sorted subpopulations after a 3-day culture in the presence of doxycycline (dox). **c**, Relative probability to generate Nanog-eGFP<sup>+</sup> iPS cell

colonies from each subpopulation compared to fully reprogrammed iPS cells. Error bars represent s.d.,  $n = 3$ . **d**, Expression of CD44, ICAM1 and Nanog-eGFP was re-analysed 24 h after sorting. **e**, Major transitions (>500 cells) of each population within 24 h. The y axis indicates relative c.f.p. after a further 10 days. Arrow size reflects relative cell numbers.



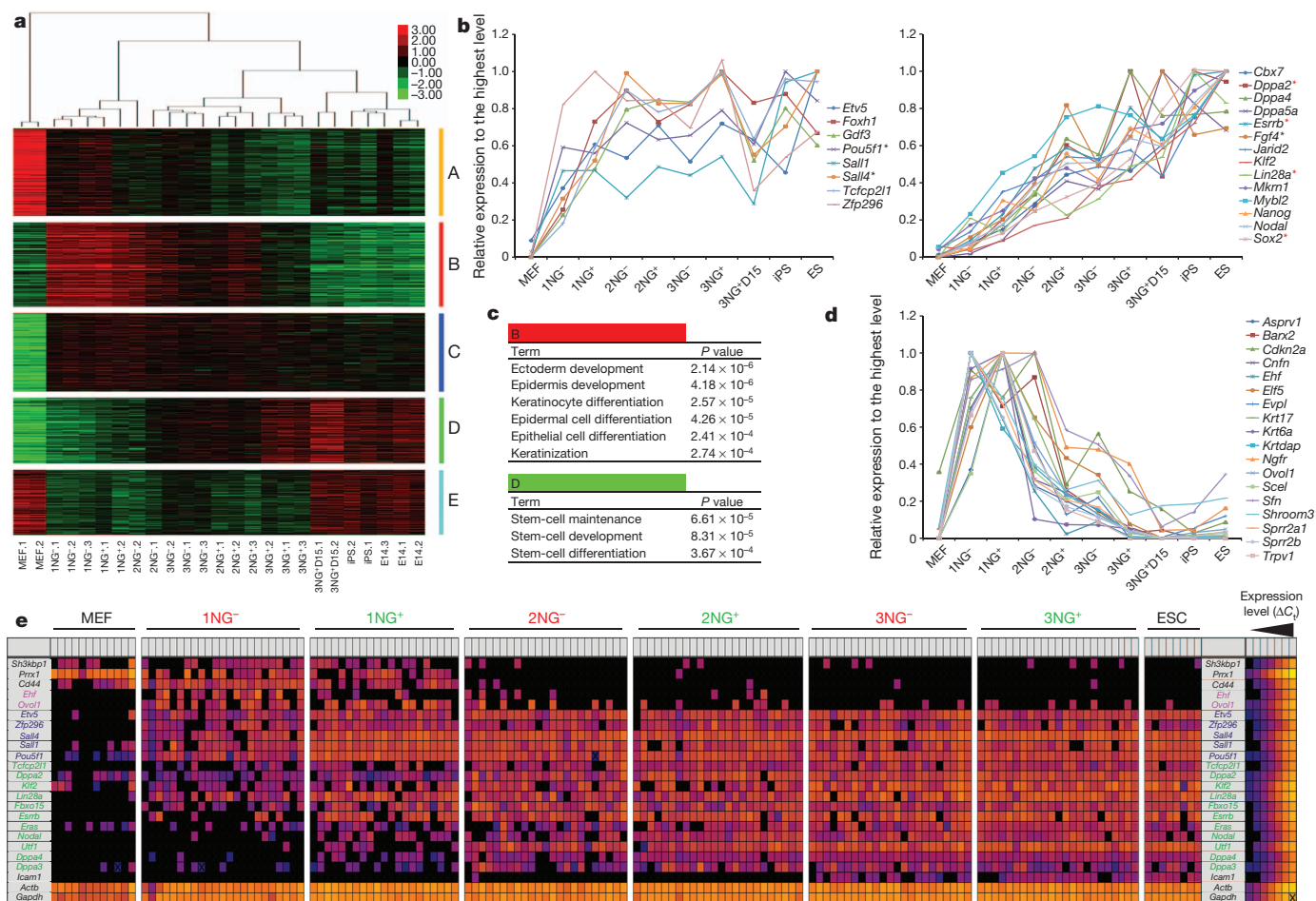


**Figure 3 | Global gene expression changes during the stage transition.** **a**, Hierarchical clustering of samples with DEGs and expression heat map. Groups A–E represent different expression patterns. **b**, Early (left) and late (right) upregulation of pluripotency-related genes. Black and red asterisks indicate early and late pluripotency genes, respectively, previously identified by

Fig. 13). The DEGs between these two populations may be involved in the establishment of an exogenous-factor-independent self-renewal state. Principal component analysis clearly distinguished  $2NG^+$  from  $3NG^-$  cells, consistent with the higher probability of the former to reach the  $3NG^+$  state within 24 h (Supplementary Figs 10 and 12b). DEGs could be classified into five distinct expression pattern groups (A–E) (Fig. 3a and Supplementary Tables 2 and 3). Group A contained readily downregulated fibroblast-related genes. Group D comprised factors gradually upregulated towards iPS cells, in which ES cell genes were highly enriched ( $P \leq 0.000367$ ) (Fig. 3c). However group C, which contained genes upregulated at early stages and maintained throughout reprogramming, also included some pluripotency-related factors. To extend this finding, we examined the expression pattern of 22 pluripotency-related genes in our data set<sup>27,28</sup>. Interestingly, 8 pluripotency genes, including endogenous *Oct4* (also known as *Pou5f1*), were already upregulated at the  $1NG^+/2NG^-$  stages to the level found in  $3NG^+$  cells (Fig. 3b, left), whereas 14 pluripotency genes were more gradually upregulated in the later stage reprogramming populations (Fig. 3b, right, and Supplementary Table 4). This early and late pluripotency gene upregulation was confirmed at the single cell level<sup>5</sup> (Fig. 3e), highlighting the high resolution of the CD44/ICAM1 sorting system.

We also identified two additional gene expression patterns displaying transient upregulation (group B) or downregulation (group E) exclusively in the intermediate stages of reprogramming. This finding indicates that reprogramming from MEFs to iPS cells is not simply the loss of MEF genes and gain of ES cell genes. Gene Ontology analysis

single-cell quantitative PCR (qPCR)<sup>5</sup>. **c**, Epidermal and stem-cell gene enrichment in gene list B and D, respectively. **d**, Transient upregulation of 18 epidermis/keratinocyte-related genes during reprogramming. **e**, Single-cell gene expression analysis. Each square represents one reaction chamber from one cell. Colour corresponds to  $\Delta C_t$  value, as shown in the legend.

revealed that genes related to ectoderm/epidermis development and keratinocyte differentiation were highly enriched in group B ( $P \leq 0.000274$ ) (Fig. 3c, d and Supplementary Tables 3–5). Although SFN and KRT17 were barely detectable by immunofluorescence in MEFs and iPS cells, transient upregulation was observed in the intermediate stages of reprogramming (Supplementary Fig. 14). Single-cell PCR confirmed the co-expression of epidermis genes (*Ehf* and *Ovol1*) with early pluripotency genes in the  $1NG^{-/+}$  stage (Fig. 3e). Consistent with our data, analysis of three published microarray data sets incorporating partially reprogrammed iPS cells<sup>1</sup>, a time course experiment<sup>3</sup> and a subpopulation analysis with Thy1, SSEA-1 and Oct4-eGFP (ref. 6) confirmed transient epidermal gene expression during reprogramming (Supplementary Figs 15–17 and Supplementary Tables 6–8). Partially reprogrammed cells from B cells also displayed similar epidermis gene expression<sup>4</sup>, whereas two factor-reprogramming (Oct4 and Sox2) of MEFs did not<sup>29</sup>. Therefore, this intermediate state could be a consequence of the use of Klf4 that is important for efficient reprogramming, and demonstrates that the reprogramming process is not simply a reversion of normal differentiation (summarized in Supplementary Fig. 1). It would be intriguing to investigate whether similar transient gene expression changes can be seen in reprogramming of ectoderm or endoderm lineages. Downregulation of these epidermis genes coincided with upregulation of ‘late’ pluripotency genes. Future examination of this rapid switch in gene expression may provide a new insight into the molecular mechanism of reprogramming.



The integrative data analysis described above demonstrated that this CD44/ICAM1/Nanog-eGFP marker system could uniquely provide high-resolution information during late pluripotency gene upregulation, enabling the discrimination of 'reprogramming' from 'expansion of reprogrammed cells' (Fig. 3b and Supplementary Figs 16b and 17f). This system also refines investigation of the kinetics of reprogramming. It has recently been shown that vitamin C increases reprogramming efficiency by facilitating histone 3 Lys 9 (H3K9) demethylation<sup>7</sup>, and that reprogramming factors fail to bind trimethylated H3K9-rich regions in the initial stages of reprogramming<sup>30</sup>. We carried out reprogramming in the absence of vitamin C and observed not only a decrease in the iPS cell colony number, but also a marked delay in the transition from one stage of reprogramming to the next (Supplementary Fig. 18). Similar analyses can be performed using our marker system to investigate the mechanism of action of other factors that alter reprogramming efficiency. Isolation and analysis of subpopulations affected by these factors could reveal the downstream genes specifically involved in, and required for, successful reprogramming. Further studies using this high-resolution analysis system have the potential to make a considerable contribution towards revealing the molecular mechanisms of reprogramming.

## METHODS SUMMARY

The vector PB-TAP IRI 2LMKOSimO, a modified version of polycistronic reprogramming vector pCAG2LMKOSimO (ref. 12), containing insulator and replicator sequences and driven by the tetO<sub>2</sub> promoter, was constructed as described in the Methods. This vector was used to generate iPS cell line D6s4B5 from reverse tetracycline transactivator (rtTA)-expressing MEFs carrying a Nanog-eGFP reporter<sup>13</sup>. D6s4B5 iPS cells were used to generate chimaeric embryos from which MEFs were isolated at embryonic day 12.5. Transgenic MEFs were cultured in doxycycline (300 ng ml<sup>-1</sup>), vitamin C (10 µg ml<sup>-1</sup>) and Alk inhibitor (500 nM), and collected for flow cytometry analysis (BD Fortessa), carried out using antibodies for CD44 and ICAM1 every 2–3 days. Cells were sorted (BD FACS Aria II) at day 10 or 15, and replated on gelatin for analysis at 24 h, or at clonal density on irradiated MEFs for Nanog-eGFP<sup>+</sup> c.f.p. 10 days after cell sorting. All flow cytometry data were analysed using FlowJo (Tree Star). Immunofluorescence was carried out using confocal microscopy (Leica TSC SP2). RNA from sorted samples was extracted using Trizol (Invitrogen), and 10 ng total RNA was used for multiplexed RNA-sequencing<sup>20,21</sup>. Data were analysed using GeneProf<sup>22</sup>, and DEGs were identified using edgeR and DESeq Bioconductor libraries<sup>23–25</sup>. Gene Ontology enrichment was calculated using DAVID<sup>26</sup>.

**Full Methods** and any associated references are available in the online version of the paper.

**Received 19 September 2012; accepted 3 May 2013.**

**Published online 2 June 2013.**

1. Sridharan, R. *et al.* Role of the murine reprogramming factors in the induction of pluripotency. *Cell* **136**, 364–377 (2009).
2. Golipour, A. *et al.* A late transition in somatic cell reprogramming requires regulators distinct from the pluripotency network. *Cell Stem Cell* **11**, 769–782 (2012).
3. Samavarchi-Tehrani, P. *et al.* Functional genomics reveals a BMP-driven mesenchymal-to-epithelial transition in the initiation of somatic cell reprogramming. *Cell Stem Cell* **7**, 64–77 (2010).
4. Mikkelsen, T. S. *et al.* Dissecting direct reprogramming through integrative genomic analysis. *Nature* **454**, 49–55 (2008).
5. Buganim, Y. *et al.* Single-cell expression analyses during cellular reprogramming reveal an early stochastic and a late hierarchic phase. *Cell* **150**, 1209–1222 (2012).
6. Polo, J. M. *et al.* A molecular roadmap of reprogramming somatic cells into iPS cells. *Cell* **151**, 1617–1632 (2012).
7. Chen, J. *et al.* H3K9 methylation is a barrier during somatic cell reprogramming into iPS cells. *Nature Genet.* **45**, 34–42 (2013).
8. Stadtfeld, M., Maherali, N., Breault, D. T. & Hochedlinger, K. Defining molecular cornerstones during fibroblast to iPS cell reprogramming in mouse. *Cell Stem Cell* **2**, 230–240 (2008).

9. Brambrink, T. *et al.* Sequential expression of pluripotency markers during direct reprogramming of mouse somatic cells. *Cell Stem Cell* **2**, 151–159 (2008).
10. Li, R. *et al.* A mesenchymal-to-epithelial transition initiates and is required for the nuclear reprogramming of mouse fibroblasts. *Cell Stem Cell* **7**, 51–63 (2010).
11. Woltjen, K. *et al.* piggyBac transposition reprograms fibroblasts to induced pluripotent stem cells. *Nature* **458**, 766–770 (2009).
12. Kaji, K. *et al.* Virus-free induction of pluripotency and subsequent excision of reprogramming factors. *Nature* **458**, 771–775 (2009).
13. Chambers, I. *et al.* Nanog safeguards pluripotency and mediates germline development. *Nature* **450**, 1230–1234 (2007).
14. Esteban, M. A. *et al.* Vitamin C enhances the generation of mouse and human induced pluripotent stem cells. *Cell Stem Cell* **6**, 71–79 (2010).
15. Maherali, N. & Hochedlinger, K. Tgfb signal inhibition cooperates in the induction of iPS cells and replaces Sox2 and cMyc. *Curr. Biol.* **19**, 1718–1723 (2009).
16. Chan, E. M. *et al.* Live cell imaging distinguishes bona fide human iPS cells from partially reprogrammed cells. *Nature Biotechnol.* **27**, 1033–1037 (2009).
17. Carey, B. W. *et al.* Reprogramming of murine and human somatic cells using a single polycistronic vector. *Proc. Natl Acad. Sci. USA* **106**, 157–162 (2009).
18. Hanna, J. *et al.* Direct cell reprogramming is a stochastic process amenable to acceleration. *Nature* **462**, 595–601 (2009).
19. Silva, J. *et al.* Nanog is the gateway to the pluripotent ground state. *Cell* **138**, 722–737 (2009).
20. Islam, S. *et al.* Characterization of the single-cell transcriptional landscape by highly multiplex RNA-seq. *Genome Res.* **21**, 1160–1167 (2011).
21. Islam, S. *et al.* Highly multiplexed and strand-specific single-cell RNA 5' end sequencing. *Nature Protocols* **7**, 813–828 (2012).
22. Halbritter, F., Vaidya, H. J. & Tomlinson, S. R. GeneProf: analysis of high-throughput sequencing experiments. *Nature Methods* **9**, 7–8 (2012).
23. Anders, S. & Huber, W. Differential expression analysis for sequence count data. *Genome Biol.* **11**, R106 (2010).
24. Robinson, M. D., McCarthy, D. J. & Smyth, G. K. edgeR: a Bioconductor package for differential expression analysis of digital gene expression data. *Bioinformatics* **26**, 139–140 (2010).
25. Gentleman, R. C. *et al.* Bioconductor: open software development for computational biology and bioinformatics. *Genome Biol.* **5**, R80 (2004).
26. Huang, d. W., Sherman, B. T. & Lempicki, R. A. Systematic and integrative analysis of large gene lists using DAVID bioinformatics resources. *Nature Protocols* **4**, 44–57 (2009).
27. Kim, J., Chu, J., Shen, X., Wang, J. & Orkin, S. H. An extended transcriptional network for pluripotency of embryonic stem cells. *Cell* **132**, 1049–1061 (2008).
28. Xu, H., Lemischka, I. R. & Ma'ayan, A. SVM classifier to predict genes important for self-renewal and pluripotency of mouse embryonic stem cells. *BMC Syst. Biol.* **4**, 173 (2010).
29. Nemajerova, A., Kim, S. Y., Petrenko, O. & Moll, U. M. Two-factor reprogramming of somatic cells to pluripotent stem cells reveals partial functional redundancy of Sox2 and Klf4. *Cell Death Differ.* **19**, 1268–1276 (2012).
30. Soufi, A., Donahue, G. & Zaret, K. S. Facilitators and impediments of the pluripotency reprogramming factors' initial engagement with the genome. *Cell* **151**, 994–1004 (2012).

**Supplementary Information** is available in the online version of the paper.

**Acknowledgements** We thank A. Nagy and K. Woltjen for providing the 6c iPS cell line, I. Chambers for providing TNG mice, S. Monard and O. Rodrigues for assistance with flow cytometry, and T. Kunath, T. Burdon, S. Lowell and N. Festuccia for discussions and comments on the manuscript. We also thank L. Robertson for technical assistance, and Biomed unit staff for mouse husbandry. This work was supported by ERC grants ROADTOIPS (no. 261075) and BRAINCELL (no. 261063), and the Anne Rowling Regenerative Neurology Clinic. J.O.'M. and T.R. are funded by an MRC PhD Studentship and a Darwin Trust of Edinburgh Scholarship, respectively.

**Author Contributions** J.O.'M. designed and performed flow cytometry analysis and sorting experiments, prepared RNA for sequencing, carried out immunofluorescence imaging, and collected, analysed and interpreted data, and wrote the manuscript. S.S. analysed RNA-sequencing and published microarray data sets. K.A.I. carried out single-cell PCR analysis. E.C. performed primary reprogramming and FACS analysis. T.R. carried out immunofluorescence and confocal imaging. S.R.T. performed microarray analysis to identify cell-surface marker candidates. A.J. and S.L. performed multiplexed RNA-sequencing and collected data. K.K. conceived the study, identified the surface markers, generated the D6s4B5 iPS cell line, analysed RNA-sequencing data, supervised experiment design and data interpretation, and wrote the manuscript.

**Author Information** RNA-sequencing data are deposited in the ArrayExpress under accession number E-MTAB-1654. Reprints and permissions information is available at [www.nature.com/reprints](http://www.nature.com/reprints). The authors declare no competing financial interests. Readers are welcome to comment on the online version of the paper. Correspondence and requests for materials should be addressed to K.K. ([keisuke.kaji@ed.ac.uk](mailto:keisuke.kaji@ed.ac.uk)).

## METHODS

**Vector construction.** The piggyBac transposon PB-TAP containing the tetO<sub>2</sub> promoter, an attR1R2 Gateway cloning cassette (Invitrogen) and rabbit  $\beta$ -globin poly A signal, was provided by A. Nagy. To minimize silencing of the reprogramming vector, a chicken  $\beta$ -globin insulator<sup>31</sup> was inserted into the PacI site between the piggyBac 3'-terminal repeat (3'-TR) and the tetO<sub>2</sub> promoter, and a human lamin B2 (LMB2) replicator<sup>32</sup> plus another chicken  $\beta$ -globin insulator were inserted into the EcoRV site between the rabbit  $\beta$ -globin poly A signal and the piggyBac 5'-TR, to generate PB-TAP IRI. The BamHI fragment containing loxP-flanked MKOS reprogramming cassette followed by ires-mOrange (2LMKOSimO) from pCAG2LMKOSimO (ref. 12) was inserted into a Gateway entry vector pENTR 2B (Life Technologies), to generate attP2LMKOSimO pENTR. Finally the attP2LMKOSimO cassette was Gateway-cloned into the PB-TAP IRI to yield reprogramming piggyBac transposon PB-TAP IRI attP2LMKOSimO. Similarly, reprogramming piggyBac transposon PB-TAP IRI 2LOSKMimO was generated after transferring the OSKM reprogramming cassette<sup>17</sup> into attP2LMKOSimO pENTR replacing the MKOS cassette. Plasmid sequences are available on request.

**Generation of a primary iPS cell line D6s4B5.** Embryos at 12.5 days post coitum (d.p.c.) were obtained from *Rosa<sup>rtTA/rtTA</sup>*, *Nanog<sup>eGFP/+</sup>*, *Col1a1<sup>+/-</sup>* mice, which were derived by crossing TNG mice<sup>13</sup> and B6;129-Gt(Rosa)26Sor<sup>tm1(rtTA\**M2*)/ae</sup> *Col1a1<sup>tm2(tetO-Fox5f1)/ae</sup>*/J (Jackson Laboratory). The embryos were decapitated, eviscerated, dissociated with 0.25% trypsin and 0.1% EDTA, and plated in MEF medium (GMEM, 10% FBS, penicillin-streptomycin, 1 $\times$  non-essential amino acids (Invitrogen), 1 mM sodium pyruvate and 0.05 mM 2-mercaptoethanol). The PB-TAP IRI attP2LMKOSimO (500 ng) and pCyl43 piggyBac transposase expression vector<sup>33</sup> (2  $\mu$ g) were introduced into the MEFs by nucleofection (Amaxa) as before<sup>12</sup>, and cells were cultured in ES cell medium (MEF medium supplemented with 1,000 U ml<sup>-1</sup> leukaemia inhibiting factor (LIF)) in the presence of 1.0  $\mu$ g ml<sup>-1</sup> doxycycline (Sigma) for an initial 8 days, and thereafter 0.5  $\mu$ g ml<sup>-1</sup> doxycycline. Pluripotency of a clonal iPS cell line D6 was confirmed by teratoma formation, and a subclone D6s4B5 was used for secondary reprogramming. To compare CD44 and ICAM1 profiles of primary reprogramming with PB-TAP IRI attP2LMKOSimO and PB-TAP IRI 2LOSKMimO vectors, MEFs were nucleofected as above and cultured in the presence of 1.0  $\mu$ g ml<sup>-1</sup> doxycycline, 10  $\mu$ g ml<sup>-1</sup> vitamin C (Sigma) and 500 nM Alk inhibitor A 83-01 (TOCRIS Bioscience).

**Secondary reprogramming.** Each chimaeric embryo was collected at 12.5 d.p.c., dissociated and cultured in MEF medium. One-twentieth of the dissociated cells were exposed to doxycycline (300 ng ml<sup>-1</sup>) for 2 days, and the proportion of transgenic MEFs was measured by FACS analysis of mOrange expression. For FACS time course and colony counting experiments, secondary transgenic MEFs were diluted to 5% and 30% by addition of 129 wild-type MEFs and plated in a gelatinized 6-well-plate at 1  $\times$  10<sup>5</sup> cells per well (5,000 and 30,000 transgenic MEFs per well, respectively). For sorting experiments, MEFs were plated at 2  $\times$  10<sup>5</sup> cells per gelatinized 100 mm plate (1  $\times$  10<sup>4</sup> transgenic MEFs per plate). Cells were cultured in reprogramming medium, which is ES cell medium supplemented with 300 ng ml<sup>-1</sup> doxycycline, 10  $\mu$ g ml<sup>-1</sup> vitamin C and 500 nM Alk inhibitor. Medium was changed every 2 days.

**Flow cytometry and cell sorting.** Cell-surface marker analysis was performed with the following eBioscience antibodies: ICAM-1-biotin (13-0541; 1/100), CD44-biotin (17-0441; 1/100), CD44- allophycocyanin (APC) (17-0441; 1/300), streptavidin-phycoerythrin (PE)-Cy7 (25-4317-82; 1/1500), SSEA-1-647 (51-8813; 1/50), E-cadherin-biotin (13-3249; 1/100), Thy1-APC (17-0902, 1/300) and CD2-biotin (13-0029; 1/100). For sorting experiments, dead cells were excluded using 4',6-diamidino-2-phenylindole (DAPI) nucleic acid stain (Invitrogen) (0.5 ng ml<sup>-1</sup>). Cells were incubated in 0.25% trypsin and 1 mM EDTA (Life Technologies) for 1–2 min at 37 °C, collected in GMEM media containing 10% FCS and counted. Staining was carried out in FACS buffer (2% FCS in PBS) at  $\sim$ 1  $\times$  10<sup>6</sup> cells ml<sup>-1</sup> for 15–30 min at 4 °C, and followed by washing with FACS buffer, sorting and/or analysis with FACSAriaII and LSRFortessa (both BD Biosciences), respectively. Excitation laser lines and filters used for each fluorophore are summarized in Supplementary Table 9. Data were analysed using FlowJo software (Tree Star). Intact cells were identified based on forward and side light scatter, and subsequently analysed for fluorescence intensity. Additional gating was carried out as outlined in Supplementary Fig. 2. For colony formation assays, sorted cells were plated on  $\gamma$ -irradiated MEFs in 12-well plates at 3.5  $\times$  10<sup>3</sup> cells per well. Nanog-eGFP<sup>+</sup> colonies were quantified 10 days after sorting. For 24 h or time-course analysis, sorted cells were plated in gelatinized 48-well plate at 1  $\times$  10<sup>4</sup> cells per well. In both cases, cells were cultured in reprogramming medium after sorting.

**Immunofluorescence and confocal microscopy imaging.** Images of cells stained with ICAM-1-biotin (1/100), CD44-APC (1/300) and streptavidin-PE-Cy7 (1/1,500) antibodies described above were captured with a confocal microscope (Leica TSC SP2) and Leica confocal software. Cells stained with anti-Krt17 (LifeSpan BioSciences) and anti-Sfn (Sigma) antibodies and anti-Rabbit IgG CF633 secondary antibody (Sigma) were imaged with a fluorescence microscopy (Olympus).

**Multiplexed RNA sequencing and data analysis.** RNA was isolated with TRI reagent (Sigma) following the manufacturer's instructions. RNA quality and concentration was determined using the Agilent 2100 Bioanalyzer (Agilent Technologies). Using 10 ng RNA, reverse transcription with bar-coded primers, complementary DNA amplification, and sequencing with Illumina HiSeq 2000 were performed as previously described<sup>20,21</sup>. Quality control of the obtained reads and alignment to the mouse reference genome (NCBI37/mm9) were performed using the GeneProf web-based analysis suite with default parameters<sup>22</sup>. Gene expression read counts were exported and analysed in R to identify DEGs, using the edgeR and DESeq Bioconductor libraries<sup>23–25</sup>. For both methods, low expression transcripts (less than 13 reads in all samples) were filtered out, and *P* values were adjusted using a threshold for false discovery rate (FDR)  $\leq$  0.05. Genes listed as DEGs by both methods in any two subpopulation comparison indicated in Supplementary Table 1 and Supplementary Fig. 12a (total 3,171) were used for further analysis. Hierarchical clustering and K-means clustering (*K* = 5) was performed using Cluster 3.0, and Java Treeview was used for visualization<sup>34,35</sup>. This multiplexed RNA-sequencing technology reads only the 5' end of transcript, thus detecting only endogenous *Oct4* and *Sox2*. *Nanog* expression was detectable in Nanog-eGFP<sup>+</sup> populations owing to the reporter system. Principal components analysis was performed in R and plotted with the scatterplot3d library<sup>36</sup>. Gene Ontology enrichment was calculated using the DAVID functional annotation bioinformatics tool<sup>26</sup>. Gene Ontology term enrichment analysis was carried out with a modified Fisher exact *P* value. The three additional published studies<sup>1,3,6</sup> (GEO accession numbers GSE21757, GSE14012 and GSE42379) were analysed in a similar way. For the time course data, the analysis was performed as following: data were robust multi-array average (RMA)<sup>37</sup> normalized using the expression console from Affymetrix and, because no replicates were provided, fold changes between two samples were calculated in Excel. Genes with more than 1.5-fold changes were classified as DEGs. For the Plath and Polo data set, data were RMA-normalized using the 'affy' package<sup>38</sup> in R, and DEGs were identified using the 'limma' package<sup>38</sup> in R with fold change  $\geq$  1.5 and FDR  $\leq$  0.05, or fold change  $\geq$  1.5 where no replicates were available. Subsequently, K-means clustering of the identified DEGs was performed for all studies. Selected gene expression data are shown as the relative expression against the highest signal among the samples using an averaged signal value (reads per million) of duplicates/triplicates.

**Single-cell gene expression analysis.** Single-cell qPCR was performed as described previously<sup>5</sup> with slight modifications. In brief, 22 sets of TaqMan gene expression assays (Applied Biosystems; Supplementary Table 9) were pooled at a final concentration of 180 nM per primer set and 50  $\mu$ M per probe. Individual cells were sorted directly into 10  $\mu$ l RT-PreAmp Master Mix (5  $\mu$ l of CellsDirect reaction mix (Invitrogen), 2.5  $\mu$ l of pooled assays, 0.2  $\mu$ l of SuperScript III (Invitrogen), 1.3  $\mu$ l of water) using FACSAria II. Cell lysis and sequence-specific reverse transcription were performed at 50 °C for 15 min. Reverse transcriptase was inactivated by heating to 95 °C for 2 min. Subsequently, in the same tube, cDNA went through sequence-specific amplification by denaturing at 95 °C for 15 s, and annealing and amplification at 60 °C for 4 min for 22 cycles. Preamplified products were diluted fivefold with water and analysed in 48.48 dynamic arrays on a biomark system (Fluidigm) following the Fluidigm protocol. *C<sub>t</sub>* values were calculated and visualized using BioMark real-time PCR analysis software (Fluidigm). Each assay was performed in replicate.

- Gaszner, M. & Felsenfeld, G. Insulators: exploiting transcriptional and epigenetic mechanisms. *Nature Rev. Genet.* **7**, 703–713 (2006).
- Fu, H. *et al.* Preventing gene silencing with human replicators. *Nature Biotechnol.* **24**, 572–576 (2006).
- Wang, W. *et al.* Chromosomal transposition of PiggyBac in mouse embryonic stem cells. *Proc. Natl Acad. Sci. USA* **105**, 9290–9295 (2008).
- Saldanha, A. J. Java Treeview—extensible visualization of microarray data. *Bioinformatics* **20**, 3246–3248 (2004).
- de Hoon, M. J., Imoto, S., Nolan, J. & Miyano, S. Open source clustering software. *Bioinformatics* **20**, 1453–1454 (2004).
- Ligges, U. & Maechler, M. scatterplot3d — an R package for visualizing multivariate data. *J. Stat. Softw.* **8**, 1–20 (2003).
- Irizarry, R. A. *et al.* Summaries of Affymetrix GeneChip probe level data. *Nucleic Acids Res.* **31**, e15 (2003).
- Gautier, L., Cope, L., Bolstad, B. M. & Irizarry, R. A. affy—analysis of Affymetrix GeneChip data at the probe level. *Bioinformatics* **20**, 307–315 (2004).

# ZFP36L2 is required for self-renewal of early burst-forming unit erythroid progenitors

Lingbo Zhang<sup>1,2,3</sup>, Lina Prak<sup>1</sup>, Violeta Rayon-Estrada<sup>1†</sup>, Prathapan Thiru<sup>1</sup>, Johan Flygare<sup>1†</sup>, Bing Lim<sup>2,3,4</sup> & Harvey F. Lodish<sup>1,2</sup>

**Stem cells and progenitors in many lineages undergo self-renewing divisions, but the extracellular and intracellular proteins that regulate this process are largely unknown. Glucocorticoids stimulate red blood cell formation by promoting self-renewal of early burst-forming unit-erythroid (BFU-E) progenitors<sup>1–4</sup>. Here we show that the RNA-binding protein ZFP36L2 is a transcriptional target of the glucocorticoid receptor (GR) in BFU-Es and is required for BFU-E self-renewal. ZFP36L2 is normally downregulated during erythroid differentiation from the BFU-E stage, but its expression is maintained by all tested GR agonists that stimulate BFU-E self-renewal, and the GR binds to several potential enhancer regions of ZFP36L2. Knockdown of ZFP36L2 in cultured BFU-E cells did not affect the rate of cell division but disrupted glucocorticoid-induced BFU-E self-renewal, and knockdown of ZFP36L2 in transplanted erythroid progenitors prevented expansion of erythroid lineage progenitors normally seen following induction of anaemia by phenylhydrazine treatment. ZFP36L2 preferentially binds to messenger RNAs that are induced or maintained at high expression levels during terminal erythroid differentiation and negatively regulates their expression levels. ZFP36L2 therefore functions as part of a molecular switch promoting BFU-E self-renewal and a subsequent increase in the total numbers of colony-forming unit-erythroid (CFU-E) progenitors and erythroid cells that are generated.**

Humans generate  $10^{11}$  erythrocytes every day, a process regulated by multiple hormones affecting several types of progenitors. Apoptosis, proliferation and terminal differentiation of CFU-E erythroid progenitors are mainly controlled by erythropoietin (EPO)<sup>5,6</sup>. In contrast, many hormones including EPO, stem cell factor (SCF), interleukin-3 (IL-3) and interleukin-6 (IL-6) regulate the earlier BFU-E progenitors, but we do not know how they interact to control BFU-E quiescence, self-renewal divisions or cell divisions yielding the later CFU-E progenitors. Under stress conditions such as acute blood loss or chronic anaemia, glucocorticoids trigger self-renewal of BFU-E progenitors in the spleen, leading to increased numbers of self-renewal divisions. This results in increased BFU-E numbers and, over time, formation of increased numbers of CFU-E progenitors and subsequently of mature erythrocytes<sup>1–4,7,8</sup>.

To identify GR-activated genes essential for BFU-E self-renewal, BFU-Es were purified<sup>1</sup> and cultured in a medium (self-renewal medium) containing SCF, EPO, insulin-like growth factor 1 (IGF-1), and several full or dissociated GR agonists. All agonists, except for one dissociated agonist, stimulate BFU-E self-renewal (Supplementary Fig. 1). Because the genes upregulated by all functional agonists represent candidates indispensable for BFU-E self-renewal, we performed deep sequencing on mRNAs from BFU-Es cultured with GR agonists for 4 h, and identified a group of genes upregulated by all functional agonists but not by nonfunctional agonists (Supplementary Table 1). We focused on three genes normally downregulated during erythroid differentiation, *Zfp36l2*, *Hopx* and *Nlrp6* (Supplementary Fig. 2, b, c). As detailed later,

knockdown of *Hopx* and *Nlrp6* resulted in a defect in BFU-E proliferation. In contrast, knockdown of *Zfp36l2*, the most abundant transcript upregulated by GR agonists, did not affect the initial rate of BFU-E division.

During erythroid differentiation *in vivo*, ZFP36L2 is downregulated from the BFU-E stage (Fig. 1a, b). BFU-Es cultured *in vitro* for 4 h with all functional GR agonists showed a ~2.5-fold upregulation of ZFP36L2 that was maintained throughout the culture (Fig. 1c–e). Given that ZFP36L2 is upregulated after only 4 h, ZFP36L2 is likely a direct transcriptional target of the GR. Thus we performed GR chromatin immunoprecipitation sequencing (ChIP-seq) on freshly isolated BFU-Es after 1 h stimulation with dexamethasone (DEX) and identified five GR binding sites near the *Zfp36l2* transcription start site (TSS), potential enhancers of *Zfp36l2* (Supplementary Fig. 3). Four of these sites responded to DEX, indicating that they are functional enhancers regulated by glucocorticoids (Fig. 1g). Together, these results indicate that ZFP36L2 is a direct transcriptional target of the GR in BFU-Es.

ZFP36L2 belongs to an RNA-binding protein family<sup>9</sup>. On the basis of RNA-seq gene expression data from purified BFU-E, CFU-E and Ter119-positive (Ter119<sup>+</sup>, also known as LY76) erythroblasts<sup>1</sup>, ZFP36L2 is ~20 times more abundant in erythroid progenitors than its other two family members, ZFP36 and ZFP36L1, and is the only member upregulated by DEX (Fig. 1f and Supplementary Fig. 4), indicating that ZFP36L2 is the major family member involved in regulation of BFU-E self-renewal. Furthermore, ZFP36L2 is gradually downregulated from the haematopoietic stem cell (HSC) to the early and late erythroid progenitor stages (Supplementary Fig. 5). In summary, glucocorticoid treatment of BFU-Es reverses normal downregulation of ZFP36L2, correlating with glucocorticoid-induced BFU-E self-renewal.

To test whether upregulation of ZFP36L2 is required for glucocorticoid-induced BFU-E self-renewal, we used two short hairpin RNAs (shRNAs) to knock down expression of ZFP36L2 in BFU-Es (Fig. 2a, b). BFU-Es cultured without DEX stop proliferating at 4 days; as shown previously<sup>1</sup>, in the absence of DEX, each BFU-E generates several CFU-Es, each of which generates 10–30 erythroid cells over a 5 to 6 day period. In contrast, BFU-Es cultured in the presence of DEX continue to proliferate and generate over 10 times more mature erythroid cells at 9 days of culture. As shown previously<sup>1</sup>, in the presence of DEX, each BFU-E generates multiple daughter BFU-Es during the first days of culture; over time these BFU-Es generate increased numbers of daughter CFU-Es, each of which generates 10–30 erythroid cells. Importantly, BFU-Es expressing either *Zfp36l2* shRNA stop proliferating at day 4, whether or not DEX is included; the proliferation kinetics are similar to those of BFU-Es cultured without DEX (Fig. 2c). This indicates that knockdown of ZFP36L2 disrupts DEX-induced self-renewal of BFU-Es.

As one control, knockdown of c-Kit, a cell surface receptor required for the survival of haematopoietic stem and progenitor cells including

<sup>1</sup>Whitehead Institute for Biomedical Research and Department of Biology, Massachusetts Institute of Technology, Cambridge, Massachusetts 02142, USA. <sup>2</sup>Computation and Systems Biology, Singapore-Massachusetts Institute of Technology Alliance, 117576 Singapore. <sup>3</sup>Stem Cell and Developmental Biology, Genome Institute of Singapore, A\*STAR, 138627 Singapore. <sup>4</sup>Beth Israel Deaconess Medical Center, Harvard Medical School, Boston, Massachusetts 02215, USA. <sup>†</sup>Present addresses: Department of Molecular Medicine and Gene Therapy, Lund Stem Cell Center, Lund University, 22184 Lund, Sweden (J.F.); The Rockefeller University, New York, New York 10065, USA (V.R.-E.).



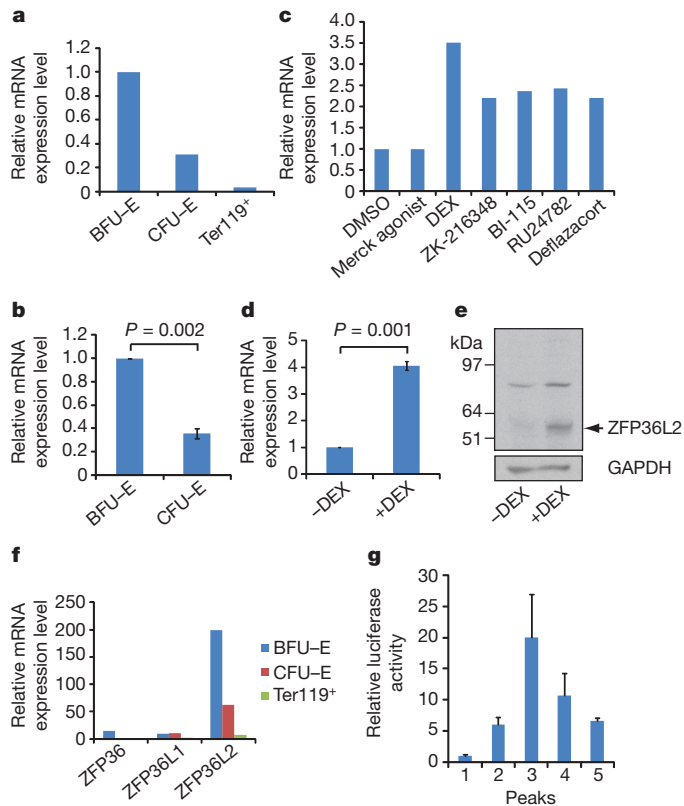


**Figure 1 | Normal downregulation of ZFP36L2 during erythroid differentiation from the BFU-E stage is reversed by functional GR agonists.** **a**, The expression levels of *Zfp36l2* mRNA in BFU-Es, CFU-Es, and Ter119<sup>+</sup> erythroblasts were measured by RNA-seq. **b**, The expression levels of *Zfp36l2* mRNA in BFU-Es and CFU-Es were measured by RT-PCR normalized to 18S ribosomal RNA (rRNA). Error bar represents standard deviation (s.d.) ( $n = 3$ ). **c**, The expression levels of *Zfp36l2* mRNA in BFU-Es after 4 h culture in self-renewal medium with indicated GR agonists were measured by RNA-seq. **d**, The expression levels of *Zfp36l2* mRNA in BFU-Es after 3 days culture in self-renewal medium with or without DEX were measured by RT-PCR normalized to 18S rRNA. Error bar represents s.d. ( $n = 3$ ). **e**, The expression levels of ZFP36L2 of samples shown in panel **d** were measured by western blot. Representative data are shown ( $n = 3$ ). **f**, The expression levels of *Zfp36*, *Zfp36l1* and *Zfp36l2* mRNAs in BFU-Es, CFU-Es and Ter119<sup>+</sup> erythroblasts were measured by RNA-seq<sup>1</sup>; data shown are relative RPKM (reads per kilobase per million mapped reads) values normalized to the expression level of *Zfp36* in Ter119<sup>+</sup> erythroblasts. **g**, Luciferase reporter vectors cloned with each GR binding site or empty vector were co-transfected with XZ-GR into 293T cells and cultured in medium containing 1  $\mu$ M DEX. Luciferase activities were measured 2 days later. Error bar represents s.d. ( $n = 3$ ). All *P* values were calculated using the two-tailed *t*-test.

BFU-Es, resulted in a blockage of BFU-E proliferation after only 1 day of culture (Supplementary Fig. 2a). HOPX and NLRP6 share similar expression patterns as ZFP36L2, are downregulated during erythroid differentiation from the BFU-E stage and upregulated by DEX, and possess promoter regions that, based on our GR ChIP-Seq data, are occupied by GR. Knockdown of these also resulted in a blockage of BFU-E proliferation after only 1 day of culture (Supplementary Fig. 2b, c).

To establish that ZFP36L2 is specifically required for BFU-E self-renewal, 3-day BFU-E cultures were tested for their number of daughter BFU-Es by colony assays. Knockdown of ZFP36L2 significantly decreased the number of BFU-Es formed in the presence of DEX (Fig. 2d). Knockdown of ZFP36L2 had no influence on apoptosis of BFU-Es (Fig. 2e) and, as expected on basis of its low level of expression in CFU-Es, knockdown of ZFP36L2 had no effect on erythroid differentiation beyond the CFU-E stage (Supplementary Fig. 6). These

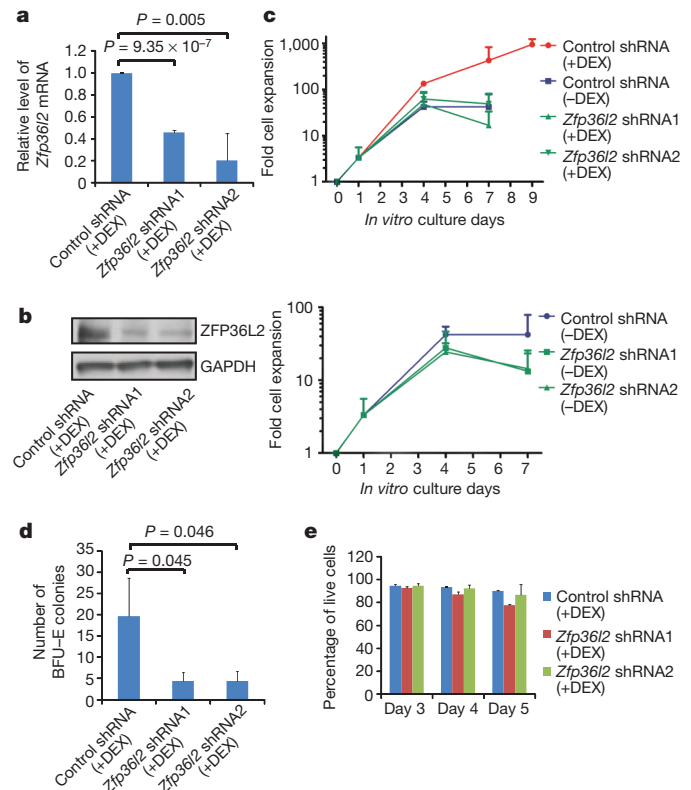


**Figure 2 | ZFP36L2 is specifically required for BFU-E self-renewal.** **a**, The expression levels of *Zfp36l2* mRNA in BFU-Es infected with viruses encoding indicated shRNAs followed with 1 day culture in self-renewal medium with DEX were measured by RT-PCR normalized to 18S rRNA. Error bar represents s.d. ( $n = 3$ ). **b**, The expression levels of ZFP36L2 in BFU-Es infected with viruses encoding indicated shRNAs followed by 3 days culture in self-renewal medium with DEX were measured by western blot. Representative data are shown ( $n = 3$ ). **c**, BFU-Es were infected with viruses encoding indicated shRNAs and cultured in self-renewal medium with or without DEX. Relative cell numbers throughout the culture are shown. Error bar represents s.d. ( $n = 3$ ). **d**, Day 3 cells from this *in vitro* BFU-E culture system were plated in methylcellulose medium; BFU-E colonies were counted 9 days later. Error bar represents s.d. ( $n = 3$ ). **e**, Day 3, 4 and 5 cells from this *in vitro* BFU-E culture system were stained with fluorophore-conjugated annexin V and 7-aminoactinomycin D (7-AAD) and the percentages of double-negative live cells are shown. Error bar represents s.d. ( $n = 3$ ). All *P* values were calculated using the two-tailed *t*-test.

data indicate that ZFP36L2 is specifically required for glucocorticoid-induced BFU-E self-renewal.

Glucocorticoids and GR are required for erythroid lineage cell expansion in the spleen during stress erythropoiesis<sup>2,4</sup>. The data in Fig. 3, using a phenylhydrazine (PHZ)-induced haemolytic anaemia mouse model, shows that ZFP36L2 is required for stress-induced erythroid lineage expansion *in vivo*. Lineage-negative (Lin<sup>-</sup>) cells were isolated and infected with viruses encoding green fluorescence protein (GFP) and either a control shRNA or *Zfp36l2* shRNAs, and then transplanted into lethally irradiated recipient mice. Six to eight weeks after transplantation, PHZ or control phosphate buffered saline (PBS) was injected intraperitoneally into transplanted mice at days 0 and 1 to induce haemolytic anaemia and erythroid lineage expansion. On day 4, spleens were dissected for flow cytometry analysis for multiple haematopoietic cells, detected by lineage specific markers (Fig. 3a). *Zfp36l2* shRNAs effectively knocked down the expression of ZFP36L2 in the Lin<sup>-</sup> cells (Supplementary Fig. 7a), and as expected, injection of PHZ resulted in a ~10-fold increase in systemic glucocorticoid levels (Fig. 3b).

In control mice transplanted with Lin<sup>-</sup> cells infected with control shRNA, the majority of control transplanted GFP<sup>+</sup> splenic cells were

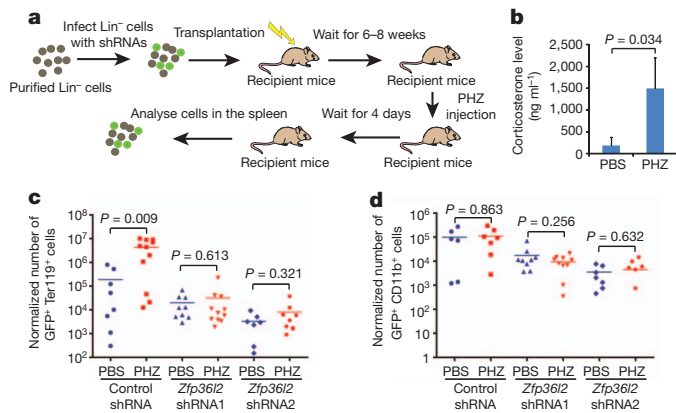


**Figure 3 | ZFP36L2 is required for erythroid lineage expansion during stress erythropoiesis *in vivo*.** **a**, Schematic diagram shows the *in vivo* bone marrow transplantation and PHZ-induced haemolytic anaemia mouse model. **b**, Corticosterone levels were measured in mouse plasma 1 h after PBS or PHZ injection. Error bar represents s.d. ( $n = 3$ ). **c**, Normalized numbers of each type of GFP<sup>+</sup> haematopoietic lineage cells were calculated as a ratio of the number of each type relative to the percentages of GFP<sup>+</sup> cells in the Lin<sup>-</sup> population before transplantation. The normalized numbers of GFP<sup>+</sup> Ter119<sup>+</sup> cells are shown. **d**, The normalized numbers of GFP<sup>+</sup> CD11b<sup>+</sup> cells are shown. All  $P$  values were calculated using the two-tailed  $t$ -test.

Ter119-negative (Ter119<sup>-</sup>) non-erythroid lineage cells as expected (Supplementary Figs 8 and 9a). PHZ-mediated haemolysis induced a ~20-fold expansion of number of erythroid lineage cells (Fig. 3c) and resulted in ~50% of GFP<sup>+</sup> cells in the spleen becoming Ter119<sup>+</sup> mature erythroid cells (Supplementary Fig. 9a).

Importantly, knockdown of ZFP36L2 significantly impaired this erythroid lineage expansion (Fig. 3c). In addition, the effects of ZFP36L2 in mediating haemolysis-induced cell expansion is specific

to the erythroid lineage, as no other haematopoietic lineages showed a difference in the number of donor-derived GFP<sup>+</sup> cells between PBS and PHZ injection groups, with or without ZFP36L2 knockdown (Fig. 3d and Supplementary Figs 10a, b and 11d–f). Consistent with the increase in the percentage of Ter119<sup>+</sup> erythroid lineage cells in control mice upon PHZ injection, the percentages of other haematopoietic lineages were decreased upon PHZ injection, and these decreases were eliminated in the absence of ZFP36L2 (Supplementary Figs 9a–d and 11a–c).

ZFP36L2 homozygous knockout mice die from HSC failure within 2 weeks after birth<sup>10</sup>, and thus this protein is likely required in early haematopoietic stem and progenitor cells. Consistent with this notion, before PHZ challenge, the percentage of GFP<sup>+</sup> splenic cells is lower in mice transplanted with Lin<sup>-</sup> cells infected with viruses encoding either *Zfp36l2* shRNA than with the control shRNA; this difference is not caused by significant differences in infection efficiency of Lin<sup>-</sup> cells before transplantation (Supplementary Fig. 7b, c).

Importantly, in mice transplanted with Lin<sup>-</sup> cells expressing the control shRNA the percentage of GFP<sup>+</sup> cells in the spleen does not significantly change after PHZ treatment, whereas in mice transplanted with Lin<sup>-</sup> cells infected with viruses encoding *Zfp36l2* shRNAs, the percentage markedly drops following PHZ treatment (Supplementary Fig. 7d), consistent with the loss of erythroid cell expansion (Fig. 3c). Together, these data indicate that ZFP36L2 is specifically required for erythroid expansion during stress erythropoiesis *in vivo* and is consistent with the notion that it is essential for glucocorticoid-induced BFU-E self-renewal.

The data in Fig. 4 show that ZFP36L2 contributes to BFU-E self-renewal by repressing expression of genes important for terminal erythroid differentiation. BFU-Es were cultured in self-renewal medium with or without DEX. At day 4, approximately 12% of the cells generated from BFU-Es cultured with DEX differentiated into Ter119<sup>+</sup> cells, whereas ~35% of the progeny of BFU-Es cultured without

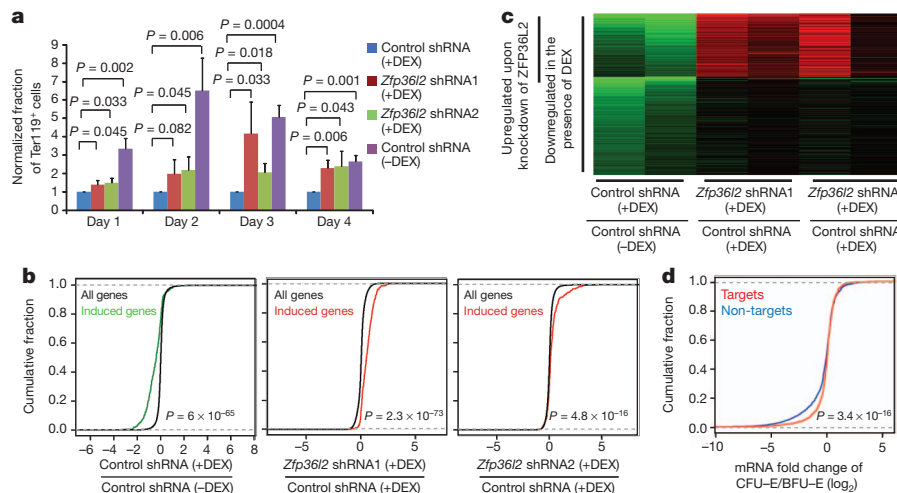


**Figure 4 | ZFP36L2 delays erythroid differentiation and preferentially binds to several mRNAs that are induced or maintained at higher expression levels during terminal erythroid differentiation.** **a**, BFU-Es were infected with viruses encoding the indicated shRNAs and cultured for 4 days in self-renewal medium with or without DEX. The fraction of Ter119<sup>+</sup> cells was measured. The normalized fraction of Ter119<sup>+</sup> cells was calculated as a ratio of the fraction of Ter119<sup>+</sup> cells in cultures of BFU-Es infected with viruses encoding the indicated shRNAs and cultured under the indicated culture conditions relative to the fraction of Ter119<sup>+</sup> cells in cultures of BFU-Es infected with control virus and cultured with DEX. Error bar represents s.d. ( $n = 3$ ).  $P$  values were calculated using the two-tailed  $t$ -test. **b**, Microarrays were performed on BFU-Es infected with viruses encoding indicated shRNAs and cultured for 3 days in self-renewal medium with or without DEX. The  $x$  axis represents the relative expression of each gene calculated as a log<sub>2</sub> ratio of its expression in the indicated samples. The cumulative fraction ( $y$  axis) is plotted

as a function of the relative expression ( $x$  axis). 'All genes' includes all of the genes in the microarray; 'Induced genes' represent a group of 340 genes most highly induced during erythroid differentiation from the CFU-E to the Ter119<sup>+</sup> erythroblast stage.  $P$  values were calculated using the Kolmogorov–Smirnov test. **c**, Genes that are downregulated by at least 20% in the presence of DEX and the subset of these genes that are upregulated by at least 20% upon knockdown of ZFP36L2 are shown through the same microarrays as those shown in **b**. **d**, The  $x$  axis represents the relative expression of each gene calculated as a log<sub>2</sub> ratio of its expression in CFU-Es relative to BFU-Es. The cumulative fraction ( $y$  axis) is plotted as a function of the relative expression ( $x$  axis). 'Targets' are the 2,000 microarray probes corresponding to mRNAs most preferentially found in the ZFP36L2 immunoprecipitate from the RIP-chip assay. 'Non-targets' represent all remaining genes.  $P$  value was calculated using the Kolmogorov–Smirnov test.

DEX became Ter119<sup>+</sup>, consistent with a DEX-triggered delay in terminal erythroid differentiation. This DEX-induced differentiation delay was eliminated by ZFP36L2 knockdown; loss of ZFP36L2 results in formation of ~30% Ter119<sup>+</sup> cells, similar to the percentage in cultures without DEX (Fig. 4a), indicating that ZFP36L2 is essential for the glucocorticoid-induced delay of erythroid differentiation from the BFU-E stage. Consistent with a differentiation delay evidenced by the Ter119 marker, DEX treatment globally repressed the expression of a group of genes most highly induced during erythroid differentiation, and knockdown of ZFP36L2 eliminated this repression (Fig. 4b).

This conclusion is further strengthened by experiments showing that overexpression of ZFP36L2 in BFU-Es significantly reduces the rate of cell proliferation (Supplementary Fig. 12a, b), but also delays erythroid differentiation. When cultured 4 days in the absence of DEX, the fraction of differentiated Ter119<sup>+</sup> cells was significantly lower in the overexpression cells than in the controls, and was similar to that from control BFU-Es cultured with DEX (Supplementary Fig. 12c). Although overexpression of ZFP36L2 led to a delay in erythroid differentiation, overexpression of ZFP36L2 in BFU-Es cultured without DEX was not able to rescue the self-renewal divisions, indicating that ZFP36L2 contributes to BFU-E self-renewal by delaying erythroid differentiation (Supplementary Fig. 12b).

To identify mRNAs in BFU-Es that directly bind to ZFP36L2, we performed an RNA-binding protein immunoprecipitation, using a verified ZFP36L2-specific antibody (Supplementary Fig. 13a, b), coupled to a microarray (RIP-chip) assay and identified many genes specifically immunoprecipitated by the ZFP36L2 antibody (Supplementary Table 2). Using this unbiased genomic approach, we showed that mRNAs containing AU-rich elements in their 3' untranslated regions (UTRs) are preferentially incorporated into the anti-ZFP36L2 immunoprecipitate (Supplementary Fig. 14); ~72% of these mRNAs indeed contain the core ZFP36L2 recognition motif ATTTA element in their 3'UTRs. This is consistent with previous reports concerning the binding specificity of ZFP36L2<sup>11,12</sup>, but we cannot eliminate the possibility that some mRNAs are binding to other unknown proteins in complexes with ZFP36L2. Strikingly, we found that in BFU-Es, ZFP36L2 preferentially binds to mRNAs that tend to be induced or maintained at higher than average expression levels during subsequent erythroid differentiation to the CFU-E stage (Fig. 4d). In addition, we found that the number of AU-rich elements of mRNAs bound by ZFP36L2 positively correlates with their extent of induction during erythroid differentiation from the BFU-E to CFU-E stage (Supplementary Fig. 15a, b). Thus, the expression pattern of ZFP36L2 negatively correlates with the expression pattern of erythroid differentiation-induced genes.

To globally identify functional targets whose expression levels are regulated by ZFP36L2, we analysed the gene expression profile of day 3 *in vitro* cultured BFU-Es with microarrays, allowing us to identify several genes with lower expression levels in BFU-Es cultured with DEX, compared with their counterparts in BFU-Es cultured without DEX (Fig. 4c). Repression of several of these DEX-repressed genes is dependent on and presumably mediated by ZFP36L2, because knockdown of ZFP36L2 eliminated this repression (Fig. 4c). A group of potential ZFP36L2 functional target genes was then identified by intersecting the set of these repressed genes with the group of genes identified by RIP-chip assay (Supplementary Fig. 16 and Supplementary Table 3). As shown in Supplementary Table 4, this group of potential functional targets contains several genes previously known to be important for or related to terminal erythropoiesis, including *Aff1*<sup>13</sup>, *Mafk*<sup>14</sup>, *Nfe2l1*<sup>15</sup>, *Sap30l*<sup>16</sup>, *Epb4.1*<sup>17</sup>, *Adar*<sup>18</sup>, *Mthfd2*<sup>19</sup> and *Mfhas*<sup>20</sup>. We performed luciferase reporter assays on selected candidates, and found that the 3'UTRs of many of these genes are ZFP36L2 responsive (Supplementary Table 4). In addition, we mutated AU-rich elements in the 3'UTR of *Aff1* and observed a statistically significant 21% increase ( $P = 0.015$ ) of luciferase activity, indicating that AU-rich elements are required for this regulation.

These data illustrate that ZFP36L2 globally negatively regulates the expression of several erythroid differentiation-induced genes, among which some are known to be required for erythroid differentiation and others are unknown but induced. Regulation by ZFP36L2 seems similar to microRNA-mediated post-transcriptional regulation. An individual microRNA binds to multiple target mRNAs and down-regulates their expression levels often by only 20–50%; collectively, however, these modulations can have important biological effects. ZFP36L2 is normally downregulated during erythroid differentiation from the BFU-E stage, thus stabilizing many mRNAs required for terminal differentiation. ZFP36L2 transcription is enhanced by glucocorticoids under stress conditions that signal erythroid lineage cell expansion. Upregulation of ZFP36L2 in turn negatively regulates multiple differentiation-induced genes, causing a delay in erythroid differentiation and ultimately contributing to BFU-E self-renewal (Supplementary Fig. 17). Altogether, our experiments uncover a novel mechanism that facilitates progenitor self-renewal: delaying differentiation by post-transcriptional downregulation of expression of mRNAs critical for progression to the next differentiation stage.

## METHODS SUMMARY

BFU-Es were isolated from embryonic day 14.5 (E14.5) mouse fetal liver<sup>1</sup>, infected with viruses encoding GFP and either control shRNA or *Zfp36l2* shRNAs, and cultured in self-renewal medium containing SCF, EPO and IGF-1 with or without DEX, and the cell numbers were counted daily throughout the *in vitro* culture. Lin<sup>−</sup> cells were isolated from mouse E14.5 fetal liver and infected with viruses encoding GFP and either control shRNA or *Zfp36l2* shRNAs and transplanted into lethally irradiated recipient mice. Six to eight weeks after transplantation, the recipient mice were intraperitoneally injected with 60 mg per kg PHZ on day 0 and day 1. On day 4, spleens were dissected and measured for multiple types of GFP<sup>+</sup> haematopoietic cells, detected by the haematopoietic lineage specific markers.

**Full Methods** and any associated references are available in the online version of the paper.

Received 10 May 2012; accepted 23 April 2013.

Published online 9 June 2013.

1. Flygare, J., Rayon Estrada, V., Shin, C., Gupta, S. & Lodish, H. F. HIF1 $\alpha$  synergizes with glucocorticoids to promote BFU-E progenitor self-renewal. *Blood* **117**, 3435–3444 (2011).
2. Bauer, A. *et al.* The glucocorticoid receptor is required for stress erythropoiesis. *Genes Dev.* **13**, 2996–3002 (1999).
3. Wessely, O., Deiner, E. M., Beug, H. & von Lindern, M. The glucocorticoid receptor is a key regulator of the decision between self-renewal and differentiation in erythroid progenitors. *EMBO J.* **16**, 267–280 (1997).
4. Reichardt, H. M. *et al.* DNA binding of the glucocorticoid receptor is not essential for survival. *Cell* **93**, 531–541 (1998).
5. Richmond, T. D., Chohan, M. & Barber, D. L. Turning cells red: signal transduction mediated by erythropoietin. *Trends Cell Biol.* **15**, 146–155 (2005).
6. Wu, H., Liu, X., Jaenisch, R. & Lodish, H. F. Generation of committed erythroid BFU-E and CFU-E progenitors does not require erythropoietin or the erythropoietin receptor. *Cell* **83**, 59–67 (1995).
7. Hattangadi, S. M., Wong, P., Zhang, L., Flygare, J. & Lodish, H. F. From stem cell to red cell: regulation of erythropoiesis at multiple levels by multiple proteins, RNAs, and chromatin modifications. *Blood* **118**, 6258–6268 (2011).
8. Narla, A. *et al.* Dexamethasone and lenalidomide have distinct functional effects on erythropoiesis. *Blood* **118**, 2296–2304 (2011).
9. Blackshear, P. J. Tristetraprolin and other CCHC tandem zinc-finger proteins in the regulation of mRNA turnover. *Biochem. Soc. Trans.* **30**, 945–952 (2002).
10. Stumpo, D. J. *et al.* Targeted disruption of *Zfp36l2*, encoding a CCHC tandem zinc finger RNA-binding protein, results in defective hematopoiesis. *Blood* **114**, 2401–2410 (2009).
11. Hudson, B. P., Martinez-Yamout, M. A., Dyson, H. J. & Wright, P. E. Recognition of the mRNA AU-rich element by the zinc finger domain of TIS11d. *Nature Struct. Mol. Biol.* **11**, 257–264 (2004).
12. Schoenberg, D. R. & Maquat, L. E. Regulation of cytoplasmic mRNA decay. *Nature Rev. Genet.* **13**, 246–259 (2012).
13. Novershtern, N. *et al.* Densely interconnected transcriptional circuits control cell states in human hematopoiesis. *Cell* **144**, 296–309 (2011).
14. Brand, M. *et al.* Dynamic changes in transcription factor complexes during erythroid differentiation revealed by quantitative proteomics. *Nature Struct. Mol. Biol.* **11**, 73–80 (2004).
15. Caterina, J. J., Donze, D., Sun, C. W., Ciavatta, D. J. & Townes, T. M. Cloning and functional characterization of LCR-F1: a bZIP transcription factor that activates erythroid-specific, human globin gene expression. *Nucleic Acids Res.* **22**, 2383–2391 (1994).



16. Teittinen, K. J. *et al.* SAP30L (Sin3A-associated protein 30-like) is involved in regulation of cardiac development and hematopoiesis in zebrafish embryos. *J. Cell. Biochem.* **113**, 3843–3852 (2012).
17. Shi, Z. T. *et al.* Protein 4.1R-deficient mice are viable but have erythroid membrane skeleton abnormalities. *J. Clin. Invest.* **103**, 331–340 (1999).
18. Wang, Q., Khillan, J., Gadue, P. & Nishikura, K. Requirement of the RNA editing deaminase ADAR1 gene for embryonic erythropoiesis. *Science* **290**, 1765–1768 (2000).
19. Tibbetts, A. S. & Appling, D. R. Compartmentalization of mammalian folate-mediated one-carbon metabolism. *Annu. Rev. Nutr.* **30**, 57–81 (2010).
20. Kumkhaek, C. *et al.* MASL1 induces erythroid differentiation in human erythropoietin-dependent CD34<sup>+</sup> cells through the Raf/MEK/ERK pathway. *Blood* **121**, 3216–3227 (2013).

**Supplementary Information** is available in the online version of the paper.

**Acknowledgements** This work is supported by NIH grant P01 HL 32262 to H.F.L.; L.Z. is supported by a graduate fellowship from Singapore-Massachusetts Institute of Technology Alliance. We thank C. Sieff, J. Zhang, and P. Ji for providing reagents, T. Chavarria and F. Reinhardt for assisting with mouse transplantation experiments,

J. Shih for helping with the making of constructs, M. Bousquet and C. Patterson for discussion and assistance with mouse transplantation experiment and antibody testing, S. Gupta, J. Kwon and I. Barrasa for processing raw RNA-seq data, processing microarray and discussion of bioinformatics analyses, and Sanofi Aventis for providing many GR agonists.

**Author Contributions** L.Z. conceived the project, designed and performed the experiments and bioinformatics analysis, analysed the data, and wrote the paper. L.P. assisted with luciferase reporter assays and BFU-E isolation. V.R.-E. performed the GR Chip-seq experiment. P.T. provided training in bioinformatics analyses. J.F. performed the initial experiments with the GR partial agonists. B.L. supervised part of the research. H.F.L. supervised the research and edited the paper.

**Author Information** All microarray data are available from the Gene Expression Omnibus database (<http://www.ncbi.nlm.nih.gov/geo>) under accession code GSE46216. Reprints and permissions information is available at [www.nature.com/reprints](http://www.nature.com/reprints). The authors declare no competing financial interests. Readers are welcome to comment on the online version of the paper. Correspondence and requests for materials should be addressed to H.F.L. ([lodish@wi.mit.edu](mailto:lodish@wi.mit.edu)).

## METHODS

**Primary BFU-Es and CFU-Es purification, retrovirus infection and *in vitro* culture.** Primary BFU-Es and CFU-Es were purified from mouse E14.5 fetal liver<sup>1</sup>. BFU-Es were then placed in virus solution in a six-well plate, followed by 37 °C overnight incubation. After incubation, virus solution was substituted by a medium (self-renewal medium) containing SCF (100 ng ml<sup>-1</sup>), EPO (2 U ml<sup>-1</sup>) and IGF-1 (40 ng ml<sup>-1</sup>) with or without full and partial GR agonists. The cells were then *in vitro* cultured at 37 °C for 9 days.

For CFU-E differentiation assay, CFU-Es were placed in virus solution, followed by 37 °C spin infection. After infection, virus solution was substituted by an EPO containing differentiation medium, and the cells were then *in vitro* cultured for 2 days<sup>21</sup>.

**Cell number counting assay and BFU-E colony formation assay.** In the BFU-E culture system, after infection with viruses encoding GFP and either control shRNA or *Zfp36l2* shRNAs, the absolute numbers of GFP<sup>+</sup> cells were counted daily by flow cytometry, where the counting beads were used as an internal counting standard. For BFU-E colony formation assay, after 3 days culture, GFP<sup>+</sup> cells were sorted by flow cytometry and cultured in methylcellulose medium (MethoCult SF M3436 from StemCell Technologies), and the number of BFU-E colonies containing a cluster of more than 20 CFU-E colonies were counted 9 days after culture.

***In vivo* PHZ induced haemolytic anaemia and bone marrow transplantation mouse model.** Lin<sup>-</sup> cells were isolated from mouse E14.5 fetal liver and infected with viruses encoding GFP and either control shRNA or *Zfp36l2* shRNAs and transplanted into lethally irradiated recipient mice. Six to eight weeks after transplantation, the recipient mice were intraperitoneally injected with 60 mg per kg PHZ or control PBS on day 0 and day 1. On day 4, spleens were dissected and measured for number and percentage of GFP<sup>+</sup> cells and of each type of GFP<sup>+</sup> haematopoietic lineage cell.

**Measurement of corticosterone level.** Mice were injected with PHZ or PBS, and plasma were prepared 1 h after injection. Corticosterone levels were measured by using an ELISA kit according to instruction by the manufacturer Immundiagnostic Systems.

**RIP-chip and data analysis.** RIP-chip was carried out according to the instruction of EZ-Magna RIP RNA-Binding Protein Immunoprecipitation Kit (Millipore). BFU-Es were lysed and incubated with ZFP36L2 antibody (Abcam ab70775; 5 µg) or control IgG (5 µg) conjugated with magnetic beads (50 µl) for 4 h. The beads, protein and mRNA complexes were immunoprecipitated and magnetically separated. The mRNAs were purified and analysed by microarray (Affymetrix mouse gene 1.0 ST array). Ratios of each microarray probe between its intensity in ZFP36L2 antibody immunoprecipitated sample and its intensity in IgG-immunoprecipitated sample were calculated.

For the AU-rich element enrichment analysis, the 2,000 microarray probes corresponding to the mRNAs most preferentially bound by ZFP36L2 antibody are listed as 'Targets'. The 2,000 microarray probes corresponding to the mRNAs most preferentially bound by control IgG are listed as 'Non-targets'. The percentages of targets and non-targets containing indicated AU-rich elements in their 3'UTR were calculated.

For the cumulative distribution plot, 'Targets' represents the 2,000 microarray probes corresponding to the mRNAs most preferentially bound by ZFP36L2 antibody in RIP-chip experiment. 'Non-targets' represents all remaining genes. The relative expressions of each gene calculated as a log<sub>2</sub> ratio between its intensity in CFU-E and its intensity in BFU-E<sup>1</sup> were calculated (*x* axis). The cumulative fraction is plotted as a function of the relative expression (*y* axis).

For the correlation analysis, the 2,000 transcripts that are most preferentially found in the ZFP36L2 immunoprecipitate in the RIP-chip experiments were ranked based on their relative expression levels calculated as a ratio of their expression levels in CFU-Es relative to BFU-Es, and were classified into 8 groups each with 250 transcripts based on their relative expression level ranking. One-way analysis of variance (ANOVA) analysis was performed to test the statistical significance of the difference among the average numbers of ATTTA elements in the 3'UTR of each gene of these 8 groups by using GraphPad software. Test for linear trend after ANOVA was performed to test the statistical significance of the linear trend, the systematic increase of the average number of ATTTA elements in the 3'UTR of each gene of these 8 groups as the rank of average relative expression levels of these 8 group increases, using GraphPad software. The average number of ATTTA elements in the 3'UTR of each gene was plotted together with the average relative expression levels of each group for these 8 groups. The percentage of genes with ATTTA elements in their 3'UTRs was plotted together with the average relative expression levels of each group for these 8 groups. The linear trend lines were drawn and the *P* values and *r*<sup>2</sup> values of the Pearson correlation test were calculated for these two plots.

**GR Chip-seq.** A total of  $\sim 7 \times 10^7$  primary BFU-E cells were purified from mouse E14.5 fetal liver<sup>1</sup>. Cells were incubated at 37 °C for 4 h in SFEM (Stem Span) medium containing SCF (100 ng ml<sup>-1</sup>), EPO (2 U ml<sup>-1</sup>) and IGF-1 (40 ng ml<sup>-1</sup>); followed by 1 h stimulation with 100 nM dexamethasone. Cells were then chemically crosslinked with 1% formaldehyde solution for 15 min at room temperature, lysed and sonicated to solubilize and shear crosslinked DNA in sonication buffer (50 mM HEPES pH 7.5, 40 mM NaCl, 1 mM EDTA, 1 mM EGTA, 1% Triton X-100, 0.1% Na-deoxycholate and 0.1% SDS). The glucocorticoid receptor (GR) was immunoprecipitated overnight at 4 °C with 10 µg of a combination of two antibodies bound to magnetic beads (Dynabeads, Invitrogen). The antibodies used were mouse monoclonal FiGR (sc-12763) and MAI-510 (BuGR clone, Thermo Scientific). The beads containing the GR bound to DNA were washed once with low salt buffer (20 mM Tris pH 8, 2 mM EDTA, 0.1% SDS, 1% Triton X100, 150 mM NaCl), once with high salt buffer (20 mM Tris pH 8, 2 mM EDTA, 0.1% SDS, 1% Triton X100, 500 mM NaCl), and once with LiCl buffer (10 mM Tris pH 8, 1 mM EDTA, 1% NaDOC, 1% NP40, 150 mM LiCl). Bound complexes were eluted from the beads by heating at 65 °C overnight in elution buffer (50 mM HEPES pH 8, 10 mM EDTA, 200 mM EDTA and 1% SDS). Whole-cell extract DNA was also treated for crosslink reversal and was used as a background control. Immunoprecipitated DNA and whole-cell extract DNA were then purified by treatment with RNase A, proteinase K and a phenol:chloroform:isoamyl alcohol extraction.

Purified DNA was prepared for sequencing according to a modified version of the Solexa Genomic DNA protocol. Fragmented DNA was end-repaired and adapters were ligated. An additional gel extraction step was added to the Illumina protocol at this step, allowing us to collect the material between 100 and 300 bp. The purified DNA was subjected to 18 cycles of linker-mediated PCR as per the Illumina protocol. Amplified fragments between 200 and 300 bp were isolated by agarose gel electrophoresis and purified. High-quality samples were confirmed by the appearance of a smooth smear of fragments from 100 to 1,000 bp, with a peak distribution between 150 and 300 bp.

Sequence reads were aligned to the mouse genome (NCBI Build 37, version mm9) using the model-based analysis of ChIP-Seq (MACS)<sup>22</sup>. Sequences uniquely mapping to the genome with zero or one mismatch were used in further analysis. Genomic bins with a normalized ChIP-Seq density greater than a defined threshold were considered enriched or "bound," based on a *P* value of less than  $10^{-8}$ .

**Luciferase reporter assay.** 293T cells were seeded into 96-well plates 24 h before transfection. For ZFP36L2 enhancer experiment, 10 ng luciferase reporter plasmid or control empty vector plasmid were co-transfected with 5 ng GR into 293T cells by using Lipofectamine 2000 transfection reagent (Invitrogen). Cells were cultured in a medium containing 1 µM DEX and lysed 48 h after transfection. For 3'UTR experiment, 10 ng luciferase reporter plasmid or control vector plasmid were co-transfected with 150 ng of XZ-ZFP36L2 into 293T cells by using Lipofectamine 2000 transfection reagent (Invitrogen) followed with 48 h culture. Luciferase activities were detected by using a dual luciferase kit (Promega).

**RNA-seq, microarray, and qRT-PCR.** For RNA-seq, samples were prepared by using the RNA Sample Prep Kit (Illumina) and sequenced by using Illumina genome analyser at Whitehead Institute.

For microarray experiments, RNA was extracted by using a miRNeasy Mini kit (Qiagen), and microarrays were performed by using the Mouse GE 4x44k microarray (Agilent) at Whitehead Institute.

For RT-PCR, RNA was extracted by using a miRNeasy Mini kit (Qiagen). Reverse transcription was carried out using SuperScript II Reverse Transcriptase (Invitrogen). Real-time PCR was performed by using SYBR Green PCR Master Mix (Applied Biosystems) and 7500 Real-Time PCR System (Applied Biosystems). The following primer sequences were used for real-time PCR: *Zfp36l2*, forward, GGCCGCACAAGCACAAAC, reverse, GAGACTCGAACCAAGATGAATAACG; *Afl1*, forward, GCCTAACACTTCCTCTGACACA, reverse, CTGCTACAGC CCAAAGTCAA; *Mafk*, forward, GCGGCGCACTCAAGA, reverse, TTTCT GTGTCACACGCTTGATG; *Nef2l1*, forward, CCCCAGAAGGCCTTTGTAAC, reverse, TCCAAGAGCATCTTCCCTTCA.

**Western blot.** Protein was extracted in lysis buffer (150 mM sodium chloride; 1.0% NP-40 or Triton X-100; 0.5% sodium deoxycholate; 0.1% SDS; 50 mM Tris, pH 8). SDS-PAGE was performed using the NuPAGE Novex Bis-Tris Gel Systems (Invitrogen). After electrophoretic transfer, the PVDF membranes with protein were incubated with the first antibody for ZFP36L2 (Abcam ab70775; at dilution of 1:1,000) or with the first antibody for GFP (Abcam ab290; at dilution of 1:1,000) at 4 °C overnight. After washing and incubating with HRP conjugated secondary antibody at room temperature for 1 h, membranes were developed.

**Immunoprecipitation experiment.** The XZ-ZFP36L2-GFP construct encoding the GFP-ZFP36L2 fusion protein was transfected into 293T cells. Two days after transfection, cells were lysed and immunoprecipitations were performed using either control IgG or ZFP36L2 antibody (Abcam ab70775) with the same amount

of input cell lysate according to the instructions for the EZ-Magna RIP RNA-Binding Protein Immunoprecipitation Kit (Millipore). Briefly, 293T cells were lysed and incubated with control IgG (5 µg) or ZFP36L2 antibody (Abcam ab70775; 5 µg) conjugated with magnetic beads (50 µl) for 4 h. The beads and proteins complexes were immunoprecipitated and magnetically separated. The proteins were purified and analysed by western blot using the ZFP36L2 antibody (Abcam ab70775).

**Plasmids.** The shRNA sequences targeting mouse *Zfp36l2*, *c-Kit*, *Hopx* and *Nlrp6* from Broad Institute RNAi consortium shRNA library were cloned into the MSCV-GFP vector. The shRNAs sequences are: *Zfp36l2*, shRNA1, aaaaCCAAACACTTAGGTCTCAGATgtcgacATCTGAGACCTAAGTGTGTTGG; shRNA2, aaaaGCACCACAACCTCAATATGAAAgtcgacTTTCATATTGAGTTGTGGTGC; *c-Kit*, shRNA1, aaaaCGGCTAACAAAGGAAGGATTgtcgacAATCCTTCCCTTGTGTAGCCG, shRNA2, aaaaCGGATCACAAAGATTTGCGATgtcgacATCGCAATCTTTGTGATCCG; *Hopx*, shRNA1, aaaaGCAGACGCAGAAATGGTTTAAgtcgacTTAAACCATTTCTGCGTCTGC, shRNA2, aaaaAGTACAACCTTCAA CAAGGTCAgtcgacTGACCTTTGTAAGTTGTA, shRNA3, aaaaCCTTCGG AATGCAGATCTGTTgtcgacAACAGATCTGCATTCCGAAGG; *Nlrp6*, shRNA1, aaaaGACCTCCAAGAGGTGATCAATgtcgacATTGATCACCTCTTGGAGGTC, shRNA2, aaaaCTGGATCATATAAAGCACAAgtcgacTTGTGCTTATGATGATCCAG. Sequences from mouse *Affl1* 3'UTR (positions 5318–6758, RefSeq NM\_001080798) that are 1,441 bp in length containing 2 'ATTTA' motifs were PCR-amplified from mouse genomic DNA and cloned into the luciferase reporter vector psiCHECK2. Following are the primers used for PCR amplification: forward, GGGCTCGAGTTCTTGGTACCTTGGTTAAATC, reverse, GGGGCGGCCGCC

CCAACTCATCTCGAATTTTCAC. For mutagenesis experiment, the two 'ATTTA' motifs of *Affl1* 3'UTR were mutated into 'TGGGC'. Sequences from mouse *Mafk* 3'UTR (positions 1730–2825, RefSeq NM\_010757) that are 1,096 bp in length containing 5 'ATTTA' motifs were PCR-amplified from mouse genomic DNA and cloned into psiCHECK2. Following are the primers for PCR amplification: forward, GGGGTTTAAACGAGCTCTGGGGCCACTGGAC, reverse, GGGGCGGCCGC CATCCCCAACAGGAAATTC. Sequences from mouse *Nfe2l1* 3'UTR (positions 3736–4614, RefSeq NM\_008686) that are 879 bp in length containing 1 'ATTTA' motif were PCR amplified from mouse genomic DNA and cloned into psiCHECK2. Following are the primers for PCR amplification: forward, GGGGTTTAAACGCTTCCTCTGCAGGGTCTAAAC, reverse, GGGGCGGCCGCGTCATGTGCTCACAGCATTTC. ZFP36L2 overexpression construct was made by inserting ORF of *Zfp36l2* into the MCD4 vector. *Zfp36l2* enhancer regions (chr17:84500031–84500271; chr17:84515492–84516478; chr17:84518538–84519282; chr17:84585041–84585584; and chr17:84595103–84595494) were each PCR-amplified from mouse genomic DNA and cloned into the luciferase reporter vector pGL3-Basic. XZ-ZFP36L2-GFP construct was made by inserting ORF of *Zfp36l2* without stop codon followed in frame with ORF of GFP into BglII and NcoI sites of XZ vector. XZ-ZFP36L2-IRES-GFP construct was made by inserting ORF of *Zfp36l2* into BglII and EcoRI sites of XZ vector.

21. Zhang, L., Flygare, J., Wong, P., Lim, B. & Lodish, H. F. miR-191 regulates mouse erythroblast enucleation by down-regulating *Rio3* and *Mxi1*. *Genes Dev.* **25**, 119–124 (2011).
22. Zhang, Y. *et al.* Model-based analysis of ChIP-Seq (MACS). *Genome Biol.* **9**, R137 (2008).



# Obesity-induced gut microbial metabolite promotes liver cancer through senescence secretome

Shin Yoshimoto<sup>1,2\*</sup>, Tze Mun Loo<sup>1,2,3</sup>, Koji Atarashi<sup>4,5</sup>, Hiroaki Kanda<sup>6</sup>, Seidai Sato<sup>1,2</sup>, Seiichi Oyadomari<sup>7</sup>, Yoichiro Iwakura<sup>8</sup>, Kenshiro Oshima<sup>9</sup>, Hidetoshi Morita<sup>10</sup>, Masahisa Hattori<sup>9</sup>, Kenya Honda<sup>2,4</sup>, Yuichi Ishikawa<sup>6</sup>, Eiji Hara<sup>1,2</sup> & Naoko Ohtani<sup>1,5\*</sup>

Obesity has become more prevalent in most developed countries over the past few decades, and is increasingly recognized as a major risk factor for several common types of cancer<sup>1</sup>. As the worldwide obesity epidemic has shown no signs of abating<sup>2</sup>, better understanding of the mechanisms underlying obesity-associated cancer is urgently needed. Although several events were proposed to be involved in obesity-associated cancer<sup>1,3</sup>, the exact molecular mechanisms that integrate these events have remained largely unclear. Here we show that senescence-associated secretory phenotype (SASP)<sup>4,5</sup> has crucial roles in promoting obesity-associated hepatocellular carcinoma (HCC) development in mice. Dietary or genetic obesity induces alterations of gut microbiota, thereby increasing the levels of deoxycholic acid (DCA), a gut bacterial metabolite known to cause DNA damage<sup>6</sup>. The enterohepatic circulation of DCA provokes SASP phenotype in hepatic stellate cells (HSCs)<sup>7</sup>, which in turn secretes various inflammatory and tumour-promoting factors in the liver, thus facilitating HCC development in mice after exposure to chemical carcinogen. Notably, blocking DCA production or reducing gut bacteria efficiently prevents HCC development in obese mice. Similar results were also observed in mice lacking an SASP inducer<sup>8</sup> or depleted of senescent HSCs, indicating that the DCA–SASP axis in HSCs has key roles in obesity-associated HCC development. Moreover, signs of SASP were also observed in the HSCs in the area of HCC arising in patients with non-alcoholic steatohepatitis<sup>3</sup>, indicating that a similar pathway may contribute to at least certain aspects of obesity-associated HCC development in humans as well. These findings provide valuable new insights into the development of obesity-associated cancer and open up new possibilities for its control.

Cellular senescence is a process occurring in normal cells in response to telomere erosion or oncogene activation, acting through checkpoint activation and stable cell-cycle arrest as a barrier to tumorigenesis<sup>9,10</sup>. Recent studies, however, reveal that senescent cells also develop a secretory profile composed mainly of inflammatory cytokines, chemokines and proteases, a typical signature termed the senescence-associated secretory phenotype (SASP)<sup>4</sup> or the senescence messaging secretome (SMS)<sup>5</sup>, hereafter referred to as SASP. Some of the SASP factors have cell-autonomous activities that reinforce senescence cell-cycle arrest<sup>5</sup> and/or promote clearance of senescent cells<sup>11,12</sup>, but other SASP factors have cell non-autonomous functions associated with inflammation and tumorigenesis promotion<sup>4</sup>, indicating that SASP contributes positively and negatively to cancer development, depending on the biological context<sup>4,5</sup>. Because some of the SASP factors, such as IL-6 and PAI-1<sup>4,5</sup>, are known to increase cancer risk in obesity<sup>1,13</sup>, we propose that SASP may contribute to obesity-associated cancer.

To explore this possibility, we first set up a system to examine the impact of dietary obesity on tumorigenesis, using wild-type C57BL/6

mice. However, we were unable to detect a statistically significant difference in cancer development between obese mice fed a high-fat diet (HFD) and lean mice fed a normal diet (data not shown), implying that a certain level of oncogenic stimuli might be required for obesity-associated cancer, especially in wild-type mice maintained in a specific pathogen free (SPF) environment. Because the Ras-pathway is frequently activated in human cancers, including hepatocellular carcinoma (HCC)<sup>14</sup>, we decided to use a treatment with DMBA (7,12-dimethylbenz(a)anthracene, a chemical carcinogen that causes an oncogenic Ras mutation) at the neonatal stage, a protocol known to generate a variety of tumours throughout the body<sup>15</sup>. In this setting, we also took advantage of using p21-*p-luc* mice, in which the expression of the *p21<sup>Waf1/Cip1</sup>* gene (a senescence inducer, also known as *Cdkn1a*) can be monitored noninvasively using a bioluminescence imaging (BLI) technique<sup>16</sup>. The neonatal p21-*p-luc* mice were therefore treated with a single application of DMBA, followed by feeding either HFD or normal diet for 30 weeks (Fig. 1a). Interestingly, a marked increase of the bioluminescent signal was observed in the abdomen of the obese mice, and it originated mainly from liver cancer (Supplementary Fig. 1). Notably, all HFD-fed mice developed HCC, whereas only 5% of mice fed normal diet developed malignant tumours in lung, but not liver (Fig. 1b–e and Supplementary Fig. 2). Importantly, moreover, similar HCC development was also observed when genetically obese (*ob/ob*, also known as *Lep<sup>ob/ob</sup>*) mice were treated with DMBA at the neonatal stage (Supplementary Fig. 3a–d), indicating that obesity, but not the HFD, promotes HCC development.

Because the induction of *p21<sup>Waf1/Cip1</sup>* expression was observed in liver, particularly in the area of liver cancer (Supplementary Fig. 1c), we speculated that senescent cells might be present in the vicinity of cancerous hepatocytes. Indeed, *p21<sup>Waf1/Cip1</sup>* expression was observed only in activated hepatic stellate cells (HSCs), which express  $\alpha$ -smooth muscle actin ( $\alpha$ -SMA) and desmin<sup>7</sup> (Fig. 1f). Furthermore, a number of other senescence markers<sup>9,10</sup>, such as p16<sup>INK4a</sup> expression, signs of DNA damage (53BP1 foci and  $\gamma$ H2AX foci) and inhibited cell proliferation (the absence of bromodeoxyuridine incorporation and Ki-67 expression), were also observed in activated HSCs despite absence of oncogenic *ras* mutation (Fig. 1f and Supplementary Figs 3e and 4). Interestingly, moreover, increased expression of IL-6, Gro- $\alpha$ , CXCL9 (major components of SASP)<sup>4,5</sup>, but not HGF (a differentiation marker)<sup>7</sup>, was observed in activated HSCs, but not in other types of liver cells (Fig. 1f and Supplementary Figs 3e and 5), indicating that these activated HSCs are senescing and may promote obesity-associated HCC development via SASP. It should be noted that, unlike the study using carbon tetrachloride (CCl<sub>4</sub>)<sup>11</sup>, fibrosis was not apparent in HFD-fed mice (Supplementary Fig. 6), precluding the possibility that the appearance of senescent HSCs was a by-product of liver fibrosis.

<sup>1</sup>Division of Cancer Biology, Cancer Institute, Japanese Foundation for Cancer Research, Koto-ku, Tokyo 135-8550, Japan. <sup>2</sup>CREST, Japan Science and Technology Agency, Kawaguchi, Saitama 332-0012, Japan. <sup>3</sup>Department of Applied Biological Science, Tokyo University of Science, Noda, Chiba 278-8510, Japan. <sup>4</sup>Research Center for Allergy and Immunology, RIKEN, Yokohama, Kanagawa 230-0045, Japan. <sup>5</sup>PRESTO, Japan Science and Technology Agency, Kawaguchi, Saitama 332-0012, Japan. <sup>6</sup>Division of Pathology, Cancer Institute, Japanese Foundation for Cancer Research, Koto-ku, Tokyo 135-8550, Japan. <sup>7</sup>Institute for Genome Research, University of Tokushima, Tokushima 770-8503, Japan. <sup>8</sup>Research Institute for Biological Science, Tokyo University of Science, Noda, Chiba 278-8510, Japan. <sup>9</sup>Graduate School of Frontier Sciences, University of Tokyo, Kashiwa, Chiba 277-8561, Japan. <sup>10</sup>School of Veterinary Medicine, Azabu University, Sagami-hara, Kanagawa 229-8501, Japan.

\*These authors contributed equally to this work.

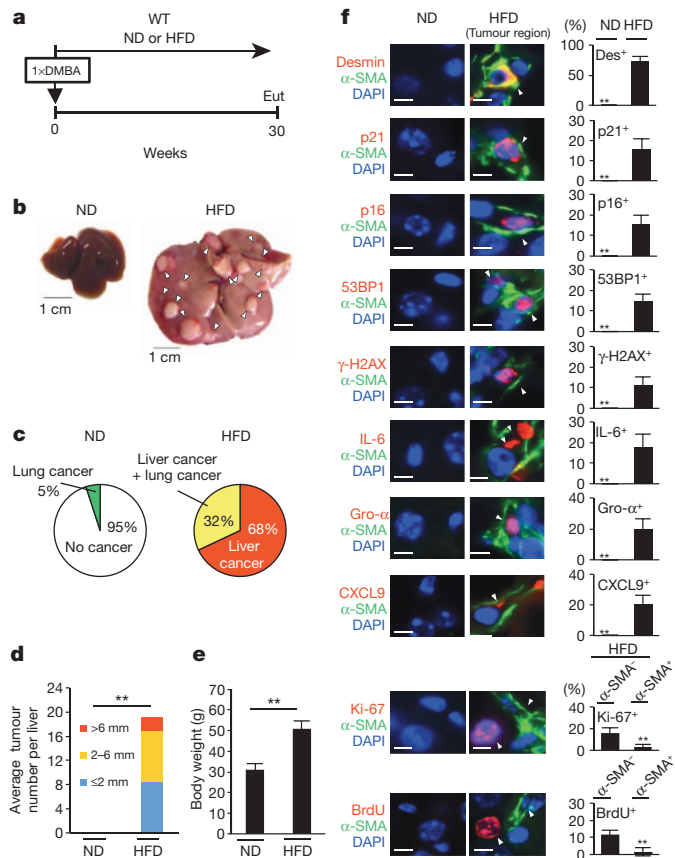


**Figure 1 | Cellular senescence in HSCs.** **a**, Timeline of the experimental procedure ( $n = 19$  per group). Eut, euthanasia; ND, normal diet. **b**, Representative macroscopic photographs of livers. Arrowheads indicate HCCs. **c**, The ratios of cancer formation. **d**, The average liver tumour numbers and their relative size distribution. **e**, The average body weights at the age of 30 weeks. **f**, Immunofluorescence analysis of liver section. HSCs were visualized by  $\alpha$ -SMA staining and DNA was stained by 4',6-diamidino-2-phenylindole (DAPI). Scale bars, 2.5  $\mu$ m. Arrowheads indicate  $\alpha$ -SMA expressing cells that were positive for indicated markers. The histograms indicate the percentages of  $\alpha$ -SMA-expressing cells that were positive for indicated markers. At least 100 cells were scored per group. For all graphs, error bars indicate mean  $\pm$  standard deviation (s.d.).  $**P < 0.01$ .

To ascertain the role of SASP in obesity-associated HCC development, we next sought evidence that the blockage of SASP can reduce obesity-associated HCC development. Although we were unable to detect the expression of IL-1 $\alpha$  (an upstream regulator of SASP induction)<sup>8</sup> in HSCs, significant induction of IL-1 $\beta$  (a functional homologue of IL-1 $\alpha$ ) and its activator, caspase-1 (an essential component of the inflammasome), was observed in senescent HSCs (Fig. 2a–c). Moreover, the addition of recombinant IL-1 $\beta$  caused the dose-dependent induction of IL-6 and *Gro- $\alpha$*  (also known as *Cxcl1*) gene expression in cultured primary murine HSCs (Supplementary Fig. 7a), indicating that inflammasome activation and subsequent IL-1 $\beta$  maturation can act as an upstream regulator of SASP induction in HSCs. Indeed, the levels of SASP factor expression in activated HSCs were substantially diminished in mice lacking the *Il-1 $\beta$*  gene (*Il-1 $\beta$ <sup>-/-</sup>* mice, also known as *Il1b<sup>-/-</sup>*) (Fig. 2c), and the numbers and sizes of the liver tumours that developed in *Il-1 $\beta$ <sup>-/-</sup>* mice were strikingly reduced, as compared with wild-type mice (Fig. 2d, e), although the degree of steatohepatitis was not attenuated (Supplementary Fig. 8a, b). It should be noted, however, that other senescence markers, such as 53BP1 foci, p21<sup>Waf1/Cip1</sup> expression and inhibited cell proliferation, were still observed in the activated HSCs of *Il-1 $\beta$ <sup>-/-</sup>* mice (Fig. 2c and Supplementary Fig. 8c). These results are somewhat consistent with a recent observation that the

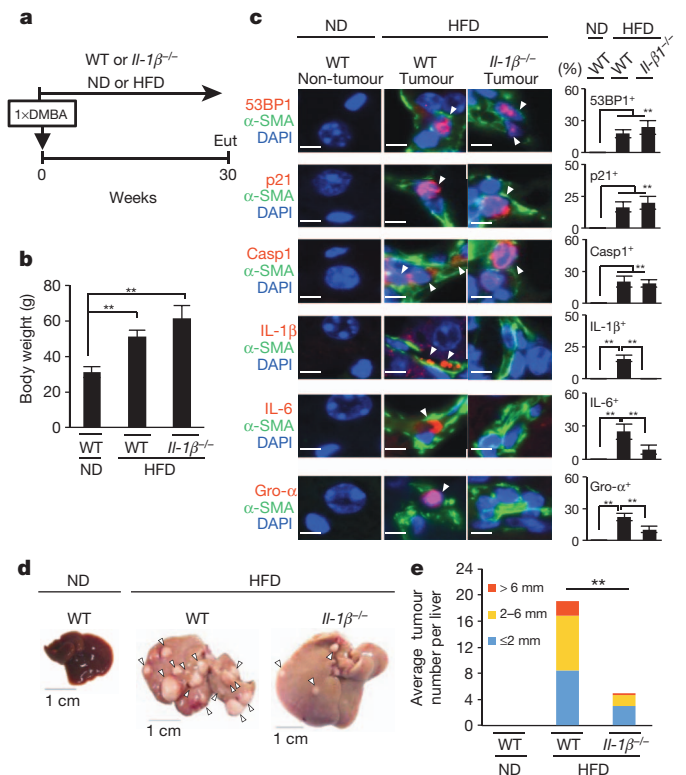


**Figure 2 | IL-1 $\beta$  deficiency alleviates obesity-induced HCC development.** **a**, Timeline of the experimental procedure (wild type (WT),  $n = 19$ ; *Il-1 $\beta$ <sup>-/-</sup>*,  $n = 9$ ). **b**, The average body weights at the age of 30 weeks. **c**, Immunofluorescence analysis of liver sections. HSCs were visualized by  $\alpha$ -SMA staining and DNA was stained by DAPI. Scale bars, 2.5  $\mu$ m. The histograms indicate the percentages of  $\alpha$ -SMA-expressing cells that were positive for indicated markers. At least 100 cells were scored per group. **d**, Representative macroscopic photographs of livers. Arrowheads indicate HCCs. **e**, The average liver tumour numbers and their relative size distribution. For all graphs, error bars indicate mean  $\pm$  s.d.  $**P < 0.01$ .

expression of p21<sup>Waf1/Cip1</sup> can induce senescence cell-cycle arrest without SASP induction<sup>17</sup>, suggesting that SASP, but not senescence cell-cycle arrest, promotes obesity-associated HCC development.

To further verify this idea, we next attempted to deplete senescent HSCs from obese wild-type mice treated with DMBA at the neonatal stage. As reported previously<sup>18</sup>, an intravenous injection of liposomes carrying small interfering RNA (siRNA) against HSP47 substantially reduced the abundance of activated HSCs, coinciding with a significant reduction of HCC development (Supplementary Fig. 9a–f). Note that this was not accompanied by an attenuation of steatohepatitis (Supplementary Fig. 9g, h). These results, along with the data from *Il-1 $\beta$ <sup>-/-</sup>* mice (Fig. 2), strongly indicate that senescent HSCs have enhancing roles in HCC development via SASP, at least in the neonatal DMBA plus obesity-induced HCC model. It is also noteworthy that neither the deletion of the *Il-1 $\beta$*  gene nor the depletion of senescent HSCs caused appreciable weight loss (Fig. 2b and Supplementary Fig. 9c), implying that there may be an indirect link between obesity and HCC development, at least in this experimental setting. These observations then raised the question of how obesity provokes SASP in HSCs.

Emerging evidence has indicated that alterations of intestinal microbiota are associated with obesity<sup>19</sup>. Furthermore, the activation of toll-like receptor (TLR) 4 by lipopolysaccharide (LPS) from intestinal Gram-negative bacteria has been shown to promote HCC development, in an HCC model using DEN (diethyl nitrosamine) plus CCl<sub>4</sub> treatment<sup>20</sup>. We thus explored the possibility that intestinal bacteria have key roles in obesity-associated HCC development. Indeed, a

treatment with a well-established oral antibiotic cocktail (4Abx), which reduces the number of commensal intestinal bacteria<sup>20</sup>, caused a marked reduction of HCC development, accompanied by a marked decrease in senescent HSCs in the neonatal DMBA plus obesity-induced HCC model (Fig. 3 and Supplementary Fig. 3). As reported<sup>20</sup>, 4Abx treatment resulted in not only a > 99.5% reduction of the presence of bacterial 16S ribosomal RNA gene in faeces, but also an enlargement of caecum commonly observed in germ-free mice (Fig. 3b and data not shown). Unexpectedly, however, a slight increase, rather than decrease, in HCC development was observed in mice lacking the *Tlr4* gene (*Tlr4*<sup>-/-</sup>) (Supplementary Fig. 10), indicating that LPS from Gram-negative bacteria is unlikely to promote HCC development in this setting. Indeed, meta 16S rRNA gene sequencing analysis of the intestinal microbiota revealed that the percentage of Gram-positive bacterial strains indigenous to the human and rodent intestinal tracts<sup>6</sup> was dramatically increased with a HFD (Fig. 4a). Moreover, a treatment with vancomycin (VCM), an antibiotic that preferentially targets Gram-positive bacteria, alone was sufficient to block HCC development and the appearance of senescent HSCs (Figs 3d–f, 4a and Supplementary Fig. 3). These results lead us to propose that the obesity-associated increase of Gram-positive bacteria may promote HCC development, presumably through the enterohepatic circulation of gut bacterial metabolites or toxins.

To substantiate this idea, the serum metabolites of HFD- and normal-diet-fed mice were analysed by liquid chromatography mass spectrometry (LC-MS). Interestingly, the level of deoxycholic acid (DCA), a secondary bile acid produced solely by the 7 $\alpha$ -dehydroxylation of

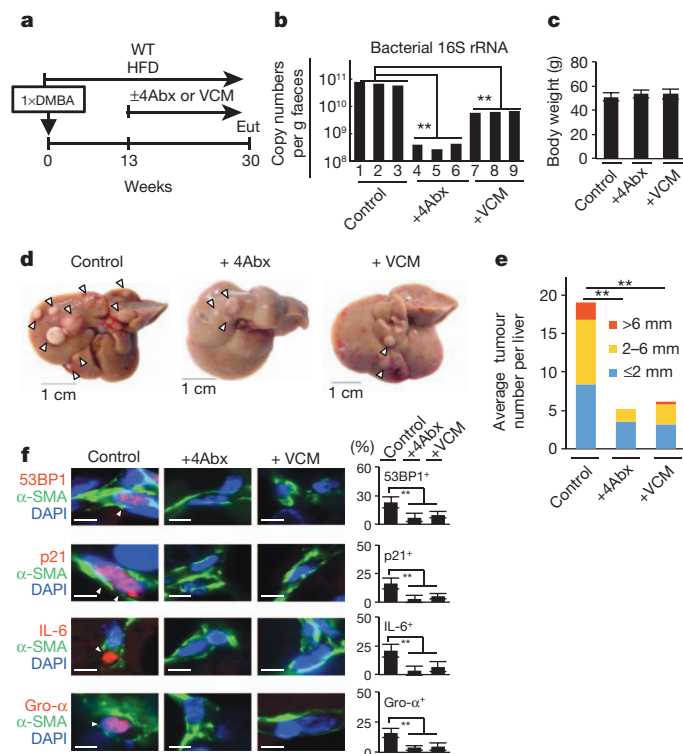


**Figure 3 | Antibiotics treatments alleviate obesity-induced HCC development.** **a**, Timeline of the experimental procedure (HFD, *n* = 19; HFD + 4Abx, *n* = 12; HFD + VCM, *n* = 6). **b**, The copy number of intestinal bacteria in faeces of indicated mice. **c**, The average body weights at the age of 30 weeks. **d**, Representative macroscopic photograph of livers. Arrowheads indicate HCCs. **e**, The average tumour numbers and their relative size distribution. **f**, Immunofluorescence analysis of liver sections. HSCs were visualized by  $\alpha$ -SMA staining and DNA was stained by DAPI. Scale bars, 2.5  $\mu$ m. The histograms indicate the percentages of  $\alpha$ -SMA expressing cells that were positive for indicated markers. At least 200 cells were scored per group. For all graphs, error bars indicate mean  $\pm$  s.d. \*\**P* < 0.01.

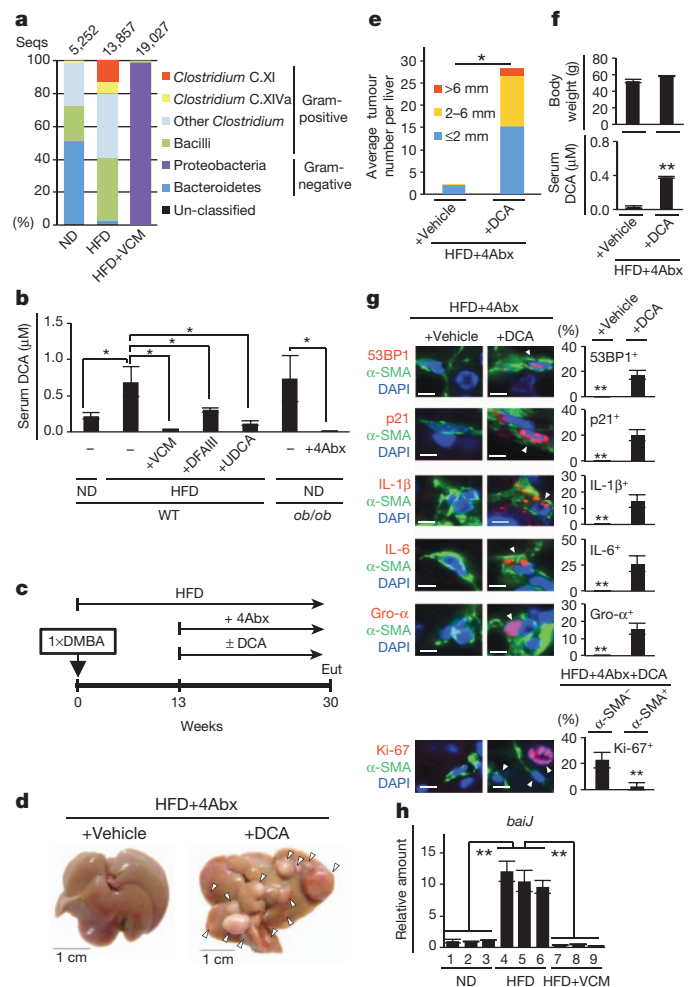


**Figure 4 | Bacterial metabolite promotes obesity-induced HCC development.** **a**, The relative abundance of OTUs (%) in the faecal bacterial community. Data are representative of five mice per group. **b**, Serum DCA concentration (ND, *n* = 4; HFD, *n* = 6; HFD + VCM, *n* = 3; HFD + DFAIII, *n* = 3; HFD + UDCA, *n* = 3; *ob/ob*, *n* = 3; *ob/ob* + 4Abx, *n* = 3). Error bars indicate mean  $\pm$  s.e.m. **c**, Timeline of the experimental procedure (*n* = 3 per group). **d**, Representative macroscopic photographs of livers. Arrowheads indicate HCCs. **e**, The average tumour numbers and their relative size distribution. **f**, The average body weight and serum DCA concentration. **g**, Immunofluorescence analysis of liver sections. Scale bars, 2.5  $\mu$ m. The histograms indicate the percentages of  $\alpha$ -SMA-expressing cells that were positive for indicated markers. At least 100 cells were scored per group. **h**, The quantitative real time PCR (qPCR) analysis of *baiJ* gene in the faeces (180 mg) of indicated mice used in **a**. For all graphs except **b**, error bars indicate mean  $\pm$  s.d. \**P* < 0.05, \*\**P* < 0.01.

primary bile acids carried out by gut bacteria such as strains belonging to *Clostridium* cluster XI and XIVa<sup>6</sup> (VCM-sensitive Gram-positive bacteria), was substantially increased by the HFD feeding, and was reduced by antibiotic treatments (Figs 3a and 4b). Note that DCA is known to cause DNA damage through reactive oxygen species production<sup>21</sup> and DNA damage is a critical inducer of SASP<sup>4,22</sup>. Moreover, in addition to colon carcinogenesis<sup>23</sup>, DCA has been shown to enhance liver carcinogenesis<sup>24</sup>. These notions prompted us to examine if DCA has key roles in obesity-associated HCC development. To this end, we attempted to lower the levels of DCA, by either decreasing the 7 $\alpha$ -dehydroxylation activity with difructose anhydride III (DFA III)<sup>25</sup> or stimulating bile acid secretion with ursodeoxycholic acid (UDCA)<sup>26</sup>. Notably, lowering the DCA concentration substantially reduced HCC development, accompanied by a marked decrease in senescent HSCs in obese mice treated with DMBA at the neonatal stage (Fig. 4b and



Supplementary Figs 11 and 12). In a reciprocal set of experiments, we also assessed whether DCA-feeding enhances HCC development in mice treated with DMBA at the neonatal stage (Fig. 4c). Intriguingly, although DCA feeding alone was insufficient to enhance HCC development in lean mice fed a normal diet at 30 weeks (data not shown), a significant enhancement of HCC development (Fig. 4c–f), accompanied by the appearance of senescence cell-cycle arrest and SASP in HSCs (Fig. 4g), was observed when HFD-fed mice treated with 4Abx were fed DCA for 17 weeks.

Notably, operational taxonomic unit (OTU)-based bacterial diversity analysis (Fig. 4a), in conjunction with a quantitative PCR analysis (Supplementary Fig. 13), revealed that the population of cluster XI of the genus *Clostridium* was strikingly increased in HFD-fed mice. Interestingly, phylogenetic analysis of the bacterial OTUs revealed that the population of *Clostridium* cluster XI is composed of a single bacterial taxon (OTU-1105) close to the DCA-producing strain *Clostridium sordellii*, and represents more than 12% of the faecal bacteria in HFD-fed mice (Supplementary Fig. 14). Concordantly, moreover, the abundance of the *baiJ* gene, a gene involved in bile acid 7 $\alpha$ -dehydroxylation<sup>27</sup>, was remarkably increased in faeces of mice fed HFD and was reduced by VCM treatment (Fig. 4h). On the other hand, a bacterial taxon (OTU-154) close to other DCA producing strains belonging to *Clostridium* cluster XIVa (*Clostridium hylemonae* and *Clostridium scindens*) represents only 0.5% of the total faecal bacteria in HFD-fed mice (Supplementary Fig. 14). Thus, although other bacteria may also be involved here, the simplest explanation for our data is that OTU-1105 belonging to *Clostridium* cluster XI contribute to an increase in the DCA level at least to some extent in HFD-fed mice.

Finally, to further support and extend our murine data to human biology, we tested whether IL-1 $\beta$  treatment can induce SASP in cultured primary human HSCs. As in murine HSCs, the addition of recombinant IL-1 $\beta$  caused the induction of *Il-6* and *Il-8* (a functional homologue of murine *Gro- $\alpha$* ) gene expression in cultured primary human HSCs (Supplementary Fig. 7b). Importantly, moreover, signs of cellular senescence and SASP were also observed in the HSCs without serious fibrosis in the area of HCC arising in patients with non-alcoholic steatohepatitis (NASH)<sup>3</sup> (8 out of 26) (Supplementary Fig. 15). This is somewhat consistent with previous observations that replicative senescence of cultured human HSCs is accompanied by a pronounced inflammatory but less fibrogenic phenotype<sup>28</sup> and a certain percentage of NASH-associated HCC arose from the non-cirrhotic liver<sup>29</sup>. Unlike rodents, the human liver cannot 7 $\alpha$ -hydroxylate DCA, forming cholic acid<sup>6</sup>. Hence, DCA can accumulate to very high levels (>50%) in the bile acid pool of humans<sup>6</sup>. These data, together with the previous observation that high fat consumption resulted in higher faecal DCA concentrations in healthy male volunteers (ages 20–60)<sup>30</sup>, suggest that DCA-induced senescent HSCs may contribute to at least certain aspects of obesity-associated HCC development via SASP in humans as well.

It should be noted that although many of the perturbations, for example, the *Il-1 $\beta$*  knockout, antibiotics treatment and lower DCA levels, significantly prevent HCC development, residual HCCs were still observed with these perturbations (Figs 2e and 3e and Supplementary Figs 11c and 12c). These results, in conjunction with the observation that DCA-feeding alone was insufficient to enhance HCC development in lean mice fed a normal diet until at least 30 weeks (data not shown), imply that an additional factor associated with obesity may exist to promote obesity-associated HCC development. Nevertheless, combining published data<sup>14,19,21,24,30</sup> with our findings, it is clear that the increased levels of DCA produced by gut bacteria play key roles in the promotion of obesity-associated HCC development via provoking SASP in HSCs, at least in the neonatal DMBA plus obesity-induced HCC model (Supplementary Fig. 16). A greater understanding of the molecular mechanisms linking gut microbial metabolite to SASP will therefore provide valuable new insights into how to bypass this undesirable side effect of cellular senescence.

## METHODS SUMMARY

**Chemically-induced carcinogenesis.** DMBA treatments<sup>15</sup> consisted of a single application of 50  $\mu$ l of a solution 0.5% DMBA (7,12-dimethylbenz [a]anthracene, Sigma) in acetone to the dorsal surface on postnatal day 4–5. Mother mice with pups were then fed either normal diet or HFD until weaning. At the age of 4 weeks old, pups were weaned and continuously fed either normal diet or HFD until euthanized.

**Bacterial 16S rRNA amplicon sequencing and analysis.** Bacterial genomic DNA was isolated from mice faeces, amplified for V1–V4 hypervariable regions of the 16S rRNA gene, and used for pyrosequencing analysis.

**Full Methods** and any associated references are available in the online version of the paper.

Received 10 December 2012; accepted 4 June 2013.

Published online 26 June 2013.

1. Khandekar, M. J., Cohen, P. & Spiegelman, B. M. Molecular mechanisms of cancer development in obesity. *Nature Rev. Cancer* **11**, 886–895 (2011).
2. Calle, E. E. & Kaaks, R. Overweight, obesity and cancer: epidemiological evidence and proposed mechanisms. *Nature Rev. Cancer* **4**, 579–591 (2004).
3. Sun, B. & Karin, M. Obesity, inflammation, and liver cancer. *J. Hepatol.* **56**, 704–713 (2012).
4. Coppé, J. P. et al. Senescence-associated secretory phenotypes reveal cell nonautonomous functions of oncogenic RAS and the p53 tumor suppressor. *PLoS Biol.* **6**, 2853–2868 (2008).
5. Kuilman, T. & Peeper, D. S. Senescence-messaging secretome: SMS-ing cellular stress. *Nature Rev. Cancer* **9**, 81–94 (2009).
6. Ridlon, J. M., Kang, D. J. & Hylemon, P. B. Bile salt biotransformations by human intestinal bacteria. *J. Lipid Res.* **47**, 241–259 (2006).
7. Friedman, S. L. Hepatic stellate cells: protean, multifunctional, and enigmatic cells of the liver. *Physiol. Rev.* **88**, 125–172 (2008).
8. Orjalo, A. V., Bhaumik, D., Gengler, B. K., Scott, G. K. & Campisi, J. Cell surface-bound IL-1 $\alpha$  is an upstream regulator of the senescence-associated IL-6/IL-8 cytokine network. *Proc. Natl Acad. Sci. USA* **106**, 17031–17036 (2009).
9. Collado, M. & Serrano, M. Senescence in tumours: evidence from mice and humans. *Nature Rev. Cancer* **10**, 51–57 (2010).
10. Kuilman, T., Michaloglou, C., Mooi, W. J. & Peeper, D. S. The essence of senescence. *Genes Dev.* **24**, 2463–2479 (2010).
11. Krizhanovskiy, V. et al. Senescence of activated stellate cells limits liver fibrosis. *Cell* **134**, 657–667 (2008).
12. Kang, T. W. et al. Senescence surveillance of pre-malignant hepatocytes limits liver cancer development. *Nature* **479**, 547–551 (2011).
13. Park, E. J. et al. Dietary and genetic obesity promote liver inflammation and tumorigenesis by enhancing IL-6 and TNF expression. *Cell* **140**, 197–208 (2010).
14. Newell, P. et al. Ras pathway activation in hepatocellular carcinoma and anti-tumoral effect of combined sorafenib and rapamycin *in vivo*. *J. Hepatol.* **51**, 725–733 (2009).
15. Serrano, M. et al. Role of the *INK4a* locus in tumor suppression and cell mortality. *Cell* **85**, 27–37 (1996).
16. Ohtani, N. et al. Visualizing the dynamics of p21<sup>Waf1/Cip1</sup> cyclin-dependent kinase inhibitor expression in living animals. *Proc. Natl Acad. Sci. USA* **104**, 15034–15039 (2007).
17. Coppé, J.-P. et al. Tumor suppressor and aging biomarker p16<sup>INK4a</sup> induces cellular senescence without the associated inflammatory secretory phenotype. *J. Biol. Chem.* **286**, 36396–36403 (2011).
18. Sato, Y. et al. Resolution of liver cirrhosis using vitamin A-coupled liposomes to deliver siRNA against a collagen-specific chaperone. *Nature Biotechnol.* **26**, 431–442 (2008).
19. Ley, R. E., Turnbaugh, P. J., Klein, S. & Gordon, J. I. Microbial ecology: human gut microbes associated with obesity. *Nature* **444**, 1022–1023 (2006).
20. Dapito, D. H. et al. Promotion of hepatocellular carcinoma by the intestinal microbiota and TLR4. *Cancer Cell* **21**, 504–516 (2012).
21. Payne, C. M. et al. Deoxycholate induces mitochondrial oxidative stress and activates NF- $\kappa$ B through multiple mechanisms in HCT-116 colon epithelial cells. *Carcinogenesis* **28**, 215–222 (2007).
22. Takahashi, A. et al. DNA damage signaling triggers degradation of histone methyltransferases through APC/C<sup>cdh1</sup> in senescent cells. *Mol. Cell* **45**, 123–131 (2012).
23. McGarr, S. E., Ridlon, J. M. & Hylemon, P. B. Diet, anaerobic bacterial metabolism, and colon cancer: a review of the literature. *J. Clin. Gastroenterol.* **39**, 98–109 (2005).
24. Kitazawa, S. et al. Enhanced preneoplastic liver lesion development under ‘selection pressure’ conditions after administration of deoxycholic or lithocholic acid in the initiation phase in rats. *Carcinogenesis* **11**, 1323–1328 (1990).
25. Minamida, K., Ohashi, M., Hara, H., Asano, K. & Tomita, F. Effects of ingestion of difructose anhydride III (DFA III) and the DFA III-assimilating bacterium *Ruminococcus productus* on rat intestine. *Biosci. Biotechnol. Biochem.* **70**, 332–339 (2006).
26. Beuers, U. Drug insight: mechanisms and sites of action of ursodeoxycholic acid in cholestasis. *Nat. Clin. Pract. Gastroenterol. Hepatol.* **3**, 318–328 (2006).
27. Ridlon, J. M. & Hylemon, P. B. Identification and characterization of two bile acid coenzyme A transferases from *Clostridium scindens*, a bile acid 7 $\alpha$ -dehydroxylating intestinal bacterium. *J. Lipid Res.* **53**, 66–76 (2012).

28. Schnabl, B., Purbeck, G. A., Choi, Y. H., Hagedorn, C. H. & Brenner, D. A. Replicative senescence of activated human hepatic stellate cells is accompanied by a pronounced inflammatory but less fibrogenic phenotype. *Hepatology* **37**, 653–664 (2003).
29. Takuma, Y. & Noso, K. Nonalcoholic steatohepatitis-associated hepatocellular carcinoma: our case series and literature review. *World J. Gastroenterol.* **16**, 1436–1441 (2010).
30. Rafter, J. J. *et al.* Cellular toxicity of fecal water depends on diet. *Am. J. Clin. Nutr.* **45**, 559–563 (1987).

**Supplementary Information** is available in the online version of the paper.

**Acknowledgements** The authors thank M. Oshima for suggestions in antibiotics treatment and members of the Hara laboratory for discussion during the preparation of this manuscript. This work was supported by grants from Japan Science and Technology Agency (JST), Ministry of Education, Culture, Sports, Science and Technology of Japan (MEXT), Ministry of Health, Labour and Welfare of Japan (MHLW), Uehara Memorial Foundation and Takeda Science Foundation. S.Y. was partly

supported by a postdoctoral fellowship from the Japan Society for Promotion of Science (JSPS). T.M.L. was partly supported by an international scholarship from the Ajinomoto Scholarship Foundation.

**Author Contributions** E.H. and N.O. designed the experiments, analysed the data and wrote the manuscript. N.O., S.Y. and T.M.L. performed obesity-induced liver cancer experiments. K.A., K.O., H.M., M.H. and K.H. performed bacterial genome data analysis. H.K., S.S. and Y.I. performed histopathological analysis of mouse and human liver cancer specimens. S.O. performed metabolite analysis. Y.I. provided *Il-1 $\beta$ <sup>-/-</sup>* mice. E.H. oversaw the projects.

**Author Information** Bacterial 16S rRNA amplicon sequence data have been deposited in DDBJ (<http://www.ddbj.nig.ac.jp/index-e.html>) with the accession number DRA000952. Reprints and permissions information is available at [www.nature.com/reprints](http://www.nature.com/reprints). The authors declare no competing financial interests. Readers are welcome to comment on the online version of the paper. Correspondence and requests for materials should be addressed to E.H. ([ejji.hara@jfc.or.jp](mailto:ejji.hara@jfc.or.jp)).

## METHODS

**Mice and diet.** The *p21-p-luc* mice (CD1)<sup>16</sup> were backcrossed with C57BL/6 mice for eight generations. The leptin-deficient (*ob/ob*) mice (C57BL/6) were purchased from Charles River Laboratories Japan, Inc. *Tlr4*<sup>-/-</sup> mice (C57BL/6) were purchased from Oriental Bioservices. *Il-1β*<sup>-/-</sup> mice (C57BL/6) were provided by Y. Iwakura<sup>31</sup>. Male mice were used for all the experiments in this study. The mice were maintained under specific pathogen-free (SPF) conditions, on a 12-h light-dark cycle, and fed normal diet (CE-2 from CLEA Japan Inc., composed of 12 kcal% fat, 29 kcal% protein, 59 kcal% carbohydrates) or high-fat diet (HFD, D12492 from Research Diets Inc., composed of 60 kcal% fat, 20 kcal% protein, 20 kcal% carbohydrates) *ad libitum*. Mice with more than 45 g weight at the age of 30 weeks old were used as obese mice for all the experiments. We measured the amount of food our mice eat and found that a 50 g HFD mouse eats 3.44 g food a day. This equates to 1.2 g of fat per day or 24 g per kg. According to the Reagan-Shaw equation<sup>32</sup> (human equivalent dose (mg kg<sup>-1</sup>) = mouse dose (mg kg<sup>-1</sup>) × mouse *K<sub>m</sub>* factor ÷ human *K<sub>m</sub>* factor; where the mouse and human *K<sub>m</sub>* factors are 3 and 37, respectively), this is equivalent to a 70 kg human eating 136 g of fat a day. The sample size used in this study was determined based on the expense of data collection, and the need to have sufficient statistical power. Randomization and blinding were not used in this study. All animal experiments were cared for by protocols approved by the Committee for the Use and Care of Experimental Animals of the Japanese Foundation for Cancer Research (JFCR).

**Chemically induced carcinogenesis.** DMBA treatments<sup>15</sup> consisted of a single application of 50 µl of a solution 0.5% DMBA (7,12-dimethylbenz(a)anthracene, Sigma) in acetone to the dorsal surface on postnatal day 4–5. After this application, mother mice with pups were fed normal diet or HFD. At the age of 4 weeks old, pups were weaned and continuously fed either normal diet or HFD until euthanized. Evaluation of tumour number and size was determined by counting the number of visible tumours and measuring the size of the tumour.

**Bioluminescence imaging.** Bioluminescence imaging was performed as previously described<sup>16,33</sup>. In brief, for the detection of luciferase expression, mice were anesthetized, injected intraperitoneally with D-luciferin sodium salt (75 mg kg<sup>-1</sup>) 5 min before beginning photon recording. Mice were placed in the light-tight chamber and a grey-scale image of the mice was first recorded with dimmed light followed by acquisition of luminescence image using a cooled charged-coupled device (CCD) camera (PIXIS 1024B; Princeton Instruments). The signal-to-noise ratio was increased by 2 × 2 binning and 5 min exposure. For colocalization of the luminescent photon emission on the animal body, grey scale and pseudo-colour images were merged by using IMAGE-PRO PLUS (Media Cybernetics).

**Antibiotics treatment.** Antibiotics treatment was performed as previously described<sup>20</sup> using a combination of four antibiotics (4Abx) of ampicillin (1 g l<sup>-1</sup>), neomycin (1 g l<sup>-1</sup>), metronidazole (1 g l<sup>-1</sup>) and vancomycin (500 mg l<sup>-1</sup>), or vancomycin (500 mg l<sup>-1</sup>) alone (VCM) in drinking water at the age of 13 weeks old until killed.

**Histology and immunofluorescence analysis.** Haematoxylin and eosin staining and immunofluorescence analysis were performed as previously described<sup>16</sup>. The primary antibodies used for mouse samples were as follows: α-SMA (Sigma A5228), desmin (abcam ab15200), p21 (abcam ab2961), p16 (Santa Cruz sc1207), 53BP1 (Santa Cruz sc22760), γ-H2AX (CST 9718), IL-6 (abcam ab6672), Gro-α (abcam ab17882), Ki-67 (Thermo RM9106), bromodeoxyuridine (abcam ab6326), caspase-1 (Millipore 06-503), IL-1β (R&D systems AF-401-NA), HSP47 (Santa Cruz sc8352), CXCL9 (abcam ab137792), F4/80 (Invitrogen BM8) and CD45 (Millipore 05-1416). The primary antibodies used for human samples were as follows: α-SMA (Dako M0851), γ-H2AX (CST 9718), p16 (Santa Cruz sc56330), p21 (CST #2947), IL-6 (abcam ab6672), IL-8 (abcam ab18672), 53BP1 (Santa Cruz sc22760) and caspase-1 (Millipore 06-503).

**Quantitative PCR.** Total RNA was extracted from mouse tissues using TRIzol reagent (Life technologies) and reverse transcription and quantitative PCR were performed as previously described<sup>22</sup>. Primers used were as follows: human *GAPDH*, 5'-CAACTACATGGTTTACATGTTTC-3' (forward) and 5'-GCCAGTGGACTCCACGAC-3' (reverse), mouse *Gapdh*, 5'-CAACTACATGGTCTACATGTTTC-3' (forward) and 5'-CACCAGTAGACTCCACGAC-3' (reverse), human *IL-6*, 5'-CTCGACGGCATCTCAGCCCTGA-3' (forward) and 5'-CTGCCAGTGCCTCTTTGCTGCTTT-3' (reverse), mouse *Il-6*, 5'-TGATTGTATGAACAACGATGATGC-3' (forward) and 5'-GGACTCTGGCTTTGTCTTTCTTGT-3' (reverse), human *IL-8*, 5'-AAGGAAATCTGGGTGCAGAG-3' (forward) and 5'-ATTGCTATCTGGCAACCCTAC-3' (reverse), mouse *Gro-α*, 5'-GCTGGGATTCACC TCAAGAA-3' (forward) and 5'-AGGTGCCATCAGAGCAGTCT-3' (reverse), bacterial *baiI*, 5'-TCAGGACGTGGAGGCGATCCA-3' (forward) and 5'-TACRTGATACTGGTAGCTCCA-3' (reverse), *Clostridium* cluster XI 16S rRNA gene 5'-TGACGGTACYNNRKAGGAAGCC-3' (forward) and 5'-ACTACGGTTRAGCCGTAGCCTTT-3' (reverse).

**In vivo RNAi experiment.** 250 µl of siRNA solution (3 mg ml<sup>-1</sup>) against HSP47 or control siRNA were mixed with 250 µl of complexation buffer and 500 µl of Invivofectamine (Life Technologies), incubated for 30 min at 50 °C, and dialysed at room temperature for 2 h in 1 l of PBS (pH 7.4). Dialysed siRNA-Invivofectamine complex was collected and 3 µg per g (weight) was injected through mice's tail vein twice a week for 15 weeks until killed. The sequences of HSP47 targeting oligo are as follows. 5'-GCACUGCUUGUGAACGCCAU GUUCU-3' (sense), 5'-AGAACAUGGCGUUCACAAGCAGUGC-3' (antisense). As a negative control, Ambion *In vivo* Negative Control #1 siRNA(4457289) was used.

**Treatment with DCA, UDCA and DFAIII.** Deoxycholic acid (DCA) was dissolved in absolute ethanol and diluted in 66% propylene glycol to reduce the concentration of alcohol to 5%. HFD-fed mice treated with DMBA at neonatal stage were fed a combination of four antibiotics (4Abx) with 40 µg per g (weight) of DCA or vehicle (control) three times per week using a plastic feeding tube at the age of 13 weeks old until killed. Ursodeoxycholic acid (UDCA) tablets (Tanabe-Mitsubishi Pharma) were powdered and dissolved in 66% propylene glycol. HFD-fed mice treated with DMBA at neonatal stage were fed 60 µg per g (weight) of UDCA or vehicle (control) using a plastic feeding tube every day at the age of 15 weeks old until killed. Diffructose anhydride III (DFAIII) was dissolved in saline. HFD-fed mice treated with DMBA at neonatal stage were fed 0.1 mg per g (weight) of DFAIII or vehicle (control) using a plastic feeding tube every day at the age of 17 weeks old until killed.

**Bacterial 16S rRNA amplicon sequencing and analysis.** Bacterial genomic DNA was isolated from faeces using a QIAamp DNA Stool mini kit (QIAGEN), and 100 ng of DNA was used for PCR for V1–V4 hyper variable regions of the 16S rRNA gene. Twenty five cycles of amplification was performed with universal 16S rRNA primers 27F 5'-AGAGTTTGATCCTGGCTCAG-3' and 519R 5'-GWATTACCGCGGCKGCTG-3' with 10-bp barcode tags using KOD Fx plus DNA polymerase (TOYOBO). All amplicons were sequenced on a 454 Genome Sequencer FLX Titanium platform (Roche Diagnostics and Beckman Coulter Genomics). Quality filter-passed sequence reads were obtained by removing reads that had no both primer sequences, had less than 500 bp in length, had the average quality value (QV) < 25, or were possible chimaeric. Of the filter-passed reads, more than 2,500 sequence reads trimming off both primer sequences for each sample were used and subjected to OTU analysis with the cutoff similarity of 97% identity using QIIME software. Representative sequences from each OTU were blasted to the database in Ribosomal Database Project (RDP) and aligned. The obtained OTU sequences were grouped at class level<sup>34,35</sup> and were subjected to phylogenetic analysis using MEGA software as described previously<sup>35</sup>.

**Determination of the copy number of faecal bacteria.** The copy number of faecal bacteria was calculated from the standard curve of known bacterial copy number by quantitative real-time PCR of 16S rRNA gene using 341f, 5'-CCTACGGGAGGC AGCAG-3' and 534r 5'-ATTACCGCGGCTGCTGG-3' primers as described previously<sup>36</sup>.

**Measurement of serum ALT and AST.** The levels of serum alanine aminotransferase (ALT) and aspartate aminotransferase (AST) were measured using kits from WAKO Pure Chemical Industries, Ltd.

**Measurement of serum deoxycholic acid.** The metabolomic analysis of mice serum were performed by liquid chromatograph mass spectrometry (LC-MS) in Human Metabolome Technologies Inc. Japan as previously described<sup>37</sup>. The amount of serum DCA was measured by gas chromatograph mass spectrometry (GC-MS) in the Bile Acid Institute of Junshin Clinic, Japan as described<sup>38</sup>.

**Human subjects.** Informed consent was obtained from all patients according to the protocol approved by the ethics committee of the Japanese Foundation for Cancer Research (JFCR).

**Statistical analysis.** Data were analysed by unpaired *t*-test with Welch correction (two-side) or Mann–Whitney test (two-side). *P*-values less than 0.05 were considered significant.

**Cell culture.** Murine primary HSCs were isolated as previously described<sup>18,39</sup>, and were cultured in Dulbecco's modified Eagle's medium supplemented with 10% fetal bovine serum in 3% O<sub>2</sub> and 5% CO<sub>2</sub> condition. Human primary HSCs were purchased from Health Science Research Resources Bank and were grown in Dulbecco's modified Eagle's medium supplemented with 10% fetal bovine serum in 3% O<sub>2</sub> and 5% CO<sub>2</sub> condition.

**H-ras sequencing.** Total RNA was prepared from HCCs and HSCs isolated from tumour regions using TRIzol reagent (Invitrogen). RNA was converted to cDNA by using oligo (dT) primer and a 330-bp PCR fragment containing exon 2 of *H-ras* gene was amplified with 5'-TGGGGCAGGAGCTCCTGGAT-3' and 5'-GAA GGACTTGGTGTGTTGA-3' primers. PCR fragments were sub-cloned using Target Clone Plus system (TOYOBO) and were sequenced by using Dye-Terminator and Big-Dye cycle sequencing system (Applied Biosystems) as described previously<sup>33</sup>.



31. Horai, R. *et al.* Production of mice deficient in genes for interleukin (IL)-1 $\alpha$ , IL-1 $\beta$ , IL-1 $\alpha/\beta$ , and IL-1 receptor antagonist shows that IL-1 $\beta$  is crucial in turpentine-induced fever development and glucocorticoid secretion. *J. Exp. Med.* **187**, 1463–1475 (1998).
32. Reagan-Shaw, S., Nihal, M. & Ahmad, N. Dose translation from animal to human studies revisited. *FASEB J.* **22**, 659–661 (2008).
33. Yamakoshi, K. *et al.* Real-time *in vivo* imaging of p16<sup>Ink4a</sup> reveals cross talk with p53. *J. Cell Biol.* **186**, 393–407 (2009).
34. Collins, M. D. *et al.* The phylogeny of the genus *Clostridium*: proposal of five new general and eleven new species combinations. *Int. J. Syst. Bacteriol.* **44**, 812–826 (1994).
35. Atarashi, K. *et al.* Induction of colonic regulatory T cells by indigenous *Clostridium* species. *Science* **331**, 337–341 (2011).
36. Song, Y., Liu, C. & Finegold, S. M. Real-time PCR quantitation of clostridia in feces of autistic children. *Appl. Environ. Microbiol.* **70**, 6459–6465 (2004).
37. Ooga, T. *et al.* Metabolomic anatomy of an animal model revealing homeostatic imbalances in dyslipidaemia. *Mol. Biosyst.* **7**, 1217–1223 (2011).
38. Muto, A. *et al.* Detection of  $\Delta^4$ -3-oxo-steroid 5 $\beta$ -reductase deficiency by LC-ESI-MS/MS measurement of urinary bile acids. *J. Chromatogr. B* **900**, 24–31 (2012).
39. Sekiya, Y. *et al.* Down-regulation of cyclin E1 expression by microRNA-195 accounts for interferon- $\beta$ -induced inhibition of hepatic stellate cell proliferation. *J. Cell. Physiol.* **226**, 2535–2542 (2011).

# Self-assembling influenza nanoparticle vaccines elicit broadly neutralizing H1N1 antibodies

Masaru Kanekiyo<sup>1</sup>, Chih-Jen Wei<sup>1</sup>, Hadi M. Yassine<sup>1</sup>, Patrick M. McTamney<sup>1†</sup>, Jeffrey C. Boyington<sup>1</sup>, James R. R. Whittle<sup>1</sup>, Srinivas S. Rao<sup>1</sup>, Wing-Pui Kong<sup>1</sup>, Lingshu Wang<sup>1</sup> & Gary J. Nabel<sup>1‡</sup>

Influenza viruses pose a significant threat to the public and are a burden on global health systems<sup>1,2</sup>. Each year, influenza vaccines must be rapidly produced to match circulating viruses, a process constrained by dated technology and vulnerable to unexpected strains emerging from humans and animal reservoirs. Here we use knowledge of protein structure to design self-assembling nanoparticles that elicit broader and more potent immunity than traditional influenza vaccines. The viral haemagglutinin was genetically fused to ferritin, a protein that naturally forms nanoparticles composed of 24 identical polypeptides<sup>3</sup>. Haemagglutinin was inserted at the interface of adjacent subunits so that it spontaneously assembled and generated eight trimeric viral spikes on its surface. Immunization with this influenza nanoparticle vaccine elicited haemagglutination inhibition antibody titres more than tenfold higher than those from the licensed inactivated vaccine. Furthermore, it elicited neutralizing antibodies to two highly conserved vulnerable haemagglutinin structures that are targets of universal vaccines: the stem<sup>4,5</sup> and the receptor binding site on the head<sup>6,7</sup>. Antibodies elicited by a 1999 haemagglutinin–nanoparticle vaccine neutralized H1N1 viruses from 1934 to 2007 and protected ferrets from an unmatched 2007 H1N1 virus challenge. This structure-based, self-assembling synthetic nanoparticle vaccine improves the potency and breadth of influenza virus immunity, and it provides a foundation for building broader vaccine protection against emerging influenza viruses and other pathogens.

Influenza outbreaks arise from viruses that evade human immunity. Advances in influenza virus structural biology, nanotechnology and gene delivery offer new opportunities to develop improved vaccines that can confer more broadly protective immunity against diverse influenza viruses<sup>4–6,8,9</sup>. Among recent innovations, several natural proteins have shown the ability to form nanoparticles well-suited for antigen presentation and immune stimulation<sup>10</sup>. One such protein is ferritin, a ubiquitous iron storage protein that self-assembles into nanoparticles<sup>3</sup>. Although ferritin has been used to display exogenous peptides<sup>11</sup>, it has not been possible to display viral glycoproteins because of their complexity and requirements for oligomerization. Additionally, recombinant ferritins made in prokaryotic cells were not subjected to mammalian glycosylation and other post-translational modifications typical of viral proteins<sup>11–13</sup>. Structural analysis of ferritin indicated that it would be possible to insert a heterologous protein, specifically influenza virus haemagglutinin (HA), so that it could assume the physiologically relevant trimeric viral spike (Fig. 1a). Ferritin forms a nearly spherical particle composed of 24 subunits arranged with octahedral symmetry around a hollow interior. The symmetry includes eight threefold axes on the surface. The aspartic acid (Asp) at residue 5 near the NH<sub>2</sub> terminus is readily solvent accessible, and the distance between each Asp 5 on the threefold axis (28 Å) is almost identical to the distance between the central axes of each HA2 subunit of trimeric HA (Fig. 1a, right). We therefore proposed that HA would trimerize properly if inserted into this structure.

To test this hypothesis, we genetically fused the ectodomain of A/New Caledonia/20/1999 (1999 NC) HA to *Helicobacter pylori* non-haem ferritin<sup>14</sup> (Fig. 1a, bottom), a ferritin that diverges highly from its mammalian counterparts (Supplementary Fig. 1). This fusion protein was expressed in mammalian cells, and self-assembly of ferritin and HA–ferritin nanoparticles was confirmed by size exclusion chromatography and dynamic light scattering (Supplementary Fig. 2a, b). HA–ferritin also had the expected apparent molecular weight of 85 kDa (Supplementary Fig. 2c). Whereas ferritin alone formed smooth spherical particles as visualized by transmission electron microscopy (TEM), HA–ferritin showed clearly visible spikes protruding from the spherical core (Fig. 1b, Ferritin np versus HA–np). Remarkably, the placement of these spikes illustrated the octahedral symmetry of the HA–nanoparticle design. Octahedral two-, three- and fourfold axes were distinctly observed in the TEM image (Fig. 1b, right). These data demonstrated the formation of trimeric HA spikes on self-assembling nanoparticles.

To verify the antigenicity of the HA spikes on the nanoparticles, we analysed their reactivity with an anti-HA head monoclonal antibody and a conformation-dependent monoclonal antibody, CR6261, which recognizes a conserved structure on the HA stem<sup>4</sup>. The HA–nanoparticle binds to the anti-head or the anti-stem monoclonal antibody with affinities similar to trimeric HA or trivalent inactivated influenza vaccine (TIV) containing the same 1999 NC HA at equimolar concentrations of HA (Supplementary Fig. 3a). Analogous to trimeric HA, the HA–nanoparticle also blocked neutralization by CR6261 and another stem-directed monoclonal single chain variable fragment antibody, F10 (ref. 5) (Supplementary Fig. 3b). These results confirmed that HA molecules on the HA–nanoparticle antigenically resembled the physiological HA viral spike.

To assess the immunogenicity of the HA–nanoparticle, mice were immunized twice with TIV or HA–nanoparticles with or without Ribi adjuvant. The HA–nanoparticles induced 1.6-fold higher haemagglutination inhibition (HAI) titres than TIV in the absence of adjuvant. Although this increase did not reach statistical significance, HAI titres were 7.2-fold higher in animals receiving HA–nanoparticles when Ribi was used (Fig. 2a, left;  $P < 0.0001$ ), and a similar effect was observed in the neutralization and enzyme-linked immunosorbent assay (ELISA) titres (Fig. 2a, middle and right;  $P < 0.0001$ ). For example, neutralization titres elicited by HA–nanoparticles as assessed by the concentration of antibody needed to inhibit viral entry by 90% (IC<sub>90</sub>) were ~34 times higher than TIV (Fig. 2a, middle). We also evaluated whether a similar immune response can be induced by HA–nanoparticles with MF59, an adjuvant that has been used in humans<sup>15</sup>. Similarly high HAI and IC<sub>90</sub> titres were observed in mice receiving MF59-adjuvanted HA–nanoparticles ( $4,608 \pm 512$  and  $47,140 \pm 22,561$ , respectively), and the titres were significantly higher than those induced by either non-adjuvanted HA–nanoparticles ( $P = 0.0005$  and  $0.0311$  for HAI and IC<sub>90</sub>, respectively) or MF59-adjuvanted TIV ( $P = 0.0016$  and  $0.0388$  for HAI and IC<sub>90</sub>, respectively) (Fig. 2b). These results demonstrated

<sup>1</sup>Vaccine Research Center, National Institute of Allergy and Infectious Diseases, National Institutes of Health, Bethesda, Maryland 20892, USA. <sup>†</sup>Present addresses: MedImmune, 1 MedImmune Way, Gaithersburg, Maryland 20878, USA (P.M.M.); Sanofi, 640 Memorial Drive, Cambridge, Massachusetts 02139, USA (G.J.N.).

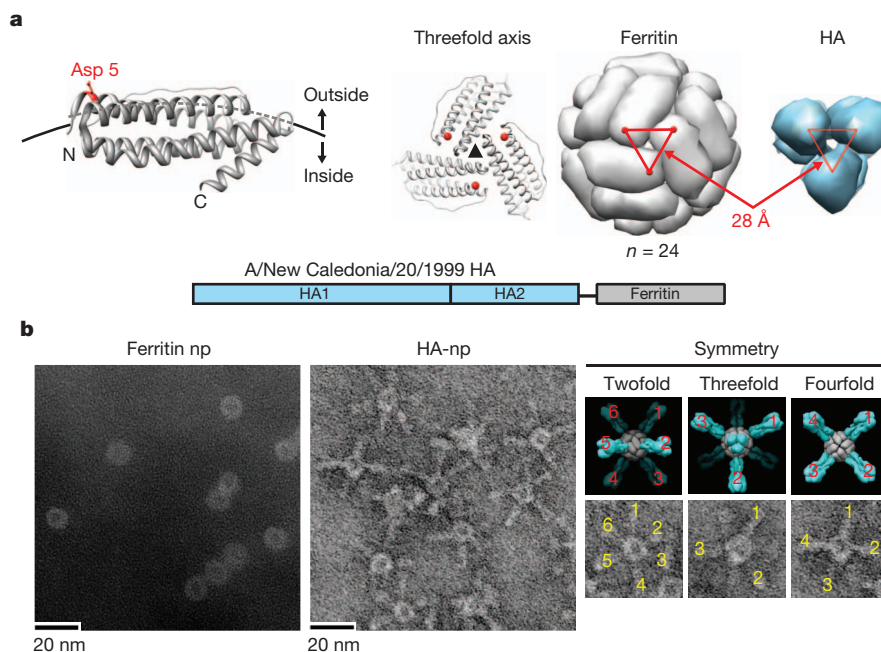


**Figure 1 | Molecular design and characterization of ferritin nanoparticles displaying influenza virus HA.** **a**, A subunit of *H. pylori* non-haem ferritin (PDB: 3bve) (left). The NH<sub>2</sub>- and COOH-termini are labelled as N and C, respectively. Three subunits surrounding a threefold axis are shown (middle) and the Asp 5 is coloured in red. An assembled ferritin nanoparticle and an HA trimer (PDB: 3sm5) (viewed from membrane proximal end) (right). A triangle connecting the Asp 5 residues at the threefold axis is shown in red. The same

triangle is drawn on the HA trimer (right). A schematic representation of the HA-ferritin fusion protein is shown (bottom). **b**, Negatively stained TEM images of nanoparticles (np) (left and middle). Computational models and observed TEM image (right, top and bottom panels) representing octahedral two-, three- and fourfold axes of HA-nanoparticles are shown as indicated. Visible HA spikes are numbered in the images.

the feasibility of using the HA-nanoparticles with an adjuvant suitable for humans<sup>16</sup>. Because higher titres were observed using either adjuvant, further comparisons were performed with adjuvant (Ribi). Neutralization against a panel of H1N1 strains revealed not only increased potency, but

also enhanced breadth, stimulated by HA-nanoparticles compared with TIV or trimeric HA (Fig. 2c). Neutralization against two unmatched, highly divergent H1N1 strains, A/Puerto Rico/8/1934 (1934 PR8) and A/Singapore/6/1986 (1986 Sing), was only observed in mice immunized

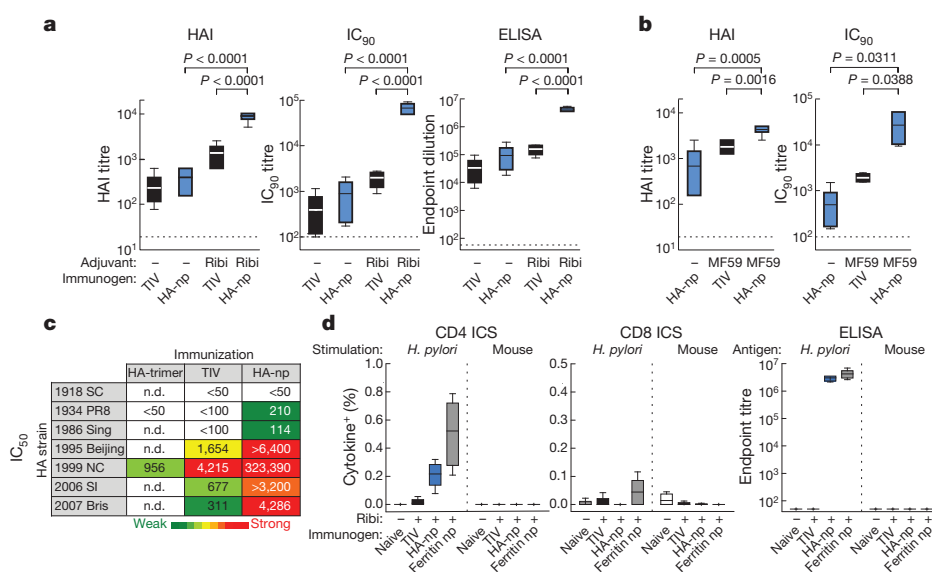


**Figure 2 | Immune responses in HA-nanoparticle-immunized mice.** **a**, HAI (left), IC<sub>90</sub> neutralization (middle) and anti-HA antibody endpoint titres (right) after two immunizations of TIV or HA-nanoparticles with or without (–) Ribi. **b**, HAI (left) and IC<sub>90</sub> (right) titres after two immunizations of TIV with MF59 or HA-nanoparticles with or without (–) MF59. Two of five mice immunized with MF59-adjuvanted HA-nanoparticles exhibited IC<sub>90</sub> titres >51,200 and were plotted as 51,200. The data are presented as box-and-whisker plots (boxed from lower to upper quartile with whiskers from minimum to maximum) with lines at the mean ( $n = 5$ ). **c**, Neutralization breadth of the immune sera (with

Ribi). IC<sub>50</sub> titres against a panel of H1N1 pseudotyped viruses were determined. Heat map is coloured in a gradient from green to yellow to red reflecting the neutralization strength. **d**, Cellular (left and middle) and humoral (right) immune responses against *H. pylori* and mouse ferritins. Cells expressing interferon  $\gamma$  (IFN- $\gamma$ ), tumour necrosis factor  $\alpha$  (TNF- $\alpha$ ) or interleukin 2 (IL-2) upon stimulation with peptides covering *H. pylori* or mouse ferritins were combined and plotted as cytokine<sup>+</sup>. The data are presented as box-and-whisker plots with lines at the mean ( $n = 5$ ). ICS, intracellular cytokine staining.



with the HA-nanoparticles, and the titre against the contemporary strain A/Brisbane/59/2007 (2007 Bris) was more than tenfold higher in mice immunized with HA-nanoparticles than with TIV (Fig. 2c).

We next examined whether pre-existing immunity to ferritin or to other HA subtypes would interfere with subsequent immunization using HA-nanoparticles. Mice pre-immunized with either H3 (A/Perth/16/2009, 2009 Perth) HA-nanoparticles or empty ferritin nanoparticles generated substantial anti-H3 HA and/or anti-*H. pylori* ferritin antibody responses (Supplementary Fig. 4a). They were then immunized with H1 (1999 NC) HA-nanoparticles. Comparable HAI, IC<sub>90</sub> and ELISA titres against 1999 NC HA were observed in naive animals as well as in groups pre-immunized with H3 HA-nanoparticles or empty ferritin nanoparticles (Supplementary Fig. 4b). These results indicated that pre-existing anti-*H. pylori* ferritin immunity did not diminish the HA-specific antibody response.

To address the concern that immunization with ferritin might abrogate immune tolerance and induce autoimmunity, we analysed T-cell and antibody responses against murine and *H. pylori* ferritins in HA-nanoparticle-immunized mice. Although we found an increase in intracellular cytokine staining of CD4<sup>+</sup> T cells stimulated with *H. pylori* ferritin peptides (Fig. 2d, left), no increase in CD4<sup>+</sup> or CD8<sup>+</sup> intracellular cytokine staining responses to murine ferritin peptides were observed (Fig. 2d, left and middle). In addition, antibodies to *H. pylori* ferritin, but not to murine ferritin, were detected in the immune sera (Fig. 2d, right). We therefore found no evidence of immunity to autologous ferritin in mice. Moreover, the HA-nanoparticles are unlikely to affect iron homeostasis *in vivo* because of their minimal iron incorporation activity (Supplementary Fig. 5).

We next generated a trivalent vaccine comprising three, separately purified HA-nanoparticles formulated into a single vaccine dose, analogous to a standard TIV. The strains chosen were H1 (A/California/04/2009, 2009 CA), H3 (2009 Perth) and influenza B (B/Florida/04/2006, 2006 FL). All three HA-nanoparticles self-assembled and showed morphology similar to 1999 NC HA-nanoparticles (Supplementary Fig. 6a). The immunogenicity of multispecific HA-nanoparticles (combination of three monospecific HA-nanoparticles) was compared to a seasonal TIV containing the same H1 and H3 strains and a mismatched influenza B (B/Brisbane/60/2008). HAI titres against homologous H1N1 and H3N2 viruses were significantly increased in animals immunized with multispecific HA-nanoparticles relative to TIV (Supplementary Fig. 6b;  $P = 0.0125$  and  $0.0036$ , respectively). When compared to animals immunized with the corresponding monospecific HA-nanoparticles, HAI titres against H1N1 and H3N2 viruses induced by multispecific HA-nanoparticles were comparable (Supplementary Fig. 6b). Therefore no substantial antigenic competition was observed with the multispecific HA-nanoparticle vaccine.

We next examined the immunogenicity of HA-nanoparticles (1999 NC) in ferrets. Three weeks after the first immunization, all ferrets receiving Ribi-adjuvanted HA-nanoparticles generated protective HAI titres against homologous virus ( $>40$ ), whereas only 50% (3/6) of Ribi-adjuvanted TIV-immunized ferrets induced titres greater than 40 (Fig. 3a, left;  $P = 0.0056$ ). The same difference was also observed for both neutralization and ELISA titres (Fig. 3a, middle and right;  $P = 0.0047$  and  $P = 0.0045$ , respectively), documenting the potency of HA-nanoparticles in a second species. After boosting, the HAI, IC<sub>90</sub> and ELISA titres of the HA-nanoparticle-immune sera were approximately tenfold higher than those of TIV-immune sera (Fig. 3a, left, middle and right;  $457 \pm 185$  versus  $5,760 \pm 1,541$ ,  $P = 0.0066$ ;  $598 \pm 229$  versus  $5,515 \pm 1,074$ ,  $P = 0.0012$ ; and  $5,902 \pm 1,851$  versus  $55,105 \pm 13,018$ ,  $P = 0.0038$ , respectively). Remarkably, a single immunization of HA-nanoparticles induced immune responses comparable to two immunizations of TIV (Fig. 3a).

To determine whether HA-nanoparticles could confer protection against an unmatched H1N1 virus, immunized ferrets were challenged with 2007 Bris virus, which had not yet evolved when 1999 NC circulated and required a different seasonal vaccine to confer protection in

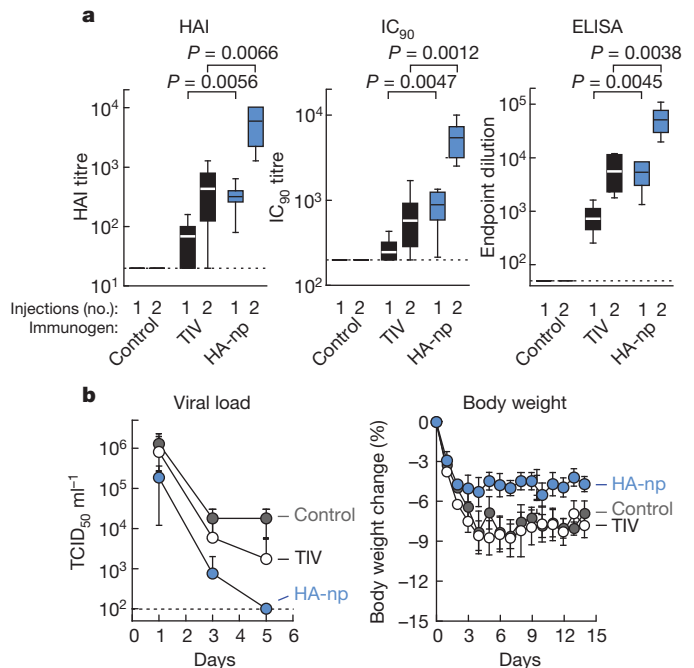


**Figure 3 | Protective immunity induced in ferrets immunized with the HA-nanoparticles.** **a**, HAI (left), IC<sub>90</sub> (middle) and anti-HA antibody endpoint titres (right) against 1999 NC HA. Immune sera were collected after the first (1) and second (2) immunizations. The data are presented as box-and-whisker plots with lines at the mean ( $n = 6$ ). **b**, Protection of immunized ferrets from 2007 Bris virus challenge. Challenge was performed with  $10^{6.5}$  EID<sub>50</sub> through intranasal inoculation. Virus titres in the nasal washes were determined by 50% tissue culture infectious dose (TCID<sub>50</sub>) assay (left). The mean viral loads with s.d. at each time point were plotted ( $n = 6$ ). Change in body weight after virus challenge was monitored (right). Each data point represents the mean percent change in body weight from day 0 (pre-challenge) with s.e.m. ( $n = 6$ ).

humans. Ferrets immunized with HA-nanoparticles showed a significant reduction in viral shedding beginning 1 day after challenge compared to the sham control group (Fig. 3b, left;  $P = 0.0259$ ). At the same time point, no significant reduction in viral shedding was seen in the TIV-immunized group (Fig. 3b, left;  $P = 0.4665$ ). In addition, HA-nanoparticle-immunized ferrets suffered less weight loss compared to the TIV-immunized and sham control animals (Fig. 3b, right), further demonstrating the protective efficacy of HA-nanoparticles.

Interestingly, unlike the TIV-immune sera which preferentially neutralized homologous 1999 NC and another closely related strain (A/Beijing/262/1995, 1995 Beijing), sera from HA-nanoparticle-immunized ferrets broadly neutralized heterologous 1986 Sing, 1995 Beijing, A/Solomon Islands/3/2006 (2006 SI) and 2007 Bris viruses (Fig. 4a, left). The recent identification of two classes of broadly neutralizing antibodies that target the highly conserved but vulnerable regions of HA suggests a potential pathway to develop influenza vaccines with broad coverage<sup>17</sup>. One class of broadly neutralizing antibodies typified by CR6261 recognizes a hydrophobic groove on the HA stem and neutralizes virus by inhibiting membrane fusion<sup>4,5,18–21</sup>. The second class recognizes the receptor binding site (RBS) on the HA head and inhibits viral entry<sup>6,7,22</sup>. To determine whether the cross-reactivity across diverse H1N1 strains induced by HA-nanoparticles included neutralizing antibodies to the HA stem epitope, ferret immune sera were pre-absorbed with cells expressing a stem mutant ( $\Delta$ Stem)<sup>8</sup> HA to remove non-stem-directed antibodies and analysed for binding to wild-type or  $\Delta$ Stem HA as previously described<sup>8</sup>. Stem-specific antibodies were detected in HA-nanoparticle-immunized ferrets (6/6) in greater frequency and magnitude than TIV-immunized ferrets (2/6) (Fig. 4b, left;  $P = 0.0056$ ). Moreover, binding of these pre-absorbed sera to HA was reduced by CR6261 (Fig. 4b, right;  $P = 0.0019$ ), further documenting the

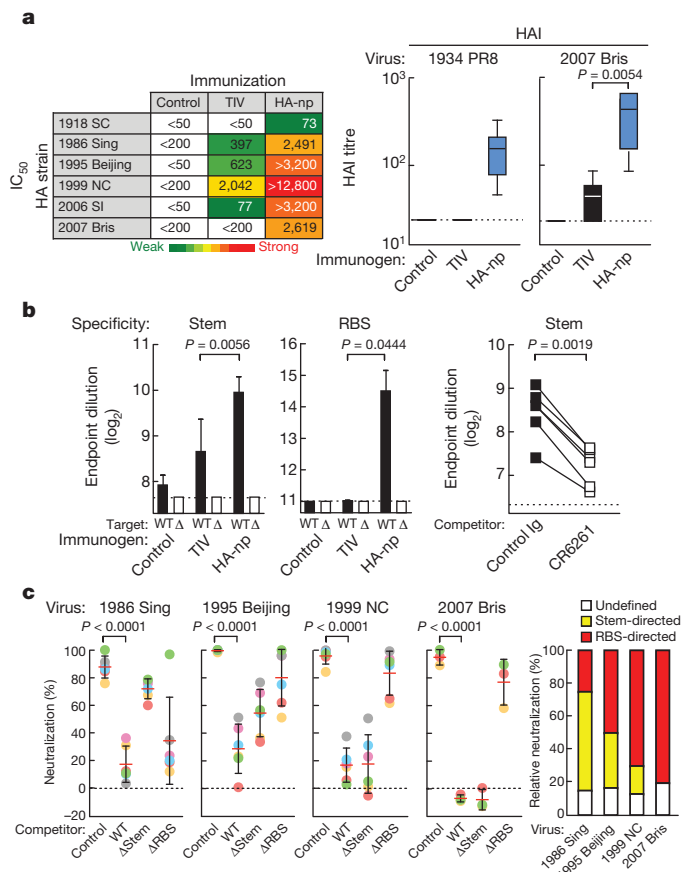


**Figure 4 | Improved neutralization breadth and detection of stem- and RBS-directed antibodies.** **a**, Breadth of serum neutralization in immune ferrets.  $IC_{50}$  titres against a panel of H1N1 pseudotyped viruses (left) and HAI titres against 1934 PR8 and 2007 Bris H1N1 viruses (right) were determined. Heat map is coloured as in Fig. 2. HAI titres are presented as box-and-whisker plots with lines at the mean ( $n = 6$ ). **b**, Stem- and RBS-directed antibodies elicited by HA-nanoparticle immunization. Immune sera were pre-absorbed with  $\Delta$ Stem (left) and  $\Delta$ RBS (middle) HA-expressing cells and analysed for their binding to wild-type and a respective mutant ( $\Delta$ ) HA. The mean endpoint titres were plotted with s.d. ( $n = 6$ ). Binding of  $\Delta$ Stem HA pre-absorbed immune sera to HA pre-incubated with a control or CR6261 monoclonal antibody (right). Each symbol represents the titre of an individual ferret ( $n = 6$ ). **c**, Neutralization competition with wild-type,  $\Delta$ Stem or  $\Delta$ RBS HA (left). The neutralization of HA-nanoparticle-immune sera was measured in the presence of indicated competitor proteins. Percent neutralization at serum dilutions of 1/200 (1986 Sing and 2007 Bris), 1/800 (1995 Beijing) or 1/3,200 (1999 NC) was plotted. Each symbol represents an individual ferret, and the mean is indicated as a red line with s.d. ( $n = 6$  except for 2007 Bris ( $n = 3$ )). The relative contributions of stem- and RBS-directed neutralization were calculated and plotted as the mean percentage ( $n = 6$ ).

presence of antibodies targeting the same epitope as CR6261. The HAI titres against heterologous 2007 Bris virus were also significantly higher in ferrets immunized with HA-nanoparticles (6/6) than with TIV (3/6) (Fig. 4a, right;  $P = 0.0054$ ). Interestingly, HA-nanoparticle-immune sera have HAI responses against a highly divergent 1934 PR8 strain, with titres  $\geq 40$  in all ferrets. However, no HAI titres against 1934 PR8 were detected in TIV-immunized ferrets (Fig. 4a, right). These data indicated that the HA-nanoparticles might elicit another class of neutralizing antibody directed towards the conserved RBS in the HA head. To dissect the specificity of the RBS-directed antibody response, we generated an RBS mutant HA ( $\Delta$ RBS) by introducing a glycosylation site in the sialic acid binding pocket at residue 190 (Supplementary Fig. 7)<sup>23</sup>. Ferret immune sera were absorbed with  $\Delta$ RBS HA-expressing cells to remove antibodies to HA outside of this region and tested for binding against wild-type or  $\Delta$ RBS HA. RBS-directed antibodies were detected

with titres of  $>2,000$  in all HA-nanoparticle-immunized ferrets, but only in 1 of 6 ferrets that received TIV (Fig. 4b, middle).

To define the relative contributions of stem- and RBS-directed antibodies to the breadth of neutralization, we performed neutralization assays in the presence of competitor proteins: wild-type,  $\Delta$ Stem or  $\Delta$ RBS HA. In the presence of excess  $\Delta$ Stem HA, only stem-directed antibodies can neutralize viruses; similarly,  $\Delta$ RBS HA interferes with all antibodies except those targeting the RBS. Four H1N1 strains were tested in this assay and the pattern of neutralization inhibition varied by strain. Neutralization of 1999 NC or 2007 Bris was mediated predominantly by RBS-directed antibodies. However, neutralization of 1986 Sing was due mainly to stem-directed antibodies. Interestingly, both stem- and RBS-directed antibodies contributed to neutralize 1995 Beijing virus (Fig. 4c). Whereas the neutralization specificities of mouse and ferret antibodies differ somewhat from previously described human anti-stem antibodies, we have observed these differences previously<sup>8</sup>. This variation is most likely due to differences in the origins of the *IGHV* genes that give rise to them and affect their fine specificity<sup>23</sup>. In particular, anti-stem antibodies isolated from humans derive predominantly from the *IGHV1-69* (*V<sub>H</sub>1-69*) gene<sup>19</sup>, which is not present in other species. Even different human *V<sub>H</sub>1-69*-derived anti-stem antibodies show differences in breadth and fine specificity among influenza subtypes<sup>19</sup>.

Based on the premise that highly ordered repetitive arrays induce yet stronger immune responses<sup>24</sup>, we have successfully designed an HA-nanoparticle to present trimeric HA spike in its native conformation, rigidly and symmetrically, with sufficient spacing to ensure optimal access to potential broadly neutralizing antibodies directed to the stem. These nanoparticles not only had the desired physical properties but also enhanced the potency and breadth of neutralizing antibody responses compared to TIV, the current commercial vaccine, and they were directed to two independent highly conserved epitopes. Although not yet a universal influenza vaccine, these nanoparticles provide a major increment in influenza protection by eliciting potent neutralizing antibodies against a broad spectrum of H1N1 viruses. Moreover, the synthetic nanoparticles are fully recombinant, eliminating the need to produce potentially dangerous virus in eggs or in cell culture, and allowing for modifications that improve immunogenicity which would otherwise not be tolerated in replication-competent viruses currently used to manufacture vaccines. HA-nanoparticle technology therefore represents a foundation for a new generation of influenza vaccines and could be adapted to create analogous vaccines for a wide variety of pathogens.

## METHODS SUMMARY

All genes used for recombinant proteins and pseudoviruses were synthesized using mammalian preferred codons. The HA-ferritin fusion gene was generated by fusing the ectodomain of HA (residues HA1 1–HA2 174, H3 numbering system) to *H. pylori* ferritin (residues 5–167) with a Ser-Gly-Gly linker. Recombinant proteins were produced by transient transfection of expression vectors in 293F cells (Invitrogen) and purified by chromatography techniques (see Methods for detail). The TIVs used in this study were 2006–2007 and 2011–2012 Fluzone (Sanofi Pasteur). Animal experiments were carried out in accordance with all federal regulations and NIH guidelines. Mice were immunized intramuscularly twice with 0.17  $\mu$ g (Fig. 2a and b) or 1.67  $\mu$ g (Fig. 2d) of HA-nanoparticles (HA amount) or matched amount of TIV with or without Ribi adjuvant system (Sigma) or with MF59 (Novartis) at a 3-week interval. Ferrets were immunized intramuscularly with 2.5  $\mu$ g of HA-nanoparticles or 7.5  $\mu$ g of TIV with Ribi at weeks 0 and 4. H1N1 virus challenge was performed 5 weeks after the last immunization with  $10^{6.5}$  50% egg infectious dose ( $EID_{50}$ ) of 2007 Bris virus via intranasal inoculation. Statistical analyses were performed using Prism 5 (GraphPad Software).

**Full Methods** and any associated references are available in the online version of the paper.

Received 28 August 2012; accepted 18 April 2013.

Published online 22 May 2013.

- Salomon, R. & Webster, R. G. The influenza virus enigma. *Cell* **136**, 402–410 (2009).

2. Lambert, L. C. & Fauci, A. S. Influenza vaccines for the future. *N. Engl. J. Med.* **363**, 2036–2044 (2010).
3. Yamashita, I., Iwahori, K. & Kumagai, S. Ferritin in the field of nanodevices. *Biochim. Biophys. Acta* **1800**, 846–857 (2010).
4. Ekiert, D. C. *et al.* Antibody recognition of a highly conserved influenza virus epitope. *Science* **324**, 246–251 (2009).
5. Sui, J. *et al.* Structural and functional bases for broad-spectrum neutralization of avian and human influenza A viruses. *Nature Struct. Mol. Biol.* **16**, 265–273 (2009).
6. Whittle, J. R. *et al.* Broadly neutralizing human antibody that recognizes the receptor-binding pocket of influenza virus hemagglutinin. *Proc. Natl Acad. Sci. USA* **108**, 14216–14221 (2011).
7. Ekiert, D. C. *et al.* Cross-neutralization of influenza A viruses mediated by a single antibody loop. *Nature* **489**, 526–532 (2012).
8. Wei, C. J. *et al.* Induction of broadly neutralizing H1N1 influenza antibodies by vaccination. *Science* **329**, 1060–1064 (2010).
9. Ledgerwood, J. E. *et al.* DNA priming and influenza vaccine immunogenicity: two phase 1 open label randomised clinical trials. *Lancet Infect. Dis.* **11**, 916–924 (2011).
10. Lee, L. A. & Wang, Q. Adaptations of nanoscale viruses and other protein cages for medical applications. *Nanomedicine* **2**, 137–149 (2006).
11. Li, C. Q., Soistman, E. & Carter, D. C. Ferritin nanoparticle technology. A new platform for antigen presentation and vaccine development. *Ind. Biotechnol.* **2**, 143–147 (2006).
12. Meldrum, F. C., Heywood, B. R. & Mann, S. Magnetoferritin: *in vitro* synthesis of a novel magnetic protein. *Science* **257**, 522–523 (1992).
13. Jääskeläinen, A. *et al.* Production of apoferritin-based bioinorganic hybrid nanoparticles by bacterial fermentation followed by self-assembly. *Small* **3**, 1362–1367 (2007).
14. Cho, K. J. *et al.* The crystal structure of ferritin from *Helicobacter pylori* reveals unusual conformational changes for iron uptake. *J. Mol. Biol.* **390**, 83–98 (2009).
15. O'Hagan, D. T., Ott, G. S., Nest, G. V., Rappuoli, R. & Giudice, G. D. The history of MF59 adjuvant: a phoenix that arose from the ashes. *Expert Rev. Vaccines* **12**, 13–30 (2013).
16. Mbow, M. L., De Gregorio, E., Valiante, N. M. & Rappuoli, R. New adjuvants for human vaccines. *Curr. Opin. Immunol.* **22**, 411–416 (2010).
17. Nabel, G. J. & Fauci, A. S. Induction of unnatural immunity: prospects for a broadly protective universal influenza vaccine. *Nature Med.* **16**, 1389–1391 (2010).
18. Okuno, Y., Isegawa, Y., Sasao, F. & Ueda, S. A common neutralizing epitope conserved between the hemagglutinins of influenza A virus H1 and H2 strains. *J. Virol.* **67**, 2552–2558 (1993).
19. Corti, D. *et al.* Heterosubtypic neutralizing antibodies are produced by individuals immunized with a seasonal influenza vaccine. *J. Clin. Invest.* **120**, 1663–1673 (2010).
20. Corti, D. *et al.* A neutralizing antibody selected from plasma cells that binds to group 1 and group 2 influenza A hemagglutinins. *Science* **333**, 850–856 (2011).
21. Ekiert, D. C. *et al.* A highly conserved neutralizing epitope on group 2 influenza A viruses. *Science* **333**, 843–850 (2011).
22. Krause, J. C. *et al.* A broadly neutralizing human monoclonal antibody that recognizes a conserved, novel epitope on the globular head of influenza H1N1 virus hemagglutinin. *J. Virol.* **85**, 10905–10908 (2011).
23. Lingwood, D. *et al.* Structural and genetic basis for development of broadly neutralizing influenza antibodies. *Nature* **489**, 566–570 (2012).
24. Bachmann, M. F. & Zinkernagel, R. M. Neutralizing antiviral B cell responses. *Annu. Rev. Immunol.* **15**, 235–270 (1997).

**Supplementary Information** is available in the online version of the paper.

**Acknowledgements** We thank H. Andersen, A. Taylor, A. Zajac and C. Chiedi for help with the animal studies; U. Baxa, K. Nagashima and A. Harned for electron microscopy studies; X. Chen for technical support; A. Panet, B. Graham, R. Schwartz and members of the Nabel lab for discussions; S. Sun and M. Rossmann for technical and conceptual advice; A. Tislerics, B. Hartman and J. Farrar for manuscript preparation. The MF59 adjuvant was kindly provided by Novartis. This work was supported by the Intramural Research Program of the Vaccine Research Center, NIAID, National Institutes of Health.

**Author Contributions** M.K., J.C.B. and G.J.N. developed the concept of HA–ferritin nanoparticles; M.K., C.-J.W. and G.J.N. designed the research studies; M.K., C.-J.W., H.M.Y., P.M.M., J.C.B., J.R.R.W., W.-P.K., L.W. and G.J.N. performed the research and analysed data; M.K., C.-J.W., H.M.Y., P.M.M., J.C.B., J.R.R.W. and G.J.N. discussed the results and implications; S.S.R. assisted in animal studies and sample collection; M.K., C.-J.W., J.C.B. and G.J.N. wrote the paper and all authors participated in manuscript revisions.

**Author Information** The authors declare that an intellectual property application has been filed by NIH based on data presented in this paper. Reprints and permissions information is available at [www.nature.com/reprints](http://www.nature.com/reprints). The authors declare competing financial interests: details accompany the full-text HTML version of the paper at [www.nature.com/nature](http://www.nature.com/nature). Readers are welcome to comment on the online version of the paper. Correspondence and requests for materials should be addressed to G.J.N. (Gary.Nabel@sanofi.com).



## METHODS

**Vector construction.** The gene encoding *Helicobacter pylori* non-haem iron-containing ferritin (GenBank NP\_223316) with a point mutation (N19Q) to abolish a potential N-linked glycosylation site was synthesized by PCR-based accurate synthesis<sup>25</sup> using human-preferred codons. The human CD5 leader sequence and a serine-glycine-glycine (Ser-Gly-Gly) spacer were fused to the gene fragment encoding ferritin (residues 5–167) to generate a secreted protein. The plasmids encoding various influenza virus HAs, including A/South Carolina/1/1918 (1918 SC), A/Puerto Rico/8/1934 (1934 PR8), A/Singapore/6/1986 (1986 Sing), A/Beijing/262/1995 (1995 Beijing), A/New Caledonia/20/1999 (1999 NC), A/Solomon Islands/3/2006 (2006 SI), A/Brisbane/59/2007 (2007 Bris), A/California/04/2009 (2009 CA), A/Perth/16/2009 (H3 2009 Perth), B/Florida/04/2006 (B 2006 Florida), and their corresponding neuraminidases (NAs) with human preferred codons were synthesized as previously reported<sup>8</sup>. HA–ferritin fusion genes were generated by fusing the ectodomain of HAs (residues HA1 1–HA2 174, H3 numbering) from 1999 NC, 2009 CA, H3 2009 Perth and B 2006 Florida to *H. pylori* ferritin (residues 5–167) with a Ser-Gly-Gly linker. Transmembrane and soluble forms of 1999 NC  $\Delta$ Stem<sup>8</sup> and  $\Delta$ RBS<sup>23</sup> HA mutants were generated by introducing an N-linked glycosylation site at residues HA2 45 (I45N/G47T) and HA1 190 (R192T), respectively. The soluble form of 2007 Bris  $\Delta$ RBS HA mutant was generated by introducing an N-linked glycosylation site at the same site. All genes were then cloned into mammalian expression vectors for efficient expression<sup>26</sup>. Plasmids encoding the monoclonal antibodies CR6261 (ref. 4), CH65 (ref. 6) and a single-chain variable fragment (scFv) F10 (ref. 5) were synthesized as described previously<sup>8</sup>.

**Protein biosynthesis and purification.** To produce ferritin nanoparticles, HA-nanoparticles and trimeric HA, the expression vectors were transfected into 293F cells (Invitrogen) using 293fectin (Invitrogen) according to the manufacturer's instructions. Matched NAs were initially co-transfected at 20:1 HA:NA (w/w) to minimize the self-aggregation of HAs often observed with the soluble trimeric HA proteins, although further analysis showed that proper formation of the HA-nanoparticles did not require NA co-expression. The cells were grown in Freestyle 293 expression medium (Invitrogen) and the culture supernatants were collected 4 days post-transfection. The supernatants were concentrated and then buffer-exchanged to a Tris buffer (20 mM Tris, 50 mM NaCl, pH 7.5 for ferritin nanoparticles; 20 mM Tris, 500 mM NaCl, pH 7.5 for HA-nanoparticles). The ferritin nanoparticles were purified by ion-exchange chromatography using a HiLoad 16/10 Q Sepharose HP column (GE Healthcare). The HA-nanoparticles were purified by affinity column chromatography using *Erythrina cristagalli* agglutinin (ECA, coral tree lectin; EY Laboratories, Inc.) specific for galactose  $\beta$ -(1,4)-N-acetylglucosamine. The ferritin nanoparticles and HA-nanoparticles were further purified by size exclusion chromatography with a Superose 6 PG XK 16/70 column (GE Healthcare) in PBS. The molecular weights of the ferritin nanoparticle and HA-nanoparticles were calculated based on two equations generated by least squares linear regression on a semi-log plot using gel filtration low and high molecular weight standards (Bio-Rad), respectively. The yield of the HA-nanoparticles was typically 2–10 mg l<sup>-1</sup> depending on the HA strains. The trimeric HA proteins were purified as described previously<sup>27</sup>. Protein purity and size were verified by SDS–PAGE and dynamic light scattering using a DynaPro system (Wyatt Technology). Monoclonal antibodies and F10 scFv were produced in 293F cells and purified as described previously<sup>8,28</sup>. Monoclonal antibodies against 1999 NC HA were purified from hybridoma supernatants as previously described<sup>8</sup>.

**Electron microscopic analysis.** Purified ferritin nanoparticles and HA-nanoparticles were negatively stained with phosphotungstic acid and ammonium molybdate, respectively, and images were recorded on a Tecnai T12 microscope (FEI) at 80 kV with a CCD camera (AMT Corp.).

**Haemagglutinin inhibition assay (HAI).** Seed stocks of the influenza viruses were obtained from the Centers for Disease Control and Prevention (Atlanta, Georgia, USA) and the viruses were expanded in embryonated chicken eggs or in Madin–Darby canine kidney (MDCK) cells. Immune sera were pretreated with receptor-destroying enzyme (RDE II; Denka Seiken Co., Ltd) and HAI assays were performed using four haemagglutinating units per well and 0.5% turkey or chicken red blood cells.

**Pseudotyped virus neutralization and protein competition assays.** The pseudotype neutralization assay was performed as previously described and has been widely accepted for defining the specificity of neutralizing antibodies targeting influenza virus HAs<sup>8,26–29</sup>. For the protein competition assay, neutralizing activity of the F10, CR6261 or immune sera was measured in the presence of competitor proteins, trimeric HA (wild type,  $\Delta$ Stem or  $\Delta$ RBS), HA-nanoparticles, ferritin nanoparticles or irrelevant protein (HIV-1 gp120) at final concentration of 20 and 25  $\mu$ g ml<sup>-1</sup> for monoclonal antibodies and immune sera, respectively.

**ELISA.** Purified trimeric HA, HA-nanoparticles, and TIV (2  $\mu$ g of H1 HA ml<sup>-1</sup>), ferritin nanoparticles (0.68  $\mu$ g ml<sup>-1</sup> for Supplementary Fig. 2 or 2  $\mu$ g ml<sup>-1</sup> for the rest), mouse liver ferritin (2  $\mu$ g ml<sup>-1</sup>, Alpha Diagnostic International, Inc.),  $\Delta$ Stem

and  $\Delta$ RBS HA trimer (2  $\mu$ g ml<sup>-1</sup>) were coated (100  $\mu$ l per well) onto MaxiSorp plates (Nunc). For the ELISA-based competition assay, HA trimer (2  $\mu$ g ml<sup>-1</sup>) was coated onto the plates and the plates were incubated with CR6261 or an isotype control (VRC01)<sup>30,31</sup> at 8  $\mu$ g ml<sup>-1</sup> before adding serially diluted pre-absorbed ferret immune sera.

**Intracellular cytokine staining assay.** CD4<sup>+</sup> and CD8<sup>+</sup> T cell responses were evaluated by intracellular cytokine staining for interferon  $\gamma$  (IFN- $\gamma$ ), tumour necrosis factor  $\alpha$  (TNF- $\alpha$ ) and interleukin 2 (IL-2) as described previously<sup>32</sup>. We used individual peptide pools (15-mer overlapping by 11 residues, 2.5  $\mu$ g ml<sup>-1</sup> for each peptide) covering *H. pylori* ferritin or murine ferritin light and heavy chains to stimulate cells.

**Immunization.** The TIV used in this study was 2006–2007 Fluzone (Sanofi Pasteur) containing HAs from A/New Caledonia/20/1999 (H1N1), A/Wisconsin/67/2005 (H3N2) and B/Malaysia/2504/2004 (influenza B), or 2011–2012 Fluzone with HAs from A/California/07/2009-like (H1N1), A/Perth/16/2009 (H3N2) and B/Brisbane/60/2008 (influenza B) (Supplementary Fig. 6). The TIV split vaccines are treated with a detergent (octoxinol-9) to solubilize membranes on influenza viruses and form rosettes that contain full-length HAs and NAs. Female BALB/c mice (6–8 weeks old; Charles River Laboratories) were immunized (five mice per group) with 0.5  $\mu$ g (0.17  $\mu$ g of H1 HA) or 0.22  $\mu$ g (0.17  $\mu$ g of HA) of TIV or HA-nanoparticles, respectively (Fig. 2a, b), or 5  $\mu$ g (1.67  $\mu$ g of H1 HA), 2.24  $\mu$ g (1.67  $\mu$ g of HA) or 0.57  $\mu$ g (equimolar to HA-nanoparticles) of TIV, HA-nanoparticles or ferritin nanoparticles, respectively (Fig. 2d). All immunizations were given intramuscularly in 100  $\mu$ l of PBS or in 100  $\mu$ l of 50% (v/v) mixture of Ribi adjuvant system (Sigma) in PBS at weeks 0 and 3. In a separate experiment, MF59 (Novartis) was used as the adjuvant in place of Ribi. A group of BALB/c mice ( $n = 4$ ) was immunized with 20  $\mu$ g of trimeric HA with Ribi adjuvant at weeks 0 and 4. For the experiment in Supplementary Fig. 6b, mice were immunized ( $n = 5$ ) with 5  $\mu$ g (1.67  $\mu$ g of each HA component) of TIV, 2.24  $\mu$ g (1.67  $\mu$ g of HA) of monospecific HA-nanoparticles or 6.72  $\mu$ g (1.67  $\mu$ g of each HA component) of multispecific HA-nanoparticles with Ribi adjuvant at weeks 0 and 3. Blood samples were collected before the first dose, and at 2 weeks after each immunization. For ferret studies, male Fitch ferrets (6 months old; Triple F Farms), seronegative for H1N1, H3N2 and influenza B viruses, were housed and cared for at BIOQUAL, Inc. (Rockville, MD). Ferrets were immunized (six ferrets per group) intramuscularly with 500  $\mu$ l of PBS, 7.5  $\mu$ g (2.5  $\mu$ g of H1 HA) of TIV or 3.35  $\mu$ g (2.5  $\mu$ g of HA) of HA-nanoparticles in 500  $\mu$ l of 50% (v/v) mixture of Ribi adjuvant in PBS at weeks 0 and 4. Blood was collected before the first dose and 3 and 2 weeks after the first and the second immunizations, respectively. Animal experiments were carried out in accordance with all federal regulations and NIH guidelines.

**Virus challenge.** Five weeks after the last immunization, the ferrets were challenged with 10<sup>6.5</sup> 50% egg infectious dose (EID<sub>50</sub>) of 2007 Bris virus. The virus was expanded in embryonated chicken eggs from a seed stock obtained from Centers for Disease Control and Prevention (Atlanta, Georgia, USA) and has a titre of 10<sup>6.5</sup> EID<sub>50</sub> ml<sup>-1</sup>. The ferrets were observed for clinical signs twice daily and weight and temperature measurements recorded daily. Nasal washes were obtained on days 1, 3 and 5 and infectious viral titres were determined by a 50% tissue culture infectious dose (TCID<sub>50</sub>) assay using MDCK cells as described previously<sup>8</sup>.

**Serum absorption.** Ferret immune sera taken 2 weeks after the second immunization were subjected to the assay. One ml of the immune sera diluted at 1:100 and 1:1,000 was incubated with 100  $\mu$ l of pre-washed  $\Delta$ Stem and  $\Delta$ RBS HA-expressing 293F cell pellets, respectively. After incubating for 1 h at 4°C, supernatants were collected by centrifugation and binding to wild-type and mutant HAs was examined by ELISA. The  $\Delta$ Stem HA-pre-absorbed sera were also used for competition ELISA.

**Statistical analysis.** All data plotted with error bars are expressed as means with s.d. unless otherwise indicated. The *P* values were generated by analysing data with a two-tail unpaired *t* test using the Prism 5 program (GraphPad Software). In Fig. 4b, right panel, the data were analysed by two-way ANOVA using Prism 5.

**Molecular representations.** All structural renderings of proteins were generated using the UCSF Chimera package<sup>33</sup>, version 1.7.0 (<http://www.cgl.ucsf.edu/chimera/>) or The PyMOL Molecular Graphics System, version 1.5.0.4 (Schrödinger, LLC; <http://www.pymol.org/>). UCSF Chimera is developed by the Resource for Bio-computing, Visualization, and Informatics at the University of California, San Francisco, California, USA (supported by NIGMS P41-GM103311).

25. Xiong, A. S. *et al.* PCR-based accurate synthesis of long DNA sequences. *Nature Protocols* **1**, 791–797 (2006).
26. Kong, W. P. *et al.* Protective immunity to lethal challenge of the 1918 pandemic influenza virus by vaccination. *Proc. Natl Acad. Sci. USA* **103**, 15987–15991 (2006).
27. Wei, C. J. *et al.* Comparative efficacy of neutralizing antibodies elicited by recombinant hemagglutinin proteins from avian H5N1 influenza virus. *J. Virol.* **82**, 6200–6208 (2008).
28. Wei, C. J. *et al.* Cross-neutralization of 1918 and 2009 influenza viruses: role of glycans in viral evolution and vaccine design. *Sci. Transl. Med.* **2**, 24ra21 (2010).
29. Yang, Z. Y. *et al.* Immunization by avian H5 influenza hemagglutinin mutants with altered receptor binding specificity. *Science* **317**, 825–828 (2007).

30. Wu, X. *et al.* Rational design of envelope identifies broadly neutralizing human monoclonal antibodies to HIV-1. *Science* **329**, 856–861 (2010).
31. Zhou, T. *et al.* Structural basis for broad and potent neutralization of HIV-1 by antibody VRC01. *Science* **329**, 811–817 (2010).
32. Kong, W. P. *et al.* Immunogenicity of multiple gene and clade human immunodeficiency virus type 1 DNA vaccines. *J. Virol.* **77**, 12764–12772 (2003).
33. Pettersen, E. F. *et al.* UCSF Chimera—a visualization system for exploratory research and analysis. *J. Comput. Chem.* **25**, 1605–1612 (2004).

# Structural basis for alternating access of a eukaryotic calcium/proton exchanger

Andrew B. Waight<sup>1</sup>, Bjørn Panyella Pedersen<sup>1</sup>, Avner Schlessinger<sup>2</sup>, Massimiliano Bonomi<sup>2</sup>, Bryant H. Chau<sup>1</sup>, Zygy Roe-Zur<sup>1</sup>, Aaron J. Risenmay<sup>1</sup>, Andrej Sali<sup>2</sup> & Robert M. Stroud<sup>1</sup>

Eukaryotic  $\text{Ca}^{2+}$  regulation involves sequestration into intracellular organelles, and expeditious  $\text{Ca}^{2+}$  release into the cytosol is a hallmark of key signalling transduction pathways. Bulk removal of  $\text{Ca}^{2+}$  after such signalling events is accomplished by members of the  $\text{Ca}^{2+}$ :cation (CaCA) superfamily<sup>1–5</sup>. The CaCA superfamily includes the  $\text{Na}^+/\text{Ca}^{2+}$  (NCX) and  $\text{Ca}^{2+}/\text{H}^+$  (CAX) antiporters, and in mammals the NCX and related proteins constitute families SLC8 and SLC24, and are responsible for the re-establishment of  $\text{Ca}^{2+}$  resting potential in muscle cells, neuronal signalling and  $\text{Ca}^{2+}$  reabsorption in the kidney<sup>1,6</sup>. The CAX family members maintain cytosolic  $\text{Ca}^{2+}$  homeostasis in plants and fungi during steep rises in intracellular  $\text{Ca}^{2+}$  due to environmental changes, or following signal transduction caused by events such as hyperosmotic shock, hormone response and response to mating pheromones<sup>7–13</sup>. The cytosol-facing conformations within the CaCA superfamily are unknown, and the transport mechanism remains speculative. Here we determine a crystal structure of the *Saccharomyces cerevisiae* vacuolar  $\text{Ca}^{2+}/\text{H}^+$  exchanger (Vcx1) at 2.3 Å resolution in a cytosol-facing, substrate-bound conformation. Vcx1 is the first structure, to our knowledge, within the CAX family, and it describes the key cytosol-facing conformation of the CaCA superfamily, providing the structural basis for a novel alternating access mechanism by which the CaCA superfamily performs high-throughput  $\text{Ca}^{2+}$  transport across membranes.

The CaCA superfamily is defined by the presence of two short, repeating homologous sequences, termed the  $\alpha$ -repeats, found in predicted transmembrane regions. The  $\alpha$ -repeats are opposite in topology and are believed to have arisen from a gene duplication event<sup>14–16</sup>. Mutagenesis and recent structural data have identified this region as essential for ion binding and transport, and specifically two key acidic residues (Glu or Asp) are implicated in coordinating  $\text{Ca}^{2+}$  ions at the active site<sup>17–20</sup>. Members of the CAX family are approximately 400 residues long with 11 predicted transmembrane helices. The first helix (MR), found in eukaryotic CAX members, has a regulatory role in plant members and is suggested to be involved in protein targeting and/or signalling in yeast<sup>12,21,22</sup>. The 10 remaining transmembrane helices (M1–M10) perform the transport function, and are composed of two symmetrically related halves (M1–M5 and M6–M10) connected through a negatively charged loop termed the ‘acidic motif’<sup>21,16,23</sup>. *Saccharomyces cerevisiae* Vcx1 catalyses low-affinity (Michaelis constant ( $K_m$ ) = ~25  $\mu\text{M}$ ), high-capacity (maximum rate ( $V_{\text{max}}$ ) = ~35  $\text{nmol Ca}^{2+} \text{ min}^{-1} \text{ mg}^{-1}$ ) vacuolar  $\text{Ca}^{2+}$  exchange<sup>3,8,24,25</sup>. To establish function of the purified protein, Vcx1 was reconstituted into liposomes and assayed for  $\text{Ca}^{2+}$  uptake activity. In this system, purified Vcx1 demonstrates  $\text{Ca}^{2+}$  uptake monotonically dependent on pH gradient (Supplementary Fig. 1). Vcx1 shares ~30% sequence identity with other members of the  $\text{Ca}^{2+}/\text{H}^+$  exchanger family, including the canonical CAX proteins of *Arabidopsis thaliana* (Supplementary Fig. 2).

Vcx1 was solved experimentally to 2.3 Å resolution ( $R_{\text{free}}$  of 22.5%) by molecular replacement, supported by iodine-based experimental

phases (Fig. 1, Supplementary Table 1 and Supplementary Fig. 3). The structure encompasses residues 22–401 with the exception of a short loop (184–191) between M4 and M5. Two identical (root mean squared deviation (r.m.s.d.) 0.21 Å over 285 C $\alpha$  atoms) monomers are found in the asymmetric unit. Six divalent cations are identified as  $\text{Ca}^{2+}$  or  $\text{Mn}^{2+}$  in the Vcx1 monomer, on the basis of their coordination geometry and anomalous scattering differences (Supplementary Fig. 4).

The shape of the Vcx1 monomer, viewed perpendicular to the membrane plane, resembles that of a wedge (Fig. 1). Viewed from the vacuolar side of the membrane, the tapered end of the wedge consists of two long antiparallel helices M1 and M6, which are intertwined and tilted ~30° with respect to the membrane normal. The central four-helix core contains the  $\alpha$ -repeats, and is comprised of M2–M3 and M7–M8. M2 and M7 are kinked at their midpoints and change direction ~35° in the middle of the membrane plane to create M2a/M2b and M7a/M7b. These two oppositely related helix kinks meet in the mid-membrane plane, forming an hourglass shape, where the CAX family display the conserved GNXXE(H) signature sequence necessary for calcium binding and transport<sup>19,20,26,27</sup>. M3 and M8 are also tilted with respect to the membrane normal and line the interior of the hourglass. M4–M5 and M9–M10 form the outer components of a right-handed bundle which flank the central core and constitute the thicker side of the wedge shape. The 20-residue ‘acidic motif’ connecting the two duplicated halves of the protein between M5 and M6 is predicted to be disordered based on sequence. However, a clearly resolved  $\alpha$ -helix (which we term the acidic helix) for this sequence is observed in the structure. This helix is oriented parallel to the membrane and lies directly underneath the  $\alpha$ -repeat regions on the cytosolic side.

A centrally located  $\text{Ca}^{2+}$  ion occupies the active site of Vcx1, coordinated by Glu 302 on M7b and Ser 325 on M8 (Fig. 2). The Ser 325 residue is generally conserved throughout the CaCA superfamily, and in NCX and NCKX family members the analogous serine residue has been shown to have an important role in  $\text{Ca}^{2+}$  transport (Supplementary Fig. 5)<sup>18,19</sup>. Three ordered water molecules complete the octahedral coordination geometry of  $\text{Ca}^{2+}$  (Supplementary Fig. 4b). The presence of water molecules at the binding site suggest that the  $\text{Ca}^{2+}$  ion reaches the active site in a partially hydrated state, balancing the stronger binding of entropically ordered side chains with more loosely bound water to complete the coordination sphere. Glu 106, Asn 299 and the backbone carbonyl of Gly 102 coordinate the three water molecules. The remainder of the  $\text{Ca}^{2+}$  active site is stabilized by specific interactions from polar residues in the transmembrane regions of M2, M3, M7 and M8. The conserved Asn 299 and His 303 of M7b form a hydrogen bond to Ser 129 and Ser 132, respectively, of the adjacent M3 helix, and the conserved Asn 103 on M2b forms a hydrogen bond to Gln 328 on M8. M2a is bent away from the bundle of helices M2b, M3, M7 and M8, and in this configuration it is not packed tightly against the protein body (Fig. 3). M2a and the connected C-terminal half of M1 are bent away from the active site, exposing the central  $\text{Ca}^{2+}$  ion to the cytosol. The M2a/M1 arrangement creates a substantial

<sup>1</sup>Department of Biochemistry and Biophysics, University of California, San Francisco, California 94158, USA. <sup>2</sup>Department of Bioengineering and Therapeutic Sciences, Department of Pharmaceutical Chemistry, California Institute for Quantitative Biosciences, University of California, San Francisco, California 94158, USA.



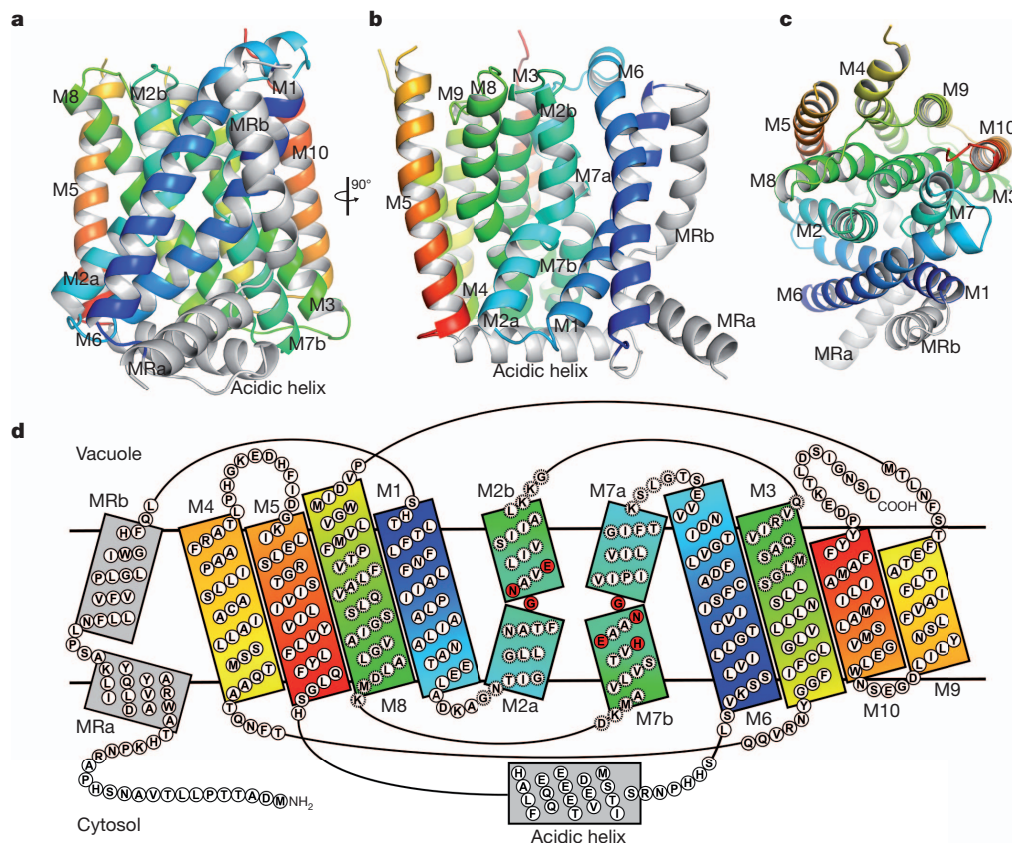


**Figure 1 | Topology and fold of the Vcx1 protein.** The symmetrically related halves of the Vcx1 monomer are coloured in a double colour spectrum from the N to C terminus. Helices of matching colour are related by symmetry. **a–c**, The Vcx1 monomer as viewed in the membrane along the axis of

symmetry (**a**), rotated by 90° (**b**) and viewed from the vacuolar side of the membrane (**c**). **d**, Topology map of the Vcx1 monomer; CAX family conserved residues are coloured in red,  $\alpha$ -repeat sequences are denoted by dashed circles.

vestibule that is accessible from the intracellular bulk solvent. This vestibule is conical in shape and has a negatively charged interior surface potential (Fig. 3c). The interior of the cavity vestibule is circumscribed by M2a, the C-terminal half of M1, M7b and the N-terminal half of M8, and allows access from the cytosol to the central  $\text{Ca}^{2+}$  binding site. Thus, the Vcx1 protein structure represents a substrate-bound, cytosol-facing conformation.

Lying across the cytosolic entrance to the vestibule, the acidic helix also coordinates two  $\text{Ca}^{2+}$  ions (Supplementary Fig. 4c). These two ions lie on the cytosolic side, 11 Å from the central  $\text{Ca}^{2+}$  site, coordinated by Asp 234 and Glu 230 of the acidic helix and by Glu 83 of M1 (Fig. 2c). The acidic motif has been suggested to have a role in  $\text{Ca}^{2+}$

binding<sup>23</sup>. In mammalian NCX members, the analogous region connecting helices M5 and M6 contains a large intracellular calcium-binding domain (CBD1) responsible for stimulating activity in the transporter domain in the presence of  $\text{Ca}^{2+}$  (ref. 28) (Supplementary Fig. 5). The CBD1  $\text{Ca}^{2+}$  binding sites are similarly formed from acidic motifs although they coordinate ions using  $\beta$ -sheets rather than  $\alpha$ -helical secondary structures<sup>29</sup>. Molecular dynamics simulations performed with the Vcx1 structure suggest that the acidic helix maintains an  $\alpha$ -helical conformation in the presence of the two coordinated  $\text{Ca}^{2+}$  ions, and becomes more flexible in their absence (Supplementary Fig. 6). The increased rigidity of the Vcx1 acidic helix at higher  $\text{Ca}^{2+}$  concentrations indicates a possible  $\text{Ca}^{2+}$ -dependent regulatory

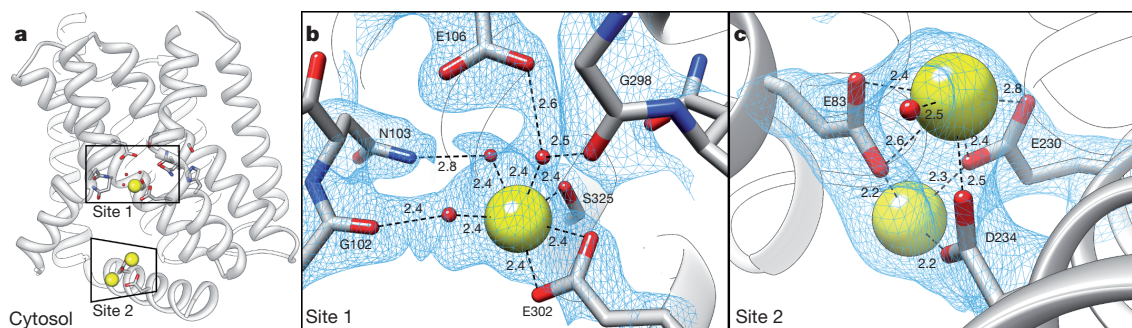


**Figure 2 | Calcium binding sites in the Vcx1 crystal structure.** **a**, Overview of site 1 and site 2 with helices MR, M1 and M6 removed for clarity. The cytosol is on the bottom of the image and  $\text{Ca}^{2+}$  ions are coloured in yellow. **b**, Active site  $\text{Ca}^{2+}$  substrate ion and interacting residues found in site 1. Hydrogen bonds are shown as dashed lines; numbers denote atomic distances (Å).  $2mF_o - DF_c$  map

is shown contoured at  $1\sigma$  (blue mesh). **c**,  $\text{Ca}^{2+}$  ions at the acidic helix in site 2 with interacting residues labelled. Hydrogen bonds are shown as dashed lines; numbers denote atomic distances (Å).  $2mF_o - DF_c$  map is shown contoured at  $1\sigma$  (blue mesh).

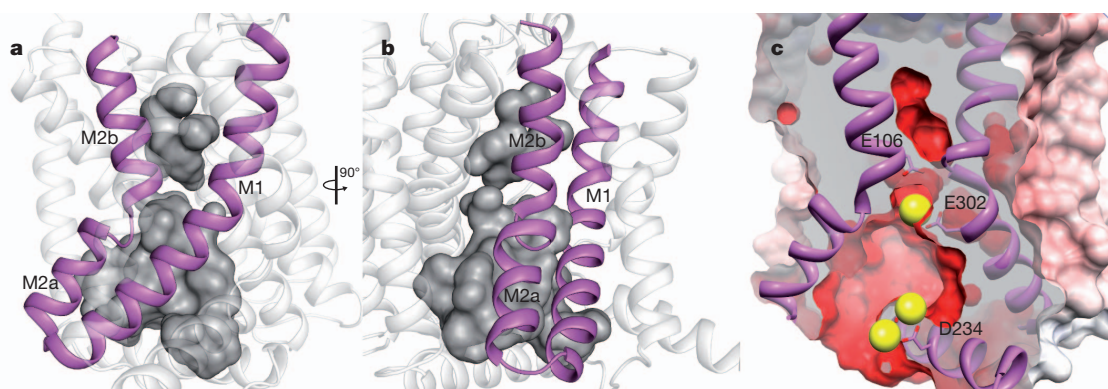


**Figure 3 | The cytoplasmic vestibule.** **a**, The protein cavity is rendered as a surface representation and is coloured grey; the helices M1 and M2 are coloured purple and are shown from the axis of symmetry. **b**, View rotated by 90°. **c**, The cytoplasmic vestibule as oriented in panel **a** and depicted with a slab surface

representation coloured by electrostatic potential (red to blue;  $-10$  to  $10 \text{ kT e}^{-1}$ ). Helices MR, M1 and M6 have been removed for clarity.  $\text{Ca}^{2+}$  ions (yellow spheres) pinpoint site 1 and site 2.

function for this region, perhaps augmenting conductance in the presence of increased cytosolic  $\text{Ca}^{2+}$ .

Comparison of the two structural repeats (M1–M5 and M6–M10) of Vcx1 reveals a structurally similar core region that is closely packed and rigid (M3–M5, M8–M10) (Supplementary Fig. 7b). In contrast, considerable differences are found in the M2a helix and C-terminal half of M1 when compared to M7a and M6. Superposition between helices M1–M2a and M6–M7a reveal a  $\sim 12^\circ$  and  $\sim 7^\circ$  asymmetric difference in the angle of M1 and M2a, respectively (Supplementary Fig. 7c, d). This structural divergence, in combination with loose packing and intracellular location, implicate this mobile region as the cytosolic gate. A dynamic straightening of the M1/M2a helices would collapse the cytosolic vestibule, and this motion could be coordinated by a structural rearrangement into a vacuole-facing conformation.

The Vcx1 conformation also sheds light on the transport cycle of CaCA proteins by comparison with the recent structure of an archaeobacterial  $\text{Na}^+/\text{Ca}^{2+}$  exchanger from *Methanococcus janaschii* (mjNCX)<sup>17</sup>. Despite low sequence identity (14%) to Vcx1, the overall fold and topology of mjNCX is similar. However, unlike Vcx1, the mjNCX exchanger is closed to the cytosolic environment and instead represents a periplasm-facing conformation, as reflected in the overall displacement between similar atoms (r.m.s.d.  $5.7 \text{ \AA}$  over 269 C $\alpha$  atoms). Structural alignment of the Vcx1 and mjNCX structures reveals a similar placement of the core region and of helices M7 and M2b (Supplementary Fig. 8). However, the M2a helix is shifted by  $\sim 16 \text{ \AA}$  towards the centre of the bilayer in Vcx1 (Fig. 4a). In addition, relative to the mjNCX structure, the position of both loosely packed

helices M1 and M6 are translated diagonally towards the vacuole by  $\sim 16 \text{ \AA}$  and  $\sim 13 \text{ \AA}$  at either end, closing a vacuole-facing portal that could otherwise expose the active site of the protein to the vacuolar environment (Fig. 4b and Supplementary Figs 8 and 9). The concerted transposition in the M1/M6 helices therefore performs a dual role of coordinating motions between the  $\alpha$ -repeats and covering/uncovering an active site entry passage (Fig. 4c). By this mechanism, translational movements of the M1/M6 helices allow alternating access to the active site of Vcx1 from both sides of the membrane. The action of the M1/M6 helices is therefore analogous to the piston of a two-stroke engine that occludes and exposes intake and efflux pathways during each turnover. Using a predicted cytosol-facing mjNCX conformation, a similar motion of the M1 and M6 helices was suggested for turnover by the mjNCX monomer<sup>17</sup>. Our data augment the proposed mechanism by including structural evidence for the M1/M6 translations and substantial conformational changes in the M2a helix. With the addition of a cytoplasmic-facing Vcx1 structure, there are now two key states in the CaCA family that suggest a trajectory for  $\text{Ca}^{2+}$  translocation, forming a strong case for the two-stroke mechanism of alternating access.

The proposed transport cycle of Vcx1 is shown in Fig. 4c (Supplementary Video 1). In the active site, Glu 106 and Glu 302 are exposed to the vacuolar side (pH  $\sim 5$ – $6$  (ref. 30)). The proton motive gradient across the vacuolar membrane provides the source of energy to drive a conformational change to the cytosol-facing conformation whereupon the glutamate residues would be expected to maintain a negative charge (at pH  $\sim 7$  (ref. 30)). Under conditions of high cytosolic  $\text{Ca}^{2+}$  concentration, as seen during signal transduction events,

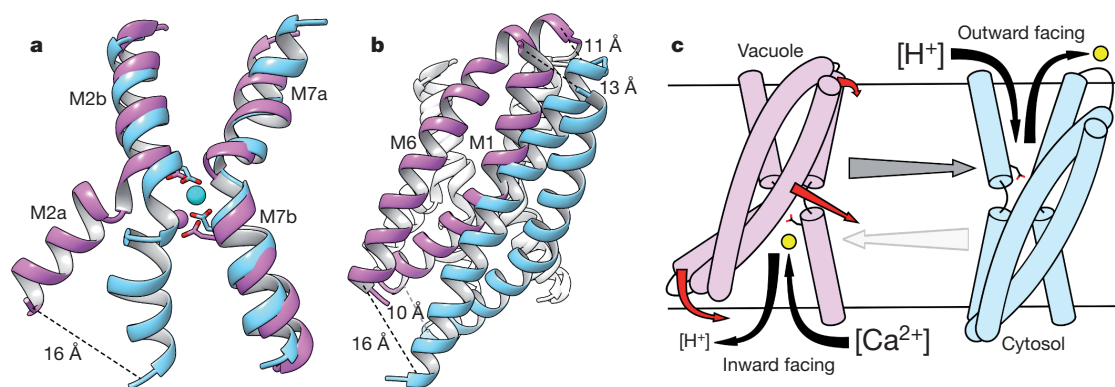


**Figure 4 | Transport cycle of Vcx1 and structural comparison to mjNCX.** **a**, Comparison of M2 and M7 and active site glutamate residues between Vcx1 (purple) and mjNCX (cyan).  $\text{Ca}^{2+}$  ions from each model are depicted as spheres. **b**, Comparison of M1 and M6 between Vcx1 (purple) and mjNCX (cyan). **c**, Schematic of Vcx1 turnover. Structures are coloured as in panel

**a**. Proposed substrate movement is denoted by black arrows, and calcium by yellow circles. Red arrows show protein movement in the cytosol-facing state of Vcx1 (left) that results in the vacuole-facing conformation on the right. Return to the cytosol-facing state presumably requires reversal of the movements denoted by the red arrows.



$\text{Ca}^{2+}$  is coordinated by the acidic helix, and  $\text{Ca}^{2+}$  is able to reach the active site. The Vcx1 side chains of Glu 302 and Ser 325 partially replace the  $\text{Ca}^{2+}$  hydration shell, and subsequent completion of coordination by Glu 106 displaces some of the remaining water molecules to bring helix M2b inward towards the active site. This movement of M2 towards the core can initiate M2a straightening and M1/M6 translation, closing the cytosolic vestibule. The translation of helices M1/M6 uncovers a vacuolar cleft and coordinates opening of M7a to expose the active site  $\text{Ca}^{2+}$  ion to the vacuole. The vacuole-facing conformation, in combination with the acidic pH in the vacuole, lowers the  $\text{Ca}^{2+}$  affinity of active site residues Glu 106 and Glu 302, leading to release of the  $\text{Ca}^{2+}$  substrate into the vacuole. The cyclical pumping action of the M1/M6 'piston', coupled to flexible helices surrounding the active site (M2a, M7a), provides an efficient framework for the rapid turnover necessary for high-throughput  $\text{Ca}^{2+}$  exchange.

In conclusion, Vcx1 is the first CAX family structure, and the first structure of the CaCA superfamily in a cytosol-facing conformation. It provides a structural basis for an alternating access mechanism for the Vcx1 protein and the CaCA superfamily in general. These findings lay the groundwork for future exploration of  $\text{Ca}^{2+}$  transport by CaCA superfamily members and lend insight into fundamental aspects of  $\text{Ca}^{2+}$  homeostasis and eukaryotic signal transduction processes.

## METHODS SUMMARY

The Vcx1 protein from *Saccharomyces cerevisiae* (Uniprot ID Q99385) was expressed in *S. cerevisiae* and purified using a decahistidine affinity-tag. Solubilization and purification were performed using dodecyl- $\beta$ -D-maltoside. Crystals were grown in-meso by combining lipidic cubic phase technique and Jeffamine M-600 sponge phase conditions with vapour phase diffusion. X-ray diffraction was collected at the Advanced Light Source beamline 8.3.1, Advanced Photon Source beamline 23-ID-B and Stanford Synchrotron Radiation Lightsource beamline 12-2. The structures were solved by single-wavelength anomalous diffraction and molecular replacement methods (MR-SAD) using mJNCX (Protein Data Bank accession 3V5U (ref. 17)) as a search model. The final structural model was refined using data to 2.3 Å to a crystallographic *R*-factor of 20.1% and free *R*-factor of 22.5% (Supplementary Table 1).

**Full Methods** and any associated references are available in the online version of the paper.

**Received 5 November 2012; accepted 30 April 2013.**

**Published online 19 May 2013.**

- Crespo, L. M., Grantham, C. J. & Cannell, M. B. Kinetics, stoichiometry and role of the Na-Ca exchange mechanism in isolated cardiac myocytes. *Nature* **345**, 618–621 (1990).
- Cui, J. *et al.* Simulating calcium influx and free calcium concentrations in yeast. *Cell Calcium* **45**, 123–132 (2009).
- Miseta, A., Kellermayer, R., Aiello, D. P., Fu, L. & Bedwell, D. M. The vacuolar  $\text{Ca}^{2+}/\text{H}^{+}$  exchanger Vcx1p/Hum1p tightly controls cytosolic  $\text{Ca}^{2+}$  levels in *S. cerevisiae*. *FEBS Lett.* **451**, 132–136 (1999).
- Philipson, K. D. & Nicoll, D. A. Sodium-calcium exchange: a molecular perspective. *Annu. Rev. Physiol.* **62**, 111–133 (2000).
- Nicoll, D. A., Longoni, S. & Philipson, K. D. Molecular cloning and functional expression of the cardiac sarcolemmal  $\text{Na}^{+}$ - $\text{Ca}^{2+}$  exchanger. *Science* **250**, 562–565 (1990).
- Lytton, J.  $\text{Na}^{+}/\text{Ca}^{2+}$  exchangers: three mammalian gene families control  $\text{Ca}^{2+}$  transport. *Biochem. J.* **406**, 365–382 (2007).
- Hirschi, K. D., Zhen, R. G., Cunningham, K. W., Rea, P. A. & Fink, G. R. CAX1, an  $\text{H}^{+}/\text{Ca}^{2+}$  antiporter from *Arabidopsis*. *Proc. Natl Acad. Sci. USA* **93**, 8782–8786 (1996).
- Pozos, T. C., Sekler, I. & Cyert, M. S. The product of HUM1, a novel yeast gene, is required for vacuolar  $\text{Ca}^{2+}/\text{H}^{+}$  exchange and is related to mammalian  $\text{Na}^{+}/\text{Ca}^{2+}$  exchangers. *Mol. Cell. Biol.* **16**, 3730–3741 (1996).
- Cheng, N.-H., Pittman, J. K., Barkla, B. J., Shigaki, T. & Hirschi, K. D. The *Arabidopsis* *cax1* mutant exhibits impaired ion homeostasis, development, and hormonal responses and reveals interplay among vacuolar transporters. *Plant Cell* **15**, 347–364 (2003).
- Cho, D. *et al.* Vacuolar CAX1 and CAX3 influence auxin transport in guard cells via regulation of apoplastic pH. *Plant Physiol.* **160**, 1293–1302 (2012).

- Cunningham, K. W. Acidic calcium stores of *Saccharomyces cerevisiae*. *Cell Calcium* **50**, 129–138 (2011).
- Shigaki, T., Rees, I., Nakhleh, L. & Hirschi, K. D. Identification of three distinct phylogenetic groups of CAX cation/proton antiporters. *J. Mol. Evol.* **63**, 815–825 (2006).
- Denis, V. & Cyert, M. S. Internal  $\text{Ca}^{2+}$  release in yeast is triggered by hypertonic shock and mediated by a TRP channel homologue. *J. Cell Biol.* **156**, 29–34 (2002).
- Schwarz, E. M. & Benzer, S. Calx, a Na-Ca exchanger gene of *Drosophila melanogaster*. *Proc. Natl Acad. Sci. USA* **94**, 10249–10254 (1997).
- Cai, X. & Lytton, J. The cation/ $\text{Ca}^{2+}$  exchanger superfamily: phylogenetic analysis and structural implications. *Mol. Biol. Evol.* **21**, 1692–1703 (2004).
- Iwamoto, T. *et al.* Unique topology of the internal repeats in the cardiac  $\text{Na}^{+}/\text{Ca}^{2+}$  exchanger. *FEBS Lett.* **446**, 264–268 (1999).
- Liao, J. *et al.* Structural insight into the ion-exchange mechanism of the sodium/calcium exchanger. *Science* **335**, 686–690 (2012).
- Nicoll, D. A., Hryshko, L. V., Matsuoka, S., Frank, J. S. & Philipson, K. D. Mutation of amino acid residues in the putative transmembrane segments of the cardiac sarcolemmal  $\text{Na}^{+}$ - $\text{Ca}^{2+}$  exchanger. *J. Biol. Chem.* **271**, 13385–13391 (1996).
- Winkfein, R. J. *et al.* Scanning mutagenesis of the alpha repeats and of the transmembrane acidic residues of the human retinal cone Na/Ca-K exchanger. *Biochemistry* **42**, 543–552 (2003).
- Kang, K.-J. Residues contributing to the  $\text{Ca}^{2+}$  and  $\text{K}^{+}$  binding pocket of the NCKX2  $\text{Na}^{+}/\text{Ca}^{2+}$ - $\text{K}^{+}$  exchanger. *J. Biol. Chem.* **280**, 6823–6833 (2005).
- Pittman, J. K., Sreevidya, C. S., Shigaki, T., Ueoka-Nakanishi, H. & Hirschi, K. D. Distinct N-terminal regulatory domains of  $\text{Ca}^{2+}/\text{H}^{+}$  antiporters. *Plant Physiol.* **130**, 1054–1062 (2002).
- Pittman, J. K. & Hirschi, K. D. Regulation of CAX1, an *Arabidopsis*  $\text{Ca}^{2+}/\text{H}^{+}$  antiporter. Identification of an N-terminal autoinhibitory domain. *Plant Physiol.* **127**, 1020–1029 (2001).
- Ivey, D. M. *et al.* Cloning and characterization of a putative  $\text{Ca}^{2+}/\text{H}^{+}$  antiporter gene from *Escherichia coli* upon functional complementation of  $\text{Na}^{+}/\text{H}^{+}$  antiporter-deficient strains by the overexpressed gene. *J. Biol. Chem.* **268**, 11296–11303 (1993).
- Ohsumi, Y. & Anraku, Y. Calcium transport driven by a proton motive force in vacuolar membrane vesicles of *Saccharomyces cerevisiae*. *J. Biol. Chem.* **258**, 5614–5617 (1983).
- Dunn, T., Gable, K. & Beeler, T. Regulation of cellular  $\text{Ca}^{2+}$  by yeast vacuoles. *J. Biol. Chem.* **269**, 7273–7278 (1994).
- Kamiya, T. & Maeshima, M. Residues in internal repeats of the rice cation/ $\text{H}^{+}$  exchanger are involved in the transport and selection of cations. *J. Biol. Chem.* **279**, 812–819 (2004).
- Shigaki, T. *et al.* Identification of a crucial histidine involved in metal transport activity in the *Arabidopsis* cation/ $\text{H}^{+}$  exchanger CAX1. *J. Biol. Chem.* **280**, 30136–30142 (2005).
- Matsuoka, S., Nicoll, D. A., Reilly, R. F., Hilgemann, D. W. & Philipson, K. D. Initial localization of regulatory regions of the cardiac sarcolemmal  $\text{Na}^{+}$ - $\text{Ca}^{2+}$  exchanger. *Proc. Natl Acad. Sci. USA* **90**, 3870–3874 (1993).
- Nicoll, D. A. *et al.* The crystal structure of the primary  $\text{Ca}^{2+}$  sensor of the  $\text{Na}^{+}/\text{Ca}^{2+}$  exchanger reveals a novel  $\text{Ca}^{2+}$  binding motif. *J. Biol. Chem.* **281**, 21577–21581 (2006).
- Martínez-Muñoz, G. A. & Kane, P. Vacuolar and plasma membrane proton pumps collaborate to achieve cytosolic pH homeostasis in yeast. *J. Biol. Chem.* **283**, 20309–20319 (2008).

**Supplementary Information** is available in the online version of the paper.

**Acknowledgements** We thank J. Holton, G. Meigs, C. Ogata, N. Venugopalan and T. Doukov for assistance with synchrotron data collection at Advanced Light Source, Advanced Photon Source and Stanford Synchrotron Radiation Lightsource; and C. Waddington and P. Wassam for technical assistance. B.P.P. was supported by a postdoctoral fellowship from the Carlsberg Foundation and later by a fellowship from the Danish Cancer Society; A.S. by NIH grants U54 GM094625 and U01 GM61390; R.M.S. by NIH grants U54 GM094625, GM24485 and GM073210.

**Author Contributions** A.B.W. optimized the yeast expression system, performed expression, purification and crystallization experiments, collected and processed the data, determined, refined and analysed the structure, and performed reconstitution and transport assays. B.P.P. performed data collection and assisted with structure solution and structural analysis. B.H.C. and A.J.R. assisted in cell collection, membrane preparation and purification experiments. B.H.C. and Z.R.-Z. did cloning and expression tests. A.Sc. constructed Vcx1 comparative models as well as performed bioinformatics and distance plot analysis. M.B. performed molecular dynamics simulations and distance plot analysis. A.B.W., B.P.P. and R.M.S. wrote the paper with input from A.Sc., M.B. and A.Sa.

**Author Information** Coordinates and structure factors have been deposited in the Protein Data Bank with the accession number 4K1C. Reprints and permissions information is available at [www.nature.com/reprints](http://www.nature.com/reprints). The authors declare no competing financial interests. Readers are welcome to comment on the online version of the paper. Correspondence and requests for materials should be addressed to R.M.S. ([stroud@msg.ucsf.edu](mailto:stroud@msg.ucsf.edu)).



## METHODS

**Expression and purification.** The Vcx1 protein from *Saccharomyces cerevisiae* (Uniprot ID Q99385) was incorporated into the 2 $\mu$  expression plasmid p423-GAL1 modified with N-terminal and C-terminal purification tags, as described<sup>31</sup>. Transformed *S. cerevisiae* (strain DSY-5; *MAT $\alpha$  his3::GAL1-GAL4 pep4 prb1-1122*) were grown in a fermenter culture vessel (Biostat C15L Sartorius AG) to high density and induction was performed via fed-batch using 40% galactose and harvested after 18–22 h. Harvested yeast (~1.8–2 kg wet cell weight) were washed in cold water, pelleted (6,000 r.p.m.) and flash frozen for storage at –80 °C. Frozen pellets were thawed in lysis buffer (100 mM Tris 7.0, 700 mM NaCl, 1 mM phenylmethylsulphonyl fluoride (PMSF) + protease inhibitors) before cell disruption using a bead mill. The homogenate was centrifuged for 25 min at 21,600g, followed by sedimentation of membranes via ultracentrifugation at 185,000g for 150 min. Membrane pellets were re-suspended in membrane re-suspension buffer (50 mM Tris pH 7.0, 600 mM NaCl, 20% glycerol) before being frozen in liquid nitrogen in 7-g aliquots. One-hundred grams of yeast cell material yielded an average of 20–25 g membrane. Membrane aliquots (8 g) were thawed and suspended in 112 ml membrane solubilization buffer (50 mM Tris pH 7.0, 600 mM NaCl, 20 mM CaCl<sub>2</sub>, 10% glycerol 1 mM PMSF + protease inhibitors) and solubilized using 1,380 mg *n*-dodecyl- $\beta$ -D-maltoside (DDM) (1:0.19 (w/w) ratio) for 30 min at 4 °C, followed by centrifugation at 120,000g for 30 min to remove unsolubilized material. The resultant lysate was supplemented with 8 mM imidazole pH 6.5 and incubated for ~3 h with 6 ml pre-equilibrated TALON Co<sup>2+</sup> resin. After incubation, the beads were collected by gravity flow-through using a Bio-Rad econocolumn and washed twice via neutation with 30 ml buffer A (50 mM Tris pH 7.0, 0.1% DDM, 20 mM CaCl<sub>2</sub>, 5 mM MnCl<sub>2</sub>, 10% glycerol) supplemented with 15 mM and 30 mM imidazole pH 6.5, respectively. The protein was eluted from the beads using three elutions of 5 ml buffer A supplemented by 500 mM imidazole pH 6.5. The elutions were pooled, bovine thrombin and 3C protease were added to cleave the tags, and dialysed with a 25-kDa cutoff into 1 l of dialysis buffer (50 mM MES pH 6.0, 20 mM CaCl<sub>2</sub>, 5 mM MnCl<sub>2</sub>, 10% glycerol) overnight at 4 °C. The following day the eluate was concentrated to 500  $\mu$ l and injected onto a size-exclusion column (Superdex 200, GE Healthcare) equilibrated SEC buffer (10 mM MES pH 6.0, 0.05% DDM, 20 mM CaCl<sub>2</sub>, 5 mM MnCl<sub>2</sub>). Peak fractions were collected and concentrated to ~30 mg ml<sup>–1</sup>.

**Reconstitution and transport assay.** Ca<sup>2+</sup> uptake into proteoliposomes using purified Vcx1 protein was performed primarily using the method described previously<sup>32</sup>. In brief, 10 mg of yeast polar lipid extract (Avanti Polar Lipids) was dried under nitrogen and re-suspended into 10 mM MOPS pH 6.5, 100 mM choline chloride, and 100  $\mu$ M Fura-2<sup>33</sup> (Sigma-Aldrich). The re-suspension was sonicated to transparency, subjected to 10 cycles of freeze–thaw, and then extruded through a 400-nm filter 10 times. The resulting liposomes were destabilized by addition of 1% octyl  $\beta$ -D-glycopyranoside (OG) and purified Vcx1 was added in a 1:500 (w/w) ratio and incubated for 1 h. OG was removed by addition of 200 mg ml<sup>–1</sup> Bio-Beads (Bio-Rad) for 3 h and replaced with 200 mg ml<sup>–1</sup> fresh Bio-Beads for incubation overnight. Proteoliposomes were harvested by centrifugation at 66,000g for 150 min and re-suspended in 10 mM MOPS pH 6.5, 100 mM choline chloride. Proton gradient was initiated by the addition of 20  $\mu$ l proteoliposome to 20  $\mu$ l reaction buffer containing 100 mM choline chloride and 10 mM MOPS pH 7.9, 7.2 or 6.5 (final pH 7.1, 6.8, 6.5) in a Corning 384 well clear bottom microplate. Transport activity followed the addition of 100  $\mu$ M CaCl<sub>2</sub>, and uptake of Ca<sup>2+</sup> was monitored at 22 °C via the changes in emission of Fura-2 at 510 nm upon excitation at 340 and 380 nm at 10-s intervals using a Molecular Devices SpectraMax microplate reader. Maximal signal was obtained via addition of 0.3% DDM, the ratio of emission intensities at the two excitation wavelengths was converted to Ca<sup>2+</sup> using a standard curve and previously described methods<sup>33</sup>.

**Crystallization.** Forty microlitres of concentrated Vcx1 was mixed with 60  $\mu$ l monoolein to prepare the lipidic cubic phase (LCP) as previously described<sup>34</sup>. Crystals were grown by adding 1  $\mu$ l Vcx1/LCP mixture to a glass coverslip and overlaid with 2  $\mu$ l crystallization solution (14% Jeffamine M600 pH 7.0, 100 mM HEPES pH 7.0, 50 mM CaCl<sub>2</sub>, 50 mM MnCl<sub>2</sub>, 200 mM NaI). Coverslips were sealed in a hanging-drop setup in 24-well trays containing 300  $\mu$ l crystallization solution. Crystals appeared in a subsequent sponge phase in approximately 3–4 days and grew to a maximum size of 250  $\mu$ m. Crystals were harvested from the trays and frozen directly in liquid nitrogen for data collection. Data were collected at Advanced Light Source beamline 8.3.1, Advanced Photon Source beamline 23-ID-B and Stanford Synchrotron Radiation Lightsource beamline 12-2. Holmium heavy-atom derivatives were obtained by adding Ho(III)Cl<sub>3</sub> to the crystals 1 h before flash-cooling, either as salt or as a concentrated, aqueous solution.

**Data processing.** Data sets were processed using XDS<sup>35</sup> in space group R3. An initial marginal molecular replacement solution was provided by the mjNCX structure (Protein Data Bank accession 3V5U; 14% identity) using the PHENIX<sup>36</sup> AutoMR program and improved upon by PHENIX<sup>36</sup> AutoBuild. Initial iodine

and holmium heavy atom sites were located in anomalous difference maps calculated in the CCP4<sup>37</sup> package using molecular replacement phases and a holmium derivative data set. The heavy atom sites were refined using the program AutoSHARP<sup>38</sup>, and subsequent density modification was performed using RESOLVE<sup>39</sup>. Refinement of the structure was performed by PHENIX<sup>36</sup> Refine and the model was built using COOT<sup>40</sup>. The assignment of ions in the model was aided by appropriate coordination by liganding side chains and anomalous scattering at Cu K $\alpha$  wavelength (8 keV  $f''(I^2) = 6.9e^-$ ,  $f''(Mn^{2+}) = 2.83e^-$ ,  $f''(Ca^{2+}) = 1.3e^-$ ). The final structural model was refined using data to 2.3 Å with a crystallographic *R*-factor of 20.1% and a free *R*-factor of 22.5% (Supplementary Table 1).

**Comparative modelling and structural analysis.** A comparative model of Vcx1 in the vacuole-facing conformation was constructed using MODELLER-9V11<sup>41</sup>, based on the mjNCX X-ray structure (Protein Data Bank accession 3V5U (ref. 17)). The alignment between the sequences of Vcx1 and mjNCX was obtained by manually editing the alignments from UCSF Chimera<sup>42</sup> and PROMALS3D<sup>43</sup>. The Vcx1 structure and model was analysed and visualized using UCSF Chimera<sup>42</sup> and PyMol<sup>44</sup>, and electrostatic surfaces were calculated using APBS<sup>45</sup>.

**Molecular dynamics simulations.** Molecular dynamics simulations were performed with GROMACS<sup>46</sup>, using the CHARMM27<sup>47</sup> all-atom force field and the TIP3P<sup>48</sup> water model. Vcx1 was oriented in an implicit lipid bilayer using PPM<sup>49</sup>, then immersed in an explicit 1,2-dimyristoyl-*sn*-glycero-3-phosphocholine (DMPC) lipid bilayer and water using CHARMM-GUI<sup>50</sup>. Periodic boundary conditions and a triclinic box with the volume of 604.326 nm<sup>3</sup> were used. Two independent simulations were carried out, one with and another one without the two Ca<sup>2+</sup> coordinating Glu 230 and Asp 234 residues. Equilibration was performed by three 10-ns-long runs, gradually increasing the temperature from 100K to 300K, in the canonical (NVT) ensemble controlled by the Berendsen<sup>51</sup> thermostat. The positions of non-hydrogen atoms of Vcx1 were restrained by a harmonic potential, with gradually decreasing force constant. A final equilibration step was carried out for 20 ns without restraints, in the isothermal–isobaric (NpT) ensemble controlled by the semi-isotropic Berendsen<sup>51</sup> barostat. Each production run was 100 ns long, in the NpT ensemble controlled by the Bussi–Donadio–Parrinello<sup>52</sup> thermostat and the semi-isotropic Parrinello–Rahman<sup>53</sup> barostat.

- Li, M. *et al.* Selecting optimum eukaryotic integral membrane proteins for structure determination by rapid expression and solubilization screening. *J. Mol. Biol.* **385**, 820–830 (2009).
- Ridilla, M., Narayanan, A., Bolin, J. T. & Yernool, D. A. Identification of the dimer interface of a bacterial Ca<sup>2+</sup>/H<sup>+</sup> antiporter. *Biochemistry* **51**, 9603–9611 (2012).
- Gryniewicz, G., Poenie, M. & Tsien, R. Y. A new generation of Ca<sup>2+</sup> indicators with greatly improved fluorescence properties. *J. Biol. Chem.* **260**, 3440–3450 (1985).
- Caffrey, M. & Cherezov, V. Crystallizing membrane proteins using lipidic mesophases. *Nature Protocols* **4**, 706–731 (2009).
- Kabsch, W. XDS. *Acta Crystallogr. D* **66**, 125–132 (2010).
- Adams, P. D. *et al.* PHENIX: a comprehensive Python-based system for macromolecular structure solution. *Acta Crystallogr. D* **66**, 213–221 (2010).
- Winn, M. D. *et al.* Overview of the CCP4 suite and current developments. *Acta Crystallogr. D* **67**, 235–242 (2011).
- Vonrhein, C., Blanc, E., Roversi, P. & Brice, G. Automated structure solution with autoSHARP. *Methods Mol. Biol.* **364**, 215–230 (2007).
- Terwilliger, T. C. Maximum-likelihood density modification. *Acta Crystallogr. D* **56**, 965–972 (2000).
- Emsley, P. & Cowtan, K. Coot: model-building tools for molecular graphics. *Acta Crystallogr. D* **60**, 2126–2132 (2004).
- Sali, A. & Blundell, T. L. Comparative protein modelling by satisfaction of spatial restraints. *J. Mol. Biol.* **234**, 779–815 (1993).
- Pettersen, E. F. *et al.* UCSF Chimera—a visualization system for exploratory research and analysis. *J. Comput. Chem.* **25**, 1605–1612 (2004).
- Pei, J., Kim, B.-H. & Grishin, N. V. PROMALS3D: a tool for multiple protein sequence and structure alignments. *Nucleic Acids Res.* **36**, 2295–2300 (2008).
- The PyMOL Molecular Graphics System, Version 1.5.0.4 Schrödinger, LLC.
- Baker, N. A., Sept, D., Joseph, S., Holst, M. J. & McCammon, J. A. Electrostatics of nanosystems: Application to microtubules and the ribosome. *Proc. Natl Acad. Sci. USA* **98**, 10037–10041 (2001).
- Hess, B., Kutzner, C., Van der Spoel, D. & Lindahl, E. GROMACS 4: Algorithms for highly efficient, load-balanced, and scalable molecular simulation. *J. Chem. Theory Comput.* **4**, 435–447 (2008).
- Bjelkmar, P., Larsson, P., Cuendet, M. A., Hess, B. & Lindahl, E. Implementation of the CHARMM force field in GROMACS: Analysis of protein stability effects from correction maps, virtual interaction sites, and water models. *J. Chem. Theory Comput.* **6**, 459–466 (2010).
- Jorgensen, W. L., Chandrasekhar, J., Madura, J. D., Impey, R. W. & Klein, M. L. Comparison of simple potential functions for simulating liquid water. *J. Chem. Phys.* **79**, 926–935 (1983).
- Lomize, M. A., Pogozheva, I. D., Joo, H., Mosberg, H. I. & Lomize, A. L. OPM database and PPM web server: resources for positioning of proteins in membranes. *Nucleic Acids Res.* **40**, D370–D376 (2012).

50. Jo, S., Lim, J. B., Klauda, J. B. & Im, W. CHARMM-GUI Membrane Builder for mixed bilayers and its application to yeast membranes. *Biophys. J.* **97**, 50–58 (2009).
51. Berendsen, H. J. C., Postma, J. P. M., Van Gunsteren, W. F., DiNola, A. & Haak, J. R. Molecular dynamics with coupling to an external bath. *J. Chem. Phys.* **81**, 3684–3690 (1984).
52. Bussi, G., Donadio, D. & Parrinello, M. Canonical sampling through velocity rescaling. *J. Chem. Phys.* **126**, 014101–014101–7 (2007).
53. Parrinello, M. & Rahman, A. Polymorphic transitions in single crystals: A new molecular dynamics method. *J. Appl. Phys.* **52**, 7182–7190 (1981).

# Structural basis of histone H2A–H2B recognition by the essential chaperone FACT

Maria Hondele<sup>1,2\*</sup>, Tobias Stuwe<sup>2†\*</sup>, Markus Hassler<sup>1,2</sup>, Felix Halbach<sup>3</sup>, Andrew Bowman<sup>1</sup>, Elisa T. Zhang<sup>2†</sup>, Bianca Nijmeijer<sup>2</sup>, Christiane Kothhoff<sup>1</sup>, Vladimir Rybin<sup>2</sup>, Stefan Amlacher<sup>4</sup>, Ed Hurt<sup>4</sup> & Andreas G. Ladurner<sup>1,2,5,6</sup>

Facilitates chromatin transcription (FACT) is a conserved histone chaperone that reorganizes nucleosomes and ensures chromatin integrity during DNA transcription, replication and repair<sup>1–6</sup>. Key to the broad functions of FACT is its recognition of histones H2A–H2B (ref. 2). However, the structural basis for how histones H2A–H2B are recognized and how this integrates with the other functions of FACT, including the recognition of histones H3–H4 and other nuclear factors, is unknown. Here we reveal the crystal structure of the evolutionarily conserved FACT chaperone domain Spt16M from *Chaetomium thermophilum*, in complex with the H2A–H2B heterodimer. A novel ‘U-turn’ motif scaffolded onto a Rtt106-like module<sup>7–10</sup> embraces the  $\alpha 1$  helix of H2B. Biochemical and *in vivo* assays validate the structure and dissect the contribution of histone tails and H3–H4 towards Spt16M binding. Furthermore, we report the structure of the FACT heterodimerization domain that connects FACT to replicative polymerases. Our results show that Spt16M makes several interactions with histones, which we suggest allow the module to invade the nucleosome gradually and block the strongest interaction of H2B with DNA. FACT would thus enhance ‘nucleosome breathing’ by re-organizing the first 30 base pairs of nucleosomal histone–DNA contacts. Our

snapshot of the engagement of the chaperone with H2A–H2B and the structures of all globular FACT domains enable the high-resolution analysis of the vital chaperoning functions of FACT, shedding light on how the complex promotes the activity of enzymes that require nucleosome reorganization.

The essential heterodimeric chaperone FACT destabilizes nucleosomes to promote polymerase progression on chromatin templates<sup>1–4,11</sup> and maintains chromatin structure *in vivo*<sup>5,6</sup>. The recognition of the histone H2A–H2B heterodimer is crucial for the molecular functions of FACT<sup>2</sup>. To map the region(s) specifically responsible for H2A–H2B binding, we tested all globular domains within FACT using pull-down assays. Biochemical dissection of yeast FACT<sup>12</sup> (composed of the Spt16–Pob3 heterodimer) had identified four globular domains (the Spt16 amino-terminal domain (Spt16N)<sup>13,14</sup>, the heterodimerization domain Spt16D–Pob3N, the middle domain of Spt16 (Spt16M) and the middle domain of Pob3 (Pob3M)<sup>12</sup>) and carboxy-terminal acidic stretches (Spt16C and Pob3C) (Fig. 1a). We find that only Spt16M, where most of the genetically identified, functionally deficient mutations cluster (Fig. 1a), recognizes H2A–H2B similarly to full-length Spt16 (Fig. 1b). Human Spt16M (encoded by the *SUPT16H* gene) also binds H2A–H2B (Fig. 1c), consistent with the evolutionary sequence

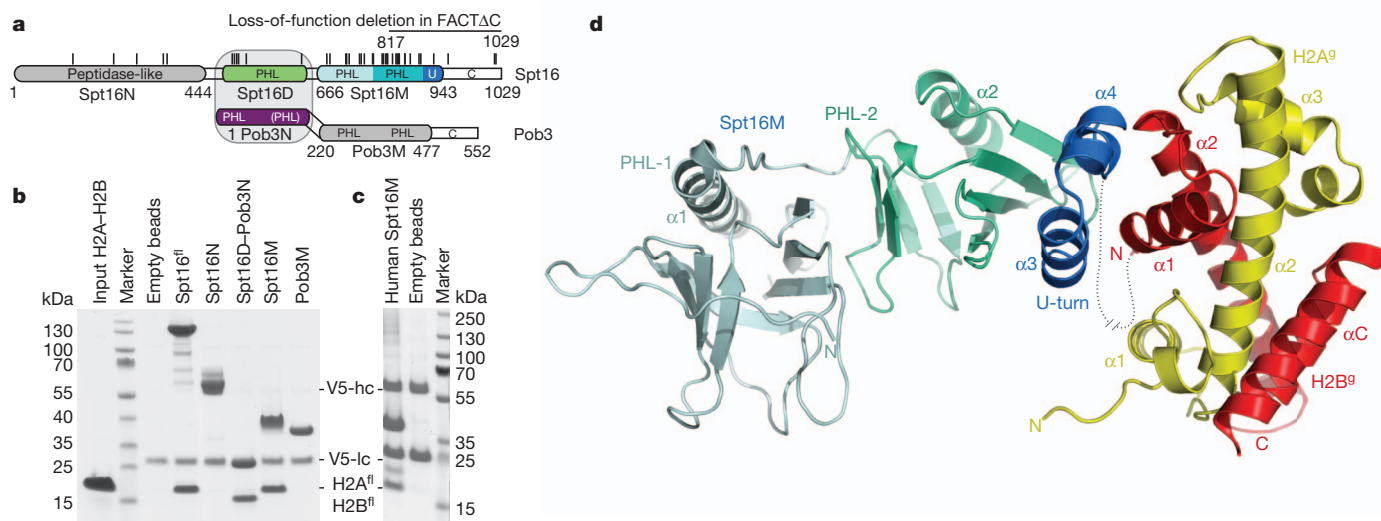


**Figure 1 | The histone chaperone complex FACT recognizes the histone H2A–H2B heterodimer through the Spt16M domain of Spt16.** **a**, Domain organization of yeast Spt16. Mutants isolated in *S. cerevisiae* (black lines) and a loss-of-function deletion in human Spt16 are indicated<sup>2,15</sup>. **b**, **c**, V5-immunoprecipitations of yeast (**b**) and human (**c**) Spt16M with H2A–H2B.

V5-hc and V5-lc denote the heavy and light chain, respectively, of the V5 antibody. **d**, Crystal structure (2.35 Å) of the tethered (~25-residue linker, no electron density observed, grey dotted line) complex between *C. thermophilum* Spt16M (residues 647–950, green and blue), histone H2A (13–106, yellow) and histone H2B (24–122, red). H2A<sup>g</sup> and H2B<sup>g</sup> denote the globular domains.

<sup>1</sup>Department of Physiological Chemistry, Butenandt Institute and LMU Biomedical Center, Faculty of Medicine, Ludwig Maximilians University of Munich, Butenandtstrasse 5, 81377 Munich, Germany. <sup>2</sup>Genome Biology Unit and Structural & Computational Biology Unit, European Molecular Biology Laboratory, Meyerhofstrasse 1, 69117 Heidelberg, Germany. <sup>3</sup>Department of Structural Cell Biology, Max Planck Institute of Biochemistry, Am Klopferspitz 18, 82152 Martinsried, Germany. <sup>4</sup>Biochemistry Center, University of Heidelberg, Im Neuenheimer Feld 328, 69120 Heidelberg, Germany. <sup>5</sup>Munich Cluster for Systems Neurology (SyNergy), 81377 Munich, Germany. <sup>6</sup>Center for Integrated Protein Science Munich (CIPSM), 81377 Munich, Germany. <sup>†</sup>Present addresses: California Institute of Technology, Division of Chemistry and Chemical Engineering, 1200 East California Boulevard, Pasadena, California 91125, USA (T.S.); Department of Molecular and Cell Biology, Howard Hughes Medical Institute, University of California at Berkeley, Berkeley, California 94720-3204, USA (E.T.Z.).

\*These authors contributed equally to this work.



conservation of FACT (Supplementary Fig. 1). This identifies Spt16M as a conserved binding module for H2A–H2B.

To characterize how Spt16M engages H2A–H2B, we determined the structures of free *Chaetomium thermophilum* Spt16M (2.0 Å resolution; Supplementary Fig. 2 and Supplementary Table 1) and a tethered complex with the globular H2A–H2B heterodimer (2.35 Å resolution; Fig. 1c and Supplementary Table 2). The core of Spt16M is composed of a tandem pleckstrin homology-like (PHL) module<sup>9</sup> (PHL-1 and PHL-2) structurally related to the H3–H4 chaperones Pob3M and Rtt106 (refs 7–10, 12 and Supplementary Fig. 3). Crucially, only Spt16M contains a C-terminal,  $\alpha$ -helical U-turn motif that is patched onto the PHL-2 scaffold and recognizes H2A–H2B (Fig. 1d and Supplementary Fig. 3b). The U-turn motif is the most conserved and only extended hydrophobic patch on Spt16M (Supplementary Fig. 2). It forms a groove complementary to a hydrophobic patch on the N-terminal  $\alpha$ 1 helix of H2B (Fig. 2a, b and Supplementary Fig. 2c). The conserved Spt16M residues Leu 915, Val 919, Ile 920, Phe 931, Phe 939 and Leu 940 engage the H2B residues Ile 36 and Tyr 39. Additional interactions include those with loop L1 and helix  $\alpha$ 2 of H2B to establish a  $\sim 660$  Å<sup>2</sup> interface with a free energy potential of  $-7.1$  kcal mol<sup>-1</sup>. Comparison of free (*C. thermophilum* and *Saccharomyces cerevisiae*) and histone-bound Spt16M reveals few differences in the backbone of either chaperone or histones (Supplementary Fig. 4), suggesting rigid docking. Isothermal titration calorimetry (ITC) reveals endothermic binding with a  $\sim 400$  nM dissociation constant ( $K_d$ ) and 1:1 stoichiometry (Supplementary Fig. 5), consistent with the observed hydrophobic contacts between Spt16M and H2B.

To validate the interactions, we used biochemical, thermodynamic, site-directed mutagenesis and *in vivo* assays. Pull-down assays show that a construct containing the U-turn motif and PHL-2 is sufficient to

recognize both full-length and tailless H2A–H2B (Supplementary Fig. 6a). Constructs consisting solely of the U-turn, or PHL-1/PHL-2 module, aggregate during purification, consistent with the hydrophobic core shared between PHL-2 and the U-turn. Wild-type Spt16M forms a complex with H2A–H2B in size-exclusion chromatography (SEC) that is consistent with 1:1:1 stoichiometry (Fig. 2c). By contrast, the Spt16M U-turn mutant Asn916Ser/Val919Ser/Ile920Ser/Thr923Ser (Spt16M<sup>NVIT</sup>) fails to form a complex with full-length histones H2A–H2B by SEC and ITC (Fig. 2c, d), although its structure is preserved (Supplementary Fig. 6b).

On the histones' side, mutation of the hydrophobic H2B  $\alpha$ 1 helix residue Ile 36 reduces affinity 30-fold (Fig. 2e and Supplementary Fig. 5). By contrast, mutation of two other prominent hydrophobic surfaces on the H2A–H2B heterodimer, the C-terminal H2A region and Tyr 80 in helix  $\alpha$ 2 of H2B, does not alter the Spt16M interaction. In agreement, a H2B peptide spanning the H2B  $\alpha$ 1 helix (residues 26–48) binds Spt16M with low micromolar affinity. Together, these assays validate the hydrophobic, globular interface established by the U-turn and H2B  $\alpha$ 1 helix as a primary interaction region between the chaperone FACT and H2A–H2B.

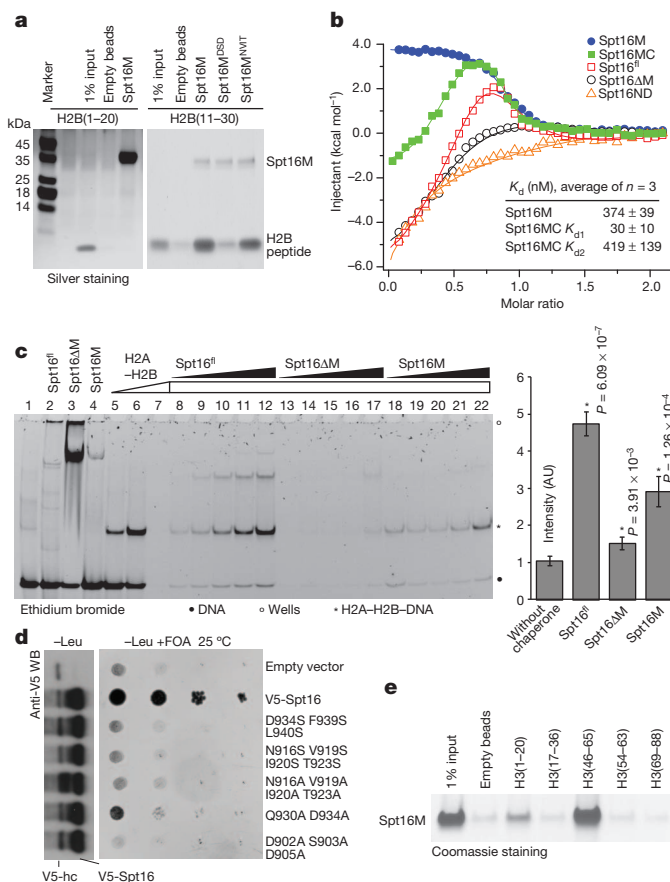


**Figure 3 | Multiple interactions support histone binding by FACT, but Spt16M-mediated contacts are key to chaperoning function.** **a**, V5–Spt16M pulls down an H2B N-terminal tail peptide encompassing residues 11–30, but not residues 1–20. Mutation of a conserved acidic patch on PHL-2 disrupts binding. **b**, ITC of various (truncated) Spt16 constructs shows that domains other than Spt16M contribute exothermically to the overall interaction with H2A–H2B. **c**, Chaperoning assay. Pre-incubation of H2A–H2B with full-length Spt16 (Spt16<sup>fl</sup>) or Spt16M, but not Spt16 $\Delta$ M, prevents histone-driven precipitation of DNA and rescues the soluble H2A–H2B–DNA complex (left). Quantification of the H2A–H2B–DNA complex (lanes 7, 12, 17 and 22) was carried out in quadruplicate (right). AU, arbitrary units. **d**, Wild-type Spt16 rescues a  $\Delta$ spt16 strain *in vivo*, whereas U-turn or acidic patch mutants mostly cannot. Protein expression was verified by western blot against an N-terminal V5-tag. FOA, 5-fluoroorotic acid. **e**, Streptavidin-mediated pull down of biotinylated H3 peptides.

**Figure 2 | A conserved, hydrophobic groove in the U-turn motif of Spt16M interacts with a hydrophobic patch of H2B.** **a**, Close-up view of the Spt16M–H2A–H2B interface. Side chains of the H2B  $\alpha$ 1 helix (H2B $\alpha$ 1; red) nestle into the hydrophobic groove formed by the Spt16M (green) U-turn motif (marine). **b**, Primary sequence of residues in the U-turn motif. Hydrophobic residues (green) tend to be conserved (pink). **c**, **d**, Wild-type (WT) Spt16M but not an engineered U-turn mutant forms a complex with full-length H2A–H2B in gel-filtration experiments (**c**) and ITC (**d**). **e**, ITC between wild-type Spt16M and various histone constructs; ITC profiles and fitting data are given in Supplementary Fig. 5. Data are mean  $\pm$  s.d.

Electrostatic interactions, often involving the basic histone tails, support histone-chaperone interactions. For Spt16M and H2A–H2B, the equilibrium dissociation constants are similar in the presence and absence of histone tails (Fig. 2e). However, deletion of the H2B N-terminal tail disrupts the chaperone–histone complex in SEC and accelerates disassembly of the complex (Supplementary Fig. 7a, b). Furthermore, a peptide encompassing H2B residues 11–30, but not 1–20, directly binds the chaperone (Fig. 3a). Interestingly, the Spt16M–H2A–H2B structure reveals an electrostatic crystal contact ( $450 \text{ \AA}^2$ , free energy potential of  $+1.2 \text{ kcal mol}^{-1}$ ) mediated by Glu 899, Asp 902 and Asp 905 on PHL-2 and H2A Arg residues (Supplementary Fig. 7c), which could be replaced by positively charged residues of the H2B tail. Consistently, mutation of the acidic patch (Spt16<sup>DS</sup>; Asp902Ala, Ser903Ala Asp905Ala), but not mutation of the U-turn, abolishes interaction with H2B (11–30) (Fig. 3a) and lowers the  $K_d$  for full-length H2A–H2B  $\sim 4$ -fold (Supplementary Fig. 7d). Our data indicate that the H2B tail mediates the kinetic stability of the complex rather than determining its equilibrium stability, which depends on the interactions between the globular cores of H2A–H2B and the Spt16M U-turn.

Deletion of the C-terminal region of human Spt16 (termed FACTAC) abrogates H2A–H2B binding, chaperone activity and cellular viability<sup>2,15</sup>. In light of our structure, it is clear that in addition to the acidic C-terminal tail of Spt16 (termed Spt16C; ref. 12), FACTAC lacks the entire and essential U-turn motif and most of PHL-2 (Fig. 1a). To refine the contribution of Spt16M to histone binding and chaperone function further, we compared H2A–H2B binding by full-length Spt16 (Spt16<sup>fl</sup>) with truncated constructs using ITC. Both Spt16M and Spt16M plus acidic C terminus (Spt16MC) display an endothermic binding site ( $K_d \sim 400 \text{ nM}$ ). However, Spt16MC adds a second, exothermic binding site ( $K_d \sim 30 \text{ nM}$ ; Fig. 3b), consistent with an independent, electrostatic histone interaction site mediated by Spt16C. These values compare favourably with the 30–90 nM H2A–H2B affinity reported for holo-FACT and full-length Spt16 using independent methods<sup>15</sup>. Furthermore, Spt16N and Spt16D together (Spt16ND) bind H2A–H2B exothermically, albeit with low affinity ( $K_d = 10$ – $100 \mu\text{M}$ ). ITC profiles of full-length Spt16 and of Spt16 lacking Spt16M (Spt16 $\Delta$ M) combine the characteristics of the isolated Spt16M, Spt16MC and Spt16ND domains. Thus, quantitative ITC reveals two high-affinity sites: the hydrophobic interaction seen in our Spt16–H2A–H2B complex, and an electrostatic Spt16C interaction.

Crucially, whereas full-length Spt16 prevents histone–DNA aggregates, a construct lacking Spt16M but containing the high-affinity, electrostatic Spt16C site (Spt16 $\Delta$ M) cannot (Fig. 3c). By contrast, Spt16M alone resolves aggregates (Fig. 3c), indicating that the interaction of Spt16M with the globular H2A–H2B core is essential to chaperone function.

To test the role of key residues *in vivo*, we rescued the lethality of a yeast *spt16* deletion strain with mutant Spt16 proteins. Mutation of U-turn or acidic patch residues does not reduce the *in vivo* stability of Spt16, but mostly fails to rescue viability (Fig. 3d). Deletion of Spt16C is also lethal. However, because Spt16C contains a putative nuclear localization signal required for nuclear localization (Supplementary Fig. 8), the lethality cannot be directly attributed to a deficient nuclear function.

In addition to binding H2A–H2B, FACT recognizes H3–H4 (ref. 2). Because the tandem PHL core of Spt16M is structurally related to the H3–H4 chaperones Pob3M (ref. 12) and Rtt106 (refs 7, 8, 10), we tested H3–H4 binding and find that Spt16M binds both full-length and tail-less H3–H4 (Supplementary Fig. 9a, b). Similarly, *S. cerevisiae* Spt16M binds H3–H4 with  $2.5 \mu\text{M}$  affinity<sup>9</sup>. Importantly, U-turn mutants retain the H3–H4 interaction (Supplementary Fig. 10), suggesting that H3–H4 and H2A–H2B have distinct binding interfaces on Spt16M.

The interaction between Spt16M and H3–H4 probably occurs through a region encompassing histone H3 residues 46–65 (Fig. 3e), which is also recognized by Rtt106, preferentially in Lys 56-acetylated form<sup>7,8</sup>. Spt16M binding of the H3(46–65) peptide is preserved after

Lys 56 acetylation (Supplementary Fig. 9d), although future work needs to clarify whether Lys 56 acetylation affects FACT function *in vivo*.

Furthermore, we solved the structure of the FACT heterodimerization domain (Fig. 4a and Supplementary Table 3). Spt16D–Pob3N also consists of PHL domains, a single PHL in Spt16D and a tandem PHL domain lacking the capping helix of the second domain in Pob3N. Interestingly, the PHL module of Spt16D–Pob3N does not interact with H2A–H2B. Nor does it bind H3–H4, in contrast to the tandem PHL modules of Spt16M, Pob3M and Rtt106 (Fig. 1b and Supplementary Fig. 9c). Yet, extended surface patches show high sequence conservation (Supplementary Fig. 11), suggesting a distinct but conserved molecular function. We used *S. cerevisiae* lysates expressing tandem affinity purification (TAP)-tagged proteins to screen for proteins co-precipitating with Spt16D–Pob3N, and identified the large subunit of the DNA polymerase  $\alpha$  complex (Pol1) as a Spt16D interactor (Fig. 4b). Our assay suggests that the FACT heterodimerization domain couples FACT to the replication machinery, promoting nucleosome deposition during replication<sup>12</sup>.

The high-resolution snapshot of the Spt16M–H2A–H2B complex, together with the structure of the FACT heterodimerization domain, completes the domain-by-domain dissection of FACT structure (Supplementary Fig. 12): Spt16N, Spt16M and Pob3M bind H3–H4, whereas Spt16M binds H2A–H2B. Consistent with the pleiotropic functions of FACT, the interaction between H2B and the Spt16M U-turn is unlikely to be directly affected by H2B heterodimers containing non-canonical H2A variants (for example, H2A.X and macroH2A) or by post-translational modifications including ubiquitination, which has a role in FACT function<sup>16,17</sup> (Supplementary Fig. 13).

Our structures serve as a platform for investigating the mechanism(s) by which holo-FACT couples H2A–H2B recognition to nucleosome reorganization. This can be illustrated by a superposition of Spt16M–H2A–H2B onto the nucleosome core particle (NCP) (Supplementary Fig. 14). We suggest that the solvent-accessible H2B N-terminal tail may mediate first interactions of FACT with the nucleosome. The Spt16M chaperone capitalizes on the dynamic nature of the NCP, in particular the constant and progressive unwrapping/rewrapping of DNA from the octamer core<sup>18</sup>, to invade the NCP gradually and develop stronger interactions with the two DNA-covered binding patches on the H3  $\alpha$ N and H2B  $\alpha$ 1 helices. Shielding of a histone's DNA-interaction site is typical for histone chaperones<sup>19–23</sup>. Together, these multiple contact points establish an extended surface that coordinates the outermost  $\sim 30$  base pairs<sup>24–26</sup>. Consistently, this DNA becomes hypersensitive to chemical modification in the presence of holo-FACT<sup>27</sup>. In perfect agreement with recent biochemical studies of FACT-facilitated Pol II transcription through nucleosomes<sup>28</sup>, our structural data rationalize how FACT promotes nucleosome ‘breathing’<sup>15,26</sup> and stabilizes reorganized, partially dissociated, more accessible nucleosome forms<sup>27,29</sup>, assisting the passage of polymerases<sup>30</sup> without NCP disassembly to ensure chromatin integrity.

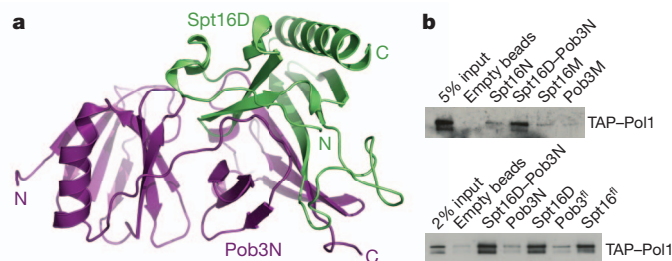


**Figure 4 | The heterodimerization domain of FACT mediates interaction with the DNA replication machinery.** **a**, Cartoon representation of the Spt16D (green) and Pob3N (magenta) PHL domains. **b**, The Spt16D domain of the FACT complex pulls down replicative Pol1 from yeast whole-cell extracts, as detected by western blot against TAP-tagged Pol1.

## METHODS SUMMARY

The *C. thermophilum* Spt16M domain (residues 651–944) was fused to histone H2B (residues 24–122) by a 12-residue linker and was co-expressed with H2A (residues 13–106). Tetragonal crystals of the native complex (space group  $P4_32_12$ ) were grown at 4 °C or 10 °C from hanging drops. High-resolution data sets were collected at beamlines PXIII (Swiss Light Source, Villigen, Switzerland) and ID23-2 (European Synchrotron Radiation Facility, Grenoble, France). ITC was performed at 20 °C in 200 mM NaCl, 25 mM Tris, pH 7.5.

**Full Methods** and any associated references are available in the online version of the paper.

**Received 14 March 2012; accepted 3 May 2013.**

**Published online 22 May 2013.**

- Orphanides, G., Wu, W. H., Lane, W. S., Hampsey, M. & Reinberg, D. The chromatin-specific transcription elongation factor FACT comprises human SPT16 and SSRP1 proteins. *Nature* **400**, 284–288 (1999).
- Belotserkovskaya, R. *et al.* FACT facilitates transcription-dependent nucleosome alteration. *Science* **301**, 1090–1093 (2003).
- Mason, P. B. & Struhl, K. The FACT complex travels with elongating RNA polymerase II and is important for the fidelity of transcriptional initiation *in vivo*. *Mol. Cell. Biol.* **23**, 8323–8333 (2003).
- Wittmeyer, J., Joss, L. & Formosa, T. Spt16 and Pob3 of *Saccharomyces cerevisiae* form an essential, abundant heterodimer that is nuclear, chromatin-associated, and copurifies with DNA polymerase alpha. *Biochemistry* **38**, 8961–8971 (1999).
- Kaplan, C. D., Laprade, L. & Winston, F. Transcription elongation factors repress transcription initiation from cryptic sites. *Science* **301**, 1096–1099 (2003).
- Lejeune, E. *et al.* The chromatin-remodeling factor FACT contributes to centromeric heterochromatin independently of RNAi. *Curr. Biol.* **17**, 1219–1224 (2007).
- Su, D. *et al.* Structural basis for recognition of H3K56-acetylated histone H3–H4 by the chaperone Rtt106. *Nature* **483**, 104–107 (2012).
- Zunder, R. M., Antczak, A. J., Berger, J. M. & Rine, J. Two surfaces on the histone chaperone Rtt106 mediate histone binding, replication, and silencing. *Proc. Natl Acad. Sci. USA* **109**, E144–E153 (2012).
- Kemble, D. J. *et al.* Structure of the Spt16 middle domain reveals functional features of the histone chaperone FACT. *J. Biol. Chem.* **288**, 10188–10194 (2013).
- Liu, Y. *et al.* Structural analysis of Rtt106p reveals a DNA binding role required for heterochromatin silencing. *J. Biol. Chem.* **285**, 4251–4262 (2010).
- Orphanides, G., LeRoy, G., Chang, C. H., Luse, D. S. & Reinberg, D. FACT, a factor that facilitates transcript elongation through nucleosomes. *Cell* **92**, 105–116 (1998).
- VanDemark, A. P. *et al.* The structure of the yFACT Pob3-M domain, its interaction with the DNA replication factor RPA, and a potential role in nucleosome deposition. *Mol. Cell* **22**, 363–374 (2006).
- Stuwe, T. *et al.* The FACT Spt16 ‘peptidase’ domain is a histone H3–H4 binding module. *Proc. Natl Acad. Sci. USA* **105**, 8884–8889 (2008).
- VanDemark, A. P. *et al.* Structural and functional analysis of the Spt16p N-terminal domain reveals overlapping roles of yFACT subunits. *J. Biol. Chem.* **283**, 5058–5068 (2008).
- Winkler, D. D., Muthurajan, U. M., Hieb, A. R. & Luger, K. Histone chaperone FACT coordinates nucleosome interaction through multiple synergistic binding events. *J. Biol. Chem.* **286**, 41883–41892 (2011).
- Pavri, R. *et al.* Histone H2B monoubiquitination functions cooperatively with FACT to regulate elongation by RNA polymerase II. *Cell* **125**, 703–717 (2006).
- Fleming, A. B., Kao, C.-F., Hillyer, C., Pikaart, M. & Osley, M. A. H2B ubiquitylation plays a role in nucleosome dynamics during transcription elongation. *Mol. Cell* **31**, 57–66 (2008).
- Koopmans, W. J. A., Buning, R., Schmidt, T. & van Noort, J. spFRET using alternating excitation and FCS reveals progressive DNA unwrapping in nucleosomes. *Biophys. J.* **97**, 195–204 (2009).
- Andrews, A. J., Chen, X., Zevin, A., Stargell, L. A. & Luger, K. The histone chaperone Nap1 promotes nucleosome assembly by eliminating nonnucleosomal histone DNA interactions. *Mol. Cell* **37**, 834–842 (2010).
- Cho, U.-S. & Harrison, S. C. Recognition of the centromere-specific histone Cse4 by the chaperone Scm3. *Proc. Natl Acad. Sci. USA* **108**, 9367–9371 (2011).
- Hu, H. *et al.* Structure of a CENP-A-histone H4 heterodimer in complex with chaperone HJURP. *Genes Dev.* **25**, 901–906 (2011).
- Hondele, M. & Ladurner, A. G. The chaperone-histone partnership: for the greater good of histone traffic and chromatin plasticity. *Curr. Opin. Struct. Biol.* **21**, 698–708 (2011).
- Zhou, Z. *et al.* NMR structure of chaperone Chz1 complexed with histones H2A.Z-H2B. *Nature Struct. Mol. Biol.* **15**, 868–869 (2008).
- Luger, K., Mäder, A. W., Richmond, R. K., Sargent, D. F. & Richmond, T. J. Crystal structure of the nucleosome core particle at 2.8 Å resolution. *Nature* **389**, 251–260 (1997).
- Killian, J. L., Li, M., Sheinin, M. Y. & Wang, M. D. Recent advances in single molecule studies of nucleosomes. *Curr. Opin. Struct. Biol.* **22**, 80–87 (2012).
- Hall, M. A. *et al.* High-resolution dynamic mapping of histone-DNA interactions in a nucleosome. *Nature Struct. Mol. Biol.* **16**, 124–129 (2009).
- Xin, H. *et al.* yFACT induces global accessibility of nucleosomal DNA without H2A–H2B displacement. *Mol. Cell* **35**, 365–376 (2009).
- Hsieh, F.-K. *et al.* Histone chaperone FACT action during transcription through chromatin by RNA polymerase II. *Proc. Natl Acad. Sci. USA* <http://dx.doi.org/10.1073/pnas.1222198110> (22 April 2013).
- Bondarenko, V. A. *et al.* Nucleosomes can form a polar barrier to transcript elongation by RNA polymerase II. *Mol. Cell* **24**, 469–479 (2006).
- Kulaeva, O. I. *et al.* Mechanism of chromatin remodeling and recovery during passage of RNA polymerase II. *Nature Struct. Mol. Biol.* **16**, 1272–1278 (2009).

**Supplementary Information** is available in the online version of the paper.

**Acknowledgements** We thank J. Basquin, E. Conti, the MPI for Biochemistry and staff at beamlines Swiss Light Source PXII and European Synchrotron Radiation Facility ID23 for crystallographic support, P. Becker, S. Hake, J. Müller and G. Schotta for H3 peptides, and F. Bonneau, P. Cramer, T. Gibson, D. Gilmour, J. Griesenbeck, C. Häring, M. Hothorn, G. Jankevicius, D. Mokranjac, R. Russell, I. Schäfer, K. Scheffzek, C. Schultz, F. Wieland, M. Winter and E. Wolf for discussion. EMBL, LMU Munich, EC FP6 Marie Curie RTN Chromatin Plasticity (to A.G.L.) and Boehringer Ingelheim Fonds (to M.Ho. and F.H.) funded this research.

**Author Contributions** Crystallography on Spt16M–H2A–H2B was conducted by M.Ho., M.Ha. and F.H.; T.S. determined the structure of free Spt16M and Spt16D–Pob3N, with assistance from M.Ho. and E.T.Z.; M.Ho. and T.S. conducted biochemical assays; A.B. conducted the chaperoning assay; M.Ho., T.S. and B.N. purified proteins; M.Ho., C.K. and T.S. conducted yeast work; M.Ho. and V.R. carried out ITC; S.A. and E.H. provided *C. thermophilum* cDNA sequences; M.Ho., T.S., M.Ha., A.B. and A.G.L. designed the study; M.Ha. and A.G.L. supervised the work; M.Ho., M.Ha., A.B. and A.G.L. wrote the manuscript.

**Author Information** Atomic coordinates and structure factors have been deposited with the Protein Data Bank under accession codes 4KHA (Spt16M–H2A–H2B), 4KHO (Spt16M) and 4KHB (Spt16D–Pob3N). Reprints and permissions information is available at [www.nature.com/reprints](http://www.nature.com/reprints). The authors declare no competing financial interests. Readers are welcome to comment on the online version of the paper. Correspondence and requests for materials should be addressed to A.G.L. ([andreas.ladurner@med.lmu.de](mailto:andreas.ladurner@med.lmu.de)).



## METHODS

**Protein expression and purification.** The *C. thermophilum* Spt16M domain (residues 651–944) was cloned into pETMCN-6xHis, carrying an N-terminal 6×His tag and tobacco etch virus (TEV) protease cleavage site (leaving an N-terminal overhang of the residues Gly-Met-Glu, in which Glu corresponds to residue 647 of Spt16M; clone CL2537). For expression of the complex, the Spt16M construct was fused to a 12-residue GGSGGGSGGS linker and the globular domain of H2B (residues 24–122). The construct (clone CL2807) was co-expressed with globular H2A lacking the hydrophobic C terminus (residues 13–106). *C. thermophilum* Pob3N (residues 1–192) was cloned into pETMCN-6xHis (ampicillin selection), carrying an N-terminal 6×His tag and TEV protease cleavage site (leaving an N-terminal overhang of the residues Gly-Met-Glu (clone CL2060) and coexpressed with an untagged version of Spt16D (residues 521–651; clone CL2558) under kanamycin selection.

Constructs were transformed and grown in *Escherichia coli* BL21-CodonPLUS(DE3)-RIL cells to an attenuation (*D*) of 0.7 nm and induced with 0.4 mM isopropyl β-D-thiogalactoside (IPTG) in rich medium at 18 °C for 16 h. Selenomethionine-labelled protein was expressed in strain B834 (DE3) and induced for 18 h with 0.5 mM IPTG in TB media with 40 μg ml<sup>-1</sup> seleno-L-methionine at 18 °C. Cells were resuspended in 50 mM Tris, pH 7.5, 500 mM NaCl, 10 mM imidazole, and EDTA-free protease inhibitor cocktail (Roche Complete), lysed by sonication, and centrifuged at 45,000g for 60 min. The supernatant was loaded onto a column packed with Ni-sepharose high performance beads (GE Healthcare), washed with lysis buffer, and eluted in the same buffer with a linear gradient of imidazole from 0 to 500 mM. Elutions were dialysed overnight in a buffer containing 25 mM Tris, pH 7.5, 400 mM NaCl and 5 mM dithiothreitol (DTT) and subsequently concentrated to 10 mg ml<sup>-1</sup> using a Vivaspinn 15R 10,000 molecular mass cut-off concentrator. The protein was then further purified on a Superdex 75 HR16/60 (for the chaperone-histone complex: SD 200 HR16/60) column (GE Healthcare). Fractions were pooled and the 6×His tag was cleaved with TEV protease for 20 h at 4 °C and dialysed into a buffer containing 25 mM Tris, pH 8.0, 150 mM NaCl and 5 mM DTT (chaperone-histone complex: 25 mM HEPES, pH 8.5, 500 mM NaCl, 2 mM DTT). The protein was bound to a MonoQ HR5/5 (heterodimerization domain: MonoS HR5/5, chaperone-histone complex: MonoS HR10/10) ion exchange column (GE Healthcare) and eluted running a linear gradient of 50 column volumes of elution buffer containing 25 mM Tris, pH 8.0, 1 M NaCl and 5 mM DTT. Fractions were pooled and dialysed against 25 mM Tris, pH 8.0, 150 mM NaCl and 5 mM DTT (complex: 25 mM HEPES, pH 8.5, 500 mM NaCl, 1 mM Tris(2-carboxyethyl)phosphine (TCEP)). Site-specific mutations were introduced by PCR and purified like wild-type Spt16M. Recombinant histones were purified and refolded, as described<sup>31</sup>.

**Crystallization and data collection.** Orthorhombic crystals belonging to space group *P*<sub>2</sub><sub>1</sub><sub>2</sub><sub>1</sub> of selenomethionine-labelled and native Spt16M (form A; Supplementary Table 1) were grown at room temperature from hanging drops composed of 1 μl of protein (3 mg ml<sup>-1</sup>) and 1 μl of crystallization buffer (6% (v/v) PEG 8000, 100 mM Na-cacodylate, pH 5.5, 200 mM Ca-acetate hydrate) suspended over 0.5 ml of the latter. Crystals were transferred in 100% parathion N and frozen in liquid nitrogen. Single-wavelength anomalous dispersion data were collected at beamline PXII (Swiss Light Source (SLS), Villigen, Switzerland). A higher-resolution native data set was acquired at beamline ID-23-1 (European Synchrotron Radiation Facility (ESRF), Grenoble, France). Data processing and scaling were done with XDS<sup>32,33</sup>. Tetragonal crystals of the native complex (space group *P*<sub>4</sub><sub>3</sub><sub>2</sub><sub>1</sub>, Supplementary Table 2) were grown at 4 °C or 10 °C from hanging drops composed of 1 μl protein (15 mg ml<sup>-1</sup>) and 1 μl crystallization buffer (7.25% (v/v) PEG 8000, 0.2 M MgCl<sub>2</sub>, 0.1 M Tris, pH 7.8) suspended over 1 ml of the latter. Crystals were frozen in glycerol, stepwise soaking up to 20% in crystallization buffer, and frozen in liquid nitrogen. High-resolution data sets were collected at beamlines PXIII (SLS, Villigen, Switzerland) and ID23-2 (ESRF, Grenoble, France). Data processing and scaling were done with XDS and Scala<sup>32,34,35</sup>. Pob3N-Spt16D crystals grew in space group *P*<sub>2</sub><sub>1</sub><sub>2</sub><sub>1</sub> (Supplementary Table 3) using the same set up as above in 2.2 M NH<sub>4</sub>SO<sub>4</sub>, 0.2 M Na-K-tartrate and 0.2 M Na<sub>3</sub>-citrate, pH 5.6. Crystals of Pob3N-Spt16D were cryoprotected in crystallization buffer supplemented with 20% ethylene-glycol. Single-wavelength anomalous dispersion data were collected at beamline PX02 (SLS, Villigen, Switzerland). A higher-resolution native data set was acquired at beamline ID-23-eh1 (ESRF, Grenoble, France). Data processing and scaling were done with XDS.

**Structure determination and refinement.** For Spt16M and Spt16D-Pob3N, single-wavelength anomalous dispersion data were used to locate six selenium sites with Phenix Auto Solve<sup>36</sup> that further carried out site refinement, phasing, density modification and phase extension. Secondary structure elements were identified and an initial model was built using Arp/Warp<sup>37,38</sup>. The structure was completed in alternating cycles of model correction in COOT and restrained refinement in Refmac5 (refs 35, 37). The model was further used to determine

the structure of the native data set by molecular replacement with PHASER<sup>33</sup>. For the structure of the complex, a PHASER molecular replacement solution was determined using the Spt16M structure determined here and the histone H2A-H2B heterodimer from the structure of the canonical nucleosome core particle<sup>39</sup>. The structure was finalized by iterative cycles of model adjustment in COOT and refinement in Refmac5 and PHENIX<sup>36</sup>. Structural visualization was done using Pymol. Electrostatic surface potentials were calculated using APBS<sup>40</sup>. Structural superpositions were calculated with 3dSS (ref. 41).

**ITC.** Binding affinities of wild-type Spt16M with H2A peptide, residues 108–130 (N-acetylated, with a C-terminal Tyr) and H2B peptides, residues 26–48 (N-acetylated, C-amidated), were determined at 25 °C by using VP-ITC and iTC200 calorimeters (GE Life Science, MicroCal). For peptide-protein interaction studies, proteins and peptides were dialysed against ITC buffer (25 mM Tris, pH 7.5, 50 mM NaCl). Injections consisted of 10 μl of peptide (600 μM) into 20 μM protein at 5-min intervals at 25 °C. For protein-protein interaction studies of Spt16M with constructs of histones H2A-H2B, proteins were dialysed against ITC buffer (25 mM Tris, pH 7.5, 200 mM NaCl). Injections on the VP-ITC instrument consisted of 10 μl of Spt16M (325 μM) into 20 μM H2A-H2B dimer at 5-min intervals at 25 °C and of 1 μl injections of 250 μM chaperone into 25 μM H2A-H2B on the iTC200. Data were analysed using Origin software (version 5.0). A single binding site model for Spt16M gave the best fit to the data, whereas Spt16MC had to be fitted with two independent binding sites. Errors are given as s.d. of the fit from the original data points.

**Histone refolding and gel filtration.** Histone refolding was performed as described<sup>31</sup>, with modifications: full-length and globular histones were mixed at equimolar ratios to a final concentration of 1 mg ml<sup>-1</sup> and refolded in 25 mM Tris, pH 7.5, 150 mM NaCl and 5 mM DTT. H2A-H2B dimers as well as (H3-H4)<sub>2</sub> tetramers were subsequently purified by gel-filtration chromatography using a Superdex75 HR16/60 column (GE Healthcare). Histones and Spt16M were mixed at equimolar ratios and incubated on ice for 30 min. Proteins were separated on a Superdex 75 or Superdex 200 10/300 GL column at 25 mM Tris, pH 7.5, 300 mM NaCl and 2 mM DTT.

**Native PAGE analysis of Spt16 chaperoning function.** Spt16<sup>fl</sup> and Spt16ΔM were expressed and purified as Spt16M. A 54-base-pair DNA fragment was synthesized as two complementary oligomers, which were then annealed. The ratio of H2A-H2B to DNA that caused close to complete precipitation was determined experimentally at a ratio of three molar equivalents of histone dimer to DNA. Histone dimer (1.2 μM) was preincubated with 0.4, 0.8, 1.6, 3.2 and 6.4 μM of Spt16<sup>fl</sup>, Spt16ΔM and Spt16M in 10 mM Tris-HCl, pH 7.4, 100 mM NaCl and 1 mM DTT. Binding of chaperone to histone was allowed to proceed at 25 °C for 15 min before the addition of DNA to a final concentration of 0.4 μM in a total reaction volume of 20 μl. In addition, controls containing chaperone at the concentration corresponding to the highest titration point with DNA alone were also carried out. Precipitation was carried out at 25 °C for 1 h before the addition of 5 μl of 20% (w/v) sucrose, removal of precipitates by centrifugation and separation of the remaining soluble complexes on a 9% polyacrylamide gel run in 0.2× TBE buffer. The gels were stained with ethidium bromide before visualization and quantification using a Fusion-FX7 Advance (PiqLab) imaging system. Statistics were calculated on a quadruplicate repeat of the experiment, with a two-tailed *t*-test assuming equal variance. Asterisks indicate *P* values of less than 0.05 when compared to the control without chaperone.

**V5 immunoprecipitations.** A total of 15 μl of anti-V5-agarose beads (Sigma) was incubated with 40 μg of *E. coli*-expressed, gel-filtration- and ion-exchange-purified V5-fused Spt16 or Pob3 construct for 30 min rotating at 4 °C in 25 mM Tris, pH 7.5, 150 mM NaCl and 0.05% Nonidet P-40 detergent. Beads were washed three times with 1 ml buffer. For interaction with histones, beads were incubated with refolded H2A-H2B in fivefold excess of histone for 1 h at 4 °C. Beads were washed five times with 25 mM Tris, pH 7.5, 200 mM NaCl and 0.05% Nonidet P-40. The samples were either directly boiled in SDS-loading buffer or eluted for 30 min with 25 μl V5 peptide (2 mg ml<sup>-1</sup>) (sequence, Ac-YGKIPINPLLGLDST) at room temperature. Samples were subsequently analysed by SDS-PAGE. For interaction with H2B or H3 peptides, beads were washed twice with 25 mM Tris, pH 7.5, 600 mM NaCl and 0.05% Nonidet P-40 and twice with 25 mM Tris, pH 7.5, 0.05% Nonidet P-40 and 75 (H2B) or 150 (H3) mM NaCl. Two microlitres of 10 mg ml<sup>-1</sup> peptide were incubated with the beads in 300 μl of the respective buffer for 2 h at 4 °C. Beads were washed four times with 1 ml buffer and bound peptides eluted twice with 10 μl 25 mM Tris, pH 7.5, 1 M NaCl and 0.05% Nonidet P-40. Samples were analysed by SDS-PAGE (NuPAGE BisTris 4–12%, run only for 75% of the length) and silver stain (Invitrogen SilverQuest kit).

**Biotin-streptavidin immunoprecipitations.** A total of 25 μl of streptavidin dynabeads (T1, Invitrogen) was saturated with 20 μl of 10 mg ml<sup>-1</sup> H3 peptides for 1 h rotating at 4 °C in 25 mM Tris, pH 7.5, 150 mM NaCl and 0.05% Nonidet P-40 detergent. Beads were washed three times with 1 ml buffer. Recombinant

Spt16M was incubated with the beads for 2 h rotating at 4 °C. Beads were washed five times with 1 ml buffer, bound protein was eluted by boiling with Laemmli SDS loading buffer and analysed by SDS–PAGE and Coomassie staining.

**Phenotypic analyses in *S. cerevisiae*.** To determine the effect of Spt16M mutations on yeast cell growth<sup>42</sup>, Spt16 was deleted from *S. cerevisiae* strain W303 by homologous recombination introducing a TRP cassette as selection marker. The associated lethal phenotype was rescued using a plasmid (YCplac33) carrying wild-type Spt16 from *S. cerevisiae* (clone CL2303) as well as the *URA3* gene that was co-transformed using the lithium acetate/PEG method. Spt16 from *C. thermophilum* (wild-type and mutants thereof; clones CL2924 (wild type), CL3046 (NVIT→A), CL3002 (NVIT→S), CL3001 (DFL→S), CL2978 (QD→A) and CL2977 (DSD→A)) with an N-terminal V5-tag was cloned into YCplac111 carrying the *LEU2* gene. The  $\Delta$ spt16 strain with the URA rescue plasmid was transformed with the mutant constructs under Leu selection and further on submitted to 5-fluoroorotic acid (FOA) selection. Thus, mutants depending on the presence of wild-type Spt16 cannot grow on FOA plates. Transformants growing on selective synthetic medium (SD – Leu) plates were grown for 5 h in YPAD medium and subsequently plated by spotting 4 µl of tenfold serial dilutions onto –Leu FOA plates and incubated at 24 °C for 4 days.

31. Dyer, P. N. *et al.* Reconstitution of nucleosome core particles from recombinant histones and DNA. *Methods Enzymol.* **375**, 23–44 (2003).

32. Kabsch, W. XDS. *Acta Crystallogr. D* **66**, 125–132 (2010).
33. McCoy, A. J. *et al.* Phaser crystallographic software. *J. Appl. Crystallogr.* **40**, 658–674 (2007).
34. Collaborative Computational Project, Number 4. The CCP4 suite: programs for protein crystallography. *Acta Crystallogr. D* **50**, 760–763 (1994).
35. Emsley, P. & Cowtan, K. Coot: model-building tools for molecular graphics. *Acta Crystallogr. D* **60**, 2126–2132 (2004).
36. Adams, P. D. *et al.* PHENIX: a comprehensive Python-based system for macromolecular structure solution. *Acta Crystallogr. D* **66**, 213–221 (2010).
37. Murshudov, G. N., Vagin, A. A. & Dodson, E. J. Refinement of macromolecular structures by the maximum-likelihood method. *Acta Crystallogr. D* **53**, 240–255 (1997).
38. Langer, G., Cohen, S. X., Lamzin, V. S. & Perrakis, A. Automated macromolecular model building for X-ray crystallography using ARP/wARP version 7. *Nature Protocols* **3**, 1171–1179 (2008).
39. Luger, K., Rechsteiner, T. J., Flaus, A. J., Waye, M. M. & Richmond, T. J. Characterization of nucleosome core particles containing histone proteins made in bacteria. *J. Mol. Biol.* **272**, 301–311 (1997).
40. Baker, N. A., Sept, D., Joseph, S., Holst, M. J. & McCammon, J. A. Electrostatics of nanosystems: application to microtubules and the ribosome. *Proc. Natl Acad. Sci. USA* **98**, 10037–10041 (2001).
41. Sumathi, K., Ananthalakshmi, P., Roshan, M. N. A. M. & Sekar, K. 3dSS: 3D structural superposition. *Nucleic Acids Res.* **34**, W128–W132 (2006).
42. Capozzo, C. *et al.* Gene disruption and basic phenotypic analysis of nine novel yeast genes from chromosome XIV. *Yeast* **16**, 1089–1097 (2000).

# CAREERS

**COLLABORATION** US–UK initiative will fund projects in emerging nations **p.117**

**RESEARCH IMPACT** Size doesn't matter when it comes to the impact of grants **p.117**

**NATUREJOBS** For the latest career listings and advice [www.naturejobs.com](http://www.naturejobs.com)



COLLABORATION

## A problem shared

*Graduate students often work alone, but programmes exist to teach them how to work towards publication in teams.*

BY CAMERON WALKER

At 4 p.m. one spring Tuesday, nine graduate students at Oregon State University (OSU) in Corvallis kick their research into gear. For more than an hour, they discuss their work on fisheries along the US west coast, moving from how data on marine biodiversity hotspots change over time to how to organize tables for a paper.

These students, who have been meeting frequently for nearly two years, are part of the Dimensions of Biodiversity Distributed

Graduate Seminar (DBDGS), a programme that ultimately included teams at 14 institutions — nine in the United States, two in Kenya and one each in Chile, Brazil and China. Each institution's group runs at least one research project, in which students, usually working outside their main field, make intensive examinations of large, mostly pre-existing biodiversity data sets. They formulate research questions, analyse data and publish the results — sometimes in multiple papers, and usually with every student in the group as a co-author. They use the DBDGS network to talk about

their work with students at other institutions, share strategies and form collaborations.

Whereas most established faculty members spend ample time collaborating with colleagues, graduate students are often required to toil alone, notes Julia Parrish, a biologist at the University of Washington in Seattle and principal investigator on the three-year, US\$1.5-million US National Science Foundation (NSF) grant that funded the DBDGS. But that means “training people to be last century’s scientists”, she says. By contrast, collaborative seminars teach students how to work together in a way that is reflective of the contemporary research world.

The distributed-seminar model originated at the US National Center for Ecological Analysis and Synthesis (NCEAS), a research centre of the University of California, Santa Barbara (UCSB), where, in 1997, graduate students from eight institutions first came together to analyse the science of different habitat-conservation plans and create a report. The DBDGS, which launched in 2011 with a pilot project at the University of Washington and is funded until the end of this year, is based on that template. Teams at each institution sent student and faculty representatives to five in-person meetings in Washington state throughout the programme — the largest, in February 2012, brought together close to 60 participants from 14 institutions. Team members learned about each other’s work, shared the data that they would use, discussed how they would approach their projects and made connections for future collaborations. Student teams are now working on almost 30 papers; two have been published.

Each team functions as an independent unit, with between 5 and 15 students working together and one or more faculty members offering guidance. Most of the students have an interest in biodiversity, but do not necessarily possess any training in the field that the project covers. At OSU, for example, students with backgrounds ranging from stream ecology to geosciences worked on fisheries data.

### LONELY PURSUIT

The road to publication can be arduous, and programmes that bring graduate students together may help them to avoid pitfalls and stay competitive. The seminars teach PhD students how to find out what gaps exist in their fields, what methods they could use to analyse their own data, what data sets are already available to work with, how to structure their writing and which journals would be receptive ►



► to a particular kind of paper.

Graduate students on the DBDGS team at the Virginia Institute of Marine Science (VIMS) in Gloucester Point, part of the College of William and Mary, read research on fish diversity before diving into records of trawling in nearby Chesapeake Bay and measuring specimens in the collection of the Smithsonian Institution National Museum of Natural History in Washington DC. That showed them what ground had already been covered on the subject, says Jonathan Lefcheck, a graduate student in marine community ecology who led the team, and demonstrated “where the gaps were, so we set ourselves up to have a marketable product”. The researchers also learned analysis methods and found appropriate citations in the literature, which they intend to use in a paper.

By looking at how previous studies were conducted, students could begin to consider how to analyse their own data sets. In some cases, DBDGS students already had experience with evaluating data, and could split up the workload according to their strengths: one student sequencing fish genes, another doing statistics.

The combined effort made it possible to tackle data sets that would overwhelm a single student, or even an individual lab. In the course of a year, the team at UCSB compiled global fisheries data from eight or nine sources — a project that few, if any, of the students would have pursued for their own dissertations, says Laura Dee, a graduate student in conservation and marine ecology at UCSB who led one of the teams.

Lefcheck taught himself new methods, from multivariate statistics to building evolutionary trees, which he would not have attempted without the backing of the group. “If it became too much of a burden, I could ask others to pitch in,” he says. Going beyond his own dissertation work, Lefcheck read primary literature and contacted authors as well as students and faculty members in the wider DBDGS network. He is now applying many of these methods to his dissertation work.

For many students, the writing process itself is daunting. Some DBDGS students went on programme-sponsored writing retreats to help them tackle the process. At one, students and faculty members on the University of Washington team collaborated on a draft of a paper abstract and introduction — one person wrote for two minutes, then passed the piece of paper to the next person. “It helped us relax

a little bit, and just get into the writing mode,” says Ailene Ettinger, a biology graduate student who co-led the team.

The OSU team broke into two groups, each working on a paper using the same data. One used a traditional approach, dividing the paper into sections for one or two students to tackle, with the team leader pulling them together. Students in the other group went to their retreat with sections that they had already written separately. They assembled the paper as a group, using a projector to put it up on the wall and edit it line by line. “Having everyone in one place may have actually sped things up a bit,” says Selina Heppell, a marine fisheries ecologist at OSU and the team’s faculty adviser. Institutions may also offer one-off presentations from editors of scientific journals, who can provide insight into the publishing process.

### WORKING TOGETHER

Throughout the DBDGS programme, students constantly practised how to interact with other researchers — whether explaining their work or negotiating how to distribute tasks — while keeping everyone on track to publication.

Determining who gets credit for what when it comes to authorship is often difficult (see *Nature* **489**, 591–593; 2012). During the DBDGS, for example, each group had to come to a consensus about what to do if people dropped out. The OSU team decided that anyone who stuck with and contributed to the project for the entire first year would be an author. Even though the students split into two groups, Heppell says, all have contributed something substantial to the work as a whole — and each of the 14 students will be on the seminar’s two papers.

The University of Washington group decided to wait until it was most of the way through the data analysis before it chose a lead author. In the end, two students were designated joint leads, and flipped a coin to see whose name would be listed first. “Really open conversations and transparency from the beginning are the way to go, so that everyone knows what the expectations are,” says Ettinger.

Cross-disciplinary collaborations have emerged between institutional teams. Parrish recalls that when students from UCSB and OSU first met, they were unsure of each other. The Oregon team was looking at what species came up in individual trawls in a single stretch of the Pacific Ocean; the Santa Barbara students were poring over global fisheries data from a conservation angle. As they discussed their projects, however, they realized that combining the scales could yield interesting results. Now students from the teams are at work on an independent project — a collaboration that Kate Boersma, a graduate student in stream ecology at OSU, calls the most rewarding aspect of the programme. It has influenced her dissertation research, and she hopes that its effects will continue after she graduates.

Parrish says that some of the international



**“Really open conversations and transparency from the beginning are the way to go.”**

Ailene Ettinger

ROBERT ETTINGER



A seminar team at Oregon State University works through the trials of collaboration.

groups have struggled because of funding, travel or infrastructure difficulties at home. However, the team at the Federal University of Rio Grande do Sul in Porto Alegre, Brazil, has thrived: taking advantage of their strong backgrounds in statistics and mathematics, its students have published a paper.

Graduate student Vanessa Weinberger, a team leader at the Pontifical Catholic University of Chile in Santiago, says that she has benefited from working with a large team of people who do not share her background in theoretical ecology, and from the opportunity to present research in English. In Chile, she says, it is relatively unusual for graduate students from different laboratories — let alone different universities — to collaborate on a project outside their theses.

### BRANCHING OUT

The DBDGS is set to end this year, but George Gilchrist, an NSF programme director, says that its good results have prompted the foundation to consider repeating the exercise. The NCEAS would also be open to hosting further distributed seminars, says deputy director Stephanie Hampton. The centre is currently hosting its first three-week institute for early-career researchers, which had more than 400 applicants from around the world. The 22 successful participants, including several graduate students, are learning skills for collaborative, data-intensive ecological research. The programme runs from 19 June to 10 July, and the NCEAS plans to offer it each year.

With a colleague, Helene Wagner, a landscape ecologist at the University of Toronto Mississauga in Canada, has led two landscape-genetics courses based on the distributed-seminar model. Students could opt to participate in group projects using existing data sets and simulation studies. The first, conducted in person and online in 2010, resulted in five papers. Unlike the mostly single-institution DBDGS groups, each team was made up of a mix of students from the 15 participating universities in North

America and Europe, including the Swiss Federal Institute of Technology in Zurich and Joseph Fourier University in Grenoble, France. The second course took place entirely online, mitigating student travel expenses; even students who were not at a participating institution could sign up. A similar course is planned for 2014.

In the United Kingdom, Vitae, a Cambridge-based organization that focuses on researchers' professional development, has offered publishing workshops with Macmillan Science Communication in London (which has the same parent company as *Nature*). It also runs a course called The Collaborative Researcher, which brings together 40 researchers at a time to learn skills including communication, cultural awareness, planning and negotiation.

### SIDE PROJECTS

Seminars such as these take up precious time, which is often in short supply for graduate students. Dee extols the skills and collaborations that she has gained from the DBDGS — but says that the process took longer than anyone expected. She estimates that it delayed her thesis by four months. But her CV, she hopes, will boast papers from both the seminar and her cross-seminar collaborations — and some of the work that she is doing with OSU students will be part of her dissertation.

Heppell told students in her team — particularly those who signed up to tackle big workloads, such as data analysis — that they needed to have a serious talk with their advisers about how much time it would take. She has not heard any complaints; in fact, advisers have commented that if students get publications, the DBDGS is a good use of their time. “I think advisers realize that the stakes are higher now,” she says, referring to research funding challenges. “The jobs are fewer.” ■

**Cameron Walker** is a freelance writer based in Santa Barbara, California.

## COLLABORATION

### US and UK join forces

The United States and Britain are launching a global research collaboration to address issues such as water supply and climate change in emerging nations. The 5-year programme will fund up to a total of 40 US and UK grants per year, says Richard Everitt, deputy director of the British Council USA in Washington DC. He did not disclose amounts but said that awards could last for up to three years. Funding will come from the British Council, the UK Department for Business, Innovation and Skills and the US Department of State. “We want to create a cadre of young researchers who can work with their counterparts from the emerging world,” says Everitt. The initiative will form partnerships with universities in nations such as China, Brazil, India and Indonesia, and will seek grant proposals in September.

## RESEARCH IMPACT

### Bang not based on buck

Grant size does not strongly predict scientific impact, according to a study published in *PLOS ONE*. The authors used four measures — publications, citations, highly cited papers and citations of the most-highly cited paper — to score the impact of 374 researchers funded between 2002 and 2006 by the Natural Sciences and Engineering Research Council of Canada. Grant sizes explained less than 30% of the variation (J.-M. Fortin and D. J. Currie *PLOS ONE* 8, e65263; 2013). Co-author David Currie, a biologist at the University of Ottawa, says, “Some very poorly funded people manage to do a great deal.”

## UNITED KINGDOM

### Funding freeze critiqued

A UK science-advocacy group says that a repeated freeze to the government's £4.6-billion (US\$7-billion) science-research budget, announced on 26 June, will damage early-career researchers' work and drive them to other nations. Science is Vital, formed to track the results of a 2010 budget freeze, polled 868 UK researchers, and found that 70% of junior scientists have lost confidence in research careers in Britain. Some 59% of respondents applying for grants said their success rate had fallen; 39% of those with labs have recruited fewer PhD students and 19% could not recruit any. “Frustrated young researchers are leaving,” says Jennifer Rohn, chair of Science is Vital and a cell biologist at University College London.



# THE OSTRACONS OF EUROPA

*A measure of life.*

BY KEN HINCKLEY

There was something transcendent about the pattern etched into the ice-bound European surface looming 53 kilometres above Ricardo Cuerta's submersible. The implacable gravity of Jupiter rewrote the great frozen palimpsest again and again, the pack ice heaved and rilled with fissures that hinted at the mysteries of the deep.

That's how he'd seen it from orbit. Now the intense blue-white glare of the spotlights seemed to be all that prevented the eternal midnight of the subsurface ocean from imploding his mind.

Particulates clouded the super-cooled brine. Flurries of malformed magnesium sulphate flakes tumbled through the cones of light cast by the submersible and vanished again into the darkness. Ricardo floated, with nothing but the spotlights of the submersible and the sheer thrall of wonder between himself and the abyss. Even now, submerged within the shattered moon, he still couldn't fathom what that pattern meant.

The black chimneys of a cryovolcano rose out of the gloom like a city of diseased skyscrapers. Ricardo torqued the joystick between his thumb and forefinger, applying just enough pressure to manoeuvre the perspex tube at the end of the armature a little closer. He needed a sample, had to bring back proof — if not for the cold gaze of Science, then at least to convince himself that he wasn't confabulating wonders in the dark.

Cold sweat drenched the polypro fabric clinging to his chest. The tang of constant anxiety oiled the fatigue lines etched into his face. The slightest mistake, the tiniest unintended twitch of a muscle, and he could easily break a chimney and bring the entire tottering structure down on the submersible. If he were lucky it would breach the observation bell and he would be dead a few tenths of a second later. If he were not so fortunate, it would cripple the craft, leaving him drifting and helpless in the dark. Communication with the rest of the crew awaiting his return at the surface was impossible. There would be no final cry for help; he would never be found.

Ricardo licked the salt from his lips. It wasn't so different, really, from the brine in which

the submersible was drifting at this very moment. He could have been floating in himself. It had been ten years since Rosa had died. His wife, his bride, so young. Why did he have to travel so far from home to exile himself from his own darkness?

And yet here he was, floating in the abyss.



The spotlights fell upon a brilliant white chevron in the silt-shrouded murk. At first he thought it was enormous — there was no sense of scale, nothing familiar and human by which to judge the size of objects. It winked out, then appeared again, and Ricardo realized it was close at hand, something partially occluded by the soot-black columns of the cryovolcano.

Something that moved.

He let the submersible drift. Whatever it was, he didn't want to startle it.

Slowly it came into view.

An alabaster-white carapace. Crimson-tipped thorns cresting sharp-jointed legs. A hooked beak framed by feathery fronds that sculled and groped at the deep.

It was a monstrosity pried from the oil-cake layers of the Burgess shale and jolted to life. The gangly and utterly alien way it moved was infused with a crawling strangeness that sent chills prickling up Ricardo's spine, across his shoulders and into the base of his brain. The words *crab* and *spider* and *giant squid* flashed through his mind, but of course it was none of these. He settled on *xeno-arachnid*, because, a man of science, he could not bring himself to call it what it was: *monster*.

Its fronds quivered and reached out. Probing. Curious. Angling his way. Suddenly Ricardo's mind flashed with comprehension: the creature had nothing that he recognized as eyes — but it, too, was dumbfounded with wonder.

Its gaping beak seemed to gnaw at the darkness. It lifted two thorned legs, not threatening, slowly extending them towards the spotlights on the front of the submersible. Ricardo was about to pull back when the xeno-arachnid halted. Its fronds undulated in the shadows cast by its limbs. The beak

repeated its gnawing motion, then again a third time. Slowly. More deliberately. Ricardo gasped and his eyes went wide.

It was trying to tell him something. But what?

Ricardo thought he glimpsed a shimmer, an iridescence just at the limits of his perception. He fingered the toggles for the spotlights and the interior lights, flicked them off one by one, and plunged himself into abject darkness.

But as his eyes adjusted, he realized the darkness was not absolute, the darkness was not eternal.

Not at all. He had only just begun to see the light.

The xeno-arachnid's legs glowed with a ghostly bioluminescence. Its carapace grew brighter and slowly turned to face him. The legs — four of them working in unison — scabbled across the surface, wove in sombre blues and muted whites a tapestry of overlapping calligraphies that became more and more complex with each pass of its limbs.

The pattern lightning-bolted in Ricardo's mind to something he recognized, to patterns larger still. The massive pack-ice shards of Europa's frozen crust. The jumbled cuneiform of pressure ridges and rifts stamped into the icy potsherds fracturing the surface.

The rafting of the European surface was not random at all.

The creature was writing its story, a small fragment of the same immense narrative that was etched into the Rosetta-stone shards that circumscribed the European globe.

Ricardo held no proof, but he knew. The xeno-arachnid was telling him. *He knew*. The light in the darkness was written on its carapace. The creature was like him, a kindred spirit, an exile, and their names were scrawled upon the ostracons of Europa. ■

**Ken Hinckley** is a writer, as well as a principal scientist at Microsoft Research, where he studies human-computer interaction, including sensors, pen computing and multi-modal input. His website is [kenhinckley.wordpress.com](http://kenhinckley.wordpress.com).

JACEY

➔ NATURE.COM

Follow Futures:

🐦 @NatureFutures

🌐 [go.nature.com/mtoodm](http://go.nature.com/mtoodm)